

AD-A239 823



DTIC FILE COPY AGARD-CP-485

①

AGARD-CP-485

Best Available Copy

AGARD CONFERENCE PROCEEDINGS No.405

**Ionospheric Modification and its  
Potential to Enhance or Degrade the  
Performance of Military Systems**

(La Modification de l'Ionosphère et son Potentiel  
d'Amélioration ou de Dégradation des  
Performances des Systèmes Militaires)

S FEB 04 1991 D

DISTRIBUTION AND AVAILABILITY  
ON BACK COVER

DISTRIBUTION STATEMENT 4

Approved for public release  
Distribution Unlimited

91 2 04 017

## **DISCLAIMER NOTICE**

**THIS DOCUMENT IS BEST QUALITY PRACTICABLE. THE COPY FURNISHED TO DTIC CONTAINED A SIGNIFICANT NUMBER OF PAGES WHICH DO NOT REPRODUCE LEGIBLY.**

AGARD-CP-485

NORTH ATLANTIC TREATY ORGANIZATION  
ADVISORY GROUP FOR AEROSPACE RESEARCH AND DEVELOPMENT  
(ORGANISATION DU TRAITE DE L'ATLANTIQUE NORD)

AGARD Conference Proceedings No.485

**Ionospheric Modification and its Potential  
to Enhance or Degrade the Performance  
of Military Systems**

(La Modification de l'Ionosphère et son Potentiel  
d'Amélioration ou de Dégradation des Performances  
des Systèmes Militaires)

Papers presented at the Electromagnetic Wave Propagation Panel Symposium, held in  
Bergen, Norway, 28th—31st May 1990.

## The Mission of AGARD

According to its Charter, the mission of AGARD is to bring together the leading personalities of the NATO nations in the fields of science and technology relating to aerospace for the following purposes:

- Recommending effective ways for the member nations to use their research and development capabilities for the common benefit of the NATO community;
- Providing scientific and technical advice and assistance to the Military Committee in the field of aerospace research and development (with particular regard to its military application);
- Continuously stimulating advances in the aerospace sciences relevant to strengthening the common defence posture;
- Improving the co-operation among member nations in aerospace research and development;
- Exchange of scientific and technical information;
- Providing assistance to member nations for the purpose of increasing their scientific and technical potential;
- Rendering scientific and technical assistance, as requested, to other NATO bodies and to member nations in connection with research and development problems in the aerospace field.

The highest authority within AGARD is the National Delegates Board consisting of officially appointed senior representatives from each member nation. The mission of AGARD is carried out through the Panels which are composed of experts appointed by the National Delegates, the Consultant and Exchange Programme and the Aerospace Applications Studies Programme. The results of AGARD work are reported to the member nations and the NATO Authorities through the AGARD series of publications of which this is one.

Participation in AGARD activities is by invitation only and is normally limited to citizens of the NATO nations.

The content of this publication has been reproduced directly from material supplied by AGARD or the authors.

Published October 1990

Copyright © AGARD 1990  
All Rights Reserved

ISBN 92-835-0590-5



Printed by Specialised Printing Services Limited  
40 Chigwell Lane, Loughborough, Leicestershire LE10 3TZ



## Theme

The propagation medium is, in effect, an integral part of many military systems. For the most part, interest in the propagation medium has been focussed on identifying and quantifying the limitations it imposes on systems, rather than on ways it might be altered, or controlled. The results of on-going theoretical and experimental research show potential for modifying selected regions of the ionosphere in order to affect radio wave propagation. A variety of modification techniques are being investigated, both ground- and space-based, to increase or decrease existing ionization or to create independent artificial plasmas. These techniques include high power radio waves, lasers, particle beams, and chemical releases. In addition, recent developments in high power RF sources raise concerns over system limitations due to self induced anomalous absorption, ray path deviation and clutter. This Symposium will present the current state of ionospheric modification technology, with emphasis on potential applications for enhancing or degrading the performance of military communications, surveillance and navigation systems.

Some topics to be covered would include:

1. General aspects of Ionospheric Modification
2. Ground-Based RF Heating including:  
HF Heating (Vertical and Oblique)  
High Power Microwave Heating
3. Chemical Modification
4. Space Based Modification
5. Wave-Particle Interaction
6. Potential Applications



Accession For	
NTIS GRA&I	<input checked="" type="checkbox"/>
DTIC TAB	<input type="checkbox"/>
Unannounced	<input type="checkbox"/>
Justification	
By	
Distribution/	
Availability Codes	
Dist	Avail and/or Special
A-1	

## Thème

Le milieu de propagation est, par ses effets, une caractéristique de beaucoup de systèmes militaires. La plupart des efforts consacrés à la recherche dans ce domaine ont porté sur l'identification et la quantification des limitations qu'il impose aux systèmes, plutôt que sur des solutions qui permettraient de le modifier ou de la contrôler. Les résultats des travaux de recherche théoriques et expérimentaux en cours laissent prévoir un certain potentiel en ce qui concerne la modification de certaines régions de l'ionosphère présélectionnées, afin d'exercer une influence sur la propagation des ondes radio-électriques.

Toute une gamme de techniques est à l'étude. Elle fait appel à des équipements basés au sol ou dans l'espace, dont le but est d'augmenter ou de réduire l'ionisation existante, ainsi que de créer des plasmas artificiels indépendants.

Ces techniques comprennent les ondes radio-électriques de grande puissance, les lasers, les faisceaux de particules et l'émission de gaz; en outre, les progrès réalisés dans le domaine des sources HF de grande puissance soulèvent un certain nombre de questions concernant les limitations imposées au systèmes par l'absorption auto-induite anormale, la déviation du parcours de l'onde et le clutter.

Ce symposium présente l'état actuel des connaissances dans le domaine de la technologie de la modification de la ionosphère. L'accent est mis sur les applications possibles en vue de l'amélioration ou la dégradation des performances des systèmes militaires de télécommunications, de surveillance et de navigation.

Parmi les sujets examinés, on distingue:

1. Aspects généraux de la modification de l'ionosphère
2. L'échauffement HF effectué à partir du sol, soit:  
L'échauffement HF (vertical et oblique)  
L'échauffement hertzien de puissance élevée
3. La modification de l'ionosphère par émission de gaz
4. La modification de l'ionosphère au moyen de matériel transporté par satellite
5. Les interactions onde-particule
6. Les applications potentielles

# Electromagnetic Wave Propagation Panel

**Chairman:** Ir H. Vissinga  
van Kempenstraat 30  
2252 Voorschoten  
Netherlands

**Deputy Chairman:** Dr J.H. Richter  
Head, Ocean and Atmospheric  
Sciences Division  
Naval Ocean Systems Center  
Code 54  
San Diego, CA 92152-5000  
United States

## TECHNICAL PROGRAMME COMMITTEE CHAIRMEN

Mr John E. Rasmussen  
Chief, Ionospheric Interactions Br.  
Ionospheric Physics Division  
Air Force Geophysics Laboratory  
Hanscom AFB, MA 01731  
United States

Prof. Tudor B. Jones  
Department of Physics  
University of Leicester  
University Road  
Leicester LE1 7RH  
United Kingdom

Dr Paul A. Kossey  
Ionospheric Interactions Branch  
Ionospheric Physics Division  
Air Force Geophysics Laboratory  
Hanscom AFB, MA 01731  
United States

## MEMBERS

Dr H.J. Albrecht  
FGAN  
Neuenahrerstrasse 20  
D-5307 Wachtberg-Werthhoven  
Germany

Dr John S. Belrose  
PO Box 11490  
Communications Research Ctr  
Station H  
Ottawa, ON K2H 8S2  
Canada

Dr Peter M. Banks  
Star Laboratory  
Stanford University  
Stanford CA 99305  
United States

Dr Asgeir Brekke  
IMR, University of Tromsø  
P.O. Box 953  
N-9001 Tromsø  
Norway

Dr Pierre Bauer  
CNRS  
BP3  
91371 Verrières Le Buisson Cedex  
France

Mr Owen R. Cote  
EOARD  
223/231 Old Marylebone Road  
London NW1 5TH  
United Kingdom

## PANEL EXECUTIVE

Lt Colonel P.A. Brunelli

**Mail from Europe:**  
AGARD—OTAN  
Attn: EPP Executive  
7, rue Ancelle  
92200 Neuilly sur Seine  
France

**Mail from US and Canada:**  
AGARD—NATO  
Attn: EPP Executive  
APO New York 09777

Tel: 33(1) 47 38 57 68  
Telex: 610176 (France)  
Telefax: 33(1) 47 38 57 99

# Contents

Theme/Thème	Page
Electromagnetic Wave Propagation Panel	iii
	iv
	Reference
SESSION I – GROUND BASED RF HEATING OVERVIEW	
Chairman: Dr W.Gordon	
The Physics of Ground Based Heating	
– The Physics of Ground Based Heating by T.B.Jones	1A
– High Power HF Modification: Geophysics by H.C.Carlson, Jr	1B
Review of Soviet Ionospheric Modification Research by L.M.Duncan and R.L.Shoven	2
SESSION II – VERTICAL HF HEATING	
Chairman: Dr A.Brekke	
Historical Overview of HF Ionospheric Modification Research by W.E.Gordon and L.M.Duncan	3
Paper 4 withdrawn	
Ionospheric Modification Research at HIPAS by R.G.Brandt	5
VLF, ELF and ULF Wave Research Using the Tromsø Heating Facility by M.T.Rietveld et al	6
Observations of the Anomalous Absorption of Diagnostic Radio Waves during Ionospheric Modification at Arecibo by A.J.Stoker, T.R.Robinson and T.B.Jones	7
Theory of a Thermal Resonance Instability in the E-Region of the Ionosphere by P.Heeg	8
On the Validity of the Weak Turbulence Approximation by A.Hanssen and E.Mjølhus	9
Theory of Large-Scale HF Heating Processes in the Unstructured and Structured Ionosphere by M.J.Keskinen, P.K.Chaturvedi and S.L.Ossakow	10
Heater Induced Plasma Lines	
– Duct Model for the Duty-Cycle Variation on the Plasma-Line Overshoot during Cyclic Heating at Arecibo by D.B.Muldrew	11A
– A Theoretical Model for the Temporal Evolution of HF-Enhanced Plasma Lines by S.P.Kuo, A.Y.Ho, M.C.Lee and F.T.Djuth	11B
Enhanced Fading Rates Produced during Ionospheric Modification by T.B.Jones and A.Wilkinson	12

	Reference
<b>Large Scale Plasma Irregularities and Airglow Enhancements from Ionospheric Heating</b> by P.A.Bernhardt, H.Rowland, L.M.Duncan and C.A.Tepley	13

### SESSION III – GROUND BASED OBLIQUE RF HEATING

Chairman: Prof. T.B.Jones

<b>Oblique HF Heating</b>	
– Ionospheric Heating with Oblique HF Waves by E.C.Field, Jr and R.M.Bloom	14A
– Modeling of HF Propagation and Heating in the Ionosphere by T.M.Smith, M.M.Shoucri and T.M.Wagner	14B
– Modeling and Design for a New Ionospheric Modification Experiment by G.S.Sales, I.G.Platt, D.M.Haines, Y.Huang and J.L.Heckscher	14C
<b>Paper 15 withdrawn</b>	
<b>Oblique Heating of the Auroral Ionosphere by LF/MF Transmitters</b> by P.S.Cannon, M.J.Rycroft and T.Turunen	16

### SESSION IV – GROUND BASED HIGH POWER MICROWAVE HEATING

Chairman: Dr L.Duncan

<b>Artificial Ionospheric Mirror (AIM)</b>	
– Concept and Issues by P.A.Kossey, J.L.Heckscher, R.A.Shanny and E.C.Field, Jr	17A
– Physics of RF Breakdown for AIM Applications by K.Papadopoulos et al	17B
<b>Laboratory Chamber Measurements of Artificial Plasmas</b>	
– Crossed-Microwave-Beam Air Ionization Laboratory Experiments by W.T.Armstrong et al	18A
– On the Feasibility of Microwave Produced Bragg Reflector: Examined by the Chamber Experiment by S.P.Kuo, Y.S.Zhang, P.A.Kossey and R.J.Barker	18B

### SESSION V – SPACE BASED MODIFICATION

Chairman: Dr P.Banks

<b>Overview of Ionospheric Modification from Space Platforms</b> by P.M.Banks	19*
<b>Plasma Density Modification by Means of Pulsed Beam CIV in the Ionosphere</b> by S.T.Lai, W.J.McNeil and E.Murad	20
<b>Plasma Density Enhancements Created by the Ionization of the Earth's Upper Atmosphere by Artificial Electron Beams</b> by T.Neubert and P.M.Banks	21
<b>Ionospheric Modification Using Relativistic Electron Beams</b> by P.M.Banks, A.C.Fraser-Smith and B.E.Gilchrist	22
<b>Electron Gyro-Harmonics Generated by Spaceborne Artificial Electron Beam</b> by D.Mourenas and C.Béghin	23

\* Abstract only.

	Reference
Vehicle Charging in Low Density Plasmas by B.N.Machum and J.Troim	24
Planning for Coordinated Space and Ground-Based Ionospheric Modification Experiments by M.C.Lee et al	25
<b>SESSION VI – WAVE PARTICLE INTERACTIONS</b>	
Wave-Particle Interactions Associated with VLF Transmitters by F.Lefevre	26
Causes and Effects of Interactions between Energetic Electrons and Whistler-Mode Waves in the Coupled Magnetosphere-Ionosphere-Atmosphere System by M.J.Rycroft	27
Ionospheric Heating for Radiation Belt Control by W.J.Burke and E.Villalon	28
Modification of the Lower Ionosphere in Lightning-Induced Electron Precipitation Events and through VLF Heating by U.S.Inan	29
<b>SESSION VII – SPECIAL MODIFICATION TOPICS</b> Chairman: Dr J.S.Belrose	
Ionospheric Chemical Releases by P.A.Bernhardt and W.A.Scales	30
Observations de Perturbations Produites par des Explosions Chimiques Puissantes dans l'Ionosphere par E.Blanc et A.R.Jacobson	31
Laboratory Simulation of High-Altitude Disruptive Effects by B.H.Ripin et al	32
Modification of Tropospheric Propagation Conditions by H.Jeske	33
<b>SESSION VIII – APPLICATIONS</b> Chairman: Dr P.Kossey	
Ionospheric Modification and Imaginable System Applications by H.J.Alfrecht	34
Paper 35 withdrawn	
Artificial Ionospheric Mirrors for Radar Applications by R.D.Short, T.Wallace, C.V.Stewart, P.Lallment and P.Koert	36
Electrojet Modulation	
– Electrojet Modulation ELF Communications by K.Papadopoulos, R.A.Shanny, L.Susman, M.Machina and P.Stamboulis	37A
– Investigation of the Polar Electrojet Current System Using Radio Wave Heating from a Ground-Based Facility by D.H.Werner, A.J.Ferraro and R.G.Brandt	37B
The Generation of ULF Waves in the Ionosphere by S.T.Noble and W.E.Gordon	38

**Paper 39 withdrawn**

**HF Propagation through Actively Modified Ionospheres Modelling and Experimental Results**  
by P.E.Argo, T.J.Fitzgerald, J.H.Wolcott and D.J.Simons

**List of Participants**

**Round Table Discussion**

**Reference**

**40**

**P**

**RTD**

## THE PHYSICS OF GROUND BASED HEATING

by

Professor T B Jones  
Department of Physics & Astronomy  
University of Leicester  
University Road  
Leicester LE1 7RH

### Introduction

The first indication that powerful radiowaves could modify the earth's ionosphere was the discovery of the Luxembourg Effect in 1933, (Tellegen, 1933). The transfer of the modulation of the high power Luxembourg broadcasts on to weaker signals propagating through the same region of the ionosphere could only be explained in terms of ionospheric "cross modulation" (Bailey & Martyn, 1934).

The ionospheric electron temperature and hence its electron density, were changed by the high power wave and these subsequently influenced other radio signals propagated through the 'modified' region. In the early 1970s, it was realized that high power radio waves could produce a many instabilities in the ionosphere in addition to the collision phenomena associated with the Luxembourg effect. These instabilities have a wide range of spatial and temporal scales and a number of heating facilities were specially built both in the West and in the Soviet Union, to study their characteristics. Special issues of a number of journals have been exclusively devoted to heating results, eg. J.Geophys.Res. 1970, Radio Science 1974, J.Atmos.Terr.Phys. 1982 and 1985.

### High Power Modification Facilities.

The strongest interaction between a radio wave and the ionospheric plasma occurs when the wave frequency is approximately equal to the local plasma frequency. Thus, heating facilities operate in the range 3 to 12 MHz to correspond with E- and F-region plasma densities. A typical 'heater' is capable of delivering about 2 MW of power into an antenna which forms a beam directed vertically into the ionosphere. Provision is made for radiating either ordinary (O), extraordinary (X) or linear polarization. The antenna gain is usually of the order of about 26 db, thus an effective radiated power (ERP) of about 200 MW can be produced. The power density  $F$  ( $\mu\text{Wm}^{-2}$ ) in the beam at a range  $R$  (km) is related to the ERP (MW) by

$$F = 82.6 \times \frac{\text{ERP}}{R^2}$$

and the electric field  $E$  ( $\text{Vm}^{-1}$ )

$$E = \frac{0.25 \sqrt{\text{ERP}}}{R}$$

Thus, an erp of 200 MW yields power fluxes of  $150 \mu\text{Wm}^{-2}$  and  $65 \mu\text{Wm}^{-2}$  at E (110km) and F (250km) layer heights respectively.

The interaction of the high power wave with the ionosphere involves a number of complicated processes which can be subdivided into four general classes as indicated in Figure 1. The time scales for these processes differ appreciably, ranging from a few milliseconds to tens of seconds as illustrated schematically in Figure 2. These various interaction processes are now considered in detail.

### Collisional Interactions (D-region).

The collisional absorption of heater wave energy in the lower ionosphere (D-region) produces a rapid increase in electron temperature which causes an increase in electron collision frequency and, hence, in the absorption coefficient, (JATP Special Issue, 1982). These changes will influence the propagation of other radio waves passing through the heated region particularly at frequencies in the HF band and below. The time constants of these heating processes are very short ( $\sim 0.5$  msec) and, thus, amplitude modulation of the heater signal can be transferred to other (low power) radio waves passing through the disturbed region as in the classical Luxembourg effect already referred to.

The electron temperature modulations produced in the D and E regions by amplitude modulating the heating wave, also produce electron density modulations via the electron temperature dependent recombination rates. Consequently, the ionospheric conductivities are modulated and in the presence of the electric field, an alternating current is generated which radiates at the modulation frequency of the modifying heater (HF) wave (Stubbe et al 1982). Significant signal levels in the ULF, ELF and VLF bands have been radiated by modulating the heater in this manner as indicated in Figure 3. Low frequency radiations have been stimulated from both auroral and equatorial electrojets and this type of radiation generation could have new applications in long distance and sub-surface communications.

#### Small scale F-region irregularities.

At high wave powers, instabilities can be generated in the ionospheric plasma by means of a variety of parametric instabilities (Fejer 1979, Robinson 1989). These occur when the frequency of the heating (pump) electromagnetic wave is close to the plasma frequency and is polarized in the ordinary (O) mode. At least one of the parametrically excited waves is an electron-acoustic wave with frequencies close to the pump frequency. Examples of such instabilities, where coupling between the wave modes is due to the Ponderomotive force (Fejer 1979), are the parametric decay instability (PDI) and the oscillating two stream instability (OTSI). The PDI is a three wave interaction in which the second decay product is a low frequency ion acoustic wave (see Figure 4). The OTSI is a four wave process in which the pump wave decays into an electron acoustic wave and, in addition, two zero frequency perturbations which constitute a spatially periodic plasma density irregularity (Dysthe et al 1983, Weatherall et al, 1982).

The time history of the development of these various instabilities is illustrated schematically in Figure 2. Initially there is a rapid growth of short wavelength electrostatic modes driven by the PDI and OTSI. These plasma disturbances can be detected by the initial enhancement of the ion line spectrum in incoherent radar backscatter (Djuth et al 1986, Kohl et al 1983). Two examples of EISCAT observations of these effects are reproduced in Figure 5.

The central panel of the figure corresponds to the ion acoustic spectrum and contains two enhanced peaks at  $\pm 10$  kHz plus new peak at zero Doppler shift (zero frequency.) These enhancements are characteristic of scatter from low frequency electrostatic modes and all three peaks have amplitudes which are much greater than the normal thermal ion acoustic spectrum. The two panels to the right and left in the figure represent the up shifted and down shifted plasma line respectively. These lines are shifted by the plasma frequency (approximately 5 MHz in the case) from the zero Doppler shift position of the 940 MHz radar frequency. The plasma line also shows considerable structure. The peak at zero Doppler shift corresponds to an enhanced plasma line signature. However, the interesting feature is the more intense peaks which are displaced by approximately 10 kHz towards the central ion line. These intense peaks have been interpreted (Kohl et al, 1983) as decay lines (PDI).

The presence of the OTSI is indicated by the existence of the 3 peaks at zero Doppler shift and, in the case of the lower panel in Figure 5, this process dominates. It must be emphasised that the spectral features reproduced in Figure 5 are highly transient and are usually observed immediately after heater turn on.

The onset and nonlinear evolution of the Thermal Oscillating Two Stream instability (TOTSI) causes the growth of small scale field aligned irregularities. These in turn give rise to anomalous absorption effects which reduce the pump power and so quench the short wavelength electrostatic modes associated with the PDI and OTSI instabilities. This quenching effect accounts for the transient nature of the spectral peaks observed in the incoherent scatter spectrum. Many theories have been proposed to account for the growth of the small scale irregularities and of the anomalous absorption effects which they produce (Graham and Fejer, 1976, Vaskov and Gurevich 1976, Robinson 1985).

Consider an electromagnetic pump wave of field  $E_0$ , ( $\omega, 0$ ) angular frequency  $\omega$  and zero wave number (i.e. large wavelength). This scatters from an initially low amplitude small scale plasma irregularity of density  $n(0, k)$  with zero frequency and wave vector  $k$  (perp to the geomagnetic field). The first order scattered wave is electrostatic and has an electric field  $E_1(\omega, k)$ . This wave can scatter from the density irregularity which subsequently produces a second order electrostatic wave with an electric field  $E_2(\omega, 2k)$ . Scattering into higher modes may also occur. Interference between the electric fields of waves with wave numbers differing by  $k$  produces heating which enhances the irregularities  $n(0, k)$ . The increasing size of  $n(0, k)$  will lead to a decrease in  $E_0$  due to anomalous absorption and an equilibrium value will be reached where the values of  $E_0$  and  $n(0, k)$  stabilize. The spatial and temporal development of  $n(0, k, t)$  can be derived from the perturbation electron and heat balance equation in which an adiabatic approximation has been invoked. This yields an expression of the form.



$$\frac{\partial n(o, k, t)}{\partial t} - \Gamma_{11} \frac{\partial^2 n(o, k, t)}{\partial z^2} + k^2 D_{\perp} n(o, k, t) = - \frac{Q(o, k, t)}{T_e + T_i} \delta(z - z_{UH})$$

When  $D_{11}$  and  $D_{\perp}$  are the diffusion coefficients parallel and perpendicular to the magnetic field,  $T_e$  and  $T_i$  are the electric and ion temperatures respectively. The right hand side term of the equation represents difference heating due to the pump and scattered waves at the upper hybrid resonance level  $z_{UH}$ . The co-ordinate  $z$  is measured in the direction of the geomagnetic field.  $Q(o, k, t)$  is the heating rate which can be written in a simplified form as

$$Q(o, k, t) = aP(t) \left( \frac{n(o, k, t)}{P_1} + \frac{n^2(o, k, t)}{n^2(o, k, t) P_2} \right) \exp(-\Gamma(t))$$

where  $P(t)$  is the pump power as a function of time  $t$ .  $P_1$  is the pump threshold power for first order scattering alone.  $P_2$  is the threshold for second order effects only and  $\Gamma$  is the coefficient of anomalous absorption which can be written as (Jones et al 1984).

$$\Gamma(t) = bn^2(o, k, t)$$

Examples of anomalous absorption of three HF diagnostic waves of different frequencies propagating through the heated volume are reproduced in Figure 6. The greatest anomalous absorption is observed on the frequency closest to the heater (pump) frequency. Note the marked change in fading rate produced during heating which is the subject of another presentation at this conference.

Anomalous absorption effects can also be detected on the reflected heater signal itself (see Figure 7). As the heater power increases, so, initially, does the reflected signal power. At about 1/4 full power, the received signal amplitude remains constant, even though the transmitted power is increased. A further increase in transmitted power, beyond about 1/2 full power, leads to a decrease in the reflected signal strength. As the power is decreased from full power, no change in the reflected signal strength occurs until the transmitted power is reduced to about 1/4 full power. This is the threshold for sustaining the irregularities and, since the transmitted power is less than this value, the irregularity generation process ceases. There is a rapid but linear decline in received signal strength as the transmitted power is further decreased to zero. This so-called Hysteresis effect can thus be explained in terms of the TOSTI as outlined by the theory presented above (Stubbe et al, 1982).

#### Large-scale Irregularities

The input of energy to the ionosphere via the anomalous absorption process quickly leads to a major increase in electron temperature. These temperature enhancements have been measured by incoherent scatter radar during heating at Tromsø and at Arecibo (Mantas et al 1981, Jones et al, 1986). Typical results for Tromsø are reproduced in Figure 8. The figure indicates that the largest enhancement occurs at heights closest to the pump reflection height and that enhancements in  $T_e$  of 500°K (corresponding to an increase of 40% over the ambient value) are quite common. The temperature increase saturates in about 1 min after heater turn on. The  $T_e$  enhancement decays less slowly with height above the pump interaction level and more rapidly below this level. This response can be explained in terms of thermal diffusion along the field line and the more rapid cooling which occurs in the lower ionosphere due to the increased collision frequency (Gurevich 1978, Shoucri et al 1984).

Changes are also observed in the electron density but these are much smaller than the temperature changes, amounting to about only 10 - 20% of the ambient value, (Figure 9). The maximum enhancement occurs at the level of the maximum enhancement in  $T_e$  and dies away rapidly above and below this level. There are major differences in the electron density and temperature responses. The values of  $\Delta N_e/N_e$  at 1 min after heater turn on are lower than those 3 min after heater turn on in the height range 150 to 225 km. This indicates that the time constants for  $N_e$  changes are greater than those for  $T_e$  changes. There is also evidence for a depletion in  $N_e$  near the altitude of the peak in  $\Delta T_e/T_e$ . This depletion in electron density is consistent with the generation of a thermal cavity by the Tromsø heater. However, the limited height resolution of the incoherent scatter radar (4km for  $N_e$ ) makes this conclusion difficult to verify experimentally.

The large scale changes in the ionospheric electron density induced by heating will change the refractive index of the ionosphere and, hence, effect the propagation characteristics of radiowaves traversing the region. It has been established that it is possible to create focussing for defocussing lenses in the ionosphere depending on what height the maximum interaction of the pump wave with the plasma occurs (Bernhardt and Duncan, 1982.)

#### Stimulated emissions

When the spectrum of the heater wave reflected from the ionosphere is measured, it is found to contain additional frequency components which are generated during the heating process (Thidé et al 1982, Stubbe et al 1984). The spectrum of these stimulated emissions exhibits considerable structure but is limited to about  $\pm 100\text{kHz}$  of the primary wave frequency. An example of such a spectrum is reproduced in Figure 10. The most prominent peak is that down shifted from the parent line by about  $10\text{kHz}$ . However, other peaks are present both up and down shifted in frequency. These new emissions have been explained as follows. Initially, the electromagnetic pump wave creates large amplitude electrostatic waves through the PDI process. Further, wave-wave interactions can then occur which involves these daughter components. These interactions give rise to new electromagnetic waves which differ in frequency from the original pump frequency. Individual peaks in the spectrum correspond to specific scatter processes.

#### Summary

Heating of the ionosphere by a high power radio wave can generate a wealth of plasma processes a few of which have been reviewed in this paper. Recent advances in theoretical understanding and in experimental techniques have lead to important new discoveries, for example, the thermal caviton. It seems that, with the development of more powerful heating facilities, even more interesting and, as yet unexpected, phenomena will be discovered.

#### References

- Bailey D K and D F Martyn, 1934, Phil.Mag. 18, 369  
 Bernhart P A and L M Duncan, 1982, J.Atmos.Terr.Phys. 44, 1061.  
 Djuth F T, C A Gonzales and H M Ierick, 1986, J.Geophys.Res. 91, 12089  
 Dysthe K B, E Mjølhus, H L Pécsell and K Rydpa, 1983, Phys.Fluids, 26, 146  
 Fejer J A, 1979, Rev.Geophys.Space Phys. 17, 135  
 Graham K N and J A Fejer, 1976, Radio Science 11, 1057  
 Gurevich A V, "Nonlinear Phenomena in the Ionosphere." Springer, New York, (1978)  
 Jones T B, T R Robinson, P Stubbe and H Kopka, 1984, J.Atmos.Terr.Phys. 46,147  
 Jones T B, T R Robinson, P Stubbe and H Kopka, 1986, J.Atmos.Terr.Phys. 48, 1027  
 Kohl H, C LaHoz, K Folkestad, T Hansen, H Kopka, G Rose and P Stubbe, 1983, In: Active Experiments in Space Symp., ESA, SP-195, 91  
 Mantas G P, H C Carlson and C H LaHoz, 1981, J.Geophys.Res. 86, 561  
 Robinson T R, 1983, J.Atmos.Terr.Phys.47, 1245  
 Robinson T R, 1989, Physics Reports 179, 79  
 Shoucri M M, G J Morales and J E Maggs, 1984, J.Geophys. Res. 89, 2907  
 Special Issues of Journals devoted to Heating:-  
     J.Gophys Res.,1970, 75  
     Radio Sci.,1974,9  
     J.Atmos.Terr.Phys.,1982, 44  
     J.Atmos.Terr.Phys.,1985, 47  
 Stubbe P, H Kopka, M T Rietveld and R L Dowden, 1982, J.Atmos.Terr.Phys.44, 1123  
 Stubbe P, H Kopka, B Thidé and Å Hedberg, 1984, J.Geophys.Res. 89, 7523  
 Stubbe P, H Kopka, H Lauch, M T Rietveld, A Brekke, O Holt, T B Jones T Rbinscn, Å Hedberg, B Thidé, M Crochet and H J Lotz, 1982, J.Atmos.Terr.Phys. 44, 1025.  
 Tellegen B D H, 1933, Nature 131, 840  
 Thidé, H Kopka and P Stubbe, 1982, Phys. Rev. Lett 49, 1561  
 Vaskov V V and AA V Gurevich, 1976, Sov.J.Plasma Phys. 2, 62  
 Weatherall J C, J P Sheerin, D R Nicholson G L Payne, M V Goldmar. and P J Hansen, 1982, J.Geophys.Res. 87, 823

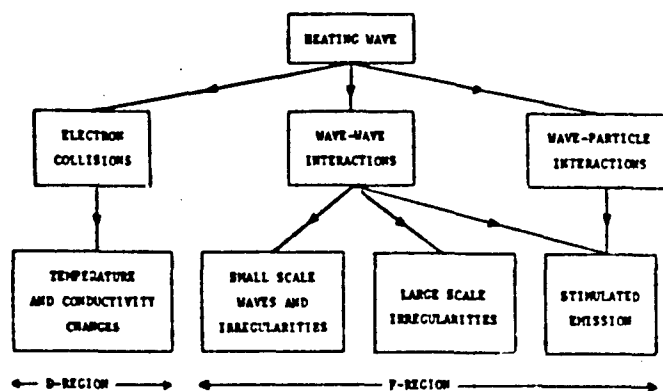


Figure 1. Schematic diagram of the various types of processes associated with ionospheric heating.

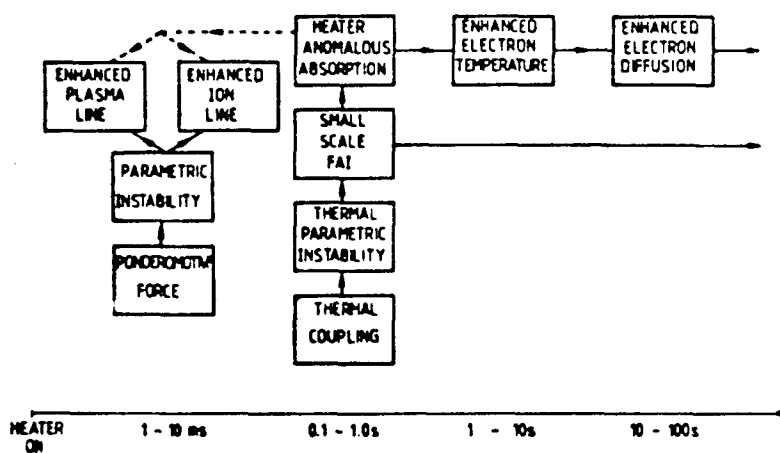


Figure 2. Schematic representation of the temporal development of the various stages observed during a typical heating experiment.

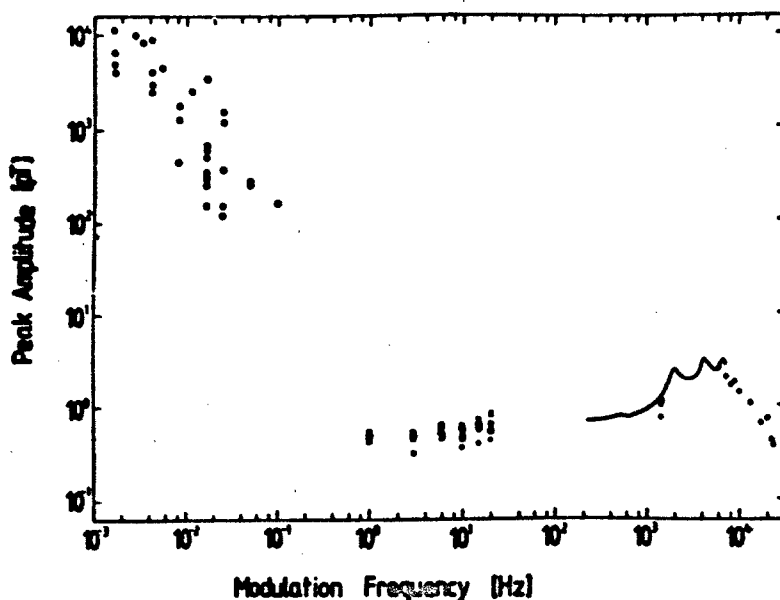


Figure 3. Relative amplitudes of low frequency emissions from modulated auroral electro-jet, Tromsø.

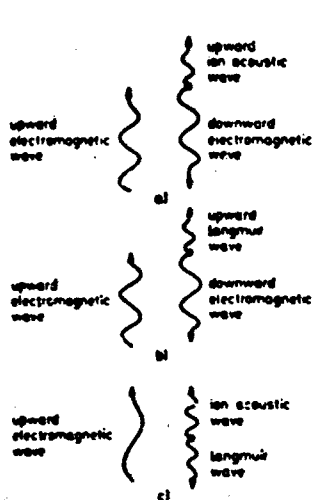


Figure 4. Schematic illustrations of (a) stimulated Brillouin scattering, (b) stimulated Raman scattering and (c) parametric decay instability.

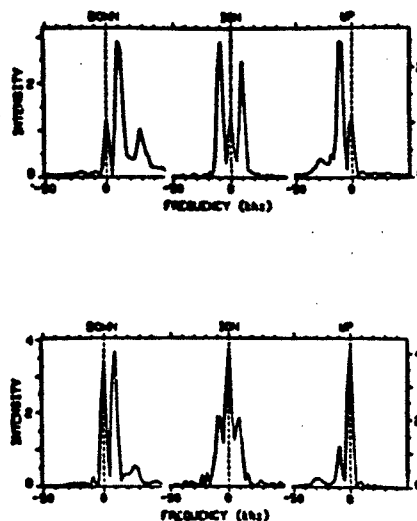


Figure 5. EISCAT spectra illustrating ion and plasma line enhancements due to heater excited PDI and OTSL.

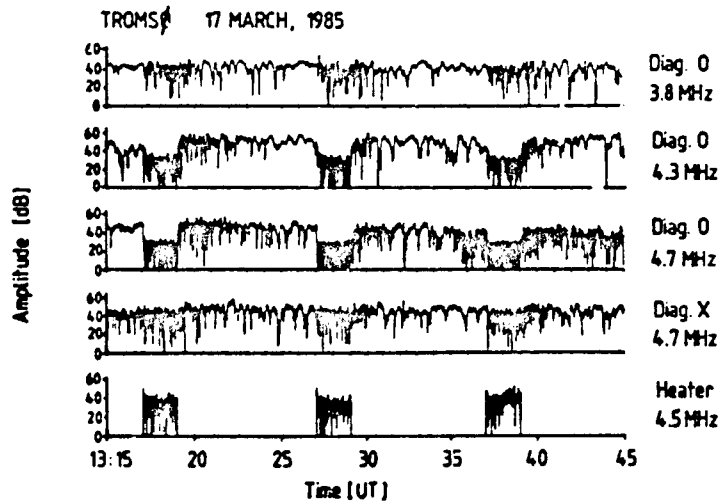


Figure 6. Amplitude changes induced in 3 diagnostic signals of a 4.5 MHz heating wave generated by the Tromsø heater.

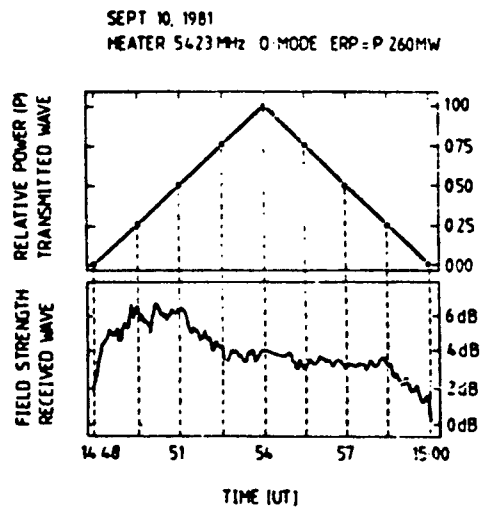


Figure 7. Ionospherically reflected heater wave amplitude data (lower panel), illustrating hysteresis between sequences of increasing and decreasing transmitted powers (upper panel).

1A-8

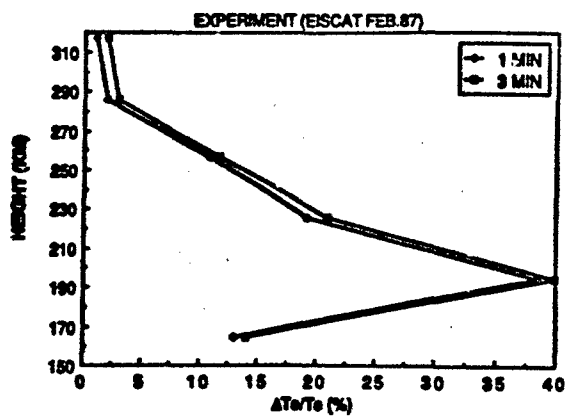


Figure 8.  $\Delta T_e/T_e$  against height after 1 and 3 min of heating obtained from EISCAT observations.

Figure 9.  $\Delta N_e/N_e$  against height after 1 and 3 min. of heating obtained from EISCAT observations.

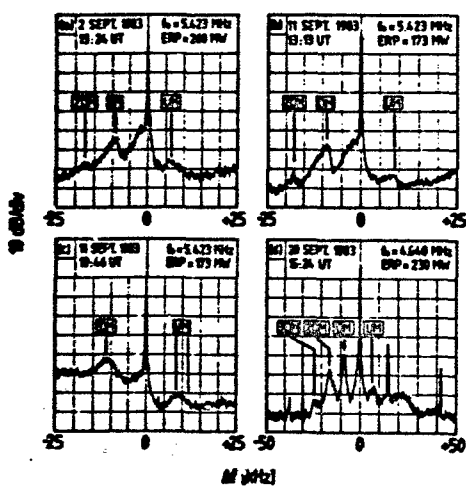
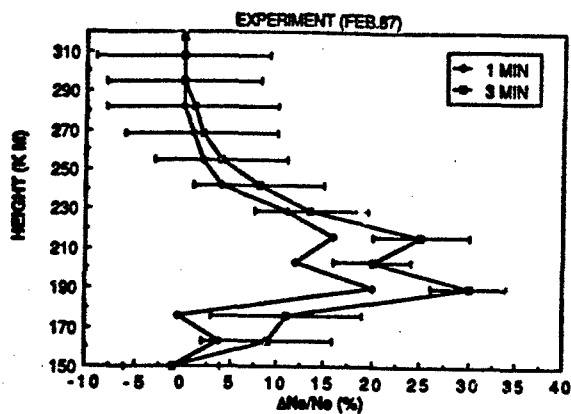


Figure 10. Four examples of richly structured stimulated electromagnetic emission [SEE] spectra.

## DISCUSSION

E. SCHWEICHER, BE

How do you prevent crosstalk between transmitter and receiver when performing reflection experiments at the heater frequency?

## AUTHOR'S REPLY

At Tromsø the heater is located in a steep valley, thus the direct ground wave at the site some 50 km south of the heater is greatly attenuated. Our measurements indicate that the ground wave is very small compared to the sky wave signal.

## HIGH POWER HF MODIFICATION: GEOPHYSICS

H.C. Carlson, Jr.  
 Ionospheric Physics Division  
 Geophysics Laboratory, Air Force Systems Command  
 Hanscom Air Force Base, MA 01731  
 USA

## SUMMARY

As the electric field and power density of radio frequency (RF) radiation increases continuously in a plasma, the response of the plasma to the incident energy changes discontinuously. This follows from a complex of competing physical processes, each generally with its own power dependent threshold, and plasma instabilities each with its own growth and decay rate. Non-linear power dependencies, boundary condition dependencies on past histories of the plasma conditions, dependence on proximity to plasma resonances, and non linear mixing in the plasma to up or down convert with respect to resonances, all conspire to make experimental guidance invaluable to theoretical development. Experiment has demonstrated that with increasing HF power one passes threshold of detectability sequentially from: passive transmission, to cross-modulation, to thermal bulk heating, to parametric and other instabilities with plasma structuring and stimulated electromagnetic radiation, to electron acceleration and airglow, to reported stimulated ionization. Theoretical understanding of these effects follows from merger of radio physics, ionospheric physics and aeronomy, plasma physics, and atomic and molecular physics. The RF propagation and emission environment is affected through the VLF to GHz range by lensing, scattering, modulation, and stimulated emission. The optical background and emission character is affected over a very wide spectrum by electron impact and temperature enhancement altering translational, rotational and vibrational temperatures (as well as raising fine structure population distribution questions). An adequate understanding of the processes, if not a predictive capability of the consequences of sending very high power density RF into the ionosphere, represents a common ground for many scientific discipline, agency, national, civilian, and defense goals and missions. This presentation addresses a set of geophysical effects over this range, and invites audience participation in anticipation of what effects lie beyond the next threshold (of ionospheric response to higher power HF illumination). The exciting upgrade of the Heater at Tromsø and emerging new HF modifier plans in the U.S. are partial motivation for such conjecture.

## 1. INTRODUCTION

As we contemplate the next generation of very high power HF ionospheric modification experiments (G watt class ERP heating experiments) it is appropriate to review where we've been and reflect on where we're headed. RF energy deposited in the ionosphere has perturbed the plasma temperature, composition, and concentration, has generated optical and RF emissions, has modified the RF propagation character, has diagnosed a number of aeronomic and plasma physics processes, and has triggered a host of instability processes. Figure 1 identifies many of the effects we will now discuss in further detail.

## 2. THERMAL ELECTRON POPULATION

## 2.1 Steady State Temperature Enhancements

The bulk electron gas temperature is enhanced by many tens of percent, or many hundreds of degrees K in the lower F region.

In fact, the thermal electron population can be heated at all altitudes in the ionosphere. The dominant immediate heating mechanism is deviative absorption. This will be strong wherever HF retardation is large (where an ionosonde virtual height is very different from the true height). Each electron alternately accepts and returns energy from and to the passing RF electric field of the HF wave. If the electron suffers a collision with a neutral particle, this ordered motion becomes disordered, i.e. heat, the heating being said due to deviative absorption.

Locally deposited heat is very quickly distributed by strong thermal conduction along magnetic field lines. This is very effective at communicating locally deposited heat to distant regions, a hundred km or more away for F region heating, where cooling may be more effective. Thus steady state electron gas temperature enhancements in the F region may balance local heating against cooling over hundreds of km. In figure 2, the dashed and solid line altitude profiles of electron temperature  $T_e$  and electron gas heating  $Q_e$  show very little difference in  $T_e$  for the same total  $Q_e$  spread over about a 10 km or a 50 km altitude region. This is because of the dominance of heat conduction in distributing the heat in altitude.

## 2.2 Response Time

The bulk thermal plasma temperature responds with a typical time constant of a fraction of a minute. This is illustrated in figure 3. Order a minute is a characteristic time for bulk plasma effects to set in, e.g. new electron and ion gas



temperatures, new plasma scale height, redistribution of new plasma pressures, plasma diffusion rates, and motion towards a new equilibrium profile, and new temperature dependent reaction rates and chemical composition.

The observed time constants for electron gas cooling agree with available theory within the observational error bars. It is important to note that this statistical error bar is set not by the measurement diagnostic (e.g. order 10K for several minutes integration at the Arecibo ISR), but by the fluctuation between the temperature in one parcel of plasma relative to the temperature in an adjacent parcel of plasma, as spacial temperature fluctuations in the heated plasma drift through the diagnostic ISR field of view (here one-sixth of a degree angular field of view, or roughly a km diameter).

The electron gas cools locally by collisions with ions in the F region, and by thermal conduction downward in altitude to where electrons collide with neutral particles below. (The heated ions in the F region pass their heat on to neutral particles locally.) The dominant F region electron gas cooling rate, collisions with ions, is proportional to the number of electrons times the number of ions with which they collide. Thus, the electron gas cooling rate is proportional to the square of the electron density,  $n_e^2$ , and thus the fourth power of the plasma frequency. For typical heating matched to near the ionospheric critical frequency  $f_{oF2}$ , one must then expect dramatically greater heating response at the low end of the heating range in view of an  $f_{oF2}^4$  dependence of cooling rate.

### 3. SUPRATHERMAL ELECTRON POPULATION

#### 3.1 Suprathermal Electron Flux Energy and Spacial Distribution

The high energy tail of the electron gas population is also enhanced. This has been most readily inferred from airglow enhancements synchronized with HF transmitter on-off cycles. In figure 4, the separation between the envelope of the alternately higher and lower 6300A intensities, roughly 20 Rayleighs, is due to electron impact excitation of atomic oxygen by electrons of greater than 1.96eV. From this measurement alone we have no information on the energy distribution of the electron flux above 2eV, and only a crude measure of the total particle or energy flux (because of competing collision cross-sections for electron impact as well as subsequent O('D) quenching by molecular nitrogen). The flux is of the same order as that which reaches a locally dark ionosphere from a sunlit conjugate midlatitude ionosphere.

Enhancements of other optical emissions, whose excitation cross sections have higher energy thresholds, are also seen. These in principle provide a crude electron energy spectrometer, and a more unambiguous lower bound on the energy above which electrons are accelerated by HF excited processes. 6300A emissions can be enhanced by Maxwellian electrons above 2eV for electron temperatures exceeding roughly 2800oK, or by non Maxwellian electrons above 2eV. 5577A emissions, with a 4eV threshold, and other higher energy threshold emissions, cannot be thermally excited.

The most direct published measurement of the energy spectrum has been by the plasma line component of the incoherent scatter radar technique. This has established that the spectrum of suprathermal electrons reaches beyond 17eV before significantly falling off (Carlson et al, 1982). There is not yet at this time an accepted theory to explain this high energy reach.

The spacial distribution of the airglow enhancements is roughly the size and shape of the HF half power beam width, and roughly collocated with it, as seen in figure 5 (Bernhardt et al, 1988). Ionospheric tilts, self-made indentations and drifts, traveling ionospheric disturbances, and gravity waves will displace the location of maximum airglow enhancement.

#### 3.2 Response Time

The 6300A enhancement response time, roughly a large fraction of a minute in figure 4, is determined by the response time of the 6300 emission process, not the time for the supra thermal electron flux to turn on. 5577A emissions show response times of a large fraction of a second, also determined by the response time of the optical emission process, not the electron flux turn on. The suprathermal electron flux turns on over plasma instability time scales (measured in ms, not s).

### 4. PARAMETRIC INSTABILITIES

#### 4.1 Spectral Identification

Among the plasma instabilities excited in the ionosphere by the HF transmitter are several at and near the height of HF reflection, identifiable in figure 6 by their spectral signature on the incoherent scatter radar plasma line echo.

The spectral peak at the HF frequency displacement is due to the two stream instability. The strongest spectral peak in this case, at the ion acoustic wave doppler displacement  $+v_i$ , is due to the decay mode instability. Plasma waves in this case are enhanced about 1011 above their thermal amplitude. The line at  $-v_i$  is the decay mode

image line. The series of relative maxima at 3, 5, 7 and 9  $\omega_i$  are harmonics of the decay mode line. That energy should cascade down (by successive pumping of each resonance by the one before) to the odd but not the even harmonics is consistent with theory, but the absolute frequency at which they are seen contradicts standard theory. These harmonics are in turn all superposed on yet another broad spectral signature of instability processes in the plasma.

This spectra from 1971 represents an average in space over many km in the ionosphere, and thus compacts down into a single spectra many instabilities that can be occurring at different altitudes. These are all observed spatially near the center of the HF main beam.

The scale size of the plasma waves sensed by the incoherent scatter radar diagnostic are those matched (0.35 $\lambda$ ) to its diagnostic radar wavelength.

#### 4.2 Response Time

The rise time of the main spectral power components just discussed is shown in figure 7. The figure shows the plasma line spectra, identifying the decay mode, harmonics of the decay mode, and the broad spectral feature, on both a linear and logarithmic power scale, vs time after HF turn-on. These parametric instabilities turn on in a matter of ms.

### 5. PLASMA IRREGULARITIES (km scale, Spread F, Scintillation)

#### 5.1 Spatial Presence

An HF imaging array sky map for the natural ionosphere is seen in the upper left hand section of figure 8. If the ionosphere were horizontally stratified and motionless the echo image would be centered in the sky map, and show zero doppler shift. The slight spatial and doppler displacement of the HF diagnostic echo is due to a slight overhead tilt and motion associated with a passing gravity wave.

The five successive frames show HF diagnostic echoes at successively greater times after turn on of a high power HF modifier with a half power beam width of order 10 degrees (roughly 40 km diameter in the F region). The HF diagnostic sky maps sense structures produced in the ionosphere by high power HF induced instability processes. In this case, the scale size of the "Spread F" structures produced are order a km across a magnetic field line B and many times greater along B.

#### 5.2 Response Time

The km scale structures in figure 7 have onset times of a fraction of a minute, the same time scale over which bulk plasma processes occur. The total number of field aligned irregularities seen continues to increase for several more minutes after HF turn on.

### 6. INSIGHTS FROM IN SITU MEASUREMENTS

#### 6.1 Satellite Measurements

There are some logistical challenges to having a satellite "thread the needle" of the heater beam. For a 100 beam (moderate antenna gain) the "target" in the sky is roughly 40 km. Successive crossings of a latitude well below the satellite inclination, for a typical 90 minute period satellite, are 22.50 of longitude apart or a couple of thousand km apart, offering half a dozen chances per year to penetrate the heater beam. Variable satellite drag can greatly complicate scheduling a pass. The number of opportunities can be greatly enhanced by having the satellite inclination a couple of degrees of latitude above that of the heater. If one wishes to penetrate the heater beam near the height of reflection, one must anticipate what ionospheric plasma frequency will be at the satellite height at the overflight time. Day to day ionospheric variability requires real time tracking and extrapolation in time based on knowledge of local ionospheric morphology (a comprehensive data base of e.g. ionosonde data for the season is valuable).

In 1976 Carlson and LaHoz obtained 3 Atmosphere Explorer-E fly-throughs of the Arecibo HF heater beam near the height of reflection during a two week period, by applications of the above considerations. Figure 8 shows the electron density measured during one such pass.

This shows some properties of the heater generated irregularities uniquely well studied by a satellite in situ pass. The background ionosphere was smooth to a small fraction of a percent. The satellite entering the heater beam from the left, encounters a sharp onset of strongly enhanced irregularity structure - many percent fluctuation in electron density. The sharp onset means a sharp HF power threshold for the instability. The satellite passing out to the right (east) samples the irregularities drifting downstream from the heater, decaying in amplitude with time and downstream distance, and losing the finer scale before the larger scale. While the incoherent scatter radar beam of the 1000 foot diameter Arecibo dish is only a km in diameter at the region sampled, indicated by the circle labeled 430 MHz radar beam in figure 9, this is too coarse to

resolve the scale size of the irregularities, which are very well resolved by the in situ AE-E diagnostic, as about half a km. (Scintillation data for other events has given the same scale size information: Basu et al, 1983, 1987.) These data of figure 5 have been interpreted (Farley et al, 1983) in terms of the thermal self focusing instability.

## 6.2 Hero Rocket Measurements

Penetrating the heated volume with a rocket requires that the rocket trajectory dispersion envelope be less than or comparable to the size of the heater beam (order tens of km diameter target at hundreds of km range).

Figure 10a shows data successfully obtained by Rose et al 1985 at the Max Planck Heater at Tromsø, with a HERO rocket flight out of Andoya. This affords a unique set of data in terms of both some individual measured parameters (supra thermal electrons directly measured, VLF measurements, electric field measurements) as well as the comprehensive composite coincident data set. The findings are summarized by Rose et al 1985 and the references therein (trajectory illustrated in figure 10b).

Chemical releases from rockets, such as will be done by the NASA CRRES experiments at Arecibo in 1991, also afford the opportunity to explore the interaction of HF energy with other than the natural earth ionosphere.

## 7. COMPETING INSTABILITY PROCESSES

While satellites and rockets provide snapshots of a set of (usually in situ vs remotely sensed) heater related parameters, incoherent scatter radar (ISR) diagnostics can provide time continuous profiles of a set of parameters. These ISR parameters include electron and ion temperatures, densities, composition, drift velocity, currents, electric fields, plasma fluctuation levels, selected plasma wave amplitudes, supra thermal electron fluxes, instability spectral signatures, neutral particle temperatures and densities at selected altitudes, and other plasma and aeronomic terms.

Figure 6 illustrated a number of plasma instabilities sensed by the ISR. However this data from 1971 compacts all these processes into a single altitude and time bin.

The incoherent scatter radar diagnostic echo offers enormous potential to diagnose HF modifier or heater related effects. However, most of this potential information is usually thrown away (because of receiver and data processing limitations). Although the ISR has been used for 20 years to study HF induced effects, only most recently has its full diagnostic potential been approached.

Figure 11 shows data recently collected at Arecibo (which has the worlds most powerful ISR diagnostic capability, vs-a-vis collecting aperture and radar sensitivity, but only a relatively modest HF modification facility). This data with better than 100m range resolution, vs the kms of figure 6, also has far better time resolution (ms vs about a minute).

This figure 11 unveils the character of the response and illustrates a key aspect of ionospheric modification. There are many competing instability processes, each with a time scale over which it sets in, and each with a level of influence at least in part also dependent on background environment parameters and history.

We see in this figure 11a the signature of an initial explosive growth of the instability leading to the observed downshifted (receding longitudinal electrostatic waves in the electron gas) plasma line. Then, after a fraction of a second, a second process takes over, quenching the initial growth phase of the first. After about 40 seconds, during which the plasma wave amplitude distribution exhibits significant variations in magnitude but a persistent character confined to within a km below the height of HF reflection, the plasma exhibits the onset of an entirely new character. The character is that of spread F, or scintillation, or thermal self focusing conditions. The onset time for this instability is a large fraction of a minute, appropriately the time scale associated with bulk plasma changes and redistributions.

Figure 11b is an expanded time plot of the same data as in figure 11a, except now shown not over the first minute after HF turn on, but detailing in ms the evolution over the first 250 ms after turn on. The spacial periodicity with a fraction of a km spacing at the onset of the parametric plasma instabilities and again at the onset of the Spread F instabilities, the temporal coherence over scales of ms and a few hundred ms, and many other critical properties are only now becoming available. Djuth and Sulzer 1990 discuss some of the implications of this new advance in extracting the information available from ISR echoes, and implications for competing plasma processes.

## 8. H.F. POWER DEPENDENCIES

Figure 12 shows two simultaneously measured HF power dependencies at Arecibo. Figure 12 shows the HF power dependence of the normalized cross section for 50 MHz VHF radar echoes of 3 m scale magnetic field aligned irregularities produced by the Arecibo heater (50 MHz echoes are observed orthogonal to the magnetic field). The power dependence is linear over the range of HF power densities available at Arecibo. No

saturation is seen. A threshold is very small or absent; that is, the intercept is nearly the origin of the graph so a finite cross section is found for even very small HF power.

Figure 12 shows simultaneously gathered data, but of a parameter which saturates while the VHF cross section continues to grow linearly with HF power. This parameter is the normalized plasma line power, that is the 35 cm scale longitudinal electrostatic plasma wave amplitude, often just called Langmuir turbulence. It too starts near the origin of the graph, also with an initially linear growth, but saturates somewhat below 100 MW ERP (effective radiated power).

Figure 13 shows data from another time, and of the 6300A emission intensity in Rayleighs vs normalized HF power density. Simultaneous ISR measurements of electron temperature verified that these airglow enhancements were not due to thermal electron impact excitation, but to a high energy non-Maxwellian suprathermal flux of electrons (order 106 electrons cm<sup>-2</sup>s<sup>-1</sup>eV<sup>-1</sup>, or comparable to a predawn photoelectron flux from a sunlit conjugate hemisphere). The HF power dependence over the limited range available is most simply fit by assuming a linear growth. If one extrapolates a linear fit to the data points, it intercepts the HF power axis somewhat below 100 kW ERP. That is, it would suggest a threshold somewhat below 100 kW ERP.

## 9. CONCLUDING REMARKS

### 9.1 General Considerations

Geophysics is intrinsic to ionospheric HF modification technology because: either controlled changes in selected geophysical parameters is the objective of the HF technology; or geophysical constraints on the HF effects must be understood in order to explain, predict, or control any other HF effects.

Coupled experiment and plasma theory is essential to: identification of consequences of high power HF irradiation of the upper atmosphere and ionosphere; and useful realization of the potential of such consequences.

Also, pivotal to research strategy in this area, as the HF power delivered to the ionosphere is increased continuously, the dissipative process dominating the response of the geophysical environment changes discontinuously. With increasing HF power, the first limiting process in the ionosphere dissipates more energy until it saturates. The ionospheric response then goes into "runaway" up to a new (the next) limiting process. The cycle repeats: after each saturation, the next major process (or class of processes) is discovered.

One cannot rely on theory to be able to predict these discontinuous leaps. Only experiment can tell us at what power the next "runaway" to new limiting processes will occur, and which property of the geophysical environment is changed, and how. At the same time one cannot expect experiment alone to guide us to realization of potential uses of high power HF modification without working within a tested theoretical framework. There are too many competing processes, and too many parameter dependencies, to allow reliance on empirical answers rather than a validated model framework.

There are a vast array of competing instability processes. If we wish to favor one over the other, we must identify the competing processes and their parameter dependencies. We will not develop the necessary theoretical framework without comprehensive diagnostics to develop, test, and validate the theoretical framework. To do this effectively, the capital costs and level of effort on the diagnostics must be matched for comparability to those of the HF modifier. A serious imbalance on either side becomes the limiting factor on both.

### 9.2 Hierarchy of Heater Thresholds

As the HF power delivered to the ionosphere is continuously increased, the dissipative process dominating the response of the geophysical environment changes discontinuously (Figure 14). At very modest HF powers, two RF waves propagating through a common volume of ionosphere will experience cross-modulation, a superposition of the amplitude modulation of one RF wave upon another.

As HF effective radiated powers available in the West, measurable bulk electron and ion gas heating is achieved, electromagnetic radiation (at frequencies other than transmitted) is stimulated, and various parametric instabilities are excited in the plasma, including those which striate or structure the ionospheric plasma so that it scatters RF energy of a wide range of wavelengths.

There is also evidence that at peak power operation in the West, parametric instabilities begin to saturate, and at the same time modest amounts of energy begin to go into electron acceleration, resulting in modest levels of electron-impact excited airglow. This suggests that at the highest HF powers available in the West, the instabilities commonly studied are approaching their maximum RF energy dissipative capability, beyond which the plasma processes will "runaway" until the next limiting process is reached. The airglow enhancements suggest that this next process then involves wave-particle interactions and electron acceleration.

The Max Planck HF facility at Tromsø, Norway, possesses power significantly greater than the Arecibo and Boulder high power heaters. Yet, it has never produced any clear airglow enhancements, as commonly produced by the US HF facilities at lower HF power, but at lower latitudes. This is attributed to the partitioning of HF energy between different competing processes as being different for the different geophysical conditions at these different latitudes. The question of experimental control to select and favor at will one process over another remains an open question and an intriguing technical challenge. The answer must lie in controlled experiments, with comprehensive diagnostics, interpreted within a tested theoretical framework.

The Soviets, operating at higher powers than the West, now have claimed significant stimulated ionization by electron-impact ionization (Migulin and Gurevich, 1985). The claim based on indirect HF propagation experiments, is that HF energy, via wave-particle interaction, accelerates ionospheric electrons to energies well in excess of 20 electron volts (eV) so that they will ionize neutral atmospheric particles with which they collide. Given that the Soviet HF facilities are several times more powerful than the Western facilities at comparable mid-latitudes, this is certainly plausible.

In summary, the range of HF power available from US and European facilities has allowed us to pass several thresholds. At the lowest HF powers, simple classical collisional heating (deviative absorption) dominates. At higher power densities in the ionosphere, a host of plasma instabilities dissipate energy. Which of these instabilities become the governing dissipative process for given geophysical conditions determines which geophysical manifestations dominate. At our previously highest available power densities (about 0.3 GW ERP), we observe energetic electrons, manifested as optical emissions, indicating that an additional, poorly-understood particle acceleration process is dissipating appreciable HF energy.

We do not know what effects are produced at still higher power densities. Plausible speculation might include: production of energetic electrons, production of substantial optical emission, production of substantial ionization and increased ionospheric densities, plasma turbulence and shock fronts, and electrical currents. However, until facilities are built to perform higher power density experiments, and diagnostics are collocated to sense the effects, we will only be able to speculate.

**Acknowledgment:** This work was partially supported by AFOSR 2310G9.

## REFERENCES

- Allen, E.M., G.D. Thome, and P.B. Rao, HF phased array observations of heater-induced spread-F, *Radio Sci.*, 9, 905-916, 1974.
- Basu, S., Su. Basu, S. Ganguly, and W.E. Gordon, Coordinated study of subkilometer and 3-m irregularities in the F region generated by high-power HF heating at Arecibo, *J. Geophys. Res.*, 88, 9217-9225, 1983.
- Basu, Sa, Su Basu, P. Stubbe, N. Kopka, and J. Vaaramaa, Daytime Scintillations Induced by High-Power HF Waves at Tromsø, Norway, *J. Geophys. Res.*, 92, 11149-11157, 1987.
- Bernhardt, P.A., L.M. Duncan, and C.A. Tepley, Artificial Airglow Excited by High-Power Radio Waves, *Science*, 242, 1022-1027, 18 November 1988.
- Carlson, H.C., and L.M. Duncan, HF Excited Instabilities in Space Plasmas, *Radio Sci.*, 12, 1001-1013, 1977.
- Carlson, H.C. and G.P. Mantas, An Experimental Test of the Ionosphere Electron Gas Cooling Rate by Excitation of the Fine Structure of the Ground State of Atomic Oxygen, *J. Geophys. Res.*, 87, 4515-4524, 1982.
- Carlson, H.C., V.B. Wickwar, and G.P. Mantas, Observations of Fluxes of Suprathermal Electrons Accelerated by HF Excited Instabilities, *J. Atmos. Terr. Phys.*, 44, 1069-1100, 1982.
- Djuth, P., and M. Sulzer, High Resolution Observations of HF Enhanced Plasma Waves in the F Region, *Geophys. Res. Letters*, in press, 1990.
- Farley, D.T., C. LaHoz, and B.G. Fejer, Studies of the self-focusing instability at Arecibo, *J. Geophys. Res.*, 88, 2093-2102, 1983.
- Mantas, G.P., H.C. Carlson, C. Lattos, Thermal Response of the F-Region Ionosphere in Artificial Modification Experiments by HF Radio Waves, *J. Geophys. Res.*, 86, 561-574, 1981.
- Migulin, V.V., and A.V. Gurevich, Investigation in the USSR of Nonlinear Phenomena in the Ionosphere, *J. Atm. Terr. Phys.*, 47, 1181-1187, 1985.
- Noble, S.T., and P. Djuth, Simultaneous Measurements of HF Enhanced Plasma Waves and Artificial Field Aligned Irregularities at Arecibo, *Geophys. Res. Letters*, in press, 1990.
- Rose, G., B. Grandal, K. Neske, W. Ott, K. Spenner, J. Holtet, K. Maseide, and J. Troim, Experimental Results From the HERO Project: In Situ Measurements of Ionosphere Modifications Using Sounding Rockets, *J. Geophys. Res.*, 90, 2851-2860, 1985.
- Shoven, R.L., Time Variations of HF Induced Plasma Waves, Ph.D. Dissertation, Rice University, Houston, TX, 1975.
- Sipler, D.P., and M.A. Biondi, Measurements of O(1D) quenching rates in the F region, *J. Geophys. Res.*, 77, 6202-6212, 1972.

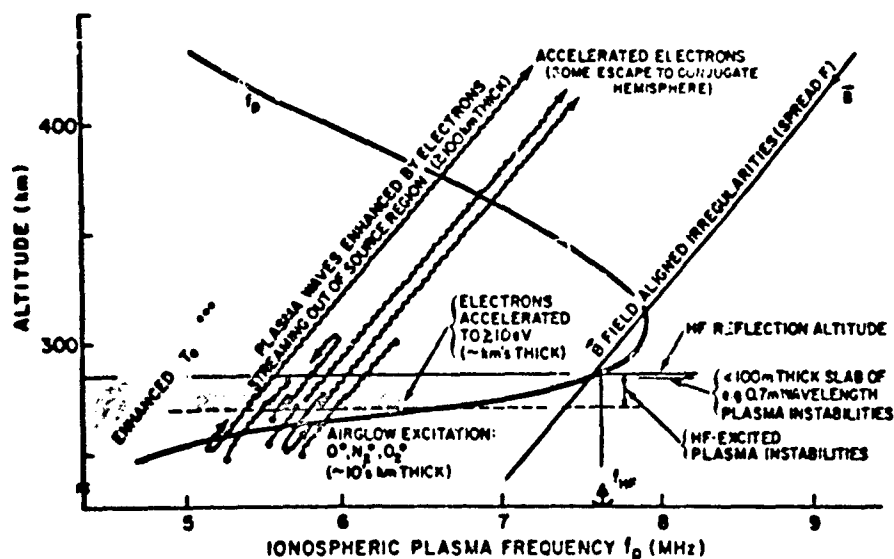


Fig. 1. Effects produced by a ground-based transmitter of power aperture of the order of  $10^4 \text{ MW}$  in the 4-12 MHz frequency range. Energy deposited in the ionospheric plasma alters both the thermal and nonthermal properties of its charged particle population. Controlled experiments have applications to aeronomy, chemical rates, atomic cross sections, communications, and a number of areas of plasma physics (Carlson and Duncan, 1977).

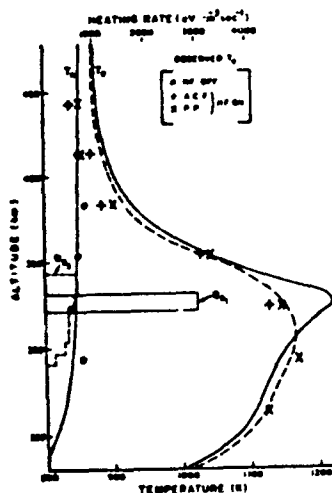


Fig. 2. Comparison of calculated and observed artificially enhanced electron temperature profiles at Arecibo on October 10, 1972. The profiles show  $T_e$  observed using two independent techniques,  $T_e$  calculated for a thick and thin heat input region, and the heating rates leading to the matched  $T_e$  calculation. (Rantaa et al. 1981).

Fig. 3. (a) Comparison of the observed and the calculated variations of the enhanced electron temperature, averaged in the altitude range 269-287 km, as the HF transmitter is periodically turned on and off every 120s. The points represent the observations and the smooth curves the predicted variation of  $T_e$  for various amounts of fine structure cooling. (b) Comparison of the observed and the calculated variations of the enhanced electron temperature. (Carlson and Rantaa 1982).

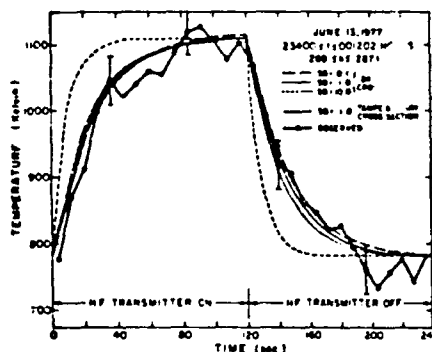


Fig. 3a

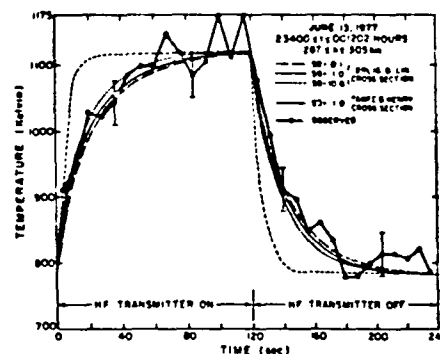


Fig. 3b

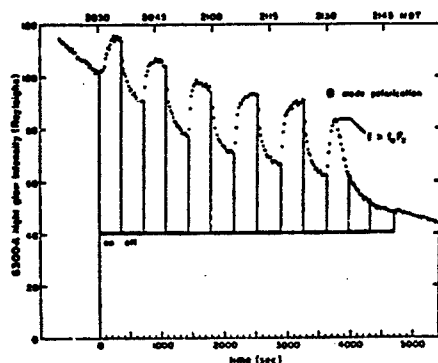


Fig. 4. The 6300-A intensity enhancements produced by ordinary polarization waves on September 25, 1970 (P 1.6 Mw and  $f = 5.3$  MHz). The critical frequency  $f^oF_2$  decreased below the transmitter frequency at 2132 hours MDT. (Sipler and Biondi, 1972).

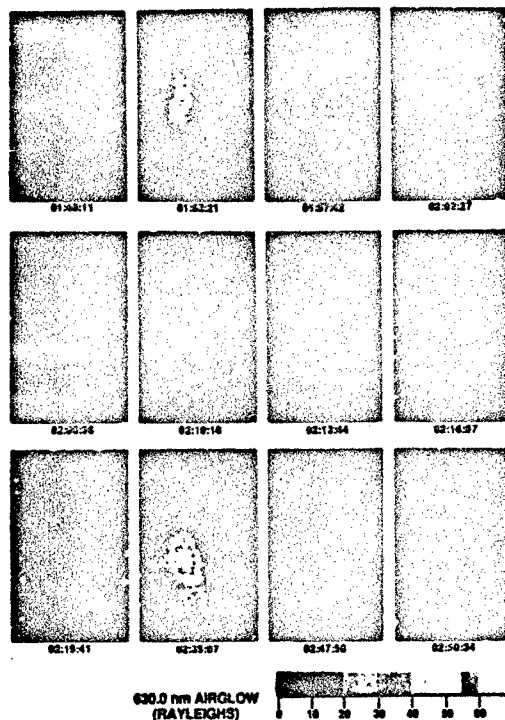


Fig. 5. 6300A airglow enhancement due to HF heater at Arecibo, showing temporal evolution of spatial distribution. (Bernhardt et al, 1988).

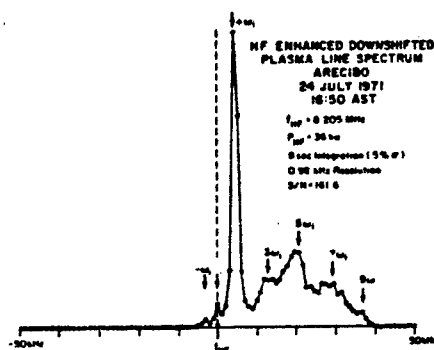


Fig. 6. Plasma wave features excited by the HF transmitter, as seen in the 430 MHz by the HF frequency corresponds to the two-stream growing mode instability. This is bracketed here by: a feature at a lower frequency displacement attributed to a decay mode parametric instability, and the image of the decay mode line. The broad spectral feature to the right, containing most of the spectral power, led to extension of the theory. It also illustrates the presence of an unexplained a physical process sometimes capable of exciting a strong set of odd  $\omega$  harmonics directly within the frame of reference of the radar line of sight. The maximum received power in the spectra is (labeled peak snr)  $\times$  (frequency resolution in kHz)  $\times$  ( $5 \times 10^{-16}$  watts  $\text{kHz}^{-1}$ ).

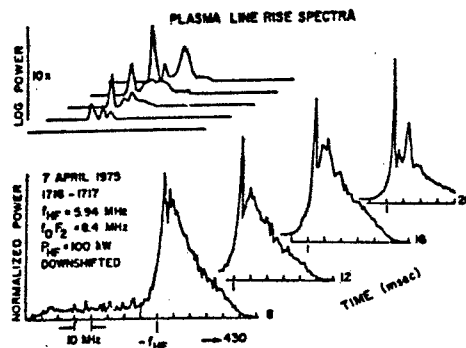


Fig. 7. Evolution of plasma line spectral shapes after HF turn-on [after Shoven, 1975]. Rise times vary with conditions but are of the order of tens of msec.



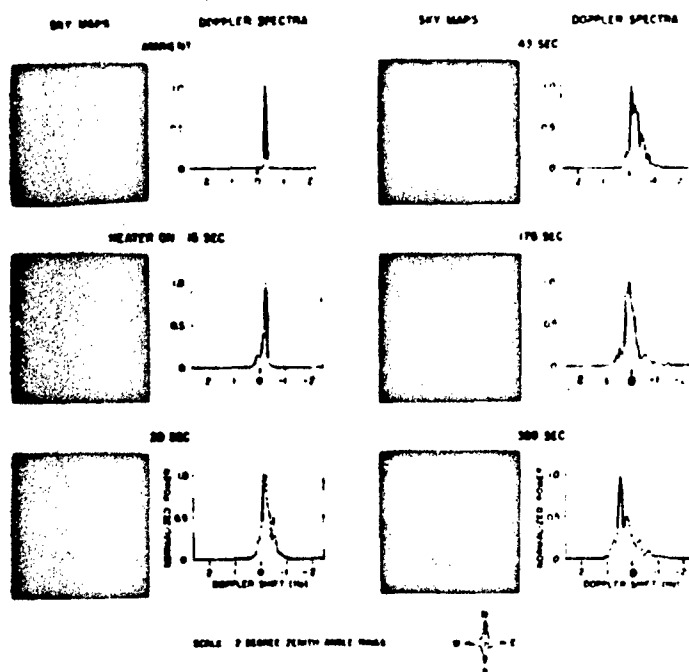


Fig. 8. Dynamic behavior of spread-F, seen with HF frequency Doppler spectra and sky map pairs during an HF turn-on time interval. With the HF off one sees the expected single echo (slightly shifted from overhead and zero Doppler shift by a passing gravity wave). Within seconds of HF turn-on, additional echoes appear, spread in location and turbulently spread in Doppler shift. The number of field aligned irregularities sensed continues to increase for several minutes [from Allen et al., 1974].

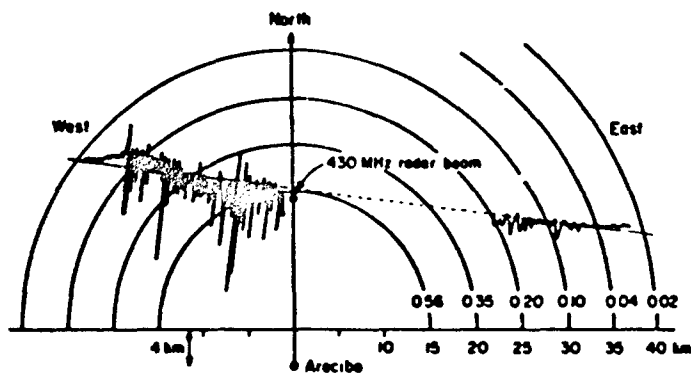


Fig. 9. The geometry at the reflection altitude (200 km) of the heating wave. The semicircles show the distance from the center of the heating beam, which is 4 km north of the point directly above Arecibo, and the relative intensity of the beam. The satellite path is shown passing 15 km north of the center, with the electron density irregularities measured in situ shown located appropriately, and the size of the 430-MHz radar beam shown approximately to scale. (Farley et al., 1983).

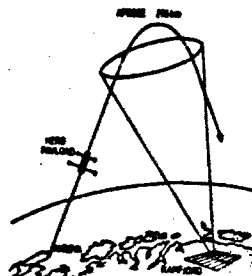
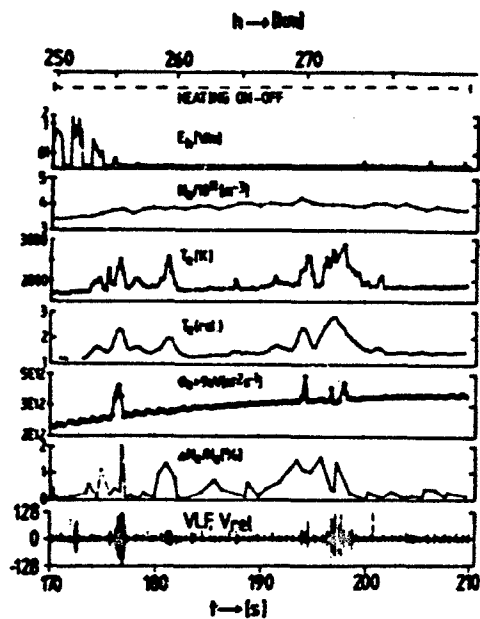
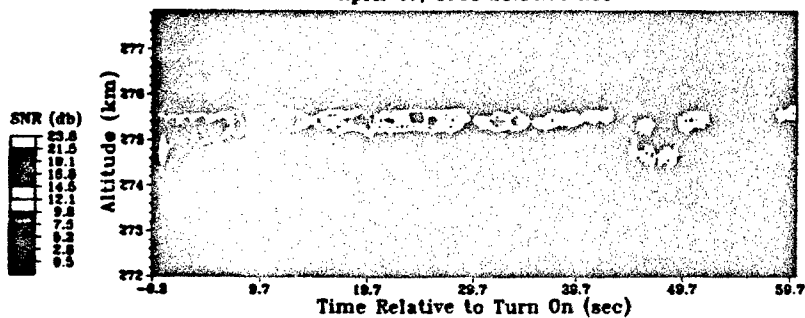


Fig. 10(a) Survey of bare rocket data obtained near and above the Tronoe HF modified region. (b) The geometry of the bare trajectory and the beam of the heating wave. (Røse et al., 1985).

Downshifted Plasma Line  
April 27, 1988 21:32:00 AST



Downshifted Plasma Line  
April 27, 1988 21:32:00 AST

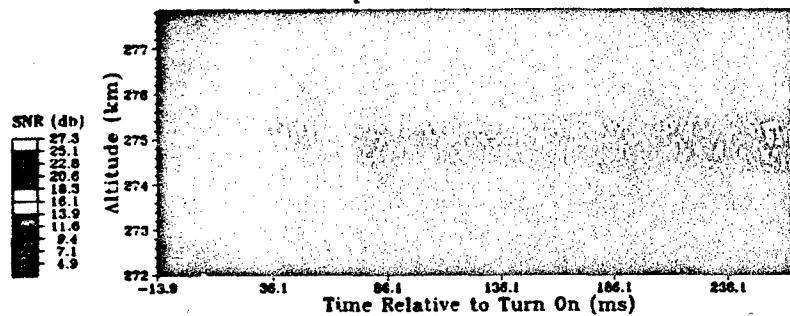


Fig. 11. Fine resolution altitude profiles showing plasma line response to HF turn-on at Arecibo, over the first minute (11a) and first 250m (11b) after turn-on. (Djuth and Sulzer, 1990).

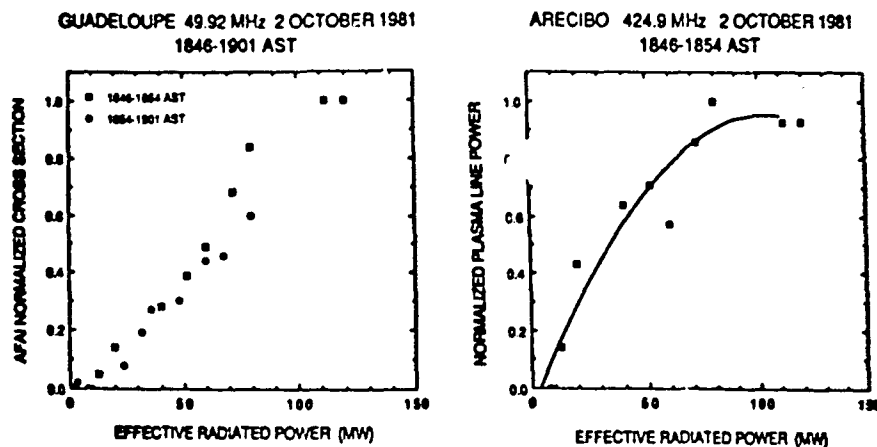


Fig. 12. HF power dependence of VHF coherent backscatter power (linear) and UHF incoherent plasma line (saturates) simultaneously measured in the same volume of space over Arecibo. (Noble and Djuth, 1990).

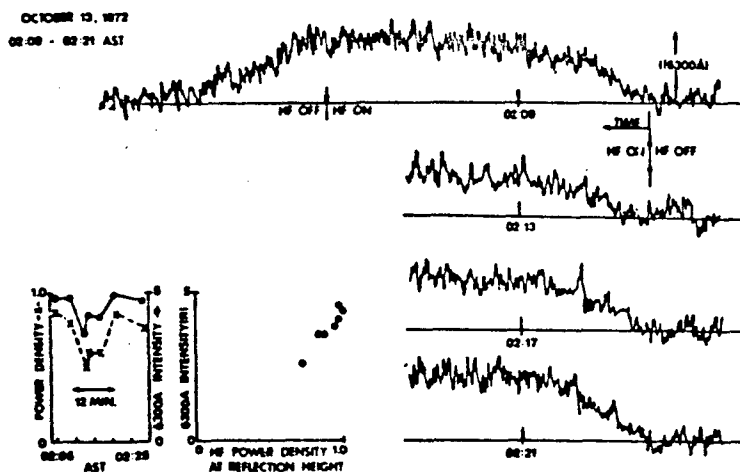


Fig. 13. HF power dependence of the 6300 Å intensity enhancement. Between 0205 and 0230 AST on 13 October 1972, there was a series of 2 min on, 2 min off cycles of the HF heater, operating in e-mode, during which the power density delivered to the ionosphere varied because of changes in HF power level and ionospheric reflection altitude. The right-hand portion of the figure shows the 6300 Å intensity data, with time increasing to the left. The left-hand insert shows the similarity of the time-variations of the 6300 Å enhancements (top line) determined after the initial exponential increase, and of the relative power density at the reflection altitude (bottom line). The right-hand insert suggests a linear relationship between these quantities. (Carlson et al, 1982).

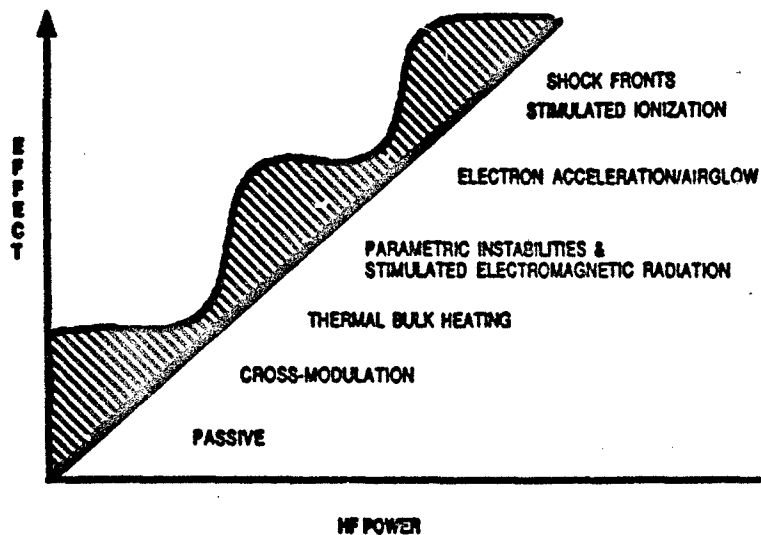


Fig. 14. Hierarchy of Heater Thresholds, illustrating discontinuous changes in plasma response to continuously increasing HF power which drives the plasma past higher-power density thresholds.

#### DISCUSSION

D. PAPADOPOULOS, US

In the time evolution of instabilities under constant HF driver, it is important to note that we are observing the evolution of the plasma state toward a "fully developed" turbulence state (i.e., interaction of Langmuir solitons, their associated cavitons and the suprathermal electrons) rather than new instabilities dominating at various times. Such situations have been analyzed over the last fifteen years in plasma physics (i.e., electron beam plasma interactions and laser fusion).

#### AUTHOR'S REPLY

It is indeed fair to say that the change in character of the observed echo (of Fig. 11a) is attributable to a change in the state of the plasma between the initial growth and the following many seconds. After tens of seconds a different instability (thermal self-focussing) interpretation best fits the data. However, to me, the main issue and challenge to the theoretical/experimental team is: to maintain a good enough dialogue to achieve theoretical definition and experimental measurement of critical discriminators to test and validate alternate theoretical hypotheses and descriptions; and to intelligently plan for future heater thresholds (Fig. 14).

E. SCHWEICHER, BE

Why do you see only odd harmonics of the ion-acoustic wave in the HF produced instabilities?

#### AUTHOR'S REPLY

It is a consequence of satisfying the geometry for reception of echoes along the incoherent scatter radar line of sight and the conservation of momentum between the interacting waves. It can be seen from construction of a  $k$  vector diagram for the waves.

# REVIEW OF SOVIET IONOSPHERIC MODIFICATION RESEARCH

by

Lewis M. Duncan and Robert L. Showen  
 Cleveland University SRI International, 30160  
 Cleveland, OH 44103 333 Ravenswood  
 United States Menlo Park, CA 94025  
 United States

## Summary

We have reviewed and provided a technical assessment of Soviet research of the past five to ten years in ionospheric modification by high-power radio waves. This review includes a comprehensive survey of Soviet published literature, conference proceedings, and direct discussions with the involved Soviet researchers. The current state of the art for Soviet research in this field is evaluated, identifying areas of potential breakthrough discoveries, and discussing implications of this work for emerging technologies and future applications. This assessment is divided into the categories of basic research, advanced research, and applications. Basic research is further subdivided into studies of the modified natural geophysical environment, nonlinear plasma physics, and polar geophysical studies. Advanced research topics include the generation of artificial ionization mirrors and high-power oblique propagation effects. A separate comparative assessment of Soviet theoretical work also is included in this analysis. Our evaluation of practical and potential applications of this research discusses the utility of ionospheric modification in creating disturbed radio wave propagation environments, and its role in current and future remote-sensing and telecommunications systems. This technical assessment does not include consideration of ionospheric modification by means other than high-power radio waves.

The Soviet effort in ionospheric modification sustains theoretical and experimental research at activity levels considerably greater than that found in comparable programs in the West. Notable strengths of the Soviet program are its breadth of coverage, large numbers of scientific participation, theoretical creativity and insight, and its powerful radio wave transmitting facilities. Weaknesses in the Soviet effort include computational limits in numerical analysis of nonlinear processes, inferior experimental diagnostic capabilities, and an apparent tendency of experimental programs to validate theoretical predictions as opposed to exploring new phenomena. A recent review of Soviet ionospheric modification research is given by Migulin and Gurevich (1).

## Introduction

Radio wave propagation through the upper atmosphere is inherently a nonlinear process. As the radio wave energy density delivered to the upper atmosphere is increased continuously, the response of the medium and its associated influence on wave propagation changes discontinuously. At sufficiently high powers, radio waves are capable of significantly modifying the medium through which they propagate. The region of the atmosphere with the greatest effect on radio waves and most susceptible to change by them is the ionosphere (roughly 50 to 1000 km), which is weakly ionized by solar radiation. This weakly ionized plasma is a subject of great interest in basic plasma physics research. Some of the nonlinear wave-plasma interactions observable in the ionosphere are fundamental processes, with application to many other areas of plasma physics, but which because of associated large spatial and temporal growth scales are not easily reproduced and investigated in traditional laboratory plasmas. Furthermore, transionospheric propagation, ionospheric reflection, and ionospheric refraction are key elements in numerous civilian and military telecommunications and remote-sensing systems operating at radio frequencies. Nonlinear self-action effects of radio waves on the medium through which they are travelling may act to enhance or degrade system performance at high frequencies, as well as to establish absolute performance limitations. In addition, induced ionospheric modifications may influence, or even disrupt, the operation of other radio frequency systems relying on propagation through the modified region. The controlled generation or accelerated dissipation of ionospheric disturbances may be used to produce new propagation paths, otherwise unavailable, appropriate for selected rf missions. As a result, the study of ionospheric modification by high-power radio waves is motivated by the diversity of applications of radio waves to perturbational investigation of the ambient atmosphere, to basic plasma physics research using the near-earth space environment as a natural plasma laboratory-without-walls, and to direct measurements of the influence of the ionosphere on rf systems operations.

The Soviet effort in ionospheric modification continues to maintain theoretical and experimental research at activity levels considerably greater than those found in comparable Western programs. The Soviets have approximately ten times as many personnel involved as are active in the United States, although the ratio is smaller (a factor of two or three) when evaluated in terms of researchers demonstrating sustained participation over several years. Soviet high-power high-frequency transmitting facilities for ionospheric modification are both more powerful and numerous than similar facilities in the West, and appear to be operated on a more regular basis. Known Soviet transmitting facilities are described in Table 1, providing our best estimates of location, frequency range, power, and other operating characteristics. Figure 1 shows schematically the location of each facility and its approximate conjugate point. In contrast to Soviet facilities, modification facilities in the West enjoy superior diagnostic capabilities, at least as needed for the study of basic physical processes. Whereas Western theoretical research has emphasized numerical analysis and computer simulations, the predominant Soviet theoretical effort has used a more intuitive analytical approach, with noteworthy successes in addressing

weakly nonlinear phenomena using approximation techniques. This approach in large part is the result of limited Soviet computational facilities. Nevertheless, the Soviets maintain a theoretical effort of exceptional quality and insight.

As terms of performance, Soviet theoretical research tends to lead their experimental ionospheric modification programs. An apparent inclination toward stressing experimental confirmation of theory is a characteristic unique to Soviet ionospheric modification research. In the West, experimental results are considered to be of greatest importance when they discover some unexpected feature or new ionospheric behavior, beyond simple confirmation of theoretical predictions. The Soviet experimental tendency toward reporting theoretically expected results may be a consequence of data selectivity based on statistical uncertainties or ambiguous diagnostic measurements (making new discoveries more difficult to substantiate or rigorously reproduce), or perhaps in some isolated cases as a conformist response to the acknowledged hierarchy of Soviet scientific research in this field, in which recognized theorists and their studies are held in high regard. For whatever reason, Soviet ionospheric modification research has not demonstrated an exploratory experimental effort to complement and challenge their theoretical creativity.

Table 1. Soviet ionospheric modification facilities.

Facility / Site	Organization	Frequency (MHz)	ERP (MW)
Zelenogradskaya (near Moscow)	NIIR	1.35	1000, pulsed 40, CW
GISSAR (Dushanbe)	IZMIRAN/IPFAN	4.5	80
SURA (near Gorkii)	IPFAN	5-10	400
ZIMENKI (near Gorkii)	IPFAN	4-6	20
Monchegorsk (near Murmansk)	PGI/IZMIRAN	3.3 15	10 •
Khar'kov	KPI	4.7-11 4.7-11	10 400

#### *Geophysical Effects*

HF modification of the ionosphere develops discontinuously. As increasing energy delivered to the ionosphere exceeds the limiting capacity of each dissipative process, the ionospheric response cascades discontinuously to ever greater nonlinear saturation processes. In addition, each new level of nonlinearity is accompanied by a host of secondary interactive phenomena. This concept, with associated nonlinear process, is shown schematically in Figure 1. Historically, theory has been relatively poor at predicting the thresholds for these discontinuous leaps in nonlinear physics behavior, as well as at anticipating what new nonlinear processes are to assume dissipative predominance at each higher level. However, theory has been comparatively quick to explain experimental results once these new nonlinearities are observed.

The Soviet Union conducts experimental research using facilities with greater frequency coverage and greater radiated power capacity than current facilities in the West, and thus enjoys a considerable potential advantage in terms of generating, studying, and exploiting new atmospheric modification effects. However, because of the general inability of theoretical analysis to predict these new processes and associated phenomena, and because of the generally less exploratory nature of Soviet experimental studies, their research has yet to apply this potential advantage into advanced systems operations. We cannot accurately assess the importance or systems applications these processes might afford, although several potential applications are being suggested and discussed in this symposium. We can speculate, based on comments found in the Soviet literature, that they are exploring the use of such geophysical modifications to alter optical (visible and infrared) background atmospheric emissions; to either enhance or degrade, controllably, selected RF communications and remote-sensing operations; to provide for low data rate communications with magnetic conjugate regions; and to affect magnetic and energetic particle activity in the near-earth space environment. That such applications have found notice in the Soviet research is in itself not surprising, since similar issues obviously have been addressed in the Western ionospheric modification research.

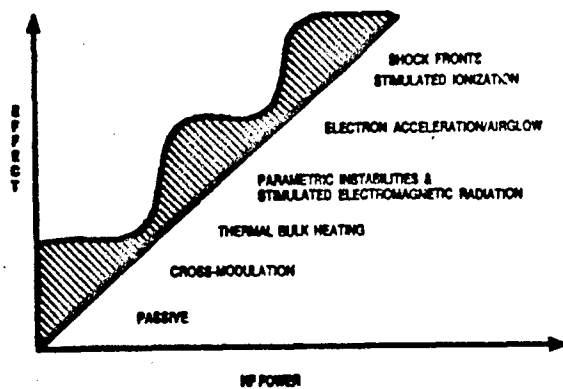


Figure 1. Hierarchy of HF ionospheric modification thresholds (H. C. Carlson, FASAC Report TAR-4040, 1983).

#### *Nonlinear Plasma Physics*

Publications and reports of Soviet studies of plasma instabilities in the ionosphere have increased dramatically in recent years. These studies are motivated more by the importance to basic plasma physics research than by a desire to better understand the natural geophysical environment. Plasma instabilities can give rise to ionospheric electron density irregularities, plasma turbulence, stimulated electromagnetic emissions, accelerated electrons, and larger-scale density redistributions. Notably, these plasma instabilities are often the driving processes behind the geophysical modifications discussed above. As such, the study of HF-induced plasma instabilities in the ionosphere is appropriately considered as an essential basic research supporting the development of practical telecommunications and remote-sensing applications. This connection is openly discussed in the Soviet literature. Recent experimental results continue to be limited by diagnostics that are relatively poor in comparison to those available in the West. However, there are exceptions, with state-of-the-art equipment such as HF digital sounders beginning to be used in some of these experiments. Another notable trend in this area is the appearance in Soviet publications of detailed information about their facilities and experimental methods, and an open willingness to participate in mutually beneficial collaborative research. Experimental observations are supported by careful data analysis and high quality theoretical calculations.

#### *Polar Region Studies*

Considerable recent attention in the West has been given to HF ionospheric modification at high latitudes, with relatively new HF facilities operating at Tromsø, Norway and Fairbanks, Alaska, and an even more powerful new facility being planned for near Fairbanks in the future. Given that ionospheric modification research is very active in the Soviet Union, and that the Soviets also maintain a vigorous program in polar ionospheric research, it is quite surprising to find so little reported activity or apparent interest in ionospheric modification in polar regions. All of the Soviet HF facilities from which data have been reported operate in mid-latitude geophysical environments. A new 15-MHz facility is under development by the Polar Geophysical Institute, but only one transmitter/antenna element has been constructed and operated. Eventually this facility may become a uniquely powerful HF transmitting site, but the pace of development is relatively slow for now.

#### *Oblique Propagation*

Oblique high-power radio wave propagation is an area of great interest, but of limited reported activity within Soviet ionospheric modification research. Its primary application is to over-the-horizon radars, and possibly to high-power short-wave radio communications over long propagation paths. At sufficiently high power densities, obliquely incident electromagnetic waves can modify the ionospheric plasma through which they propagate so as to affect their system performance, as well as the performance of other systems relying on radio propagation through this modified region. Currently reported Soviet research results typically come from either very dated or unusually low power experiments. Although basic experimental and theoretical research in high-power oblique propagation has obvious telecommunications and radar applications, no specific reference to these systems is found within the published Soviet literature. This may be a consequence of strong organizational distinctions between Soviet basic research and systems applications, or the result of a more deliberate programmatic separation of research.

### *Theoretical Research*

Soviet theoretical work on ionospheric modification encompasses many different fields of research. These studies must address a diverse spectrum of nonlinear processes and phenomena, often mutually interactive and operating over a wide range of spatial and temporal scales. There is no decisive superiority of the Soviet or Western theoretical programs. As noted earlier, experimental observations frequently serve to motivate theoretical research. Soviet theoretical efforts have in the past often responded to observations reported from experiments in the West. However, as modification science in the West becomes increasingly interested in highly nonlinear processes such as strong Langmuir turbulence effects, Soviet theoretical analyses are significantly disadvantaged by their lack of access to sophisticated computer simulations.

### *Artificial Ionization*

High-power electromagnetic radiation is capable of producing and maintaining regions of artificial ionization in the middle atmosphere and lower ionosphere. The Soviets have conducted an orderly and innovative program combining theoretical studies, numerical modeling, laboratory observations, and atmospheric experiments. The concept of using dual intersecting high-power microwave beams to define and sustain an ionized region originated in the Soviet Union (2,3). Achieving steady progress over the past decade, the Soviets have developed a well-defined recommendation for a prototype facility using a multiple-pulse intersecting beam method of ionizing the neutral atmosphere. This approach, leading to artificial ionization radio reflectors, has been described in the Soviet literature as offering new propagation paths for a wide variety of civilian and military RF applications, including enhanced long-range communications, improved over-the-horizon radar coverage, and the possibility of secure military communications avoiding disturbed environments. A decision to proceed with facility development has not yet been made. Artificial ionization studies in the West have been pursued only for about the last five years, but to our advantage the artificial ionization process is physically complex and best can be accurately treated using nonlinear kinetic theory and sophisticated computer simulations. Many difficult problems remain for both Soviet and Western programs to convert a basic physics research concept into applied operational systems. However, the potential reward and scope of application is so great, to the point of revolutionizing selected areas of RF propagation and remote-sensing, that continued study of artificial ionization processes seems assured. Opportunities for cooperative research studies with the Soviets in this area appear very realistic, with a joint symposium recently held discussing artificial ionization research results and future plans (as part of the International Workshop on Nonlinear and Turbulent Processes in Physics, Kiev, USSR, October, 1989) and additional meetings scheduled (International Workshop on Strong Microwaves in Plasmas, Suzdal, USSR, September, 1990).

Table 2. Summary of ionospheric modification effects.

Ionospheric Region	Altitude (km)	Perturbing Frequency	Practical Effects
•	20-90	1 MHz - 10 GHz	Electron density production
D	70-95	10 kHz - 30 MHz	Micropulsation to VLF generation Increase electron energy, density Nonlinear interactions HF absorption Self-action effects
E	95-120	3 MHz - 10 MHz	Ionization irregularities Increase electron energy Modify electron density Instability excitation HF-VHF refraction
F	150-450	3 MHz - 30 MHz	HF-VHF refraction and backscatter Increase electron energy Modify electron density Field-aligned striations Optical emissions Instability excitation Plasma and em emissions Strong Langmuir turbulence



### Applications

Ionospheric modification research is motivated in part by its practical and potential applications. As long as systems rely on atmospheric propagation as an integral component of their overall performance, the study of atmospheric disturbances, both natural and man-made, will be an important field of study. As described in the preceding sections, ionospheric modification offers opportunities to introduce controlled perturbations into the ionosphere, selectively enhancing or degrading specific telecommunications systems performance. Soviet studies openly discuss this motivation for their research;

... there are sure to be a number of practical applications of effects resulting from radio wave modifications of the ionosphere. Here it is sufficient to point out the application to radio communications at distances up to 3000 km, using aspect-sensitive field-aligned scattering from artificial small-scale irregularities, the use of the same effect for radio wave injection into the ionospheric waveguides, and the improvement of very long-range HF communications with satellites. Such reasons underlie the considerable Soviet interest in investigations of nonlinear phenomena ... (4)

As described, research goals with system applications include establishing limitations imposed by radio wave self-action effects, controlling disturbed environments through which other systems must operate, and providing propagation paths otherwise unavailable for new RF systems operations. A summary of possible controlled atmospheric perturbations, as discussed in the Soviet literature, is presented in Table 2. At this time, the most promising practical applications of ionospheric modification appear to be radio frequency generation by modulation of ionospheric currents or nonlinear beat wave mixing; enhanced VHF/UHF propagation using artificial irregularities and field-aligned scatter; ionospheric studies exploiting HF-induced optical emissions; and HF over-the-horizon range foreshortening and VHF/UHF range extension using scatter from artificially ionized regions. Within these topics, most Soviet applied work seems to be in the area of exploring field-aligned scatter, with a number of recent reports investigating various qualities and conditions of the irregularity development and its scattering characteristics. Potential applications of such research are shown schematically in Figure 2. Recent renovation and upgrading of the gyrofrequency high-power facility near Moscow indicates a renewed interest in D- and E-region heating, with direct applications to radio frequency generation. This application is illustrated schematically in Figure 3. The Soviets have conducted the most thorough analysis to date on expected artificially excited optical emissions, but no evidence suggests that an active experimental program exists in this area (5). The Soviet work on artificial ionization is quite advanced, with open discussion of the many possible telecommunications applications such a system might support. However, any accelerated efforts toward construction of a prototype facility is not apparent. Proposed applications geometries are shown in Figure 4, and a Soviet cartoon of applications is presented in Figure 5. Applications to selected system degradations are shown schematically in Figure 6. Clearly the range of potential applications is diverse, and Soviet science seems well aware of these opportunities.

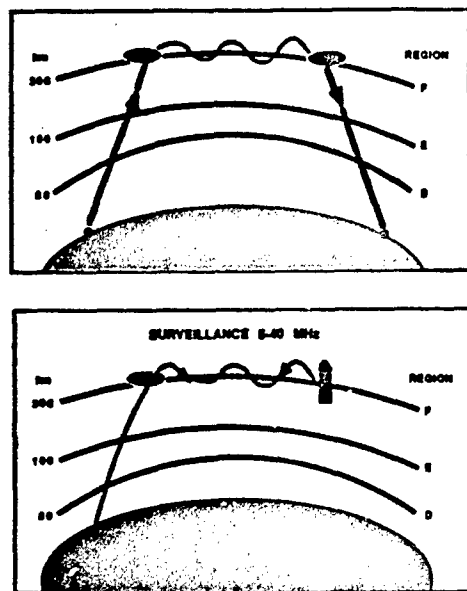


Figure 2. Long-range HF propagation (N. C. Gerson, FASAC Report TAR-4040, 1988).

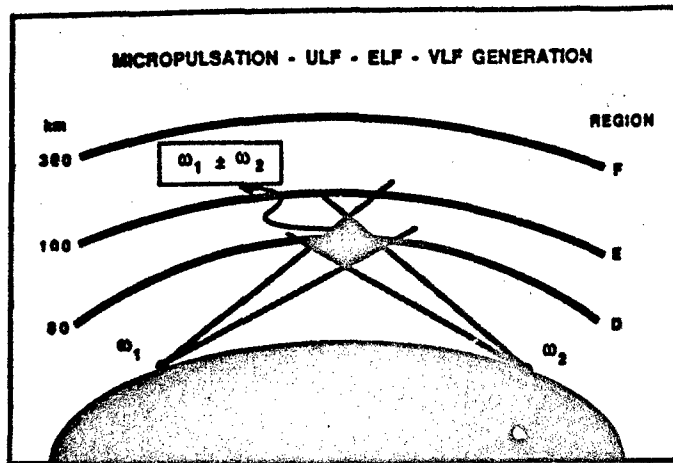


Figure 3. Radio wave generation in the perturbed ionosphere (N. C. Gerson, FASAC Report TAR-4040, 1988).

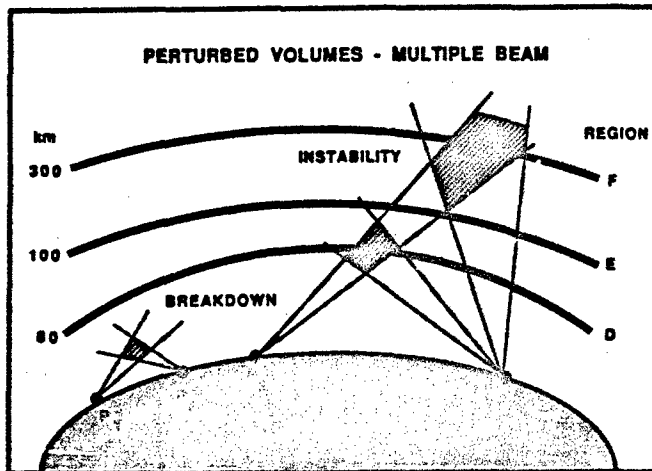


Figure 4. Crossed-beam ionospheric modification application geometries (N. C. Gerson, FASAC Report TAR-4040, 1988).

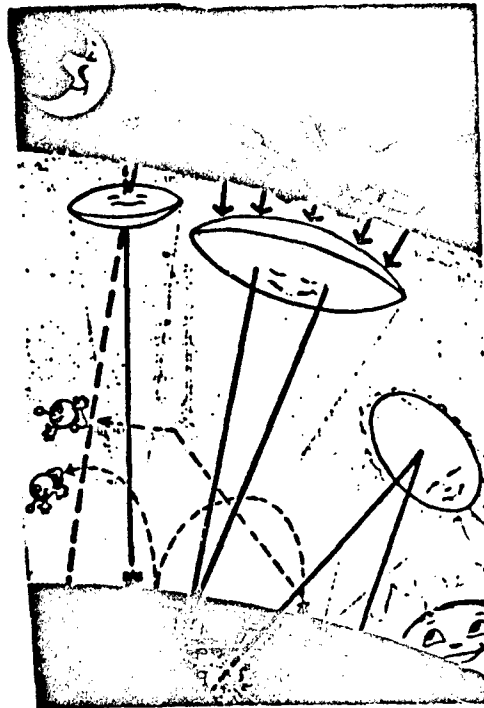


Figure 5. Cartoon of telecommunications applications of artificial ionization (A. Spiridonov, "To control the ionosphere," *Sputnik*, November, 1986).

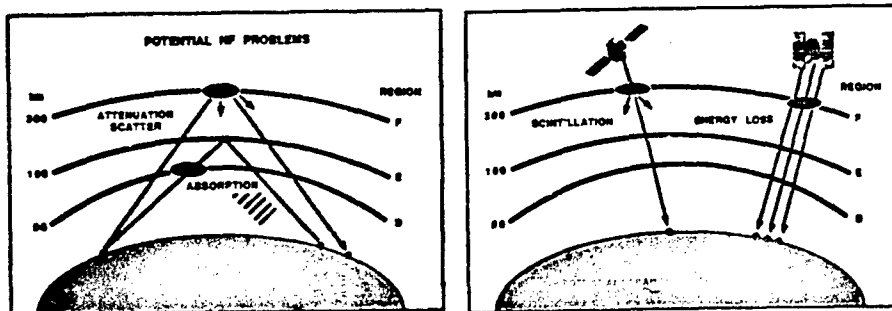


Figure 6. Scenarios for telecommunications degradations using HF ionospheric modification (N. C. Gerson, FASAC Report TAR-4040, 1988).

### Conclusions

Soviet research in ionospheric modification continues both to address fundamental problems in plasma physics and geophysical research, and to demonstrate the application of this approach as a means of controlling the natural environment, providing enhanced or new opportunities in remote-sensing and telecommunications. Applied work in ionospheric modification tends to be in areas of emerging technologies, not breakthrough technologies. Because of efforts in the past several years to openly discuss ongoing studies and exchange research results, to hold joint research symposia, and to support collaborative research programs, we do not believe the West is imminently susceptible to significant technological surprise from Soviet ionospheric modification research. Indeed, the opportunities for cooperative and mutually beneficial research have never been better.

**Acknowledgments.** This study is the outgrowth of work initiated under contract to the Foreign Applied Sciences Assessment Center, Science Applications International Corporation. The current study was conducted with support from the U.S. Air Force Geophysics Laboratory (AFGL) through Los Alamos National Laboratory. The author gratefully acknowledges the original contributions to the FASAC technical assessment report TAR-4040 (1983) by H. C. Carlson, Jr., F. T. Djuth, J. A. Fejer, N. C. Gerson, T. Hagfors, and D. B. Newman, Jr. We also wish to thank P. A. Kossey, W. T. Armstrong, and G. Milikh for helpful comments and suggestions.

### References

- (1) Migulin, V. V. and A. V. Gurevich, "Investigation in the USSR of nonlinear phenomena in the ionosphere," *J. Atm. Terr. Phys.* 47 (1985), 1181.
- (2) Gurevich, A. V., Nonlinear Phenomena in the Ionosphere, New York-Berlin, Springer-Verlag, 1978.
- (3) Gurevich, A. V., "Ionization of the lower ionosphere under the effect of strong radio pulses," *Geomagn. Aeron.* 12 (1979), 428.
- (4) Gurevich, A. V. and V. V. Migulin, "Investigations in the USSR of nonlinear phenomena in the ionosphere," *J. Atm. Terr. Phys.* 44 (1982), 1019.
- (5) Gurevich, A. V. and G. Milikh, "Spectroscopy of the ionosphere perturbed by powerful radio waves," *Geomagn. Aeron.* 24 (1984), 602.

## DISCUSSION

R. F. BENSON, UK

Scientists from the USSR have also been active in ionospheric modification due to satellite-borne transmitters, i.e., ionospheric topside sounders. In this case the high power is due to the in-situ nature of the transmitter. Indeed, one of the main effects they have studied concerns electron acceleration due to the sounder pulse, and electron acceleration was one of the effects in the high power portion of your "Effect vs RF Power" figure (taken from H. C. Carlson). They [Gal'perin et al., Detection of electron acceleration in the ionospheric plasma under the influence of high-power radio radiation near the local plasma frequency aboard the space vehicle Interkosmos 19, Cosmic Res., 19, 22-29, 1981] were the first to investigate this effect which has also been observed with the ISIS topside sounders [James, H. G., Sounder-accelerated particles observed on ISIS, J. Geophys. Res., 88, 4027-4040, 1983]. More recently they have correlated the electron heating with the frequency of the responsible sounder pulse and attempted to relate them to specific sounder-stimulated plasma resonances [Shuiskaya et al., Resonant heating of the ionospheric plasma by powerful radiopulses aboard the Interkosmos-19 and Cosmos-1809 satellites, Planet. Space Sci., 38, 173-180, 1990]. Their continued interest in space-borne transmitters for research is illustrated by the recent mission "ACTIVE".

## AUTHOR'S REPLY

No reply needed.

D. PAPADOPOULOS, US

In your report there was a mention of one gyrofrequency facility with more than 1 GW of power at Dushanbe. Is this still correct?

## AUTHOR'S REPLY

The report refers to a gyrofrequency heating facility at Zelenogradskaya, near Moscow, with a pulsed ERP of 1 GW. This facility has an antenna array with approximate gain  $G = 20$  dB. The pulse durations are 500 microseconds with a pulse repetition period of 20 milliseconds. The CW ERP of this facility is 40 MW.

## HISTORICAL OVERVIEW OF HF IONOSPHERIC MODIFICATION RESEARCH

by

William E. Gordon  
Rice University, P.O. Box 1892  
Houston, Texas 77251  
United States

and

Lewis M. Duncan  
Department of Physics and Astronomy  
Clemson University  
Clemson, SC 29634-1901  
United States

Radio waves have inadvertently modified the Earth's ionosphere since the Luxembourg observations of Tellegen in 1933 and perhaps since Marconi in 1901. The history of ionospheric modification by radio waves is reviewed, beginning with Marconi, describing the Luxembourg effect and its explanations, and its early use to deduce the properties of the lower ionosphere in the 1930s. The measurements became more sophisticated in the 1950s, leading to the call for high-power high-frequency modification experiments in the upper ionosphere. Beginning in 1970, radio facilities became available of sufficient powers to induce changes in the ionospheric plasma detectable by a wide array of diagnostic instruments and techniques. A summary of these effects is presented based upon work up to 1990. These studies were originally motivated as a means of better understanding the natural ionosphere using a weak perturbational approach. However, a rich spectrum of nonlinear wave-plasma interactions was quickly discovered and ionospheric modification research became strongly motivated by issues in basic plasma physics. The ionosphere and near-Earth space are now exploited as an exceptional plasma laboratory-without-walls for the study of fundamental plasma processes requiring large spatial or temporal scales. Here we present a brief overview of these processes and phenomena, illustrated using results obtained from the Arecibo ionospheric modification facilities. The lessons learned and phenomena explored thus far offer many opportunities for controlling the ionospheric environment critical to many civilian and military telecommunications systems, both to disrupt systems normally operational and to create new propagation paths otherwise unavailable.

### 1. INTRODUCTION

Modification of the ionosphere by high-power high-frequency (HF) radio waves has been intensively investigated over the past two decades. This research has yielded direct advances in aeronomy, geophysics, and plasma physics with applications to telecommunications, remote sensing, laser fusion physics, and astrophysics. In addition, ionospheric modification has historically provided for fruitful interactions of plasma theorists and radio experimentalists.

There being almost no linear effects of powerful radio waves on the ionosphere, we will concentrate on the nonlinear effects. To put the subject in perspective we trace its history beginning in the early 1930s and highlight the important events up to the late 1960s. We then shift to a phenomenological approach and deal, in order, with ohmic heating, parametric instabilities, self-focusing and kilometer-scale filamentation irregularities, meter-scale irregularities, strong Langmuir turbulence, pump modulation and wave generation effects, and a collection of recently discovered phenomena. Many of these processes are illustrated using results from the Arecibo ionospheric modification facilities. We conclude with a brief discussion of the diverse range of telecommunications applications to which ionospheric modification techniques might contribute.

#### 1.1 HISTORICAL PERSPECTIVE

On December 12, 1901, in a bold experiment that he felt would work, but was not prepared to explain, Marconi transmitted the code letter "S" from Cornwall, England and received it in St. Johns, Newfoundland, a distance of about 3000 km around the curvature of the Earth's surface. The success of this pioneering venture, although not a demonstration of a nonlinear ionospheric effect, started a revolution in long distance communication, ushered in an era of international science, and started a pattern of experimental observation stimulating rapid development of radio science theory. In this case, Kennelly<sup>1</sup> and Heaviside<sup>2</sup> quickly responded by independently postulating in 1902 the presence of a conducting reflecting layer aloft.

The proper beginning for radio modification of the ionosphere, however, is the report by Tellegen<sup>3</sup> in 1933 of the inadvertent modulation of the Beromünster (625 kHz) signal by the powerful signal of the Luxembourg transmitter (Figure 1). Tellegen interestingly titled his report "Interaction Between Radio Waves?" and within a year Bailey and Martyn<sup>4</sup> properly ascribed the observed cross-modulation to ionospheric changes produced by the Luxembourg radio waves. In particular, the Luxembourg wave changed the instantaneous electron collision frequency and thus the attenuation suffered by the Beromünster wave as it passed through the ionosphere near the Luxembourg transmitter, producing a modulation of the Beromünster signal patterned on the Luxembourg modulation.

In 1937 Bailey,<sup>5</sup> developing further the Luxembourg effect, suggested that if the disturbing waves were at a frequency near the gyrofrequency, the cross-modulation would be abnormally large. Some simple experiments supported this prediction<sup>6</sup> and it was later rigorously confirmed by Cutolo.<sup>7</sup>

Fejer<sup>8</sup> described a method using the cross-modulation techniques to obtain electron density and collision frequency profiles (Figure 2) in the D region ionosphere under certain assumptions. This technique compares the amplitude of a disturbed wave and an undisturbed train of wanted waves while altering the interaction height through changes in the relative time of the wanted wave and disturbing pulses. A powerful radio wave in the ionosphere not only is capable of applying its modulation to other signals passing through the same plasma, but also distorts itself in ways that have been described as self-demodulation<sup>9</sup> and nonlinear distortion.<sup>10</sup>

### 1.3 ACTIVE EXPERIMENTS

As the phenomenon of cross-modulation and wave self-interaction became better understood, a number of researchers began to recognize the potential of using high-power radio waves to modify the ionosphere in controlled experiments. In a direct extrapolation of the developing cross-modulation theory, Bailey and Goldstein<sup>11</sup> suggested using radio waves near the electron gyrofrequency to control ionospheric electron temperatures, thereby affecting temperature-dependent ionospheric processes such as diffusion, attachment, and recombination. They also suggested the complementary nature of controlled ionospheric experiments and laboratory plasma studies.

High-power radio-wave modification of the F-region ionosphere was proposed by Ginzburg and Gurevich<sup>12</sup> in 1960. Specific heating effects were investigated by Farley<sup>13</sup> and Gurevich,<sup>14</sup> estimating the expected increases in F-region electron temperatures and associated density redistribution resulting from plasma diffusion along the geomagnetic field lines. Bailey<sup>15</sup> also suggested using powerful radio waves to generate artificial airglow in the nocturnal E-region. Ginzburg<sup>16</sup> and Lombardini<sup>17</sup> investigated in detail the possibility of artificially ionizing the lower ionosphere by acceleration of electrons in the electric field of high-power radio waves, concluding that impractically high radiation power densities were necessary.

A collection of ionospheric modification techniques, known somewhat imprecisely as "ionospheric heating," began to emerge from the cross-modulation and wave-interaction studies. An early attempt (1963) to detect ionospheric heating effects with a relatively weak 7.7 MHz system was unsuccessful.<sup>18</sup> In an experiment investigating ionospheric absorption and associated recovery time constants, Klemperer<sup>19</sup> used the 50-MHz Jicamarca Radio Observatory facility to modulate the measured cosmic radio-noise intensity. And using Arecibo incoherent scatter radar measurements to infer changes in the electron temperature, Showers<sup>20</sup> investigated changes in the ionosphere under the influence of a high-power 40-MHz radio wave. These early experiments demonstrated that controlled ionospheric modification experiments were possible using suitably powerful facilities. Modern radio transmitters were being constructed capable of generating these powerful radio waves, leading to the development of several dedicated ground-based ionospheric modification facilities in the late sixties and early seventies.<sup>21-23</sup> More recently, new modification facilities have been operated at Arecibo, Puerto Rico; Tromsø, Norway and Fairbanks, Alaska.

### 2. HEATING

The original ionospheric modification experiments using high-power HF radio waves were intended to produce small perturbations in the local thermal balance as a tool to study heating and cooling processes, collision rates, and scattering cross-sections. The ionospheric D, E and F regions have been disturbed and then allowed to relax to ambient conditions (Figure 3) yielding heating and cooling time constants and electron density variations.<sup>24</sup>

As the electrons are heated in the lower ionosphere, the collision rate increases and hence the radio wave absorption becomes even more efficient. This amplification may lead to a process known as "thermal runaway" in which electron temperatures can rise to very high levels.<sup>25</sup> Experimentally, large temperature rises have been reported,<sup>26</sup> accompanied by increases of 25-30 dB absorption of radio waves passing through this region.

Cohen and Whitehead<sup>27</sup> reported a drop in signal strength of 10 dB for a wave reflected at the height of the disturbed F region. A similar result<sup>28</sup> is shown in Figure 4. Stubbe et al.<sup>29</sup> reported that the intensity of a wave reflected in the disturbed F region drops by up to 15 dB when the disturbing transmitter is turned on. Varying the transmitter power of the disturbing wave produced no change in the reflected wave field-strength when the ionosphere was "quiet," but the attenuation decreased when the disturbing wave power was decreased and the ionosphere was variable. Such results support the view that some signal losses in the ionospheric F region may be attributed to enhanced wave scattering from induced irregularities.<sup>30</sup>

Direct measurement of the ionospheric electron-temperature changes has been attempted using incoherent scatter radar techniques. Initial studies examined the heating and cooling time dependence on high-power HF pulsing near the HF reflection height.<sup>31</sup> Subsequent studies by Mantas et al.<sup>24</sup> extended this approach to include analysis of heating and cooling effects away from the reflection altitude, where heat conduction is responsible for spreading of the electron temperature enhancement outside of the region where the radio wave energy is deposited (Figure 5).

### 3. ENHANCED PLASMA WAVES

One of the more remarkable discoveries<sup>32</sup> of the early HF ionospheric modification experiments was the detection of a rich spectrum of plasma instabilities excited near the HF reflection height. These nonlinear wave-plasma interactions are usually attributed collectively to parametric instabilities, characterized by a pump or driving field whose energy cascades into plasma oscillations at lower natural resonant plasma frequencies and additional electromagnetic waves. In the present ionospheric modification experiments, the high-power HF electromagnetic radiation provides the initial driving field. The parametrically driven product waves include the longitudinal electrostatic electron plasma-wave and an ion-acoustic wave (parametric decay instability), the electron plasma-wave and a zero-frequency ion mode (oscillating two-stream instability), two electron plasma-waves at the quarter-critical density height (two plasmon decay instability), an ion acoustic wave and a scattered electromagnetic wave (stimulated Brillouin scattering), and an electron plasma-wave and a scattered electromagnetic wave (stimulated Raman scattering). In addition, the excited electrostatic plasma waves can reach sufficient intensities so as to act as pump waves for further parametric cascades.

These instabilities are driven by the ponderomotive or striction force.<sup>33,34</sup> The possibility of excitation of such instabilities in the ionosphere was first suggested by Perkins and Kaw.<sup>35</sup> Further refinements of this nonlinear wave-plasma interaction theory, as applied specifically to high-power ionospheric modification experiments, were contributed by DuBois and Goldman<sup>36</sup> and Fejer and Leer.<sup>37</sup> The experimental excitation of plasma waves (Figure 6) was first observed by Carlson et al.<sup>38</sup> and Wong and Taylor.<sup>39</sup> The resulting enhanced electrostatic turbulence is easily detected and studied using incoherent scatter radars. Echoes enhanced by up to several orders of magnitude are routinely observed at both the ion-acoustic and electron plasma-wave frequencies, at an altitude just below the HF reflection height (Figure 7). These enhancements are excited only for ordinary polarization of the incident pump radiation; extraordinary polarized waves do not reach the proper altitude for generation of these phenomena.

The enhanced electrostatic turbulence observed in radar experiments is generally attributed to parametric instabilities excited by the powerful HF pump wave. Many of the features observed in the fluctuation spectrum seem to correspond very closely with predicted parametric excitations. However, parametric processes are generally dominant in a weak turbulence

regime, as we shall discuss in a later section, some aspects of the high-power HF ionospheric modification results may require consideration of strong Langmuir turbulence effects.

Radar measurements of the spectra of the enhanced plasma waves (Figure 8) indicate a complex enhanced plasma wave structure. Additional spectral features have been associated with the saturation of the parametrically enhanced oscillations based on secondary parametric decay interactions, with the enhanced electrostatic plasma oscillations acting as new pump waves.<sup>40-42</sup> Additional spectral effects have been suggested based upon plasma wave propagation through the reflected pump wave Airy standing wave pattern,<sup>43</sup> and through natural or HF-induced ionospheric density ducts.<sup>44</sup>

Studies of the enhanced plasma line rise and decay time behavior have been conducted in a continuing series of pulsed HF experiments, beginning with initial measurements by Kantor.<sup>32</sup> Greatest interest among these studies has been given to understanding a process known as plasma-line overshoot. Immediately following turn-on of the HF pump wave, the observed enhanced plasma-line signal increases rapidly to a maximum and then relaxes back to a lower steady-state level. The specific time scales and overshoot amplitudes are variable depending on the background ionospheric conditions, HF pump frequency and power, and the length of the preceding HF off time. An example of the plasma-line overshoot is shown in Figure 9 from Duncan and Sherrin.<sup>45</sup> The spectrum of the developing enhanced plasma line overshoot was studied by Showen and Kim,<sup>46</sup> showing an evolution from a broad diffuse spectrum to one of sharp spectral peaks at the predicted parametric instability matching frequencies. The height of the enhanced plasma line during overshoot has been investigated by Duncan and Sherrin<sup>45</sup> and Djuth et al.<sup>47</sup> They found that a weak early signal originated from a height several kilometers above the main instability height, that the main overshoot instability developed in tens of milliseconds during which time the excitation height rose by about one kilometer above its initial appearance height, and that the excitation altitude range began as a very narrow layer but grew over several hundred milliseconds to encompass several hundred meters (Figure 10). A new observational technique has been developed more recently relying on an incoherent-scatter radar chirped frequency,<sup>48,49</sup> indicating that the HF-induced plasma-line signal originates at a height several kilometers above the natural plasma-line height at the pump frequency. These results, consistent with more steady-state observations of Muldrew and Showen<sup>50</sup> have been used to argue for the existence of ionospheric cavitons, and will be discussed below. An alternative explanation using wave ducting has also been proposed by Muldrew.<sup>51</sup> Observational limits on the role of Langmuir cavitons was discussed by Sulzer et al.<sup>52</sup> in particular describing detection of enhanced plasma line bursts occurring regularly with a quasi-period of 20-50 ms. Such regular repeatable features in space and time require significant additional theoretical and experimental work.

#### 4. SELF-FOCUSING

Large-scale (kilometer-size) field-aligned ionospheric electron-density irregularities are commonly generated during HF ionospheric modification experiments. These large-scale structures are believed to be responsible for the artificial spread-F detected by Utlaut et al.<sup>53</sup> with subsequent investigations by Utlaut and Violette,<sup>54</sup> Wright<sup>55</sup> and Rufensch.<sup>56</sup> Thome and Perkins<sup>57</sup> demonstrated the spatial relationship of large-scale irregularities to self-focussing processes. Complementary investigations have used incoherent-scatter radar observations to map the density irregularity structure,<sup>58</sup> while more recently incoherent-scatter radar results have been combined with AE satellite observations,<sup>59</sup> and radio-star scintillation measurements.<sup>60</sup> From these studies has emerged a consistent description of production of kilometer-scale irregularities attributable to thermal self-focusing of the incident HF pump radiation. Supporting theoretical studies have been conducted by Perkins and Valeo,<sup>60</sup> Crugin and Fejer,<sup>61</sup> and Perkins and Goldman.<sup>62</sup> More recently computer simulations of HF pump wave propagation through the ionospheric plasma have accurately modelled the self-focusing process.<sup>63</sup> Thermal self-focusing of the pump wave, leading to beam filamentation and density striation, develops on time scales of seconds to tens of seconds, but once excited can persist for tens of minutes. Pump power enhancement by self-focusing has been suggested as an explanation of the pre-conditioning phenomenon report by Morales et al.<sup>64</sup>

Incoherent scatter radar studies of HF-induced ionospheric irregularities rely on measurements of the pump-enhanced plasma waves discussed in Section 3. The amplitude of the enhanced plasma waves directly depends upon the local power of the pump electric field. In addition, because these enhanced waves are detected at only one altitude, systematic scanning of the narrow radar beam across the HF interaction region can yield a cross-sectional map representative of the local electric-field intensity. These two-dimensional maps of plasma-line intensity clearly show focusing of the incident HF beam and large-scale structuring of the illuminated plasma. As the radar beam remains fixed, ionospheric winds drift the large-scale structures through the beam. Combinations of fixed and scanning radar measurements, as shown in Figure 11, have been used to determine typical striation scale sizes of 0.5-1.5 km, as well as to monitor the background drift velocities. Variations in the height of the enhanced plasma lines also have been used to infer associated electron density variations of a few percent.

The influence of beam self-focusing and large-scale ionospheric irregularities, both natural and HF-induced, on other instability processes has been addressed by Muldrew.<sup>51</sup> The role of these ionospheric ducts in determining the interaction altitude and associated enhanced plasma-line amplitude appears to be an important consideration. In particular, HF ducting may help to explain the difference in observation height between natural photoelectron-enhanced plasma waves and HF-enhanced waves for the same observing frequency, and the high signal amplitudes detected for the Arecibo radar observational geometry.

#### 5. SHORT-SCALE IRREGULARITIES

One of the unexpected effects of the early HF ionospheric modification experiments was the generation of intense short-scale (metre-size) field-aligned density striations.<sup>65-67</sup> A number of theoretical models have since been proposed to explain their development.<sup>30,68-70</sup> Despite a great deal of experimental information on these aspect-sensitive short-scale striations, the responsible excitation mechanism has not yet been resolved.

Experimental studies of short-scale striations have involved the measurement of HF, VHF, and UHF coherent radar backscatter from the E- and F-region HF interaction volume. These echoes are highly aspect sensitive, indicating that the scattering structures are closely aligned to the magnetic field. Recent studies have concentrated on measurements of the striation growth and decay time constants, drift velocity, and dependence on incident HF wave power and polarization (Figure 12). Growth and decay time constants have been measured to be of the order of 10 ms.<sup>71</sup> The short-scale striations, similar to the parametrically enhanced plasma waves, develop only for O-mode HF polarization and only when the pump frequency is less than the ionospheric critical frequency. A strong correlation exists between the incident pump power and the short-scale striation scatter, as shown in Figure 13.



Belevov et al.<sup>67</sup> working with scattering from striations having cross-sections of 12 to 25 m find time constants of the order of 10 s using disturbing transmitter cycles of 7 min on and 8 min off and time constants of seconds when the disturbing transmitter is cycled 1 min on, 1 min off suggesting an "accumulation" effect. Coster<sup>73</sup> reports E- and F-region time constants of milliseconds and seconds, respectively, for scattering from 3 m diameter striations when the ionosphere is "pre-conditioned" (i.e., accumulation effect operating). Coster calculates that the observed time constants do not agree by one or more orders of magnitude with the values predicted by Grach et al.<sup>74</sup> or by Das and Fejer<sup>30</sup> for an inhomogeneous medium (horizontally stratified ionosphere).

The striation drift velocity has been found to be independent of the HF radiated power, but well correlated with the general F-region ionization drift.<sup>75</sup> A comparison of short-scale striation and large-scale irregularity drift velocities during a period of simultaneous observations, presented in Figure 14, shows reasonably good agreement between the two measurements.

## 6. STIMULATED ELECTROMAGNETIC EMISSIONS

In addition to the use of incoherent scatter radars to study the excitation of plasma waves in the ionosphere, recent studies have utilized direct observation of the scattered electromagnetic signals near the HF pump frequency. These signals accompany the instabilities responsible for the enhanced plasma oscillations reported by radar studies, and generally are described as stimulated electromagnetic emissions. Observations include reports of detection of signals associated with the parametric decay instability, stimulated Brillouin backscattering, and possibly ion Bernstein modes.<sup>76,77</sup> Experimental studies of this process continue, with recent studies reporting on harmonic and subharmonic excitations.<sup>78</sup>

## 7. AIRGLOW

High-power electromagnetic waves are also capable of generating enhanced nighttime airglow through a complex process, beginning with HF wave-particle interactions near the reflection height, accelerating electrons into a suprathermal distribution, transporting these energetic electrons down geomagnetic field lines out of the heated region, collisional excitation and de-excitation of ambient species such as atomic oxygen, and subsequent airglow radiation. The magnitude of the effect depends upon the amplitude, frequency and polarization of the incident pump wave. Extraordinary mode polarization waves collisionally heat the plasma without exciting plasma instabilities. Correspondingly this increase in electron temperature temporarily reduces the rate of ambient dissociative recombination, subsequently reducing the natural red (630.0 nm) and green (557.7 nm) line emissions. High-power ordinary mode pump waves excite plasma instabilities near the reflection height that result in acceleration of thermal electrons to energies of several eV. Collisional excitation of atomic oxygen then results in substantial airglow enhancements. This process is depicted schematically in Figure 15. Both thermal suppression and energetic electron enhancement effects have been reported in previous airglow emission studies.<sup>22,79</sup> More recently, significant airglow enhancements have been used to image the HF modification region using a charge-coupled device (CCD) camera.<sup>80,81</sup> Additionally, these observations have been associated with large-scale ionospheric plasma-density cavities recently detected in incoherent-scatter radar studies. Trapping and focusing of electromagnetic waves in these cavities is believed to produce relatively large populations of accelerated electrons. Convection of plasma cavities across geomagnetic field lines is believed to cause an accompanying refraction of the HF pump beam, giving rise to a quasi-cyclic process of cavity formation, convection, dissipation and reappearance. This process is shown in 630.0 nm airglow images in Figure 16. The dynamic nature of this process on time scales of tens of minutes is now believed to represent a major source of long-term variability in ionospheric modification experiments.

## 8. CAVITIES

HF-induced temperature fluctuations and density profile modifications generally are observed to be no larger than a few hundred Kelvin and a few percent  $\Delta n/n$ . However, under special HF and ionospheric conditions much larger modifications have been observed. Large density cavities have been measured in the nighttime F-region ionosphere with density depletions exceeding 50 per cent, extending hundreds of kilometers along the geomagnetic field.<sup>82</sup> These cavities are thermally driven, with electron temperatures in the depletions increased by factors of 3 to 4. Examples of this phenomenon are shown in Figs. 17 and 18. The depletion dynamics exhibit many of the characteristics associated with thermal cavities. Cavities are seen to develop on time scales of minutes and to decay on time scales of tens of minutes. Numerical modeling of large-scale ionospheric cavities has contributed to an improved understanding of the geometry and generation conditions specific to these features. As described above, the large-scale cavities also are observed to be capable of entraining the incident HF beam, allowing large refraction effects and substantial spatial displacements of the beam, as detected by the airglow observations. These measurements thus indicate that sufficiently high-power radio beams are more susceptible to large-scale directional errors because of these self-action effects and ionospheric cavity development.

Isaacs et al.<sup>49</sup> have developed a sensitive observing technique for observing irregularities in the variation of the electron density with height. The technique involves varying the frequency of the HF wave that generates plasma lines, i.e., Langmuir waves, in the ionosphere at a rate that matches the variation with height of the plasma as observed by a diagnostic radar (430 MHz) pulse traversing the medium. The frequency of the plasma-line receiver of the radar is varied at the same rate. Thus if the rate matches the height variation of the plasma over some interval, the contributions from each height in the interval will add up giving a single line in the output. Departures of the height variation from that used in the observing technique produce additional components to the narrow line associated with the match.

Having observed returns that have the additional component, they conclude by eliminating various other possible explanations that their observations are evidence of caviton production and Langmuir wave trapping. They are unable to give size or shape information since the diagnostic has beam width of the order of a kilometer and the technique averages along the beam path.

Isaacs's results are given an alternate interpretation by Fejer in a paper by Salzer et al.<sup>82</sup> that uses Mulkrew's pre-existing ducts<sup>51</sup> along the field lines.

## 9. STRONG LANGMUIR TURBULENCE

Undoubtedly one of the most exciting developments in ionospheric modification research in recent years has been the introduction of theoretical modelling and observational studies of strong Langmuir turbulence (SLT).<sup>83</sup> SLT is predicted to occur at thresholds only marginally above those of parametric instabilities. However, the SLT approach represents a significant departure from the conventional concepts associated with parametric instabilities and weak turbulence cascades. In particular, SLT offers new opportunities to explain experimental results apparently inconsistent with established modification region models relying primarily on weak turbulence theory.

In the strong Langmuir turbulence regime, a significant part of the excited high-frequency density fluctuations is expected to take the form of localized states, called cavitons, consisting of a high-frequency Langmuir field trapped in a self-consistent density depletion. The developed turbulent state is sustained by a dynamic cycle of nucleation, collapse and burnout. In this process, the localized fields are trapped in self-consistently evolving density wells which collapse to small dimensions as the nonlinear ponderomotive force dominates the linear pressure force. At scale sizes of 5-10 electron Debye lengths the trapped electrostatic energy is rapidly dissipated through electron acceleration. This electrostatic burnout leaves an empty density cavity which then evolves as a free ion sound pulse. Subsequently, the residual ion density wells provide nucleation centers for the excitation of new collapsing cavitons.

Several aspects of the experimental observations have been used to suggest that SLT effects are present. The spectrum of the HF-enhanced plasma lines show broad features at early times or weak powers that indicate the presence of excitation processes different than conventional parametric decay. The theoretically modelled dependence of excited signal intensities with orientation to the geomagnetic field predicted that enhancements would be  $10^4$  larger when measured along the field, but instead have been found to be of comparable magnitude in Arecibo's observations at an angle of  $45^\circ$  and EISCAT observations with an angle  $< 18^\circ$ . Furthermore, the HF-enhanced plasma lines are measured to come from altitudes 1-2 km higher than the natural photoelectron-enhanced plasma lines, and occasionally contain a "free mode" peak above the HF pump frequency corresponding to the free Langmuir wave dispersion. Weak turbulence theory generally evokes the influence of macroscopic density irregularities to qualitatively explain some of these effects; however, the growth time of the irregularities is at least several tens of milliseconds and cannot completely explain the described observations, particularly at very early times following HF turn-on.

Several of these observational effects are explainable in terms of Langmuir waves localized in cavitons.<sup>84,85</sup> However, these early studies often oversimplified soliton dynamic processes such as burnout accompanying Langmuir dissipation through Landau damping. The residual density cavities then could act as nucleation centers for new cycles of caviton growth and collapse.<sup>86,87,88</sup> Under some conditions it has been speculated that spatial correlations of caviton formation and collapse may develop. Allowance for all such processes is necessary to adequately study the longer-time dynamics of collapsing caviton turbulence.

## 10. ULF WAVES GENERATED BY TWO FREQUENCY HEATING OF THE IONOSPHERE

Non-linear mixing of two HF waves separated by a frequency difference of a Hertz to a kilohertz in the ionospheric plasma near the height where the HF matches the local plasma frequency is expected to produce ULF waves that may be observed on the ground.<sup>89</sup> Details are available in the Proceedings of this meeting.<sup>90</sup>

## 11. HF INDUCED STRIATIONS

Frey [private communication] has observed electron density profiles continuously over Arecibo while the HF transmitter is cycled on and off. Figure 19 shows the observations of density in shades of gray (dark is high density) on coordinates of local time and height running linearly from 70 to 500 km. The sudden changes with HF turn-on are due in part from increases in electron temperature of the plasma which has not been removed from the data in the figure. The figure is derived from power profiles observed by the diagnostic radar pointing essentially vertically and corrected for range. The striations are obvious.

## 12. THE FUTURE

Strong Langmuir turbulence effects have been demonstrated to contribute to the variety of phenomena and nonlinear interactions excited during high-power HF ionospheric modification experiments. Continuing investigations, both theoretical and experimental, will determine the spatial and temporal scales over which SLT effects are dominant in comparison to weak turbulence theory. Regardless of the outcome of these studies, the SLT work to date has conclusively demonstrated the vitality and richness of basic physics research ongoing in ionospheric modification investigations today. The ionosphere and near-Earth space environment will continue to serve as an exceptional plasma laboratory-without-walls.

## REFERENCES

1. Kennelly, A. E., On the elevation of the electrically-conducting strata of the Earth's atmosphere, *Elect. World (USA)*, 39 (1902) 473.
2. Heaviside, O., Telegraphy, *Enycl. Brit. (USA)*, 33 (1902) 215.
3. Tellegen, B. D. H., Interaction between radio waves?, *Nature (GB)*, 6 (1933) 840.
4. Bailey, V. A. and Martyn, D. F., Influence of electric waves in the ionosphere, *Phil. Mag. (GB)*, 26 (1934) 369.
5. Bailey, V. A., On some effects caused in the ionosphere by electric waves - Part 1, *Phil. Mag. (GB)*, 23 (1937) 929.
6. Bailey, V. A., Resonance in the interaction of radio waves (observational results), *Nature (GB)*, 139 (1937) 838.

7. Osoiko, M., Gyro-interaction of radio waves obtained by the pulse method, *Nature (GB)*, 160 (1947) 834.
8. Fejer, J. A., The interaction of pulsed radio waves in the ionosphere, *J. Atmos. and Terr. Phys. (GB)*, 7 (1955) 322.
9. King, I. W., Ionospheric self-demodulation and self-distortion of radio waves, *J. Atmos. and Terr. Phys. (GB)*, 14 (1959) 41.
10. Vilenkii, I. M., Nonlinear distortion of high-power radio waves propagated through the ionosphere, *Izv. VUZ Radiofiz. (USSR)*, 9 (1966) 649.
11. Bailey, V. A. and Goldsack, L., Control of the ionosphere by means of radio waves, *J. Atmos. and Terr. Phys. (GB)*, 12 (1956) 216.
12. Glasburg, V. L. and Gurevich, A. V., Nonlinear phenomena in a plasma located in an alternating electromagnetic field, *Usp. Fiz. Nauk. (USSR)*, 70 201; *Sov. Phys. Usp. (USA) (English Translation)*, 3 (1960) 115 and 175.
13. Farley, D. T., Artificial heating of the electrons in the F-region of the ionosphere, *J. Geophys. Res. (USA)*, 68 (1963) 401.
14. Gurevich, A. V., Effect of radio waves on the ionosphere in the vicinity of the F-layer, *Geomagn. and Aeron. (USA)*, 7 (1967) 230.
15. Bailey, V. A., Some possible effects caused by strong gyro-waves in the ionosphere, *J. Atmos. and Terr. Phys. (GB)*, 14 (1959) 299.
16. Glasburg, V. L., *Propagation of Electromagnet. Waves in Plasmas* (Pergamon, New York) 1960.
17. Lombardini, P. P., Alteration of the electron density of the lower ionosphere with ground-based transmitter, *Radio Sci. (USA)*, 69D (1965) 83.
18. Potemra, T., *Tech. Rep. 75* (Stanford Electronics and Radioscience Laboratory, USA) 1963.
19. Klemperer, W. K., Ionospheric cross modulation on the geomagnetic equator, *Tech. Note 211* (National Bureau of Standards, USA), 3 (1964).
20. Showen, R. L., Artificial heating of the lower ionosphere, *J. Geophys. Res. (USA)*, 77 (1972) 1923.
21. Gurevich, A. V. and Shlyuger, I. S., Investigation of nonlinear phenomena when powerful radio pulses propagate in the lower layers of the ionosphere, *Izv. VUZ Radiofiz. (USSR)*, 18 (1975) 1237.
22. Utisut, W. F. and Cohen, R., Modifying the ionosphere with intense radio waves, *Science (USA)*, 174 (1971) 245.
23. Gordon, W. E., Carlson, H. C. and Showen, R. L., Ionospheric heating at Arecibo: First tests, *J. Geophys. Res. (USA)*, 76 (1971) 7808.
24. Mantas, G. P., Carlson, H. C. and LaHoz, C. A., Thermal response of the F region ionosphere in artificial modification experiments by HF radio waves, *J. Geophys. Res. (USA)*, 86 (1981) 561.
25. Perkins, F. S. and Roble, R. G., Ionospheric heating by radio waves, *J. Geophys. Res. (USA)*, 83 (1978) 1611.
26. Shlyuger, I. S., Certain results of investigations of nonlinear effects in the E layer of the ionosphere, *Sov. Phys. JETP Lett. (USA)*, 20 (1975) 334.
27. Cohen, R. and Whitehead, J. D., Radio-reflectivity detection of artificial modification of the ionospheric F layer, *J. Geophys. Res. (USA)*, 75 (1970) 6439.
28. Utisut, W. F. and Violette, E. J., Some ionosonde observations of ionospheric modification by very high power, high frequency ground-based transmission, *Radio Sci. (USA)*, 9, (1974) 355.
29. Stubbe, P., Kopka, H., Jones, T. B. and Robinson, T., Wideband attenuation of radio waves caused by powerful HF waves: Saturation and dependence on ionospheric variability, *J. Geophys. Res. (USA)*, 87 (1982) 1551.
30. Dea, A. C. and Fejer, J. A., Resonance instability of small-scale field-aligned irregularities, *J. Geophys. Res. (USA)*, 84 (1979) 6701.
31. Showen, R. L. and Behnke, R. A., The effect of HF-induced plasma instabilities on ionospheric electron temperatures, *J. Geophys. Res. (USA)*, 83 (1978) 207.
32. Kasner, I. J., High-frequency induced enhancements of the incoherent scatter spectrum at Arecibo, *J. Geophys. Res. (USA)*, 79 (1974) 199.
33. Silin, V. P., Parametric resonance in a plasma, *Sov. Phys. JETP (USA)*, 21 (1965) 1127.
34. DuBois, D. F. and Goldman, M. V., Radiation-induced instability of electron plasma oscillations, *Phys. Rev. Lett. (USA)*, 14 (1965) 544.
35. Perkins, F. W. and Kaw, P. K., On the role of plasma instabilities in ionospheric heating by radio waves, *J. Geophys. Res. (USA)*, 76 (1971) 282.
36. DuBois, D. F. and Goldman, M. V., Nonlinear saturation of parametric instability: Basic theory and application to the ionosphere, *Phys. Fluids (USA)*, 15 (1972) 919.

37. Fejer, J. A. and Leer, E., Excitation of parametric instabilities by radio waves in the ionosphere, *Radio Sci. (USA)*, 7 (1972) 481.
38. Carlson, H. C., Gordon, W. E. and Showen, R. L., High frequency induced enhancements of the incoherent scatter spectrum at Arecibo, *J. Geophys. Res. (USA)*, 77 (1972) 1242.
39. Wong, A. Y. and Taylor, R. J., Parametric excitation in the ionosphere, *Phys. Rev. Lett. (USA)*, 27 (1971) 644.
40. Perkins, F. W. and Valeo, E. J., Thermal self-focusing of electromagnetic waves in plasmas, *Phys. Rev. Lett. (USA)*, 32 (1974) 1234.
41. Fejer, J. A. and Kuo, Y., Structure in the nonlinear spectrum of parametric instabilities, *Phys. Fluids (USA)*, 16 (1973) 1490.
42. Krueer, W. L. and Valeo, E. J., Nonlinear evolution of the decay instability in a plasma with comparable electron and ion temperatures, *Phys. Fluids (USA)*, 16 (1973) 675.
43. Arnush, D. B., Fried D. and Kennel, C. F., Parametric amplification of propagating electron plasma waves in the ionosphere, *J. Geophys. Res. (USA)*, 79 (1974) 1885.
44. Muldrew, D. B., The role of field-aligned ionization irregularities in the generation of the HF-induced plasma line at Arecibo, *J. Geophys. Res. (USA)*, 83 (1978) 2552.
45. Duncan, L. M. and Sheerin, J. P., High resolution studies of the HF ionospheric modification interaction region, *J. Geophys. Res. (USA)*, 90 (1985) 8371.
46. Showen, R. L. and Kim, D. M., Time variations of HF-induced plasma waves, *J. Geophys. Res. (USA)*, 83 (1978) 623.
47. Djuth, F. T., Gonzales, C. A., and Ierkic, H. M., Temporal evolution of the HF-enhanced plasma line in the Arecibo F region, *J. Geophys. Res. (USA)*, 91 (1986) 12089.
48. Birkmayer, W., Hagfors, T. and Kofman, W., Small-scale plasma-density depletions in Arecibo high-frequency modification experiments, *Phys. Rev. Lett. (USA)*, 57 (1986) 1008.
49. Isham, B., Birkmayer, W., Hagfors, T., and Kofman, W., Observations of small scale plasma density depletions in Arecibo HF experiments, *J. Geophys. Res. (USA)*, 92 (1987) 4629.
50. Muldrew, D. B., and Showen, R. L., Height of the HF-enhanced plasma line at Arecibo, *J. Geophys. Res. (USA)*, 82 (1977) 4793.
51. Muldrew, D. B., Duct-model explanation of the plasma line overshoot observed at Arecibo, *J. Geophys. Res. (USA)*, 93 (1988) 7598.
52. Salzer, M. P., Ierkic, H. M., and Fejer, J. A., Observational limitations on the role of Langmuir cavitons in ionospheric modification experiments at Arecibo, *J. Geophys. Res. (USA)*, 94 (1989) 6841.
53. Utlaut, W. F., Violette, E. J., and Paul, A. K., Some ionosonde observations of ionosphere modification by very high-power, high-frequency ground-based transmission, *J. Geophys. Res. (USA)*, 75 (1970) 6435.
54. Utlaut, W. F., and Violette, E. J., Further observations of ionospheric modification by a high-powered HF transmission, *J. Geophys. Res. (USA)*, 77 (1972) 6804.
55. Wright, J. W., Kinesonde observations of ionosphere modification by intense electromagnetic fields from Plateville, Colorado, *J. Geophys. Res. (USA)*, 78 (1973) 5622.
56. Rufenach, C. L., Radio scintillation of stellar signals during artificial ionospheric modification, *J. Geophys. Res. (USA)*, 78 (1973), 5611.
57. Thome, G. D. and Perkins, F. W., Production of ionospheric striations by self-focusing of intense radio waves, *Phys. Rev. Lett. (USA)*, 32 (1974) 1238.
58. Duncan, L. M., and Behnke, R. A., Observations of self-focusing electromagnetic waves in the ionosphere, *Phys. Rev. Lett. (USA)*, 41 (1978) 998.
59. Farley, D. T., LaHoz, C. and Fejer, B. G., Studies of the self-focusing instability at Arecibo, *J. Geophys. Res. (USA)*, 88 (1983) 2093.
60. Basu, S., Basu, S., Johnson, A. L., Klobuchar, J. A., and Rush, C. M., Preliminary results of scintillation measurements associated with ionospheric heating and possible implications for the solar power satellite, *Geophys. Res. Lett. (USA)*, 7 (1980) 609.
61. Cragin, B. L., and Fejer, J. A., Generation of large-scale field-aligned irregularities in ionospheric modification experiments, *Radio Sci. (USA)*, 9 (1974) 1071.
62. Perkins, F. W., and Goldman, M. V., Self-focusing of radio waves in an underdense ionosphere, *J. Geophys. Res. (USA)*, 86 (1981) 600.
63. Bernhardt, P. A. and Duncan, L. M., The feedback diffraction theory of ionospheric heating, *J. Atmos. and Terr. Phys. (UK)*, 44 (1982) 1061.

64. Morales, G. I., Wong, A. Y., Santoru, J., Wang, L. and Duncan, L. M., Dependence of plasma line enhancement on HF pulse length and ionospheric preconditioning, *Radio Sci. (USA)*, 17 (1982) 1313.
65. Fialer, P. A., Field-aligned scattering from a heated region of the ionosphere - Observations at HF and VHF, *Radio Sci. (USA)*, 9 (1974) 923.
66. Minkoff, J., Kugelmann, P. and Weissman, L., Radio frequency scattering from a heated volume, 1. VHF/UHF field-aligned and plasma-line backscatter measurements, *Radio Sci. (USA)*, 9 (1974) 941.
67. Belezov, A. F., Bubnov, V. A., Erukhimov, L. M., Kiselev, Y. V., Komranov, G. P., Mityakova, E. E., Rubtsov, L. N., Uryadov, R. P., Frolov, V. L., Chugunov, Y. V., and Yakhmatov, B. V., Parameters of artificial small-scale ionospheric irregularities, *Izv. Vysst. Uchebn. Zaved. Radiofiz. (USSR)*, 20 (1977) 1805.
68. Perkins, F. W., A theoretical model for short-scale field-aligned plasma density striations, *Radio Sci. (USA)*, 9 (1974) 1069.
69. Vashov, V. V., and Gurevich, A. V., Nonlinear resonant instability of a plasma in the field of an ordinary electromagnetic wave, *Soviet Phys. JETP Lett. (USSR)*, 42 (1975) 91.
70. Lee, M. C., and Fejer, J. A., Theory of short-scale field-aligned density striations due to ionospheric heating, *Radio Sci. (USA)*, 13 (1978) 893.
71. Frey, A., Ph.D. thesis, Rice University, Houston, Texas, 1982.
72. Djuth, F. T., Jost, R. J., Noble, S. T., Gordon, W. E., Stubbe, P., Kopka, H., Nielsen, E., Bostrom, R., Derblom, H., Hedberg, A. and Thide, B., Observations of E-region irregularities generated at auroral latitudes by a high-power radio wave, *J. Geophys. Res. (USA)*, 90 (1985) 12,293.
73. Coster, A. J., Ph.D. thesis, Rice University, Houston, Texas, 1983.
74. Grach, S. M., Karashina, A. N., Mityshkov, N. A., Rapoport, V. O., and Trukhtengerts, V. Y., Parametric excitation of ionospheric irregularities extended along the magnetic field, *Izv. Vysst. Zaved. Radiofiz. (USSR)*, 18 (1975) 1283.
75. Coster, A. J., M.S. thesis, Rice University, Houston, Texas, 1981.
76. Thide, B., Kopka, H. and Stubbe, P., Observations of stimulated scattering of a strong high frequency radio wave in the ionosphere, *Phys. Rev. Lett. (USA)*, 49 (1982) 1561.
77. Thide, B., Derblom, H., Hedberg, A., Kopka, H. and Stubbe, P., Observations of stimulated electromagnetic emissions in ionospheric heating experiments, *Radio Sci. (USA)*, 18 (1983) 851.
78. Derblom, H., Thide, B., Hedberg, A., Kopka, H. and Stubbe, P., Tromsø heating experiments: stimulated emissions at HF pump harmonic and subharmonic frequencies, *J. Geophys. Res. (USA)*, 94 (1989) 10,111.
79. Heston, J. C. and McGill, L. R., A model of the enhanced airglow excited by RF radiation, *Radio Sci. (USA)*, 9 (1974) 1005.
80. Bernhardt, P. A., Duncan, L. M., and Tepley, C. A., Artificial airglow excited by high-power radio waves, *Science (USA)*, 242 (1988) 1022.
81. Bernhardt, P. A., Duncan, L. M., and Tepley, C. A., Airglow enhancements associated with plasma cavities formed during ionospheric heating experiments, *J. Geophys. Res. (USA)*, 94 (1989) 9071.
82. Duncan, L. M., Sheerin, J. P., and Behnke, R. A., Observations of ionospheric cavities generated by high-power radio waves, *Phys. Rev. Lett. (USA)*, 61 (1988) 239.
83. D'bois, D. F., Rose, H. A., and Russell, D., Excitation of strong Langmuir turbulence in plasmas near critical density, LA-U-89-1419 (1989) Los Alamos National Laboratory.
84. Weatherall, J. C., Sheerin, J. P., Nicholson, D. R., Payne, G. L., Goldman, M. V., and Hansen, P. J., Solitons and ionospheric heating, *J. Geophys. Res. (USA)*, 87 (1982) 823.
85. Sheerin, J. P., Weatherall, J. C., Nicholson, D. R., Payne, G. L., Goldman, M. V., and Hansen, P. J., Solitons and ionospheric modification, *J. Atmos. Terr. Phys. (UK)*, 44 (1982) 1043.
86. DuBois, D. F., DuBois, D. F., and Rose, H. A., Nucleation of cavitons in strong Langmuir turbulence, *Phys. Rev. Lett. (USA)*, 54 (1985) 804.
87. Russell, D. D., DuBois, D. F., Rose, H. A., Collapsing caviton turbulence in one dimension, *Phys. Rev. Lett. (USA)*, 56 (1986) 838.
88. Russell, D. D., DuBois, D. F., Rose, H. A., Nucleation in two-dimensional Langmuir turbulence, *Phys. Rev. Lett. (USA)*, 60 (1988) 581.
89. Kuo, J., Menyuk, C. R., Reiman, A., Tripathi, V., Palmadesso, P., and Papadopoulos, K., ELF generation in the lower ionosphere via collisional parametric decay, *J. Geophys. Res. (USA)*, 91 (1986) 10,097.
90. Noble, S. N., and Gordon, W. E., The generation of ULF waves in the ionosphere, Paper #38 *Proceedings AGARD Symposium on Ionospheric Modification*, Spring 1990.

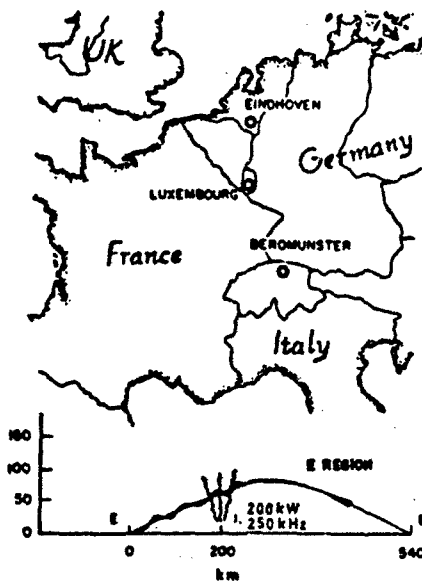


Fig. 1—Geometry of the Luxembourg effect as described by Tellegen

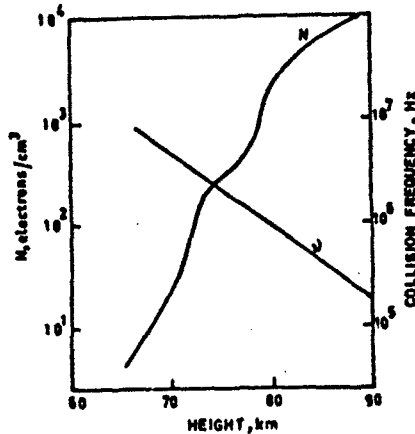


Fig. 2—D-region collision frequency and electron density profiles as measured by the cross-modulation technique

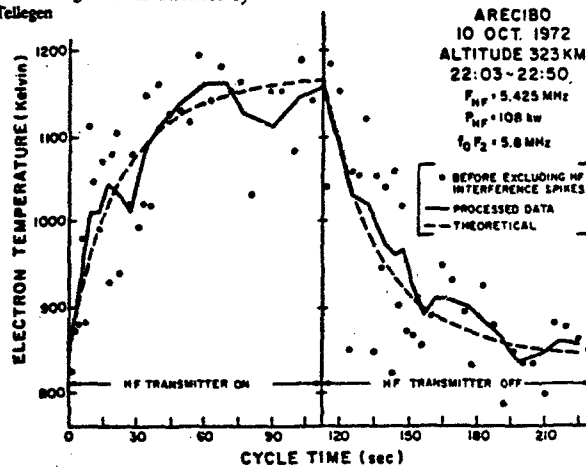


Fig. 3—Comparison of the calculated and the observed artificially enhanced electron temperatures at Arecibo on October 10, 1972.

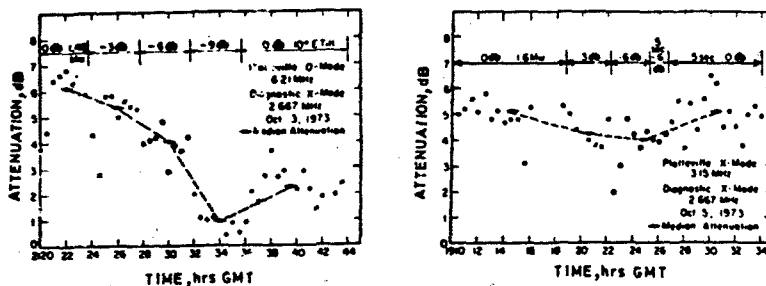


Fig. 4—Attenuation of signal strength resulting from HF ionospheric heating

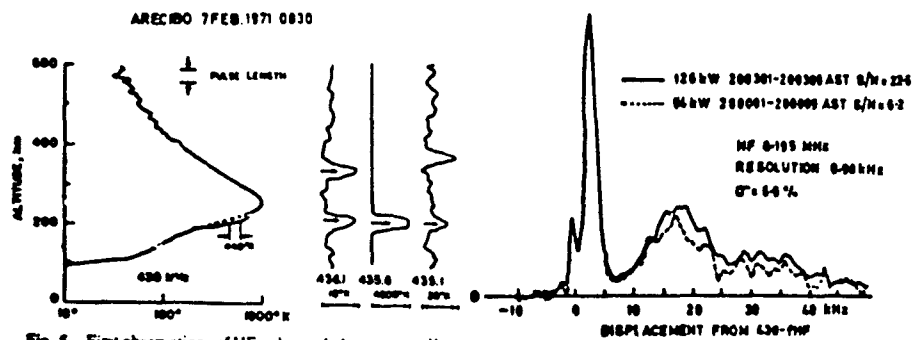
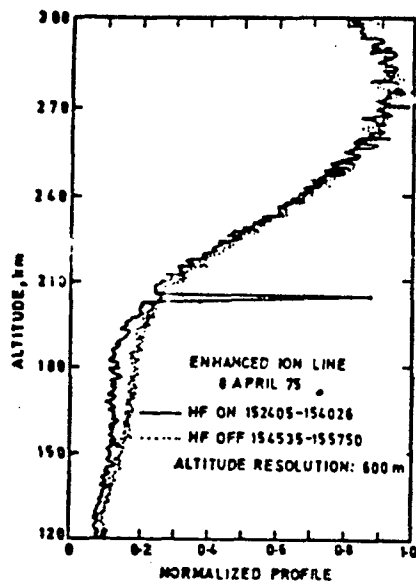
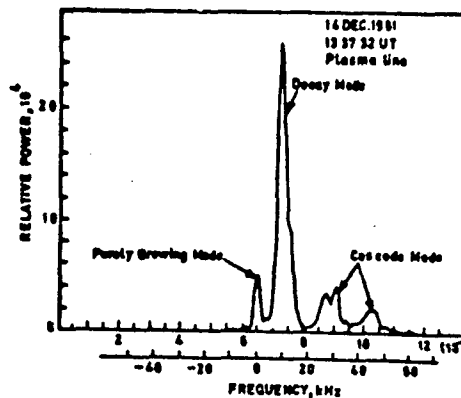
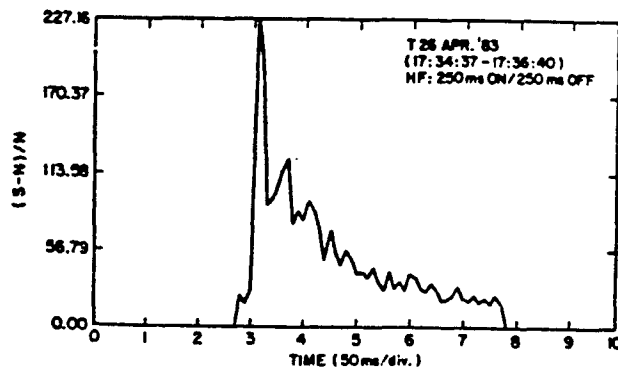
Fig. 5—First observations of HF-enhanced plasma waves<sup>11</sup>Fig. 7—HF-enhanced plasma wave spectrum as measured with Arecibo's 430 MHz radar<sup>11</sup>Fig. 6—Typical incoherent backscatter radar return, including HF-enhanced ion line<sup>10</sup>Fig. 8—Observations of enhanced plasma line spectrum at Esca during heating experiments<sup>11</sup>

Fig. 9—Plasma line overshoot enhancements for 250 ms on/off HF pulsing and 5-ms radar data resolution.

Downshifted Plasma Line  
April 27, 1988 21:32:00 AST

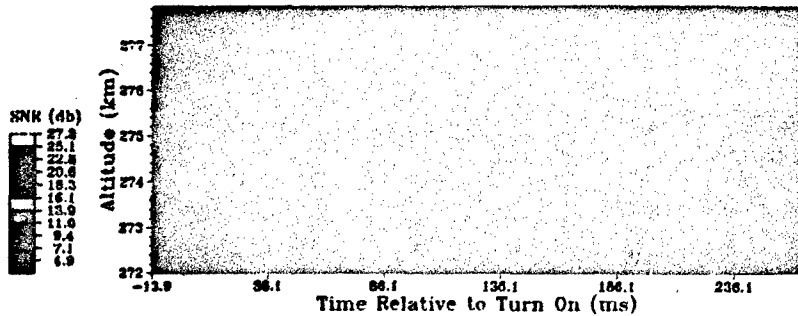


Fig. 10—Plasma line development in height and time.

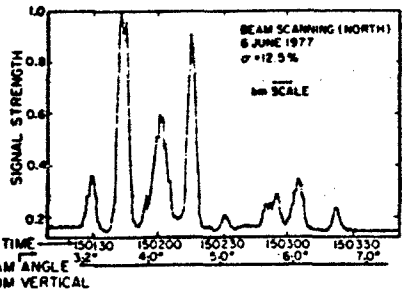
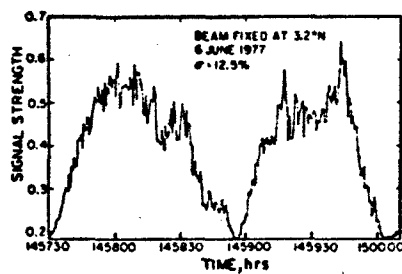


Fig. 11—Observations of the enhanced plasma-line signal strength in relative power using both fixed and scanning radar measurements, showing the beam self-focusing effects<sup>48</sup>

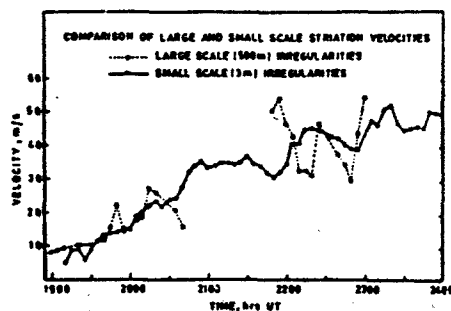


Fig. 14—Comparison of short scale (3 m) and large-scale (0.5-1.5 km) striation drift velocities<sup>49</sup>

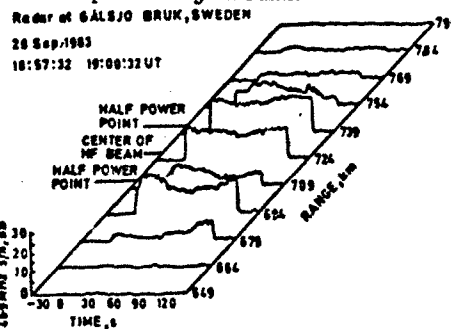


Fig. 12—Observations of E-region irregularities generated at auroral latitudes<sup>52</sup>

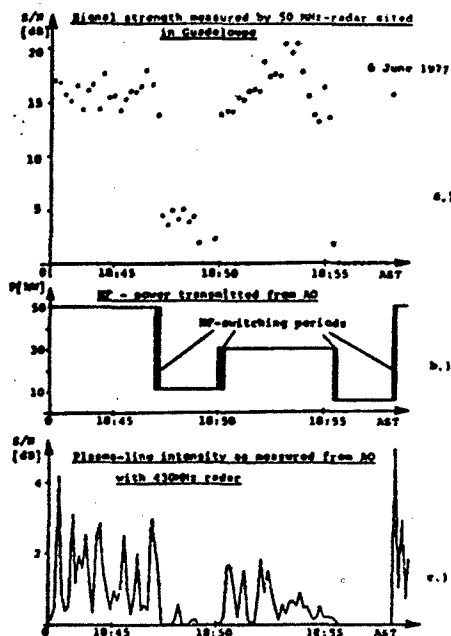


Fig. 13—Correlation of incident HF power, enhanced plasma line intensity and short-scale (3 m) striation-scatter signal-strength<sup>53</sup>



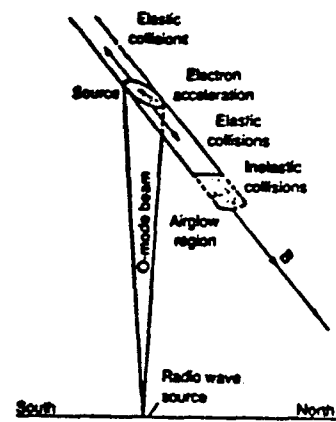


Fig. 15-Airglow generation schematic

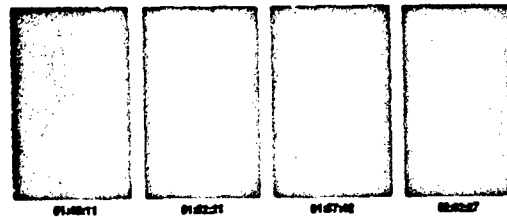


Fig. 16-Airglow clouds in a drifting plasma

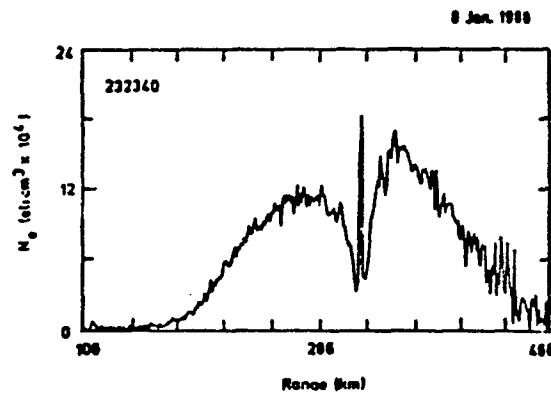


Fig. 18-HF enhanced ion-acoustic waves in a cavity

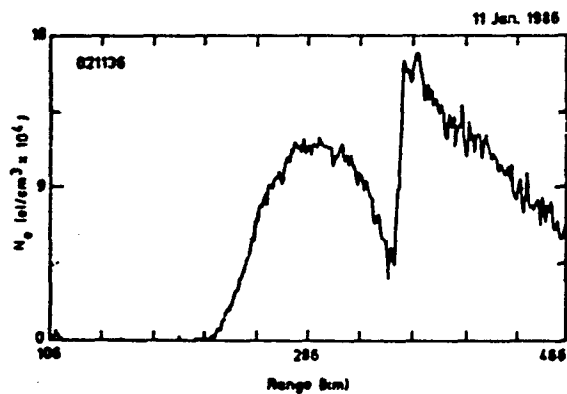


Fig. 17-Steady-state induced cavity

PAPER NO. 3

## DISCUSSION

R. SHOWN, US

In your Figure showing a depletion of  $n_e$  near the height of HF wave reflection, what fraction of the effect is due to a density drop, and what fraction to an increase in  $T_e$ ?

AUTHOR'S REPLY

The issue is well taken that, because of the temperature dependence of the electron scattering cross-section, an increase in electron temperature or a decrease in electron density can produce a reduction in the radar backscattered power. Separation of these two effects can be made using a variety of approaches, the simplest relying on the relatively fast temperature response at HF turn-ons and turn-offs compared to the electron density changes. These estimates are supported by direct  $T_e$  measurements, at substantially reduced range resolution, and  $n$  estimates based upon the change in height of the HF-enhanced ion line. Our best estimates for  $n/n_e$ , even several minutes after HF-off so that  $T_e$  is not a significant factor, are that typically  $\Delta n/n \approx 50\%$ .

W. GORDON, US

In view of your remarks about funding of institutions in USSR, do you think that Lebedev and/or IZMIRAN are threatened?

AUTHOR'S REPLY

Just as in the West, during times of constricting national budgets the funding for science in the Soviet Union will become tighter. I do not believe this immediately threatens the institutes involved in ionospheric modification research, in large part because of the kinds of potential applications that we are discussing at this symposium. However the pace of research, and particularly the development of new experimental facilities, certainly will be affected. If anything, these economic changes place an even greater emphasis on cooperative research with the West.

## IONOSPHERIC MODIFICATION RESEARCH AT HIPAS

by  
Richard G. Brandt  
Office of Naval Research  
800 N. Quincy Street  
Arlington, VA 22217  
U.S.A.

### SUMMARY

The HIPAS ionospheric heating facility radiates a total power of 1.2 MW with an ERP of 84 MW. It presently operates at an HF frequency of 2.85 MHz but is tunable to about 5 MHz. Electrojet modulation experiments have been conducted at frequencies from 5 Hz to 5 kHz. The magnetic field amplitudes, measured close to the heater, can be 1 pT or larger under very strong electrojet conditions. Even under much weaker conditions when the amplitudes are highly variable, the phase of the ELF signal is relatively stable. The efficiency of converting HF to ELF is presently too low for a practical communication system. Beam painting has been proposed as a method for improving the conversion efficiency in D region heating by causing a much larger area of the ionosphere to radiate coherently; this concept will be tested using microsecond beam steering. Use of shorter heating pulses (lower duty cycle) already seems promising. Even larger gains are expected for E region heating as compared to D region heating.

### PREFACE

This review of ionospheric modification research at HIPAS starts with a brief description of the facility which began operating at the megawatt average power level in 1986. The research conducted at HIPAS since that time is described. This research has focused on the generation of ELF radiation. The review concludes with an indication of future research directions.

### 1. THE HIPAS FACILITY

The HIPAS ionospheric heater is located in the auroral zone 40 km east of Fairbanks, Alaska. The acronym HIPAS stands for High Power Auroral Stimulation. It was originally conceived as a high pulse power heater, rather than high average power, because of the recognition that many plasma nonlinearities are excited by large instantaneous electric fields [Wong and Santoru, 1981]. When HIPAS became operational in October 1981, it delivered 1 ms HF pulses with a peak power of 2 MW at a pulse repetition rate of 1 Hz. The average power, therefore, was only 2 kW, and the antenna gain was 17.7 dB at a radiating frequency of 4.905 MHz. This facility was initially used for probing short-term nonlinear plasma phenomena, especially enhancement of the incident electric fields at the resonant altitude and creation of electromagnetic cavitons via ponderomotive forces. These cavitons are localized depletions in electron density with scale sizes from 1 to 100 m.

In 1982 several events occurred which altered the original research plan. First, in March 1982 the incoherent scatter radar at Chatanika was moved to Greenland. Much of the detailed work on caviton structure and dynamics was subsequently carried out at the Arecibo facility with its excellent incoherent scatter radar. Second, in late 1982 the HF transmitters from the Platteville heater became available, and a decision was made to incorporate these transmitters in the HIPAS facility, transforming it into a high average power heating facility.

Eight of the Platteville transmitters are now operating at HIPAS, each connected to an individual element in the transmitting antenna array [Wong et al, 1990]. This modular design allows the phase of the high power radiation emitted by each element in the array to be controlled at the low-level input to each transmitter and thus permits rapid beam steering and related modulation techniques. Each transmitter is normally operated continuously at 100 to 150 kW, although the maximum rating is 200 kW. Instead of relying on commercial prime power, two megawatt diesel electric generators were installed at HIPAS so that operational costs would be minimized.

The antenna consists of a circular (208 m diameter) array of seven crossed half-wave dipoles approximately one quarter of a wavelength above the ground plus one similar crossed dipole in the center. Although the antenna elements were designed to be resonant at 4.905 MHz, a novel scheme was developed [2] for retuning the antenna to lower frequencies by making use of a pair of wires attached to the end of each dipole element; the angle between these two wires and the angle these

wires make with the ground determine the new resonant frequency. Using this technique, the array has been successfully retuned and operated at the additional frequencies of 4.503, 3.349 and 2.805 MHz. The antenna gain remains essentially constant at about 18 dB. At 2.85 MHz the calculated effective radiated power (ERP) is 84 MW at a total radiated power of 1.2 MW.

With the upgrade of HIPAS to the megawatt average power level, the research directions changed. These new research activities capitalized on the existing diagnostic capabilities which included ionosondes, an HF imaging radar, magnetometer chain data, riometer data, and ELF receivers. More recently, a 50 MHz coherent radar has become operational. In addition, satellite receivers and beacons have been utilized at various times. The initial scientific studies were concerned with optimal approaches for coupling energy into the ionospheric plasma [Wong et al, 1989]. Beginning in 1987 the research has focused on the subject of generation of ELF radiation in the ionosphere by modulation of the powerful electrojet current flowing in the auroral region.

## 2. ELF/VLF GENERATION

The ELF generation experiments at HIPAS began in 1987. This team effort involved A. Ferraro (Pennsylvania State University), A. Wong (University of California, Los Angeles), D. Papadopoulos (Science Applications International Corporation), J. Olson (University of Alaska) and coworkers. In these experiments the ELF receivers were located about 50 km west of HIPAS. The receivers used standard coherent detection techniques, and the heater and the receivers were synchronized using separate frequency standards. Most of the measurements were made at modulation frequencies between 1 and 5 kHz where the detection sensitivity was best. The heater was almost always amplitude modulated with 100 percent modulation depth.

These experiments continued through 1989 during which time progressively more sophisticated beam steering capability was implemented. Initially, the heater beam could be steered by manually adjusting the eight phaseshifters in the lines leading to the individual antenna elements. In 1988 electronic phaseshifters were introduced and placed under computer control, and a beamforming time of 10 ms was achieved. In 1989 this capability was upgraded to provide 15 ms beamforming time.

The initial experiments [Ferraro et al, 1989] served to demonstrate the ability to generate ELF and confirm earlier results obtained by the Tromsø group. As an illustration, Figure 1 shows data obtained at a modulation rate of 2.5 kHz during a strong electrojet event which occurred overhead of the HIPAS facility as indicated by magnetometer data. We see that the amplitude and phase of the ELF signal remain constant during the 2-minute period of modulation, after which the amplitude falls to zero and the phase becomes random. The magnetic signal strength is 0.6 pT. Even when the electrojet is very weak and the amplitude of the ELF signal is small and highly variable, the phase remains remarkably constant as illustrated in Figure 2.

This phase stability of the ELF signal suggests that phaseshift keying might be a viable signal modulation technique for an ELF communication system based on ionospheric generation. To explore this hypothesis, several phase shifting experiments were performed. The tests performed in 1987 were relatively simple, consisting of periodically changing the phase of the ELF signal by 180 degrees. Some of these data [5] are illustrated in Figure 3 and indicate a very stable phase for periods of 0.5 minute. Following these initial biphasic stability tests, various quadphase tests were conducted in 1989 in which the phase was periodically switched from 180 to 90 to 0 to -90 to -180 degrees. Representative data [5] are shown in Figure 4 and again indicate phase stability for periods of 0.5 minute. All these measurements were made at the receiving site 50 km from HIPAS and at a frequency of 2.5 kHz. In 1989 several attempts were made to receive data using a mobile receiving station located at more remote sites in Alaska. Data obtained from Cantwell, Alaska, about 210 km from HIPAS [5] are shown in Figure 5. Switching between the various phase states is clearly evident, although the transitions between these states are less sharp.

Other experiments were performed to determine whether these ELF signals could be generated at less than full power levels. Some of these data [5] are shown in Figure 6. The curious spikes in the data were caused by a local thunderstorm. In this experiment the modulation frequency was 2.5 kHz, and the total radiated power was varied from a maximum of 800 kW to a minimum of 80 kW. At maximum power the measured magnetic field amplitude was less than 0.1 pT which indicates that there was no strong overhead electrojet. Nonetheless, ELF signals were generated at all HF transmitter power levels including at 80 kW when the measured magnetic field amplitude was less than 0.02 pT. There is some indication that the effect is beginning to saturate at the higher power levels, suggesting that there would be little advantage in using a heater with an even higher ERP.

### 3. BEAM PAINTING/LOW DUTY CYCLE HEATING

The experimental results described above clearly demonstrate the ability to generate ELF signals under a variety of ionospheric conditions. Although the amplitude of these signals may be variable, the phase is reasonably stable. The efficiency of the generation process, however, is quite low. The total radiated HF power is approximately 1 MW. Except under strong electrojet conditions, the ELF power is very modest. When there is no strong electrojet directly overhead, the ELF power is no more than 10 mW, corresponding to a conversion efficiency of  $10^{-8}$ . This ELF power is calculated from the measured near-field amplitudes using a far-field formula for dipole radiation in free space.

Papadopoulos and coworkers [Papadopoulos et al, 1990] have developed a theory which suggests an approach for achieving dramatic improvements in HF-to-ELF conversion efficiency, namely, beam painting. For low altitude heating they conclude that the ERP of the current HIPAS heater is sufficient to achieve the full saturated value of Hall conductivity modulation. Any further increase in power density would be wasted. Papadopoulos et al [6] conclude that the only way to achieve an increase in conversion efficiency in low altitude heating is to cause a much larger area of the ionosphere to radiate coherently. The predicted ELF power is then proportional to the square of the radiating area. In principle, this can be accomplished by beam painting, that is, using the present beam spot size but rapidly steering the beam such that many different spots are heated and not allowed to cool off before they radiate. At 75 km altitude the time required to increase the electron temperature by a factor of 2 (a sufficient increase to produce most of the conductivity change) is typically about 10 ms; this heating time decreases somewhat at higher power densities. At the same altitude the cooling time is of the order of 100 ms, at least for temperatures below 2000 K. The concept of beam painting, therefore, requires that many spots be visited and that the temperature rise produced during each visit is not dissipated before that same spot is revisited. The total time available for heating is a half cycle of the ELF modulation or about 5 ms. During that time the temperature of each spot must be increased, in cumulative fashion, by at least a factor of 2.

Papadopoulos and coworkers [6] have also analyzed the case of heating at 100 km, the altitude at which the electrojet flows. Here the situation is more complex. At these altitudes the Pederson conductivity modulation dominates over the Hall conductivity modulation and does not saturate until power densities of at least  $10 \text{ mW/m}^2$  are reached, a factor of 10 higher than that available at HIPAS. When saturation occurs, the predicted increase in conductivity modulation is by a factor of 100 which leads to an increase in the efficiency of ELF generation by a factor of  $10^4$ . This increase would be obtained without beam painting. The practical difficulty in realizing the high altitude scheme, especially under day time conditions, is the fact that self absorption at lower heights could deplete the power density before reaching the higher altitudes. Another potential disadvantage of high altitude heating is that the coupling of the ELF fields into the earth-ionosphere waveguide may be more inefficient. Nonetheless, the potential gain in generation efficiency by a factor of  $10^4$  is a significant prize worth pursuing, and several schemes for defeating the self absorption problem have been suggested. However, none of these ideas for increasing the efficiency of high altitude generation of ELF has yet been tested experimentally.

The recent HIPAS experiments were designed to maximize the heating in the low altitude regime because of the choice of operating frequency (2.85 MHz which is near the second harmonic of the electron cyclotron frequency) and the use of X mode polarization (same sense of rotation as the electron cyclotron motion). An initial effort was made to demonstrate that beam painting could produce an efficiency enhancement in generation of ELF at low altitudes. At present the beam forming time at HIPAS is 15 ms. Each spot must be heated almost 10 ms during each visit. Therefore, in order to heat 10 spots, for example, about 250 ms is required which is longer than the cooling time of each spot. This simple arithmetic clearly illustrates that a significantly faster beam forming time is required before an efficiency enhancement can be demonstrated. The initial tests at HIPAS, therefore, did not yield an efficiency enhancement, but the dependence of generated signal strength on beam painting parameters was in accordance with theory.

Other experiments were performed [Papadopoulos and Ferraro, 1989] which directly relate to the beam painting concept. A series of measurements were made in which the duty cycle of the ELF modulation of the HF waves was varied. The ELF modulation frequency was 833 Hz, and the duty cycles selected were 50 percent (600 ms on, 600 ms off), 37.5 percent (450 ms on, 750 ms off), 25 percent (300 ms on, 900 ms off), 12.5 percent (150 ms on, 1050 ms off), 6.25 percent (75 ms on, 1125 ms off), 2.5 percent (30 ms on, 1170 ms off), and 1.25 percent (15 ms on, 1185 ms off). The amplitudes of the generated ELF signals were measured for all duty cycles, and the data are shown in Figure 7. The error bars represent the scatter in the results for repeated measurements. The results clearly show that the same ELF signal strengths are generated at 25 percent duty cycle as at 50 percent duty cycle. Below 25 percent duty cycle the amplitudes fall off approximately linearly. The conclusion is that the efficiency of generating magnetic field signals can be increased by a factor of 2 and thus the efficiency of generating ELF power can be increased by a factor of 4 merely by decreasing the duty cycle from 50 percent to 25 percent, that is, by reducing the average HF power by a factor of 2. For this

single spot only about the first 300 ms of the heating pulse is effective; the rest is wasted. Pulses shorter than 300 ms do not saturate the conductivity modulation although they do produce a measurable effect. The time between heating pulses is longer than the cooling time, and thus energy cannot be accumulated.

#### 4. ULF/ELF GENERATION

ELF generation was also investigated in the frequency range below 100 Hz [McCarrick et al, 1990]. In these experiments it was initially not possible to use full amplitude modulation as in the higher frequency experiments because of various transmitter system resonances. Instead, an alternate procedure was developed known as beam-dephasing modulation. In this procedure all eight transmitters were operated continuously, while the phase of four of these transmitters was switched in a square-wave fashion between 0 and 180 degrees with respect to the phase of the other transmitters. In this way the beam was alternately focused and defocused at the desired modulation rate. When the beam is defocused, there still is some residual heating of the ionosphere, both overhead and in the sidelobes, and thus the effective modulation depth is less than in 100-percent amplitude modulation. It was calculated that the power density in the main lobe is reduced by more than 75 percent during the out-of-phase half-period.

The receiver used in these experiments is located at the NOAA Gilmore Creek Facility, 35 km from HIPAS. The system was developed by D. Sentman for the purpose of studying the natural Schumann resonances of the earth-ionosphere waveguide. The receiver consists of a pair of orthogonal magnetic coils, a vertical electric field sensor, associated amplifiers and signal conditioning electronics, and a dedicated data acquisition and storage system. To reduce the sensitivity to 60 Hz background radiation, a low-pass filter is placed between the coils and the amplifiers. The attenuation is 4.4 dB at 76 Hz and becomes very large above 100 Hz. The data obtained at this site are transmitted in real time to the HIPAS control room where they are displayed together with environmental data from the ionosondes, the magnetometer chain, and, more recently, from the coherent radars.

Using the dephasing modulation technique and the receiving system just described, experiments were performed at the frequencies of 5, 11, 21, 23, 41, and 76 Hz. In Figure 8 is shown a typical background noise spectrum obtained from a 4-minute incoherent average of the east-west coil output [8]. The first three Schumann resonance peaks at 7.5, 14 and 21 Hz are well defined. In order to observe the generated ELF signals which are often weaker than the natural atmospheric noise background, coherent detection techniques were used, including conventional lock-in amplifiers and digital signal processing routines. A typical coherent ELF spectrum from the east-west coil [6] is shown in Figure 9. Here we see the 11 Hz signal generated by HIPAS as well as the third harmonic of this signal at 33 Hz. A 4-minute averaging period was used. Similar quality data were obtained from the north-south magnetic sensor as well as the vertical electric field sensor. Note that the measured magnetic field strength at 11 Hz is in excess of 1 pT.

These experiments were performed under a variety of ionospheric conditions in order to correlate the strength of the observed signals with measures of geomagnetic activity. Basically, whenever the magnetic activity is high enough, as determined by the Kp index or by magnetometer chain data, large ELF signals can be generated. In terms of Kp index, which is an indication of how far south in geomagnetic latitude the auroral oval has expanded, it was found that signals in excess of 1 pT could be generated whenever the Kp index exceeded 3. Similarly, ELF signal strength correlates strongly with strength of the electrojet as determined from magnetometer chain data. Figure 10 shows data for the north-south magnetometer at College, Alaska during a time period corresponding to an ELF generation experiment [8]. Data from a single ground-based magnetometer are somewhat difficult to interpret since the ionospheric currents move in geographic location as well as increase and decrease in amplitude throughout the day. However, in Figure 11 we see the measured ELF amplitudes during the same time period. Both signals begin at high levels and then fall to minimum values at 0700 UT, followed by a significant rise. Finally, as the magnetometer output decreases and then changes sign corresponding to a reversal of electrojet current direction, there is a decrease and then a very rapid increase in ELF amplitude. At the same time as this current reversal is occurring, the otherwise steady phase of the ELF signal experiences a discontinuous phase shift.

Other favorable situations for ELF generation include the occurrence of visible aurora and the existence of a sporadic E layer as determined by ionosondes. An unfavorable time for ELF generation is under high absorption conditions, as indicated by riometer readings. Such high absorption conditions are caused by high-energy proton and electron precipitation during major solar events. Under these conditions most of the HF power appears to be absorbed at a very low altitude and cannot effectively modulate the conductivity where ionospheric currents are flowing.

These measurements prove that the beam-dephasing modulation technique works successfully, but with an effective modulation depth of less than 100 percent. Very recently [Wong et al, 1990] it has been demonstrated that the transmitters can be amplitude modulated at frequencies down to 50 Hz by increasing the filter capacitance in the high voltage power supplies. At the present time four of the eight transmitters have been so modified. Initial tests have been performed to compare the performance of amplitude modulation with dephasing modulation at 76 Hz. The resultant electric field signal amplitudes are shown in Figure 12. In all cases the total radiated power was kept constant at 400 kW. The data labeled 8DM indicates that all eight transmitters were operated at the 50 kW level and modulated by dephasing. The label 4DM denotes that four transmitters were modulated by dephasing, each operated at the 100 kW level. When four transmitters were full amplitude modulated and operated at the 100 kW level, the resultant signal amplitudes are labeled 4AM. Comparing the 4AM results with the 4DM results, we see that the 4AM amplitudes are larger than the 4DM amplitudes by a factor of more than 3, corresponding to an increase in ELF power by at least a factor of 10. This increase is achieved at the same total radiated power and the same ERP. The only change is an improvement in effective modulation depth. In the 8DM case the ERP is much higher and even larger amplitudes are obtained, indicating that the conductivity modulation effect is not saturated at the lower power density. It is anticipated that similar gains can be realized when all eight transmitters are converted to full amplitude modulation.

### 5. FUTURE RESEARCH DIRECTIONS

Additional ELF generation experiments will be performed at HIPAS later this year in order to investigate more fully various approaches for enhancing the HF-to-ELF conversion efficiency. The beam steering capability will be upgraded to a 2 ms beam forming time, allowing more definitive tests of the beam painting concept. Other experiments will evaluate the use of short pulses (low duty cycle heating) to improve efficiency. All transmitters will be modified to allow full amplitude modulation down to 50 Hz. The receivers will be optimized for detection in the 75 to 150 Hz range, and measurements will be made at distances of hundreds of kilometers from the heater using a mobile receiving station. It is anticipated that a single HF heating frequency will be used, chosen to maximize absorption in the D region, although dual frequency operation would permit exploration of some of the concepts for improved efficiency via E region heating. The measured ELF amplitudes will be correlated with real-time environmental data from ionosondes, the riometer and magnetometer chain, plus data from 50-MHz coherent radars operating near Anchorage and at HIPAS. The understanding gained from these new measurements and their interpretation will be valuable in future research planning and in the design of new facilities.

### REFERENCES

1. Wong, A. Y., and J. Santoru, Active Stimulation of the Auroral Plasma, *J. Geophys. Res.*, vol. 86, no. A9, pp. 7718-7732, 1981.
2. Wong, A. Y., J. Carroll, R. Dickman, W. Harrison, W. Huhn, B. Lum, M. McCarrick, J. Santoru, C. Schock, G. Wang and R.F. Wuerker, High Power Radiating Facility at the HIPAS Observatory, to be published in a special issue of *Radio Sci.*, 1990.
3. Wong, A. Y., F. Y. Cheung, M. J. McCarrick, J. Stanley, R. F. Wuerker, R. Close, B. Baker, E. Fremouw, W. Kruer and B. Langdon, Large-Scale Modification in the Polar Ionosphere by Electromagnetic Waves, *Phys. Rev. Lett.*, vol. 63, pp. 271-274, 1989.
4. Baker, M. R., T. W. Collins, H. S. Lee and A. J. Ferraro, A Diagnostic System for the Study of Extremely Long Wavelength Emission Produced by Ionospheric Modification, to be published in a special issue of *Radio Sci.*, 1990.
5. Ferraro, A. J., H. S. Lee, T. W. Collins, M. Baker, D. Werner, F. M. Zain and P. J. Li, Measurements of Extremely Low Frequency Signals from Modulation of the Polar Electrojet Above Fairbanks, Alaska, *IEEE Trans. Antennas Propagat.*, vol. 37, pp. 802-805, 1989; other data provided prior to publication by A. J. Ferraro, 1989.
6. Papadopoulos, K., A. S. Sharma and C. L. Chang, On the Efficient Operation of a Plasma ELF Antenna Driven by Modulation of Ionospheric Currents, *Comments Plasma Phys. Controlled Fusion*, vol. 13, no. 1, pp. 1-17, 1989; Papadopoulos, K., C. L. Chang, P. Vitello and A. Drobot, On the Efficiency of Ionospheric ELF Generation, to be published in a special issue of *Radio Sci.*, 1990.
7. Papadopoulos, K., and A. J. Ferraro, Summary of July-August 1989 HIPAS Campaign, preliminary report provided by the authors, 1989.
8. McCarrick, M. J., A. Y. Wong, R. F. Wuerker, B. Chouinard and D. D. Serriman, Excitation of ELF Waves in the Schumann Resonance Range by Modulated HF Heating of the Polar Electrojet, to be published in a special issue of *Radio Sci.*, 1990.
9. Wong, A. Y., et al, data provided prior to publication, 1990.

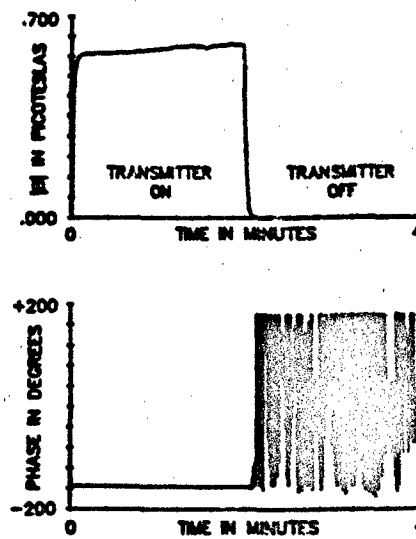


Figure 1: Magnitude and phase of strong 2.5 kHz signal.

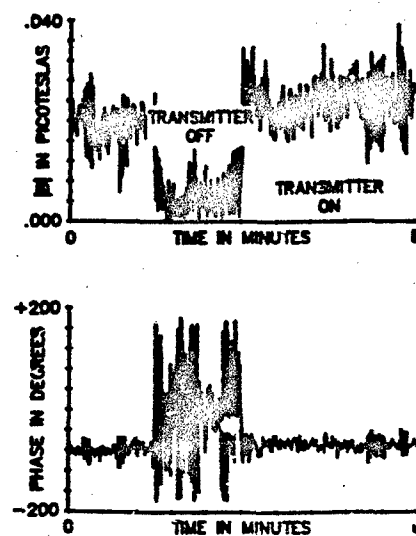


Figure 2: Magnitude and phase of weak 2.5 kHz signal.



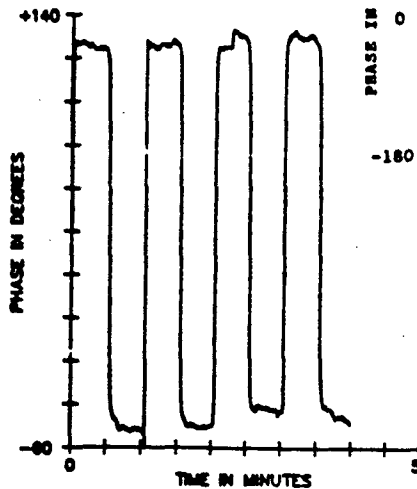


Figure 3: Detected phase of 2.5 kHz signal in phase keying test. Phase inverted by 180 degrees at 30 second intervals.

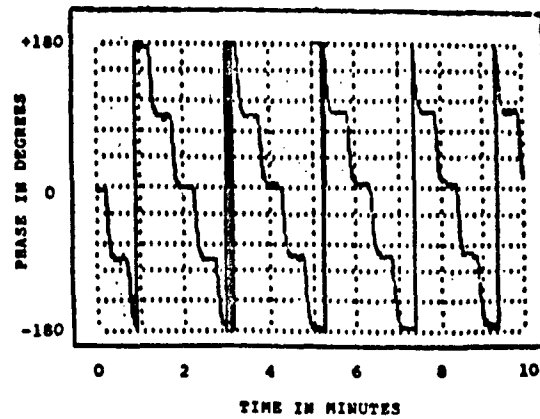


Figure 4: Detected phase of 2.5 kHz signal in phase shift keying test. The phase is shifted from 180 to 90 to 0 to -90 to -180 degrees.

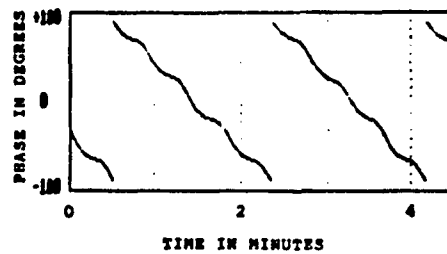


Figure 5: Detected phase of 2 kHz signal in phase shift keying test. The phase is shifted from 180 to 90 to 0 to -90 to -180 degrees. The receiver is located 210 km from the heater.

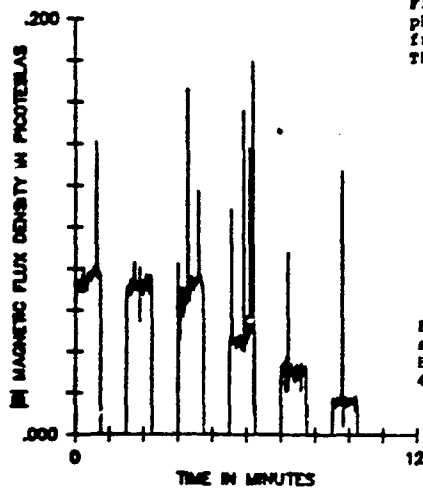


Figure 6: Magnitude of received 2.5 kHz signals in power reduction test. Total HF power is reduced from 800 to 640 to 480 to 320 to 160 to 80 kW.

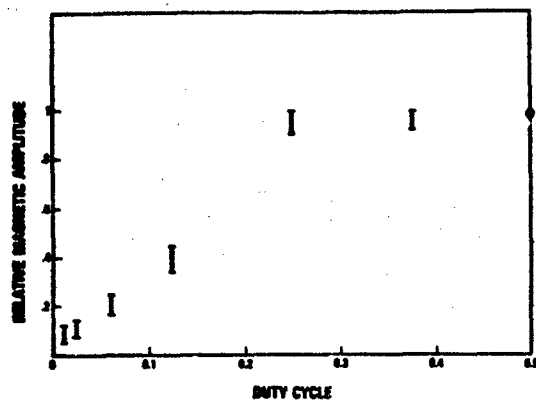


Figure 7: Relative signal amplitudes at various heater duty cycles

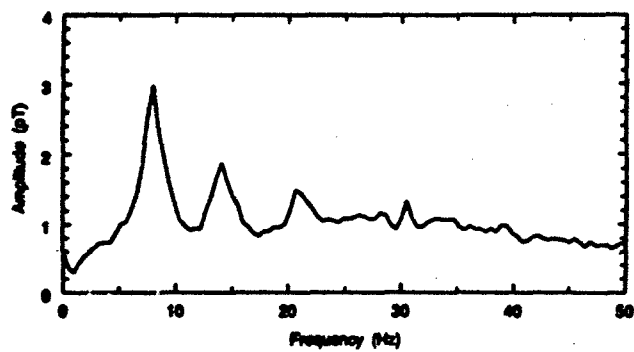


Figure 8: Background noise spectrum

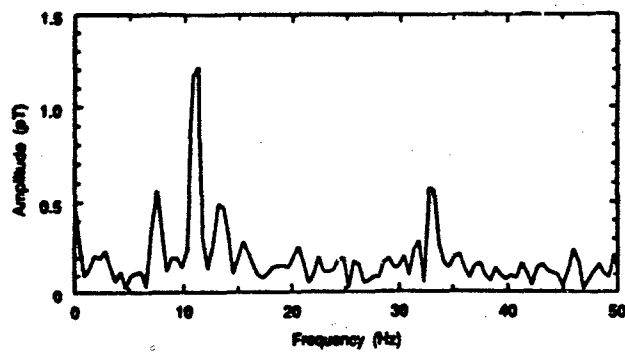


Figure 9: Signal spectrum resulting from modulation at 11 Hz.

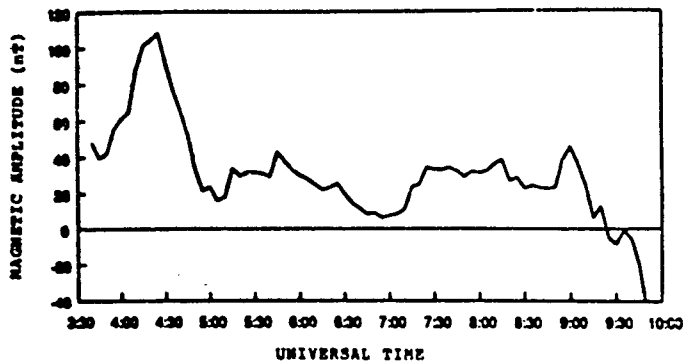


Figure 10: H-axis output of magnetometer at College, Alaska

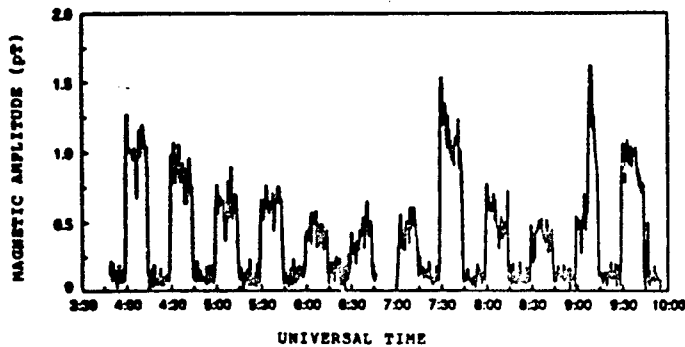


Figure 11: Signal strength at 11 Hz for same time period as in Figure 10.

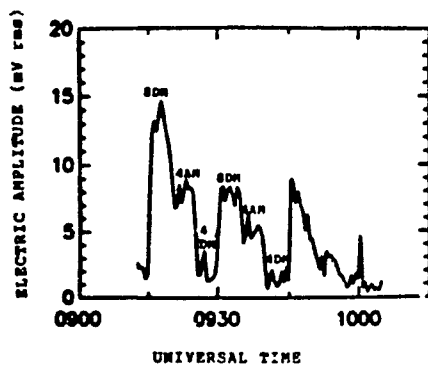


Figure 12: Signal amplitude at 76 Hz for various modulation schemes. AM denotes amplitude modulation; DM denotes dephasing modulation; 4 and 8 indicate number of transmitters being modulated. The total radiated power in all cases is 400 kW.

## DISCUSSION

U. C. IKEN, US

When you make ground-based measurements, say at ELF, were there any phase delay measurements to determine that the source was in the ionosphere?

## AUTHOR'S REPLY

Phase height measurements were made by Sonstaby and Ferraro of Penn State during a campaign at HIPAS in July 1988. These measurements, made at a heater modulation frequency of 5 kHz, indicate that the source was located at a height of 70 km in the ionosphere.

W. ARMSTRONG, US

What fraction of time (in tens of percent) is the electrojet conveniently located for ELF experiments?

## AUTHOR'S REPLY

Although the data are available to answer this question, in the form of magnetometer chain records, these data have not been systematically analyzed for the region near Fairbanks, Alaska. During good periods, such as September 1989, for example, the electrojet was essentially overhead about 50 percent of each day. During solar minimum conditions and during summer months, on the other hand, the electrojet is accessible less than 10% of the time.

M. BYCROFT, UK

The correlation between ELF (11 Hz) signal strength radiated by the electrojet (Figure 11) and the change in the H-component of a ground-based magnetometer (Figure 10) relies on the baseline (zero magnetic amplitude in Figure 10) chosen. How was this baseline determined?

## AUTHOR'S REPLY

The zero level was set by comparison with earlier, quiet traces.

W. GORDON, US

Antenna gain has been overestimated by 5 or 6 dB. Brandt's eight dipoles if perfectly operated without losses above a perfect ground at the right height (possible for one frequency in the range he covers) yields 14 dB, not 19 dB, maximum. With losses for "wrong" height above ground of 2 or 3 dB, the actual gain will be in range 11 to 14 dB rather than 19 dB.

## AUTHOR'S REPLY

In the limit of a uniformly illuminated aperture, the HIPAS array would have a gain of about 20 dB at its design frequency of 4.9 MHz and a gain of about 16 dB at the present operating frequency of 2.85 MHz. There is an additional gain due to the dipole elements of about 2 dB and an additional gain due to the ground plane. At 4.9 MHz the ground plane gain is 6 dB, while at 2.85 MHz the ground plane gain is substantially reduced, perhaps to 3 dB. Therefore, the maximum possible gain of the array is about 28 dB at 4.9 MHz and 21 dB at 2.85 MHz. However, the spacing of elements in the array is much greater than a half wavelength so that the gain is substantially reduced from these maximum values. Calculations performed using the NEC electromagnetic code give values of about 17 dB at 4.9 MHz and 18 dB at 2.85 MHz. The reduction at 2.85 MHz is less severe because the aperture is somewhat better filled at this longer wavelength.

# VLF, ELF AND ULF WAVE RESEARCH USING THE TROMSØ HEATING FACILITY

by

M.T. Rietveld

EISCAT

N-9027 Ramfjordbotn

Norway

R. Barr\*, P. Stubbe, A. Maul, H. Kopka

Max-Planck-Institut für Aeronomie

Postfach 20

D3411 Katlenburg-Lindau

Germany

and

R.L. Dowden

c/o Main Author

EISCAT

N-9027 Ramfjordbotn

Norway

## SUMMARY

A review is presented of results from the Tromsø Heating facility in the areas of wave generation from ULF (mHz) to VLF (kHz) frequencies, as well as VLF wave propagation under heated ionospheres. Results from similar facilities in the USSR and USA will not be included.

## 1. INTRODUCTION

High power high frequency (HF) radio waves heat the electrons in the lower ionosphere through non-deviative absorption on the time-scale of microseconds resulting in the enhancement of the electron-neutral collision frequency. The heated region, typically 25 km diameter at 80 km altitude, can act as a perturbation on the upper wall of the Earth-ionosphere waveguide, thereby affecting the propagation of VLF waves. On the other hand, by amplitude modulating the heating wave the heated region can act as an oscillating current source, if there is an external driving electric field, which can itself radiate waves at the modulation frequency into the waveguide or into the magnetosphere. The auroral zone is ideally situated for experiments of the second type because of the frequent presence of large (tens of mV/m) electric fields. For experiments of the first type, the auroral zone is not quite so ideal since large natural ionospheric variations can mask the artificially produced ones. We shall review results from both types of experiment performed using the heating facility of the Max-Planck-Institut für Aeronomie, a description of which can be found in Stubbe and Kopka (1979) and Stubbe et al. (1982a, 1985). This facility will be operated by the EISCAT scientific association from 1993 onwards.

## 2. D-REGION PERTURBATIONS

The effect of heating with about 300 MW of effective radiated power (ERP) at, say 4 MHz, is to increase the electron collision frequency by more than an order of magnitude at 80 km, corresponding to a change in height of the collision frequency profile by about 10 km. The effective change in VLF reflection height is, however, not so large since it depends on the ionospheric refractive index which above 65 km depends more on the magnetic than the collisional properties of the plasma. The effect is, nevertheless, to increase the reflection height by about 4 km over a circle of radius 25 km in diameter. Such heating-induced perturbations are analogous to localised natural decreases in the VLF reflector height caused by lightning-induced electron precipitation, called Trimp events (Inan and Carpenter, 1987; Dowden and Adam, 1988). Whatever the cause of the perturbation, they effect changes in the phase and amplitude of signals from VLF transmitter with varying sign and degree depending on where the perturbation is located with respect to the transmitter-receiver path. A good didactic explanation of scattering of VLF waves by such perturbations is given by Dowden et al. (1990).

In order to test the theory of VLF wave scattering off such perturbations, Barr et al. (1984) used the north-south beam steering ability of the Tromsø heater to make the first observations of the effect of a moveable ionospheric anomaly on VLF propagation. They observed small (typically .1 dB in amplitude and 0.5° in phase) but clear diffraction effects on signals at 12.1 kHz from the Omega transmitter at Aldra, Norway, received at Skibotn which is 52 km east of the heater site. In more extensive work, Barr et al. (1985a) studied the temporal variability of the perturbations for a fixed heater deflection angle such that the perturbation was on the propagation path. They found that at times of a marked reduction in the VLF field strength, i.e. during times of modal interference usually after sunset, much larger perturbations of up to 6 dB in amplitude and 50° in phase could be caused by heating. Figure 1 shows how the strongest perturbations occurred during times of the amplitude minima.

Both the normal and enhanced amplitude and phase perturbations were successfully modelled in the same paper by computing the effect on multimode VLF propagation of heating a series of ionospheres ranging from day to night conditions. Multimode propagation was necessary in this case because of the short (< 500 km) path. Values of the waveguide propagation constant were obtained for each mode under heated and unheated ionospheres by solving the waveguide modal equation (Budden, 1961), using an implementation described by Barr (1971). The effect of RF heating is to reduce the phase velocity of the modes which is the cause of the scattering. The effect of moving the perturbation at right angles to the path under stable conditions was to change the phase of the scattered signal relative to that of the direct signal in proportion to the change in echo path length. This results in a diffraction pattern which could be fairly well reproduced by the model for small deflection angles up to 40° (Barr et al. 1985a).

Dowden et al. (1990) also analysed data from a similar beam deflection experiment using a different approach. They showed that the heating-induced perturbation acts as a steerable receiver and can be used to study the VLF mode structure and parameters (phase velocity and excitation phase) at high altitudes (~75 km).

In all the experiments performed so far, only the changes caused by collision frequency enhancement on the time scale of ~0.5 s were monitored. This was necessary to overcome the drift due to ionospheric variability. Comparatively high speed changes in electron density at low altitudes in the D-region, which may also occur (see the partial reflection experiment results in Stubbe et al., 1982a), are a subject for future research.

\* On leave from DSIR Physics and Engineering Laboratory, Lower Hutt, New Zealand.

### 3. MODULATION OF IONOSPHERIC CURRENTS

Besides being able to produce stationary D-region perturbations, the heater can be used to produce a modulated conductivity perturbation in the D- or E-region. The time constant for electron temperature ( $T_e$ ) enhancement is very short, typically 10  $\mu$ s at 60 km and 1 ms at 90 km with an exponential height variation. The electron density ( $N_e$ ), on the other hand, has a long time constant which, below the E-region peak, decreases with increasing altitude. For modulation frequencies greater than a few Hz the collision frequency modulation is dominant whereas less than a few Hz electron density modulation may dominate if the heater wave reaches high enough altitudes. The conductivity modulation caused by electron temperature enhancement is quite well understood (Stubbe and Kopka, 1977; Stubbe et al., 1982b) and that caused by electron density through modulation of the  $O_2^+$  and  $NO^+$  temperature-dependent recombination rates reasonably well understood. The primary source currents, driven by an external horizontal electric field, are simply proportional to these conductivity perturbations. The closure of these currents depends very much on the frequency involved, as is shown by Figures 2 and 3 of Stubbe et al., (1982b). In general we may say that at low ULF frequencies ( $\ll 1$  Hz) currents flowing around the heated region (polarization currents) and to some extent into the magnetosphere are important. The theory of Stubbe and Kopka (1977), which uses height-integrated currents, can then be applied to calculate the magnetic effect on the ground if one ignores the magnetospheric path and self inductance. These latter effects are considered by Fejer and Krenzien (1982).

At the other end of the spectrum, the primary source currents in the hundreds of Hz to kHz range are closed through the wave impedance and are limited mainly by self inductance. The radiation from these currents cannot be calculated using the approach above, but must be done by considering elementary current sheets and solving Maxwell's equations at each layer. Such a full wave calculation for plane wave propagation, and then correcting the results for the limited size of the heated region, was performed by Rietveld et al. (1987, 1989) to calculate the wave field on the ground underneath the heated region. Multiple reflections of the waves between Earth and ionosphere were also included. The same model can also be used to calculate the upward propagating whistler-mode waves in the upper E-region. In another approach, used for calculating the wave fields excited in the Earth-ionosphere waveguide, the primary Hall and Pedersen source currents are integrated over the heated volume to get an integrated dipole moment at some effective height in the ionosphere, which can then be used to get the efficiency of waveguide excitation by the principle of reciprocity (Barr and Stubbe, 1984a, 1984b).

In the intermediate frequency range (0.1-10 Hz) neither of the above approaches seems to work well (Rietveld et al., 1989). The consideration of all the currents necessary in this range is a complicated task and has not been done yet.

The ionospheric antenna produced by the alternating current, often called "polar electrojet antenna", is non-resonant so there is no low frequency limit as in conventional ground based antennas. This is one of its advantages, but otherwise it is an inefficient ELF/VLF source as the following work shows.

### 4. NEAR FIELD ELF/VLF RESULTS

After the first reports of artificial ionospheric ELF wave generation by Soviet workers (e.g. Getmantsev et al., 1974), Stubbe et al. (1980, 1981, 1982c) and Dowden et al. (1981) measured both amplitude and phase of ELF signals recorded at Lavangsdalen, 17 km from the Tromsø heater, and proved that they were of ionospheric origin. They used north-south and east-west oriented loop antennas. By varying the modulation frequency continuously from a few hundred Hz to about 6 kHz it was found that the amplitude showed pronounced peaks near 2 kHz and higher multiples. Measurements of phase as a function of frequency enabled the group delay and thereby the effective generation height of the waves, typically 75 km, to be determined. An example of such a sweep is shown in Figure 2 (from Figure 6 of Rietveld et al., 1989). The signals from the two antennas were resolved into their right- and left-handed circular components labelled R and L in the figure. The data (solid lines) illustrate the following typical features. The amplitudes are typically 1  $\mu$ T under disturbed geomagnetic conditions. Ionospheric electric fields were greater than about 20 mV/m in this case as deduced from the STARE auroral radar data. The R-mode (whistler mode in the plasma) is slightly stronger than the L-mode (which is evanescent in a plasma) but the L-mode has sharper peaks at the 2 kHz resonances. The waves are usually elliptically polarized since the R and L-modes are comparable in strength. The effective source heights, obtained from the rate of change of phase with frequency, are larger for the R-mode on average.

The dotted lines in figure 2 are the results of the full wave calculation described in Rietveld et al. (1989). The inclusion of multiple Earth-ionosphere reflections reproduces the peaks reasonably well in both amplitude and phase (or height) and shows that an interpretation of the phase in terms of source height needs to be done with care. Occasionally frequency sweeps show more structure in the R-mode than in the L-mode (figure 7 of Rietveld et al., 1989). This could also be modelled and explained by the presence of ionization at heights above that where the waves are generated. For example sporadic E-layers could cause the upward propagating whistler mode waves to be reflected and interfere with the downward propagating waves.

Other features of the ELF/VLF waves are that they are usually stronger for X-mode than O-mode heating and stronger at lower HF frequencies, because the D-region absorption is more efficient in both cases. Modulating with lower average HF power is more efficient than with higher average power because of the non-linear relation between electron temperature enhancement and HF energy input (Stubbe et al., 1982b; Papadopoulos et al., 1989).

An alternative way of examining the VLF waves from ionospheric heating is to look at the broad-band temporal response to pulsed heating, rather than the narrow band fixed frequency waves. This was first done by Stubbe et al., (1982b) and repeated in more detail by Rietveld et al. (1986). Figure 3 shows the average ELF/VLF response from one loop antenna to 50, 300- $\mu$ s heater pulses. Up to 6 multiple Earth-ionosphere reflections of the wave radiated by the transient current perturbation are evident and labelled. The difference in response to heater-on and heater-off transitions were used to deduce that the electron heating time constant was about half that for cooling. It was also suggested that this technique could find more general use with other radar systems in the auroral zone since it can use rather low duty cycle transmissions (Rietveld and Stubbe, 1987).

Many studies were made of the temporal behaviour of waves generated at a small number of fixed modulation frequencies. By comparing the variation with other measurements (mainly magnetometers and electric field estimates from STARE) it was shown that both the amplitude and phase can be modulated by large scale electric fields on time-scales from seconds to many hours. For example Rietveld et al. (1983, 1987) showed that natural Pc-5 pulsations could be monitored in this way and Rietveld et al. (1988) showed Pc-1 pulsations of 3 s period. On one occasion an experiment lasting 32 hours during a Polar Cap Absorption (PCA) event showed how the source height varied from the rather low altitude of 55 km during the day to about 75 km at night (Rietveld et al., 1987).

## 5. FAR FIELD ELF/VLF RESULTS

To demonstrate the successful excitation of waveguide modes by the ionospheric ELF/VLF antenna, measurements were made in Sweden at Kiruna, Lycksele, and Uppsala at distances of 205, 554, and about 1000 km respectively from the heating facility. Signals have been detected at Uppsala but no quantitative analysis has yet been made. Data in the frequency range 1-1.6 kHz from Kiruna and Lycksele were used to determine, not only the effective power radiated by the ionospheric antenna, but also the propagation constant of the Earth-ionosphere waveguide (Barr et al., 1983b). During a 2-day period the radiated power ranged from  $< 100 \mu\text{W}$  to  $> 2 \text{ W}$ . The upper value compares favourably with theoretical values of a few watts computed by Barr and Stubbe (1984b) for a constant ionospheric electric field of 25 mV/m. For a HF power input of about 1 MW this represents a power efficiency of  $\sim 0.0001\%$ . The amplitude was highly variable but the high correlation coefficient of 0.87 and 0.8 at 1.04 and 1.57 kHz respectively between signals from Kiruna and Lycksele shows that the variation is provided by the source rather than the propagation medium. This conclusion is confirmed by simultaneous local measurements at Lavingsdalen.

The frequency dependence of signals at Lycksele from the "polar electrojet antenna" was examined at frequencies from 223 Hz to 5.44 kHz (Barr et al., 1986). Frequencies over the whole range were received with maximum amplitudes  $\sim 50 \text{ fT}$ . Both azimuthal and radial magnetic field components were recorded allowing their ratio, commonly termed polarization, to be determined. The data were modelled using the theory of Barr and Stubbe (1984b) in which a point dipole of 30 amp-km was located at the height of the maximum modulated Hall current at a certain angle to the propagation path (north-south). Figure 4 shows the cutoff frequency near 2 kHz of the first-order quasi-transverse-electric (QTE) mode (Budden, 1961) very clearly in the radial component. This frequency is determined by the ionospheric height and was used to find the appropriate density profile. Changes of this cutoff frequency, which is related to the first waveguide resonance near 2 kHz in Figure 2, is correlated with auroral precipitation and with diurnal changes in the ionospheric height. A dipole located at 69 km and oriented at  $120^\circ$  to the propagation path gave the fit shown. That the theory underestimates the radial magnetic flux density below 2 kHz may be due to neglect of near-field effects in the model. The minima between 2 and 4 kHz in the azimuthal data are caused by modal interference as the propagation changes from the zero-order quasi-transverse-magnetic (QTM) mode to the first-order QTM mode. Overall, they conclude that the simple model of a single point-dipole in the ionosphere located at the height of the ELF/VLF Hall current maximum is excellent in explaining the experimental results, especially above 1 kHz. Using waveguide mode theory to extrapolate our results to longer distances leads to discrepancies with other published claims of far-field measurements (e.g. Ferraro et al., 1982; Lunnen et al., 1984).

## 6. MULTIPLE AND MOVEABLE ELF/VLF SOURCES

The Tromsø heating facility is able to tilt the antenna beam in the north-south plane by phasing the 6 rows of HF antennas appropriately. This can in fact be done at rates up to about 5 kHz. Experiments were performed where the beam was swept in a 1 minute cycle  $35^\circ$  about the zenith while ELF signals were being generated near 2 kHz by amplitude modulation. Signals recorded under this moving source of ELF radiation sometimes showed an amplitude variation with deflection angle which were interpreted, with the help of STARE electric field data, as being caused by spatial variations in the ionospheric electric field (Rietveld et al., 1984).

Similar experiments were performed under more uniform and stable ionospheric conditions but using a receiver at Lycksele, 554 km away. The phase variation with beam deflection angle was obtained and used to derive the phase velocity of ELF waves between 1 and 6 kHz in the Earth-ionosphere waveguide (Barr et al., 1987). The simple point-ELF-dipole model they used to relate measured phase, ionospheric height, beam deflection angle and phase velocity, fitted most of the data very well and gave phase velocities that agreed with those calculated from waveguide theory. The simple theory failed to fit the phase at large northerly deflections, suggesting that the HF antenna side lobe structure may be contributing to total ELF signal radiated. The idea is that when the main beam is pointing far to the north, the lower power side lobe structure illuminates the ionosphere to the south and effectively generates ELF signals in the ionosphere with shorter propagation paths to the receiver. Also the larger the deflection, the larger the power in the side lobes becomes so that these secondary sources can interfere significantly with the source from the main beam.

A more realistic model was presented by Barr et al. (1988) where the ELF/VLF source was assumed to be continuous with contributions from the majority of the HF radiation pattern as depicted in Figure 5. The improved fit to the phase data is demonstrated in Figure 6 which shows the simple theory on the left and the full theory at the right. In addition the amplitude data could be reasonably well explained, which was not the case with the simple theory. The most important feature in the amplitude data, that the signals from deflections  $37^\circ$  south were about 6 dB stronger than for vertical beam could be explained by less phase path difference across the source directed to the south than for vertical beam. It would thus appear that deflecting the HF beam in the required direction of ELF/VLF propagation is a good technique for improving the ELF/VLF signal output especially at the shorter wavelengths.

By deflecting the HF beam in square wave fashion without amplitude modulation, it is possible to illuminate two separated patches in the ionosphere in antiphase. Barr et al. (1987) used a switching frequency of 2.94 kHz to produce two antiphase sources of ELF radiation in the waveguide and thus produce a directional source of ELF radiation. They varied the separation between the patches from 0 to more than 100 km and found a maximum in received signal at Lycksele at about 54 km assuming a source height of 78 km. With free space propagation velocities, two antiphase sources at 2.94 kHz would need to be 51 km (half a wavelength) apart to produce a maximum signal in the line joining them. The maximum signal was also twice as much as obtained from a single amplitude modulated patch, indicating the two heated patches were operating efficiently as two independent ELF sources. Furthermore, the amplitude measured near the midpoint between the two patches was much less than for the single amplitude modulated patch, as one would expect.

## 7. MAGNETOSPHERIC ELF/VLF RESULTS

The ELF/VLF waves produced in the lower ionosphere also propagate in the whistler mode upwards where they may be detected on satellites or even on the ground in the conjugate hemisphere if suitable ducting of the signals occurs. During an extensive campaign in December 1981 a detailed search was made for ground signals at Mawson, Antarctica, near the conjugate point to Tromsø. No signals were found probably because ducted whistler-mode propagation, which is usually necessary for ground reception, is rare outside the plasmapause.

Whistler mode signals have, however, been seen on three satellite passes in 1981: Aureole 3 on 3 Dec (Lefevre et al., 1985), ISIS 1 on 9 Dec (James et al., 1984), and DE-1 on 12 Dec (Inan and Helliwell, 1985; James et al., 1990). ISIS 1 detected signals from 525 to 5850 Hz near 1200 km altitude on a magnetic field line close to the Heater with amplitudes from 3-30  $\mu\text{V/m}$ . Aureole 3 detected waves from 525 to 1425 Hz at 1890 km altitude with about 5  $\mu\text{V/m}$ ; while DE-1 detected waves from 1525 to 5925 Hz at 11000 km

with 0.4-0.7  $\mu\text{V/m}$ . Some aspects of the satellite observations remain unexplained. The amplitudes measured on ISIS 1 were stronger than implied by simultaneous ground measurements, and the harmonic signal ratios from the square wave modulation were different in space and on the ground (James et al., 1984).

The DE-1 results were compared with 10.2 kHz signals from the Omega transmitter in Aldra, Norway, which were received at the same time, to deduce a radiated power of about 30 W. This is somewhat higher than that measured in the Earth-ionosphere waveguide (Barr et al., 1985b) which is typically a few watts, suggesting that the "polar electrojet antenna" is a more efficient generator of magnetospheric than sub-ionospheric radiation. Nevertheless the signal levels were still a factor of about 6 smaller than the signals from the 10 kW Omega transmitter. Spectral broadening of about 10 Hz and pulse stretching by a few hundred milliseconds could not be explained by propagation in a smooth magnetosphere, but required scattering off density irregularities.

## 8. ULF RESULTS

Measuring the effects of modulating currents in the ULF range (less than a few Hz) has been more difficult mainly because the natural noise level is much higher than at ELF/VLF frequencies. Ionospherically produced oscillations in the magnetic field on the ground under the heated region have been clearly measured in the 1 to 20 Hz range (Stubbe et al., 1982b; Rietveld, 1985; Maul et al., 1990) and most features can be shown to be caused by ionospheric current modulation (Maul et al., 1990) involving temperature modulation and some density modulation at the lower frequencies. Amplitudes are typically a few pT, similar to those in the hundreds of Hz range, but are not so well reproduced by our models.

Long period oscillations have been recorded by magnetometers close to the heated region with periods from 10 to 600 seconds (Stubbe and Kopka, 1981; Stubbe et al., 1982b; Lotz-Iwen, 1983; Maul et al., 1990). Some of these events have had amplitudes up to 10 nT which are much larger than expected on the basis of the current modulation theory of Stubbe and Kopka, 1977 (Stubbe et al., 1982b; 1985). Sometimes they showed an abrupt onset, suggesting that an instability may be involved. One possible mechanism investigated by Secker (1985), involving feedback to the original perturbation by electron precipitation from the magnetosphere, appeared unlikely to explain the observations but could not be completely excluded.

On the other hand, approximately 1 nT amplitude of a 120 s period event could be explained by the current modulation theory quite well (Maul et al., 1990). During the same experiment 1425 Hz and 1 Hz modulations were also used every half hour with successful results. This example, shown in Figure 6, illustrates that the conditions required for strong ULF current modulation are quite different from those required for strong ELF/VLF excitation because the 1425 Hz waves are quite weak ( $\sim 0.15$  pT) compared to those usually seen. Low electron densities in the lower D-region, which were measured by EISCAT, resulted in weak 1425 Hz signals, but allowed the HF wave to modulate the electron density in the E-region, as the modelling of Maul et al. (1990) showed.

The launching of Alfvén waves into the magnetosphere by such periodic ionospheric perturbations has never been demonstrated experimentally although a search was made for Pc-5 perturbations on the GEOS-2 synchronous orbit satellite, and for Pc-1 perturbations at the conjugate point in Mawson, Antarctica (Webster et al., 1987). The chances of detecting these waves in the magnetosphere are thought to be remote because of the small extent of the perturbed region (Fejer and Krenzien, 1982). Although we cannot completely exclude other mechanisms that do not rely on current modulation as the source of ULF or ELF waves, most of our data seem to be explainable in terms of such current modulation.

## 9. CONCLUSIONS

Perturbing the D-region on the propagation path of VLF waves by HF heating has been shown to provide a useful tool in furthering our understanding of VLF wave propagation. In particular the effects of modal interference, the displacement from the propagation path, and the size of the perturbed ionosphere on the signal amplitude and phase have been elucidated.

The excitation of ELF/VLF waves provides an interesting diagnostic of ionospheric conditions and another tool for studying the propagation properties of the Earth-ionosphere waveguide. The mechanism is not very efficient in exciting waveguide modes and is perhaps more efficient at exciting the whistler-mode in the magnetosphere. Some methods of improving the power radiated into the Earth-ionosphere waveguide by factors of up to about 3 using antenna beam steering have been demonstrated. Recent ideas to improve further the efficiency of radiation into the Earth-ionosphere waveguide from the ionospheric ELF antenna (Papadopoulos et al., 1989) have not yet been tested experimentally.

The excitation of detectable ULF oscillations on the ground requires more restrictive conditions than for ELF/VLF. There are probably more unanswered questions in this area than in the two above.

## 10. REFERENCES

- Barr, R., 1971, The propagation of ELF and VLF radio-waves beneath an inhomogeneous anisotropic ionosphere, *J. Atmos. Terr. Phys.*, 33, 343-353.
- Barr, R., and P. Stubbe, 1984a, The 'Polar Electrojet Antenna' as a source of ELF radiation in the Earth-ionosphere waveguide, *J. Atmos. Terr. Phys.*, 46, 315-320.
- Barr, R., and P. Stubbe, 1984b, ELF and VLF radiation from the "polar electrojet antenna", *Radio Sci.*, 19, 1111-1122.
- Barr, R., M. T. Rietveld, H. Kopka, and P. Stubbe, 1984, The effect of a heated patch of auroral ionosphere on VLF radio wave propagation, *Nature*, 309, 534-536.
- Barr, R., M. T. Rietveld, P. Stubbe, and H. Kopka, 1985a, The Diffraction of VLF Radio Waves by a Patch of Ionosphere Illuminated by a Powerful HF Transmitter, *J. Geophys. Res.*, 90, 2861-2875.
- Barr, R., M. T. Rietveld, H. Kopka, P. Stubbe, and E. Nielsen, 1985b, Extra-low-frequency radiation from the polar electrojet antenna, *Nature*, 317, 155-157.
- Barr, R., P. Stubbe, M. T. Rietveld, and H. Kopka, 1986, ELF and VLF Signals Radiated by the 'Polar Electrojet Antenna': Experimental Results, *J. Geophys. Res.*, 91, 4451-4459.



- Barr, R., M. T. Rievers, P. Stubbe and H. Kopka, 1987, Ionospheric heater beam scanning: A mobile source of ELF radiation, *Radio Sci.*, 22(6), 1073-1083.
- Barr, R., M. T. Rievers, P. Stubbe, and H. Kopka, 1988, Ionospheric heater beam scanning: A realistic model of this mobile source of ELF/VLF radiation, *Radio Sci.*, 23(3), 379-388.
- Budden, K. G., 1961, *The Waveguide Mode Theory of Propagation*, 150 pp., Prentice-Hall, New Jersey.
- Dowden, R. L., P. Stubbe, and H. Kopka, 1981, VLF Wave Generation by Modulated RF Heating of the Electrojet Ionosphere, *Adv. Space Res.*, Vol. 1, pp 221-223, COSPAR.
- Dowden, R. L., C. D. D. Adams, M. T. Rievers, P. Stubbe, and H. Kopka, 1990, Phase and Amplitude Perturbations on Subionospheric Signals Produced by a Moving Patch of Artificially Heated Ionosphere, in press, *J. Geophys. Res.*
- Fejer, J. A., and E. Kneizlen, 1982, Theory of generation of ULF pulsations by ionospheric modulation experiments, *J. Atmos. Terr. Phys.*, 44, 1075-1087.
- Ferraro, A. J., H. S. Lee, R. Allshouse, K. Carroll, A. A. Tomko, F. J. Kelly, R. G. Joiner, 1982, VLF/ELF radiation from the ionospheric dynamo current system modulated by powerful HF signals, *J. Atmos. Terr. Phys.*, 44, 1113-1122.
- Germantsev, G. G., N. A. Zulkov, D. S. Kotik, L. F. Mironenko, N. A. Miryakov, V. A. Rapoport, Yu. A. Sazonov, V. Yu. Trakhtengerts, and V. Ya. Eidman, 1974, Combination frequencies in the interaction between high-power short-wave radiation and ionospheric plasma, *JETP Lett.*, 20, 101-102.
- Inan, U. S., and D. L. Carpenter, 1987, Lightning-Induced Electron Precipitation Events Observed at L=2.4 as Phase and Amplitude Perturbations on Subionospheric VLF Signals, *J. Geophys. Res.*, 92, 3293-3303.
- Inan, U. S., and R. A. Helliwell, 1985, Active Experiments from Ground, in *Results of the Arcad 3 Project and of the Recent Programmes in Magnetospheric and Ionospheric Physics*, Cepadues-Editions, Toulouse, France, pp 599-607.
- James, H. G., R. L. Dowden, M. T. Rievers, P. Stubbe and J. H. Kopka, 1984, Simultaneous Observations of ELF waves from an Artificially Modulated Auroral Electrojet in Space and on the Ground, *J. Geophys. Res.*, 89, 1655-1666.
- James, H. G., U. S. Inan, and M. T. Rievers, 1990, Observations on the DE-1 spacecraft of ELF/VLF waves generated by an ionospheric heater, in press, *J. Geophys. Res.*
- Lefevre, P., J. L. Fauch, V. L. Dee, E. E. Tlova, V. E. Yurov, O. A. Molchanov, M. M. Mogilevsky, O. A. Maltseva, L. V. Zinin, H. Kopka, M. T. Rievers, P. Stubbe, and R. L. Dowden, 1985, Detection from Aureol-3 of the Modulation of Auroral Electrojet by HF-Heating from ELF Signals in the Upper Ionosphere above Tromsø, in *Results of the Arcad 3 Project and of the Recent Programmes in Magnetospheric and Ionospheric Physics*, Cepadues Editions, Toulouse, France, pp 609-619.
- H.-J. Lotz-Iwen, 1983, *Anregung Erdmagnetischer Pulsationen durch lokales aufheizen der polaren Ionosphäre mit energiereichen Hochfrequenzwellen*, Doctoral thesis, Universität Göttingen.
- Lumen, R. J., H. S. Lee, A. J. Ferraro, T. W. Collins, and R. F. Woodman, 1984, Detection of radiation from a heated and modulated equatorial electrojet current system, *Nature*, 311, 134-135.
- Maul, A.-A., M. T. Rievers, P. Stubbe, and H. Kopka, 1990, Excitation of periodic magnetic field oscillations in the ULF range by suprathermal modulated HF waves, in press, *Annales Geophysicae*.
- Papadopoulos, K., A. S. Sharma, and C. L. Chang, 1989, On the Efficient Operation of a Plasma ELF Antenna Driven by Modulation of Ionospheric Currents, *Comments Plasma Phys. Controlled Fusion*, 13, 1, 1-17.
- Rievers, M. T., H. Kopka, E. Nielsen, P. Stubbe, and R. L. Dowden, 1983, Ionospheric Electric Field Pulsations: A Comparison Between VLF Results From an Ionospheric Heating Experiment and STARE, *J. Geophys. Res.*, 88, 2140-2146.
- Rievers, M. T., R. Barr, H. Kopka, E. Nielsen, P. Stubbe, and R. L. Dowden, 1984, Heater Beam Scanning: A new Technique for ELF Studies of the Auroral Ionosphere, *Radio Sci.*, 19(4), 1069-1077.
- Rievers, M. T., 1985, Ground and in situ excitation of waves in the ionospheric plasma, *J. Atmos. Terr. Phys.*, 47, 1283-1296.
- Rievers, M. T., H. Kopka, and P. Stubbe, 1986, D-region characteristics deduced from pulsed ionospheric heating under auroral electrojet conditions, *J. Atmos. Terr. Phys.*, 48, 311-326.
- Rievers, M. T., H.-P. Manelshagen, P. Stubbe, H. Kopka, and E. Nielsen, 1987, The Characteristics of Ionospheric Heating-Produced ELF/VLF Waves Over 32 Hours, *J. Geophys. Res.*, 92, 8707-8722.
- Rievers, M. T., and P. Stubbe, 1987, Ionospheric demodulation of powerful pulsed radio waves: A potential new diagnostic for radars suggested by Tromsø heater results, *Radio Sci.*, 22(6), 1084-1090.
- Rievers, M. T., H. Kopka, and P. Stubbe, 1988, Pc 1 ionospheric electric field oscillations, *Annales Geophysicae*, 6(4), 381-388.
- Rievers, M. T., P. Stubbe, and H. Kopka, 1989, On the frequency dependence of ELF/VLF wave, produced by modulated ionospheric heating, *Radio Sci.*, 24(3), 270-278.
- J. Seckler, 1985, *Verstärkung einer durch starke HF-Wellen induzierten Elektronenflüstörung in der polaren E-Schicht*, Doctoral thesis, Universität Göttingen.

- Stubbe, P., and H. Kopka, 1977, Modulation of the polar electrojet by powerful HF waves, *J. Geophys. Res.*, 82, 2319-2325.
- Stubbe, P., and H. Kopka, 1981, Generation of Pc 5 Pulsations by Polar Electrojet Modulation: First Experimental Evidence, *J. Geophys. Res.*, 86, 1606-1608.
- Stubbe, P., H. Kopka, and R. L. Dowden, 1981, Generation of ELF and VLF waves by polar electrojet modulation: experimental results, *J. Geophys. Res.*, 86, 9073-9078.
- Stubbe, P., H. Kopka, H. Lauche, M. T. Rietveld, A. Brekke, O. Holt, T. B. Jones, T. Robinson, A. Hedberg, B. Thidé, B. Crochet and H.-J. Lotz, 1982a, Ionospheric modification experiments in northern Scandinavia, *J. Atmos. Terr. Phys.*, 44, 1025-1041.
- Stubbe, P., H. Kopka, M. T. Rietveld and R. L. Dowden, 1982b, ELF and VLF wave generation by modulated heating of the current carrying lower ionosphere, *J. Atmos. Terr. Phys.*, 44, 1123-1135.
- Stubbe, P., H. Kopka, M. T. Rietveld and R. L. Dowden, 1982c, Generation of ELF and VLF waves by modulated HF heating of the polar electrojet, AGARD Conf. Proceedings No. 305.
- Stubbe, P., H. Kopka, M. T. Rietveld, A. Frey, P. Hoeg, H. Kohl, E. Nielsen, G. Rose, C. La Hoz, R. Barr, H. Derblom, A. Hedberg, B. Thidé, T. B. Jones, T. Robinson, A. Brekke, T. Hansen and O. Holt, 1985, Ionospheric modification experiments with the Tromsø heating facility, *J. Atmos. Terr. Phys.*, 47, 1151-1163.
- Webster, D. J., B. J. Fraser, M. T. Rietveld, and F. W. Menk, 1987, Conjugate effects from ground excitation of ULF waves in the ionosphere, in ANARE Research Notes 48, (ed G.B. Burns and M. Craven) The Publications Office, Antarctic Division, Channel Highway, Kingston, Tasmania 7150, Australia, pp 34-40.

## 11. ACKNOWLEDGEMENTS

We thank the staff at the Max-Planck Institut für Aeronomie, especially L. Bemmman, H. Gegner, and K. Eulig for their assistance in making these experiments possible. The Heating project was supported by the Deutsche Forschungsgemeinschaft (DFG).

## DISCUSSION

D. PAPADOPOULOS, US

A discrepancy of about one order of magnitude in the ratio of amplitude observed on the ground vs the one observed by satellite and the theoretically expected has been noted in a 1984 paper by James. Has the discrepancy been resolved?

AUTHOR'S REPLY

For the ISIS-1 data you mention, the discrepancy has not been resolved.

U. S. INAN, US

Is the excitation of magnetospheric ELF/VLF waves really more efficient than that of exciting waves into the waveguide? Are the wave intensities observed on the ground inconsistent with satellite observations where one takes into account the absorption during transionospheric propagation?

AUTHOR'S REPLY

The estimate of radiated power into the magnetosphere from the DE-1 data do suggest about an order of magnitude more efficient excitation than into the waveguide. I think, however, that there is room for better modelling. The intensities are not inconsistent, considering the uncertainties in the absorption during transionospheric propagation.

M. CARLSON, US

Could you say more about the null result of Alfvén wave detection (heater induced)?

AUTHOR'S REPLY

The search for artificial pulsations using the GEOS-2 geostationary satellite yielded a null result for the long period pulsations. The chance of detecting such pulsations is very low, however, because the small spatial extent of the modified ionosphere maps to a region near the equator which is also very small. Fejer and Krenn (1982) discuss the probabilities of detection by satellites. The amplitudes are also expected to be very small. I do not remember what the detection limits for the satellite observations were.

J. S. BELROSE, CA

You have described VLF transmission (12.1 kHz over a 425 km path) in terms of multimode propagation. While this is one interpretation, propagation over this short distance range can more simply be described in terms of a ground- and a once reflected sky-wave. In this interpretation, the direction of phase changes at the time of a sunset minimum in amplitude of the total field can be simply explained. It depends on whether the skywave or groundwave is the stronger. Hence the positive or negative phase perturbation with heating can more simply be visualized.

AUTHOR'S REPLY

We used the multimode waveguide propagation approach because we had the programs for such calculations available, and this approach is easily extended to longer distances, where the number of rays necessary becomes large. I agree that for a short path one could use the ray approach.

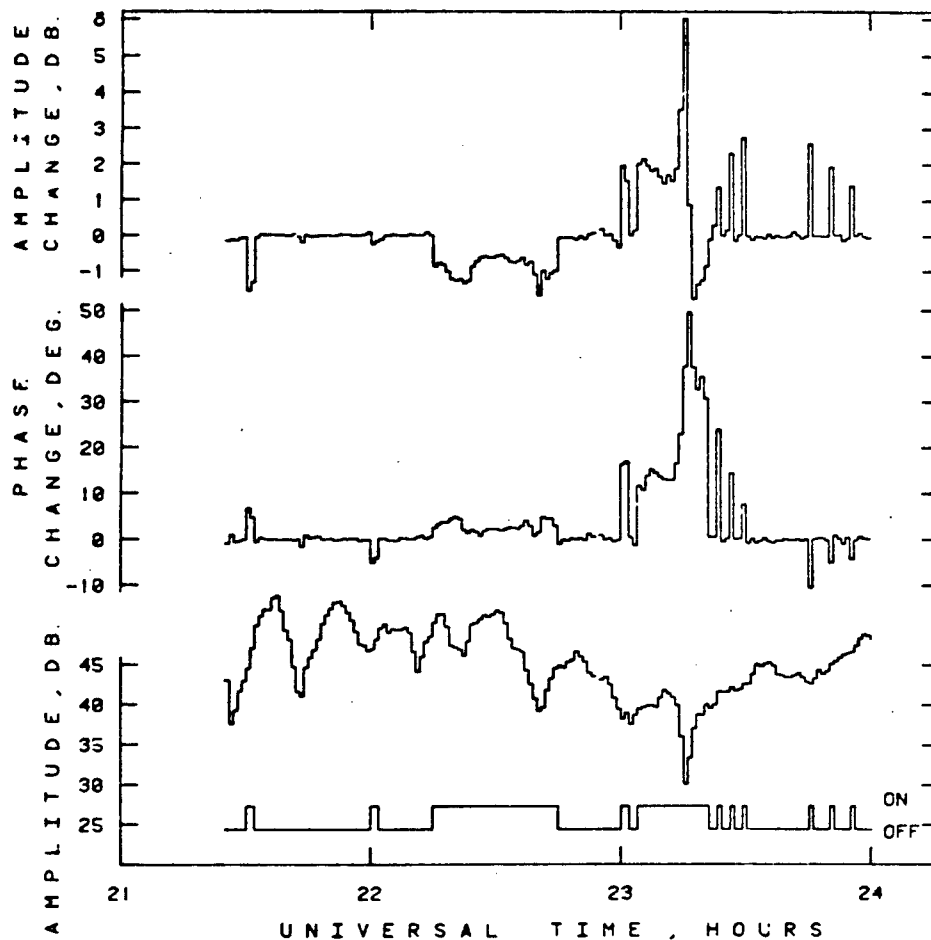


Figure 1. Heater-induced amplitude and phase perturbations of 12.1 kHz Omega signals on 29 Sept. 1983. The heater on times, with X-mode at 2.759 MHz and ERP=260 MW, are indicated at the lower edge. Heater on was during segments D and G of the Norwegian Omega transmission format. Upper panel: relative amplitude change, derived from successive short on/off periods. Middle panel: corresponding phase change. Lower panel: field strength during heater-off.

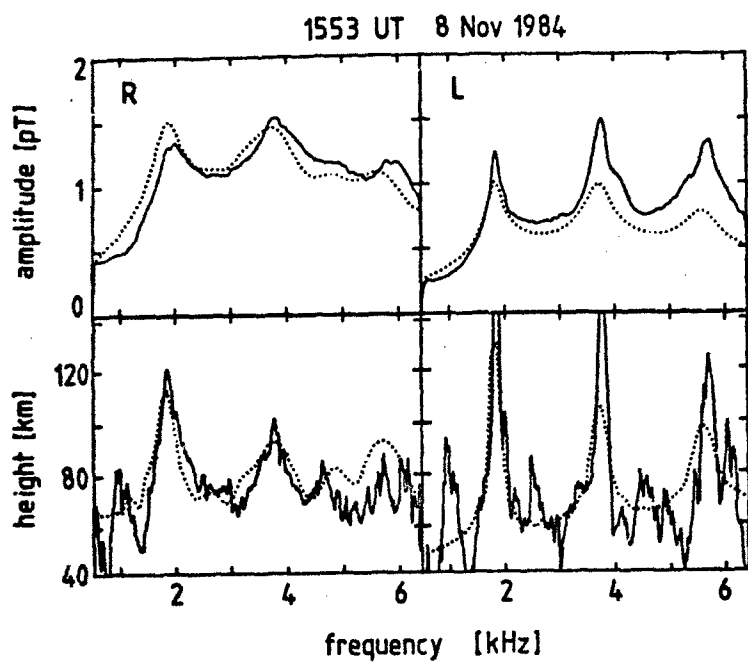


Figure 2. Experimental frequency sweep (solid line) separated into the right- (R) and left- (L) handed circular components. The dotted lines show the results of our model. Upper panels: amplitude. Lower panel: Apparent source height derived from the phase variation with frequency.

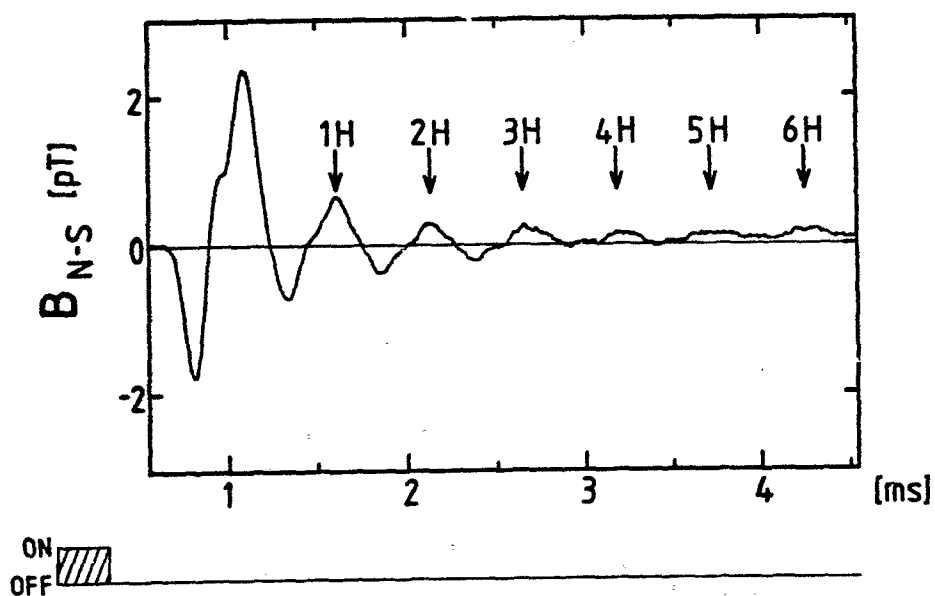


Figure 3. ELF/VLF broadband response to a 300  $\mu$ s heating pulse (indicated at bottom). An average over 50 pulses is shown. Multiple reflections between ground and ionosphere of the direct ionospheric signal are indicated up to the sixth hop.

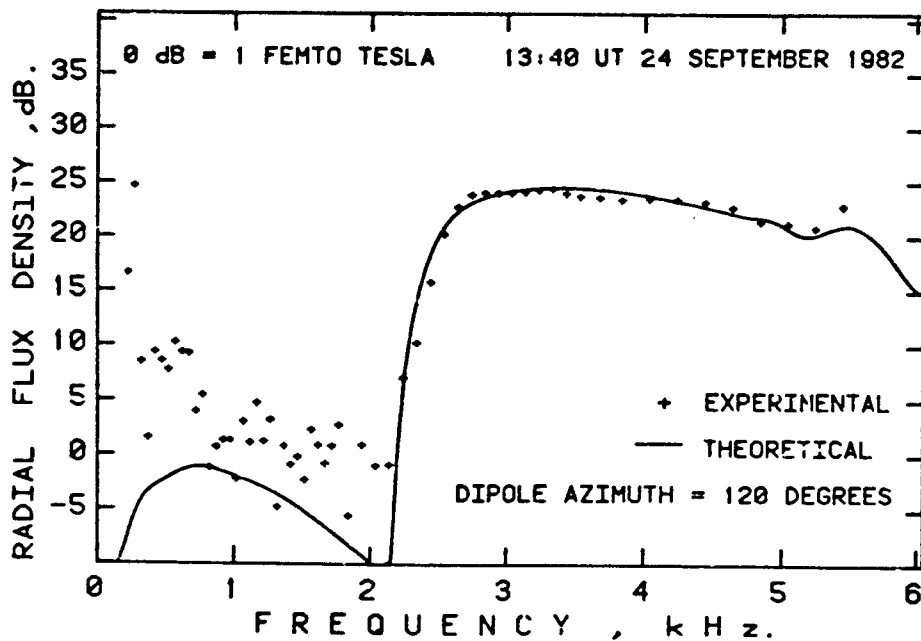
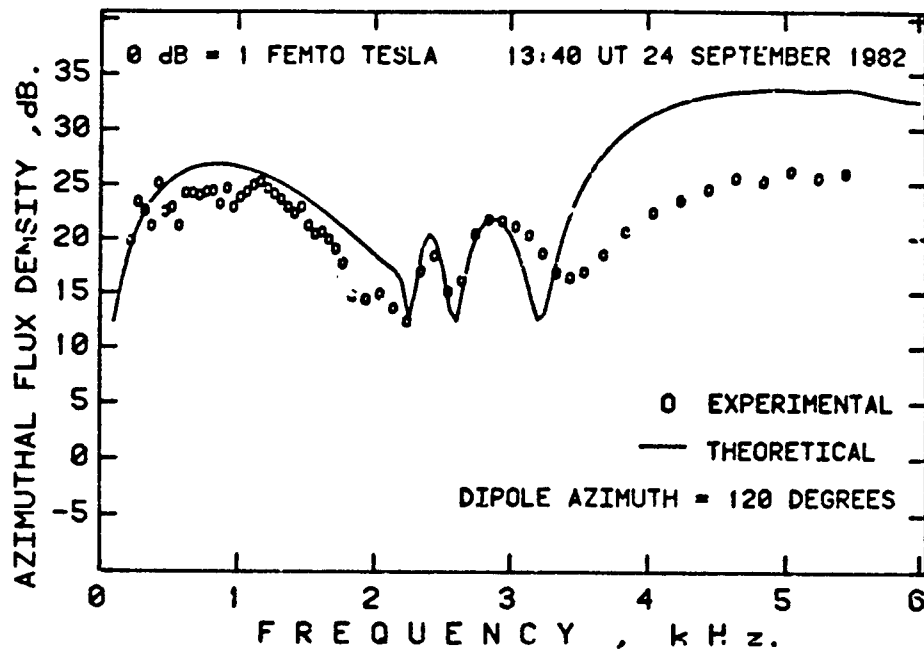


Figure 4. Comparisons of theoretical estimates of radial and azimuthal magnetic fields 554 km from the source, as a function of frequency, with experimental daytime observations.

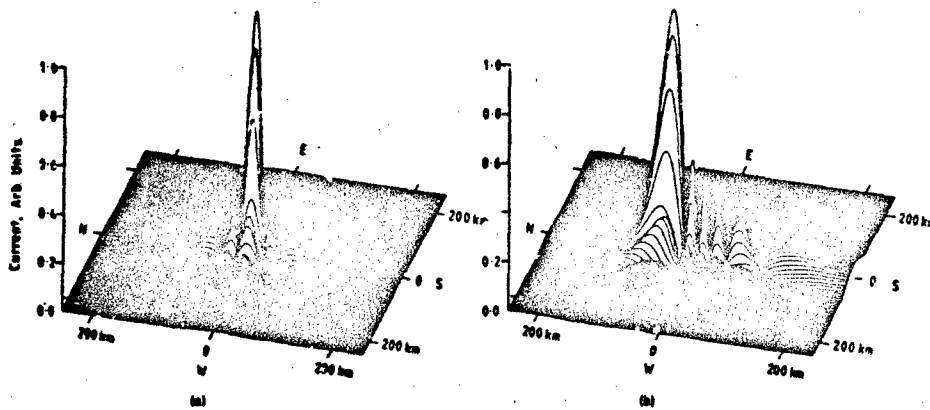


Figure 5. Effective ELF/VLF source current at 71 km assuming the current is proportional to the square root of the HF power. (a) Antenna directed vertically. (b) Antenna beam deflected 37° northward from vertical.

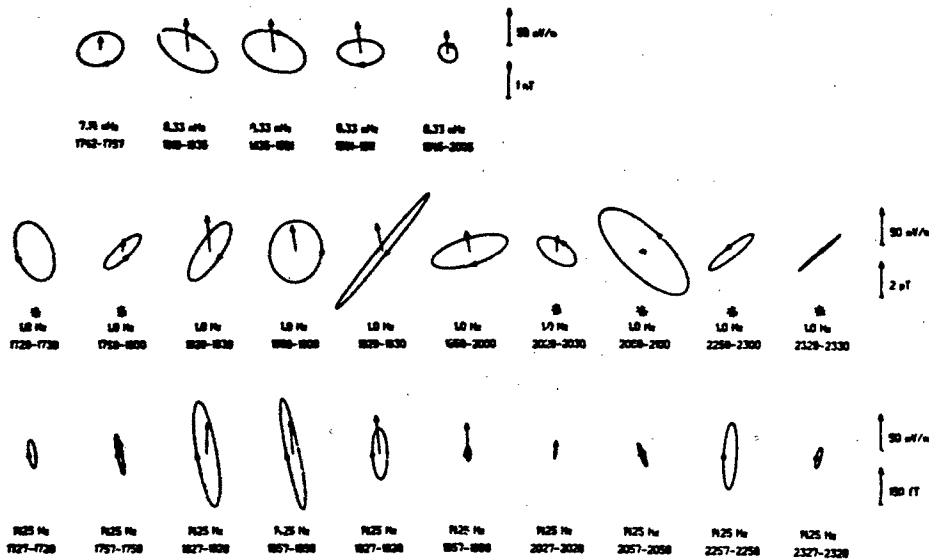


Figure 6. Magnetic Polarization ellipses for an experiment on 26 October 1984 covering 5 decades in frequency. The electric field arrows are derived from EISCAT radar measurements. Upper row: 120 s period oscillations. Middle row: 1 Hz oscillations. Bottom row: 1425 Hz waves. The ellipses marked with asterisks have a degree of polarization less than 0.5.

Observations of the anomalous absorption of diagnostic radio waves during ionospheric modification at Arecibo

A.J. Stocker, T.R. Arbinson and T.B. Jones  
 Department of Physics  
 University of Leicester  
 University Road  
 Leicester, LE1 7RH, U.K.

### Abstract

Theory indicates that the anomalous absorption produced during modification of the ionosphere by means of high power radio waves is dependent on the magnetic dip angle. Recent measurements of the anomalous absorption at Arecibo, Puerto Rico, are found to be considerably smaller in magnitude than those previously reported for the high latitude site at Tromsø, Norway.

### 1) Introduction

The anomalous (or wideband) absorption of low power HF diagnostic radio waves propagating through an F-region illuminated by a high power radio wave (heater) was discovered during some of the earliest heating experiments at mid-latitudes at Platteville (eg Cohen and Whitehead 1970; Utlaut and Violette 1974). Heater induced anomalous absorption has also been a regular feature of heating experiments performed at high-latitudes at the MFI heating facility at Tromsø (Stubbe *et al* 1982; Robinson 1985; Jones *et al* 1986). Simultaneous observations of large scale heating and anomalous absorption at Tromsø led Robinson (1989) to suggest that at high latitudes anomalous absorption of the pump wave itself plays a far more significant role in heating the plasma than deviative absorption. Theoretical studies (Robinson 1989) also predict that for the same ionospheric conditions, anomalous absorption and therefore anomalous heating, should be much smaller at low-latitudes (eg Arecibo, dip angle  $50^\circ$ ) than at high latitudes (eg Tromsø, dip angle  $78^\circ$ ), due to the role played by the direction of the geomagnetic field.

A wide variety of heating experiments have been undertaken with the heating facility at Arecibo but no direct observations of anomalous absorption have been reported. However, Fejer *et al* (1989) have measured a reduction of about 4 dB in the reflected heater wave after a few seconds of heating and Coster *et al* (1985) have observed the growth of field aligned irregularities (FAI) during heating at Arecibo. Heater generated FAIs are currently held to be responsible for anomalous absorption (eg Vas'kov and Gurevich 1975, 1977; Graham and Fejer 1978; Jones *et al* 1984; Mjølhus 1985; Robinson 1989). Mantas *et al* (1981) have inferred, from measurements of electron heating at Arecibo, that weak anomalous heating comparable in size with deviative heating does occur.

In this paper the first direct observations of anomalous absorption from an HF propagation experiment at Arecibo are presented.

### 2) Experimental Results

The experiment reported below was performed on 16 May 1989 and ran from 1630 until 1900 AST (Atlantic Standard Time, AST = IJT - 4). The interval of interest occurred towards the end of this experimental period from about 1800 AST onwards. The heater, which is located at Islote (17 km northeast of the Arecibo Observatory), transmitted O-mode polarized signals at a frequency of 7.4 MHz. From 1700 AST the heater was repeatedly turned on for five minutes and then off for ten minutes. Four HF transmitters were operated, each with a power of 100 kW resulting in an effective radiated power (ERP) of approximately 80 MW (assuming an antenna gain of 23 dB).

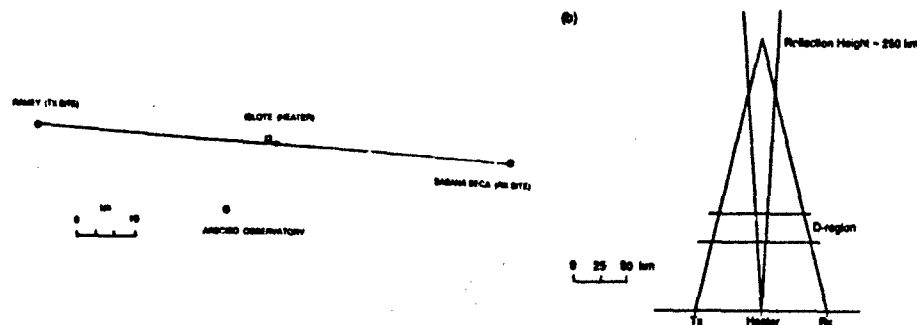


Figure 1. a) Map showing the location of the diagnostic transmitter and receiver sites, the heater and the 430 MHz radar at the Arecibo Observatory.  
b) A schematic of the diagnostic ray paths in relation to the 3 dB contour of the heater.

The diagnostic equipment, which consists of 3 low power (30 W) transmitters and 5 receivers, has been described in detail by Robinson (1989) for experiments at Tromsø. This equipment was deployed for the experiment described here with the transmitters located at Ramey Solar Observatory and the receivers and data logging apparatus at Sabana Seca Naval Base (Figure 1a). This experimental geometry ensures that the diagnostic waves do not propagate through the heated D-region (Figure 1b) and thus only F-region modification effects will be observed. During the interval in question the three diagnostic frequencies were approximately, 6.77, 7.65 and 7.95 MHz. O-mode polarized waves were monitored for all three of these frequencies. A further receiver monitored the reflected heater signal strength.

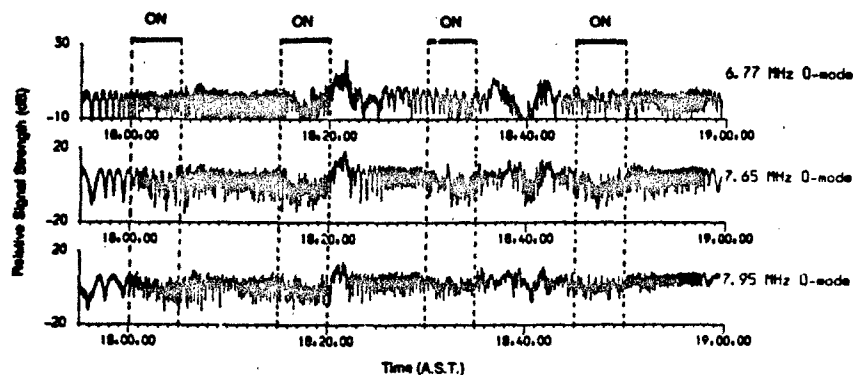
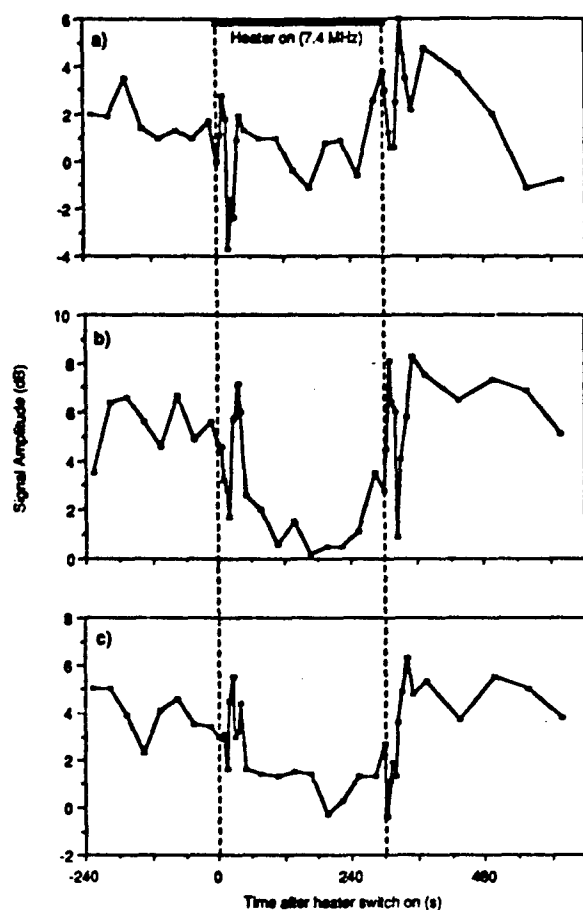


Figure 2. Amplitude variation of the diagnostic signals versus time on 16 May 1989. The heater was operated in O-mode with an ERP of 80 MW and at a frequency of 7.4 MHz.

The diagnostic O-mode signal amplitudes recorded by the receivers and integrated over a 1 second period are presented in Figure 2. It is clear that the diagnostic signals have been absorbed and the fading rate has changed during heating. However, the depth of fading before heater turn on is similar in magnitude to the heater-induced absorption making it difficult to identify the precise onset time of the heating effects. In an effort to identify the systematic heating effects more clearly the data from four consecutive heater cycles between 1800 and 1900 AST have been overlaid and averaged (Figure 3). The heater induced absorption for each of these three diagnostics has been estimated from Figure 3 and the results presented in Table 1. The level of absorption is highest at the diagnostic frequency closest to the heater frequency.





**Figure 3.** Superimposed O-mode diagnostic field strength from four heater cycles between 1800 - 1900 AST, 16 May 1989. Heater on time is indicated by the dashed lines. a) 6.77 MHz; b) 7.65 MHz; c) 7.95 MHz.

$\omega_p / 2\pi$ (MHz)	6.77	7.65	7.95
Absorption (dB)	1.5	4.8	2.5

**Table 1.** Anomalous Absorption in dB of three diagnostic frequencies for 4 heater cycles between 1800-1900 AST, 16 May 1989.

The amplitude variation immediately after heater turn on appears to oscillate in a manner similar to damped SHM (Figure 3a). At heater turn off a similar oscillatory feature is observed in the amplitude but this time the phase of the oscillations is the opposite to that at heater turn on. A similar response occurs for the interval reproduced in Figure 3b. In Figure 3c oscillatory features are still evident but do not exhibit the marked phase reversal between on and off conditions noted in the other two cases. A detailed analysis of these features is beyond the scope of the present work, however, further investigation of this phenomena will be the subject of a future paper.

### 3) Discussion

Robinson (1989) has discussed three possible mechanisms which could lead to the reduction of diagnostic signal amplitude in experiments of the type described,

- i) Enhanced D-region absorption
- ii) F-region defocussing due to large scale plasma density change
- iii) F-region scattering of EM waves into Langmuir waves from small scale FAI, ie anomalous absorption.

For the current experiment the spacing of the transmitter and receiver stations (Figure 1) should ensure that the diagnostic waves do not pass through the heated D-region. In addition the diagnostic signal response to this D-region absorption has a much shorter time constant than that exhibited by the data.

Mechanism (ii) requires large scale changes in the plasma density. There is some evidence for such changes, as a heater-induced increase in electron temperature of close to 200 K has been measured by the 430 MHz radar. However, no diagnostic phase changes were observed in these experiments, a result which is consistent with no change, or a very small change, in electron density (Jones *et al* 1982). It should be noted that large changes in the electron density are not required for defocussing to occur. Robinson (1989) eliminated defocussing as an amplitude reduction mechanism for the Tromsø experiment on the grounds that the absorption time constants were much less than the times measured for large scale changes in the density to occur. For the experiments reported here there was no measurable change in the electron density and therefore it was not possible to deduce the relevant time constants. However, in previous experiments at Arecibo, Mantas *et al* (1981) reported growth and decay times of the modified electron temperature of between 17 and 30 s. The recovery time of the diagnostic amplitude is much less than this (Figure 3), although the onset time is similar. Therefore, it is likely that defocussing can be eliminated as a significant source of the observed amplitude reduction.

By eliminating mechanisms (i) and (ii), it remains probable that the reduction in the diagnostic amplitude is a result of anomalous absorption.

### 4) Conclusions

Measurements of the reflected signal strength of low power HF radio-waves propagating through the modified ionosphere have yielded the first direct observations of anomalous absorption at Arecibo. The absorption levels were smaller than those typically observed at high latitudes as predicted by theory (Robinson 1989).

### References

- Cohen R. and Whitehead J.D., *J. Geophys. Res.*, 75, 6439, 1970.
- Coster A.J., Djuth F.T., Jost R.J., and Gordon W.E., *J. Geophys. Res.*, 90, 2807, 1985.
- Fejer J.A., Djuth F.T., Ierkic H.M., and Sutzer M.P., *J. Atmos. Terr. Phys.*, 51, 721, 1989.
- Graham K.N. and Fejer J.A., *Radio Sci.*, 11, 1057, 1976.
- Jones T.B., Robinson T., Stubbe P. and Kopka H., *J. Geophys. Res.*, 87, 1557, 1982.
- Jones T.B., Robinson T., Stubbe P. and Kopka H., *J. Atmos. Terr. Phys.*, 46, 147, 1984.

Jones T.B., Robinson T., Stubbe P. and Kopka H., J. Atmos. Terr. Phys., 48, 1027, 1986.

Mantas G.P., Carlson Jr. H.C. and LaHoz C.H., J. Geophys. Res., 86, 561, 1981.

Mjølhus E., J. Geophys. Res., 90, 4269, 1985.

Robinson T.R., J. Atmos. Terr. Phys., 47, 1245, 1985.

Robinson T.R., Physics Reports, 179, 81, 1989.

Stubbe P., Kopka H., Jones T.B., and Robinson T., J. Geophys. Res., 87, 1551, 1982.

Utlaut W.F. and Violette E.J., Radio Sci., 9, 895, 1974.

Vas'kov V.V. and Gurevich A.V., Sov. Phys. JETP, 42, 91, 1975.

Vas'kov V.V. and Gurevich A.V., Sov. Phys. JETP, 48, 487, 1977.

#### Acknowledgments

We would like to thank the personnel at the Sabana Seca Naval Base and Ramey Solar Observatory for their assistance and for providing the sites for the equipment. The Arecibo Observatory is part of the National Astronomy and Ionosphere Center, which is operated by Cornell University under contract with the National Science Foundation.

#### DISCUSSION

E. MJØLHUS, NO

In Tromsø, a certain maximum level of absorption has been found, at - 18 dB as far as I remember. Do you have a similar kind of result in Arecibo?

AUTHOR'S REPLY

Experimentally the maximum absorption observed so far is approximately 6 dB. Theoretically, for an intensity of irregularity similar to those observed at Tromsø, the anomalous absorption would be about 5 dB.

L. DUNCAN, US

The Arecibo beam pattern is such that the first sidelobe, with significant power density and opposite polarization from the main beam, occurs at about 15° from vertical. This gives a possible secondary D-region heated volume at about the intersection of your probe waves with the D-region. Therefore great care is needed, such as your O/X mode and time constant comparisons, so as to ensure that D-region effects are excluded.

AUTHOR'S REPLY

We feel confident that the effects are not due to D-region heating: (i) the time constants in the D-region are very much less (~ milliseconds) than those observed (~ 40 seconds); and (ii) tuning the heater to X-mode (and the sidelobe to O-mode) produces no effects.

M. SHOUCRI, US

You assume absorption caused by striations. Is it not possible that large scale striations cause signal scattering rather than absorption? After all striations are associated only with O-mode heating and not X-mode.

AUTHOR'S REPLY

Our results are for O-mode heating. We use both O & X modes for the low power diagnostic signals. We usually see anomalous absorption only for O-mode diagnostic and not for the X-mode diagnostic. However, fading rate changes are observed on both O & X diagnostics, suggesting that scatter effects are observed on both O & X, but absorption, i.e., a general reduction in the signal amplitude is seen on O-mode only. At Arecibo we do see some changes in the amplitude of the X-mode diagnostic (never seen at Tromsø). This effect is, we think, due to the fact that fortuitously the reflection height of the X-mode diagnostic frequency is the same as that of the O-mode pump frequency and thus some strange effects may be expected.

## THEORY OF A THERMAL RESONANCE INSTABILITY IN THE E-REGION OF THE IONOSPHERE.

P. Heeq

Danish Meteorological Institute, Dept. of Geophysics,  
Copenhagen, DK-2100, Denmark

## ABSTRACT

Auroral region modulation experiments have shown, that strong electromagnetic HF waves are generating short-scale field-aligned irregularities in the E region of the high latitude ionosphere. For overdense conditions the instabilities are excited close to the reflection altitude of the O-mode heating wave. The theory presented here for a thermal resonance instability are capable of explaining these observations for magnetically quiet to moderate disturbed conditions. We consider the dispersion relation for a thermal resonance instability, where differential heating by collisional dissipation is more important than the action of the ponderomotive force. Thus special attention is paid to the transport theory, when a constant ambient electric field is applied to the plasma. For irregularities with transverse scale lengths much smaller than the wavelength of the heating wave, thermal nonlinearity causes strongly enhanced electron density fluctuations in regions of excess heating wave intensity. In the region, where the upper hybrid frequency of the plasma matches the heating wave frequency, the initial growth of irregularities takes place. The dispersion relation for the electrostatic response of the heating wave together with the full theory of transport lead to criteria for the threshold electric heating wave field, growth rate and drift velocity of the instabilities. Numeric simulations of the theory demonstrate, the magnitude of the threshold electric field as function of altitude in the ionosphere, the magnitude and direction of the phase velocity of unstable waves and the influence of the constant ambient electric field on the threshold criteria.

## 1. INTRODUCTION.

Vertical HF heating of the high latitude ionosphere with frequencies, just below the maximum plasma frequency of the E region, have been able to generate unstable waves propagating close to the direction of the drift of the ambient plasma [1,2,3,4]. Series of experiments with the Heating Facility near Tromsø, Norway showed a preference of HF modulation plasma processes, when the ambient plasma irregularities were small or moderate [4]. The aim of this paper is to present a theory for the observations done during magnetically quiet to moderate disturbed conditions ( $K_p < 3$ ).

The theory of the thermal resonance instability is derived from the fluid approximation to the full dispersion relation. Similar results for a simpler model have already been presented in the literature [5,6]. But since the E region of the ionosphere is relatively dense, this paper will demonstrate the importance of including all thermal forces and the spatial extend of the pump wave in the upper-hybrid resonance region. Thus section 2 will treat the transport equations in detail and the possible approximations needed to explain the modulation experiments. In section 3, we will present the electrostatic pump wave relations to the electron density perturbations. The necessary spatial extend of the pump wave electric field will be verified [6]. Section 4 briefly discusses an approximation to the linearized dielectric tensor, when a constant ambient convectional electric field is present in the plasma. Finally, in section 5, we show the simulation results of the theory. Additional we summarize the results.

## 2. THE TRANSPORT EQUATIONS.

To describe the ionospheric plasma, when the heater wave is present, we have assumed a plasma consisting of electrons, one species of single ionized ions and neutrals. Due to the geometry at high latitudes the pump wave modulations is thought to generate irregularities with a spatial extend, along the Earth magnetic field direction, that is larger than the parallel diffusion length of the electrons. The ions are considered unmagnetized and the electron gyroradius is small compared to the wavelengths of the

instabilities. Together with the assumptions that electrons and ions behave isothermal and that the time scale of the instability process is larger than the plasma collision times, the set of equations describing the dynamics can be divided into sets of equations parallel and perpendicular to the ambient magnetic field  $B_0$ . Figure 1 outlines the geometry of the experiment.

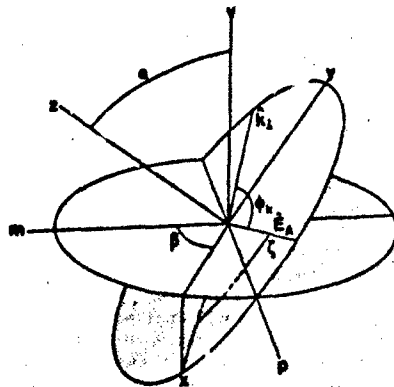


Fig. 1 The geometric relations used in the theory. The direction of the Earth's magnetic field is along the z-axis.  $s, z$  and  $v$  form the magnetic meridian plane.  $v$  is in the vertical direction, while  $[s, p]$  constitute the horizontal plane. The unit vector  $\hat{s}_1$  indicates the direction of the constant ambient convectional electric field.  $\hat{s}_2$  represents the unit vector of the perpendicular wave number vector of the irregularities.

The fluid momentum equations for the electrons and ions, parallel and perpendicular to  $B_0$ , become (7)

$$m_e \frac{\partial v_{ez}}{\partial t} - e \nabla_z \phi + \nabla_z T_e + \frac{T_e}{N_e} \nabla_z N_e =$$

$$-m_e v_{e\perp} (v_{e\perp} - v_{i\perp}) - m_e v_{e\perp} v_{e\perp} - \hat{g}_T \nabla_z T_e$$

$$m_i \frac{\partial v_{iz}}{\partial t} + e \nabla_z \phi + \nabla_z T_i + \frac{T_i}{N_i} \nabla_z N_i =$$

$$m_i v_{i\perp} (v_{e\perp} - v_{i\perp}) - m_i v_{i\perp} v_{i\perp} + \hat{g}_T \nabla_z T_i$$

$$m_e \frac{\partial v_{e\perp}}{\partial t} + e \nabla_{\perp} \phi + \nabla_{\perp} T_e + \frac{T_e}{N_e} \nabla_{\perp} N_e - m_e \Omega_e (\hat{s} \times v_{e\perp}) =$$

$$-m_e v_{e\perp} (v_{e\perp} - v_{i\perp}) - m_e v_{e\perp} v_{e\perp} + \frac{\partial^2}{\partial s^2} \hat{s} (\hat{s} \times \nabla T_e)$$

$$m_e \frac{\partial \mathbf{v}_e}{\partial t} - e \mathbf{E}_0 + e \nabla \phi + \nabla T_e + \frac{T_e}{N_e} \nabla N_e + m_e \Omega_e (\hat{\mathbf{b}} \times \mathbf{v}_e) =$$

$$m_e \nu_{ee} (\mathbf{v}_e - \mathbf{v}_i) - m_e \nu_{ei} \mathbf{v}_i - \frac{1}{N_e} \nabla \cdot (\hat{\mathbf{b}} \times \nabla T_e)$$

The temperatures are defined as  $k_B T$ , where  $k_B$  is the Boltzmann constant.  $\phi$  is the electric potential defined as  $\mathbf{E} = -\nabla \phi$ .  $\mathbf{E}_0$  is the constant electric field in the plasma,  $\hat{\mathbf{b}}$  is a unit vector along the direction of  $\mathbf{E}_0$  ( $\hat{\mathbf{b}} = \mathbf{E}_0/|\mathbf{E}_0|$ ).  $\mathbf{v}_{e,i}$  represents the electron and ion velocities in the reference frame of the neutral gas.  $\Omega_e$  is the electron gyrofrequency,  $\nu_{ee}$ ,  $\nu_{ei}$ ,  $\nu_{ii}$  represent the considered collision frequencies and  $N_i$ ,  $N_e$  the ion and electron densities. We have assumed a neutrality condition for the steady-state densities of ions and electrons, i.e.  $N_{e0} = N_{i0}$ . The thermal forces included in the above equations originate from the velocity dependence of the collision frequencies and the temperature gradients [7]. It leads to the thermal derivatives given in appendix A. Here  $\nu_{ei}$  refers to the averaged electron-ion collision frequency.

Perturbation calculations together with quasi neutrality and the continuity equations result in the relation for the temporal changes in the electron density.

$$\frac{1}{N_e} \frac{\partial N_e}{\partial t} = \left[ \epsilon_n \frac{\partial N_e}{\partial t} + \epsilon_T \frac{\partial T_e}{\partial t} \right] - \nabla \cdot \frac{1}{N_e} \nabla N_e$$

with

$$\epsilon_n = D_e^* (1 + \hat{D}_{ee}) (\alpha_n \alpha_e - 1)$$

$$\epsilon_T = D_e^* \left[ (1 + \hat{D}_{ee}) (\alpha_n \alpha_e - 1) + (\alpha_e - \hat{D}_{ee}) \right]$$

$D_e^*$  and  $\hat{D}_{ee}$  are given in appendix A. They consist of the product of the electron diffusion coefficients and the squared wave number of the irregularities perpendicular and parallel to the Earth magnetic field. The  $\alpha_i$  terms are also given in appendix A.

The last term on the right-hand side of the equation for  $\partial N_e / \partial t$  becomes a function of the diffusion coefficients, the wave number vector, collision frequencies and  $(\delta N_e / N_e)^2$ . Since the term is of second order, it is normally omitted. But for the whole possible parameter space, it is not trivial to discard the last term. For typical E region parameters together with  $|\delta N_e / N_e| < 0.1$  the last term becomes small.

The second moment transport equation, the energy equation, reduces for the electrons to,

$$\frac{1}{T_e} \frac{\partial T_e}{\partial t} - \frac{1}{N_e} \frac{\partial N_e}{\partial t} + \nu \frac{m_e}{m_i} \left[ \frac{1}{2} \epsilon_T \frac{\partial T_e}{\partial t} + \epsilon_n \frac{\partial N_e}{\partial t} \right]$$

$$+ \frac{1}{2} \nabla \cdot \frac{1}{T_e} \nabla T_e = \frac{1}{N_e T_e} \left[ -\nabla \cdot \mathbf{q} + \epsilon Q_e \right]$$

$\mathbf{q}$  represents the heat flux. The cooling terms have been included in  $\epsilon_T$  and  $\epsilon_n$  (see appendix A). The  $\epsilon_T$  and  $\epsilon_n$  terms are also related to the density and temperature dependence of the collision frequencies. Thus they will be influenced by the steady-state heating of the plasma caused by the strong pump wave and the ambient convective electric field.

Together with the electron heat flux expressions, we have established a closed system of equations for determining the transport processes in the plasma. The heat flux equations are

$$\frac{1}{N_e T_e} q_{e1} = -\kappa_1^* \frac{1}{T_e} \nabla T_e + \hat{g}_1 [\mathbf{v}_e - \mathbf{v}_i],$$

$$\frac{1}{N_e T_e} q_{e2} = -\kappa_1^* \frac{1}{T_e} \nabla T_e - \kappa_A^* \left[ \hat{\mathbf{b}} \times \frac{1}{T_e} \nabla T_e \right] - \alpha_e \left[ \hat{\mathbf{b}} \times [\mathbf{v}_e - \mathbf{v}_i] \right]$$

The thermal heat flux coefficients  $\kappa_1^*$ ,  $\kappa_1^*$  and  $\kappa_A^*$  are defined as

$$\kappa_1^* = A_1 \nu l_e^2$$

$$\kappa_1^* = A_1 \nu r_e^2$$

$$\kappa_A^* = A_A \nu r_e l_e$$

The approximations to the transport constant,  $A_1$  and  $A_A$ , for the conditions in the ionosphere are given in appendix A.  $l_e$  is the mean free path of the electron and  $r_e$  is the electron gyroradius.

Substituting the expressions for the heat flux into the energy equation gives the following result

$$\begin{aligned} \frac{3}{2} \frac{1}{T_e} \frac{\partial T_e}{\partial t} - \frac{1}{N_e} \frac{\partial N_e}{\partial t} \\ + \left[ \frac{3}{2} \frac{m_e}{m_i} \delta_T + D_e^* [\delta_T + \hat{D}_{ee}^{-1} \delta_T] \right] \frac{\delta T_e}{T_e} \\ + \left[ \frac{m_e}{m_i} \delta_N + D_e^* [\delta_N + \hat{D}_{ee}^{-1} \delta_N] \right] \frac{\delta N_e}{N_e} = \frac{\delta Q_e}{N_e T_e} \end{aligned}$$

$\delta_{T,1}$ ,  $\delta_{T,2}$ ,  $\delta_{N,1}$  and  $\delta_{N,2}$  are given in appendix A.

The next step is to express  $\delta Q_e$  as density and temperature fluctuations. The heat source are divided into two terms.

$$\delta Q_e = \delta Q_p + \delta Q_A$$

$\delta Q_p$  is the differential heating of the pump wave and  $\delta Q_A$  the ambient heat source of the currents in the plasma. In section 3, a relation is given for the differential heating in the resonance region and the density fluctuations for a linear electron density profile in the interaction region.

Perturbation calculations of the closed set of equations gives the characteristic equation.



$$\underline{T} \begin{pmatrix} \frac{\delta T_e}{T_e} \\ \frac{\delta N_e}{N_e} \end{pmatrix} = \lambda \begin{pmatrix} \frac{\delta T_e}{T_e} \\ \frac{\delta N_e}{N_e} \end{pmatrix}$$

$$\underline{T} = \begin{pmatrix} [Q - i\frac{1}{2}\omega] & [H + i\omega] \\ \epsilon_T & [\epsilon_N + i\omega] \end{pmatrix}$$

where

$$Q = Q_{A_0} [N_e T_e]^{-1} + \frac{1}{2} \frac{m_e}{m_i} \delta_T + D_e^* [\delta_{T_e} + \widehat{D}_{ee}^{-1} \delta_{T_e}]$$

$$H = [Q_e - 2Q_{A_0}] [N_e T_e]^{-1} + \frac{m_e}{m_i} \delta_N$$

$$+ D_e^* [\delta_{N_e} + \widehat{D}_{ee}^{-1} \delta_{N_e}]$$

The threshold for the instability can be found for  $\gamma = 0$  or  $\gamma = -A$ , where

$$A = \frac{1}{2} [Q - [\frac{1}{2}\epsilon_N + \epsilon_T]]$$

The threshold condition for marginal growth of the instability becomes

$$\left| \frac{Q_e}{N_e T_e} \right|_{\text{max}} = Q_{A_0} [N_e T_e]^{-1} [\frac{1}{2}\epsilon_N + 2]$$

$$+ \frac{m_e}{m_i} [\frac{1}{2}\frac{\epsilon_N}{\epsilon_T} \delta_T - \delta_N]$$

$$+ D_e^* \left[ \frac{\epsilon_N}{\epsilon_T} [\delta_{T_e} + \widehat{D}_{ee} \delta_{T_e}] - [\delta_{N_e} + \widehat{D}_{ee} \delta_{N_e}] \right]$$

Solutions to the threshold depends on the sign of  $\epsilon_T$  and the magnitude of  $\omega_r$ , which represents the phase velocity of the unstable waves. For  $\omega_r = 0$ , the growth rate becomes

$$\gamma = [\epsilon_N + \frac{1}{2}\epsilon_T] - \frac{1}{2} Q_{A_0} [N_e T_e]^{-1}$$

$$- \frac{m_e}{m_i} \delta_T - \frac{1}{2} D_e^* [\delta_{T_e} + \widehat{D}_{ee} \delta_{T_e}]$$

For  $\omega_r = 0$  and  $\epsilon_r < 0$ , the growth rates increase for increasing  $Q_{re}$ . While the growth rates decrease for  $\epsilon_r > 0$  and for  $Q_{re} \rightarrow (Q_{re})_{max}$ .

$$|Q_{re}|_{\omega_r=0} = |Q_{re}|_{max} + \frac{1}{2} N_e T_e \epsilon_r' \left( \frac{\gamma_r}{2} \right)^2$$

For  $\omega_r \neq 0$ , we find the growth and the phase velocity to become

$$\gamma_r = \frac{1}{2} \gamma_e$$

$$\left( \frac{\omega_r}{k_r} \right)^2 = \frac{1}{2} \epsilon_r' (N_e T_e)^{-1} \left[ Q_{re} - |Q_{re}|_{max} \right] - \left( \frac{\gamma_r}{k_r} \right)^2$$

$$\epsilon_r'' = \epsilon_r k_r^{-2}$$

$\epsilon_r < 0$ , the instabilities will only have the phase velocity of the electron gas caused by the ambient convective electric field. For  $\epsilon_r > 0$ , the threshold condition and the phase velocity become

$$Q_{re} > |Q_{re}|_{max}$$

$$\left| \frac{\omega_r}{k_r} \right| = \left\{ \left[ \frac{1}{2} \epsilon_r' (N_e T_e)^{-1} |Q_{re}|_{max} \right] \cdot [\epsilon - 1] \right\}^{1/2}$$

$$\epsilon = \frac{Q_{re}}{|Q_{re}|_{max}}$$

### 3. THE WAVE EQUATION.

Small density perturbations create together with the strong pump wave field a polarization charge, which gives rise to the electrostatic field fluctuation  $E_1$ . Under the assumptions,  $\underline{\epsilon} = \underline{\epsilon}_0 + \delta \underline{\epsilon}$  and  $\underline{N} = \underline{N}_0 + \underline{N}_1$ ,

$$\underline{E}_1 = \underline{\epsilon}_0 \cdot \frac{\delta \underline{N}_0}{N_0}$$

$\underline{\epsilon}$  is the dielectric tensor and  $\underline{E}_0$ , the constant pump wave field. Neglecting higher order perturbation terms for a quasi one dimensional model, gives

$$\underline{\epsilon}_0 \cdot \underline{E}_1 = \epsilon_0 \frac{\chi}{1 - \chi} \frac{\delta N_0}{N_0} \left( \underline{E}_0 + i \gamma \underline{E}_0 \right)$$

X and Y are given in appendix B. The above is valid for slow spatial variations in  $\underline{E}_0$  and for  $(\omega/k)_{\text{pump}} = v_{\text{ph}} = |\delta v_e|$ , where  $\delta v_e$  refers to velocity fluctuations in the electron population.

We now want to find a relation between  $E_1$  and  $\delta N_e/N_e$  at the level of the upper-hybrid resonance. In this region the real part of the refractive index goes to infinity. As the wave approaches the resonance region, both its phase velocity and group velocity goes to zero, and the pump wave energy is converted into upper-hybrid oscillations. These waves will in a inhomogeneous plasma be absorbed in the resonance region.

For perpendicular propagation of the pump wave to  $B_0$ , resonance occurs for

$$R + L = 0$$

R and L are given in appendix B. To simplify the conditions at the resonance region, we assume the electron density to be linearly dependent of the altitude h,

$$X = (1 - Y^2) \left(1 + \frac{h}{L_n}\right)$$

$$L_n = \left(\frac{1}{N_e} \frac{\partial N_e}{\partial z}\right)^{-1}$$

This gives a relation for the pump wave electric field and the electron density fluctuations.

$$E_1 = -\frac{\frac{h}{L_n} + i\delta}{|\Delta|^2} (E_0 + iY E_0) \frac{\delta N_e}{N_{e0}}$$

$$\Delta = -\frac{h}{L_n} + i\delta$$

$$\delta = Z \frac{1 - Y^2}{1 - Y}$$

The differential heating amounts to

$$Q = 2 \mathbf{E}^* \cdot \mathbf{E}$$

When taking the upward and the downward propagating pump wave into account in the resonance region [5,6], the differential heating becomes

$$Q_p = P_0 P_1 |E_0|^2$$

where

$$P_0 = 8\pi r^2 \epsilon_0 L \exp(-2kL\delta) \frac{1}{\cos\alpha}$$

$$P_1 = r \sin\varphi (a - b \cos^2\delta) + \frac{1}{2} \left[ (1-r^2) \exp(2kL\delta) + 2r \cos\varphi \right] \frac{1}{2} c \sin(2\delta)$$

$$a = [1 - Y^2 \cdot 2Y^2 \Gamma^2 \cdot Y(3 \cdot Y^2) \Gamma] [1 - Y^2]^{-1}$$

$$b = 1 - \Gamma^2$$

$$c = Y[1 - \Gamma^2]$$

$$\Gamma = \frac{1}{2Y \cos^2\alpha} \left[ (\sin^4\alpha + 4Y^2 \cos^2\alpha)^{1/2} - \sin^2\alpha \right]$$

$\alpha$  is the angle between vertical and the direction of the constant ambient magnetic field  $H_0$ .  $\beta$  is the angle between the magnetic meridian plane and the pump wave electric field. Figure 1 outlines the geometrical relations, when the magnetic field coordinate system is tilted with respect to the Earth reference frame.  $\varphi$  is the angle between the pump wave electric field vector along the x-axis and the constant ambient electric field.

In [6] they show that the differential heating calculated this way gives the same result as for the full two-dimensional analysis.

Recalculating the above expressions for the differential heating of the pump wave with the modified dielectric tensor, given in section 4, result in the below equations.

$$Q_2 = P_0 \left[ P_1 |E_0^*| - \delta E_A [4Y^2(1 - \Gamma^2)]^{-1/2} P_2 \right] |E_0^*|$$

where

$$P_1 = \left\{ 2r \sin\varphi \left[ \frac{1}{2} V_1 \cdot V_2 \cdot \Gamma V_3 \right] + \left[ (1-r^2) \exp(2kL\delta) + 2r \cos\varphi \right] \left[ \frac{1}{2} V_4 \cdot |V_5 \cdot \Gamma^2 V_6| \cdot |V_6 - V_5| [1 - \Gamma^2] \cos^2\beta \cdot \Gamma V_7 \right] \right\}$$

All the  $V_i$  terms (see appendix B) are relations of the geometry of the experiment in the resonance region, the dielectric tensor,  $\epsilon_A$  and  $\epsilon_0$ .

#### 4. THE LINEARISED DIELECTRIC TENSOR.

In most theories the local dielectric tensor with no external forces is used [6,8]. In order to take account for the ambient electric fields influence on the instability threshold and growth rate, we have calculated a linearized dielectric tensor  $\underline{\epsilon}$ , where pressure perturbations and the forces, due to the ambient convectional electric field  $\mathbf{E}_A$  and the pump wave electric field perturbations  $\mathbf{E}_1$ , only are related to electron density fluctuations. The expression for  $\underline{\epsilon}$  is only valid for ionospheric E region conditions with a moderate vertical electron density gradient and for a phase velocity of the pump wave, much larger than the electron thermal velocity of the plasma. For magnitudes of  $\mathbf{E}_A$  smaller than the magnitude of the pump wave electric field  $\mathbf{E}_1$ , we find for the resonance region the current fluctuations.

$$\mathbf{J}_1 = \epsilon_0 \frac{\omega_p^2 \omega'}{\omega_c^2 - \omega'^2} \left[ \mathbf{E}_1 + i \frac{\omega'}{\omega_c} \mathbf{E}_1 \times \hat{\mathbf{b}} - \frac{\omega_c^2}{\omega'^2} [\mathbf{E}_1 \cdot \hat{\mathbf{b}}] \hat{\mathbf{b}} \right] + \epsilon_0 \frac{\omega_p^2}{\omega_c} [\mathbf{E}_A \times \hat{\mathbf{b}}] \frac{\delta N_e}{N_{e0}}$$

$\omega_p$  is the angular plasma frequency,  $\omega_c$  the angular cyclotron frequency. The approximation to the dielectric tensor gets the form

$$\underline{\epsilon} = \epsilon_0 \begin{vmatrix} S\lambda_1 & iD\lambda_2 & 0 \\ -iD\lambda_2 & S\lambda_1 & 0 \\ 0 & 0 & P \end{vmatrix}$$

where

$$\lambda_1 = 1 - i \left[ Y(Y^2 - 1) \{ hL^{-1} - i\delta \} \sin^2 E_A E_0^{-1} \right]$$

$$\lambda_2 = 1 - [Y^2 - 1] \{ hL^{-1} - i\delta \} \cos^2 E_A E_0^{-1}$$

#### 5. SIMULATION RESULTS.

We performed numerical simulations of the thermal resonance instability, as described in the above sections. Some of the results will be presented here.

All the simulations have been done for the Earth's magnetic field tilted 12 degrees with vertical. This is the geometry in the ionosphere at the latitude of Tromsø, Norway. The angle  $\beta$ , defined as the direction of the pump wave electric field with respect to the magnetic meridian plane in the resonance region, has been fixed to 45 degrees. The phase shift between the upward propagating wave and the reflected wave is kept equal to zero, i.e. the lowest threshold condition is estimated. The collision frequencies and their derivatives are deduced from the collision models given in [9,10]. Furthermore, the composition of the neutral ionosphere has been derived from the CIRA 1972 reference atmosphere model. The electron density profile used in all the simulations equals a summertime profile at high latitudes.

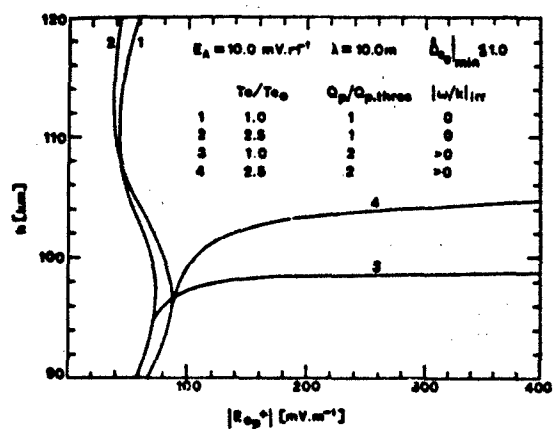


Fig. 2 Threshold of the horizontal pump wave field as function of altitude for 10 m wavelength irregularities. The calculations are done for a ambient convective electric field  $E_A$  of 10 mV/m.

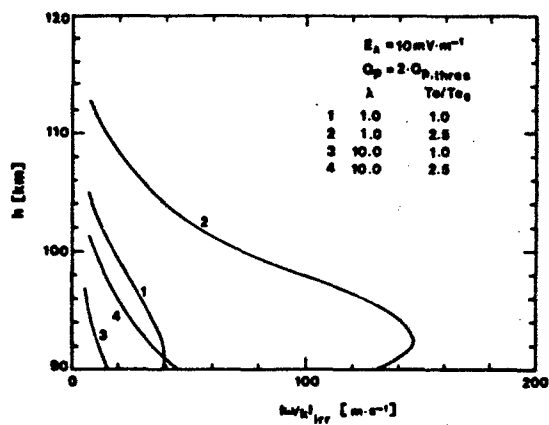


Fig. 3 Magnitudes of the drift velocity of the striations as function of altitude.

Figure 2 shows the threshold pump wave electric field  $|E_{0,p}|$  as function of the altitude. The perpendicular scale size of the instabilities is equal to 10 m, while the parallel length equals the diffusion length of the electrons, which in turn is a function of the altitude.

Below the altitude of 95 km the growth rates for all scale sizes of the unstable waves becomes so small, that damping processes will stabilize the plasma. For altitudes between 95 km and 110 km, increasing  $T_e$  in the heated volume gives higher threshold pump wave electric field for  $|\omega/k|_{irr} = 0$  (graph 1 and 2). While for  $|\omega/k|_{irr} > 0$ , the threshold decreases (graph 3 and 4) for the same altitudes. The calculated thresholds is obtainable with the Heating Facility in Tromsø, Norway. In fact, instabilities can be generated up to an altitude of 110 km with the Heating Facility. If the enhanced  $T_e$  is caused by the heating wave, the plasma may grow unstable for relatively high threshold, for  $|\omega/k|_{irr} > 0$ , since the threshold wave field to maintain the instability is smaller than  $|E_{0,p}|_{thres}$  shown in graph 3 and 4. But this depends strongly on the magnitude and sign of  $\epsilon_2/\epsilon_1$ , given in section 2, and the growth time in reference to the response time of the plasma to react to the strong pump wave modulations.

In general the growth rates increase with altitude. We find growth times less than a second for optimal conditions in altitudes from 102 km to 108 km. For shorter wavelengths of the unstable waves, the average growth time can be less than 100 ns. The growth times decrease for increasing ambient electric field  $E_A$ .

For  $h < 110$  km, the growth rate varies strongly as function of  $\hat{B}_{\infty}$ . Thus the striations have to have a parallel scale size, which is larger than the diffusion length of electrons along  $B_0$ . This means that  $l_{\parallel}$  has to be at least of the order of 0.5 km to 1 km.

Figure 3 gives the phase velocity of the unstable waves in the rest frame of the ambient current, driven by  $E_A$ . The magnitude of 1 m waves are in agreement with the measured phase velocities [4].

Figure 4 shows the influence of  $E_A$  on the threshold pump wave electric field  $|E_{0,p}|$ . The angle  $\theta$  has been set to zero, i.e. the ambient electric field is along the direction of the pump wave electric field. In general we see an increase in the threshold conditions for increasing  $E_A$ . While for  $115 \text{ km} < h < 125 \text{ km}$ ,  $|E_{0,p}|_{thres}$  decreases for  $5 \text{ mV/m} < |E_A| < 20 \text{ mV/m}$ . The decrease amounts to 5 % for  $|E_A| = 12 \text{ mV/m}$ . For another geometry of the experiment, it is possible that even larger changes occur. Here, we have only analyzed this geometry to verify, that it is possible to decrease the threshold pump wave field for increasing  $E_A$ .

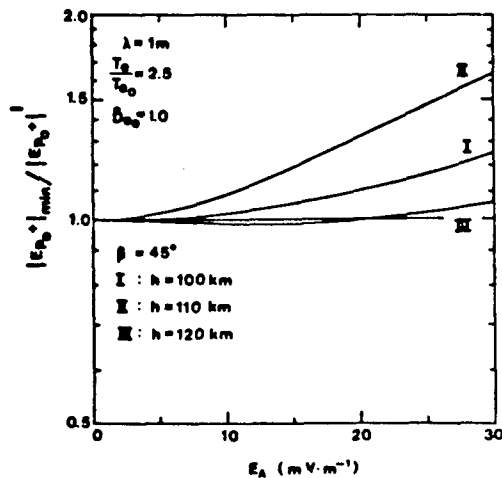


Fig. 4 The relative change in the pump wave threshold field as function of the constant ambient electric field  $E_A$ . The given data are for 1 m wavelength irregularities.

## 6. SUMMARY.

We have presented the theory for the thermal resonance instability in the E region of the high latitude ionosphere. We have demonstrated, that differential heating by collisional dissipation is more important than processes caused by the ponderomotive force. For overdense E region conditions, the theory are capable of explaining the observations done for magnetically quiet to moderate disturbed conditions. For most parameter space, increasing ambient convectional electric fields enhance the threshold of the thermal resonance instability.

In all, the theory shows that existing heaters can modulate the E region of the ionosphere for the presented instability.

## 7. REFERENCES.

1. Nibberd, F.N., E. Nielsen, P. Stubbe, H. Kopka, M.T. Rietveld, Production of auroral zone E-region irregularities by powerful HF heating, J. Geophys. Res., 88, 6347, 1983.
2. Djuth, F.T., R.F. Jost, S.T. Noble, W.E. Gordon, P. Stubbe, H. Kopka, E. Nielsen, R. Boström, H. Derblom, Å. Hedberg, B. Thidé, Observations of E-region irregularities generated at auroral latitudes by a high-power radio wave, J. Geophys. Res., 90, 12293, 1985.
3. Stubbe, P., H. Kopka, M.T. Rietveld, A. Frey, P. Heeg, H. Kohl, E. Nielsen, G. Rose, C. LaHos, R. Barr, H. Derblom, Å. Hedberg, B. Thidé, T.B. Jones, T. Robinson, A. Brakke, T. Hansen, O. Holt, Ionospheric modification experiments with the Tromsø Heating Facility, J. Atmos. Terr. Phys., 47, 1151, 1985.
4. Heeg, P., E. Nielsen, P. Stubbe, H. Kopka, Heater-induced 1-meter irregularities, J. Geophys. Res., 91, 11309, 1986.
5. Das, A.C. and J.A. Fejer, Resonance instability of small-scale field-aligned irregularities, J. Geophys. Res., 84, 6701, 1979.
6. Dysthe, K.B., E. Mjølhus, M. Pécseli, K. Rypdal, A thermal oscillating two-stream instability, Phys. Fluids, 26, 146, 1983.
7. Golants, V.E., A.P. Zhilinsky, I.E. Sakharov, Fundamentals of plasma physics, J. Wiley & Sons, New York, 1980.
8. Gurevich, A.V., Non-linear phenomena in the ionosphere, Springer-Verlag, New York, 1978.
9. Schunk, R.W. and A.P. Nagy, Electron temperatures in the F-region of the ionosphere: Theory and observations, Rev. Geophys. Space Phys., 16, 355, 1978.
10. Schunk, R.W. and J.C.G. Walker, Theoretical ion densities in the lower ionosphere, Planet. Space Sci., 21, 1875, 1973.



## B. APPENDIX A.

$$\hat{e}_0 = \frac{p}{p_0} \hat{Q}_0^T + \hat{Q}_{0n}^T$$

$$\hat{e}_1 = \frac{p}{p_0} \hat{Q}_1^T - \hat{Q}_{1n}^T$$

$$\hat{Q}_T = \frac{2}{3} \frac{\hat{e}_0}{\hat{e}_{0n} + 1.67 \hat{e}_{01}}$$

$$\hat{e}_n = \hat{e}_0 \frac{\hat{e}_{0n} + 0.97 \hat{e}_{01}}{\hat{e}_{0n} + 1.67 \hat{e}_{01}}$$

$$\hat{Q}_{0n}^T = \frac{T_0}{\hat{e}_0} \frac{\partial \hat{e}_0}{\partial T_0}$$

$$\hat{Q}_{1n}^T = \frac{T_1}{\hat{e}_n} \frac{\partial \hat{e}_n}{\partial T_1}$$

$$\hat{Q}_{nn}^T = \frac{T_0}{\hat{e}_{nn}} \frac{\partial \hat{e}_{nn}}{\partial T_0}$$

$$\hat{e} = \hat{e}_0 + \hat{e}_{nn}$$

$$\hat{e} = \hat{e}_0 + \frac{m}{m_0} \hat{e}_{nn}$$

$$D_0^* = k_1^2 \frac{T_0}{m_0 \hat{e}_0^2}$$

$$D_1^* = k_1^2 \frac{T_1}{m_0 \hat{e}_0^2}$$

$$\hat{D}_0 = D_0^* / D_1^*$$

$$\hat{D}_{nn} = D_0^* / D_1^*$$

$$D_0^* = k_1^2 \frac{T_0}{m_0 \hat{e}_0^2}$$

$$A_0 = \frac{2}{3} \cdot \hat{Q}_T$$

$$A_1 = \frac{2}{3} \cdot \hat{Q}_T - \frac{\hat{e}_{01}}{p} \hat{Q}_0^T$$

$$\delta_{N_0} = \hat{Q}_T [1 - \alpha_1 \alpha_3]$$

$$\delta_{T_0} = A_0 + \hat{Q}_T [1 + \hat{Q}_T - \alpha_1 \alpha_4]$$

$$\delta_{N_1} = -\alpha_7 [\alpha_3' + \alpha_1' \alpha_3]$$

$$\delta_{T_1} = A_1 - \alpha_7 [\alpha_4' + \alpha_1' \alpha_4]$$

$$\delta_T = 1 + \alpha_7 \left[ \left( 1 - \frac{T_0}{T_1} \right) - \frac{1}{2} \frac{m}{m_0} \frac{Q_{T_0}}{N_0 T_0} \right]$$

$$\delta_N = \frac{2}{3} \left[ 1 - \frac{T_0}{T_1} \right] - \frac{m}{m_0} \frac{Q_{T_0}}{N_0 T_0}$$

$$\alpha_0' = \left[ 1 + \left( \frac{p}{\hat{e}_0} \right)^2 \right]^{-1}$$

$$\alpha_1 = \left[ \alpha_0' + \hat{D}_{nn} + \frac{p}{\hat{e}} \right]^{-1}$$

$$\alpha_2 = \frac{k_1}{k_0} \hat{D}_{nn} - \left[ \alpha_0' \frac{m}{m_0} \left[ \frac{k_0 \delta v_{0x} + k_1 \delta v_{1y}}{k_1 \delta v_{0x}} \right] \frac{\delta v_{0x}}{\delta v_0} \right. \\ \left. - \frac{p}{\hat{e}} \left[ \frac{k_0 \delta v_{0x} + k_1 \delta v_{0y}}{k_1 \delta v_0} \right] \right]$$

$$\alpha_3 = \hat{D}_{nn} - \left[ \alpha_0' \frac{T_0}{T_1} \frac{\delta N_1}{\delta N_0} - \frac{p}{\hat{e}} \right]$$

$$\alpha_4 = \hat{D}_{nn} (1 + \hat{Q}_T) - \left[ \left( \alpha_0' \frac{\delta T_0}{\delta T_1} - \frac{p}{\hat{e}} \right) \right. \\ \left. - \frac{1}{\hat{e}} (\hat{e}_{nn} \hat{e}_0 + \alpha_0' \hat{e}_{nn} \hat{e}_1) \left( \frac{k_1^2 - k_0^2}{k_1^2} \right) \right]$$

$$\alpha_5 = \frac{k_0 \delta v_{0x} + k_1 \delta v_{0y}}{k_1 \delta v_0}$$

$$\alpha_6 = \alpha_7 \alpha_8$$

$$\alpha_7 = \frac{x_{nn} \hat{e}_0}{p}$$

$$\alpha_8 = \frac{k_1^2 - k_0^2}{k_1^2}$$

## 9. APPENDIX B.

$$S = \frac{1}{2}[R+L]$$

$$D = \frac{1}{2}[R-L]$$

$$R = 1 - \frac{X}{1-Y-IZ}$$

$$L = 1 - \frac{X}{1-Y-IZ}$$

$$P = 1 - \frac{X}{1-IZ}$$

$$X = \frac{e_1^2}{e_0^2}$$

$$Y = \frac{e_1^2}{e_0^2}$$

$$Z = \frac{e_1}{e_0}$$

$$V_1 = (1-Y)Y^{-1}\cos\delta\sin 2\beta(1-\Gamma^2)$$

$$V_2 = 2e\sin\delta \cdot \Gamma^2 e_1 Y Z^{-1} \cos\delta$$

$$\cdot [e_1 \sin\delta - e_1 Y Z^{-1} \cos\delta] [1-\Gamma^2] \cos^2\beta$$

$$V_3 = [1-\delta Y^{-1} \sin\delta \frac{E_A}{E_0}] e_1 Z^{-1} \cos\delta - [1-(e_1-2e_1^{-1})] Y \sin\delta$$

$$V_4 = (1-Y) \sin\delta \sin 2\beta (1-\Gamma^2)$$

$$V_5 = [1-2\delta Y^{-1} \sin\delta \frac{E_A}{E_0}] e_1 Z^{-1} \sin\delta$$

$$V_6 = [1-e_1 Y^{-2} \cos\delta \frac{E_A}{E_0}] 2e_1 Y \cos\delta$$

$$V_7 = e_1 Z^{-1} Y \sin\delta - [1-4e_1^{-1}] \cos\delta$$

$$+ [\delta(2Y)^{-1} \sin 2\delta + (1-e_1 Y^{-2} \cos^2\delta) e_1 e_1] \frac{E_A}{E_0}$$

## DISCUSSION

S. KEO, US

Usually, OTSI can only be excited by dipole pump and in the overdense region of the plasma. The instability considered by the author is, in fact, a filamentation instability since the pump is an electrostatic wave ( $E_0 \parallel B_0$ ) and the excited low frequency wave propagates perpendicular to  $B_0$ .

AUTHOR'S REPLY

I refer to the paper by Dysthe et al, 1987, where they suggest the name, the thermal oscillating two stream instability, for a similar instability as the one presented here. The TRI is dominated by collisional heating processes instead of the ponderomotive force.

E. NYSLIUS, NO

I only wished to comment to Dr. Kuo that what the speaker has in mind, is probably what has been called "the Thermal Oscillating Two Stream Instability", where the dominant nonlinearity is ohmic instead of ponderomotive, but which is otherwise quite analogous to the ordinary Oscillating Two Stream Instability.

AUTHOR'S REPLY

Yes, I agree with Dr. Nyslius.

D. PAPADOPOULOS, US

You described a situation that OTSI has a finite phase velocity due to the fact that it is driven by the ohmic nonlinearity. I would then expect that when the phase velocity approaches  $c_s$  (~ 200-300 m/s) it would couple directly to the Farley-Buneman instability. Have you examined this theoretically or experimentally?

AUTHOR'S REPLY

Yes, the theory predicts for the high latitude E-region, that enhanced ambient electric field stabilizes the plasma for the thermal resonance instability. Using the STARE twin-radar as the diagnostic system, experimentally it has been difficult to determine if the TRI occurs when the two-stream instabilities are observed in the STARE field-of-view.

# ON THE VALIDITY OF THE WEAK TURBULENCE APPROXIMATION

A. Hansen and E. Mjølhus  
University of Tromsø  
N-9000 Tromsø  
NORWAY

## SUMMARY

The weak Langmuir turbulence approach to explain the artificial plasma line in ionospheric radio modification experiments, is examined. The mathematical model is a version of the one dimensional Zakharov equations, including damping and a nonlinear a.c. driving. Numerical full wave solutions to this set of equations are compared with the saturation spectrum determined by a wave kinetic equation derived from the same set of equations. We found that a distance below the O-mode reflection level,  $\omega - \omega_p \gg (m/M)\omega_p$  ( $\omega$  applied frequency;  $\omega_p$  plasma frequency;  $m, M$  electron and ion masses), the full wave solution is in good qualitative agreement with the cascade theory. The number of cascades seen in the full wave solution is generally smaller than that of the saturation spectrum of the wave kinetic equation. On the other hand, in the reflection region  $\omega - \omega_p < (m/M)\omega_p$ , a qualitatively different process takes place, describable as many localized cycles of nucleation, (one dimensional driven) collapse, and burnout, similar to the results of Doolen et al. [8]. These findings are discussed with respect to the experiments performed in Arecibo and Tromsø.

## 1 INTRODUCTION

The conventionally accepted theory for the plasma process responsible for the artificial plasma line backscatter in ionospheric radio modification experiments (e.g. [1] and [2]), is the weak Langmuir turbulence, or cascade theory, as developed in e.g. Kruev and Valeo [3], Fejer and Kuo [4], and Perkins et al. [5]. This interpretation is presently being debated. First, there are certain features observed in the experiments that are not consistent with this kind of theory. In particular, this concerns the observed height in the ionosphere from which the plasma line comes [6],[7]. Second, the above mentioned picture has recently been challenged theoretically [8-11]. These authors claim that the cascade theory has a very limited validity and must be replaced by a theory of strong Langmuir turbulence. According to the latter theory, the turbulence consists of a large number of localized cycles of nucleation, Langmuir collapse, and burnout.

The objective of this presentation is to report a study of the question of internal consistency mentioned above. The set of equations known as the Zakharov model [12] is a well studied mathematical model that contains the basic elements which are of importance in a Langmuir turbulence driven by an electromagnetic field oscillating near the plasma frequency. With respect to the present application of ionospheric radio modification, this model was first invoked by Weatherall et al. [13], and the same model was also used by the Los Alamos group [8-11]. This model certainly contains the relevant initial parametric instabilities [14], and furthermore allows the construction of a cascade theory in a way completely similar to that developed in [3-5], as will be demonstrated below.

Our specific aim will thus be to compute numerically the Fourier spectra of full wave solutions to the Zakharov model, then compute the saturation spectrum from the wave kinetic equation that is derived from the Zakharov model, in order to compare these. A study of this kind was recently reported in [15]. However, these authors considered the initial value problem for a conservative version of the Zakharov model. The present work differs by considering a version of the Zakharov model which contains damping terms, and which includes a pumping oscillating electric field, thus giving a driven and damped system.

The emphasis will be on the effect of the parameter

$$\Delta\Omega = \omega - \omega_p, \quad (1)$$

where  $\omega$  is the frequency of the pump, and  $\omega_p$  is the local plasma frequency. Since  $\omega_p$  depends on height,  $\Delta\Omega$  can be interpreted as the height relative to the reflection level  $\omega = \omega_p$  of the ordinary polarized pump, being positive (negative) below (above) the reflection level.

For a positive value of  $\Delta\Omega$ , corresponding to a height below the reflection level, a decay instability will start up around a certain wave number  $k_1(\Delta\Omega)$  selected uniquely by the resonance condition and the dispersion relation (see Eq. (6) below). A natural expectation is that when  $\Delta\Omega$  is large enough, this instability will saturate by cascading into successively smaller wave numbers of opposite signs  $-k_2 < k_1$ ,  $k_3 < -k_2$ , each satisfying the resonance condition for parametric decay from the former mode, and the dispersion relation. This picture was indeed qualitatively verified by our full wave solution, although the number of cascades turned out to be smaller than that predicted by the corresponding wave kinetic theory.

On the other hand, in the reflection region  $\Delta\Omega \approx 0$ , the expectation is that the nucleation process described in [8] will dominate. Our numerical results confirm these earlier findings, and also show that the wave number spectrum produced in the  $\Delta\Omega \approx 0$  region is broad enough to contain the wave lengths detected by the backscatter radars used in this type of experiments, such as the EISCAT VHF radar (see Fig. 8).

## 2 ZAKHAROV'S MODEL, AND A CASCADE THEORY

The version of the one dimensional Zakharov's equations that is appropriate for the present work, reads

$$\begin{aligned} \left[ i \left( \frac{\partial}{\partial t} + v_e \right) + (\Delta \Omega - \alpha_e) + \frac{\partial^2}{\partial x^2} \right] S &= \alpha_e S - \langle \alpha_e S \rangle \quad (a) \\ \left( \frac{\partial^2}{\partial x^2} + 2\alpha_e \frac{\partial}{\partial x} - \frac{\partial^2}{\partial x^2} \right) n &= \frac{\partial^2}{\partial x^2} |S + E_0|^2 \quad (b) \end{aligned} \quad (7)$$

In Eqs. (7), one-dimensional variables have been introduced, and their units are given in Table 1, together with their magnitude for typical values of the ionospheric F-region plasma parameters. The electric field is presented as  $(S + E_0) \exp(-i\omega t) + c.c.$ , where  $E_0$  is the infinite wave length driving electric field, polarized along the  $x$ -direction; the complex valued  $S(x, t)$  represents the perturbed potential electric field, and the real valued  $n(x, t)$  represents the quasineutral slow time scale electron density perturbation. The parameters  $v_e$ ,  $\alpha_e$ , and  $\Delta \Omega$  are the electron and ion damping rates and the before mentioned frequency mismatch, measured in units of  $\omega_p^{-1}$  of Table 1. The brackets of the last term of Eq. (2a) mean spatial mean value.  $\alpha$  and  $E$  are chosen to have mean value by definition, then this term must be included for consistency. This formulation ensures that the driving field  $E_0$  is externally controlled; if  $E$  were allowed to have a nonvanishing mean value, the driving field would be  $E_0 + \langle E \rangle$ , i.e. it would be self-modifying, which would not be appropriate for the process that we wish to investigate.

Time:	$\omega_p = (4\pi/3) (M/m) (1/\omega_p)$	$\approx 10^{-8} \text{ s}$
Space:	$\lambda_D = (3/2) (M/m) (1/\omega_p) \lambda_D$	$\approx 1.3 \text{ m}$
E-field:	$E_0 = q(m/M)^{1/2} (10 n_0 T_e / 2 \omega_p)^{1/2}$	$\approx 6.72 \text{ V/m}$
Density:	$n_0 = 4\pi m_0 / 3M$	$\approx 1.65 \cdot 10^7 \text{ m}^{-3}$

Physical quantities:

- $m$  electron mass
- $M$  ion mass
- $q = 1 + 3T_e/T_i$
- $T_e, T_i$  electron and ion temperatures
- $\lambda_D$  Debye length
- $n_0$  ambient electron number density
- $\omega_p$  dielectric constant of free space

Table 1: Units for the quantities occurring in Eqs. (7). The numerical values correspond to a plasma with electron density  $n_0 = 2 \cdot 10^{11} \text{ m}^{-3}$ , electron temperature  $T_e = 2000 \text{ K}$ , ion temperature  $T_i = T_e/2$ , and ion mass number 22 (mixture of one quarter of  $O_2^+$ , and three quarters of  $NO^+$ ), leading to an effective mass ratio  $M/m = 4 \cdot 10^4$ .

A dispersion relation which determines the growth rate of the parametric decay instability can easily be deduced from Eqs. (7): Assuming

$$\begin{aligned} S &= E^{(0)} \exp(i\theta_0) + E^{(1)} \exp(i\theta_1) + E^{(-1)} \exp(-i\theta_1^*) \\ n &= n_0 \exp(i\theta_0) + n_1^* \exp(-i\theta_1^*) \\ \theta_j &= k_j x - \omega_j t; j = 0, 1, 2 \end{aligned} \quad (8)$$

where the  $\theta_j$  satisfy the resonance condition

$$\theta_1 = \theta_0 - \theta_2^* \quad (9)$$

one can derive the dispersion relation

$$\omega_1 + \omega_0 + \Delta \Omega - k_1^2 = \frac{(k_0 - k_1)^2 |E^{(0)}|^2}{(\omega_0 - \omega_1)^2 - \omega_1(\omega_0 - \omega_1) - (k_0 - k_1)^2} \quad (10)$$

Putting  $E^{(0)} = E_0$ ,  $k_0 = 0$ ,  $\omega_0 = 0$ , (10) becomes the dispersion relation for the parametric decay of the pump. However, the formulation (8) also allows a Langmuir wave of amplitude  $E^{(0)}$ , frequency shift  $\omega_0$ , and wave number  $k_0$  to be the mod.  $x$  wave.

One could also use  $\omega_0 \neq 0$  in the pump, but as easily seen from Eqs. (2), this frequency can be included in  $\Delta \Omega$ , so one can with no loss of generality put  $\omega_0 = 0$  in the external pump.

Using the resonance condition and the dispersion relation (10) (in which the nonlinear coupling and damping is neglected), one finds

$$k_1(\Delta \Omega) = \pm \frac{1}{2} (\sqrt{4\Delta \Omega + 1} - 1) \quad (11)$$

for the wave number of the first decay.

On the basis of Eq. (8), one can formulate a wave kinetic equation in a way parallel to that of Perkins et al. [5]. It reads

$$\frac{dI(k)}{dt} = \left[ \gamma_0(k) - \nu_e(k) + \sum_{k'} M(k, k') I(k') \right] I(k), \quad (12)$$

where

$$\gamma_0(h) = \frac{h^2(\Delta\Omega - h^2) |E|^2}{[(\Delta\Omega - h^2)^2 - h^2]^2 + (\Delta\Omega - h^2)^2 \nu_{ei}^2(h)} \quad (a)$$

$$M(h, h') = \frac{h^2 - h'^2}{(h - h')^2 [(h + h')^2 - 1]^2 + (h + h')^2 \nu_{ei}^2(\Delta h)} \quad (b) \quad (8)$$

and the spectral intensity is  $I(h) = |E(h)|^2$ . The rates  $\gamma_0(h)$  and  $M(h, h')I(h')$  are determined as the imaginary part of  $\omega_1$  as determined by (5). Following Krueer and Valeo [3] and Perkins et al. [5], the additional approximation of neglecting the imaginary part of  $\omega_1$  when it occurs in the denominator of (8) is applied.  $\gamma_0(h)$  is obtained by assigning  $h_0 = 0$ ,  $E^{(0)} \rightarrow E_0$ ,  $h_1 \rightarrow h$ , while  $\gamma(h, h') = M(h, h')I(h')$  is obtained by assigning  $E^{(0)} \rightarrow E(h')$ ,  $h_0 \rightarrow h'$ ,  $h_1 \rightarrow h$ ,  $\Delta h = h - h'$ . Note that in (8),  $\nu_{ei}$  are considered  $h$  dependent, thus allowing kinetically determined Landau damping, hence  $\nu_{ei}$  occurring in (2) should be considered as linear operators (convolutions).

Note that, besides the random phase approximation which leads to a set of equations like (7) in terms of the wave intensities alone, there are also drastic approximations behind the growth rates (8). In particular, the approximation leading from (5) to (8) mentioned above, requires that the growth rates  $\gamma$  satisfies  $\gamma \ll \omega_1$ , this lies behind the interpretation of the saturation mechanism as "nonlinear Landau damping" (Krueer and Valeo [3], Perkins et al. [5]). This condition will not necessarily be satisfied at high intensities.

### 3 NUMERICAL RESULTS

In order to solve the set of equations (2) numerically, we assume periodic boundary conditions, and apply a pseudo-spectral method to solve for the Fourier components of  $E$  and  $n$ , at each time step. The method chosen, is a second order explicit scheme, and is a variation of the method presented by Payne et al. [17]. It is again important to note that the damping decrements  $\nu_{ei}$ , are assumed to be non-local in configuration space (convolutions), and hence products in wave number space.

The following changes must be made in the Payne et al. [17] method, in order to solve our particular choice of Zakharov model. In their Eq. (6):  $h^2 \rightarrow h^2 - \Delta\Omega$ , and  $(nE)_h \rightarrow [n(E + E_0)] - \langle nE \rangle > h$ . In their Eq. (7):  $E \rightarrow E + E_0$ . This will lead to a number of changes in the resulting algorithm.

The wave kinetic equation, Eq. (7), is solved by means of a standard vectorial fourth-order Runge-Kutta method (e.g. Burden and Faires [16]).

The spectral method was applied with  $N = 512$  grid points. Of these, only 340 of the Fourier modes (centered around  $h = 0$ ) were used, since for a quadratic nonlinearity, 1/3 of the modes will suffer from aliasing errors. At  $t = 0$ , we start from a low background noise level in the Langmuir wave Fourier components

$$E(h, t = 0) = A \exp(2\pi i \theta_0), \quad (9)$$

where  $A \ll E_0$ , and  $\theta_0$  is a random variable uniformly distributed on  $[0, 1]$ . The ion density fluctuations at  $t=0$  are assumed to be zero.

In the Runge-Kutta solution to Eq. (7), we choose  $N = 340$  coupled coupled equations to be solved simultaneously. The initial condition is taken as  $I(h, t = 0) = A^2$ , for the same choice of  $A$  as in Eq. (9).

The damping operators in Fourier space are chosen to be the following: For the electrons, we use a collisional type damping,  $\nu_{ei} = 0.7$  (700 Hz in physical units), and the linear electron Landau damping. The ion damping is chosen as the collisionless damping of ion acoustic waves, obtained from linear kinetic theory. The length of the system is  $L = 112.5$ .

In Figs. 1-3, we show numerical solutions to the full wave model and the weak turbulence approximation for different pump powers. We have chosen the frequency mismatch to be  $\Delta\Omega = 163.59$  in dimensionless units. This particular choice will ensure that the first decay mode  $h_1$  as determined by (6) is detectable with the EISCAT VHF radar ( $h_{MFP} = 2h_1 = 12.3$  in dimensionless units, where  $h_1$  is the radar wave number).

Fig. 1 shows the results for a pump electric field of  $E_0 = 0.5$ , which gives a ratio  $P = E_0^2/E_{th}^2 = 3.2$  between the pump power and the threshold power for onset of the parametric decay instability. Here we note that both the full wave solution and the wave kinetic solution yield cascade spectra. The spacing between the cascades is roughly the same,  $\Delta h \approx 1$  as predicted from the  $M(h, h')$ -term in the weak turbulence model. Note, however, that the solution to the full wave model give fewer cascades than what we get from the weak turbulence approximation.

Fig. 2 is for  $E_0 = 0.75$ , or a power ratio of  $P = 8$ . Again, the full wave solution produces fewer cascades than the weak turbulence solution. Furthermore, the full wave solution exhibits weak up-shifted features, the so-called Anti-Stokes lines. Note also that we start to see a continuous band of excitations between the cascades from the full wave solution, which is not present in the weak turbulence results.

Fig. 3 shows a comparison between the two models for  $E_0 = 1$ , or a power ratio of  $P = 9$ . In this case, we see that in the weak turbulence approximation, the cascades extend down to  $h = 0$ . This is the Langmuir condensate, and once this is reached, the weak turbulence approximation is no longer valid. Our full wave result in this case still exhibits a cascade, but the continuous band of excitations is much more prominent.

In Fig. 4, we see a comparison between the total electrostatic Langmuir wave energies for a driving field of  $E_0 = 1$ .

Figs. 5-7 show calculations for  $\Delta\Omega = 0$ , corresponding to the reflection region in the ionospheric RF-heating experiments. The pump field is chosen to be  $E_0 = 1$ . In these solutions, we see the cavity nucleation-collapse-burnout cycles as described earlier by Dooley et al. [8] in a one dimensional treatment, and Russell et al. [9] and DuBois et al. [10, 11] in multi dimensional treatments.

In Fig. 8, we see the wave number spectrum for the Langmuir waves, for the fully developed turbulence.

The nucleation state consists of trapping of Langmuir waves in low-density depressions. The trapped Langmuir fields will continue to grow, which in turn "blows" away more plasma, hence, the density depressions become even deeper. This is the collapse stage. At some instant, the trapped Langmuir wave energy suddenly disappears, and we are left with an empty low-density depression. This is the burnout. The empty low-density holes will no longer be supported by the trapped Langmuir waves, and they will start to damp away. Some of the density depressions may break into two low-density pulses propagating in opposite directions. At some time instant, the density depression again has the correct form for a trapped wave resonance, and the cycle starts again.

#### 4 CONCLUSIONS AND DISCUSSION

Our numerical study demonstrates two different mechanisms by which a Langmuir wave spectrum can be produced by a long wave height e.m. pump.

One mechanism takes place under the condition  $\Delta\Omega \gg 1$ , i.e.

$$\omega - \omega_p \gg (m/M)\omega_p, \quad (10)$$

In dimensional quantities, which is satisfied a distance below the reflection level. It has the characteristics of a cascade process: the spectrum has a line structure, the highest wave number is the one that satisfies the selection rule for the decay instability of the pump (Eq. (6)), and the lower lines satisfy the resonance conditions for the further decays of parametrically driven Langmuir waves. The total number of cascades increases with pump intensity. When the pump intensity is so high that the whole wave number range down to  $k = 0$  is filled with cascade lines, i.e. the Langmuir condensate is reached, then also the bands between the cascade lines become filled. On the other hand, comparing the results of the full wave solution with those of the wave kinetic equation (7), it is found that a smaller number of cascades is produced in the full wave model than predicted by the wave kinetic approach.

The other process takes place under the condition  $\Delta\Omega \approx 0$ , that is, in the region of reflection ( $\omega = \omega_p$ ), of an ordinary polarized incident pump. This process starts with an oscillating two stream instability, but in the fully developed stage, it consists of many localized cycles of nucleation, (one dimensionally driven) collapse, and burnout, similar to what was reported in [5]. The  $k$ -spectrum of Langmuir waves in this case is broadbanded, starting around  $k \approx 0$ , and extending to higher  $k$  as a function of time. In a stationary state, the spectrum extends out to the range where Landau damping is important [8].

In the experiments that have been performed in Arecibo, Puerto Rico, and at Ranzjordmoen, near Tromsø, Norway, one wave number component selected by the Eragy condition for the probing radar, is observed. According to the theory presented above, the conventional interpretation in the form of a cascade process, requires that the echo comes from a height a distance below the reflection height. This is in conflict with the observations in Arecibo, where the conclusion has been drawn that the echo comes from the reflection region [6,7]. A crucial point in the previous discussion of these results, has been that the polarization of the O-polarized pump wave under Arecibo conditions (magnetic field forms  $\sim 40^\circ$  with the vertical), is along the magnetic field. This is exact at the reflection level, and a good approximation for the whole range of altitudes of interest here. In addition, multi dimensional wave kinetic calculations [4,5] show that the angular spread of the cascade is not large enough to be observed with the Arecibo radar. Instead, the old interpretation has been in terms of an enhanced thermal fluctuation spectrum [3].

In the new interpretation [11], the observations are explained by a multi dimensional version of the  $\Delta\Omega \approx 0$  process. The numerical calculations of Refs. [9-11] show that spectral features observable by the Arecibo radar can be produced by this process, because the multi dimensional collapse stage leads to a broadening of the Fourier spectrum both in magnitude and angular distribution. In addition to giving an explanation of the observed height of the plasma line, there are also other observations that are explained by this model [10], in particular, the so-called "free-mode" feature should be mentioned.

In this discussion, the contribution of the present work is to demonstrate that the two processes are not "conflicting theories", nor "competing processes". They both can coexist, but in separate height regions, and they are also described within the same mathematical model. It may also seem inappropriate to name the two processes "weak" versus "strong" turbulence theories, because, as has been shown here, both are excited at similar pump powers. It is the value of  $\Delta\Omega$  that matters. Neither is this a novel finding, similar observations were made in [14] and [15].

Turning to the Tromsø observations, the magnetic field geometry is such that both types of turbulence should be observable by the EISCAT radars. It seems most reasonable that in the observations that have so far been reported, is the  $\Delta\Omega \gg 1$  type that has been seen, because of the pronounced line structure of the spectra [18]. This might be explained by the higher degree of coherence in the waves generated in this type of process, giving rise to stronger backscatter, drowning echoes coming from the reflection region. We wish, however, to point out that a feature including a height separation has been observed in Tromsø [21]. The EISCAT UHF enhanced plasma line was observed to come from a height ca. 7 km below that which the enhanced ion line came from. One might speculate that this could be explained by a difference in the backscatter efficiency of the low and high frequency sections in the two types of turbulence. This, however, remains to be investigated.

In conclusion, it should be stressed that the work reported here, still is at an early stage, and will certainly be continued. In addition to a more detailed exploration of the present model, magnetic field and multi dimensional features need to be considered.

#### 5 ACKNOWLEDGEMENTS

This work is supported by the Norwegian Research Council (NAVF/RNF), under project 436.90/002. Discussions with C.LaRoc, H.Bjorndal, K.B.Dyrhaug, and K.Rypdal are appreciated.

## 6 REFERENCES

- [1] H.C. Carlson, W.E. Gordon, and R.L. Showen, High frequency induced enhancements of the incoherent scatter spectrum at Arecibo, *J. Geophys. Res.* 77, 1242 (1972).
- [2] T. Hagfors, W. Kofman, H. Kopka, P. Stubbe, and T. Aljanen, Observations of enhanced plasma loss by EISCAT during heating experiments, *Radio Sci.* 18, 641 (1983).
- [3] W.L. Krueer, and E.J. Valeo, Nonlinear evolution of the decay instability in a plasma with comparable electron and ion temperatures, *Phys. Fluids* 16, 675 (1973).
- [4] J.A. Pajer, and Yu-Yun Kuo, Structure in the nonlinear saturation spectrum of parametric instabilities, *Phys. Fluids* 16, 1480 (1973).
- [5] F.W. Perkins, C. Oberman, and E.J. Valeo, Parametric instabilities and ionospheric modification, *J. Geophys. Res.* 79, 1475 (1974).
- [6] D.B. Maltrew, and R.L. Showen, Height of the HF-enhanced plasma line at Arecibo, *J. Geophys. Res.* 82, 4793 (1977).
- [7] B. Isham, W. Birkmayr, T. Hagfors, and W. Kofman, Observations of small-scale plasma density depletions in Arecibo HF heating experiments, *J. Geophys. Res.* 82A, 4629 (1987).
- [8] G.D. Doek, D.F. DuBois, and Harvey A. Rose, Nucleation of cavitons in strong Langmuir turbulence, *Phys. Rev. Lett.* 54, 904 (1985).
- [9] D. Russell, D.F. DuBois, and H.A. Rose, Nucleation in two-dimensional Langmuir turbulence, *Phys. Rev. Lett.* 60, 541 (1988).
- [10] D.F. DuBois, H.A. Rose, and D. Russell, Power spectra of fluctuations in strong Langmuir turbulence, *Phys. Rev. Lett.* 61, 2209 (1988).
- [11] D.F. DuBois, Harvey A. Rose, and David Russell, Excitation of strong Langmuir turbulence in plasmas near critical density: application to HF heating of the ionosphere, *Report LA-UR-89-1419, Los Alamos National Laboratory* (1989).
- [12] V.E. Zakharov, Collapse of Langmuir waves, *Soviet Phys. JETP* 55, 908 (1972).
- [13] J.C. Weatherall, J.P. Sheridan, D.R. Nicholson, G.L. Payne, M.V. Goldman, and J.P. Hanson, Solitons and ionospheric heating, *J. Geophys. Res.* 82B, 623 (1982).
- [14] D.R. Nicholson, and M.V. Goldman, Cascade and collapse of Langmuir waves in two dimensions, *Phys. Fluids* 21, 1766 (1978).
- [15] G.L. Payne, D.R. Nicholson, and Mei-Mei Shen, Numerical test of weak turbulence theory, *Phys. Fluids B1*, 1797 (1989).
- [16] L.M. Degtyarev, R.S. Sagdeev, G.I. Solov'ev, V.D. Shapiro, and V.I. Shvetschenko, One-dimensional Langmuir turbulence, *Sov. J. Plasma Phys.* 6, 363 (1980).
- [17] G.L. Payne, D.R. Nicholson, and R.M. Downie, Numerical solution of the Zakharov equations, *J. Comput. Phys.* 50, 482 (1983).
- [18] R.L. Burden, and J.D. Faires, *Numerical Analysis*, Prentice, Weber & Schmidt, Boston (1985).
- [19] P. Stubbe, *Talk at 8th Sunda URSI Symposium, Tromsø, Sept. 1988.*
- [20] P.Y. Cheung, A.Y. Wong, T. Tanikawa, J. Santoru, D.F. DuBois, H.A. Rose, and D. Russell, Short-time-scale evidence for strong Langmuir turbulence during HF heating of the ionosphere, *Phys. Rev. Lett.* 63, 2676 (1989).



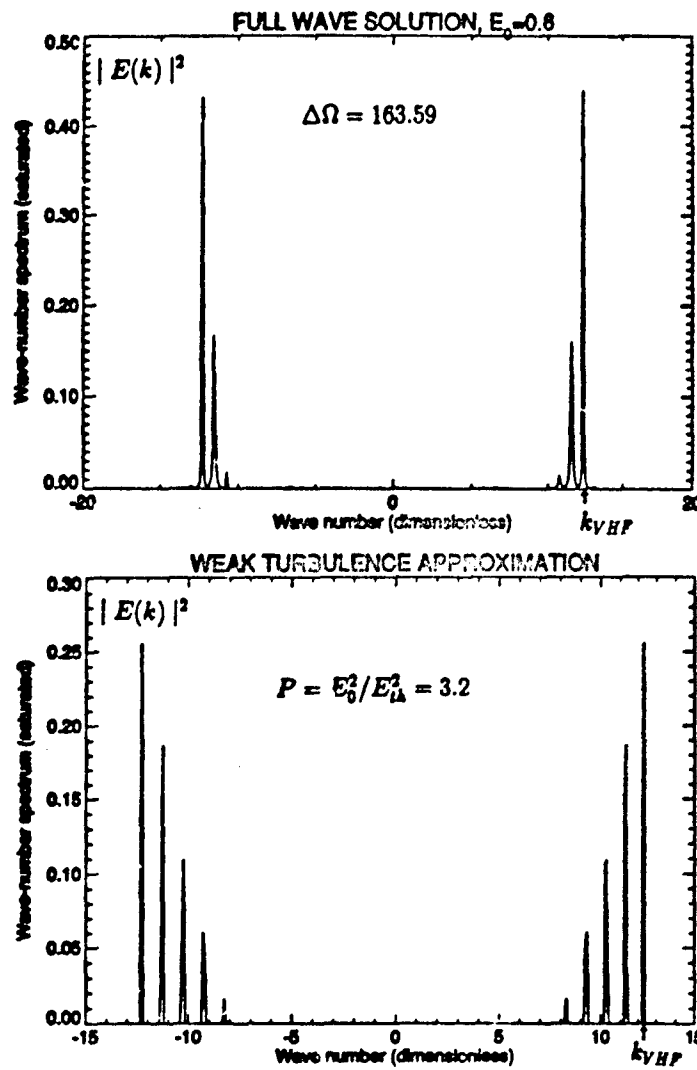


Fig. 1 Wave number spectra of Langmuir turbulence calculated from (a) the full wave model, (b) the wave kinetic equation. Parameters:  $E_0 = 0.8$  ( $P = 3.2$ ),  $\Delta\Omega = 163.59$ . (Note that the scales on the y-axes are different.)

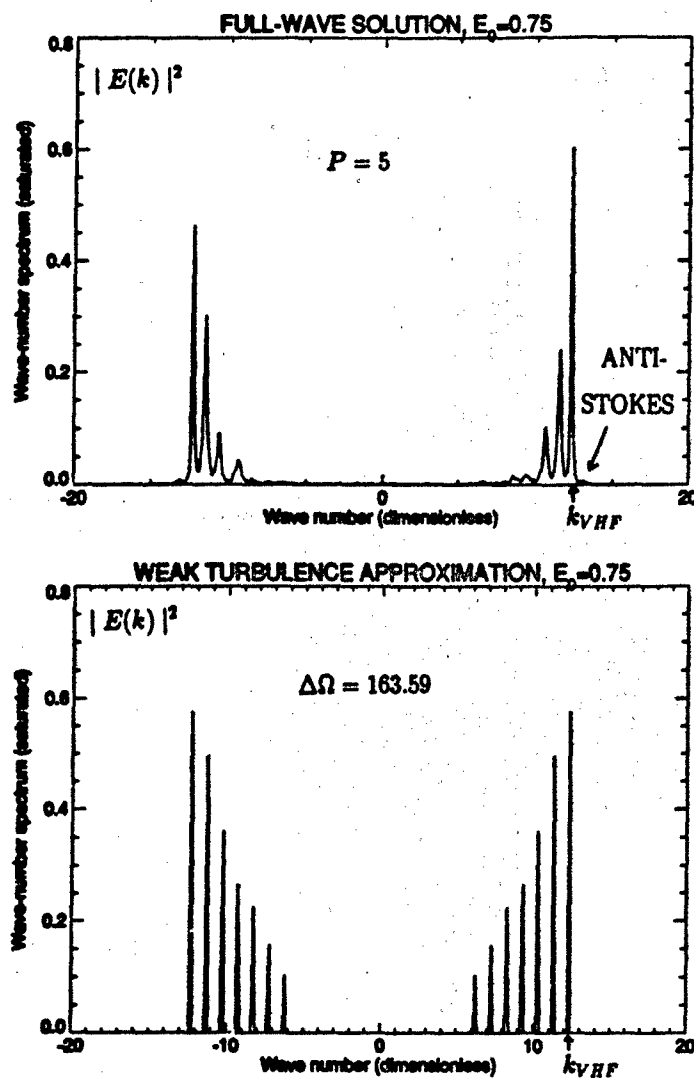


Fig. 2 Same as Fig. 1, but  $E_0 = 0.75$  ( $P = 5$ ).

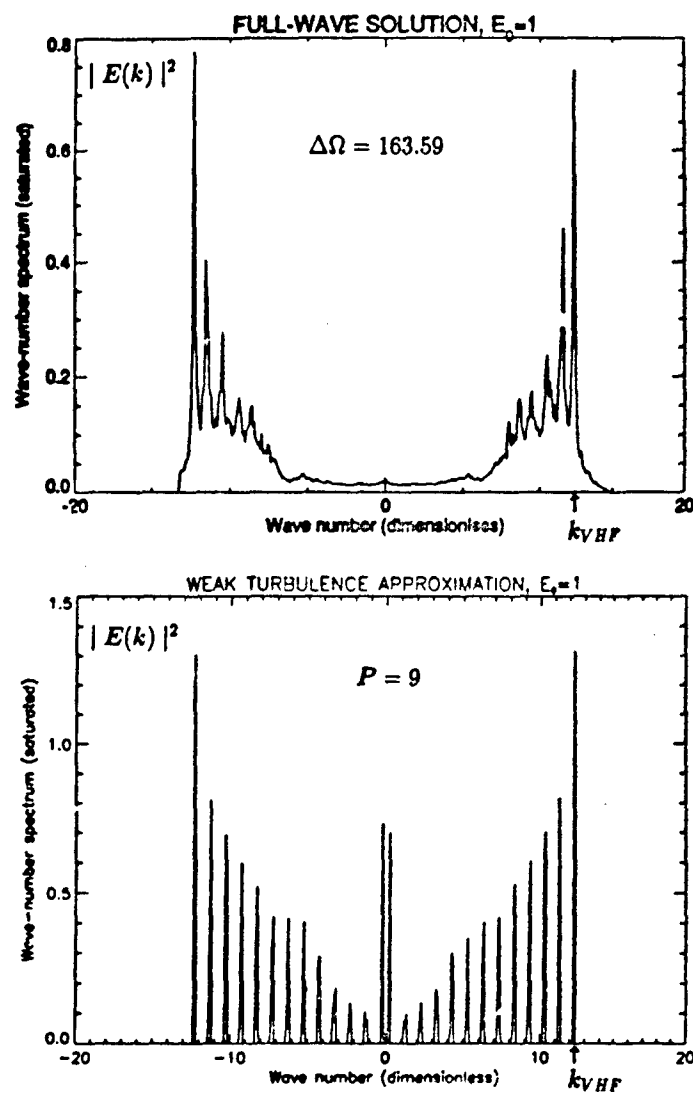


Fig. 2 Same as Fig. 1, but  $E_0 = 1$  ( $P = 9$ ).

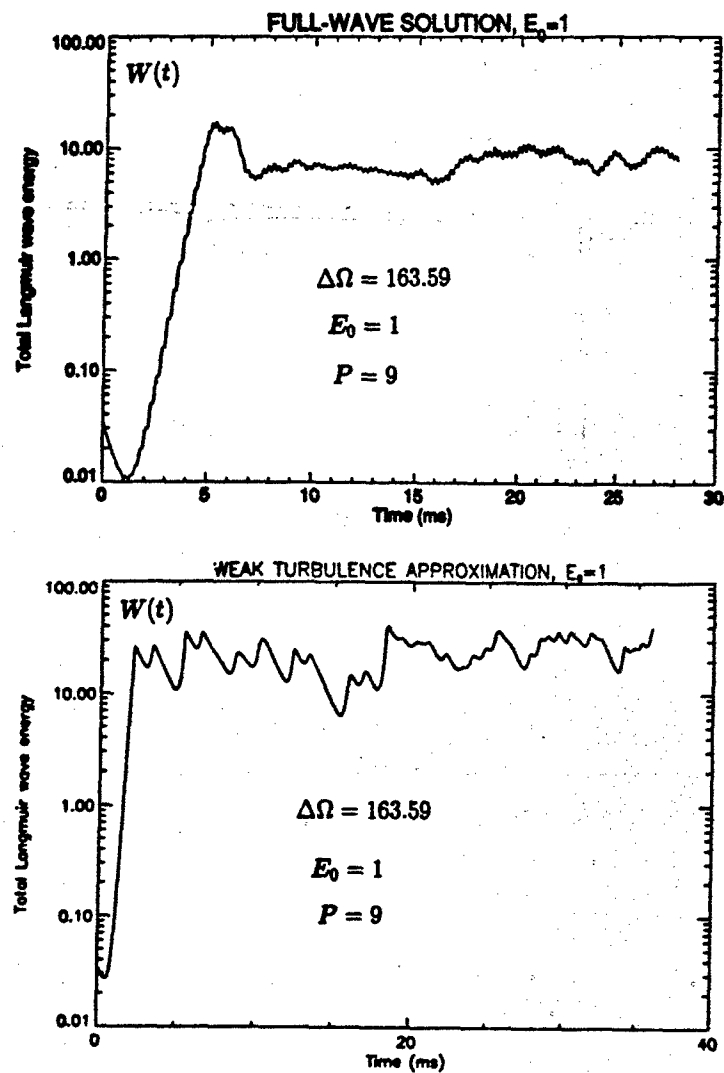
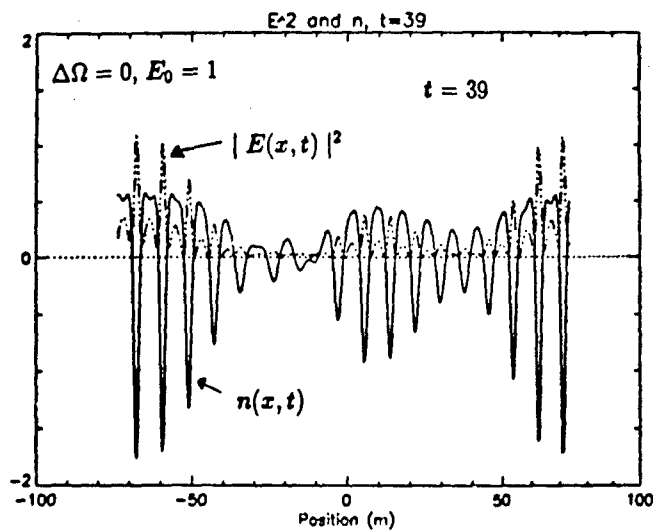
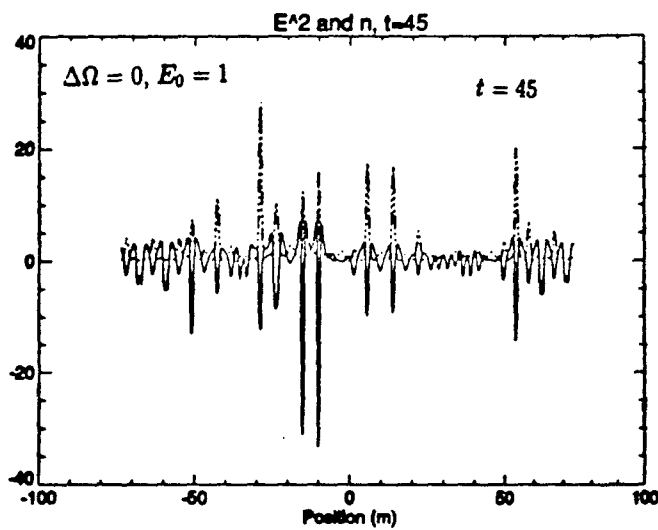


Fig. 4 Time evolution of the total Langmuir wave energy,  $W(t) = \sum_k |E(k, t)|^2$ , for (a) the full wave solution, (b) the wave kinetic equation. ( $E_0 = 1$ ,  $\Delta\Omega = 163.59$ ).



**Fig. 5** Solutions of  $|E(x,t)|^2$  and  $n(x,t)$  (configuration space) from the full wave model in the reflection region ( $\Delta\Omega = 0$ ), at time  $t = 39$ . Pump power is  $E_0 = 1$ .



**Fig. 6** Same as Fig. 5, but at  $t = 45$ .

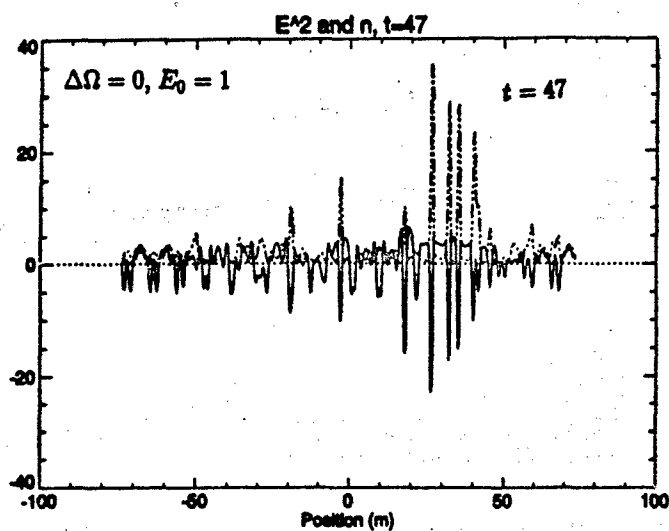


Fig. 7 Same as Fig. 6, but at  $t = 47$ .

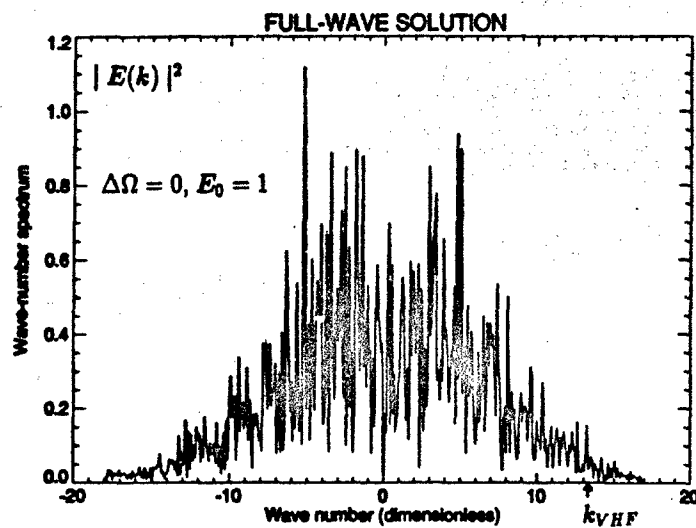


Fig. 8 Wave number spectrum for the Langmuir waves in the fully developed turbulence,  $\Delta\Omega = 0$ ,  $E_0 = 1$ .

## DISCUSSION

W. T. ARMSTRONG, US

How do "full wave theory" predictions compare to Djuth's detailed measurements of height dependence of turbulence development?

## AUTHOR'S REPLY

(Reply by Mjølhus) First of all, we have wanted to examine the consistency of the "weak turbulence" theory of the "plasma line" experiments. I have focussed upon the fact that the echoes of the Djuth experiment start at the "highest" height and expand downwards. If this height is the reflection height, it is consistent with a "strong turbulence" theory. The expansion might be explained by distortion of the density profile by the heating wave and/or the turbulence.

D. PAPADOPOULOS, US

This is a very nice comprehensive work. However its applicability to the ionosphere as well as the applicability of the DuBois-Rose work is at best doubtful. The magnetic energy  $B^2/8\mu$  is at least 1000 times stronger than the plasma energy density. As a result transverse collapse would be easily prevented. The dynamics would then be 1-D, as described in Rowland and Papadopoulos (1984) for beam plasma interactions, namely, multisoliton state for  $W/WT < 0.1$  and chaotic state resembling 3-D collapse for  $W/WT > 0.1$ .

## AUTHOR'S REPLY

I agree with you that the magnetic field effects are very important. We will include the magnetic field in our model, and I thank you for the reference to your work!

R. L. SHOWN, US

I want to be cautious with the assumption that theory is in agreement with the heating observations in respect to plasma line altitude. I'm not sure that the recent plasma line reports have indicated accurately the enhancement altitude, but I do think that such measurements should be made.

L. DUNCAN, US

Some care must be taken in interpretation of the radar data shown with regard to enhanced plasma line excitation heights and the HF pump wave reflection height. The pump reflection height is inferred rather than measured directly. The usual technique for measuring this height relies on looking at the natural plasma line at the pump frequency, but this range cannot be resolved with the accuracy used in the HF-enhanced plasma line data.

## AUTHOR'S REPLY

Thank you for pointing this out for us. This then, appears to be an important task for good experimentalists to resolve. On the other hand, since you CANNOT resolve the height difference between the natural and the enhanced plasma lines, they must be quite close to each other, which is again consistent with our assumption  $\Delta n = 0$  in the Arecibo experiments.

# THEORY OF LARGE-SCALE HF HEATING PROCESSES IN THE UNSTRUCTURED AND STRUCTURED IONOSPHERE

M.J. Kackinen<sup>1</sup>, P.K. Chaturvedi<sup>1</sup>, and S.L. Ossakov<sup>2</sup>

<sup>1</sup>Space Plasma Branch  
<sup>2</sup>Plasma Physics Division  
 Naval Research Laboratory  
 Washington, DC 20375-5000

## ABSTRACT

Theoretical aspects of large-scale HF heating processes in the unstructured and structured ionosphere have been studied. For the unstructured case, we present an analytical model for the generation, convection, and steepening of E-induced density cavities. We discuss the nonlinear propagation of high power HF in steepened cavities. Properties of thermal self-focusing instabilities in the presence of a convecting and steepened cavity is studied. For the structured ionosphere, we discuss parametric coupling processes of a large amplitude HF pump wave with both F-region, i.e., interchange, current-convective, and ion cyclotron and E-region, i.e., two-stream and gradient-drift ionospheric instabilities which instabilities have been proposed to account, in part, for naturally occurring ionospheric irregularities. We show that these instabilities may be stabilized or destabilized using high power HF heaters.

## 1. INTRODUCTION

Recently, much attention, both experimental<sup>1-6</sup> and theoretical<sup>7-12</sup> has been directed towards a more complete understanding of the physics of the interaction of high power radio waves and the ionosphere. Several diverse phenomena, e.g., stimulated electromagnetic emissions<sup>3</sup>, modification of the polar electrojet and ELF/VLF generation<sup>13</sup>, artificial airglow emissions<sup>2</sup>, ionospheric cavity formation<sup>4,5</sup>, large temperature enhancements<sup>3</sup> and artificial control of naturally occurring ionospheric waves and irregularities<sup>7-9,11,12</sup> have been investigated.

For the general topic of plasma structure development and irregularity generation during ionospheric heating by high-power radio waves, observational and theoretical studies can generally be classified as emphasizing either large scale, i.e., hundreds of meters to kilometers, or small scale, i.e., centimeters to tens of meters, phenomena. For the large scale case, it is generally agreed<sup>4,14</sup> that the thermal self-focusing instability<sup>15</sup> plays a major role in generating kilometer-scale plasma fluctuations and structure. Indeed, Wright et al.<sup>4</sup> have recently presented experimental observations that suggest that neutral thermospheric gravity waves may act as a "seed" for the initiation of the thermal self-focusing instability.

However, the majority of studies on the large scale aspects and phenomenology of ionospheric heating have not considered, in a self-consistent manner, the role of ambient ionospheric electric fields, neutral thermospheric winds, gravitational drifts and associated convective effects on the evolution of the heated regions. For long time scale radio wave heating, e.g., for tens of seconds to minutes in duration, and over sufficiently large spatial scales (tens of kilometers), polarization electric fields due to ionosphere-thermosphere interactions and coupling will become important in the evolution of the structure and dynamics in heater-induced plasma depletions and cavities in the ionosphere. Several effects, e.g., cavity steepening and electrical decoupling from the surrounding ionosphere and thermosphere may arise. These effects may, in turn, lead to changes in high power radio wave propagation and thresholds for instabilities, e.g., self-focusing. As a result, it is important to develop a self-consistent theoretical model of late-time ionospheric heating by high power radio waves.

In addition, it is well known that the ionosphere can be structured, both parallel and perpendicular to the geomagnetic field, prior to high power radio wave injection. Such structure can be caused, in part, by plasma fluid and kinetic instabilities and processes. However, very few studies have considered the interaction of high power radio waves with ionospheric instabilities and associated irregularities. Consequently, it is important to develop models of the physics of the interaction of high power HF waves and ionospheric instabilities and processes.

The outline of this paper is as follows: In Section 2, we discuss aspects of late-time large-scale HF heating processes in an unstructured ionosphere. We study both beam propagation and stability. In Section 3, we study aspects of HF heating in a structured ionosphere and consider the effect of HF waves on low frequency ionospheric instabilities. Finally, in Section 4, we summarize and discuss our results.

## 2. HF HEATING IN AN UNSTRUCTURED IONOSPHERE

We take the ionospheric plasma, in the presence of high-power radio waves, to be low  $\beta$  and weakly ionized. We assume that the radio wave beam power density  $I = E_0^2$  changes little over an electron mean-free path  $\lambda_e$ , i.e.,  $I^{-1} dI/dx \ll \lambda_e^{-1}$ . We also consider temporal changes in the beam power density to occur on time scales longer than an electron collision time  $\nu_e^{-1}$  with  $\nu_e$  a typical collision frequency.

The set of equations describing our model can then be written<sup>17-18</sup>

$$\frac{\partial \mathbf{N}_0}{\partial t} + \nabla \cdot (\mathbf{N}_0 \mathbf{V}_0) = s_0 - l_0 \quad (1)$$

$$\frac{\partial \mathbf{N}_1}{\partial t} + \nabla \cdot (\mathbf{N}_1 \mathbf{V}_1) = s_1 - l_1 \quad (2)$$



$$m_e N_e \left( \frac{\partial}{\partial t} + \mathbf{V}_e \cdot \nabla \right) \mathbf{V}_e = - \nabla p_e - \nabla \cdot \mathbf{P}_e - m_e (\mathbf{E} + c^{-1} \mathbf{V}_e \times \mathbf{B}) + \mathbf{E}_g \quad (3)$$

$$m_i N_i \left( \frac{\partial}{\partial t} + \mathbf{V}_i \cdot \nabla \right) \mathbf{V}_i = - \nabla p_i + N_i m_i \mathbf{g} - \nabla \cdot \mathbf{P}_i + e N_i (\mathbf{E} + c^{-1} \mathbf{V}_i \times \mathbf{B}) - \mathbf{E}_g \quad (4)$$

$$\frac{3}{2} N_e \left( \frac{\partial}{\partial t} + \mathbf{V}_e \cdot \nabla \right) T_e + N_e T_e \nabla \cdot \mathbf{V}_e + \nabla \cdot \mathbf{q}_e = Q_e - L_e \quad (5)$$

$$\frac{3}{2} N_i \left( \frac{\partial}{\partial t} + \mathbf{V}_i \cdot \nabla \right) T_i + N_i T_i \nabla \cdot \mathbf{V}_i + \nabla \cdot \mathbf{q}_i = Q_i - L_i \quad (6)$$

$$\nabla \cdot \mathbf{j} = \nabla \cdot e N (\mathbf{V}_e - \mathbf{V}_i) = 0 \quad (7)$$

For  $\alpha = e, i$ ,  $N_\alpha$  is the plasma density,  $\mathbf{V}_\alpha$  is the velocity,  $s_\alpha$  is ionization production rate,  $l_\alpha$  is the ionization loss rate,  $m_\alpha$  is the mass,  $p_\alpha = N_\alpha T_\alpha$ ,  $\mathbf{P}_\alpha$  is the stress tensor,  $\mathbf{B}$  is the magnetic field,  $\mathbf{g}$  is the acceleration due to gravity,  $\mathbf{E}$  is the electric field,  $\mathbf{E}_g$  is the electron-ion (ion-neutral) collision frequency,  $\mathbf{E}_i$  is the electron-neutral (ion-neutral) collision frequency,  $\mathbf{U}$  is the thermospheric wind velocity,  $\mathbf{E}$  is the electric field,  $T_\alpha$  is the temperature,  $\mathbf{q}_\alpha$  is the heat flow vector,  $Q_\alpha$  is the heating rate with  $Q_e = E \cdot \mathbf{j}$  and  $Q_i = E \cdot \mathbf{j}$  and  $c_\alpha$  the a.c. plasma conductivity,  $L_\alpha$  is the cooling rate with  $L_e = \nu_{ei}(T_e - T_i)$  and  $L_i = \nu_{in}(T_i - T_n)$  with  $T_n$  the neutral temperature. Equations (1) - (7) are supplemented by the wave equation in the limit  $\omega_0 \gg \nu_{ei}, \nu_{in}$

$$\nabla^2 \mathbf{E} - \nabla(\nabla \cdot \mathbf{E}) + \frac{\omega_0^2}{c^2} \mathbf{E} = 0 \quad (8)$$

with  $\omega_0$  the frequency of the electromagnetic wave and  $\epsilon$  is the dielectric tensor. Eq. (1) - (8) with exclusion of Eq. (7) are similar to those used in previous studies<sup>14,15</sup>.

## 2.1 CONVECTION AND STEEPENING OF HEATER-INDUCED DENSITY CAVITIES

It is well-known that high power radio waves can produce large scale density cavities and depletions in the ionosphere<sup>2,4</sup>. We now show<sup>20</sup> that, for long-time scale heating, these density depletions can steepen perpendicular to the geomagnetic field due to polarization electric fields caused by gravity and/or neutral thermospheric winds.

Using Eqs. (3) and (4), Eq. (7), for current conservation at F-region altitudes, can be written to lowest order,

$$\nabla \cdot \mathbf{j}_1 = 0 \quad (9)$$

with

$$\mathbf{j}_1 = \frac{v_{in} N_0}{b} \left( \mathbf{E}_1 + \frac{b}{c v_{in}} (\mathbf{E} + v_{in} \mathbf{U}) \times \hat{\mathbf{b}} \right) \quad (10)$$

where  $b_1 = eB/m_1 c$  is the ion cyclotron frequency and  $\hat{\mathbf{b}} = \mathbf{B}/|\mathbf{B}|$ . The first term on the right-hand side is due to electric field-induced Pedersen drifts, the second term due to gravity-induced drift and the third term due to neutral winds. Equation (9) can then be written, after separating  $\mathbf{E}$ , i.e.,  $\mathbf{E} = \mathbf{E}_{OT} + \delta \mathbf{E}$ ,

$$\nabla \cdot N \delta \mathbf{E} = - \mathbf{E}_{OT} \cdot \nabla N \quad (11)$$

with  $\mathbf{E}_{OT} = \mathbf{E}_{OP} + (B/c v_{in})(\mathbf{g} + v_{in} \mathbf{U}) \times \hat{\mathbf{b}}$  and  $\mathbf{E}_{OP}$  a constant polarization field. Linearizing Eq. (11) with  $N = N_0 - \delta n$  for a depletion  $\delta n \ll N_0$  and taking  $|\delta \mathbf{E}| \ll \mathbf{E}_{OT}$  we find

$$\delta \mathbf{E} = \frac{\delta n}{N_0 - \delta n} \mathbf{E}_{OT} \quad (12)$$

The total electric field  $\mathbf{E}_T$  in the density depletion can then be written

$$\begin{aligned} \mathbf{E}_T &= \mathbf{E}_{OT} + \delta \mathbf{E} \\ &= \frac{N_0}{N_0 - \delta n} \mathbf{E}_{OT} \end{aligned} \quad (13)$$

As a result, the total electric field inside the depletion is greater than the total field outside the depletion. This implies that the center of the depletion moves faster than the outside portions and results in a steepening of the depletion or cavity as depicted in Fig. 1. The steepening will occur in the  $\mathbf{E}_{OT} \times \hat{\mathbf{b}}$  direction. This analysis is similar to that applied to

naturally occurring ionospheric depletions in equatorial spread-F by Ossakov and Chaturvedi<sup>21</sup> who computed depletion and cavity velocities for various cavity shapes, e.g., cylinders, sheets, ellipses.

In order to estimate the steepening time  $t_s$  we take  $t_s = L/|V_B - V_A|$  where  $V_B$  and  $V_A$  is the velocity of region B (large  $\Delta n$ ) and A (small  $\Delta n$ ), respectively. Here  $L$  is a typical scale length for the depletion. Now  $V_B = c/B [N_0/(N_0 - \Delta n)]E_0$  and  $V_A = c/B [N_0/(N_0 - \Delta n)]E_0 = cE_0/B$ . For a 50 percent depletion, i.e.,  $\Delta n/N_0 = 0.5$ ,  $cE_0/B = 100$  msec<sup>-1</sup>,  $L = 10$  km, we find a steepening time  $t_s = 10^{-4}$  sec. The steepening time can vary depending on the shape of the depletion<sup>21</sup>. However, the variation will involve factors of two to three and will not change this estimate appreciably. As a result of steepening, the cavities will develop strong density gradients in the direction of convection. In the next section, we discuss the effects of this steepening on high power radio wave propagation.

## PLASMA DENSITY N

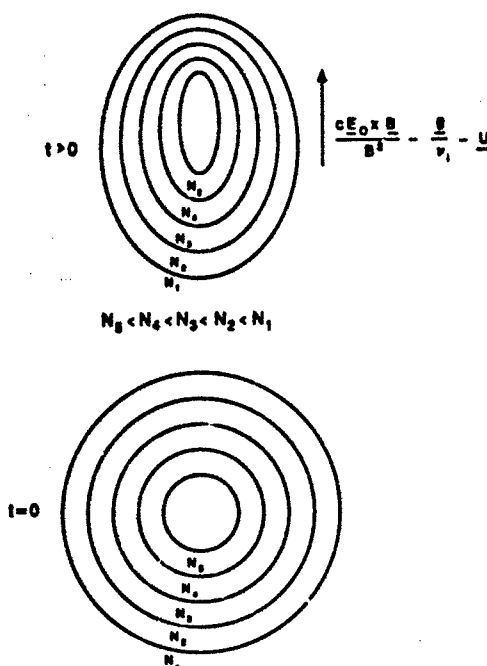


Fig. 1 Sketch of steepened plasma cavity. The  $N_i$ ,  $i = 1, 3$ , denote plasma densities.

### 2.2 PROPAGATION OF HIGH POWER RADIO WAVES IN CONVECTING AND STEEPENED DENSITY CAVITIES

We now consider the effects<sup>20</sup> of a steepened ionospheric density cavity on the propagation of high power radio waves assumed to be propagating in the  $z$ -direction. In Eq. (8) we take

$$E(z) = E(z) \exp(i \int_0^z k dz) \quad (14)$$

in the geometrical optics approximation where now  $E$  refers to the wave electric field. Inserting Eq. (14) into Eq. (8) we find

$$\frac{\partial^2 E}{\partial z^2} + 2ik \frac{\partial E}{\partial z} + iE \frac{dk}{dz} + \frac{v^2 E}{c^2} + \frac{\epsilon^2}{2} E = 0 \quad (15)$$

with  $\epsilon = \epsilon_2 + i\epsilon_1$  the complex dielectric. Further decomposing  $E = E_0 \exp(ikS)$  we find

$$\frac{\partial I}{\partial s} + \zeta \cdot \nabla I + I \nabla \cdot \zeta = 0 \quad (16)$$

$$\left(\frac{\partial}{\partial s} + \zeta \cdot \nabla\right) \zeta = (2\epsilon_0)^{-1} \nabla \delta \epsilon \quad (17)$$

where we have defined  $\zeta = \nabla I$ ,  $I = E_0^2$ ,  $\nabla$  is the gradient operator transverse to the ray vector  $\zeta$ , and  $s = s_0 + \delta s$  with  $\delta s$  due to large amplitude effects. Equations (16) - (17) determine the nonlinear geometrical optics of radio-wave ionospheric heating with  $\delta \epsilon$  determined by Eqs. (1) - (7). In Eq. (17) we have ignored refraction and diffraction. Equation (17) is simply an expression for energy balance.

By integrating Eq. (16), using (17) we find

$$I(x, y, s) = I_0(x, y, s) \exp\left[-\int_0^s d\eta h(\eta)\right] \quad (18)$$

with

$$h(\eta) = (\nabla \cdot I^{-1} \nabla I) \cdot \int_0^\eta d\eta' (2\epsilon_0)^{-1} \nabla \delta \epsilon \quad (19)$$

$I_0(x, y, \cdot)$  is the intensity associated with a homogeneous medium. We take  $s = 1 - (\omega_p^2/\omega^2)$  with the remark that

$$\delta \epsilon = -\frac{4\pi e^2}{m_e \omega^2} \delta n \quad (20)$$

We take a model for  $\delta n$  to be of the form

$$\delta n = n_0 \frac{\partial T}{\partial T_0} f(x, y, s) \quad (21)$$

with<sup>14</sup>

$$\frac{\partial T}{\partial T_0} = \frac{E_0^2}{E_p^2} \quad (22)$$

with  $E_p = [3T_e n_0 (\omega^2 + \omega_c^2)/e^2]^{1/2}$  with  $m_e$  the electron mass,  $\omega_0$  the wave frequency,  $T_e$  the electron temperature,  $\omega_c$  the electron collision frequency, and  $n_0$  is the average fraction of the energy lost by electrons in one collision. In Eq. (21)  $f(x, y, s)$  is used to describe a steepened cavity. Since  $\partial T_0 = E_0^2$  we have  $\delta n = E_0^2 \cdot I$ . Using Eq. (21) in Eq. (20) we have

$$\delta \epsilon = \alpha f(x, y, s) \quad (23)$$

where we have normalized  $I = E_0^2$  by  $\omega^2/\omega_p^2 E_p^2$ . Using Eq. (23) and (19) we have from Eq. (18)

$$I(x, y, s) = I_0(x, y, s) \exp\left[-\beta \int_0^s [g_1(\eta) + g_2(\eta)] d\eta\right] \quad (24)$$

with

$$g_1(\eta) = \int_0^\eta d\eta' \nabla_1^2 f(\eta')$$

$$g_2(\eta) = \int_0^\eta d\eta' \{ \nabla_1 I \cdot \nabla_1 f + I^{-1} (\nabla_1 I)^2 \}$$

where  $\nabla_1 = \frac{\partial}{\partial x} \frac{\partial}{\partial x} + \frac{\partial}{\partial y} \frac{\partial}{\partial y}$ . In the following we take the steepened cavity to be axisymmetric about the  $s$ -direction and model the steepened profile in the  $xy$ -plane using the analytical expression

$$\delta n(x, y) = f(x, y) = \exp(-y^2) \exp(-x^2) \int_0^x d\tau \exp(\tau^2)$$

A plot of this functional form is shown in Fig. 2.

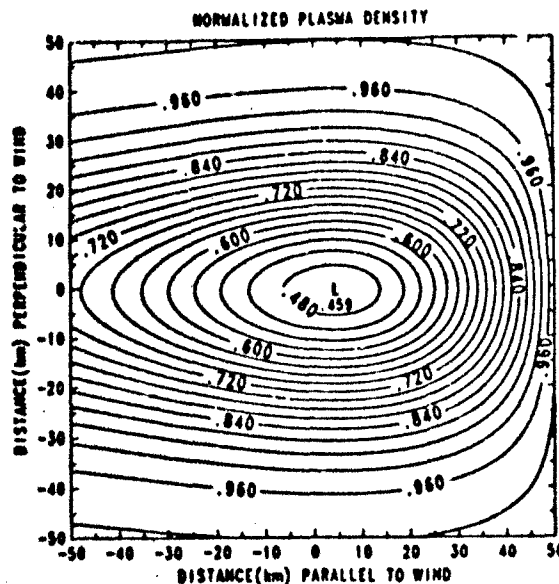


Fig. 2. Plot of analytic profile of steepened plasma cavity..

We can now find a solution to Eq. (24) using perturbation theory by assuming  $I = I_0 + \delta I_1 + \dots$  with  $\delta \ll 1$ . This amounts to inserting  $I_0$  in the expressions for  $g_1$  and  $g_2$  on the right-hand side of Eq. (24). In the  $xy$ -plane we take an initial Gaussian beam profile

$$I_0(x,y) = I_0(0) \exp[-(x^2 + y^2)/a^2] \quad (25)$$

which is shown in Fig. 3. In Fig. 4 we show the beam intensity  $I(x,y,z)$  as given in Eq. (24) with  $g_1$  and  $g_2$  evaluated using  $I = I_0$  as given by Eq. (25). In Fig. 4 we use  $\beta = 0.6$ . For  $\beta = 0.1$  we note only small distortion of the beam intensity with a shift in beam peak intensity along the flow direction. In addition, there is some spreading of the beam and associated decrease in peak beam intensity. On the other hand for strong beam  $\beta = 0.6$  in Fig. 4 we find stronger focusing together with an increase and shift of beam peak intensity. This shift in beam intensity is consistent with the recent observations<sup>2</sup> of beam shift and "snap-backs" during long-time high power HF heating experiments.

### 2.3 BEAM FILAMENTATION INSTABILITY IN THE PRESENCE OF CONVECTION AND STEEPENING

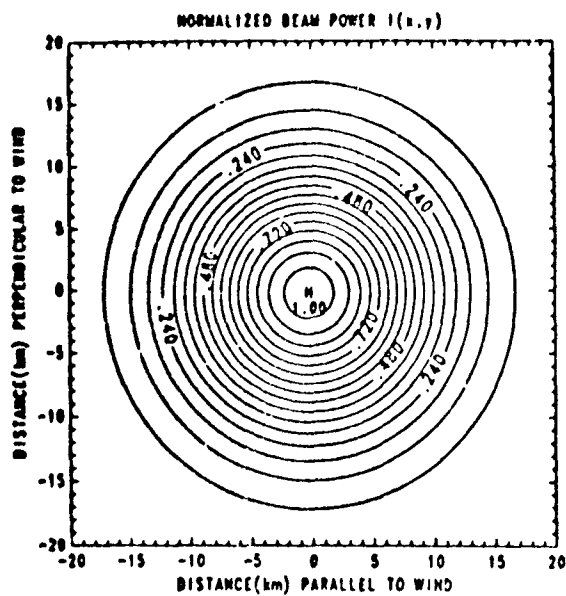
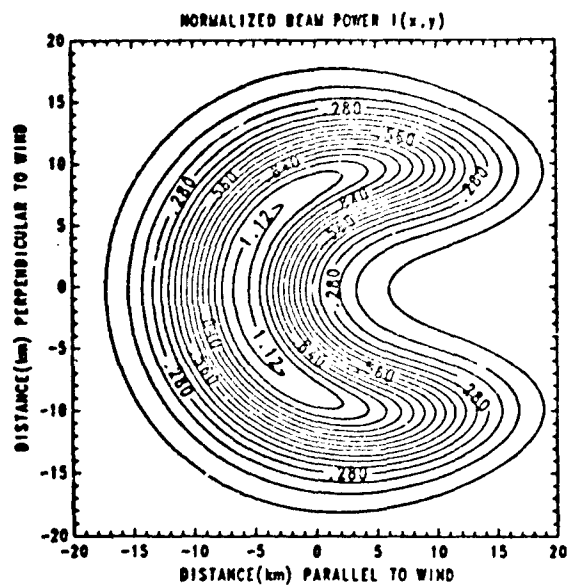
We have also studied<sup>20</sup> the effect of convection and steepening on the thermal filamentation instability. Density depletions in the ionosphere are known to be unstable to the Rayleigh-Taylor instability, an interchange-like plasma instability driven by gravity in conjunction with neutral thermospheric winds. The growth rate of the thermal filamentation instability in the presence of interchange instability can be written<sup>20</sup>

$$\gamma = (\Omega_e \Omega_i + k_x^2 v_e^2)^{-1} [\gamma_0 (8/3) (n_i/n_e) (v_e/c)^2 n_i^2 - k_x^2 C_s^2] - \gamma_0 \Omega_e \Omega_i \quad (26)$$

where  $\Omega_e(\Omega_i)$  is the electron (ion) gyrofrequency,  $B = B_0$ ,  $v_e$  is the electron thermal speed,  $\nu_e$  the electron collision frequency,  $m_i(m_e)$  the ion (electron) mass,  $v_e$  the electron quiver velocity,  $\omega_{pi}$  the ion plasma frequency,  $C_s$  the sound speed, and  $v_0 = v_e/L$  with  $v_0 = (g/v_i) + u$  and  $g$  is gravity,  $\nu_i$  the ion collision frequency,  $u$  is the neutral thermospheric wind, and  $L$  is the density gradient scale length perpendicular to the geomagnetic field. From Eq. (26) the threshold pump field for filamentation can be written

$$(v_0/c)^2 > (8/3) (n_i/n_e) [k_x^2 \lambda_D^2 + (\nu_e/\nu_i) (\Omega_e \Omega_i / n_i^2)] \quad (27)$$

with  $\lambda_D$  the Debye length. Equation (26) reduces to the standard result<sup>14,16</sup> when  $v_0 = 0$ . We see that the growth rate  $\gamma_0$  of interchange instability can increase the threshold for excitation of the thermal filamentation instability.

Fig. 3. Plot of  $I(x,y)$  with  $\theta = 0$ .Fig. 4. Plot of  $I(x,y)$  with  $\theta = 0.6$ .

### 3. HF HEATING IN A STRUCTURED IONOSPHERE

In this section we discuss the possibility of influencing the development of natural low frequency plasma modes in the F-region and E-region ionosphere by a high power HF pump wave. These modes are believed to be excited by various instability processes at different times and in different regions, resulting in structured fields in the medium that have been detected by various experimental techniques for decades. It is hoped that a controlled experiment using external HF waves to study the development of low frequency ionospheric instabilities may enhance the understanding and identification of these processes as a step towards development of an ionospheric model with predictive capabilities.<sup>22</sup>

We consider a situation in which an HF pump wave is resonantly mode converted into an electrostatic mode near the region where its frequency is close to the ambient upper-hybrid frequency. Further, we neglect the effects of ambient magnetic field on the high-frequency modes, an approximation made for simplicity. The standard mode coupling analysis is performed for the interaction between low-frequency modes ( $\omega_1, k_1$ ) and high frequency sideband modes ( $\omega_2, k_2$ ) in the presence of an HF pump ( $\omega_0, k_0$ ). In the low-altitude ionosphere, the thermal nonlinearity is dominant (when  $v_0 > \omega_1$ ) while in the high-altitude ionosphere, ponderomotive effects are dominant ( $v_0 < \omega_1$ ). In the following, we present results of the linear stability analysis for various low-frequency modes in the presence of HF pump waves and their probable regions of occurrence.

#### 3.1 INTERCHANGE INSTABILITIES IN THE F-REGION

The dispersion relation of interchange modes in the presence of a high power HF pump in the local approximation is given by<sup>23,24</sup>

$$\omega_1^2 = i(\Gamma_L - D_A k_1^2) - i\Gamma_{HL} \quad (28)$$

where  $\Gamma_L = (\frac{1}{2} \frac{v_0}{\omega_1}) (k_1^2 / \omega_1^2)$ ,  $k_{0L} = (\frac{1}{2} \frac{v_0}{\omega_1}) \frac{k_1}{\omega_1} = \frac{k_1}{\omega_1} \frac{v_0}{\omega_1}$ ,  $\Gamma_{HL} = \frac{1}{2} \frac{v_0}{\omega_1} \frac{k_1}{\omega_1} \frac{v_0}{\omega_1} \frac{k_1}{\omega_1}$ ,  $v_0 = v_1 / \omega_1$ ,  $v_d$  is the plasma drift velocity in the frame of the neutrals,  $D_A = \frac{1}{2} \frac{v_0}{\omega_1} \frac{k_1}{\omega_1} \frac{v_0}{\omega_1} \frac{k_1}{\omega_1}$ , and

$$\Gamma_{HL} = [4(v_0/\omega_1)k_1^2 \omega_1^2 v_0^2 \omega_1^2] / [\omega_1^2 (\omega_1^2 + v_0^2 \omega_1^2)] \quad (29)$$

with  $\delta = \omega_1^2 - \omega_0^2$ ,  $\theta = 3(n_0/n_1)v_0$ . Interchange instabilities are believed to cause ionospheric irregularities both in the low latitude and high latitude ionosphere. In the low latitude ionosphere, gravity-driven Rayleigh-Taylor modes are believed<sup>24</sup> to cause equatorial spread-F for scale sizes 100 m - 10 km while at high latitudes electric field-driven interchange modes<sup>25</sup> are believed to lead to density irregularities on the edges of convecting plasma inhomogeneities. The pump induced structure at altitudes ~ 300 km, requires threshold pump power (pump electric field) of 0.1 mV/m<sup>2</sup> (2 mV/m). The pump destabilizes interchange modes in overdense regions ( $\delta < 0$ ,  $\omega_1 < \omega_{pe}$ ) while it is stabilizing in the underdense region ( $\delta > 0$ ,  $\omega_1 > \omega_{pe}$ ). Thus the unstable modes would have a structure in altitude such that the mode is localized in the overdense region (in a situation similar to the natural instability associated with the "blobs" which have a finite altitude extent).<sup>25</sup> This situation favors destabilization of modes with scales comparable to the localization region (~ 100 m). For longer scale sizes, nonlocal effects play an important role and the growth rates (pump wave thresholds) are reduced (enhanced). Figure 3 gives a plot of Eq. (28) for typical parameters for underdense heating ( $\delta > 0$ ).

#### 3.2 INSTABILITIES AND PROCESSES IN THE E-REGION

The two-stream instability in the E-region is favored at electrojet altitudes (105 - 115 km) when electron Hall drift ( $v_{d1}$ ) exceeds the local ion-sound speed ( $C_s$ ),  $v_{d1} > C_s$ . The presence of HF pump wave may result in its excitation for sub-threshold conditions ( $v_{d1} < C_s$ ). The dispersion relation for the two-stream instability in presence of HF pump wave is<sup>26</sup>

$$\omega_1^2 + \omega_2^2 + i(\Gamma_L k_1^2 - \frac{1}{2} \frac{v_0}{\omega_1} \frac{k_1}{\omega_1} \frac{v_0}{\omega_1} \frac{k_1}{\omega_1}) = \frac{1}{2} \frac{v_0}{\omega_1} \frac{k_1}{\omega_1} \frac{v_0}{\omega_1} \frac{k_1}{\omega_1} (1 - \frac{1}{2} \frac{A}{\omega_1}) \quad (30)$$

where  $\Gamma_L = 3/2 D_A$ ,  $\omega_1 = v_0/\omega_1$ ,  $v_1 \gg \omega_1$ ,  $v_0 \ll \omega_1$ ,  $v_{d1} = 0$ ,  $k_{d1} = 0$ ,  $\omega_{d1} = \omega_1 - k \cdot v_d$ . The HF pump wave destabilizes these modes in the overdense region ( $\delta < 0$ ,  $\omega_1 < \omega_{pe}$ ) and the required threshold pump wave power (electric field) is 5 mV/m<sup>2</sup> (60 mV/m) (for  $\lambda_1 = 3$  m,  $v_{d1} = 350$  m/s,  $v_0 = 4 \times 10^4$  s<sup>-1</sup>,  $v_1 = 2.5 \times 10^3$  s<sup>-1</sup>). The natural two-stream instability has been associated with observations of enhanced electron temperatures ("hot spots") in the region.<sup>26</sup> Some experiments on HF effects on E-region have indicated observations of type I-like irregularities (associated with the two-stream instability).<sup>27-29</sup> A future experiment may be considered to verify the association of "hot spots" with the two-stream instability.

At larger scale sizes the gradient-drift instability may be excited in the E-region electrojet. The HF pump wave may also be used to influence the large scale size modes (~ 100 m) in the E-region. The gradient drift instability is associated with the electrojet current (100 - 120 km altitude) and the current-convective instability (CCI) is associated with the presence of parallel currents (> 130 km). These modes may be detected by VHF-radar (type II echoes) or scintillation measurement, and require pump wave field strengths of ~ 15 mV/m (for gradient-drift instability, at ~ 110 km) and ~ 2 mV/m (for CCI at ~ 130 km). Some E-region experiments

have apparently detected such effects.

In the upper electrojet region, it has been suggested that parallel currents may play a role in the irregularity generation<sup>10</sup>. At altitudes where  $v_1 = \Omega_1$  (~120 km), electrostatic ion-cyclotron (EIC) modes are heavily damped due to  $v_{1y}$  while ion-acoustic waves (IA) may be excited (with  $u_1 = k_1 C_s > v_1$ ). At higher altitudes (>150 km), EIC modes have been mentioned as a possible source of irregularities detected by various techniques (VEP, HF radars, in-situ probes<sup>11</sup>). Thus an HF-pump may destabilize IA waves with a pump electric field ~ 20 mV/m at ~120 km and EIC modes at higher altitudes (~150 km) by pump wave fields ~ 5 mV/m. The pump wave is further destabilizing to the linearly unstable modes in the overdense region ( $\delta < 0$ ,  $\omega_p < \omega_{UH}$ ) while it may destabilize linearly stable modes in the underdense region ( $\delta > 0$ ,  $\omega_p > \omega_{UH}$ ). The EIC instability in high-latitude ionosphere has been associated with the observations of magnetic lens<sup>11</sup>. Thus a controlled experiment using an HF pump and excitation of the EIC mode may be carried out to verify this proposition.

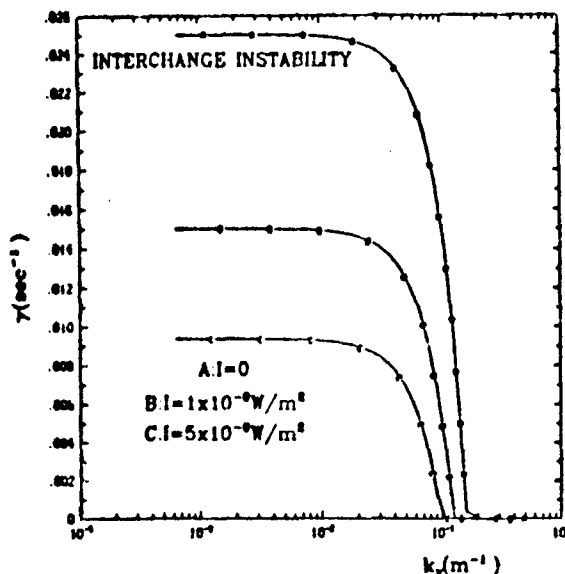


Fig. 9. Plot of growth rates from Eq. (17). Here  $I = cE_0^2/8\pi$  with  $v_1 = cE_0/\omega_1 B_0$ . The following parameters are used:  $B_1 = 1 \text{ m}^2/\text{s}$ ,  $v_1/B_1 = 10^{-2}$ ,  $v_2/B_2 = 10^{-2}$ ,  $v_3 = 3 \times 10^{-2} \text{ m/s}$ ,  $\omega_1 = 20 \text{ Hz}$ ,  $\omega_2$  is in the  $\hat{x}$ -direction,  $\omega_3$  is the  $\hat{y}$ -direction,  $\omega_4 = 3 \times 10^6 \text{ Hz}$ ,  $\omega_5 = 3 \times 10^6 \text{ Hz}$ ,  $\Omega_1 = 10^2 \text{ sec}^{-1}$ .

#### 4. SUMMARY AND DISCUSSION

We have discussed features of large-scale HF heating processes in the unstructured and structured ionosphere. For the unstructured problem, for large scale long-time HF heating, we have shown that polarization fields due to ionosphere-thermosphere interactions and coupling will be important in the evolution of the structure and dynamics of heater-induced plasma cavities in the ionosphere. Several effects, e.g., cavity steepening, convection, and electrical decoupling from the ambient ionosphere may arise. We have shown that typical steepening time for heater-induced density cavities are on the order of a few minutes. Plasma convection and steepening induced by both gravity and neutral winds have been investigated. The propagation of high power radio waves in a steepened depletion has been studied. It is found that an initially collimated radio wave beam is shifted in the direction of convection due to a steepened plasma cavity. For low beam powers, this convection and steepening causes a decrease in peak beam intensity while at higher power an increase in peak beam intensity is seen, i.e., beam focusing is increased. In addition, we have also computed the growth rate of the generalized thermal self-focusing instability in the presence of both convection and a plasma density gradient induced by steepening, perpendicular to the geomagnetic field. We find that interchange processes can increase the threshold and reduce the growth rate of the generalized thermal self-focusing instability.

For the structured ionosphere, we show that instabilities and processes in both the F-region and E-region and associated irregularities may be stabilized or destabilized using high power HF waves. HF pump amplitudes may be accessible using existing heaters.

#### 5. REFERENCES

1. Bass, S., Su, Suo, P. Stubbe, N. Kopka, and J. Vaaramaa, Daytime scintillations induced by high-power HF waves at Tromsø, Norway, *J. Geophys. Res.*, **92**, 11149, 1987.

2. Bernhardt, P., L.N. Duncan, and C.A. Topley, Artificial airglow excited by high-power radio waves, Science, **242**, 1022, 1988.
3. Djuth, P.T., B. Thide, E.N. Ierke, and M.P. Sulzer, Large F-region electron temperature enhancements generated by high-power HF radio waves, Geophys. Res. Lett., **14**, 933, 1987.
4. Wright, J.V., B. Kopka, and P. Stubbe, A large-scale ionospheric depletion by intense radio wave heating, Geophys. Res. Lett., **15**, 1531, 1988.
5. Wang, A.Y., T. Zanikava, and A. Kuthi, Observation of ionospheric cavitons, Phys. Rev. Lett., **29**, 1373, 1987.
6. Thide, B., B. Kopka, and P. Stubbe, Observations of stimulated scattering of a strong high-frequency radio wave in the ionosphere, Phys. Rev. Lett., **49**, 1561, 1982.
7. Kaskinen, M.J., P.K. Chaturvedi, and S.L. Ossakow, Parametric excitation and suppression of convective plasma instabilities in the high latitude F-region ionosphere, J. Geophys. Res., **88**, 7239, 1983.
8. Chaturvedi, P.K., M.J. Kaskinen, and S.L. Ossakow, Production and control of ion-cyclotron instabilities in the high latitude ionosphere by high power radio waves, J. Atmos. and Terr. Phys., **49**, 37, 1987.
9. Chaturvedi, P.K. and S.L. Ossakow, Plasma instabilities in the high latitude E-region induced by high power radio waves, J. Geophys. Res. (submitted), 1990.
10. Shuecri, N.H., G.J. Morales, and J.E. Faggs, Ohmic heating of the polar F region by HF pulses, J. Geophys. Res., **92**, 2907, 1987.
11. Stenflo, L., Stimulated scattering by collisional modes in the ionosphere, Radio Sci., **18**, 1379, 1983.
12. Lenz, V.N. and V.K. Tripathi, Radio wave heating and equatorial spread-F, J. Atmos. and Terr. Phys., **49**, 1071, 1987.
13. Stubbe, P., B. Kopka, and R.L. Doubien, Generation of ELF and VLF waves by polar electrojet modulation: experimental results, J. Geophys. Res., **86**, 9073, 1981.
14. Gurevich, A., Nonlinear Phenomena in the Ionosphere, Springer-Verlag, New York, 1978.
15. Fejer, J.A., Ionospheric modification and parametric instabilities, Rev. Geophys. Space Phys., **17**, 135, 1979.
16. Perkins, F.W., and E.J. Valeo, Thermal self-focusing of electromagnetic waves in plasmas, Phys. Rev. Lett., **32**, 1234, 1974.
17. Braginskii, S.I., Transport processes in a plasma, Reviews of Plasma Physics, Vol. 1, ed. N.A. Leontovich, Consultants Bureau, New York, 1963.
18. Banks, P.N. and G. Eckhardt, Aeronomy, Vol. A and B, Academic, San Diego, Ca., 1973.
19. Bernhardt, P.N. and L.N. Duncan, Feedback diffraction theory of radio wave heating, J. Atmos. and Terr. Phys., **44**, 1061, 1982.
20. Kaskinen, M.J., and P. Bernhardt, Late time ionospheric heating by high power radio waves, Radio Sci. (to be submitted).
21. Ossakow, S.L. and P.K. Chaturvedi, Morphological studies of rising equator-to-l spread F bubbles, J. Geophys. Res., **83**, 2085, 1978.
22. Wilent, V.F., An ionospheric modification experiment using very high power, high frequency transmission, J. Geophys. Res., **75**, 6402, 1970.
23. Lee, K., P.K. Ray, and C.F. Kennel, External production and control of electrojet irregularities, J. Geophys. Res., **77**, 4197, 1972.
24. Ossakow, S.L., Spread F theories: A review, J. Atmos. Terr. Phys., **43**, 437, 1981.
25. Chaturvedi, P.K. and J.D. Dube, The interchange instability in high-latitude plasma blobs, J. Geophys. Res., **92**, 3357, 1987.
26. D'Angelo, N. and E.L. Merline, Comments on "Are observed broadband plasma wave amplitudes large enough to explain the enhanced electron temperatures of the high-latitude E region?" by J.-P. St.-Maurice and R. Lahar, J. Geophys. Res., **92**, 321, 1987.
27. Song, P., E. Nielsen, P. Stubbe, and B. Kopka, Heater-induced 1 meter irregularities, J. Geophys. Res., **91**, 11309, 1986.
28. Djuth, P.T., R.J. Jost, S.T. Moble, W.K. Gordon, P. Stubbe, B. Kopka, E. Nielsen, R. Bestron, M. Derblom, A. Hedberg, and B. Thide, Observations of E region irregularities generated at auroral latitudes by a high-power radio wave, J. Geophys. Res., **90**, 12293, 1985.



29. Elford, P.H., S. Nielson, P. Stubbe, H. Kocka, and M.T. Rietveld, Production of auroral zone E region irregularities by powerful HF-heating, J. Geophys. Res., 88, 6347, 1983.
30. Chattervedi, P.R., J.D. Riba, S.L. Gusev, P. Satyanarayana, and J.A. Fodor, Parallel current effects on two-stream electrojet plasma instabilities, J. Geophys. Res., 92, 8700, 1987.
31. Shelley, E.G., R.D. Sharp, and R.G. Johnson, Satellite observations of a ionospheric acceleration mechanism, Geophys. Res. Lett., 3, 454, 1976.

## DUCT MODEL FOR THE DUTY-CYCLE VARIATION OF THE PLASMA-LINE OVERSHOOT DURING CYCLIC HEATING AT ARECIBO

by  
D. B. Muldrew  
Communications Research Centre  
Department of Communications  
P.O. Box 11490, Station 'H'  
Ottawa, Ontario K2H 8S2  
Canada

### SUMMARY

In a recent publication on ionospheric heating by Sulzer et al. [1989] the effects of suddenly changing the duty cycle, during on-off cycling of the HF transmitter, on the plasma-line (PL) overshoot are strikingly illustrated. When the duty cycle was suddenly decreased, the overshoot lifetime changed gradually over about 1 min from roughly 0.1 s to more than 0.5 s. When the duty cycle was suddenly increased, the lifetime changed gradually from more than 0.5 s to roughly 0.1 s. For a still higher duty cycle, the PL intensity began to pulsate dramatically. The Langmuir (L) waves responsible for the PL grow by the parametric-decay instability and propagate in magnetic-field-aligned ionization ducts having a density decrement relative to the ambient density outside the duct. The change in the decrement depends both on the ponderomotive force of the trapped L waves and on heating due to damping of the L waves. When the HF is on, the decrement increases. When the HF is off, the decrement decreases. Rapid decay of the L waves (i.e. decay of the overshoot) by Landau damping begins when the decrement exceeds a certain level. The duty-cycle observations can be explained with this model.

### INTRODUCTION

The PL overshoot was first observed and described by Showen [1975] and Showen and Kim [1978]. Graham and Fejer [1978] suggest that short-scale field-aligned irregularities with a growth time of a few seconds scatter the EM waves into L waves and hence reduce the EM field at greater heights after a few seconds. However, the existence of overshoots combined with a lack of a measurable reduction in reflected EM power has been demonstrated [Djuth et al., 1981; Fejer et al., 1982]. Kuo et al. [1987] suggest that L waves, with growth rates larger than the growth rates of L waves detected by the radar, randomise electron motion; this increases the threshold of the detected waves and causes the drop in PL intensity. Caviton theory [Dubois et al., 1988; Dubois et al., 1989] does not explain the overshoot. The limitations of the role of cavitons in explaining ionospheric-heating observations are discussed by Sulzer et al. [1989].

The duct model in conjunction with the parametric decay instability have been able to explain qualitatively many of the observed characteristics of the plasma line observed at Arecibo [Muldrew and Showen, 1977; Muldrew, 1978, 1979, 1986] including an explanation of the PL overshoot [Muldrew, 1988]. Sulzer et al. [1989] present data illustrating the effect on the PL overshoot of suddenly changing the duty cycle during cycling of the heating transmitter. A brief explanation of these results using the duct model was given by Sulzer et al. based on a preprint of Muldrew [1988] and correspondence between J.A. Fejer and the author [1988]. A more detailed explanation is given here.

### OBSERVATIONS OF SULZER ET AL. [1989]

Figures 6, 7 and 1 of Sulzer et al. [1989] with their captions are reproduced here in Figures 1, 2 and 3, respectively. In Figure 1 the duty cycle of the HF transmitter was changed from 0.5-s on, 5.5-s off (duty cycle A) to 0.5-s on, 19.5-s off (B) at 2015:49 (time = 0 s in the figure). Only times near the 0.5-s on periods are shown in the figure; hence, the time scale can only be used for comparing received pulses. The gradual lengthening of the overshoot from about 0.1 s to 0.5 s takes about 2 min (time = 6 s in the figure). See remarks in the caption regarding the third and fourth pulses. In Figure 2 the duty cycle of the HF transmitter was changed from B to A at 2027:28 (time = 0 s in the figure). The gradual shortening of the overshoot from greater than 0.5 s to about 0.1 s takes about 1.5 min (time = 9 s in the figure).

In Figure 3 the HF duty cycle is 2-s on, 2-s off with an effective radiated power of 40 MW at 5.1 MHz. The 430-MHz radar pulses have an inter-pulse period of 1 ms giving a time resolution of 1 ms. The HF transmission starts shortly after 400 ms in the figure. The PL disappears about 1200 ms after the start of the HF. Between about 1200 and 1700 ms on the time scale the pulses are extremely regular with less-than-10-ms pulses separated by about 42 ms.

### DUCT-MODEL EXPLANATION

Figure 4 is taken from Muldrew [1988] and is a modified version of a schematic of a representative overshoot for the early Arecibo experiments with relatively weak HF power as determined by Showen [1975]. The evolution of a duct during ionospheric heating can be divided into four time domains [Muldrew, 1988]. The first three of these which constitute the growth stage are shown in the figure. The fourth is the recovery stage when the heater is off.

Consider the start of HF cycling after the transmitter has been off sufficiently long (eg. more than 10 min) that no HF-enhanced ducts exist. Natural field-aligned ducts are always present in the ionosphere having a variety of cross-field diameters and electron-density enhancements or decrements. These ducts are too small to affect the HF field distribution. In the presence of a powerful HF field the parametric-decay instability can

occur inside three ducts at the height of maximum field strength (first Airy maximum) at a plasma frequency which is only slightly less than the L-wave frequency. Initially, only small wavenumber Langmuir waves will grow parametrically due to the small density decrement. These will be damped, raising the electron temperature  $T_e$  inside the duct and consequently decreasing the electron density by the expansion of plasma along the magnetic-field direction. Larger-wavenumber L waves can then grow parametrically. The duct acts like a waveguide. As the L waves are guided along the duct their wavenumbers vary back and forth over a large angle relative to the magnetic-field direction. When the duct has grown sufficiently, L waves will exist (PL waves) which have the appropriate direction and wavenumber to backscatter the 430-MHz radar signal. After the start of HF cycling it may take several HF pulses before a PL is detected; the duct continues to grow during each pulse until an approximate steady state is reached. Ducts with relatively large density decrements will permit a larger range of L waves to be trapped than those with smaller density decrements. This means ducts with larger density decrements will be heated more by damping and will grow more rapidly than smaller ducts. Consequently, only the largest natural ducts existing before the initial HF turn-on will end up as the ducts responsible for the PL. This probably explains the large separation of PL ducts (roughly 0.5 km) which is clearly indicated by the observed approximate 1-min fading rate of PL intensity.

As mentioned above, after the HF transmitter has been cycling for some time the ducts reach the 'steady state' in which the duct characteristics repeat approximately each HF cycle. As soon as an HF pulse starts, L waves begin to grow by the parametric-decay instability in the ducts and they reach an observable level in about 2 ms (region 1, Figure 4). They become nonlinearly saturated in another few milliseconds and start to exert an appreciable ponderomotive force on the plasma in the duct. This force drives plasma in both directions along the magnetic field away from the maximum HF field strength at the first Airy maximum. This lasts for approximately the time it takes an electron-ion pair to travel at thermal velocity across one half of the first Airy maximum, or about 100 ms (region 2, Figure 4). The increase in  $T_e$  due to L-wave damping begins to become significant after about 300 ms and duct density gradually decreases even further. As the density decrement increases, Landau damping of the L waves increases (Figure 2, Muldrew, 1933) and at some point becomes severe, causing the steep drop in PL intensity shown in Figure 4 near 3 s (region 3, Figure 4).

Using the above description of the PL overshoot based on Muldrew [1933], the observations in Figures 1 to 3 will be explained. At  $t = 0$  in Figure 1 the duty cycle suddenly decreases. The heating integrated effect of the previous pulses thus decreases and  $T_e$  and the density decrement  $\delta n$  due to thermal effects decreases from pulse to pulse. For the left-hand side of Figure 1,  $\delta n$  is relatively large. The ponderomotive force produces an additional density decrement  $\delta n_p$  which reaches its peak value tens of milliseconds after the start of each pulse;  $\delta n + \delta n_p$  is sufficiently high that the L waves responsible for the PL are severely Landau damped after about 0.1 s. For the right-hand side of Figure 1,  $\delta n$  is relatively small and  $\delta n + \delta n_p$  is not sufficiently large for the PL waves to be severely damped in less than 0.5 s.

At the higher duty cycle starting at  $t = 0$  in Figure 2,  $T_e$  and hence  $\delta n$  in the duct rise from pulse to pulse until after about six 0.5-s pulses,  $\delta n + \delta n_p$  becomes high enough near the end of the 0.5-s pulses to initiate Landau damping of the PL waves.  $\delta n$  at the start of the pulse continues to increase for the next seven pulses and severe Landau damping of PL waves occurs at progressively earlier times from pulse to pulse. On the right-hand side of Figure 2,  $\delta n$  is sufficiently large at the start of the pulse that when  $\delta n_p$  maximizes in some tens of milliseconds,  $\delta n + \delta n_p$  is great enough to initiate severe damping of PL waves. The Langmuir waves whose wavenumbers make small angles with the duct axis and hence cannot be observed by the radar suffer considerably less damping than the PL waves. Hence, the ponderomotive force is maintained.

At the still higher duty cycle of Figure 3, even the L waves whose wavenumbers make small angles with the duct axis can be damped, cutting off the ponderomotive force. At the start of the HF pulse (at about 450 ms),  $\delta n$  is quite close to the value at which severe damping of PL waves takes place. Shortly after the ponderomotive force starts to reduce the density, severe damping of all waves sets in and the ponderomotive force is almost eliminated. The PL waves are observed for a short time before they are absorbed. Due to plasma inertia  $\delta n + \delta n_p$  remains high for tens of milliseconds (in this case about 30 ms) before  $\delta n + \delta n_p$  decreases to where L waves can grow again. The process is repeated resulting in the observed periodicity. It is interesting that for  $t > 1200$  ms the PL intensity between PL spikes has fallen to the HF-off noise level. This is likely due to the enhanced temperature near the middle of the 2-s pulse which ensures that the PL waves are completely eliminated between the peaks.

There is another important observation: the spikes from 1200 to 1700 ms are clean and evenly spaced. This is probably because there is only one PL duct in the radar beam. Duct spacing is roughly one-half to one kilometer and beam diameter is about one kilometer; hence at a given time there may be anywhere from zero to a few ducts in the beam at the height of the first Airy maximum. If there were two ducts in the beam the spacing might appear irregular (see Figure 3 for  $t < 1200$  ms). If there were three or more ducts the spacing might appear random.

## CONCLUSIONS

The duct model for the PL overshoot at Arecibo is capable of explaining qualitatively the rather complex evolution of the PL intensity when the duty cycle of HF cycling is suddenly changed.

To the author's knowledge no good data have yet been published on PL intensity following the start of HF cycling after the transmitter has been off for at least 10 min. For ionospheric conditions, HF power, frequency, and cycling periods similar to those corresponding to Figures 1 and 2, it is predicted that if a PL is observed it will probably take 1 to 2 min for the PL overshoot to appear and reach minimum lifetime.

For a high duty cycle such as the one corresponding to Figure 3, it is occasionally possible to get rapid PL pulsing. This occurs when the duct density decrement due to heating is just low enough to allow weakly damped L waves, which can be observed by the radar, to exist but high enough so that all L waves become severely damped when the density decrement is increased further by the ponderomotive force.

## REFERENCES

- Djuth, F. T., C. A. Gonzalez, and H. M. Ierkie, Temporal evolution of the HF-enhanced plasma line in the Arecibo F region, *J. Geophys. Res.*, 91, 12089-12107, 1986.
- DuBois, D. F., H. A. Rose, and D. Russell, Power spectra of fluctuations in strong Langmuir turbulence, *Phys. Rev. Lett.*, 61, 2209-2212, 1988.
- DuBois, D. F., H. A. Rose, and D. Russell, Excitation of strong plasma turbulence in plasmas near critical density: application to HF heating of the ionosphere, Report LA-UR-89-1419, Los Alamos National Laboratory, 1989.
- Fejer, J. A., F. T. Djuth, H. M. Ierkie, and M. P. Sulzer, Simultaneous observations of the enhanced plasma line and of the reflected HF wave at Arecibo, *J. Atmos. Terr. Phys.*, 51, 721-725, 1989.
- Graham, K. N., and J. A. Fejer, Anomalous radio wave absorption due to ionospheric heating effects, *Radio Sci.*, 11, 1057-1063, 1976.
- Kuo, S. P., M. C. Lee, and F. T. Djuth, A new interpretation of plasma-line phenomena, *Geophys. Res. Lett.*, 14, 961-964, 1987.
- Muldrew, D. B., The role of field-aligned ionization irregularities in the generation of the HF-induced plasma line at Arecibo, *J. Geophys. Res.*, 83, 2552-2560, 1978.
- Muldrew, D. B., Frequency asymmetry in the upshifted and downshifted plasma lines induced by an HF wave at Arecibo, *J. Geophys. Res.*, 84, 2705-2714, 1979.
- Muldrew, D. B., An ionization duct explanation of some plasma line observations with a 40.8-MHz radar and with a 430-MHz radar, *J. Geophys. Res.*, 90, 6662-6668, 1985.
- Muldrew, D. B., Duct model explanation of the plasma-line overshoot observed at Arecibo, *J. Geophys. Res.*, 93, 7593, 1988.
- Muldrew, D. B., and R. L. Showen, Height of the HF-enhanced plasma line at Arecibo, *J. Geophys. Res.*, 82, 4723-4804, 1977.
- Showen, R. L., Time variations of the HF induced plasma waves, Ph.D. thesis, Rice University, Houston Tex., 1978.
- Showen, R. L., and D. M. Kim, Time variations of HF-induced plasma waves, *J. Geophys. Res.*, 83, 623-628, 1978.
- Sulzer, M. P., H. M. Ierkie, and J. A. Fejer, Observational limitations on the role of Langmuir cavitons in ionospheric modification experiments at Arecibo, *J. Geophys. Res.*, 94, 6841, 1989.

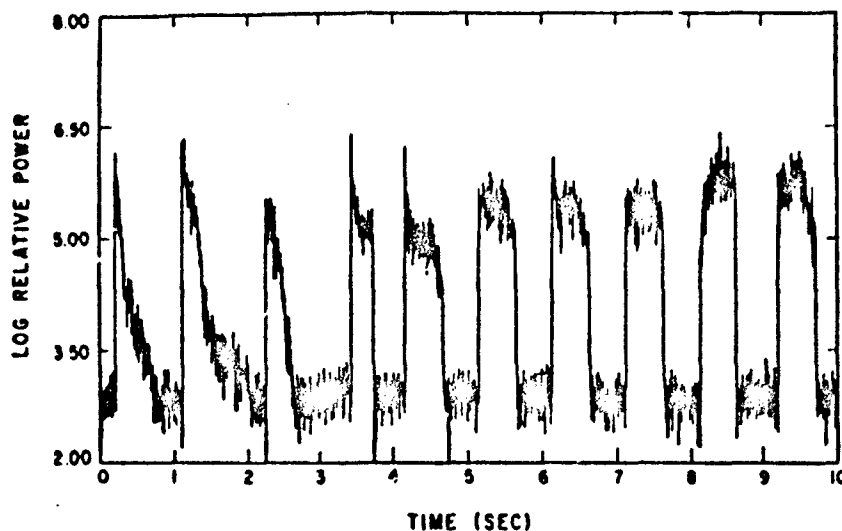


Fig. 1. The logarithm of the power in the enhanced plasma line as a function of time. The data are displayed only near the 0.5-s on periods, starting 2015:49 on 18 January, 1987 when the HF transmission sequence was changed from 0.5-s on, 8.5-s off to 0.5-s on, 10.5-s off. As a result of the nature of the data taking program, the beginning of the third and end of the fourth 0.5-s on periods were not recorded. After Sulzer et al. [1989].

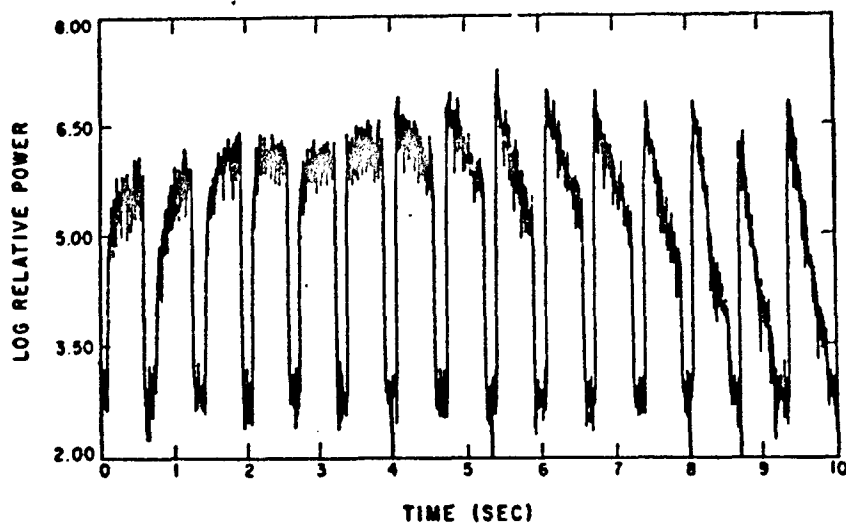


Fig. 2. The logarithm of the power in the enhanced plasma line as a function of time. The data are displayed only near the 0.5-s on periods, starting 2027:23 on 18 January, 1987 when the HF transmission sequence was changed from 0.5-s on, 10.5-s off to 0.5-s on, 8.5-s off. After Sulzer et al. [1989].

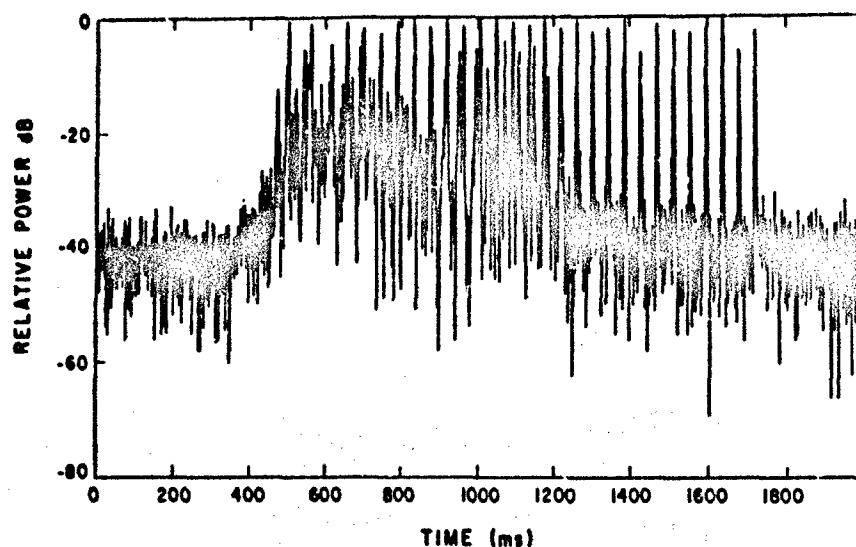


Fig. 3. Quasi-periodically recurring pulses in the relative power in decibels of the enhanced plasma line with a 2-s on, 2-s off transmitting sequence, sampling the power every millisecond. A 2-s long period starting at 1632:08 on January 19, 1967 is displayed. After Sulzer et al. [1969].

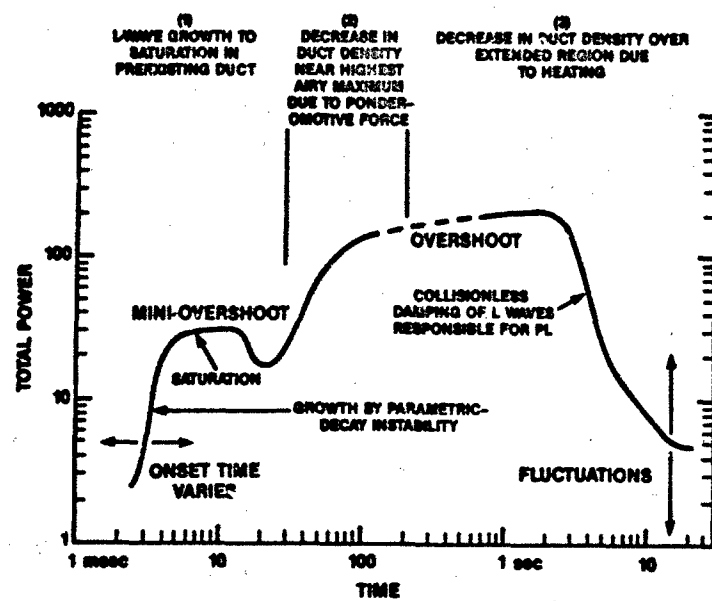


Fig. 4. Schematic of overshoot total PL power based on observations with transmitter on-off cycle times of about 20-60 s. After Showen [1975] as modified by Muldrew [1988].

## DISCUSSION

N. SHOUCRI, US

You refer to ducts being an explanation for the observations of Duncan and Bahrke (1978). However, their drifting striations are kilocycles in size, while the ducts you are discussing are 25 m in size. How do you account for the difference?

AUTHOR'S REPLY

Although the ducts are about 25 m in diameter, individual ducts are separated by about 0.5 to 1 km. Consequently, the fading peaks are separated by about the same amount as that which would be expected from the self-focussing instability.

L. DUNCAN, US

In fact, there have been measurements showing height variations of the enhanced plasma line consistent with structures of  $\Delta n/n$  - few % drifting through the radar beam. However, there appears some reasons to believe that the intermediate scale structures associated with self-focussing (~ km) and smaller structures you are calling ducts (~ 25 m) may both be present as components of a multi-scale irregularity environment. There is no inconsistency between these models.

AUTHOR'S REPLY

Perhaps ducts and self-focussing irregularities could co-exist. The data I referred to showing no height variation of the PL during ~ 1 min fading were recorded with a height resolution of 600 m. Since this was observed in several sets of data, the height variation is probably considerably less than 600 m. This implies density variation for self-focussing of less than about 1%. Your observations had a height resolution of 200 m, I believe, so that our observations could be consistent. However quite small values of  $\Delta n/n$  are implied.

## A THEORETICAL MODEL FOR THE TEMPORAL EVOLUTION OF HF-ENHANCED PLASMA LINES

by

S.P.Kuo and A.Y.Ho  
Weber Research Institute  
Polytechnic University  
Route 110, Farmingdale, NY 11735  
United States

M.C.Lee  
Plasma Fusion Center (NW16-234)  
Massachusetts Institute of Technology  
Cambridge, MA 02139  
United States

and

F.T.Djuth  
c/o Main Author

Abstract

The HF-enhanced plasma lines (HFPLs) observed in the Arecibo heating experiments refer to the radar returns at frequencies near the sum and difference of the radar frequency and the HF-heater frequency. These enhanced spectral lines are caused by backscatter of radar signals from parametrically excited plasma waves having a wavenumber of  $18\text{m}^{-1}$ . A nonlinear theory has been developed to describe the temporal evolution of those specified plasma waves and their originating altitude interval. Both phenomena of intensity overshoot and expansion of originating altitude interval of HFPLs observed at Arecibo, Puerto Rico are explained. The theoretical results agree well with the observation [Djuth and Sulzer, 1989].

1. Introduction

It is generally believed that parametric decay instability plays an essentially role responsible for various nonlinear plasma phenomena observed during the ionospheric HF-heating experiments [Carlson et al., 1972]. One of the most pronounced signature of such an instability is the observation of HF-enhanced plasma lines (HFPLs) during the heating experiments. In the Arecibo heating experiments, these lines correspond to the enhanced backscatter spectrum of the Arecibo 430MHz radar signals at frequencies near  $430\text{ MHz} \pm f_{\text{HF}}$ , where  $f_{\text{HF}}$  is the frequency of the HF heater wave. The enhanced radar returns at these two sidebands then provide useful information on the characteristic features of those upgoing and downgoing components of the parametrically excited plasma waves. One of the interesting features associated with the HFPLs in the F region over Arecibo is the so-called main plasma line overshoot [Showen and Behnke, 1978; Showen and Kim, 1978]. It has been described in detail by the recent study of temporal evolution of HFPLs [Djuth et al., 1986]. The experimental results at high HF power (80 MW ERP) show that the HFPL signal exhibits an initial growth lasting for a few tens of milliseconds before reaching a maximum value, and then greatly reduces its strength in the order of a few seconds. A theoretical interpretation of this phenomenon has been suggested in terms of a mode competition process which results from anomalous damping introduced by incoherent scattering of electron orbits by the total excited plasma waves [Kuo et al., 1989]. Electron diffusion in the velocity space along the magnetic field together with the cross-field diffusion in the coordinate space are results of the incoherent scattering. On one hand, these diffusion processes appear as an enhanced viscosity to the electron motion. But, on the other hand, they broaden the resonance interaction between the electrons and waves and lead to anomalous damping of waves. The mode competition process can be understood from the fact that the anomalous damping introduced by enhanced electron cross-field diffusion to each spectral line of excited plasma waves is proportional to the total spectral intensity of excited plasma waves. This is because the enhanced electron cross field diffusion is determined by the total spectral intensity. The increase of the anomalous damping on the slowly growing plasma line can result from the fast growth of other lines in the same region. Consequently, plasma waves with smaller growth rates will be suppressed by those with larger growth rates. Such a mode competition process is believed to be responsible for the overshoot of HFPLs observed with the Arecibo 430 MHz radar. With the improvement in the altitude and temporal resolution of radar measurements, the time evolution of the intensity and height location of HFPLs can be investigated. The experiments for such a study were performed by Djuth in the April, 1988 heating campaign with an HF pulsing sequence of 9 minutes off and 1 minute on. During these observations, the HF heater was operated at 5.1 MHz and approximately 80 MW effective radiated power was transmitted. The results show that during the first few seconds following HF turn-on, the HFPLs exhibits a transient response wherein it overshoots in intensity over a time scale of a second. During this period the HFPLs also occupy an extended altitude interval which is much larger than that predicted by linear theory. The upper cutoff altitude of HFPLs ( $\sim 275.8\text{ Km}$ ) is very close to the point of HF reflection in the plasma. The location of HFPLs never extends above the upper cutoff altitude (HF reflection). In general, the altitude interval extends only downward over 1 to 2 Km in about 30 to 50 milliseconds following HF turn-on. A common experimental result showing the evolution of the altitude interval of HFPLs is demonstrated in Figure 1.

In the present work, a detail study of plasma line overshoot is given and a theoretical interpretation on the expansion of originating altitude interval of HFPLs is suggested. The proposed



theory is based on the "tail" heating of the bulk plasma [e.g., Sagdeev and Galeev, 1969, pp 67-68] by excited Langmuir waves whose temporal evolution is described by the model equations derived in our previous work addressing the plasma line overshoot phenomena [Kuo et al., 1987]. The increase of the "equivalent temperature" of the plasma which is proportional to the energy density of Langmuir waves causes the downshift of the matching location of plasma wave dispersion relation with frequency and wavevector fixed by heater wave and radar signal, respectively. Thus, the plasma waves responsible for HFPLs are excited not only from the original matching location but also from the newly established matching height. It results in an expansion of originating altitude interval of HFPLs following the growth and saturation of Langmuir waves. The theory and formulation are presented in section II. The numerical results presented in section III have reproduced both the overshoot and altitude expansion phenomena. A summary of the work is given in section IV.

## II. Theory and Formulation

As plasma waves are excited through the parametric decay instability, their wave fields affect the motion of electrons and introduce electron diffusion in the velocity space. Such a diffusion process can be described by a quasi-linear diffusion equation wherein the diffusion coefficient can be separated into two parts. The resonant interaction of waves and electrons contribute to the resonant part of the diffusion coefficient. However, only very few electrons are involved in the interaction. On the other hand, the nonresonant (or adiabatic) interaction involves the main body of the plasma distribution in the plasma oscillations. The oscillatory kinetic energy associated with the excited Langmuir waves increases as the amplitude of the waves increase and the main body of the plasma appears to be heated. One can show that the main body of the plasma electrons is effectively heated in

the presence of plasma waves by the temperature increment  $\propto \sum E_s^2 / 4\pi n_0$ , where  $E_s^2$  is the spectral intensity of plasma waves and  $n_0$  is the background electron density [e.g., Sagdeev and Galeev, 1969]. Consequently, the dispersion relation of plasma wave is modified to be:

$\omega_p^2 = \omega_{pe}^2 + \Omega_e^2 \sin^2 \theta + 3k^2 (T_e + \tau) / m_e$ , where  $\omega_p$ ,  $\omega_{pe}$ ,  $k$ ,  $\theta$ ,  $\Omega_e$ ,  $m_e$ , and  $T_e$  are the Langmuir wave frequency, electron plasma frequency, Langmuir wave number, the propagation angle of Langmuir wave with respect to the geomagnetic field, the electron gyrofrequency, the electron mass, and the unperturbed electron temperature, respectively. Since  $\omega_p = \omega_{pe}$  required by the frequency matching condition of the parametric instability and  $k_z = \pm 2k_y$  required for being able to be detected by the backscatter radar, where  $k_y$  is the wavevector of the radar signal, the dispersion relation is reduced to  $\omega_{pe}^2 + 3k^2 \tau / m_e = \text{const}$ . It implies that the modification of the dispersion relation of the plasma wave due to finite  $\tau$  is going to change the matching height location of the plasma waves responsible for HFPLs. As  $\tau$  increases in time, the matching height location also moves in time

according to the rate equation  $\frac{d\omega_{pe}^2}{dt} = -3 \frac{k^2}{m_e} \frac{d\tau}{dt}$ . It is noted that the plasma waves which are responsible for HFPLs in the early time will continue to grow at the original location as long as the pump field still exceeds the enhanced threshold field of the parametric instability. If a linear density profile is assumed for the heated ionosphere, i.e.,  $n_0 = n_{00}(1+x/L)$  where  $L$  is the linear scale height of the ionospheric density and  $n_{00}$  is the electron plasma frequency at the original matching location, we then have the rate equation for the originating altitude of HFPLs as

$$\frac{dx}{dt} = -Ck^2 L / m_e \omega_{pe0}^2 \frac{d\tau}{dt} \quad (1)$$

Equation (1) indicates that the originating altitude of HFPLs is going to move downward as  $\tau$  increases. This represents a downward expansion of the originating altitude interval of HFPLs.

Let  $I_0 = 4\pi \sin^2 \theta \int dk k^2 E_s^2$  represent the spectral intensity of Langmuir waves propagating at the same angle  $\theta$  with respect to the earth's magnetic field, thus,  $\tau$  can be expressed in terms of  $I_0$  as  $\tau = \left[ \int I_0 d\theta \right] / 4\pi n_0$ , where  $\theta_0$  is the averaged maximum spectral angle of excited plasma waves. Substituting this expression of  $\tau$  into (1), yields

$$\frac{dx}{dt} = -Ck^2 L / 4\pi n_0 \omega_{pe0}^2 \left( \int I_0 d\theta \right) \frac{d\theta}{dt} \quad (2)$$

The rate equations for  $\theta_0$  and  $I_0$  (i.e.  $\frac{d\theta_0}{dt}$  and  $\frac{dI_0}{dt}$ ) were already derived in our early work [Kuo et al., 1987] on the study of HFPL overshoot phenomenon. In the following, a brief summary of the previous derivation is included.

The linear growth rate of parametric instability for the spectral line  $\bar{k}$  is found to be

$$\gamma_{\bar{k}}^L = \alpha k^{1/2} \cos \theta - \beta_0 - \beta_1 k \quad (3)$$

where  $\alpha = eE_0/2(m_e m_e c_s)^{1/2}$ ,  $\beta_0 = v_A^2/4$ ,  $\beta_1 = \frac{1}{4}(\kappa/\bar{\omega})^{1/2} c_s (T_e/T_i)^{1/2} v_A^{-1} \pi^{-1/2}$ ,  $\omega_e = kc_s$ , and  $v_A$  is the electron collision frequency.

The linear growth rate is then given by  $\gamma_{\bar{k}, \max}^L = (\alpha^2/4\beta_1) \cos^2 \theta - \beta_0$  for  $k = k_0 = \alpha^2 \cos^2 \theta / 4\beta_1$ . It is seen that the linear growth rate of the spectral line is a function of the propagation angle  $\theta$  and the wavenumber  $k$ , and the growth rate is maximized for each  $k$  at  $\theta = 0$ . For a pump field exceeding the threshold field, the maximum angle for the unstable  $|\bar{k}|$  modes is given by  $\theta_{0k} = \cos^{-1}[(\beta_0 + \beta_1 k)/\alpha k^{1/2}]$ , where  $\beta_0 + \beta_1 k \leq \alpha k^{1/2}$  is required for the instability.

Two nonlinear damping mechanisms will be considered to obtain the net growth rate of the instability. The first one is the cascading of the plasma lines which occurs when the amplitude of the excited plasma wave exceeds the threshold of parametric decay process. The daughter plasma wave of each cascading process then takes energy away from its corresponding mother plasma wave, and eventually, the total energy drained by all the decay waves becomes large enough to stop the growth of the first mother plasma wave. Based on the balance relation, the anomalous damping rate  $\gamma_{\bar{k},0}^*$  on the starting decay process is deduced to be

$$\gamma_{\bar{k},0}^* = (\Delta k)^{3/2} k^{1/2} e E_0 / 2(m_e m_i c_s)^{1/2} \quad (4)$$

where  $\Delta k$  is the spectral width of each spectral line and given by  $\Delta k/k_0 = \sqrt{2} \alpha \beta_1 / k_0 v_A^2$ ;  $v_A^2 = T_e/m_e$ .

Since  $\gamma_{\bar{k},0}^*$  is proportional to  $E_0$  only, the cascading process can only lead to the saturation of the instability. The second non-linear damping mechanism which originates from the broadening of wave-electron resonances in the presence of random scattering of electrons in the excited turbulent field is considered to be the cause of HFPL overshoot phenomenon. It has been shown by Dum and Dupree [1970] that the field-dependent resonance broadening can be expressed in terms of diffusion coefficients which broaden the resonance function in a similar way as collisional damping does. In the magnetized plasma, the cross-field diffusion will be the major response of electrons to the incoherent scattering by waves. The diffusion damping rate to the  $\bar{k}$  line is thus obtained to be

$$d_0(k) = \bar{k}_1 \cdot \bar{D}_1 \cdot \bar{k}_1 \quad (5)$$

where  $\bar{D}_1 = \sum_k [c^2 (\partial E_k / \partial E_{\bar{k}}) (\partial E_{\bar{k}} / \partial E_k) (2\gamma_{k,\bar{k}}^2) (\omega_k^2 + \gamma_{k,\bar{k}}^2)]$ ,  $\gamma_{k,\bar{k}}^2 = k^{1/2} \alpha \cos \theta$ , and  $\Omega_e^2 \ll \omega_k^2$  is assumed.

Replacing the summation by integral, we can rewrite (5) as

$$d_0(k) = [\alpha c^2 \sin^2 \theta / 8 \omega_k^2] \int [2 \alpha k^{3/2} \sin^2 \theta \cos \theta E_{\bar{k}}^2 dk' d\theta' \quad (6)$$

From (3), (4) and (6), the nonlinear growth rate of the  $\bar{k}$  line can be defined by

$$\gamma_{\bar{k}} = \gamma_{\bar{k}}^L - \gamma_{\bar{k},0}^* - d_0(k) \quad (7)$$

The rate equation for describing the nonlinear evolution of  $E_{\bar{k},0}$  is then given by

$$\frac{dE_{\bar{k},0}}{dt} = \gamma_{\bar{k}} E_{\bar{k},0} \quad (8)$$

In terms of  $I_0$ , equation (8) becomes approximately

$$\frac{d\bar{I}_0}{dt} = (\bar{\alpha}_0 \cos \theta_0 - 2\bar{\beta}_0 - \bar{\eta}_0^{1/2}) \bar{I}_0 \quad (9)$$

where  $\bar{\alpha}_0 = 2\alpha_1^{1/2}$ ,  $\bar{\beta}_0 = 2(\beta_0 + \beta_1 k_0)$ ,  $\bar{\eta}_0 = e(\Delta k/k_0)^{1/2} / (4\pi \sin \theta_0 m_e \omega_0 c_0)^{1/2}$  and  $\bar{I}_0 = (\cos^2 \theta_0^{1/2} \sin^2 \theta_0 / 2B_1^{1/2}) \int_0^{\pi/2} I_0 \sin^2 \theta \cos \theta d\theta$ ;  $k_0 = \alpha^2 \cos^2 / 4\beta_1^2$  and  $b = 2k_0 / \Delta k_{\text{max}}$ ;  $\theta_0$  is defined by  $\bar{\alpha}_0 \cos \theta_0 - \bar{\beta}_0 - 2\bar{\beta}_0 - \bar{\eta}_0^{1/2} = 0$  which leads to the rate equation for  $\theta_0$  as

$$\begin{aligned} \frac{d\theta_0}{dt} = & - (B \sin^2 \theta_0 \cos^2 \theta_0 / [\bar{\alpha}_0 \sin^2 \theta_0 + B \bar{I}_0 \sin^2 \theta_0 \cos^2 \theta_0] \\ & + (2 - 5 \sin^2 \theta_0 / \cos^2 \theta_0) (\bar{\alpha}_0 \cos \theta_0 - \bar{\beta}_0 - \bar{\eta}_0^{1/2}) \\ & \int_0^{\pi/2} (\bar{\alpha}_0 \cos \theta - \bar{\beta}_0 - 2\bar{\beta}_0 - \bar{\eta}_0^{1/2}) I_0 \sin^2 \theta \cos \theta d\theta \end{aligned} \quad (10)$$

with the coefficients  $b = \alpha^2 c^2 / 32 \pi^2 B_1^{1/2} \alpha_1^2 \bar{\alpha} = \alpha^2 / \beta_1$ .

Equations (2), (9) and (10) represent three coupled equations for describing the temporal evolution of the spectral intensity of plasma waves oriented at the angle  $\theta$  and the height of HFPLs. These equations will be solved numerically. In terms of dimensionless variables:  $\bar{x} = x/L$ ,  $\bar{t} = 2\pi \omega_0 t$  and  $\bar{I}_0 = I_0 / 4\pi \omega_0 T_e$ , equations (2), (9) and (10) are normalized for numerical analysis to be

$$\frac{d\bar{I}_0}{d\bar{t}} = -A [\bar{I}_0 \frac{d\theta_0}{d\bar{t}} + \int_0^{\pi/2} (\frac{d\bar{I}_0}{d\bar{t}}) d\theta] \quad (11)$$

$$\begin{aligned} \frac{d\bar{I}_0}{d\bar{t}} = & [\alpha_1^2 \cos^2 \theta_0 - 1 - B \cos^2 \theta_0 \sin^2 \theta_0 \int_0^{\pi/2} I_0 \sin^2 \theta \cos \theta d\theta \\ & - C \cos^2 \theta_0 \sin^{-1/2} \theta_0 \bar{I}_0^{1/2}] \bar{I}_0 \end{aligned} \quad (12)$$

$$\begin{aligned} \frac{d\theta_0}{d\bar{t}} = & - (B \sin^2 \theta_0 \cos^2 \theta_0 / [2\alpha_1^2 \sin^2 \theta_0 + B \bar{I}_0 \sin^2 \theta_0 \cos^2 \theta_0] \\ & + (2 - 5 \sin^2 \theta_0 / \cos^2 \theta_0) (\alpha_1^2 \cos^2 \theta_0 - 1) \\ & - C(5/2 - 7 \sin^2 \theta_0 / \cos^2 \theta_0) \cos^2 \theta_0 \sin^{-1/2} \theta_0 \bar{I}_0^{1/2}) \\ & \int_0^{\pi/2} (\frac{d\bar{I}_0}{d\bar{t}}) \sin^2 \theta \cos \theta d\theta \end{aligned} \quad (13)$$

where  $\alpha_1 = \alpha / \alpha_{ch}$ ,  $\alpha_{ch} = 2(\beta_0 \beta_1)^{1/2}$ ,  $A = 3k_0^2 v_{th}^2 / \omega_{pe}^2$ ,  $B = \sqrt{2} \alpha_1^2 v_{th}^4 \omega_{pe}^2 / \beta_1^2 \alpha_{ch}^2$  and  $C = \beta_1^2 \omega_{pe} / 20 \alpha_1^2 \beta_1^2 v_{th}^2$ .

### III. Results

Using the following parameters relevant to the Arecibo heating experiments:  $v_{th} = 1.3 \times 10^7$  cm/sec,  $c_s = 1.5 \times 10^5$  cm/sec,  $T_e = T_i = 1100^\circ$  K,  $\omega_0 / 2\pi = 5.1 \times 10^6$  sec<sup>-1</sup>,  $\lambda_p = 35$  cm (for 430 MHz radar), and  $\nu_{rf} = 500$  Hz and  $\alpha_1 = 2$ , we then have  $\beta_0 = 125$  Hz,  $\beta_1 = 0.0212 c_s$ ,  $A = 1/50$ ,  $B = 120$  and  $C = 0.325$ . Equations (11)-(13) are then integrated to determine the time dependence of the reflection height and intensity of HFPLs.

Shown in Figure 2(a) and (b) are the numerical results describing the  $L_{\text{app}}$  and the fake temperature increment  $\tau$ , where  $L_{\text{app}}$  simulates the plasma line detected by the Arecibo 430 MHz backscatter radar since the vertical lines of sight of the Arecibo radar makes  $40^\circ$  angle with the geomagnetic field. The observed overshoot phenomenon of HFPLs is successfully reproduced by the numerical result of our theoretical model. It is noted from equation (2) that the matching height location of the plasma lines responsible for HFPLs is going to move downward during the growth of plasma waves. This observation is demonstrated by a numerical result evaluated for the Arecibo situation. This result is presented in Figure 3. It shows that the matching height location indeed moves downward as the total intensity of plasma waves grows. This location eventually settles at a distance 0.05L below the original altitude after the HF heater is turned on for about 50 milliseconds. As mentioned before, this represents the expansion of the originating altitude of HFPLs because the plasma lines responsible for HFPLs are continuously excited not only from their original location but also, at the same time, extending to a lower altitude due to the "fake heating" of electrons by the excited plasma waves. The ionosphere scale height L, deduced from the experiments is about 22 Kilometers [Djuth et al., 1986], leading to the calculated expansion of the originating altitude interval

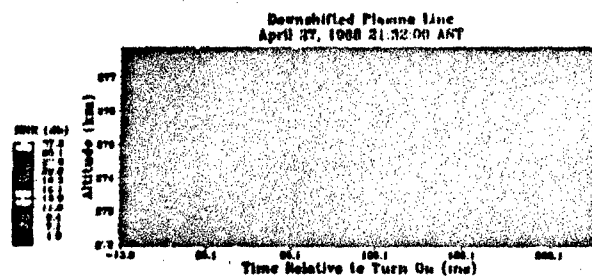
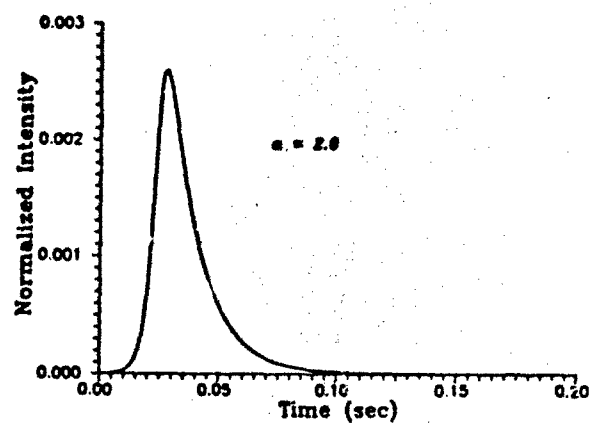
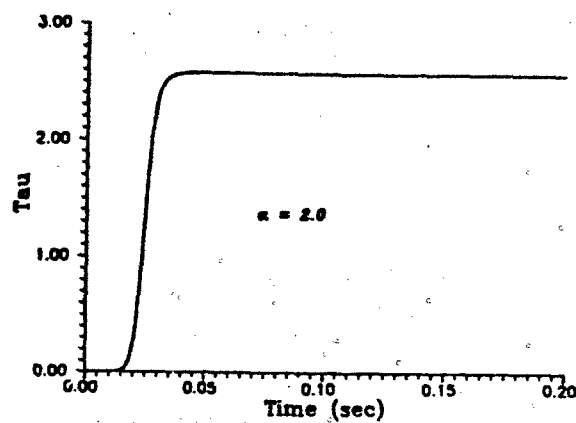


Figure 1. Typical overshoot experimental data

Figure 2(a) Intensity  $I_{40^\circ}$  vs. timeFigure 2(b) Temperature increment  $\tau$  vs. time

11B-6

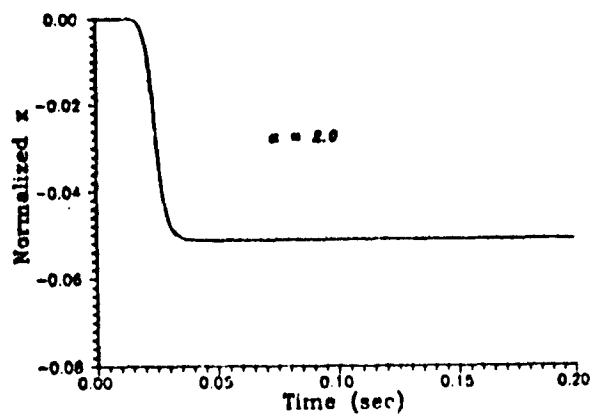


Figure 3 Matching Altitude  $x$  vs. time

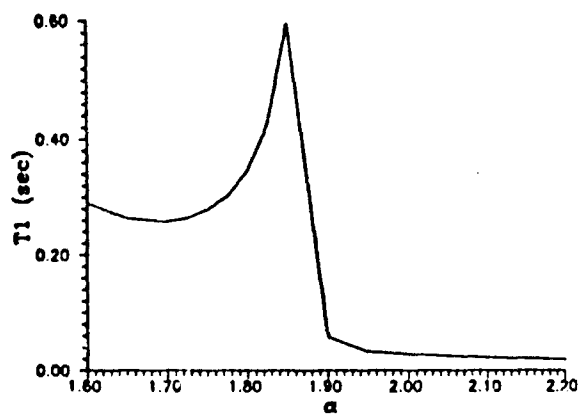


Figure 4(a) Overshoot time  $t_1$  vs.  $\alpha$

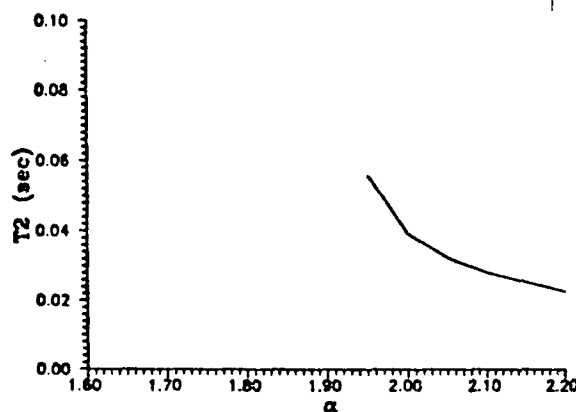


Figure 4(b) Time to half-peak intensity  $t_2$  vs.  $\alpha$

of HFPLs to be 1.1 Kilometers. These theoretical results agree well both qualitatively and quantitatively with the observation shown in Figure 1.

In the present theory, two nonlinear effects are included. Mode competition mechanism is responsible for overshoot while cascading mechanism is responsible for the saturation of the plasma lines. Only when the first mechanism dominates over the second mechanism, overshoot can occur. Therefore, it is useful to find out the relationship between overshoot phenomenon and the heater intensity. The dependence of the overshoot intensity and overshoot time on the pump intensity are concerned.

Let  $t_1$ ,  $t_2$  and  $t_3$  represent the times for the plasma line to reach its peak intensity, then drop its intensity to one-half and then one-tenth of its peak value, respectively. According to our theoretical model,  $t_1$  approaches infinity if this plasma line does not overshoot. The dependence of these three characteristic times on the heater intensity is displayed in Figures 4(a)-4(c). Shown in Figure 5 is the dependence of the peak intensity of HFPLs on the heater intensity. The results show that both overshoot times and peak intensity of HFPLs decrease generally with the heater intensity.

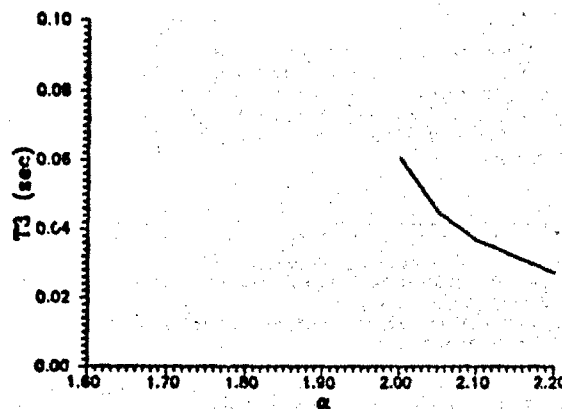


Figure 4(c) Time to tenth-peak intensity  $t_3$  vs.  $\alpha$

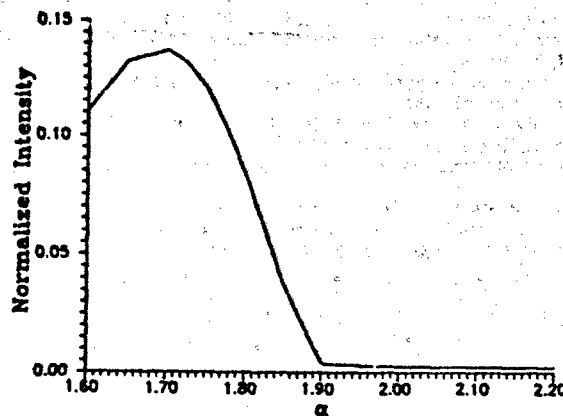


Figure 5. Peak Intensity vs.  $\alpha$

## IV. Summary

Our theoretical model [Kuo et al., 1987] developed originally for explaining the intensity overshoot of the HFPLs has been extended. The extension of the model is based on the fact that nonresonant heating of plasma electrons by the parametrically excited Langmuir wave can yield an apparent increment in electron temperature. This fake heating of electrons introduces an extra term into the dispersion relation of Langmuir waves. The modification of the dispersion relation moves the matching location of the HFPLs to a lower altitude where the plasma density is less than that at their initial location. This extended model is intended to explain the newly observed expansion in the originated altitude interval of HFPLs. This model can successfully reproduce both the intensity overshoot and the expansion of the originating altitude interval of HFPLs in good agreement with the observations. The numerical results of the theoretical model also show that both the overshoot time and intensity decrease generally with the pump intensity.

It is noted that thermal filamentation instability can generate large scale density perturbation ( $> 1$  Km scale length) which may also cause the shift of the plasma line altitude. However, two facts stand on the way to rule out the possibility of this instability as the cause mechanism for the observed phenomena. One is its growth time. It takes at least a few seconds for the development of large scale density irregularities through thermal filamentation instability [Kuo and Schmidt, 1983]. The other one is the filamentation direction which is shown to be perpendicular to the magnetic meridian plane for an O-mode pump [Kuo and Schmidt, 1983].

**Acknowledgments:** This work was supported by the National Science Foundation under Grant No. ATM-8516457 and by the Air Force Office of Scientific Research under the Grant No. AFOSR-85-0316 and AFOSR-85-0127 at the Polytechnic University, and by the NASA under Grant No. NAG5-1055 at the Massachusetts Institute of Technology, and by the Aerospace-sponsored Research program. The numerical work was performed at the Pittsburgh Supercomputing Center which is supported by the National Science Foundation.

## References

- Carlson, H. C., Gordon, W. E., and Showen, R. C., High frequency induced enhancements of the incoherent scatter spectrum at Arecibo, *J. Geophys. Res.*, **77**, 1242, 1972.
- Djuth, F. T., Gonzales, C. A., and Ierkie, H. M., Temporal evolution of HF-enhanced plasma line in the Arecibo F region, *J. Geophys. Res.*, **91**, 12059, 1986.
- Djuth, F. T., and Selzer, M. P., High-resolution observations of HF-enhanced plasma waves at Arecibo, *Geophys. Res. Lett.*, submitted, 1989.
- Dubois, D. F., Rose, H. A., and Russel, D., Excitation of strong Langmuir turbulence in plasmas near critical density: Application to HF heating of the ionosphere, *J. Geophys. Res.*, submitted, 1989.
- Dum, C. T. and Dupree, T. H., Nonlinear stabilization of high frequency instabilities in a magnetized field, *Phys. Fluids*, **13**, 2064, 1970.
- Kuo, S. P. and Schmidt, G., Filamentation instability in magnetized plasmas, *Phys. Fluids*, **26**, 2529, 1983.
- Kuo, S. P., Lee, M. C., and Djuth, F. T., A new interpretation of plasma-line overshoot phenomena, *Geophys. Res. Lett.*, **14**, 961, 1987.
- Payne, G. L., Nicholson, D. R., Downie, R. M., and Sheerin, J. P., Modulation instability and soliton formation during ionospheric heating, *J. Geophys. Res.*, **89**, 1092, 1984.
- Perkins, F. W., Oberman, C. and Valso, Parametric instabilities and ionospheric modification, *J. Geophys. Res.*, **79**, 1478, 1974.
- Sagdeev, R. Z., and Galeev, A. A., *Nonlinear plasma theory*, edited by T. M. O'Neil and D. L. Book, Benjamin Publications, New York, 1969.
- Showen, R. L. and Behnke, R. A., The effect of HF-induced plasma instabilities on ionospheric electron temperatures, *J. Geophys. Res.*, **83**, 207, 1978.
- Showen, R. L., and Kim, D. M., Time variations of HF-enhanced plasma waves, *J. Geophys. Res.*, **83**, 623, 1978.
- Showen, R. L., The spectral measurement of plasma lines, *Radio Sci.*, **14**, 503, 1979.
- Weatherall, J. C., Sheerin, J. P., Nicholson, D. R., Payne, G. L., Goldman, M. V., and Hansen, P. J., Solitons and ionospheric heating, *J. Geophys. Res.*, **87**, 823, 1982.

## DISCUSSION

R. L. SHOWN, US

I wanted to point out, relevant to your last conclusion, that when the plasma line strength is moderate, the overshoot durations were several seconds, and when the strengths were strong the overshoots were "sharp", with duration of  $\sim \frac{1}{2}$  sec. I should also ask the last speaker, Don Muldrew, if these observations are consistent with his duct theory.

## AUTHOR'S REPLY

[Rao] Our results are consistent with your remarks. As we have shown, both the overshoot time and plasma line strength are pump power dependent. In the region  $1.42 < E_p/E_{th} < 1.7$ , the overshoot time decreases with the pump power, while the plasma line strength increases with the pump intensity. For  $E_p/E_{th} = 1.7$ , the plasma line reaches the peak in less than  $\frac{1}{2}$  sec.

[Muldrew] The observations are consistent with the duct theory. Moderate PL strength implies moderate L-wave intensity in the duct and a strong PL implies strong L-wave intensity. Electron heating in the duct would occur more quickly with strong L-wave intensity and hence duct electron density would decrease more quickly than with moderate L-wave intensity. Landau damping of the trapped Langmuir waves responsible for backscattering the radar would thus also occur sooner for the strong PL case, i.e., the overshoot would be shorter or sharper.

L. BUNCAN, US

The fast thermal effect due to your 'fake' heating from enhanced Langmuir waves is very interesting and helps explain a number of features of the overshoot. However, there are also other features which indicate a role for density structures in overshoot such as in the previous talk. These data note a strong dependence on the character of overshoot based upon off times of the pump waves for seconds to tens of seconds time scales, consistent with diffusion relaxation of structures.

## AUTHOR'S REPLY

The two phenomena, plasma line overshoot and expansion of altitude interval of HF PLs discussed in my talk, were observed simultaneously in the Arecibo heating experiments only when the ionosphere is not pre-conditioned. The experiments were performed with heater one minute on and nine minutes off. Such an arrangement was intended to eliminate the possible role of heater induced irregularities (or ducts) on the observed phenomena. The possible role of naturally occurred irregularities as the cause of the observed phenomena was also not likely because the background plasma during the experiments was very quiet and the two phenomena were observed persistently over the long experimental period.

A. HANSEN, NO

Kruer & Valeo (1972), Perkins et al. (1974), Chen & Fejer (?) and other authors consistently see strong oscillations in the intensity of numerical solutions to the wave-kinetic equations. Your calculations do not show that. Why?

## AUTHOR'S REPLY

Two nonlinear processes are included in our theory. One is cascading of plasma lines responsible for the saturation of plasma lines. The other one is mode competition among plasma lines responsible for overshoot of plasma lines. These two nonlinear processes are competing and pump power dependent. When pump power is low, cascading process is dominant and there is no overshoot. In this region the energy of Langmuir waves oscillates in time before reaching a constant saturation level. As pump power increases, mode competition process gradually takes over and the oscillations of Langmuir wave energy becomes less apparent. This trend is shown by our calculations.



# ENHANCED FADING RATES PRODUCED DURING IONOSPHERIC MODIFICATION

by

T.B. Jones and A. Wilkinson  
Department of Physics and Astronomy  
University of Leicester  
University Road  
Leicester, LE1 7RH  
United Kingdom

## Introduction

When very high power radiowaves are reflected from the ionosphere, modifications in the physical characteristics of the ambient plasma are produced. These include the production of field aligned plasma striations with scale sizes across the geomagnetic field lines ranging from a few metres to a few kilometres. The presence of these striations produces anomalous absorption of both the heater wave itself and of other HF signals propagating through the modified region. During experiments at Tromsø, Norway, with the heating facility constructed by the Max Planck Institut für Aeronomie, Lindau, West Germany, marked changes in the fading rate of HF signals reflected from the heated volume have been noted. These rapid fluctuations in signal amplitudes are thought to be produced by medium scale striations generated during the heating process. An estimate of scale size of these striations is made from the experimental data.

## Measurements of fading rates

Small scale irregularities with wavelengths between (1 - 100m) are generated by instabilities which involve the excitation of electrostatic plasma waves (Des and Fejer, 1979, Inhester et al, 1981, Perkins and Valeo, 1974). These irregularities produce anomalous absorption of an O-mode wave propagating through the disturbed region, (Graham and Fejer, 1976, Jones et al, 1984, Robinson, 1989). The X-mode, however, does not suffer anomalous absorption and the amplitude fading rates observed are produced by changes in the electron density structure rather than by anomalous absorption. Since an X-mode signal is reflected at a lower height (smaller electron density) than an O-mode of the same frequency, the X-mode diagnostic signal is transmitted at a frequency some 0.25 MHz above the O-mode heater (pump) frequency. This ensures that the X-mode signal is reflected at a height close to that at which the heating wave interacts most strongly with the ionospheric plasma. The heater and diagnostic geometry is illustrated in Figure 1.

Typical examples of the changes produced by the Heater in X mode fading rates measured during quiet ionospheric conditions on the 17 and 22 March, 1985, are reproduced in Figure 2. The heater was operated at full power (4.544 MHz, ERP = 360 MW) in a 2 min on, 6 min off cycle on 17 March and a 3 min on 7 min off cycle on 22 March. There is no overall change in signal level indicating the absence of anomalous absorption. There is, however, a very marked change in the fading rate during times of heater on. The increased fading rate persists even after the heater has been switched off. Ionograms taken during the experiment indicate that there is no change in propagation mode structure is during heating. It is, therefore, concluded that the enhanced fading rate is a direct consequence of multiple field aligned scatters created within the heated region. It becomes more difficult to distinguish the enhanced fading rate from the background fluctuations during disturbed ionospheric conditions.

## Spectral characteristic of the X-mode signal

The complex spectrum of the 4.7 MHz diagnostic signal was obtained from samples of the real and imaginary output of the receiver by means of an FFT. Two effects are apparent. At heater turn-on there is a bulk downward displacement in the reflection level (+ Doppler) which decays away during the on period. At switch-off there is an upward movement (- Doppler) which gradually decays as the ionosphere recovers. Such changes have been reported by many authors (eg. Jones et al, 1982, Robinson, 1989).

The second effect is the spread in the frequency of the signal during the on period. This is due to the enhanced fading present at this time. It persists throughout the heater on time and takes over 1 minute to decay after heater turn-off. It is this spectral spreading that forms the basis of this study.

Following the procedures for studying of the scintillation of trans-ionospheric propagation, (eg. Aarons et al 1971, Procello et al 1968, Frey & Duncan 1984, Booker 1979), it is possible to assign a spectral power index to the power spectrum of the X-mode fading. An example of this type of spectrum is reproduced in Figure 3 together with a schematic diagram which illustrates the main features. The FFT technique was applied to 2048 data samples representing a 120 sec interval resulting in a frequency resolution of 0.031 Hz over the range 0 to 16 Hz.

The scintillation spectral density is constant, as expected, for dimensions larger than the Fresnel scale size  $\lambda_e k_f = 2\pi/\lambda_e$ , which corresponds to a frequency of 0.4 Hz in Figure 3. The scintillation frequency  $f_s$  can be written in terms of the ionospheric drift velocity,  $U_d$ , as

$$f_s = \frac{U_d}{2\pi} k_f$$

For a drift velocity of  $150 \text{ ms}^{-1}$  this corresponds to a Fresnel dimension  $k_f$  of  $2 \times 10^{-3} \text{ m}^{-1}$ . For the parameters of the Tromas heater, radiating a frequency of 4.5 MHz ( $\lambda = 65 \text{ m}$ ) and a reflection height  $z = 200 \text{ km}$ , the value of the Fresnel zone parameter  $k_f$  is expected to be about  $1.17 \times 10^{-3} \text{ m}^{-1}$ . The difference between the two values for the Fresnel zone can be attributed to both the "Fresnel Filtering" effect and the focussing effects observed during strong refractive scattering (Briggs 1975). It should be noted that the noise cut-off in the spectrum of Figure 3 occurs at about 4 Hz and that all the important information is contained in the range 0 to 8 Hz.

The spectral power index  $p$  has been obtained by applying a least squares fit to the spectrum between the interval 0.5 to 3.0 Hz. The S4 index was obtained by integrating the area under the power spectrum (from 0.01 to 16 Hz) as indicated by the shaded region of Figure 3. The values obtained for this spectrum,  $p = 2.94$  and  $S4 = 1.47$ , indicate that a strong scattering regime exists during heater on times (Booker et al 1986, Singleton 1969).

A comparison of the scintillation parameters during heater on and off periods has been made from data collected between 11.46 and 14.37 UT on 17 March, 1985. During this period the heater radiated an X-mode at a frequency of 4.544 MHz with an ERP of 360 MW. The diagnostic frequency was 4.7 MHz and the fading characteristics were measured for the X-mode component which was isolated by means of a polarimeter at the receiver. A 7 min on 8 min off heating cycle was employed. Examples of the fading spectra obtained during this period are reproduced in Figures 4 (a) to (d). The derived S4 and spectral index parameters are presented in Table 1.

Both the S4 and spectral index increase during the period of heater on. The steepening of the spectral slope (over the interval 0.5 to 1.3 Hz) during the times of heater on suggests that more power has been deposited in the intermediate scale irregularities than was present before heating commenced. It is not clear, however, whether the power increase in the intermediate scale irregularities is due to the cascading of the larger scale irregularities into smaller scale sizes or to the growth of the small scale irregularities. The theory of self focussing instabilities suggests that the break-up of large scale irregularities would occur due to stimulation by the heater. However, the consistent increase in the S4 index during heater on times indicates that a stronger scattering regime exists when the heater is on. This effect is seen more clearly by considering the spectra reproduced in Figure 5, in which five of the 120-sec interval spectra presented in Figure 4 are averaged to illustrate the principal changes in the spectral characteristics of the diagnostic signal between periods of heater on and off. The general trend observed is for the spectral slope to become steeper ( $p$  increases) and the  $S_4$  index to exceed one, indicating that saturation and focusing is occurring, (Salpeter 1967) for periods when the heater is on.

A similar experiment was performed on 22 March 1985 from 11:54 (UT) until 13:24 (UT) in which a 4.70 MHz X-mode diagnostic signal was received while the heater (4.91 MHz, ERP=360 MW) was operated at full power in a 3-min on, 7-min off switching sequence. The spectra, obtained by averaging over five individual 120-sec spectra corresponding to times of heater on and off, are presented in Figure 6. The steepening of the spectral slope between periods of heater off ( $p = 2.06$ ) and heater on ( $p = 2.83$ ) once again indicates that more power is present in the intermediate scale irregularities when the heater is on. The concurrent increase in  $S_4$  index (0.48 (off) - 1.05 (on)) confirms the need for a strong scattering theory to explain the observed scintillation of the diagnostic signal.

### Summary

The values of the spectral and S4 indices obtained from the fading rates of an X-mode diagnostic signal, indicate that the heater induces a strong scattering regime in the ionosphere. Saturation and focussing mechanisms must also be considered since the S4 index is frequently greater than unity. The steepening of the spectral slope between heater on and heater off periods suggests that power is being deposited into the intermediate scale irregularities during heating. The change from slow to fast fading induced by the heater suggest that large scale structures are broken up due to stimulation of filamentation instabilities and a scale size of the order of 1 km is observed.

### Acknowledgement

We would like to thank the Max Planck Institut für Aeronomie, Lindau, for making the *Faser* available and Drs P Stubbe and H Kopka for their help in this project. One of us, Angela Wilkinson, acknowledges the receipt of an SERC studentship.

### References

- Aarons J, H E Whitney and R S Allen, 1971, *Proc. IEEE*, 59, 159  
 Booker H G, 1979, *J. Atmos. Terr. Phys.* 41, 501  
 Booker H G, P K Pasricha and W J Powers, 1986, *J. Atmos. Terr. Phys.* 48, 327  
 Briggs B H, 1975, *Contemp. Phys.* 16, 469  
 Das A C and J A Fejer, 1979, *J. Geophys. Res.* 84, 6701  
 Frey A and L M Duncan, 1984, *Geophys. Res. Lett.* 11, 677  
 Graham K N and J A Fejer, 1976, *Radio Science* 11, 1057  
 Inhester B, A C Das and J A Fejer, 1981, *J. Geophys. Res.* 86, 9101  
 Jones T B, T Robinson, H Kopka and P Stubbe, 1982, *J. Geophys. Res.* 87, 1557  
 Jones T B, T Robinson, P Stubbe and H Kopka, 1984, *J. Atmos. Terr. Phys.* 46, 147  
 Perkins F W and E J Valeo, 1974, *Phys. Rev. Letters*, 32, 1234  
 Procello L J and L R Hughes, 1963, *J. Geophys. Res.* 74, 4105  
 Robinson T, 1989, *Physics Reports*, 179, 79  
 Saltpeter E E, 1967, *Astrophys. J.* 147, 433  
 Singleton D G, 1969, *J. Geophys. Res.* 74, 1772

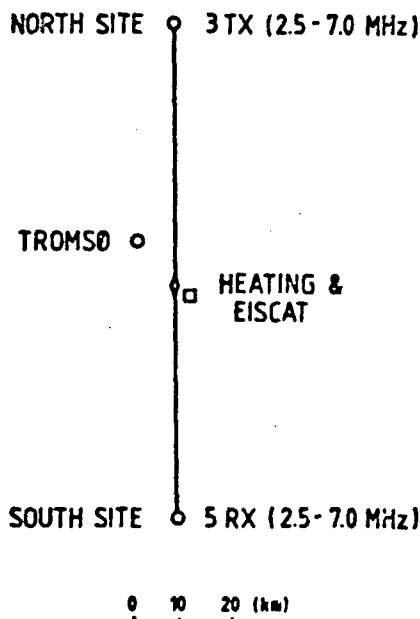


Fig. 1 Plan of the positions of the diagnostic transmitters and receivers relative to the Heating Facility at Ramfjordmoen during the March 1985 campaign.

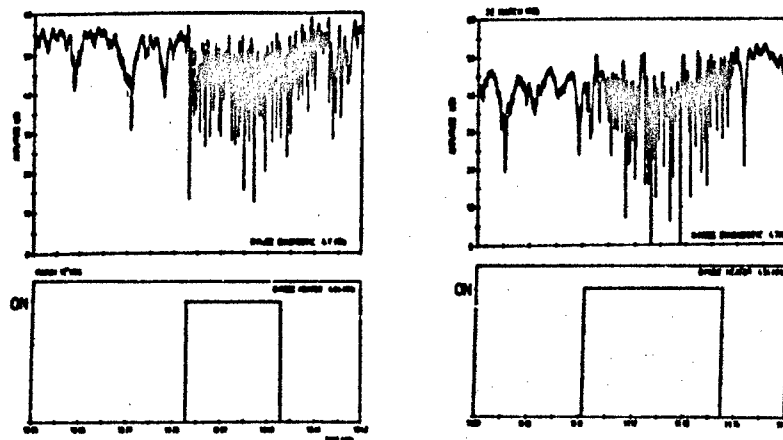


Fig. 2 Increase observed in the fading rate of an X-mode diagnostic signal (upper panel) corresponding to the switch on of the heater (lower panel), under quiet ionospheric conditions.

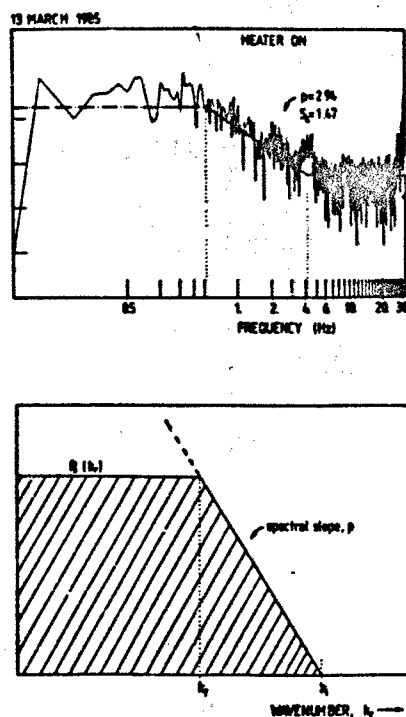


Fig. 3 (a) Typical example of the power law type spectrum obtained from a 4.40 MHz X-mode diagnostic signal on 13 March, 1985.  
(b) Schematic diagram highlighting the expected features in (a).

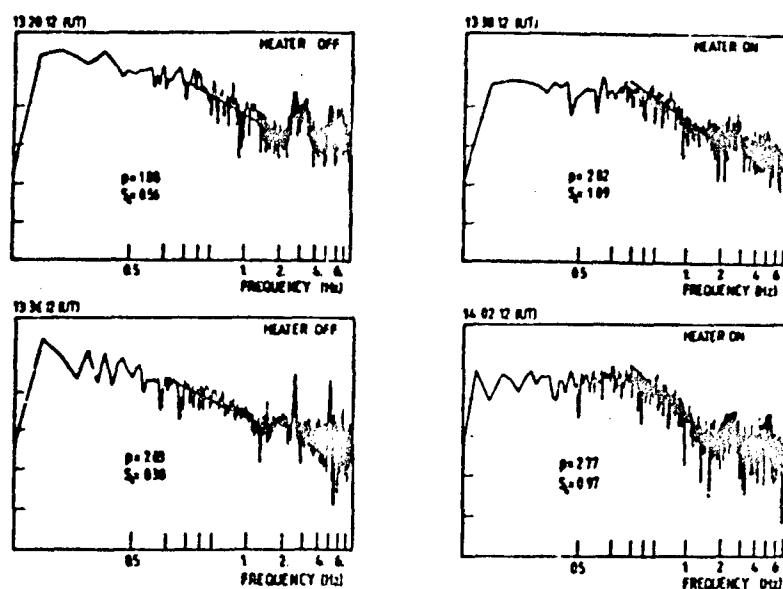


Fig. 4 (a) - (d) Typical examples of the differences observed in the power law spectra of an X-mode signal between periods of heater switch on and switch off 11:46 to 14:37 (UT) on 17 March, 1985.

TIME (UT)	HEATER MODE	SPECTRAL INDEX, -P		S <sub>4</sub> INDEX
		FREQUENCY INTERVAL (Hz)		
		(0.5-1.3)	(0.8-2.0)	
13:18:12	ON	2.08	2.18	0.98
13:20:12	OFF	1.88	1.58	0.73
13:25:12	OFF	1.13	0.30	0.56
13:28:12	ON	1.80	2.19	0.99
13:30:12	OFF	1.54	2.06	0.68
13:35:12	OFF	1.23	0.41	0.38
13:38:12	ON	2.82	0.63	1.09

(a) 17<sup>th</sup> March 1985

HEATER MODE	SPECTRAL INDEX, -P			S <sub>4</sub> INDEX
	FREQUENCY INTERVAL (Hz)			
	(0.5-1.3)	(0.8-2.0)	(0.9-3.0)	
ON	3.20	2.24	2.38	1.09
OFF	1.90	0.35	1.42	0.61

(b) 17<sup>th</sup> March 1985 (11:59-12:40 (UT))

Table 1 (a) Spectral- and S<sub>4</sub>-indices derived from the data presented in Figure 4 (a) - (d).  
(b) The average change in the spectral and S<sub>4</sub> indices observed between periods of heater on and off obtained between 11:46 - 14:37 (UT) on 17 March, 1985.

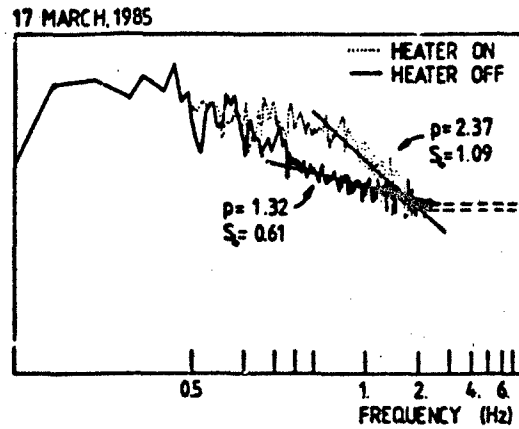


Fig. 5

The characteristic power spectra of an X-mode diagnostic signal obtained during periods of heater on and off by averaging data over 5 consecutive heating cycles. The shift in spectral index from  $p = 1.32$  (off) to  $p = 2.37$  (on) indicates that more power is being deposited into smaller scale irregularities during periods of heating.

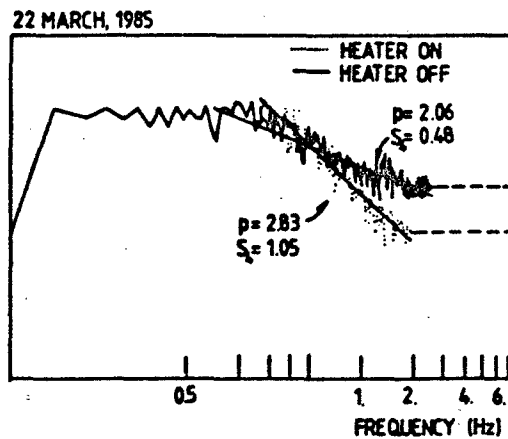


Fig. 6

As for (5) but obtained on 22 March, 1985. Each spectrum is an average over 5 consecutive heater switching sequences.

## DISCUSSION

W. GORDON, US

Do you explore height variation of "strong" scatterers by selecting frequency of diagnostics? What happens for paths below HF-induced strong scatterers?

## AUTHOR'S REPLY

Yes we usually employ three or four frequencies selected so that they have reflection points above and below the heater reflection height. The effects observed decay more rapidly as you move downward below the heating level than they do with increasing distance (height) above the reflection level.

G. SALES, US

Given that you measure the quadrature components out of the receiver, have you looked at the full spectrum,  $\pm$  frequency shifts and is there any deviation from a symmetrical shape and are there any offsets from zero Doppler which might indicate drifts through the heated regions?

## AUTHOR'S REPLY

There is little overall frequency shift. There are of course large frequency changes in the diagnostic associated with heater turn on and turn off. We have found no evidence of a drift induced by heating although we have looked for this using a spaced receiver method.

K. C. YEN, US

Your fading measurements such as S, and the spectrum seem to refer to amplitude only. Do you have phase measurements? If so, what is the behavior on the phase data?

## AUTHOR'S REPLY

My remarks referred to the amplitude only. We have the phase information, but have not done a similar analysis on these data. Note that the phase change is usually slower than the amplitude effect.

G. S. SALES, US

Using the quadrature components of the received signal, have you looked at the actual spectrum of the signals, i.e., with positive and negative Doppler, do you see an offset and approximately how wide is that spectrum? You might be able to say something about the drifts driving these across the pattern.

## AUTHOR'S REPLY

This is just the amplitude spectrum. We deliberately introduce a 2.3 Hz offset between the transmitted frequency and the receiver local oscillator, and you can see that there is a spreading of about half a Hertz during heater on. It's more sometimes -- these are particularly strong examples, but they don't usually show that big. More typically it's about half a Hertz. There is not a shift from zero Hertz, just the spreading. This doesn't show you where the energy is distributed -- the dynamic range in our plot is zero.

# LARGE SCALE PLASMA IRREGULARITIES AND AIRGLOW ENHANCEMENTS FROM IONOSPHERIC HEATING

Paul A. Bernhardt and Harvey Rowland  
Space Plasma Branch, Code 4780  
Plasma Physics Division  
Naval Research Laboratory  
Washington, DC 20375-5000

Levin W. Duncan  
Department of Physics and Astronomy  
Clemson University,  
Clemson, SC 29634-1911

Craig A. Topley  
Arecibo Observatory  
Arecibo, PR 00613

## SUMMARY

Ionospheric modification with high power radio waves may generate plasma irregularities and airglow clouds. Large scale irregularities are produced in a convecting F-layer by a mechanism called the plasma-relaxation-oscillator. When a continuous beam of powerful electromagnetic waves heats the ionosphere, a cavity is produced by thermal pressure gradients. The cavity drifts under the influence of ambient electric fields causing the vertically-incident, radio beam to be refracted from the zenith. At some point, the cavity can no longer "capture" the beam and it returns to the zenith to form another cavity. This relaxation process repeats to yield irregularities on the scale of the heater beam diameter. Airglow enhancements are produced by energetic electrons accelerated out of the heated region. Large amplitude electrostatic waves may be excited by linear mode coupling, by parametric decay instabilities, and by strong plasma turbulence. This occurs near the point where the plasma frequency of the ionosphere matches wave frequency. The electrostatic waves accelerate ambient electrons to high enough energy to collisionally excite ambient oxygen atoms. Clouds of enhanced red-line (630.0 nm) and green-line (537.7 nm) emissions have been recorded with low-light-level imaging systems located at Arecibo, Puerto Rico. Comparison of the imager data with data from the Arecibo incoherent scatter radar shows that artificial airglow clouds are physically tied to the density cavities and to regions of enhanced electrostatic waves by the earth's magnetic field lines. At currently available power levels (around 80 MW effective radiated power), HF modification yields 10-30% fluctuations in density and 10-100 Rayleigh enhancements in airglow intensity.

## 1. INTRODUCTION

Ionospheric heating by high power radio waves produces a wide variety of phenomena through nonlinear processes. These include generation of enhanced ion-acoustic and Langmuir wave turbulence, production of field-aligned irregularities from meter to kilometer scale sizes, stimulation of electromagnetic emissions, and excitation of enhanced airglow emissions. The study of artificially generated ionospheric irregularities is of practical interest because they can affect a communication channel by inducing amplitude or phase fluctuations as a result of multipath mixing or scattering. Artificial modification of the F-region can be used to generate artificial density structures, control existing irregularities or to study processes which govern the evolution of both natural and artificial plasma structures.

During nighttime, winter solar-minimum, experiments were conducted with high-power HF heating frequencies near 3 MHz and effective radiated powers on the order of 80 MW. Observations by Djuth et al. [1987] and Duncan et al. [1988] at the Arecibo Observatory in Puerto Rico have demonstrated that significant (factors of 3 or 4) electron temperature enhancements and large (10 - 30 percent) density reductions can be generated with high power electromagnetic waves. Bernhardt et al., [1988] have reported large airglow enhancements which accompany the artificially created density cavities.

These anomalously large effects have been attributed to the low nighttime plasma densities which occurred during the winter of 1986-1987. Calculations by Mantas et al. [1981] and Neuman et al. [1988] show that electron heat loss occurs through thermal conduction and electron-ion collisions. It is well known that the electron-ion energy transfer rate is proportional to  $n^2$  where  $n = n_e = n_i$  is the plasma density [Banks and Kockarts, 1973]. For a constant heat input from high power radio waves, a lower density F-region will yield higher electron temperatures because of reduced electron to ion cooling. Thermal pressure gradients will drive plasma from the heated region leaving density cavities.

Cavities generated in a drifting plasma will convect away from the zenith of the heating facility. The beam of high power electromagnetic waves will be deflected by the sides of the cavity. The interactions of the cavity and the radio beam leads to the generation of large scale periodic structures. These have been detected with ground-based optical and radar diagnostics.

This paper describes the physical process thought to be responsible for cavity formation in a drifting plasma. In the next section, the fluid and wave equations which describe F-region heating by powerful radio waves are solved numerically to yield a large scale thermal cavity. In the following section, a phenomenological model treats the waves as packets to demonstrate relaxation oscillator behavior in the plasma.



## 2. THE HIGH FREQUENCY WAVE INTERACTION MODEL

Ionospheric modification using the transmission of high power radio waves into the F-region can be understood in terms of coupled fluid and wave equations. The electron and ion continuity equations have the form

$$\frac{dn_j}{dt} + \nabla \cdot (n_j \mathbf{v}_j) = P_j - L_j \quad (1)$$

where the subscript "j" refers to electrons to ions,  $n_j$  is the concentration,  $\mathbf{v}_j$  is the velocity,  $P_j$  is the production rate and  $L_j$  is the loss rate for the plasma species. Powerful radio waves can affect the electron production by accelerating electrons to high enough energies to cause neutral breakdown but this does not occur in the ionosphere for facilities currently in existence. Temperature dependent electron-ion recombination rates are modified in the artificially heated environment.

High power radio waves most directly couple to the electron densities in the ionosphere by modifying the transport term  $[\nabla \cdot (n_e \mathbf{v}_e)]$  in the continuity equation for electrons. The velocity of each plasma species is determined by the equation of motion:

$$\frac{d\mathbf{v}_j}{dt} + (\mathbf{v}_j \cdot \nabla) \mathbf{v}_j = - \frac{\nabla P_j}{\rho_j} + \frac{q_j}{m_j} (\mathbf{E} + \mathbf{v}_j \times \mathbf{B}) + \mathbf{g} - \nu_{jn}(\mathbf{v}_j - \mathbf{v}) - \nu_{ji}(\mathbf{v}_j - \mathbf{v}_i) \quad (2)$$

where  $P_j = n_j k T_j$  is pressure,  $\rho_j = n_j m_j$  is mass density,  $T_j$  is electron or ion temperature,  $m_j$  is mass,  $q_j$  is charge,  $\mathbf{E}$  is electric field,  $\mathbf{B}$  is ambient magnetic flux density,  $\mathbf{g}$  is gravitational acceleration,  $\nu_{jn}$  is the electron- (or ion-) neutral collision frequency,  $\mathbf{v}$  is neutral velocity,  $\nu_{ji}$  is the electron- (or ion-) ion collision frequency, and  $\mathbf{v}_i$  is the velocity of the other plasma species. Most of the terms on the right side of (2) can be artificially changed. The flow of plasma out of a region of high power radio waves is a result of enhanced plasma pressure in the heated region. Suprathermal electron fluxes are produced by large amplitude electric fields near the regions where the electromagnetic waves resonate with the electron plasma.

Resistive heating by high power radio waves provides an energy source in the ionosphere to form large scale cavities [Duncan et al., 1958]. The resulting thermal cavities can refract the incident radio wave causing self-focussing. Simulation of these effects require coupling continuity equations (1) and equations of motion (2) to equations which describe the electron and ion temperatures and the propagating electromagnetic wave.

The energy equation for the electron gas is derived in a reference frame which moves with the  $\mathbf{E} \times \mathbf{B}$  drift of the plasma. Heat flow is restricted to the direction of the ambient magnetic field. The one dimensional heat equation is

$$n_e \frac{\partial}{\partial s} \left( \frac{\kappa_e}{T_e} \right) + n_e \mathbf{v}_e \cdot \frac{\partial}{\partial s} \left( \frac{\kappa_e}{T_e} \right) + n_e k T_e \frac{\partial}{\partial s} \left( \frac{\mathbf{v}_e \cdot \nabla}{T_e} \right) - \frac{\partial}{\partial s} \left[ \kappa_e \frac{\partial T_e}{\partial s} \right] = Q_e - L_e \quad (3)$$

where the coordinate "s" is along the magnetic field,  $\mathbf{v}_e$  is the field aligned component of electron drift,  $\kappa_e$  is the electron thermal conductivity,  $Q_e$  is the heat input to the electrons, and  $L_e$  is the heat lost to ions and to neutrals. A similar equation describes the ion temperatures. The artificial heat source for ohmic heating from high power radio waves is given by

$$Q_{oh} = e_0 |\mathbf{E}_0|^2 \nu_e / 2 \quad (4)$$

where  $|\mathbf{E}_0|$  is the magnitude of the electric field of the electromagnetic wave with frequency  $\omega$ ,  $\mathbf{E} = \mathbf{E}_0 e^{i\omega t}$ ,  $\nu_e$  is the plasma frequency,  $\epsilon_0$  is the dielectric constant of free space, and  $\nu_e$  is the total electron collision frequency. Conversion of electromagnetic waves to slowly propagating plasma waves can be another heat source to the plasma.

For a single frequency time variation  $e^{i\omega t}$ , the wave equation which describes both electromagnetic and electrostatic wave propagation is written as:

$$-\nabla^2 \mathbf{E}_0 + [I - \frac{1}{2} \frac{\nu_e}{\omega} (\nabla \cdot \mathbf{E}_0)] \mathbf{E}_0 - k_0^2 (I - \frac{1}{2} \frac{\nu_e}{\omega}) \mathbf{E}_0 = 0 \quad (5)$$

where

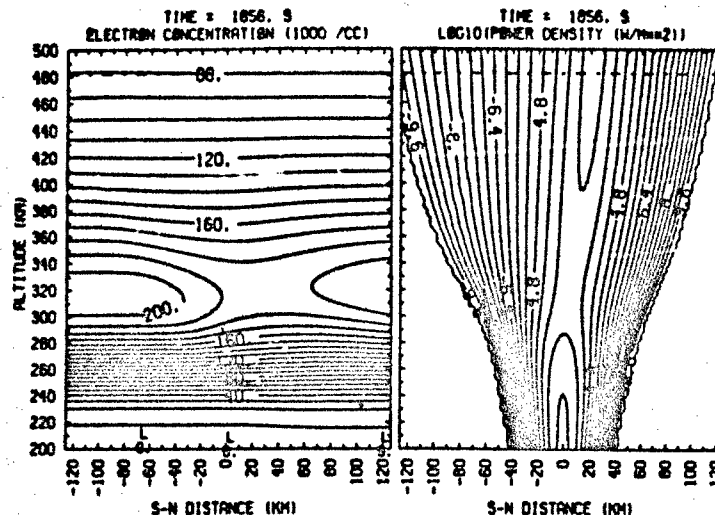
$$\mathbf{H} = \begin{bmatrix} U & iY_x & -iY_y \\ -iY_x & U & iY_z \\ iY_y & -iY_z & U \end{bmatrix}^{-1}$$

$U = (1 - i\nu_e/\omega)$ ,  $\mathbf{H}$  has the same form as  $\mathbf{H}$  except that Landau damping is incorporated into  $U$ ,  $\gamma = \omega/\omega_p$ ,  $k_0 = \omega/c$ ,  $\mathbf{I} = \mathbf{v}_e^2/c^2$ ,  $\nu_e$  is the electron thermal velocity, and  $c$  is the speed of light. Details about the wave equation and the notation are given by Yeh and Liu [1972]. Equation (5) should be used for a complete electrostatic and magnetoionic treatment of radio wave coupling to the plasma.

Bernhardt and Duncan [1982, 1987] have developed a model of ionospheric heating which incorporates equations (1) through (5) with the following simplifications:

- (1) The propagation is assumed to be isotropic so  $\gamma$  is set to zero.
- (2) The heating is underdense ( $\omega < \omega_p$ ) so that  $X < 1$  everywhere.
- (3) The conversion to plasma waves is neglected.

The thermal cavity produced by a  $40 \text{ MW/m}^2$  beam at 4.4 MHz is shown in Figure 1. The HF electromagnetic waves heat the plasma continuously for 1600 seconds. The electron temperature near the center of the beam at the peak of the layer is elevated by 400 K. The maximum density is reduced by ten percent. For this simulation, the ambient plasma is drifting northward at 50 m/s. Asymmetric thermal cavities are produced by the 50 degree inclination of the ambient magnetic field and by an imposed 50 m/s northward plasma drift. Continuous wave heating of the drifting ionospheric should eventually cause a depression in the plasma down stream from the heated region.



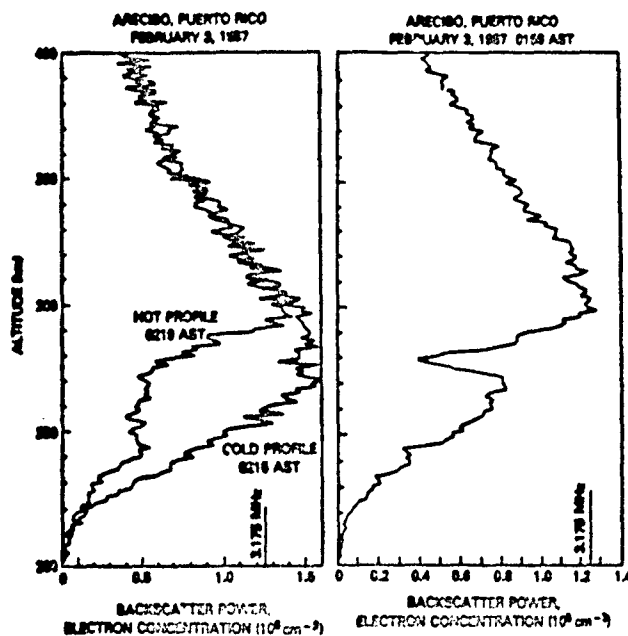


Figure 2. Artificial, thermal cavities produced by the high power radio waves from the Arecibo RF Facility. The frequency of the electromagnetic wave is 3.175 MHz. Comparison of the hot and cold profiles on the left shows the effects of the  $50 \mu\text{V}/\text{m}^2$  beam after 4 minutes of heating. A more localized cavity is seen on the right.

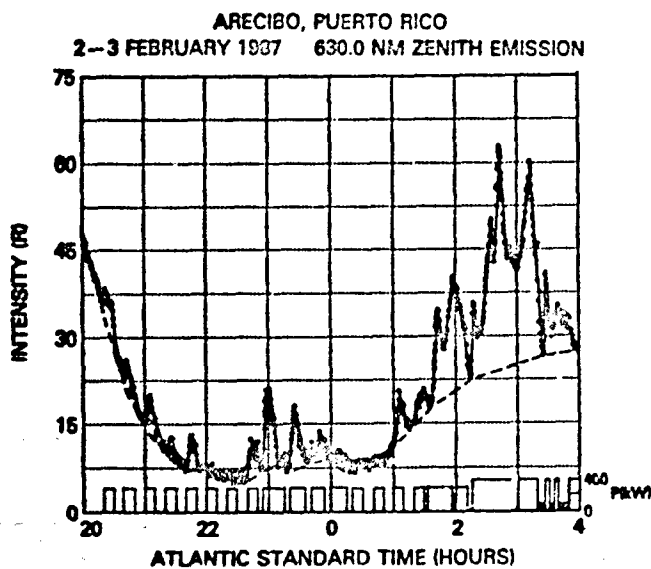
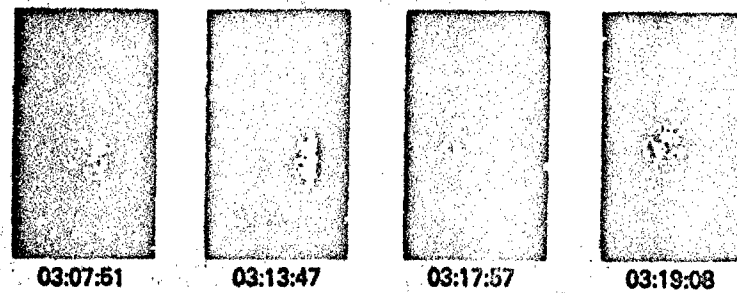


Figure 3. Time history of the 630.0 nm airglow from ionospheric heating. Between 0219 and 0320 AST, continuous wave heating at 400 kW transmitter power produced large fluctuations in airglow intensity.

## 630.0 nm AIRGLOW



FEBRUARY 3, 1987 AST 3.175 MHz HF  
ARECIBO, PUERTO RICO

Figure 4. One cycle of the drifting airglow clouds produced by ionospheric heating. The airglow clouds outline the elliptical beam which has a major axis in the north-south (top-bottom) direction. The airglow clouds and associated cavities drift to the west (right) at 50 m/s. A snap-back occurs at the third panel when the west most cloud vanishes and a new one forms at the south of the heater.

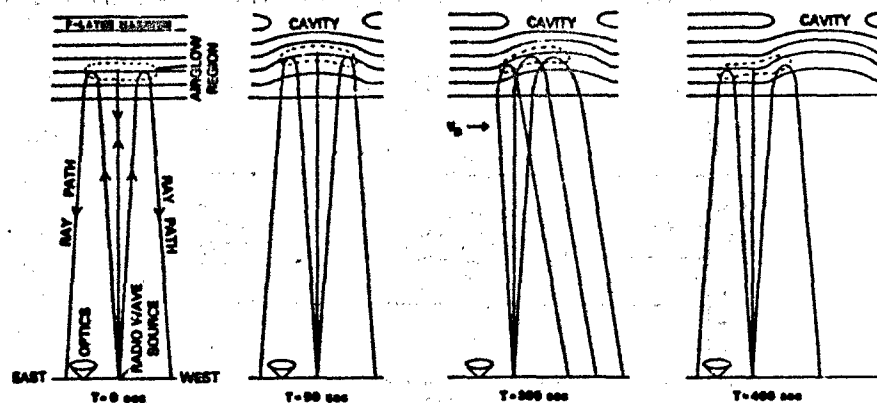


Figure 5. Schematic of the snap-back process during continuous ionospheric heating. This process leads to the generation of periodic irregularities.

Lifshitz, 1971). For the case of a wave packet travelling through a plasma, the equations of motion can be written in the same form as those for a single particle moving through a potential (Stix, 1963). Beyond the requirements that the spatial gradients be long compared to the wavelength of the radiation and that changes in the medium occur on time scales long compared to the radiation's frequency, to be able to use this approach, one must be able to differentiate the local dispersion relation for the mode of interest. This opens up the possibility of using many of the techniques of particle simulations to study the large scale propagation of electromagnetic waves in spatial and time varying plasmas.

The case of a high frequency electromagnetic mode in an unmagnetized plasma is particularly straightforward. This branch obeys a dispersion relation

$$\omega^2 = \omega_p^2(s) + (kc)^2, \quad (6)$$

where  $\omega$  is the frequency of the wave,  $\omega_p$  is the local plasma frequency,  $k$  is the local wavevector,  $s$  is the vertical coordinate, and  $c$  is the speed of light. The motion of the wavepacket is  $\partial s / \partial t = v_g$  where  $v_g$  is the group velocity. The group velocity is  $\partial \omega / \partial k$ . Therefore,

$$\partial \omega / \partial t = (c^2 / \omega) k. \quad (7)$$

We need an equation of motion for  $k$  which can be obtained by differentiating the dispersion relation,

$$2c^2k \left( \frac{\partial k}{\partial t} \right) \left( \frac{\partial t}{\partial z} \right) = -\partial n_p^2(z)/\partial z. \quad (8)$$

This reduces to

$$\partial k / \partial t = -(2u)^{-1} \partial c^2(z)/\partial z. \quad (9)$$

Now  $n_p^2(z) = (e_0/n_0) n(z)$ . Letting  $v' = c^2k/u$  and  $n'(z) = n(z)/n_0$ , the equations of motion for the wave packet is

$$\partial n / \partial t = v' \text{ and } \partial v' / \partial t = -u \partial n'(z) / \partial z, \quad (10)$$

where  $u = (1/2)(c_0^2/n_0)^2$ . The density of the plasma acts as a potential field which determines the motion of the packet.

To perform a preliminary study of the effects of resonant heating by the RF beam, a simple model of a drifting plasma was constructed. The density is initialized as an increasing Gaussian in the  $z$ -direction and uniform in the horizontal  $x$ -direction. The initial normalized temperature is uniform ( $= 1.0$ ). A third array,  $C(x,z)$ , is the product of  $n(x,z)$  and  $T(x,z)$  and does not change in time. These three arrays are shifted to the right in the  $x$  direction by one cell each time step. The values of the three arrays on the left hand boundary are not changed so that an unperturbed plasma flows into the simulation box. The wave packets are injected into the plasma at a constant rate of eight packets per time step at  $z=0$  and at  $x=15$  cells.  $v_z'$  is chosen so that the critical layer is approximately half way up the density gradient.  $v_z'$  has a magnitude of 20% of  $v_z'$  and is multiplied by a uniform random number between -1 and +1 so that the beam has an angular spread. Each wave packet carries a fixed amount of energy (80). When  $v_z' < 0$ , this indicates that the particle has reached the critical layer and the energy is deposited in the plasma. This is done by increasing the temperature at the nearest grid point and its six closest neighbors.

$$T(x,z) = T(x,z) + V^2 \delta 0 \quad (11)$$

where  $V$  is a linear weighting. The particle is then removed from the simulation. The density is changed by  $n(x,z) = C(x,z) / T(x,z)$ . This new density determines the forces acting on the wave packets.

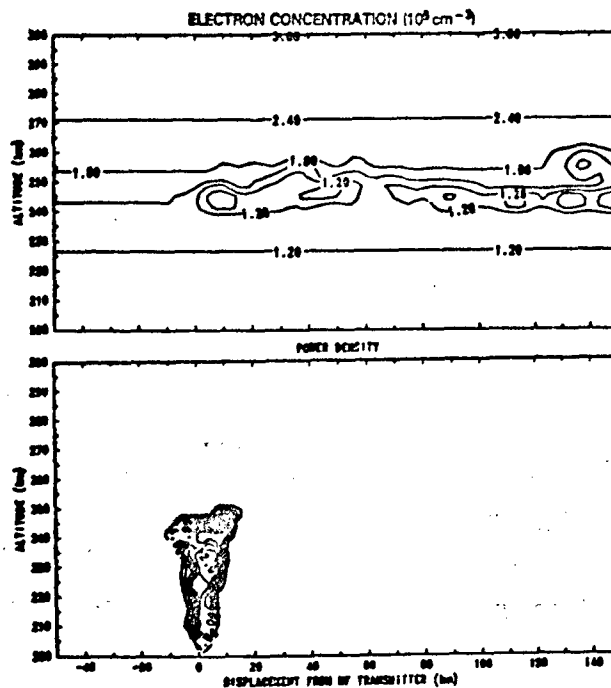


Figure 6. Simulation of a structured plasma layer produced by continuous wave heating. The irregularities tend to form with a spatial period of 40 km. The ambient plasma drift is 100 m/s from left to right.

Figure 6 shows the electron density contours and the shaved radio beam at  $t=1500$  seconds. An unperturbed plasma flows in from the left hand boundary. As it flows over the transmitter energy is absorbed at the critical layer, the temperature increases and a cavity is formed. At the critical layer the width of the beam is approximately 20 km. The plasma is flowing to the right and the structures to the right of the transmitter were formed at earlier times. The modification of the density is not smooth but is bursty in nature forming localized cavities. The density gradients in the  $x$  direction act to focus the beam. The plasma drift then acts to bend the beam to the right. By reducing the density at the critical layer it is possible for the beam to reach higher altitudes. This can be seen in the structure at 140 km where a cavity was formed above the ambient critical layer.

The dynamics of this interaction is still being studied. Injecting the same number of wave packets but reducing the amount of energy carried by each wave packet by 2 orders of magnitude leads to a much smoother response. The density at the critical layer is reduced by one percent and one does not see the large oscillations and cavity structures. Also, one does not see the bending of the beam.

The ionospheric cavities produced by high power radio waves are subject to the effects of polarization by neutral winds. This has been discussed in a previous section with reference to ionospheric holes produced by chemical releases. A neutral wind can polarize a thermal cavity to cause it to steepen on the up wind side. We are currently investigating the effects of this steepening on the high power radio waves with respect to beam propagation and beam stability, e.g., thermal self-focussing instabilities. In a stationary heated ionosphere, a plasma depression acts like a convergent lens to further intensify the electromagnetic beam. Neutral convection relative to the plasma may induce cross-B drifts which further intensify the density gradients on one side of the cavity. As a result, temperature gradients due to ohmic heating will appear across the cavity. Preliminary calculations show that these density and temperature gradients, in conjunction with convection, will have a stabilizing influence on the thermal self-focussing instability [Keshinen et al., 1990].

#### A. CONCLUSIONS

When anomalously lower densities occur in the midlatitude ionosphere, ground based HF transmitters with equivalent radiated powers of 80 MW or more can produce thermal cavities near where the wave frequency equals the plasma frequency of the ionosphere. At high enough powers, continuous wave transmissions can produce periodic irregularities in a convecting F-layer of any density. This will be the result of a relaxation oscillator type process that produces multiple snap-backs of the heater beam. Once a large scale cavity is formed,  $E \times B$  gradient drift instability may yield shorter scale sizes along their edges. Our future research is directed to upgrading our coupled fluid-wave model to simulate overdense ionospheric heating. With this model, we hope to be able to predict the radio wave powers required to generate large scale F-region cavities under all conditions.

#### ACKNOWLEDGMENTS

This work is supported by the Office of Naval Research.

#### REFERENCES

- Bernhardt, P.A. and L.N. Duncan, "The feedback-diffraction theory of ionospheric heating," *J. Atmos. and Terr. Phys.*, 44, No. 12, 1061, 1982.
- Bernhardt, P.A. and L.N. Duncan, "Ionospheric focused heating - a hybrid modification experiment," *J. Atmos. Terr. Phys.*, 49, 1107, 1987.
- Bernhardt, P.A., L.N. Duncan, and C.A. Tepley, "Artificial Airglow Excited by High-Power Radio Waves," *Science*, Volume 242, pp 1022-1027, 18 November 1988.
- Bernhardt, P.A., L.N. Duncan, and C.A. Tepley, "Heater-induced cavities as optical tracers of plasma drifts," *J. Geophys. Res.*, 94, 7003-7010, 1989a.
- Bernhardt, P.A., C.A. Tepley, and L.N. Duncan, "Airglow enhancements associated with plasma cavities formed during ionospheric heating experiments," *J. Geophys. Res.*, 94, 9071-9092, 1989b.
- Djuth, F.T., B. Thidé, E. M. Ierkic, and N. P. Sulzer, Large F-region electron temperature enhancements generated by high-power HF radio waves, *Geophys. Res. Lett.*, 14, 953-956, 1987.
- Duncan, L.N., J.P. Sheerin, R.A. Behnke, Observations of ionospheric cavities generated by high-power radio waves, *Phys. Rev. Lett.*, 61, 239-242, 1988.
- Keshinen, M.M., P.K. Chaturvedi, and S.L. Ossakov, Theory of large-scale heating processing the in unstructured and structured ionosphere, 46th EPP Symposium, Bergen, Norway, 28 May - 1 June 1990.
- Newman, A.L., E. C. Carlson, Jr., G.P. Mantas, and F.T. Djuth, Thermal response of the F-region ionosphere for conditions of large HF-induced electron-temperature enhancements, *Geophys. Res. Lett.*, 15, 311, 1988.
- Stix, T.D., *The Theory of Plasma Waves*, McGraw-Hill Book Company, New York, pp. 55-59, 1962.
- Yeh, K.C., and C.N. Liu, *Theory of Ionospheric Waves*, Academic Press, New York, pp. 130-307, 1972.

## DISCUSSION

W. T. ARMSTRONG, US

1. Is the scale size of ambient irregularities indicated by airglow maintained during heating or reduced, as suggested by paper 12?
2. Do the ambient irregularities indicated by airglow appear correlated with any class of acoustic gravity waves?

## AUTHOR'S REPLY

1. The airglow technique can only measure structures with scale sizes greater than 1 to 10 km. In this limit, the scale size of the irregularities seems to be maintained by the heater. Future experiments should use simultaneous optical and HF radio diagnostics for comparison.
2. The gravity waves at mid latitudes have 1000 km wave lengths which can tilt the ionosphere to have a small effect on the radio wave reflection point. No study of the effects of gravity waves on optically measured irregularities has been performed.

T. B. JONES, UK

I think the point about the ambient ionosphere is a very important one, especially here in Norway and Tromsø. You should liken the idea of a heating experiment to throwing stones into the sea. If you want to see a good effect, you don't throw a stone into a stormy sea, you throw it into a millpond, and you'll see the effect very well. Similarly for a very quiet and calm ionosphere. If you try to heat a disturbed ionosphere, for example if there is a lot of aurora about and a lot of disturbance, you will never see any heating effects because the inherent energy of the system is much bigger than anything you can put in from a radio transmitter on the ground.

M. J. KESKINEN, US

Two comments: the mid-latitude F-region ionosphere in terms of naturally occurring structures is very poorly understood; and second, gravity waves at Arcoibo usually are typically hundreds of thousands of kilometers in wavelength, and I don't think they could be a seed for 10-20 km type fluctuations, you have to look for some other plasma processes.

## AUTHOR'S REPLY

Tilts of the ionosphere from the gravity wave could affect the region where the airglow is seen, where the wave reflects, but you're right, large scale structures would probably not act as the initial seed. Most of the time that we've made the large cavities, the heater beam itself produced its own seed.

IONOSPHERIC HEATING WITH OBLIQUE HF WAVES

Edward C. Field, Jr.  
 Ron M. Bloom  
 Pacific-Sierra Research Corporation  
 12340 Santa Monica Boulevard  
 Los Angeles, CA 90025

SUMMARY

This paper presents calculations of ionospheric electron density perturbations and ground-level signal changes produced by intense oblique high-frequency (HF) transmitters. Our analysis takes into account radio field focusing at caustics, the consequent joule-heating of the surrounding plasma, heat conduction, diffusion, and recombination processes--these being the effects of a powerful oblique "modifying" wave. It neglects whatever plasma instabilities might occur. We then seek effects on a secondary "test" wave that is propagated along the same path as the first. Our calculations predict ground-level field-strength reductions of several dB in the test wave for modifying waves having ERP in the 85-to-90 dBW range. These field-strength changes are similar in sign, magnitude, and location to ones measured in Soviet experiments. Our results are sensitive to the model ionosphere assumed, so future experiments should employ the widest possible range of frequencies and propagation conditions. An effective power of 90 dBW seems to be a sort of threshold that, if exceeded, results in substantial rather than small signal changes. Our conclusions are based solely on joule-heating and subsequent defocusing of waves passing through caustic regions.

1. INTRODUCTION

During the past two decades a number of powerful high-frequency (HF) radio transmitters have been developed solely to transmit waves strong enough to produce measurable nonlinear effects in the ionosphere. The early tests were called heating experiments, but many types of nonlinear effects were observed, and such tests are now called ionospheric modification experiments. Several authors [Gurevich, 1978; Utlaut and Violette, 1974; Duncan and Gordon, 1982] have summarized the phenomena observed in modification experiments performed at vertical incidence.

The nonlinear processes that lead to ionospheric modification are often divided into two categories: (1) heating, which alters temperature and hence, reaction rates, collision frequencies, and particle densities, and (2) generation of parametric instabilities, which cause a myriad of phenomena, including spread-F and geomagnetic-field-aligned irregularities. Both categories behave differently at oblique incidence than at vertical incidence.

As the incidence angle is increased, heating is affected by two competing trends: the field is weakened by the increased path length, but strengthened by focusing near caustics. Field and Warber [1985] showed that such focusing can overcome geometric spreading and produce intense--albeit localized--fields in the ionosphere. However, certain parametric instabilities--important for vertical heating--cannot be excited by oblique waves, because only vertical waves can reach heights where matching conditions on frequency are met.

The most intense focusing occurs along the Ray-Bundle, just beyond the wave-group reflection height in the ionosphere. What plasma density perturbations may occur as a result of the field will therefore be most pronounced in the vicinity of this region. Subtle shifts in the density and dimension of the plasma near the ray-reflectrix will be manifested in more profound effects in ground-level signal strength.

Except for the experiments of Bochkarev et al., [1982], all modification experiments have transmitted the powerful modifying wave at vertical incidence. Radar and communication transmitters operate at oblique incidence, however. Accordingly, this paper examines the effects of a strong oblique wave on the ionosphere and on waves that propagate through the modified region. The two goals of this paper are: first, to illustrate through a parameter study the signal changes that might be caused by powerful HF transmitters; and second, to explain the amplitude changes measured by Bochkarev.

Our analysis takes into account focusing at caustics, the consequent joule-heating of the surrounding plasma, heat conduction, diffusion, and recombination processes--these being the effects of a powerful oblique "modifying" wave. We then seek effects on a secondary "test" wave, which is propagated along the same path as the first. The test wave could, in fact, be the modifying wave itself, in which case the calculation would be of the "self-effect" of a powerful transmitter.

Our calculations use what might be called a "first-order" approximation to nonlinear wave propagation. Hereover, we neglect heating-induced changes in kinetic and recombination coefficients, thereby linearizing certain equations. The controlling hypothesis is that, should first-order calculations fail to predict detectable heating effects, higher-order nonlinear effects would probably not increase the magnitude of the heating to a detectable level. Plasma instabilities are omitted from our calculations.

2. TECHNIQUE OF CALCULATION

Our calculations are accomplished through an aggregation of three separate procedures, each previously discussed in the literature and producing data used as input by the next procedure. The first procedure computes an electric field distribution in the caustic region, given an oblique HF transmitter and a horizontally stratified ionospheric profile. The second, which closely follows Gurevich [1978], calculates the temperature and electron density changes caused by the focussed fields near the caustic. The third procedure estimates the change in ground-level signal caused by the density perturbation.



## 2.1. Calculation Of Fields Near Caustics

We evaluate the electric field in the caustic region as a superposition of quasi-plane-wave components, each component being an asymptotic solution to the wave equation in a medium with specified (field-independent) refractive index. Budden [1976] shows that a field component  $E$  in an isotropic medium whose complex refractive index  $n$  varies only in height  $z$  can be approximated as the plane-wave spectral integral

$$E(x, y, z) = \iint G(s_1, s_2) (C/q)^{1/2} 2\pi^{1/2} \zeta^{1/4} Ai(\zeta) \cdot \exp \left\{ -ik \left[ s_1 x + s_2 y + \int_0^z q \, dz \right] \right\} ds_1 ds_2 \quad (1)$$

where  $s_1, s_2, C$  are complex direction cosines in free space;  $G$  is essentially the radiation pattern of the transmitter;  $x, y, z$  are Cartesian coordinates of the field point; and  $k = 2\pi/\lambda$  is the free space wave number. The function  $q$  is

$$q^2 = n^2(z) - s_1^2 - s_2^2.$$

the variable  $\zeta$  is

$$\zeta = \left( \frac{3}{2} ik \int_{z_0}^z q \, dz \right)^{2/3}.$$

$Ai$  is Airy's integral, and  $z_0(s_1, s_2)$  is the reflection height [ $q(z_0) = 0$ ] for the plane wave component labeled by  $s_1, s_2$ . Equation (1) is a uniformly valid approximation throughout a reflection region if: (a) higher-order derivatives of the refractive index with respect to height are well behaved; and (b) the height is not too close to roots of  $q$ . Maslin [1976a; 1976b] proves that caustic regions are always associated with envelopes of downgoing rays for which  $q < 0$ . We evaluate the integrals in Eq. (1) numerically, using the method of Warren, DeWitt and Warber [1982]. The calculation is valid both in the region of geometrical optics and across caustics. This method allows us to calculate field magnitudes throughout large regions of space without having to piece together boundary conditions and higher-order asymptotics inside and outside areas of strong focusing. The method cannot be used, however, to calculate the wave field when the refractive index  $n$  varies in more than one coordinate direction.

## 2.2 Transport Calculation

The second procedure is the "diffusion" calculation, using as a source term the horizontal electric field  $E$  calculated as above. The equations are similar to those given by Gurevich [1978], and are recapitulated in Appendix A to define notation. Aside from the electric field, the main parameters are characteristic plasma field  $E_p$ , the relaxation times  $\tau_T$  and  $\tau_N$ , the diffusion lengths  $L_T$  and  $L_N$ , and a parameter  $\gamma$  that accounts for the change in equilibrium density due to a change in de-ionization rate. The subscripts  $T$  and  $N$  denote whether a given parameter is associated with temperature or electron-density fluctuation. We numerically integrate the transport equations A-8 and A-19 to evaluate  $\Delta T/T_0$  and  $\Delta n/n_0$ , the relative changes in temperature and electron density, respectively.

## 2.3. Ground Level Signal Change

The final procedure is the estimation of the ground-level electric field intensity change due to the ionospheric perturbation  $n/N_0$ . As mentioned above, Eq. (1) cannot accommodate ionospheric profiles that have gradients in other than the vertical ( $z$ ) direction, so we use a well-tested ray tracing program (Jones, and Stephenson [1985]), first with the ambient complex refractive index  $n(z)$ , then with the perturbed one  $n(x, z)$ .

In conjunction with the ray trace, we integrate certain quantities measuring the rate of change of ray coordinate with respect to infinitesimal changes in ray initial conditions (i.e., launch and azimuth). This allows for the continuous calculation of the relative convergence of a small pencil of rays around the main ray. This convergence (or divergence) factor is proportional to the Poynting vector. We make this calculation at ground level for both the ambient and perturbed ionosphere and obtain the change in field intensity caused by the modifying wave. We have applied the methods of Nickisch and Buckley [1982].

Several points must be stressed. First, the geometrical optics field intensity becomes unbounded at the skip distance, both at the interior caustic and at the horizon. The region of validity is wherever the fractional change in adjacent ray spacing per wavelength is much less than unity. The method may correctly predict a shift in the interior skip distance, but cannot predict accurate fields there. Second, in the illuminated region past the interior skip, there are typically two rays landing at each point. This gives rise to rapidly varying interference phenomena that depend on the phase difference between the high and low rays. The field amplitude lies in the envelope formed by the sum and difference of the component ray amplitudes. It may be assumed that the resultant amplitude is, on the average, the root-mean-square of the two components.

A related, though different, approach to weakly nonlinear wave propagation can be found in work by Bochkarev [1979; 1980; 1982]. Here, the nonlinearity in dielectric constant is assumed, a priori, to be proportional to the electric field intensity  $|E|^2$ . That is,  $n'^2 = n^2 + \alpha |E|^2$ , where  $\alpha$  is the coefficient of nonlinearity. Except for the region immediately surrounding the caustic, the field is found by classical geometrical optics with the ambient refractive index and is used as a boundary condition on a small rectangular domain around the caustic. Therein, a technique known as the *Method of Parabolic Equations* is used to approximate the field [Gurevich 1978]. It would appear that our method of solution has the advantage of providing insight into the constitution of the nonlinearity that Bochkarev has bottled up into the ad hoc constant  $\alpha$ .

For a treatment analogous to ours, with a deeper analysis of HF wave energy deposition as well as estimates of nonlinear absorption due to plasma instabilities, see Meltz, Molway, and Tomljanovich [1974]. For an adaptation of this class of calculations to an automatic, feedback-propelled computational scheme, see Barnhardt and Duncan [1982]. Both of these papers apply to vertical incidence, however.

### 3. THE BOCHKAREV EXPERIMENT

To our knowledge, only Bochkarev et al [1979; 1980; 1982] have used an oblique modifying wave. In order to ensure that the diagnostic wave passed through the caustic of the modifying wave, they transmitted both waves between the same terminals with the diagnostic wave having a frequency within a few kilohertz of the modifying wave. The single-hop path length was about 1800 km, the launch angle was about 18 deg, the location was mid-latitude, and the experiment was performed with "ordinary short-wave equipment with gains of about 100". No values were given for power or frequency. However, in order to interpret their data, Bochkarev et al. [1982] present a ray-trace diagram and a corresponding daytime model ionosphere. By means of trial and error comparisons with Bochkarev's ray-trace, we have inferred a frequency near 15 MHz.

Bochkarev obtained 15 measurements for the situation where the frequency  $F_M$  of the modifying wave exceeded the frequency  $F_D$  of the diagnostic wave by a few kilohertz, and two samples where  $F_D > F_M$ . Figures 1a and 1b show averaged results for  $F_D < F_M$  and  $F_D > F_M$ , respectively. The vertical dotted line shows the instant when the modifying transmitter was turned off. We concur with Bochkarev that Fig. 1a shows the field about doubled within 40 sec of the transmitter being turned off, and then slowly decayed. We cannot, however, clearly see the 2-to-3 deg change in  $\theta$ , that Bochkarev attributes to the transmitter being turned off. Nor can we see any transmitter-induced change on Fig. 1b, although Bochkarev (1979) claims a rapid (10-to-20 sec) increase, followed by a decrease after about 60 sec. Rather than debate the point, we simply reproduce Bochkarev's figures.

Bochkarev attributes the differences between Figs. 1a and 1b to an interaction between the diagnostic wave and a standing-wave pattern set up by the incident and reflected components of the modifying wave, the magnitude of that interaction depending on whether  $F_D$  is less or greater than  $F_M$ . In our model, the tiny differences between  $F_D$  and  $F_M$  are of no consequence, and the self-effect would be the same as the effect on a diagnostic wave of similar frequency. Therefore, all we need say about Bochkarev's results are: a) depending on conditions, the ground-level signal at a range of about 1800 km is up to several decibels larger when the modifying transmitter is off than when it is on; and b) small changes ( $\pm 2$  deg) might occur in vertical arrival angle, but such data are inconclusive.

### 4. NUMERICAL RESULTS

We have performed calculations using several daytime and nighttime model ionospheres and antenna patterns. Depending on the model used, a wide range of values are possible for the characteristic field  $E_p$ , the characteristic times  $\tau_T$  and  $\tau_R$ , the characteristic lengths  $L_T$  and  $L_R$ , and the ionization-equilibrium shift factor  $\gamma$ . The characteristic times indicate how long it takes for a steady state to be reached; the lengths  $L_T$  and  $L_R$  characterize the distances over which heat is conducted or electrons diffuse in times  $\tau_T$  and  $\tau_R$ , respectively.

In the interest of brevity, we will show detailed results only for the model F-region shown in Fig. 2, which is the one used by Bochkarev. Table 1 shows the nominal parameter values that we use, which are those suggested by Gurevich for an altitude of 200 km, near the altitude of peak heating. Although a D-layer is not shown in Fig. 2, our results include D-layer absorption. We will assume a frequency of 15 MHz, and use the antenna pattern shown in Fig. 3 that has a maximum when the launch angle is 18 deg and a gain of 25 dB, which is 5 dB larger than the nominal value quoted by Bochkarev. The pattern shown in Fig. 3 is representative of modern curtain antennas, as described by Kershner [1988]. The precise value of the assumed gain is unimportant, because we will treat power-gain product (effective radiated power [ERP]) as a parameter. Our main example assumes propagation perpendicular to the magnetic field vector, a magnetic dip angle of 60°, and an ERP of 85 dBW. Later in this paper we show parametric studies of field change vs. ERP and dip angle.

Figure 4 shows the ray-trace at 15 MHz for the model ionosphere shown in Fig. 2. Such traces are essential to the construction of wave phase and for locating the caustic regions. Fig. 4 indicates intense focussing at a range of about 800 km and an altitude of about 200 km. Because the frequency greatly exceeds the gyrofrequency, we assumed isotropic propagation.

Figure 5 shows calculated electric field strength contours for ERP = 85 dBW. The diagram is centered at the wave reflection height and caustic region, i.e., at the region of maximum focussing. Appendix A shows that ratio  $E^2/E_p^2$  governs the strength of the temperature and density perturbations. Because the ratio is small ( $\approx 0.4$ ), our linearization is acceptable for the 85 dBW ERP assumed. If there were only geometric spreading and absorption without focussing, the maximum field strength in Fig. 4 would be about 0.08 v/m, so focussing increases the field by nearly an order of magnitude.

Figure 6 shows calculated electron steady-state temperature changes caused by the electric fields in Fig. 5. The largest relative temperature changes are 0.16, about half the maximum value of  $E^2/E_p^2$ , which is

Table 1. Characteristic Fields, Times, and Lengths for an Altitude of 200 km and a Frequency of 15 MHz.

$E_p$ (V/m)	$\tau_T$ (s)	$\tau_N$ (s)	$L_T$ (km)	$L_N$ (km)	$\delta$
1.2	3.2	32	17	2.3	0.04

what the maximum relative temperature change would be if there were no heat conduction. Conduction reduces that ratio by a factor on the order of  $a/\lambda_T$ , where  $a$  is the characteristic width of the focussed electric field--5-to-10 km in Fig. 5.

Figure 7 shows the calculated relative electron density perturbations,  $n/N_0$ , which do not exceed one percent. While the iso-contours of field strength conform to the downward-curving pattern of the caustic, those of the density perturbation appear elongated in roughly a vertical direction. This is because diffusion occurs mainly along magnetic field lines and appears vertical in the 2-d projection. It is shown in Appendix A

$$\frac{n}{N_0} \approx \frac{1}{2} \frac{L_N}{L_T} \frac{\Delta T}{T_0}$$

which agrees well with the numerical results of Figs. 6 and 7.

Figure 8a shows the calculated change in the geometrical optics field intensity at the ground caused by the heater-induced ionospheric perturbation. In addition to the region just past the skip distance, where the calculation is unreliable, the greatest change is predicted to occur at around 1800 km. For ERPs of 85-to-90 dBW, the calculated fields are reduced by 2-to-4 dB. Thus, the location (~1800 km), size (few dB), and sense (negative) of the ground-level field change agrees with Bochkarev's data. Moreover, the time scale  $\tau_T \sim 30$  sec (see Table 1) appears about right.

Figure 8b indicates the trend in field-strength change as ERP is increased to 95 dBW. As expected, the greater the effective power, the greater the field change. Note, however, that increasing ERP much beyond 85 dBW abuses our method, because the differential equations we solve for  $n/N_0$  are valid only when  $\Delta T/T_0$  is much less than unity. One can infer that the 90 dBW prediction (where  $E^2/E_0^2 \sim 1$  and  $\Delta T/T_0 \sim 0.5$ ) gives an upper bound on effects which can occur as a result of linear kinetic processes alone. Figure 8b does, however, give a hint that ERP = 90 dBW is a sort of threshold, beyond which substantial field changes might be caused.

Figure 9 shows the dependence of the ground-level field-strength change upon the geomagnetic dip angle. Recall that the direction of propagation has been taken as east-west. The diffusion decreases as the dip angle tends toward the horizontal, because the strongest gradients in  $E$  become nearly perpendicular to the magnetic field. That diminishment in diffusion tends to concentrate the density perturbation and thus increase the maximum value of  $n/N_0$ . However, one must not assume that the ground-level field change will necessarily be monotonic in response. In fact, a complex relationship holds between the maximum magnitude of  $n/N_0$ , the size of the region over which the density change diffuses, and the signal change on the ground. That complex behavior is evident in Fig. 9.

Finally, we have calculated the change in angle-of-arrival at a range of 1800 km for the parameters used above. In no case did the calculated change exceed a few tenths of a degree.

### 3. CONCLUSIONS

Our calculations indicate ground-level field-strength reductions of up to several dB might be produced by joule-heating of the ionosphere by intense oblique HF waves having ERP in the 85-to-90 dBW range. These calculated field-strength changes are similar in sign and magnitude to the 0-to-several-dB reductions in field strengths measured by Bochkarev and associates [1982, 1980, 1975]. Moreover, by using ionospheric parameters pertinent to the Soviet experiments, our predicted signal reductions occur at a range of about 1800 km, which also agrees with the published data. Our calculated vertical arrival-angle are much smaller than the 2-to-3 deg change claimed by Bochkarev, but are not necessarily inconsistent with his data (see Fig. 1).

Results for several day and night model ionospheres not shown here indicate similar results, although the size and location of the change in ground level field depends on the model ionosphere assumed, and future experiments should therefore employ the widest possible range of frequencies and propagation conditions. An effective power of 90 dBW seems to be a sort of threshold that, if exceeded, results in substantial rather than small signal changes. Our conclusions are based solely on joule-heating and subsequent defocusing of waves passing through caustic regions.

Our results pertain to times long enough for a steady-state to occur. That time scale is roughly the characteristic diffusion time at ionospheric heights where the strongest electric field focusing has occurred. This time,  $\tau_N$ , depends on the ambient recombination coefficient and plasma density, and is a few tens of seconds for the model ionosphere that we assumed. This characteristic time is in agreement with the roughly 40 sec onset time measured by Bochkarev.

# APPENDIX A: EQUATIONS GOVERNING ELECTRON HEATING AND TRANSPORT

The equations that govern the changes in electron temperature and density produced by an intense radio wave in the ionosphere are presented in this section. Approximate solutions for limiting cases are also provided. The equations below are similar to those used by Gurevich [1978] whose notation we use whenever convenient.

We consider only field-aligned particle motion and energy transport, ignoring the small cross-field drift and thermal conduction. We use a coordinate system with the x-direction along the geomagnetic field. That coordinate is related to height  $z$  by  $x \sin \phi = z$ , where  $\phi$  is the dip angle. Equations are numbered separately from those in the text.

## A.1. ELECTRON TEMPERATURE

If we neglect ion heating, the electron temperature  $T$  is described by the following equation (e.g., Melts and LeLievre, [1970]):

$$\frac{\partial T}{\partial t} = \frac{\partial}{\partial x} \left( \kappa \frac{\partial T}{\partial x} \right) + \delta \nu_e T_0 \left[ \frac{E^2}{E_p^2} - \frac{(T - T_0)}{T_0} \right], \quad (1)$$

where  $T_0$  is the ambient electron temperature,  $E$  is the electric field of the modifier wave,  $\delta$  is the fractional energy lost by an electron per collision, and  $\nu_e$  the electron collision frequency.

The quantity  $E_p$  in Eq. (1) is called the characteristic plasma field and is defined as

$$E_p^2 = \frac{m k T_0 \omega^2}{e^2}, \quad (2)$$

where  $k$  is Boltzmann's constant,  $m$  is the electron mass,  $e$  is the electron charge, and  $\omega$  is the modifier wave angular frequency. The quantity  $\kappa$  is the thermal diffusivity and is given by

$$\kappa = A \frac{k T_0}{m \nu_e}, \quad (3)$$

where  $A$  can be as large as 2, but is often assumed to be unity.

The quantities  $\kappa$  and  $\nu_e$  both depend on temperature, so Eq. (1) is non linear. Moreover, the dependence of  $\kappa$  on  $x$  prevents Eq. (1) from assuming the form of a canonical diffusion equation. The criterion for linearizing Eq. (1) is that  $\Delta T = T - T_0 \ll T$ , which is always true if  $E^2/E_p^2$  is small, and in the presence of strong heat conduction can be true even if  $E^2/E_p^2$  is of order unity. The  $x$ -dependence of the thermal diffusivity  $\kappa$  can then be ignored if the gradients in the ambient ionosphere are weaker than those caused by the modifying wave. We make both of these simplifications and rewrite Eq. (1) in the form

$$\tau_T \frac{\partial \Delta T}{\partial t} - L_T^2 \frac{\partial^2 \Delta T}{\partial x^2} = T_0 \left[ \frac{E^2}{E_p^2} - \frac{\Delta T}{T_0} \right], \quad (4)$$

where, following Gurevich [1978], we have defined

$$\tau_T = (\delta \nu_e)^{-1} \quad \text{and} \quad (5)$$

$$L_T^2 = \tau_T \kappa = \frac{\kappa}{\delta \nu_e} \quad \text{and} \quad (6)$$

and  $\nu_e$  is computed using  $T = T_0$ .

Equation (4) can be solved by Fourier Transformation. The result is:

$$\Delta T(x, t) = \frac{T_0}{\tau_T} \int_0^t ds \int_{-\infty}^{\infty} d\xi \left[ \frac{E^2(\xi, s)}{E_p^2} \right] \frac{\exp \left[ -\frac{(x - \xi)^2}{4\kappa(t - s)} - \frac{(t - s)}{\tau_T} \right]}{\sqrt{4\kappa(t - s)}}. \quad (7)$$

Once the field  $E$  of the modifying wave has been calculated, Eq. (7) can be used to calculate both the time and space dependence of electron temperature.

The asymptotic behavior of Eq. (7) is found by performing the  $ds$  integration:

$$\Delta T(x) \frac{t \gg \tau_T}{\tau_T} \int_{-\infty}^{\infty} dx' \left[ \frac{E^2(x')}{E^2(x)} \right] \exp \left( -\frac{|x' - x|}{L_T} \right). \quad (8)$$

where  $E(x, t) \rightarrow E(x)$  as  $t \rightarrow \infty$ .

### A.2. ELECTRON DENSITY

If we again use locally height-averaged values for ambient ionospheric properties, we can write the equation that governs the electron density in the following form:

$$\frac{\partial n}{\partial t} - D_A \frac{\partial^2 n}{\partial x^2} - \frac{n}{T} D_{TA} \frac{\partial^2 T}{\partial x^2} = P - \alpha n^2 - \beta n. \quad (9)$$

In Eq. (9),  $P$  is the ion-pair production rate,  $\alpha$  is the electron-ion recombination coefficient, and  $\beta$  is a loss rate that accounts for interactions between the ion  $O^+$  and the molecules  $N_2$  and  $O_2$ . The ambipolar diffusion coefficient is

$$D_A = \frac{K(T_0 + T_i)}{N \nu_i}, \quad (10)$$

and the ambipolar thermal diffusivity is

$$D_{TA} = \frac{KT}{N \nu_i} - D_A D_0. \quad (11)$$

where  $D_0 = T_0/(T_0 + T_i)$ ,  $N$  is the mean ion mass,  $T_i$  is the ion temperature, and  $\nu_i$  is the ion-neutral collision frequency. Equation (9) thus accounts for diffusion caused by excess particle concentrations, diffusion driven by thermal gradients, and density changes brought about through the temperature dependence of reaction rates.

The fractional density change is always small, so we can write

$$n = n_0 + n. \quad (12)$$

where  $n$  and  $n_0$  are the perturbation and ambient electron density, and use the fact that  $n \ll n_0$  to linearize Eq. (9). The result is:

$$\frac{\partial n}{\partial t} - D_A \frac{\partial^2 n}{\partial x^2} - \frac{n_0}{T} D_A \frac{\partial^2 \Delta T}{\partial x^2} = -(2\alpha n_0 \beta) n - [\alpha(T) - \alpha_0] n_0^2, \quad (13)$$

where  $\alpha_0 = \alpha(T_0)$  is the unperturbed recombination coefficient and we have used

$$P = \alpha_0 n_0^2 + \beta_0 n_0. \quad (14)$$

Because  $\beta$  is virtually independent of temperature, we have neglected a term proportional to  $\beta - \beta_0$ . By defining

$$\nu_n = (2\alpha_0 n_0 + \beta)^{-1}, \quad (15)$$

$$L_n^2 = \nu_n D_A, \quad (16)$$

and

$$\gamma = -\frac{\nu_n (\alpha - \alpha_0) n_0 T}{\Delta T} \quad (17a)$$

$$= -\nu_n n_0 T \frac{\partial \alpha}{\partial T}, \quad (17b)$$

we can rewrite Eq. (13) in a form analogous to Eq. (4):

$$\nu_n \frac{\partial n}{\partial t} - L_n^2 \frac{\partial^2 n}{\partial x^2} - \frac{n_0}{T} \frac{\partial^2 \Delta T}{\partial x^2} = -n + \gamma \frac{n_0}{T} \Delta T. \quad (18)$$

We reconcile Eq. (17) with the definition of  $\gamma$  used by Gurevich [1978] by noting that the electron loss

rate is  $q_r = \kappa n^2 + \beta n$ , so  $v_n = (\partial q_r / \partial n)^{-1}$  and  $\partial n / \partial T = n^{-2} \partial q_r / \partial T$ . The time-dependent solution to Eq. (18) can be written in terms of a Green's function, but that result is too complicated to be useful. Therefore, we restrict attention to the following steady-state solution:

$$\begin{aligned} \frac{n}{n_0} &= \frac{\gamma L_M L_T}{2(L_M^2 - L_T^2)} \int_{-\infty}^{\infty} dy \left[ \frac{E^2(y)}{E_p^2} \right] \left[ \frac{\exp(-|x-y|/L_M)}{L_T} - \frac{\exp(-|x-y|/L_T)}{L_M} \right] \\ &- \frac{E_T L_M}{2(L_M^2 - L_T^2)} \int_{-\infty}^{\infty} dy \left[ \frac{E^2(y)}{E_p^2} \right] \left[ \frac{\exp(-|x-y|/L_M)}{L_M} - \frac{\exp(-|x-y|/L_T)}{L_T} \right]. \end{aligned} \quad (19)$$

### A.3. PEAK TEMPERATURE AND DENSITY PERTURBATIONS

Although our numerical results pertain to the actual electric-field structure, it is instructive to consider heating pulse with a "square wave" shape given by,

$$E(x) = \begin{cases} E_0 & |x| \leq a \\ 0 & |x| > a \end{cases} \quad (20)$$

where  $E_0$  is constant and  $2a$  is the width of the heated region, then Eqs. (7), (8), and (19) can be integrated straightforwardly. The details are given by Field, Bloom and Meikes [1988]. Here we give results for some limiting cases.

#### A.3.1. Weak Transport

The peak values of  $\Delta T$  and  $n$  usually occur at the origin ( $x = 0$ ). For that case it can be shown that the following expressions pertain to the square heating pulse given in Eq. (20).

$$\frac{\Delta T}{T_0} = \frac{E_0^2}{E_p^2} \left[ 1 - e^{-a/L_T} \right] \quad (21)$$

and

$$\frac{n}{n_0} = \frac{E_0^2}{E_p^2} \left[ \gamma \left( 1 - e^{-a/L_M} \right) + \frac{E_T^2 L_M^2 + \gamma L_T^2}{L_T^2 - L_M^2} \left( e^{-a/L_M} - e^{-a/L_T} \right) \right]. \quad (22)$$

The limit of weak heat conduction and diffusion is reached when  $a \gg L_M$  and  $L_T$ , which can occur either if the heating pulse is very wide or the diffusion and conduction lengths are small. In that limit,

$$\frac{\Delta T}{T_0} = \frac{E_0^2}{E_p^2} \quad (23)$$

and

$$\frac{n}{n_0} \rightarrow \gamma \frac{\Delta T}{T_0} \quad (24)$$

#### A.3.2 Strong Transport

The limit of strong transport is reached when  $L_M$  and  $L_T \gg a$  and  $\gamma \ll 1$ , in which case Eqs. (21) and (22) become

$$\frac{\Delta T}{T_0} = \frac{E_0^2}{E_p^2} \left( \frac{L_M}{L_T} \right), \quad (25)$$

$$\left| \frac{n}{n_0} \right| = E_T \left( \frac{L_M}{L_T + L_M} \right) \frac{\Delta T}{T_0}. \quad (26)$$

Note that  $L_M$  seldom exceeds  $L_T$  in the F-region, and is usually much smaller. Therefore Eq. (24) and (26) show that

$$\frac{n}{n_0} \ll \frac{4T}{T_0}$$

regardless of whether transport is strong or weak.

#### APPENDIX B: ELECTRON LOSS RATES

In order to define the ionization-equilibrium shift factor  $\gamma$  we must choose values for various electron loss rates. Gurevich [1978] suggests the following formulas for the loss rates  $\alpha$  and  $\beta$ :

$$\alpha = \alpha_1 \left( \frac{n_{\text{NO}^+}}{n_0} \right) + \alpha_2 \left( \frac{n_{\text{O}_2^+}}{n_0} \right) \quad (1)$$

where

$$\alpha_1 = 3 \times 10^{-7} \left( \frac{300}{T} \right)^{1.2} \quad (2a)$$

$$\alpha_2 = 2.2 \times 10^{-7} \left( \frac{300}{T} \right)^{0.7} \quad (2b)$$

and

$$\beta = 10^{-12} n_{\text{H}_2} + 2 \times 10^{-11} n_{\text{O}_2} \quad (2c)$$

Other authors give somewhat different values for the above loss rates. For example, McEvan and Phillips [1975] indicate that  $\alpha_1$  behaves as  $(300/T)^{1.0}$ , whereas Bates [1988] uses the relationships

$$\alpha_1 = 4.2 \times 10^{-7} \left( \frac{300}{T} \right)^{\lambda_1} \quad (3)$$

$$\alpha_2 = 1.6 \times 10^{-7} \left( \frac{300}{T} \right)^{\lambda_2} \quad (4)$$

where  $0.37 \leq \lambda_1 \leq 0.9$  and  $0.55 \leq \lambda_2 \leq 0.7$ .

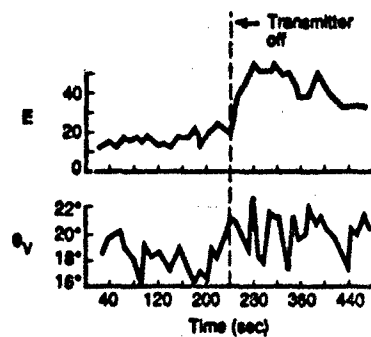


Fig 1a. Measured Change in Field Strength (Relative Units) and Arrival Angle When Modifying Wave Turned Off.  $F_D < F_M$  (Bochkarev, et al., [1979]).

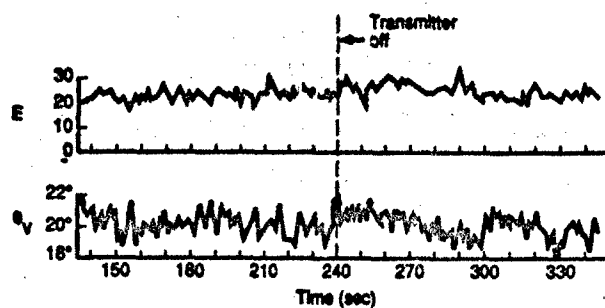


Fig 1b. Measured Change in Field Strength (Relative Units) and Arrival Angle when Modifying Wave Turned Off.  $F_D > F_M$  (Bochkarev, et al., [1979]).

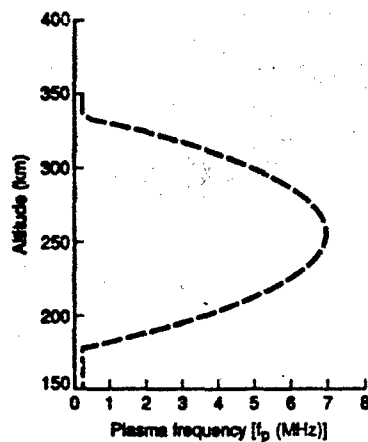


Fig 2. Model F-region.



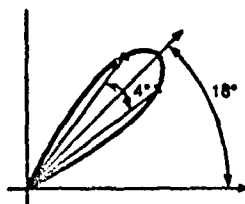


Fig 3. Antenna Pattern.

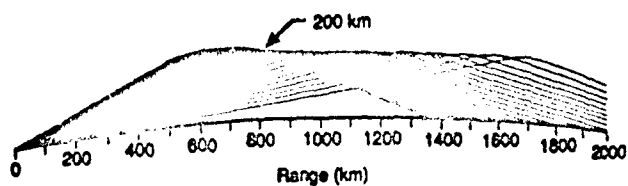


Fig 4. Ray Trace at a Frequency of 15 MHz

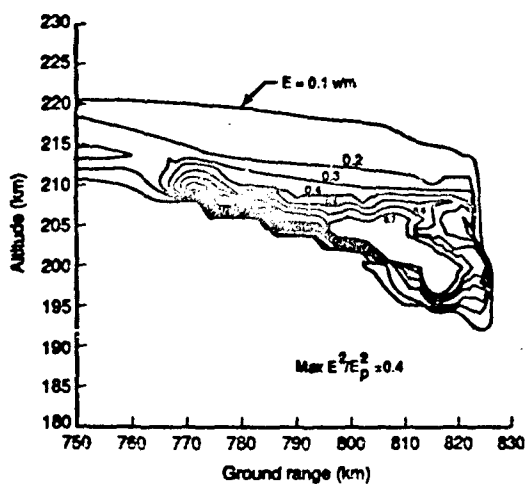


Fig 5. Calculated Contours of Electric Field Strength: Frequency = 15 MHz; ERP = 45 dBV; Geomagnetic Dip = 60°; E-W Propagation.

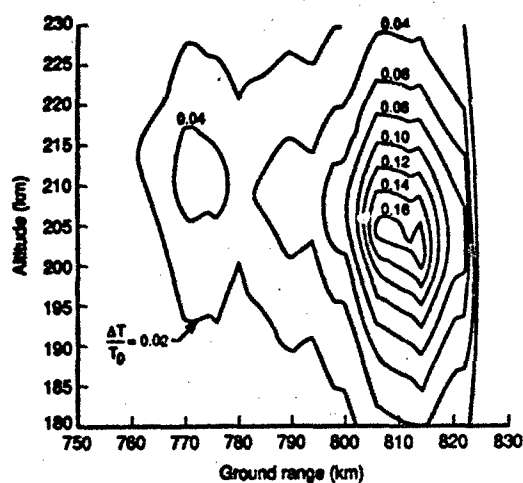


Fig 6. Calculated Contours of Steady-State Relative Temperature Change: Frequency = 15 MHz; ERP = 85 dBW; Geomagnetic Dip = 60°; E-W Propagation.

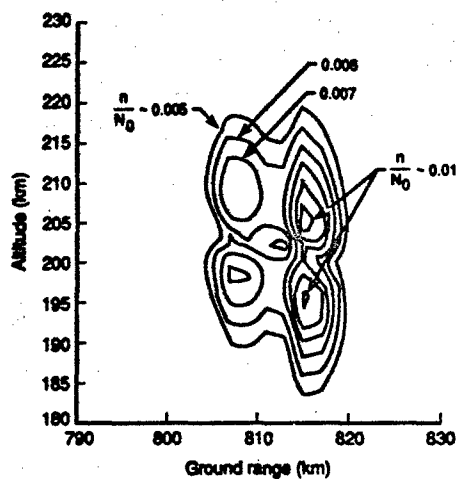


Fig 7. Calculated Contours of Steady-State Relative Electron-Density Change: Frequency = 15 MHz; ERP = 85 dBW; Geomagnetic Dip = 60°; E-W Propagation.

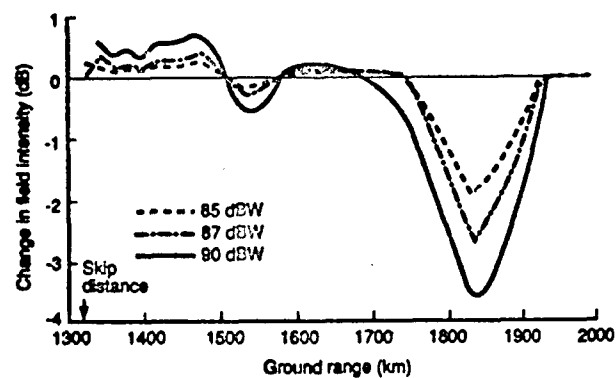


Fig 8a. Calculated Steady-State Change in Ground-Level Signal for Various Values of ERP: Frequency = 15 MHz; Geomagnetic Dip = 60°; E-W Propagation.

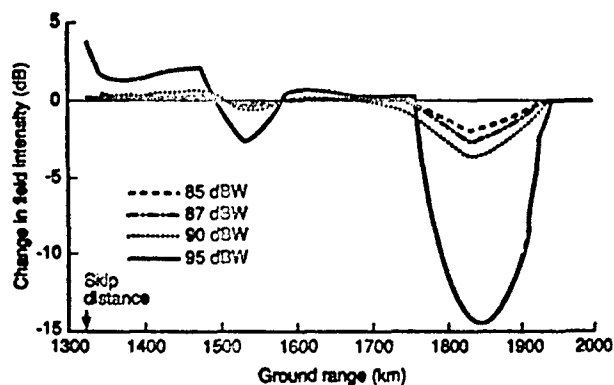


Fig 8b. Calculated Steady-State Change in Ground-Level Signal for Various Values of ERP: Frequency = 15 MHz; Geomagnetic Dip = 60°; E-W Propagation.

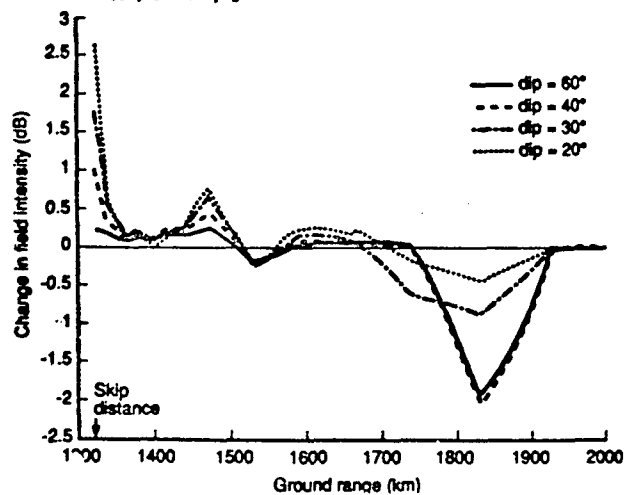


Fig 9. Calculated Steady-State Change in Ground-Level Signal for Various Magnetic Dip Angles: Frequency = 15 MHz; ERP = 85 dBW; E-W Propagation.

## REFERENCES

- Bates, David R., "Recombination in the Normal E and F Layers of the Ionosphere," *Planet. Space Sci.*, Vol. 36, No. 1, 1988, pp. 55-63.
- Bernhardt, P. A., and L. M. Duncan, "The Feedback-Diffraction Theory of Ionospheric Heating," *J. of Atmos. and Terr. Phys.*, Vol. 44, No. 12, 1982, pp. 1061-1074.
- Bochkarev, G. S., et al., "Nonlinear Interaction of Decametre Radio Wave at Close Frequencies in Oblique Propagation," *J. Atmos. Terr. Phys.*, Vol. 44, December 1982, pp. 1137-1141.
- Bochkarev, G. S., et al., "Simulation of the Action of a Strong Obliquely Incident Wave on the Ionosphere," *Geomagnet. Aeron.*, Vol. 20, No. 5, 1980, pp. 592-595.
- Bochkarev, G. S., et al., "Interaction of Decametric Radio Waves on Frequencies Close to the MUF of F2 During Oblique Propagation," *Geomagnet. Aeron.*, Vol. 19, No. 5, 1979, pp. 557-559.
- Buckley, R., "On the Calculation of Intensity in Dispersive Inhomogeneous Media in the Ray Approximation," *Proc. R. Soc. Lond.*, Vol. A 380, 1982, pp. 201-209.
- Budden, K. G., "Radio Caustics and Cusps in the Ionosphere," *Proc. R. Soc. London, Sec A*, 350, 1976, 275-301.
- Duncan, L. M., and W. E. Gordon, "Ionospheric Modification by High Power Radio Waves," *J. Atmos. Terr. Phys.*, Vol. 44, December 1982, pp. 1009-1017.
- Field, E. C., and C. R. Warber, "Ionospheric Heating with Obliquely Incident Waves," *Geophys. Res. Lett.*, Vol. 12, No. 11, November 1985, pp. 761-763.
- Field, E. C., R. M. Bloom, and K. E. Meikes, *Ionospheric Heating with Oblique Waves*, Vol. 1. *Electron Density Perturbations*, Pacific-Sierra Research Corporation, Report 1864, September 1988, AFGL-TR-88-0336.
- Gurevich, A. V., *Nonlinear Phenomena in the Ionosphere*, Springer Verlag, New York City, 1978.
- Jones, R. M., and J. J. Stephenson, *A Versatile Three-Dimensional Ray Tracing Computer Program for Radio Waves in the Ionosphere*, U.S. Department of Commerce, Washington, DC, OT Report 75-76, October 1975.
- Karshner, S. W., "High Performance Antenna Systems for New VOA Stations," *IEEE Trans. on Broadcasting*, Vol. 34, No. 2, June 1988.
- Maslin, M. M., "Caustics and Cusps in an Isotropic Ionosphere," *J. Atmos. Terr. Phys.*, 38, 239-250, 1976a.
- Maslin, M. M., "Fields Near a Caustic and Cusp in an Isotropic Ionosphere," *J. Atmos. Terr. Phys.*, 38, 1251-1263, 1976b.
- McEwan, M. J., and L. F. Phillips, *Chemistry of the Atmosphere*, Chap. 6, Edward Arnold Ltd., London, 1975.
- Melts, G., L. H. Holway, Jr., and M. M. Tomjanovich, "Ionospheric Heating by Powerful Radio Waves," *Radio Sci.*, Vol. 9, No. 11, November 1974, pp. 1049-1063.
- Nickisch, L. J., "Focusing in the Stationary Phase Approximation," *Radio Sci.*, Vol. 23, No. 2, March-April 1938, pp. 171-182.
- Utlaut, W. F., and E. J. Violette, "A Summer of Vertical Incidence Radio Observations of Ionospheric Modification," *Radio Sci.*, Vol. 9, November 1974, pp. 895-903.
- Warren, R. E., R. M. DeWitt, and C. R. Warber, "A Numerical Method for Extending Ray Trace Calculations of Radio Fields into Strong Focusing Regions," *Radio Sci.*, Vol. 17, May-June 1982, pp. 514-520.

## DISCUSSION

M. J. KESKINEN, US

Have you looked at beam self-action effects at 90 and 95 dBW?

## AUTHOR'S REPLY

No. There should be some, but we have not.

# MODELING OF HF PROPAGATION AND HEATING IN THE IONOSPHERE

by  
Timothy M. Smith, Merit M. Shoucri,  
and Thomas M. Wagner

TRW, Inc  
Space and Technology Group  
Applied Technology Division  
One Space Park  
Redondo Beach, CA 90278  
USA

## SUMMARY

A comprehensive numerical implementation of plasma geometric optics is being enhanced and adapted to the problem of self-consistent ionospheric propagation of high power, high frequency (HF) radar signals. The emphasis in this work is on realistic and rigorous description of the propagating waves so that geometric and spectral characteristics of nonlinear ionospheric effects can be predicted in detail. When improvements are complete, a plasma geometric optics code will be used in conjunction with an ionospheric transport code to determine self-consistently the HF radiation field and quasilinear modifications of ionospheric plasma properties due to ohmic dissipation of the HF radiation. This allows detailed study of nonlinear phenomena such as beam self-focusing, formation of large-scale density cavities and striations, and induced wave ducting. An overview of the theory underlying the modeling of radiation propagation and ohmic power deposition is given, and current results from the plasma geometric optics code together with associated ionospheric power deposition profiles are presented. Detailed structure of ordinary and extraordinary mode caustics formed in a manner consistent with a realistic antenna pattern and birefringence upon entrance into the ionosphere are evident.

## 1. INTRODUCTION

The ionosphere is an inhomogeneous, anisotropic, and dissipative medium which is frequently used as a propagation channel by electromagnetic waves. When the wave power is low, little interaction with the plasma occurs, and the propagation is qualified as linear. When the wave power is high, the wave interacts with the medium and changes its properties, and a nonlinear theory is required to describe the process. This nonlinear action can be either disruptive to an operating system using the ionosphere, or it can be intentionally produced, as is done in ionospheric modification experiments.

In the HF frequency regime, nonlinear phenomena have been identified both theoretically and experimentally. They can be categorized according to their length and time scales into two distinct regimes: large scale electromagnetic phenomena, occurring on scales larger than 1 kilometer and 1 second, and small scale electrostatic phenomena, occurring on scales of the order of meters and milliseconds. It is useful to assess the contribution of each phenomenon to the nonlinear HF heating of the ionosphere and to determine which mechanism is more likely to dominate under given HF parameters and ionospheric conditions. For example, parametric instabilities have long been thought to play a major role in plasma heating<sup>[1]</sup>. Specifically, two major instabilities, parametric decay and thermal self-focusing, have been frequently invoked to account for experimental results. Although the former belongs to the category of small scale electrostatic phenomena<sup>[2]</sup>, the latter is observed as large scale structures (1 - 5 kilometers) drifting across the ionosphere with a time scale of the order of one minute<sup>[3]</sup>. Different theories of thermal self-focusing provide different estimates of scale length for the resulting striations, varying from meters to kilometers<sup>[4]</sup>. To date, the relative contribution of electrostatic and electromagnetic phenomena in producing the observed striations is still unclear. More recently, strong turbulence theory of caviton collapse and burnout<sup>[5]</sup> has been used with new experimental data to put forward a mechanism for HF energy absorption which is finding favor over the more traditional assumption of weak turbulence. Because of the collisional nature of the ionosphere, it is estimated that a large amount of the energy carried by the HF waves is dissipated ohmically<sup>[6]</sup>, first in the highly collisional D and E regions, and then in the F region. In the F region ohmic heating produces plasma transport primarily along the magnetic field lines. This can create, among other things, large scale, field-aligned thermal density cavities which can also cause self-focusing and can induce wave ducting.

For all the processes mentioned above, a self-consistent analysis which relates the HF waves emanating from the transmitter antenna to the local region in the plasma where the energy is deposited is crucial. Such an analysis permits a true estimation of the pump field amplitude, polarization, and phase needed to initiate the instabilities discussed. A self-consistent analysis also traces the different mechanisms to a common HF beam injected into the ionosphere so that the relative importance of the competing processes can be correctly assessed. Calculation of wave-plasma interaction processes can be made more meaningful in the context of consistent wave and background plasma information.

In the current work, we have addressed these issues by further enhancing and adapting a numerical implementation of plasma geometric optics, initially developed at Yale University<sup>[7]</sup>, which uses the geometric optics approximation to calculate wave amplitude, phase, and polarization in inhomogeneous, anisotropic, three-dimensional media. We apply this code to the specific problem of oblique ohmic heating of the ionosphere by powerful HF waves such as those generated by HF radar transmitters. We intend to use the power dissipation determined from output of the geometric optics field as input to a transport code which predicts the corresponding ohmic heating of the ionosphere. A block diagram outlining the procedure for a self-consistent analysis of ionospheric HF heating is shown in Figure 1. The plasma dielectric tensor is implemented as a separate module invoked by the geometric optics code. This modular aspect permits the use of various types of background plasma models in the radiation calculations. For the current effort we use an inhomogeneous, magnetized and dissipative cold plasma dielectric tensor, which adequately represents the actual ionosphere, and use existing standard models to obtain the necessary ionospheric parameters.

In Section 2, a description of the theory underlying the plasma geometric optics code is presented. Section 3 describes the models used for the background ionosphere and ionospheric transport. Section 4 describes numerical results and shows

calculations of HF power deposition profiles, and the Conclusion points toward future work.

## 2. OVERVIEW OF THE RADIATION DESCRIPTION

Plasma geometric optics is an asymptotic theory of linear electromagnetic waves in plasmas with weak space and time dependence based upon the well-known WKB approximation techniques. Despite the relative simplicity of the computational prescription resulting from this asymptotic theory, complications associated with anisotropy of plasma media and vectorial wave fields require that nontrivial fields be generated by numerical rather than analytical means. A technique known as ray tracing is used for numerical description of high frequency wave propagation in the geometric optics limit.

Although many ray tracing computations have been performed and reported<sup>[5]</sup>, the code utilized here is the first to determine fully the variation of the amplitude and polarization of the field. The code generates boundary data describing transmitted radiation in a form compatible with the asymptotic theory of propagation, launches geometric optics rays, decomposes them into geometric optics modes, and propagates each of these along separate refracted ray trajectories. The amplitudes and polarizations of the radiation modes are calculated along the way, which is essential for the correct determination of power deposition resulting from coherent superposition of several waves. The code is compatible with an arbitrary model of background plasma properties as they contribute to the local plasma conductivity tensor, since roots of the local plasma wave dispersion relation are tracked through parameter space by performing computations directly with the components of the conductivity tensor itself. In addition, the code admits general weak space and time variation of the background plasma and fields. This latter property allows the direct prediction of spurious radar doppler shifts caused by time-dependent density fluctuations in the ionosphere. The code detects the occurrence of caustics and implements the asymptotic matching which results from a local boundary layer analysis, permitting graceful continuation of the geometric optics calculation as shown in Figure 2. For ionospheric heating calculations, this capability must be extended beyond the limitations of geometric optics so that accurate field values are obtained everywhere near the caustic surfaces. This may be accomplished in a straightforward manner *a posteriori* by patching the geometric optics amplitude in the neighborhood of the caustic singularity with an amplitude obtained from an appropriate boundary layer analysis. Birefringence and Faraday rotation are treated in a fully automated and general fashion. An appropriate modification of the asymptotic theory is automatically implemented in nearly degenerate environments, where two different modes have nearly the same local dispersion relation. Figure 3 illustrates the results of this procedure when an electromagnetic wave enters a magnetized plasma. This procedure results in a correct accounting for linear mode conversion in weakly anisotropic plasmas. It also allows the prediction of large scale spatial modulation of wave dissipation rates due to long wavelength Faraday rotation in the lower ionosphere.

The asymptotic theory upon which the geometric optics code is based may be summarized as follows. An equation governing linear waves in a magnetized, weakly nonuniform plasma follows directly from Maxwell's equations and an appropriate linear constitutive relation,

$$\nabla \times \nabla \times \mathbf{E} + \frac{1}{c^2} \partial_t^2 \mathbf{E} = -\frac{4\pi}{c^2} \partial_t \int d^3 \mathbf{r}' \hat{\mathbf{g}}(\mathbf{r} - \mathbf{r}', t - t'; \mathbf{r}', t') \cdot \mathbf{E}(\mathbf{r}', t'). \quad (1)$$

If the dependence of  $\hat{\mathbf{g}}$  on its last two arguments is weak then nearly plane wave solutions to (1) may be sought of the form

$$\mathbf{E}(\mathbf{r}, t) = \mathbf{E}_0(\mathbf{r}, t) e^{i\psi(\mathbf{r}, t)} \quad (2)$$

where the complex amplitude vector  $\mathbf{E}_0$  is slowly varying in space and time and the real phase function  $\psi$  is a nearly linear function of space and time. When the ansatz (2) is used in the wave equation (1) there results

$$i\hat{\Delta} \cdot \mathbf{E}_0 = \hat{L}(\mathbf{E}_0) \quad (3)$$

accurate through first order in small inverse space and time scales. Here the operator  $\hat{L}$  may be written

$$\begin{aligned} \hat{L}(\mathbf{E}_0) = & \frac{1}{2} \partial_t (\partial_\alpha \Delta^T \cdot \mathbf{E}_0) + \frac{1}{2} \hat{\Delta} (\partial_\alpha \Delta^T \cdot \mathbf{E}_0) \\ & - \frac{1}{2} \nabla \cdot (\partial_\alpha \Delta^T \cdot \mathbf{E}_0) - \frac{1}{2} \hat{\nabla} \cdot (\partial_\alpha \Delta^T \cdot \mathbf{E}_0) - \Delta \hat{\Delta} \cdot \mathbf{E}_0 \end{aligned} \quad (4)$$

where

$$\hat{\mathbf{k}} \equiv \nabla \psi, \quad \omega \equiv -\partial_t \psi. \quad (5)$$

The operators with hats are understood to act only on explicit space and time dependences, whereas those without hats act on the implicit dependences through  $\hat{\mathbf{k}}$  and  $\omega$  as well. If the plasma is perfectly uniform then the right hand side of (3) vanishes. The tensor  $\hat{\Delta}$  has the form

$$\hat{\Delta} = \left( \frac{\omega}{c} - \frac{1}{\omega} k^2 \right) \mathbf{I} + \frac{1}{\omega} \mathbf{k} \mathbf{k} + \frac{4\pi i}{c} \hat{\mathbf{g}}(\mathbf{k}, \omega, \mathbf{r}, t), \quad (6)$$

where  $\hat{\mathbf{g}}$  is the uniform plasma conductivity tensor evaluated using the local space-dependent and time-dependent plasma properties. In a cold, magnetized electron plasma with Krook type dissipation  $\hat{\mathbf{g}}$  governed by collision frequency  $\nu_e$ , the conductivity tensor takes the form

$$\hat{\mathbf{g}} = \frac{\omega_p^2}{4\pi\omega(\omega^2 - \Omega_e^2)} \{ \omega^2 \mathbf{I} - \Omega_e \Omega_e - i\omega \Omega_e \times \mathbf{k} \} \quad (7)$$

where

$$\tilde{\omega} = \omega + i\nu_e, \quad \Omega_e = \frac{e}{mc} \mathbf{B}, \quad \omega_p^2 = \frac{4\pi e^2 n}{m} \quad (8)$$

and  $\mathbf{B}$  is the background magnetic field,  $e$  is the magnitude of the electron charge,  $m$  is the electron mass,  $c$  is the speed of light, and  $n$  is the electron density. The tensor  $\Delta \hat{\Delta}$  vanishes in the cold plasma limit, and in general is not simply expressible in terms of the tensor  $\hat{\Delta}$ .

A series solution to (3) is developed based upon the smallness of the right hand side, whence

$$i\Delta \cdot E_0^{(0)} = 0 \quad (9)$$

and

$$i\Delta \cdot E_0^{(1)} = L(E_0^{(0)}). \quad (10)$$

In order for the phase function  $\psi$  to be real when the conductivity tensor  $g$  is not completely antihermitian, an additional small term may be consistently introduced in both zero and first order which contains a free parameter  $\nu$ , so that the system (9)-(10) becomes

$$i\Delta \cdot E_0^{(0)} = -i\nu \partial_\nu \Delta \cdot E_0^{(0)} \quad (11)$$

and

$$i\Delta \cdot E_0^{(1)} = L(E_0^{(0)}) + i\nu \partial_\nu \Delta \cdot E_0^{(0)}. \quad (12)$$

The zero order equation (11) has nontrivial solutions only when

$$\det(\Delta + i\nu \partial_\nu \Delta) = 0 \quad (13)$$

which defines a local dispersion relation

$$\omega = \Omega(k, r, t), \quad (14)$$

a dissipation parameter  $\nu(k, r, t)$ , and a polarization vector  $U$  such that

$$(\Delta + \nu \partial_\nu \Delta) \cdot U = 0 \quad (15)$$

where

$$E_0^{(0)} = \alpha U \quad (16)$$

and  $\alpha$  is a complex scalar amplitude. The polarization vector  $U$  has an adjoint  $U^\dagger$  such that

$$U^\dagger \cdot (\Delta + \nu \partial_\nu \Delta) = 0. \quad (17)$$

When the first order equation (12) is projected onto  $U^\dagger$  there results, after some manipulations,

$$\partial_t \alpha + (\partial_k \Omega) \cdot \nabla \alpha + \frac{1}{2} (\nabla \cdot \partial_k \Omega) \alpha = \beta \alpha \quad (18)$$

where

$$\begin{aligned} \beta = & \nu + \frac{1}{(\partial_\nu \lambda)} \left\{ -\frac{1}{2} (\partial_k \Omega) \cdot (\nabla \partial_\nu \lambda) - \frac{1}{2} (\partial_t \partial_\nu \lambda) \right. \\ & + \frac{1}{2} [(\partial_t U)^\dagger : (\partial_k \Delta^T) \cdot U^* - (\partial_t U)^\dagger : (\partial_k \Delta) \cdot U] \\ & - \frac{1}{2} [(\partial_t U)^\dagger : (\partial_\nu \Delta^T) \cdot U^* - (\partial_t U)^\dagger : (\partial_\nu \Delta) \cdot U] \\ & \left. + \frac{1}{2} [U^\dagger \cdot (\partial_t \partial_k \Delta) \cdot U - U^\dagger \cdot (\partial_t \partial_\nu \Delta) \cdot U] \right. \\ & \left. - U^\dagger \cdot (\Delta \Delta) \cdot U \right\} \quad (19) \end{aligned}$$

and  $\lambda$  is that singular value of  $\Delta + i\nu \partial_\nu \Delta$  which vanishes when (13) is satisfied. Application of the method of characteristics to (18) yields the ordinary differential equation

$$\partial_r \alpha + \frac{1}{2} (\nabla \cdot \partial_k \Omega) \alpha = \beta \alpha \quad (20)$$

with characteristic curves defined by

$$\partial_r r = \partial_k \Omega. \quad (21)$$

Differentiation of (13) leads to

$$\partial_r \lambda = -\partial_t \Omega \quad (22)$$

which formally completes the system of ray and amplitude equations. The polarization of the wave is transported along the ray by differentiating (15) with respect to  $r$  and solving for the derivative of  $U$ . Finally, if coordinates  $s_1$  and  $s_2$  are defined which parameterize the boundary surface from which rays are launched, then it can be shown that

$$\partial_r J = (\nabla \cdot \partial_k \Omega) J \quad (23)$$

where

$$J = \partial_{s_1} r \times \partial_{s_2} r \cdot \partial_r r. \quad (24)$$

Equation (23) can be used to simplify (20), which becomes

$$\partial_r [((\partial_\nu \lambda) J)^{1/2} \alpha] = \beta' [((\partial_\nu \lambda) J)^{1/2} \alpha] \quad (25)$$

where

$$\begin{aligned} \beta' = & \nu + \frac{1}{(\partial_\nu \lambda)} \left\{ \frac{1}{2} [(\partial_t U)^\dagger : (\partial_k \Delta^T) \cdot U^* - (\partial_t U)^\dagger : (\partial_k \Delta) \cdot U] \right. \\ & \left. - \frac{1}{2} [(\partial_t U)^\dagger : (\partial_\nu \Delta^T) \cdot U^* - (\partial_t U)^\dagger : (\partial_\nu \Delta) \cdot U] \right. \end{aligned}$$

$$+\frac{1}{2}[Y^t \cdot (\nabla \cdot \partial_k \Delta) \cdot U - Y^t \cdot (\partial_k \Delta) \cdot U] - Y^t \cdot (\Delta \Delta) \cdot U \} \quad (26)$$

The divergence of the group velocity appearing in (23) becomes infinite on a caustic surface. In practice, therefore, (25) is integrated along with the ray equations, the jacobian  $J$  is calculated from (24), and equations determining the partial derivatives in (24) are also integrated,

$$\partial_r \rho = \rho \cdot (\nabla \partial_k \Omega) + \eta \cdot (\partial_k \partial_k \Omega) \quad (27)$$

and

$$\partial_r \eta = -\rho \cdot (\nabla \nabla \Omega) - \eta \cdot (\partial_k \nabla \Omega) \quad (28)$$

where  $\rho$  is any one of the partial derivative vectors appearing in (24) and  $\eta$  is the corresponding partial derivative of  $k$ . The advantage of using (25), (27), and (28) is that all of the coefficients and dependent variables are bounded on a caustic surface.

When the background is isotropic or nearly isotropic the foregoing analysis breaks down and the analysis must be repeated for the case in which two singular values of the wave equation tensor vanish or are both small. One result of switching between the two formalisms is the bifurcation of rays on entry into an anisotropic medium.

The ray tracing code described by the block diagram in Figure 4 has been constructed using the formalism described above. Examples of its capabilities are displayed in Figure 5.

Electromagnetic fields at the boundary surface from which rays are launched must conform to the assumptions of slowly varying amplitude and nearly linear phase which underly the geometric optics theory. Fields radiated from a transmitting antenna must therefore be expressed in their far field form on the boundary surface. The far field form in conjunction with the local dispersion relation serve to determine the geometric optics phase, amplitude, polarization, and associated properties of the transmitted wave on the exterior of a sphere surrounding the antenna. The sphere is chosen to be large compared to the antenna but does not extend into the ionosphere. Geometric optics rays are launched from the surface of this sphere and the prescribed amplitude and polarization data are transported into the ionosphere.

The procedure for evaluating the radiation electric field and associated volumetric power deposition once the ray tracing results are in hand is not trivial. Each geometric optics ray must be considered as a member of a family of rays which describes a single geometric optics mode  $j$  having the form

$$E_j = E_{0j}(r, t) e^{i\psi_j(r, t)} \quad (29)$$

where the amplitude vector is nearly constant and the phase function is nearly linear. The transport of the wave phase, amplitude, and polarization along a ray constitutes evaluation of a single geometric optics mode along the ray path. In numerical practice, values of these wave parameters are available at discrete points along the ray path. Thus, for each geometric optics mode there is a three dimensional grid of points at which the wave parameters are available. This grid is generated by tracing rays launched from a two dimensional boundary surface. The field of each mode at an arbitrary point in space and time must be determined by a three dimensional interpolation procedure. The procedure is as follows. Let  $s_1$  and  $s_2$  be coordinates parameterizing the boundary surface, and let  $\tau$  be a coordinate parameterizing each ray. Then wave parameters for a given mode may be made available on a regular grid in the three dimensional ray space  $(s_1, s_2, \tau)$  after rays have been traced. Likewise, the position coordinates of these gridpoints are tabulated as  $r(s_1, s_2, \tau)$ . Suppose that the field of that mode is desired at a point  $r_0$ . First it is necessary to determine ray space coordinate values  $(s_{10}, s_{20}, \tau_0)$  corresponding to the field point  $r_0$  such that

$$r_0 = r(s_{10}, s_{20}, \tau_0). \quad (30)$$

This must be done by inverse interpolation. If interpolation is justifiable, a straightforward three dimensional numerical rootfinding scheme will solve this problem with any reasonable initial guess. In particular, a Newton iteration based on the relation

$$\delta r = \delta s_1 \partial_{s_1} r + \delta s_2 \partial_{s_2} r + \delta \tau \partial_\tau r \quad (31)$$

where

$$\delta r = r_0 - r(s_1, s_2, \tau) \quad (32)$$

works well. Here the partial derivatives can be evaluated using tabulated ray coordinate data. The increment  $\delta \tau$ , for example, may be determined by taking the inner product of the total variation  $\delta r$  above with the vector  $\partial_{s_1} r \times \partial_{s_2} r$ . This vector is perpendicular to both  $\partial_{s_1} r$  and  $\partial_{s_2} r$ , and the result is

$$\delta \tau = (\partial_{s_1} r \times \partial_{s_2} r) \cdot \delta r / (\partial_{s_1} r \times \partial_{s_2} r) \cdot \partial_\tau r. \quad (33)$$

Increments  $\delta s_1$  and  $\delta s_2$  may be similarly determined. The coordinates  $s_1$ ,  $s_2$ , and  $\tau$  are repeatedly incremented until they reach  $s_{10}$ ,  $s_{20}$ , and  $\tau_0$ .

Having determined  $s_{10}$ ,  $s_{20}$ , and  $\tau_0$  in this fashion, the wave parameters of the geometric optics mode may be forward interpolated in three dimensions. That is, the phase, amplitude, and polarization at  $s_{10}$ ,  $s_{20}$ , and  $\tau_0$  may be found from corresponding values at nearby points in the three dimensional ray space grid determined by the ray tracing. The entire process of inverse interpolation followed by forward interpolation must be repeated for each geometric optics mode which passes across the field point. In a typical oblique propagation scenario there may be four modes passing through a field point: upward launched and downward reflected instances of ordinary and extraordinary magnetized plasma waves. Coherent superposition of these waves is necessary in order to display such features as Faraday rotation of the polarization vector and associated spatial oscillation of the power deposition.

The time averaged volumetric power deposition is expressed in terms of the total electric field as

$$P = \frac{1}{2} E^* \cdot E \quad (34)$$



where

$$E = \sum_j E_j \quad (35)$$

and

$$I = \sum_j g_j \cdot E_j \quad (36)$$

In order to evaluate the power deposition at an arbitrary field point, the conductivity tensor  $g_j$  must also be interpolated for each radiation mode.

### 3. IONOSPHERIC PLASMA BACKGROUND AND TRANSPORT

As already mentioned, the geometric optics code uses a modular conductivity tensor, that is, the dielectric properties of the medium are incorporated in the code entirely through an isolated module. Of the various ionosphere models currently in usage<sup>[9]</sup>, we have chosen the International Reference Ionosphere (IRI) model<sup>[10]</sup>. It provides electron and ion densities and temperatures as well as neutral temperature as functions of geographic or geomagnetic location and altitude. Parameters are time of day, time of year, and sunspot number. The geomagnetic field is also evaluated by these routines. The IRI is an empirical model that gives the most flexibility and generality for applications of interest. The IRI version used was obtained through the courtesy of D. Bilitza at the National Space Science Data Center at NASA Goddard Space Flight Center. The neutral density model was obtained from the Mean CIRA Reference Atmosphere model<sup>[11]</sup> and provides densities of molecular nitrogen and oxygen, atomic oxygen, argon, helium, and hydrogen at various altitudes. The electron collision frequency has contributions from the Coulomb collisions with ions as well as short range collisions with the neutrals. The former is important in the F region, while the latter dominates the D and E regions as well as the lower F region of the ionosphere. The magnetic field is calculated from the 1963 POGO spherical harmonic model<sup>[12]</sup>. Together these routines provide a basis for the determination of the electron collision frequency and dielectric properties of the ionosphere. Figure 6 shows densities, temperatures and collision frequency profiles used in our computations and derived from the IRI routines.

Calculations of radiation power deposition will serve as input to the plasma transport computations. The transport analysis in the ionosphere is best carried out by a one-dimensional model along the earth's magnetic field lines. The lower boundary is chosen in the E region where local electron cooling by the high concentration of neutrals is a dominant effect which reduces plasma heating by the HF waves to a minimum. The transport code includes all the major elastic and inelastic local loss mechanisms existing in the ionosphere as well as the effects of convection and thermal conduction along the earth's magnetic field lines. It calculates the corresponding bulk changes in the plasma temperature and density. Such a model was initially developed for polar heating of the ionosphere<sup>[8]</sup> and is currently generalized for a two-dimensional mid-latitude geometry<sup>[13]</sup>. Other transport codes<sup>[13,14]</sup> could be used with our radiation model in a similar manner, using power deposition profiles as a heating source for energy balance transport equations.

### 4. ILLUSTRATIVE EXAMPLES

In this section we show some illustrative calculations simulating an HF radar beam propagating in the ionosphere. All examples use the ionospheric conditions shown in Figure 6. Rays are transmitted from a location 45° North and 70° West during the month of January at 8:00 AM local transmitter time. The sunspot number is 100. Figure 7 shows an angular scan of ten rays transmitted at 10 MHz with horizontal transmitter polarization. Since the reflection layer altitude is a function of frequency and angle of incidence, some rays reflect from the ionosphere and others pass through it. All rays bifurcate into distinct ordinary and extraordinary mode rays because of the anisotropy of the magnetized ionospheric plasma. Figure 8 shows multiple bounces of a radar-like beam. Notice that while rays incident at steeper angles are about to complete four hops, grazing incidence rays are barely completing two hops. A full layout of the different projections of a single hop beam of rays is shown in Figure 9. Details of the caustic surface geometry, splitting of the beam into ordinary and extraordinary modes, and shifting of the beam pattern toward the direction of the earth's magnetic field are clearly apparent. Figure 10 shows contours of constant ohmic power deposition along the equatorial x-z plane. Here the contributions from different waves are incoherently superposed since the interference terms are rapidly oscillating in space. Large absorption of the HF energy occurs at low altitude in the D and E regions due to large collision frequencies. Caustic swelling at higher altitudes is also a cause of enhanced absorption of the wave energy. These regions are therefore likely locations for thermal modification of the ionosphere. Finally, Figure 11 shows an example of results from the polar heating transport code where both electron temperature and density are changed by 90 seconds of heating at 5 MHz. Similar effects are expected to occur in the mid-latitude case using powerful radar beams since the power absorbed by the ionosphere is comparable, if not larger, in the latter case.

### 5. CONCLUSION

We have shown oblique HF ionospheric wave propagation and ohmic heating rate results from a comprehensive numerical implementation of plasma geometric optics. The completeness of the numerical implementation allows modeling of wave propagation and absorption with novel realism and detail, and is suitable for self-consistent prediction of quasilinear ionospheric modifications and associated effects. Future work will focus on coupling the radiation computations to transport computations in order to achieve self-consistency.

## REFERENCES

1. *Radio Science*, Special Issue on Ionospheric Modification, 9, 11, 1974.
2. I. J. Kantor, High Frequency Induced Enhancements of the Incoherent Scatter Spectrum at Arecibo, *J. Geophys. Res.*, 79, 199, 1974.
3. L. M. Duncan and R. A. Behnke, Observations of Self-focusing Electromagnetic Waves in the Ionosphere, *Phys. Rev. Lett.*, 41, 998, 1978.
4. D. T. Farley, C. LaHoz, and B. G. Fejer, Studies of the Self-focusing Instability at Arecibo, *J. Geophys. Res.*, 88, 2093, 1983.
5. D. F. Dubois, H. A. Rose, and D. Russell, Power Spectra of Fluctuations in Strong Langmuir Turbulence, *Phys. Rev. Lett.*, 61, 2209, 1988.
6. M. M. Shoucri, G. J. Morales, and J. E. Maggs, Ohmic Heating of the Polar F region by HF pulses, *J. Geophys. Res.*, 89, 2907, 1984.
7. T. M. Smith, Plasma Geometric Optics Analysis and Computation, Ph. D. Dissertation, Yale University, Dec. 1983.
8. K. G. Budden, *The Propagation of Radio Waves*, Cambridge, Cambridge University Press, 1985.
9. C. M. Rush, Ionospheric Radio Propagation Models and Predictions - A Mini-Review, *IEEE Trans. Ant. and Prop.*, AP-34, 1163, 1986.
10. D. Bilitza, International Reference Ionosphere: Recent Developments, *Radio Sci.*, 21, 343, 1986.
11. K. S. W. Champion, A. E. Cole, and A. J. Kantor, Standard Reference Atmospheres, Ch. 14 in *Handbook of Geophysics and the Space Environment*, A. S. Jursa ed., AFGL/AFSC, USA, 1985.
12. J. D. Hansen, Large Scale Ionospheric Modifications by High Power Radio Waves: Theory and Observation, UCLA-PPG Report No. 1298, April, 1990.
13. P. A. Bernhardt and L. M. Duncan, The Feedback-Diffraction Theory of Ionospheric Heating, *J. Atmos. and Terr. Phys.*, 44, 1061, 1982.
14. G. P. Mantas, H. C. Carlson and C. H. LaHoz, Thermal Response of F region Ionosphere in Artificial Modification Experiments by HF Radio Waves, *J. Geophys. Res.* 86, 561, 1981.

## ACKNOWLEDGEMENT

This work is sponsored by the Electromagnetics Directorate of the Rome Air Development Center at Hanscom Air Force Base, Massachusetts, USA.

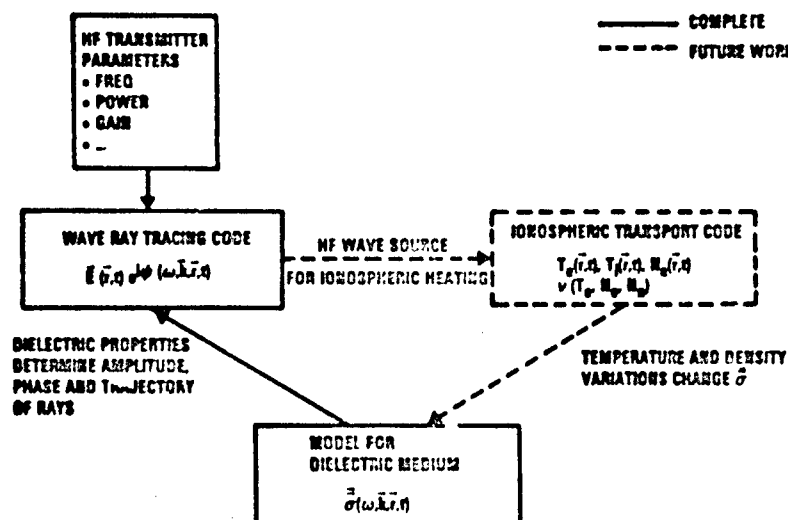


Figure 1. Block Diagram for the HF Ionospheric Propagation Code

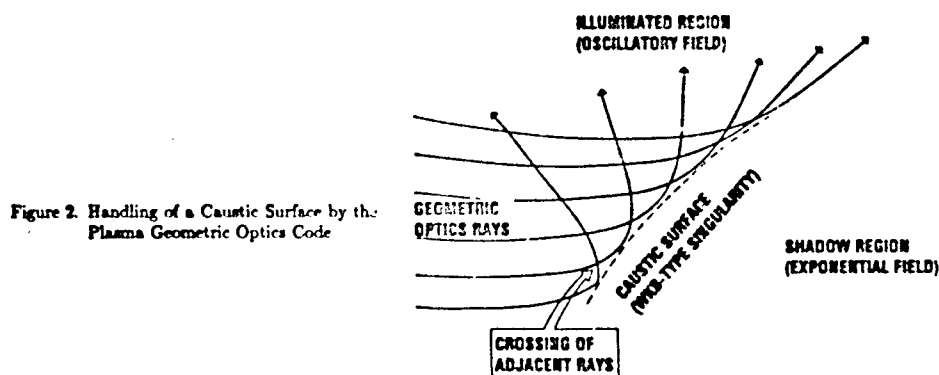


Figure 2. Handling of a Caustic Surface by the Plasma Geometric Optics Code

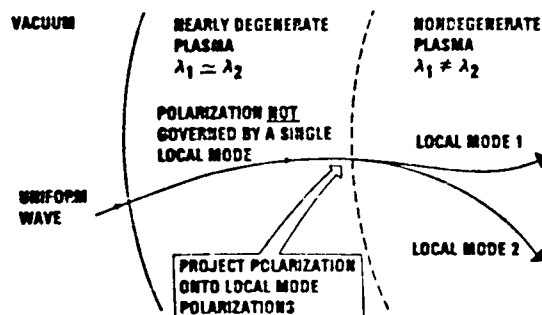


Figure 3. Treatment of Birefringence by the Plasma Geometric Optics Code

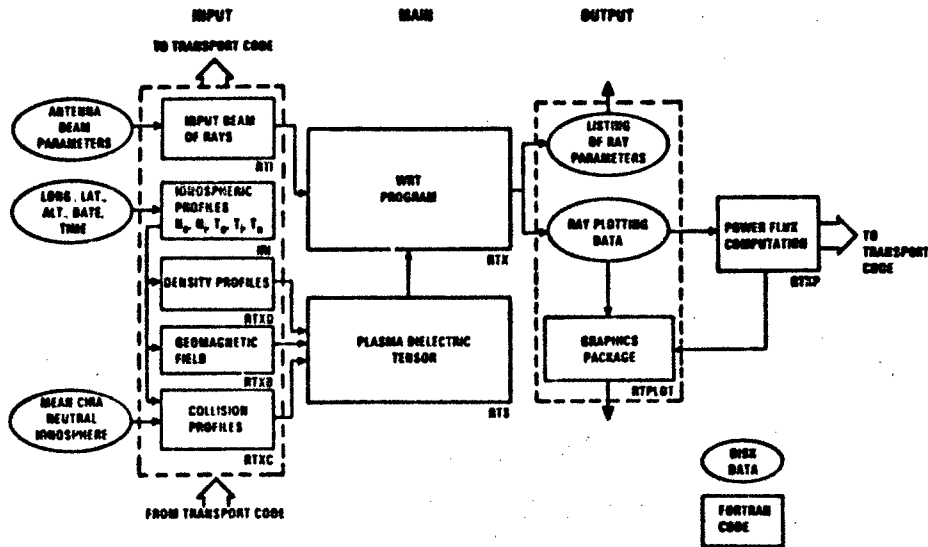


Figure 4. Block Diagram for the Plasma Geometric Optics Code Showing its Main Modules, Input and Output Routines, and Interfaces with the Transport Code

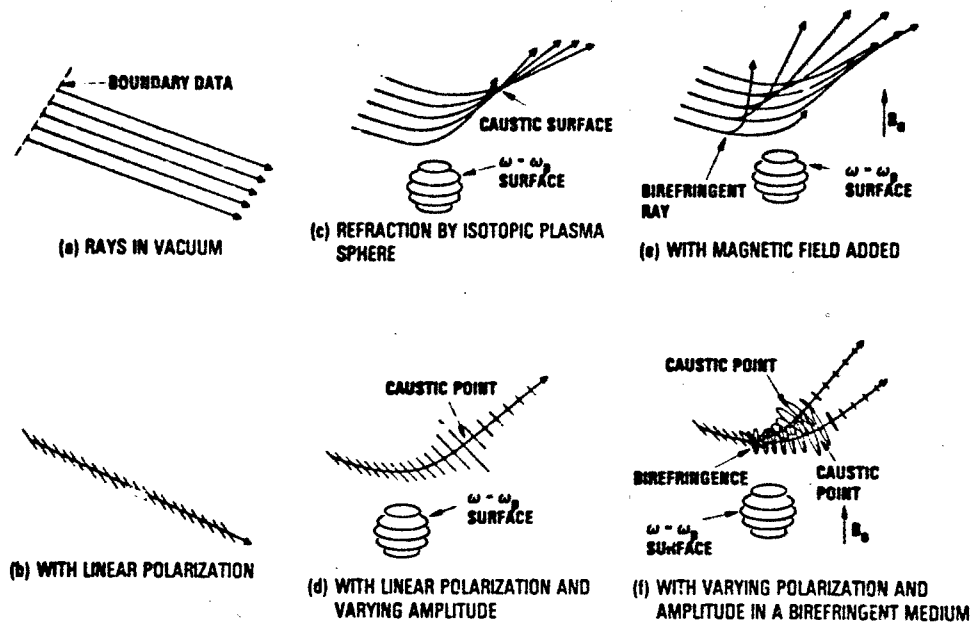


Figure 5. Examples of Plasma Geometric Optics Code Capabilities

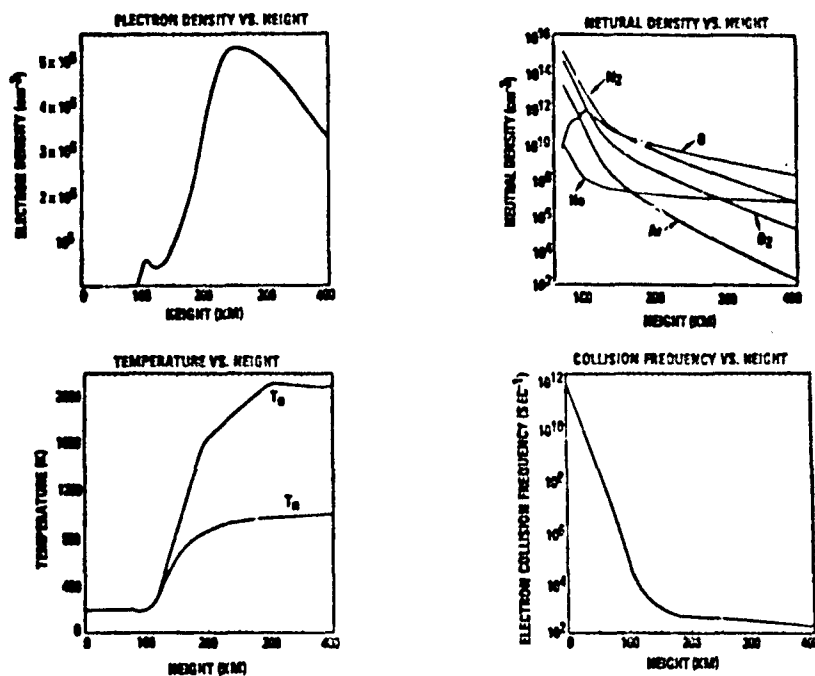


Figure 6 Ionospheric Parameters Calculated at 45° North and 70° West for the Month of January at 8:00 AM Local Time and Sunspot No. 100

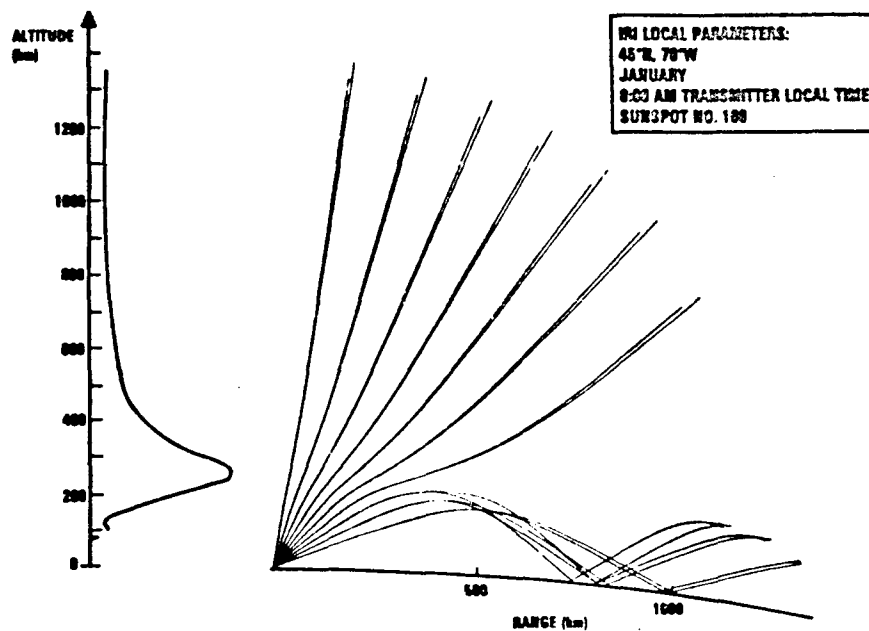


Figure 7. Angular Scan of Eastward Propagating, Horizontally Polarized Rays at 10 MHz; Rays Reflected from the Ionosphere are Reflected Again from a Curved Earth Surface Assumed to Be a Perfect Conductor

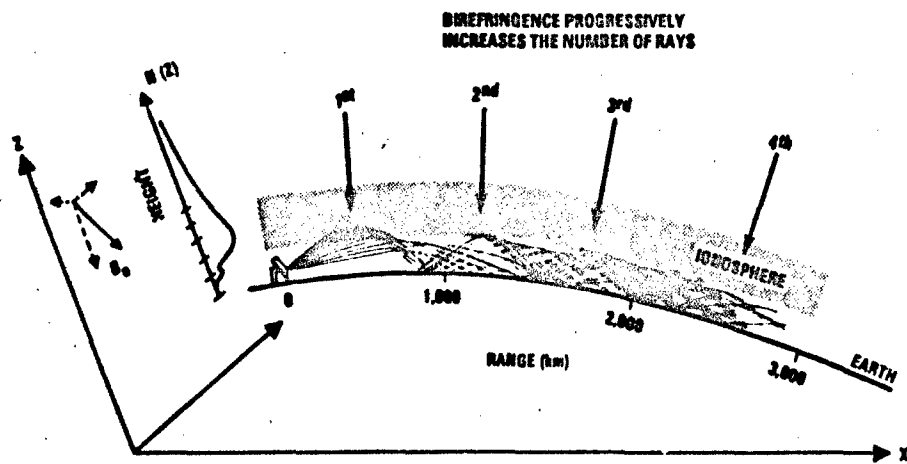


Figure 8. Multiple Hops of Radar Rays

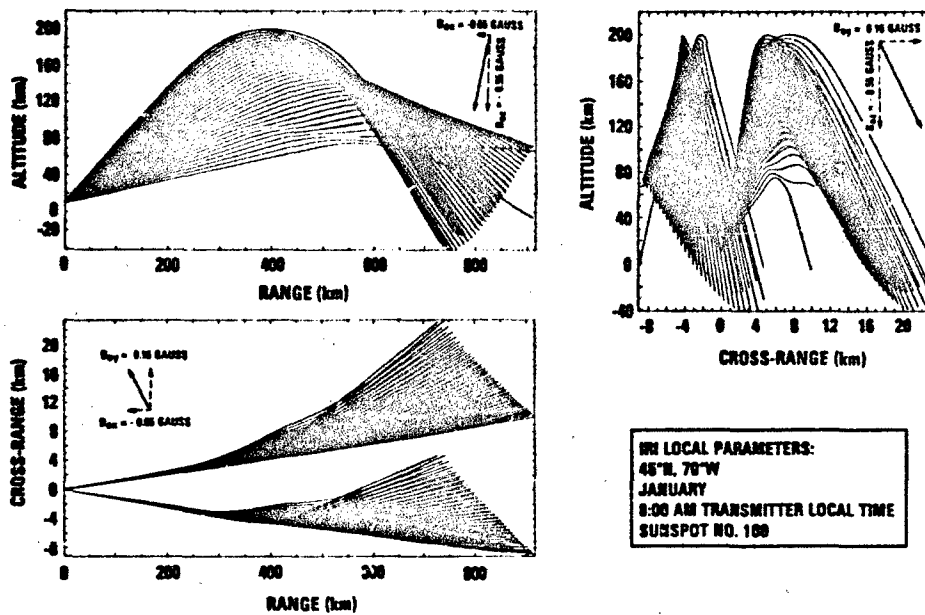


Figure 9. Projections of 10 MHz, Horizontally Polarized, Eastward Propagating Beam of Rays

## CONTOUR PLOTS ALONG X-Z PLANE

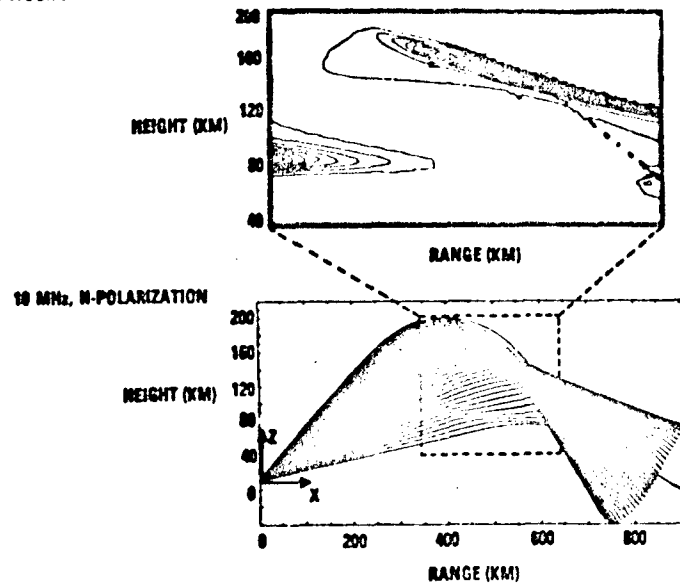
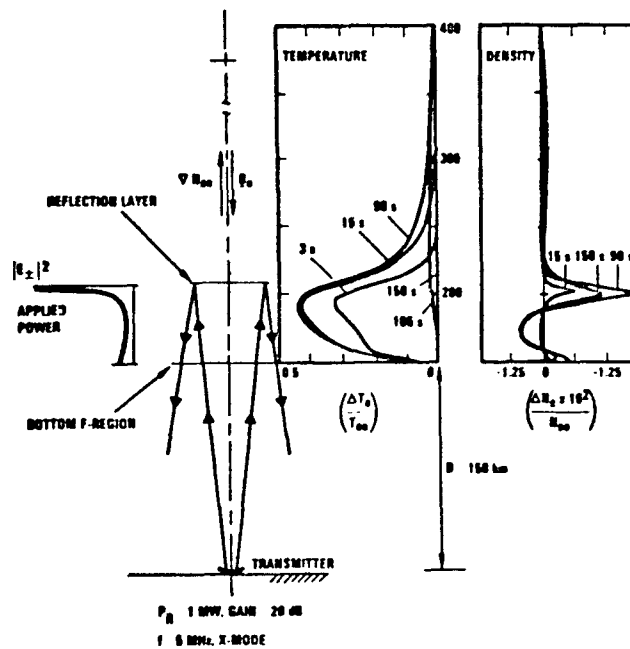


Figure 10. Power Deposition Contours along the Equatorial x-z Plane



(FROM SHOUCHI ET AL. JGR, '94)

Figure 11. Deformation of the Plasma Temperature and Density Under 90 sec. of HF Heating Followed by 60 sec. of Cooling; HF Signal is 5 MHz, ERP = 100 MWatt, from Reference No. 6

DISCUSSION

E. MJSIHUS, NO

1. Comment: This kind of code must also be useful for studies of large thermal cavity formation, large scale field aligned irregularities, "thermal self focussing" and so on. Your comment?
2. Question: My feeling is that coupling to Z mode and access to plasma resonance must be undesired, and difficult to handle in this very general code. Your comment?

AUTHOR'S REPLY

Yes, this is one of the major phenomena that we would like to be able to analyze using the code. As far as handling electrostatic wave effects (plasma resonance, Z-mode, etc...), the code will go as far as the geometric optics approximation permits, i.e., it will calculate any longitudinal field component as long as longitudinal oscillations are small with respect to spatial variations in the medium.



# MODELING AND DESIGN FOR A NEW IONOSPHERIC MODIFICATION EXPERIMENT

Gary S. Sales<sup>1</sup>, Ian G. Platt<sup>1</sup>, D. Mark Haines<sup>1</sup>, Yuming Huang<sup>1</sup> and John L. Heckscher<sup>2</sup>

<sup>1</sup>University of Lowell Center for Atmospheric Research, Lowell, MA 01854, USA

<sup>2</sup>Geophysics Laboratory/U.S. Air Force, Hanscom AFB, MA. 01731, USA

## ABSTRACT

Plans are now underway to carry out new HF oblique ionospheric modification experiments with increased radiated power using a new high gain antenna system and a 1 MW transmitter. The output of this large transmitting system will approach 90 dBW. An important part of this program is to determine the existence of a threshold for non-linear effects by varying the transmitter output.

For these experiments we are introducing a new HF probe system, a low power oblique sounder, to be used along the same propagation path as the high power disturbing transmitter. This concept was first used by soviet researchers to insure that this diagnostic signal always passes through the modified region of the ionosphere. The HF probe system will use a low power (150 W) CW signal shifted by approximately 40 kHz from the frequency used by the high power system. The transmitter for the probe system will be at the same location as the high power transmitter while the probe receiver will be 2400 km down range. The probe receiving system uses multiple antennas to measure the the vertical and azimuthal angle of arrival as well the Doppler frequency shift of the arriving probe signal. The three antenna array will be in an "L" configuration to measure the phase differences between the antennas. At the midpath point a vertical sounder will provide the ionospheric information necessary for the frequency management of the experiment.

Real-time signal processing will permit the site operators to evaluate the performance of the system and make adjustments during the experiment. A special ray tracing computer will be used to provide real-time frequencies and elevation beam steering during the experiment.

A description of the system and the analysis used in the design of the experiment are presented.

## Introduction

This oblique HF ionospheric "heating" project is designed to investigate the modification of the ionosphere using high power HF communications and radar systems that operate in long range propagation mode. In this particular case, for the F-region, we are attempting to "disturb" the ionosphere some 1200 km down range at a bearing of 90° T from the high power transmitter located at the Voice of America (VOA) station in Delano, California. This places the modified region of the ionosphere over the Albuquerque, New Mexico area.

Based on the theoretical work of Gurevich (1978) and Field et al. (1985) it is expected that the "heating" process manifests itself in two different ways. In the F-region of the ionosphere, above about 220 km, the primary effect is to heat the electrons in a volume (approximately 20 km in height and 100 km in diameter, depending on the two dimensional beamwidth of the transmitting antenna) located in the vicinity of the caustic region formed at the reflection altitude just beyond the midpath for the skip rays of the high power transmitter. At these F-region altitudes the heated electrons result in a depleted region with an electron density which is about 5% below the ambient density. Figure 1 shows, in pictorial form, the relative positions of the transmitter ray path and the heated region. As will be shown below, other radio signals propagating through this "hole" generated by the high power HF transmission can be affected.

In addition to the depletion effect we expect instabilities to develop resulting from the likely presence of small scale perturbations in the ambient plasma. The self-focusing instability mechanism appears to have a relatively low threshold ( $\sim 1$  mV/m) and should produce enhanced irregularities which are capable of scattering radio waves.

The basic plan to detect the presence of the disturbed regions is to observe changes on a probe signal passing through the modified region as the high power transmitter is cycled on and off. As will be discussed later the probe transmitter is colocated with the high power (VOA) transmitter, and uses a frequency only slightly removed from the frequency of the "disturbing" transmitter. This arrangement insures that the probe signal follows the same ray path as the disturbing signal and passes directly through the modified region on its way to the ground receiving station some 2400 km away from Delano.

In addition to the probe signal we also monitor the midpath ionosphere using a vertical incidence Digisonde to provide profiles of the ambient electron density for frequency management of the high power transmitter and for control of the elevation steering of the VOA 2-D antenna array. The ability to control these

two factors makes it possible to maximize the energy deposited in the ionosphere at the desired location. The Digisonde can also be used as a vertical looking HF radar to detect the smaller scale irregularities.

#### High Power Transmitting System

The 5% modification of the background F-region ionosphere by a high power HF transmission requires an effective radiated power level of the order of 90 dBW. The Voice of America facility at Delano, California has this capability. Using their new 2-D antenna array which consists of three vertical bays of 4 V 6 elements each, it is possible to achieve 25 to 30 dB of directive gain depending on the specific frequency selected within the frequency band for the array. Each of the three bays can be driven in phase with a separate transmitter each having a maximum power of 375 kW to give a total transmitter power of 1.1 MW.

The elevation antenna pattern of this array is steerable by phasing the horizontal rows of elements relative to each other. This permits the beamed energy to be deposited at the desired location relative to the midpath and down range stations. The choice for the specific elevation angle depends on the separation between the transmitter site and the down range receiving sites as well as the height and critical frequency of the ionosphere. In addition, theoretical modeling of the heated region with the ray tracing through the disturbed region leads to the conclusion that the largest effects occur when the skip distance is adjusted so that it lies some 200 km short of the down range site, i.e. at approximately 2200 km down range from Delano. This degree of experimental management requires a near midpath vertical sounding to specify the ionosphere in that region.

#### Midpath Vertical Incidence Sounder

##### Frequency Management

A University of Lowell Center for Atmospheric Research (ULCAR) Digisonde 256 is located at Kirtland AFB in Albuquerque, NM., some 1200 km from the Delano VOA station. This midpath site was selected because it lies almost exactly on the great circle path to Barksdale AFB near Shreveport, LA (2400 km from Delano) which serves as the ground point for the probe system discussed in the next section.

The primary mode of operation for the Digisonde is the vertical incidence (VI) ionogram made each 15 minutes and it is planned to control and receive the sounder data via a modem at the Barksdale AFB site. As a backup to the remote control and monitoring of the Digisonde for the frequency management part of the experiment, voice telephone can be used after each VI ionogram. These available data include the layer critical frequency, foF2, the true height for the maximum of the layer (derived from the automatically scaled and inverted ionogram) and the height of the bottom of the layer which for these experiments is chosen to be the lowest virtual height corresponding to the bottom of the F-layer; all these proposed measurements will be made at night during these campaigns. An example of the summary of these data are shown in Figure 2. For 31 Jan. 1990, from just after 03 UT to just before 10 UT, we see the edited vertical sounder data specification for the nighttime ionosphere. The lowest trace is the modelled E-layer, of no great significance for these experiments. Moving upward we see the variation of foF2, the height of the bottom of the F-layer and finally the height of the peak of the layer; a very typical behavior.

The received data, foF2, hmax and  $Y_m = (f_{max} - h_{min})$  will be put into a simple quasi-parabolic ray tracing program and for each selected frequency the program is run through a sequence of elevation angles beginning at 3° and increasing in 1° steps until the rays penetrated the F-layer. This set of rays is examined to determine the frequency that placed the skip distance some 200 km closer to Delano than Barksdale. At the same time the vertical take-off angle to the skip is also calculated from the program and this information is telephonically transmitted to the Delano operators so that they can adjust the high power transmitter frequency and elevation steer angle.

##### Skymap Mode

As part of the routine Digisonde mode, F-layer drift measurements are made during the time between the VI soundings. This means that some twelve minutes of drift data is recorded during each 15 minute period using the four antenna receiving array at a frequency whose virtual height is at the same virtual reflection height of the oblique heating frequency. This approach insures that the skymap measurements are made in the same altitude regime as the oblique heating process.

Skymaps are displays of the location of the several reflecting sources in the ionosphere near the reflection layer detected by the phase difference between the four Digisonde receive antennas. The signals on each antenna are spectrally processed and then the phase differences between the antennas for the strongest spectrum lines are calculated. This phase difference is then converted to elevation angle.

The spatial distribution of the observed sources can be understood as a measure of the irregular structure in the reflection region. When the ionosphere is relatively free of irregularities the skymaps will appear as a closely spaced group of reflections and the source locations will all coincide. On the other hand, when the ionosphere is highly irregular, the skymap will show a wide spread of sources over a significant fraction of the total observation angle, typically 45° measured from the zenith. For these heating experiments it is expected that

the self-focusing instability mechanism will increase the number of irregularities in the observation area and the count of the number of sources will increase during the heating part of the cycle.

During the part of the heating cycle when the high power transmitter is turned off the number of skymap sources are expected to decrease. We must recognize at this point in the analysis that we do not know the time constants associated with the decay of these instabilities and therefore the skymaps may or may not show a variation comparable with heater power cycling.

#### Oblique Sounder

An oblique swept frequency sounder was established over the same path as the Probe system, i.e., from Delano to Barksdale. This sounder sweeping from 6 to 30 MHz provided an independent measure of the maximum observable frequency (MOF) that can be compared with the values derived from the vertical incidence midpath ionogram using transmission curve overlays for 2400 km. These oblique ionograms, made every 15 minutes, helped provide a basis for the frequency management decisions, but these data had to be extrapolated to determine the MOF for 2200 km (i.e. to put the skip range approximately 200 km closer to Delano). In addition the oblique ionograms can not provide any estimate of the elevation angles that must be used to maximize the energy deposition over the Kirtland site.

#### HF Probe System

A low power (150 W) CW transmission was provided over the 2400 km path from Delano to Barksdale. These transmissions at a frequency only slightly different from the high power "heating" transmitter, would not be interrupted as the heater transmitter was cycled on and off with a five minute period. The probe signal passes through the modified ionospheric region and the signal received on the ground at Barksdale is processed for changes in Doppler frequency shift, amplitude and arrival angle that correlate with the heater cycling.

The A-D convertor at the IF output of the receiver samples the in-phase (I) and the shifted quadrature (Q) components of the signal and these complex samples are stored until the system has accumulated 4096 data points. In the Zenith computer, these 4096 complex points are used in a Fourier transform analysis. The 400 spectrum lines centered on 0 Hz are stored on the system for real-time display and also recorded on floppy disc for subsequent analysis. It is necessary to retain only the center portion of the spectrum around  $\pm 10$  Hz, since we expect the natural fluctuations of the ionosphere to cause only small Doppler frequency shifts. Again, the heating can be expected to superimpose an additional small Doppler frequency shift (certainly less than  $\pm 10$  Hz) that varies with the heating cycle.

#### Experimental Plan

The first test of the entire system was carried out during the period from 25 Jan. 1990 through 2 Feb. 1990. Five campaigns were held on alternate nights, each ran for about 5 hours beginning around 04 UT (at the midpoint heating region the local time is -7 hours from UT). This particular time period was selected for the following reasons.

1. The heating process is enhanced when the heating frequency is low.
2. The ionosphere has stabilized to some degree after the sunset period.
3. No D-region absorption is present during these hours.

This first test period is considered a dry-run for the upcoming full power tests planned for the Fall, 1990. During this test the VOA high power transmitter ran with only 375 kW total power. In addition the transmission azimuthal array beamwidth was wider than planned, thus reducing the power density on the ionosphere by an additional 5 dB. For the Jan. 1990 campaign the ERP was about 10 dB below the system's maximum power level.

The spectrum data stored on the computer hard disk during the mission are transferred to a floppy disk and are brought back to the laboratory for additional processing.

#### HF Probe Transmitting System

The transmitter is a 150 W amplifier driven by a 10 W amplifier. The frequency is obtained from a tuneable synthesizer locked to a very stable atomic frequency standard. The amplified signals are delivered to a slant-V antenna with two 400 ft balanced elements suspended from a 25 m triangular metal tower to the ground sloping outward in the direction from Delano to Barksdale (90° T). A balun was installed near the top of the tower to provide an impedance transformation from the unbalanced shielded coaxial cable to the balanced two long wire elements.

The frequency for these probe transmissions was usually set to be just below the heater frequency (i.e. 30 to 60 kHz) to keep the high power heater transmissions from overloading the probe receivers.

### HF Probe Receiver and Antenna System

To receive the probe signals at Barksdale AFB outside of Shreveport, LA we established a 3 antenna/receiver system. The three antennas are placed in two lines, one in the direction of Delano and the other perpendicular to the direction to Delano. One antenna is common to both arrays and acts as a reference antenna. The two element array along the great circle path to Delano serves as an interferometer, measuring the vertical angle of arrival of the probe signal. The interferometer measures the phase difference between the two antennas spaced approximately 100 m apart and converts this phase difference to an angle of arrival. As with any interferometer, there will be some ambiguity in this measurement and for the frequencies used in this heating experiment these foldovers due to aliasing are located outside the range of expected elevation angles.

The second array of two antennas elements spaced 30 m apart, is oriented perpendicular to the great circle path from Delano to Barksdale. This pair of antennas serve as an interferometer to measure the changes in the azimuthal arrival angle. These three antennas are simple vertical, 1 m monopoles with an active amplifier at the base of each. Three RACAL receivers, one for each antenna, use a 150 Hz bandpass filter and amplify the received signals and convert the transmission frequency down to the IF. The receivers are run in a manual gain mode and are all automatically phase calibrated at the beginning of each change in the probe frequency. This change also initiates a new file on the computer hard disk. To be useful for later signal processing these files should be least 30 minutes long.

The A-D converter at the IF output of the receiver samples the in-phase (I) and the shifted quadrature (Q) components of the signal and these complex samples are stored until the system has accumulated 4096 data points. In the Zenith computer, these 4096 complex points are used in a Fourier transform analysis. The 400 spectrum lines centered on 0 Hz are stored on the system for real-time display and also recorded on floppy disc for subsequent analysis. It is necessary to retain only the center portion of the spectrum around  $\pm 10$  Hz, since we expect the natural fluctuations of the ionosphere to cause only small Doppler frequency shifts. Again, the heating can be expected to superimpose an additional small Doppler frequency shift (certainly less than  $\pm 10$  Hz) that varies with the heating cycle.

### Experimental Plan

The first test of the entire system was carried out during the period from 25 Jan. 1990 through 2 Feb. 1990. Five campaigns were held on alternate nights, each ran for about 5 hours beginning around 04 UT (at the midpoint heating region the local time is -7 hours from UT). This particular time period was selected for the following reasons.

1. The heating process is enhanced when the heating frequency is low.
2. The ionosphere has stabilized to some degree after the sunset period.
3. No D-region absorption is present during these hours.

This first test period is considered a dry-run for the upcoming full power tests planned for the Fall, 1990. During this test the VOA high power transmitter ran with only 375 kW total power. In addition the transmission azimuthal array beamwidth was wider than planned, thus reducing the power density on the ionosphere by an additional 5 dB. For the Jan. 1990 campaign the ERP was about 10 dB below the system's maximum power level.

The spectrum data stored on the computer hard disk during the mission are transferred to a floppy disk and are brought back to the laboratory for additional processing.

### Experimental Data Processing and Interpretation

The basic approach to the data signal processing is to detect the presence of the heating cycle (5 minute period) against the background of natural ionospheric fluctuations using spectrum analysis. This analysis is in the very low frequency domain where the basic unit is millihertz, e.g. the five minute heating period is 3.3 mHz and the spectrum range is from 0 to 22 mHz. The natural background fluctuations caused by acoustic gravity waves (AGW) in the ionosphere have periods of one hour or greater to a minimum of about 7 minutes or, in the frequency domain, from 0.27 mHz to 2.4 mHz respectively. The choice of 5 minutes for the heating period is to push the frequency of the desired signal above the highest frequencies associated with the passage of AGW through the midpath region. It was found not to be feasible to move the heater cycling frequency any higher in order to get further away from the upper limit of the AGW. A higher cycling rate would reduce the heating time so that we would not be sure of reaching the saturation point for the maximum growth of the induced instabilities.

### HF Probe

For the HF probe system, the sampling time is dictated by the requirement to gather 4096 complex data points to generate the spectrum of the signal received at each of the three antennas. It takes 23.3 sec. to gather the data for all the antenna spectra. When the spectra are completed (in real-time) then the peak of the spectrum is identified and the I and Q components at that frequency are combined to give the amplitude of the peak and the

phases on the elevation pair of antennas to give the elevation angle associated with that Doppler frequency bin. When 64 of these spectra are completed, covering a period of 24 minutes, the 64 peak amplitudes are spectrally analyzed as described above.

#### Amplitude

The composite amplitude variations of the peak signal are shown in Figure 3. These data include two frequency changes following the time when the skip passes beyond Barksdale as the ionosphere decays moving into the night. The first frequency change was from 15.0 MHz to 12.1 MHz at 0630 UT and the second change occurred at 0710 when the heater and probe frequency was reduced again, this time from 12.1 MHz to 9.48 MHz. A large spectrum of "fading" characteristics can be readily observed and this manifests itself in the spectrum of pieces of these data.

The actual frequency management of the heating and the probe systems during the 31 Jan. campaign is shown in Figure 4. The three frequency steps in the heater are shown to follow the changing MOF on the oblique sounder over the Delano to Barksdale path.

Figure 5 shows a typical spectrum of the peak signal fluctuations on the reference antenna. There is no reason to expect that the spectra from either of the other two antennas will differ significantly. Often we see a relatively high power level at the lowest frequencies in these spectra corresponding to the long period fading of the peak signal. These long (~ 10 minutes or longer) fades, associated with the AGW propagation over Kirtland, will not interfere with the detection of the heating cycle frequency.

The individual campaigns are of the order of 5 hours and since each individual spectra takes 24 minutes of data, we obtain 12 spectra over the full period of operation. In order to smooth these spectra we have taken the overlapping data, i.e. the last 12 minutes from one set and the first 12 minutes from the following set of data and produce an intermediate spectrum. In Figure 5 the second spectrum overlaps the first by 12 minutes and yet we see significant changes in the structure of the power. These observations will be supported later when the skymaps are discussed.

All of the resulting spectra are then displayed in a time sequence with frequency as the ordinate and time of day as the abscissa. The spectrum power is displayed as intensity shading. Figure 6 is for the 31 Jan. 1990 campaign. We see in this figure that the most intense shadings are at the low frequency end of the spectra corresponding to natural background long period fluctuations. The shaded area represent power levels of less than 40 % below the peak power. The solid bars drawn in the shaded areas indicate the location of the peaks in each spectrum. A horizontal dashed line is drawn at the expected heating cycle frequency. If these spectra included power at the heating cycle frequency (3.3 MHz) this would show up as a horizontal trace in the figure over the time interval when heating process was effective.

As discussed earlier, the periods of effective heating will likely be when the heater frequency is close to the MOF for the path from Delano to Barksdale. On these plots, particular attention is paid to those those somewhat brief times when the heating frequency approaches the MOF for the somewhat shorter path length (2200 km) than the 2400 km from Delano to Barksdale. The difference between the MOF and the heater frequency is displayed in these figures above the spectra.

#### Elevation Angle

Using both the reference and the elevation antennas, separated by 100 m along the great circle path from Delano to Barksdale, we measure the phase difference of the arriving probe signal after passing through the heated area and reflecting from the F-region of the ionosphere. The elevation angle for the peak of the several spectrally resolved components is calculated in real time and presented with the central portion of the 23.3 second coherently integrated spectrum. Figure 7 shows the variation of the elevation angle and the 23.3 sec. spectra as a function of time during the 31 January 1990 campaign for the period 0633 UT to 0719 UT. The heater and probe systems operated at 9.5 MHz and we see two modes interweaving on the spectrum with a systematic frequency shift 0.5 to 1.0 Hz. At this point it is speculated that the two modes are the low and high rays. They eventually merge just before that frequency drops out and the spectrum just becomes noisy before 0719 UT. The elevation angle variations are shown below the spectrum and we see two angles associated with the two modes on the spectrum (low and high ray). The low ray elevation angle varies around 18° to 20° while the high ray angles are larger approaching 30° when the skip distance is relatively far from Barksdale and merges with the low ray angles as the skip approaches Barksdale just before 0719 UT.

#### Digisonde Skymaps

The Digisonde skymaps, made at Kirtland, under the heated area present a very dynamic view of the F-region of the ionosphere. Figure 8 a composite of 42 skymaps for 31 Jan. 1990 from 0502 to 0551 UT. Typically we see a strong cluster of sources near the overhead position indicating a relatively smooth ionosphere with little tilting. The pattern of sources is rapidly changing in form and in the number of sources seen in the 1 minute integration time for each map. A plot of the number of sources for the entire 31 Jan. campaign is shown in Figure 9. Large excursions in the number of sources occur frequently indicating dynamic activity under what would

14C-6

normally be recognized as quiet conditions with little or no spread-F. These variations confirm the results of the spectrum analysis of the fading of the signal peak.

Summary and Future Plans

The completed operation and analysis of this "test" experiment, using a relatively low power for the disturbing transmitter, are important to the success of the upcoming full power campaigns scheduled for the Summer, 1990. The data processing for these experiments has been designed to facilitate the detection of the heating effects in a straight forward manner. The dominance at the lowest frequencies corresponding to the ubiquitous short period AGW activity has been recognized and the upcoming campaigns will insure that the heating effects are separated sufficiently from this "noise".

WIND CASTER ACQUISITION DATA (14 HOURS)  
STARTER CODE 000 LAT 30 10 LONG 253 42 DATE 0000-000

The graph displays three data series over time from 05 to 12. The top series (likely wind speed) starts at approximately 40, remains relatively flat until 06, then rises sharply to a peak of about 80 at 08, before fluctuating between 60 and 80. The middle series (likely wind direction) starts at approximately 40, remains flat until 06, then rises steadily to about 60 at 08, and then fluctuates between 50 and 60. The bottom series (likely air pressure) starts at approximately 1000, remains flat until 06, then decreases steadily to about 950 at 08, and then fluctuates between 940 and 960.

Master Freq: 15.04  
Probe Freq: 15.040  
File: 01310427

Figure 3. Composite amplitude variations for the 31 January 1990 campaign. These data include two frequency changes during the period of operation.

14C-H

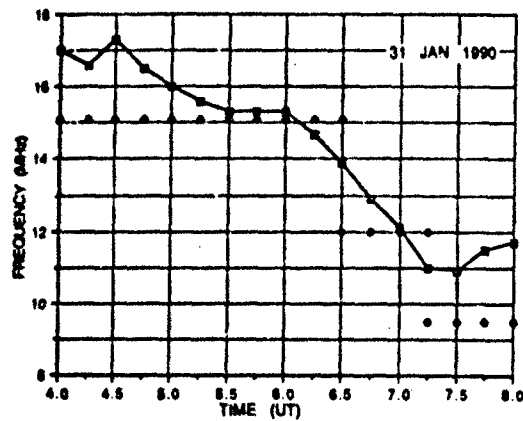


Figure 4. Probe and heater frequencies as a function of time during the 31 January 1990 campaign. Twice during the night we see the MOF pass through the heater frequency.

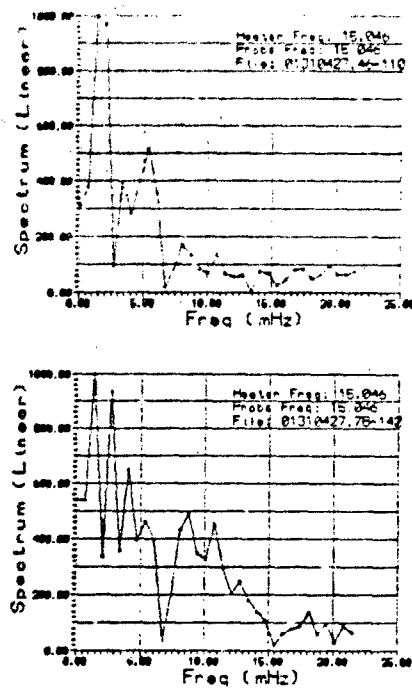


Figure 5. Sample spectra of the peak amplitude fluctuations at adjacent times 0436 UT and at 0448 UT.



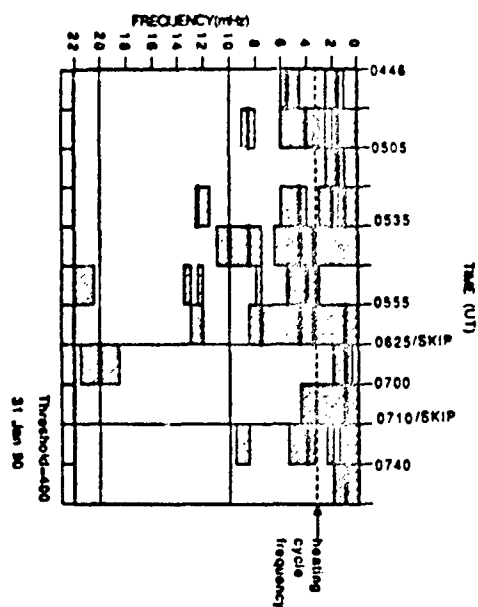


Figure 6. Variation of peak spectrum power as a function of time for 31 January 1990.

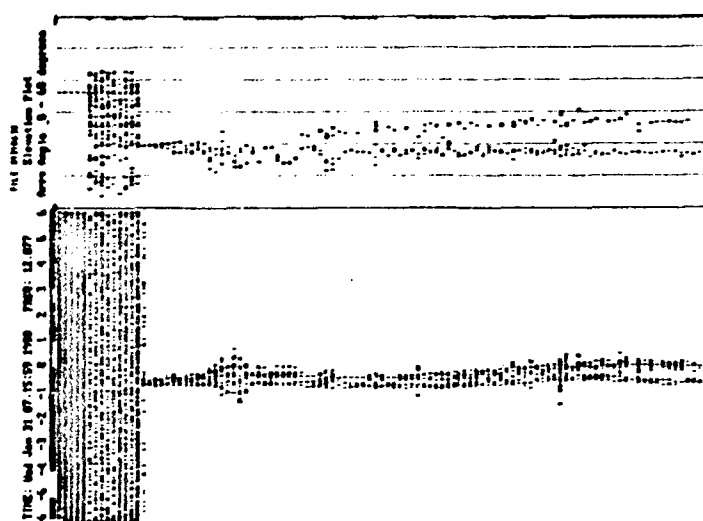


Figure 7. Time variation of spectrum of signal on Reference antenna for 31 January 1990 from 0633 to 0719 UT. The elevation angle is plotted for the strongest spectrum components.

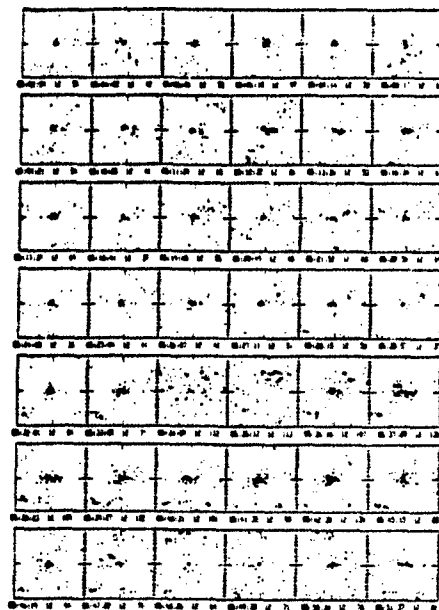


Figure 8. Composite of 42 skymaps for 31 January 1990 for the period 0502 to 0551 UT showing dynamic structure in the overhead ionosphere with periods down to 10 minutes.

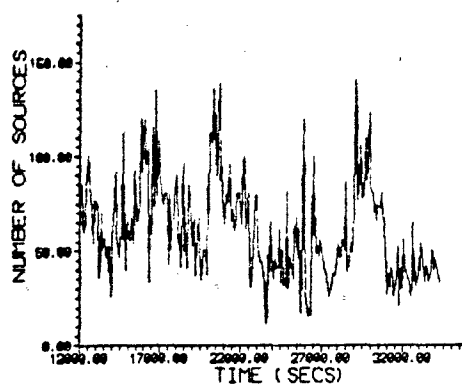


Figure 9. Variation of the number of sources as a function of time from 0320 UT to 0930 UT on 31 January 1990.

PAPER NO. 14C

## DISCUSSION

T. B. JONES, UK

If the effects are this small, do we really care?

## AUTHOR'S REPLY

Yes. If this is preliminary to 95 dBW systems which may be coming along, then I think we are in a region where things may become more serious.

W. GORDON, US

Antenna gains have been overstated in both papers (#5 and #14C) by 5 or 6 dB. 3 arrays of 4 x 6 dipoles if operated without losses will give maximum gain of 24 dB (This with  $-10^6$  W transmitters gives ERP of 84 dBW).

## AUTHOR'S REPLY

We have taken the word of TCI that the gains are as advertised. Wilenski [IEEE Trans. Broadcast., 34, No. 2, June 1988, pp. 201-209] claims a gain of 30.6 dBi at 1.35 times the design center frequency, see Table III of the reference.

## OBLIQUE HEATING OF THE AURORAL IONOSPHERE BY LF/MF TRANSMITTERS

P. S. Cannon

Applied Ionospheric Physics, Flight Management Department,  
Royal Aerospace Establishment,  
Farnborough, Hampshire GU14 6TD, United Kingdom

M. J. Rycroft

College of Aeronautics,  
Cranfield Institute of Technology,  
Cranfield, Bedford MK43 0AL, United Kingdom

T. Turunen

Sodankylä Geophysical Observatory,  
Sodankylä, SF 99600, Finland

### SUMMARY

The paper describes the generation of ELF signals due to oblique heating of the auroral ionosphere by signals from ELF modulated LF/MF radio transmitters. Apart from signals of natural origin, timing signals (six pips which occurred on the hour) were received. The pips of frequency 1 kHz, duration 105 ms and field strength  $\sim 0.1$  pT exhibit a favoured source location  $\sim 150$  km south-south-east of Sodankylä. The pips are shown to occur only when there is significant local magnetic activity and when the auroral electrojet is enhanced. The originating signals are demonstrated to be of Soviet origin and due to LF/MF broadcast transmitters several hundred kilometres away from the ELF source location. Various mechanisms which could account for a localised generation region far from the transmitters are discussed. The favoured mechanism involves in-phase heating due to two or more transmitters.

### 1 INTRODUCTION

Eleven years ago (14 March to 4 April 1979), close to the peak of the previous sunspot cycle, a network of ELF/VLF goniometer (direction finding) receivers was operated in Northern Scandinavia. These receivers were designed to be sensitive to whistlers and chorus which occur in these frequency bands. Apart from these signals of natural origin, 6 pips, which occurred on the hour, were also sometimes received. The pips had a frequency of 1 kHz and each lasted 105 ms. On some occasions distorted music was heard prior to the pips.

Turunen *et al* (1980), Cannon (1982) and Cannon *et al* (1982) presented evidence that these pips were propagating ELF signals produced by a nonlinear demodulation mechanism in the auroral E and D regions. The distorted music was used to identify the signals as Soviet LF and MF transmissions which could have originated from a number of stations. Table 1 and Fig 1 describe the most powerful of these candidate transmitters within a 1500 km radius of Sodankylä. Stubbe and Kopka (1977) and Cannon *et al* (1982) showed that the ELF field strength is related to the auroral electrojet current density which is expected to be statistically higher during periods of high geomagnetic activity (see also Barr and Stubbe (1984)). Such were the conditions 11 years ago. This paper reviews the phenomenon of oblique heating of the auroral ionosphere as identified in those earlier papers.

**Table 1**  
**Candidate transmitters**

LF transmitter Location	Geographic coordinates of transmitter	Power (kW)	Frequency (kHz)
Kaliningrad	54° 45'N 20° 30'E	1000	173
Moscow	55° 45'N 37° 38'E	500	173
Syktyvkar	61° 41'N 50° 31'E	300	173
Leningrad	59° 59'N 30° 21'E	1000	236
Moscow	55° 45'N 37° 08'E	2000	263
Minsk	53° 54'N 27° 34'E	500	281
Minsk	53° 54'N 27° 34'E	1000	549
Murmansk	68° 58'N 33° 56'E	50	657

## 2 EXPERIMENTAL CONFIGURATION

Three different types of equipment were used in the study. Bullough and Sagredo (1973) describe the ELF/VLF goniometer (direction finding) receivers used near Sodankyla (Finland), near Tromsø (Norway) and near Arjeplog (Sweden). All goniometer receivers operated between 19 and 00 UT over the period 14 March to 1 April 1979 inclusive and from 20 to 00 UT on 2, 3 and 4 April 1979. Additional scheduled recordings were made between 11 and 16 UT on 28 March 1979. Outside of these periods each station operated independently whenever feasible. Measurements were also made using an ELF/VLF receiver designed and built at the Sodankyla Geophysical Observatory and using a separate ELF receiver (Cannon, 1981). Pips were detected on all three types of instruments, but not on every hour. Noise at Arjeplog interfered with the measurements and precluded using these signals for detailed studies.

Several series of tests were carried out on the goniometer system to establish that the ELF pips were not the result of demodulation of LF or MF signals within the receiving system. The LF/MF signal strength was estimated and 173 kHz signals ~50 dB stronger than those predicted for Sodankyla were injected through a dummy ELF/VLF antenna. No demodulated output at 1 kHz was noted.

## 3 RESULTS

### *Pip occurrence*

Pips were found to occur when the geomagnetic activity was high, but not when it was low. In Fig 2 the number of occasions that pips were detected at either Sodankyla or Tromsø in one day are shown in the top panel. In the bottom panel the daily sum of the eight Sodankyla indices  $K_{40Z}$  are given. There is a strong positive correlation between pip detection and geomagnetic activity.

Fig 3 illustrates the number of times on each hour that pips were recorded at either Tromsø or Sodankyla. The period 15 March to 21 March 1979 has not been included because at no time were pips detected. The probability of hearing pips maximises in the evening sector; magnetic midnight at Sodankyla occurs at ~21:30 UT.

### *STARE and magnetometer analyses*

Goniometer measurements described below place the pip generation regions 20 minutes in longitude away from the STARE (Scandinavian Twin Auroral Radar Experiment) VHF coherent radar (Gjerwald *et al*, 1978) viewing window. The STARE window covers the region 68° to 72°N and 14° to 23°E. Notwithstanding this difference, the absence or detection of pips has been plotted on a compass projection (Fig 4) as a function of the electrojet direction determined by STARE. Each point is the

visual average of 50 individual vectors within the window; the error bars indicate the variation of vector direction within the window. The occurrence of the pips shows a high positive correlation with the eastward flowing electrojet.

Somewhat simplistically, positive bays in Sodankyla and Kiruna (Sweden) magnetometer data were interpreted as indication of a nearby eastward electrojet (Rostoker and Kisabeth, 1973). Similarly, negative bays were interpreted as due to a westward system. Pips were found to occur during both positive and negative bays; this does not corroborate the findings from the STARE analysis, where the correlation was with the eastward electrojet. It does, however, substantiate the view that a strong electrojet is needed for pip generation.

#### *Pip generation regions*

When the pip amplitude was high the goniometer receivers were used to obtain a bearing and an error on the source. When two bearings were available the source location was determined. Fig 5 shows the location of the triangulated source, together with the worst case envelope of standard errors determined from all bearings. All but one of the six triangulated source regions are located in a group to the south of Sodankyla.

#### *Field strength*

The mean pip field strengths were determined for each group of six pips (Fig 6). Field strengths at Sodankyla were higher than those at Tromsø - in agreement with the direction finding measurements which show a favoured source location close to Sodankyla. In general, on one night, variations of field strength observed at one station are mimicked by the other.

### 4 REVIEW OF EXPERIMENTAL RESULTS

It was established that the 1 kHz ELF pips received by three goniometer receivers were not the result of nonlinear demodulation of a strong broadcast service radio signal in any part of the receiving equipment. Two other instruments also received the pips. It was consequently proposed that these ELF pips of strength 0.1 pT were produced by nonlinear ionospheric demodulation of signals from one or more LF and/or MF transmitters.

Since all candidate transmission frequencies are <700 kHz, the ionospheric interaction must take place in the D-region or lower E-region.

The period of the experiment was characterised by two levels of local geomagnetic activity. During the period 14 to 21 March, when no pips were recorded, the daily sum of the  $K_{HPZ}$  indices at Sodankyla varied between 2 and 20. From 22 March to 4 April the corresponding values varied between 20 and 45 and, with the exception of 1 April, pips were recorded each day. Pips were, therefore, only recorded when the high latitude magnetic activity was high, i.e. when the ionospheric currents were strong. Analysis of STARE and magnetometer data corroborate this view.

The probability of pip occurrence was greatest in the local evening, between 19 and 20 UT (around 22 MLT) and, on a number of occasions, the source location was determined. On most of these occasions they fell south-south-east of Sodankyla at a distance of ~150 km.

### 5 INTERPRETATION

Most ionospheric heating experiments utilise a vertically incident wave from a high gain antenna in order to produce a localised hot spot overhead. The cause of the ELF pips has, however, been identified as LF/MF transmitters located several hundred kilometres distant from the generation region. It is reasonable to suppose that the LF/MF antennas are low gain, capacitively loaded verticals, the radiation pattern of which will be vertically polarised and omni-directional in azimuth. The main lobe may be expected to occur at 10 to 20 degrees elevation. Any heating mechanism must, therefore, explain how a distant localised region of the ionosphere could be heated preferentially to all others. Additionally, any proposed theory must explain why the five triangulated pip sources were approximately co-located. Four mechanisms were considered.

**Mechanism one**

In this model consider the LF/MF wave propagating from the south and incident directly (no reflections) upon an electrojet flowing essentially east-west. No reflections are assumed. Demodulation might then occur on the southerly edge of the electrojet, where there is adequate current flow but low radio wave absorption, thus allowing the incident wave to attain the electrojet altitude. Primarily, however, localisation of the generation area will be in latitude. Localisation in longitude will only occur as the result of the fall off in field strength with distance. Additionally, the distance from the transmitter to each element of the electrojet is different from that of the neighbouring elements. Consequently, each element will be out of phase with its neighbour and it is difficult to visualise how a localised, and coherent, ionospheric radiator could be formed.

**Mechanism two**

In this mechanism (Fig 7) a single transmitter is also considered, but the possibility of waves multiply reflected from the ground is considered. In certain regions the periodic heating effect of a wave having suffered  $m$  reflections may be in phase with the periodic heating of a wave having suffered  $n$  reflections ( $n \neq m$ ). In a homogeneous ionosphere, with planar geometry, a pattern of heated rings (hot rings) concentric with the transmitter would result. Localised demodulation would be expected to occur where the electrojet and the hot rings overlap. Demodulation would be forbidden within a cold ring.

**Mechanism three**

For the third mechanism (Fig 8) two transmitters are considered such that the modulated signal is broadcast with some constant phase difference which could be zero. This is the same situation that pertains in hyperbolic navigation systems. Lines defining equal phase will occur. A localised demodulation region will exist where a hot strip, due to in-phase heating, overlaps the electrojet.

**Mechanism four**

If three or more phased transmitters exist, then a set of hot spots will occur where the signals from all the transmitters are in phase (Fig 9). A fixed demodulation region is now defined by the crossing of one of these hot spots by the electrojet. Only a finite number of locations now exist, in contrast to mechanisms two or three.

Mechanisms three and four do not require that the transmitters use the same carrier frequency or have the same carrier phase - only the modulation frequency needs to be phased. It is reasonable to suppose that this is so for the transmission of timing pips. It is important, however, for a mechanism involving several transmission frequencies that the transmitters are not greatly separated in frequency. Otherwise their reflection and interaction with the ionosphere may take place at different altitudes and their effects cannot be aggregated.

**6 DETERMINATION OF MECHANISM**

The mean distance of each generation region from the principal LF/MF Soviet transmitters, within 1500 km of Sodankyla, are given in Table 2. The mean generation to transmitter distances  $d_1 - d_6$  are also given. Evidently,  $d_1 - d_2 - d_3 - d_6$  which suggests generation via mechanisms three or four. The Syktyvkar transmitter ( $d_6$ ) is, however, of lower output power than the others under consideration. The analysis of variance and Fisher's F-distribution were used to determine the probability that the various distances could be considered to be samples of the same population, i.e. represent estimates of the same mean distance. The transmission schedule on 173 kHz best fits the detection of pips and the above test was applied to the transmissions from Kaliningrad and Moscow. This showed that as large a difference as 30 km ( $d_1 - d_2$ ) would occur with a probability of  $p = 0.4$ . This discrepancy is hardly significant, lending support to mechanism three. If the powerful transmitters at Minsk are also included then the probability reduces to  $p = 0.2$ . We conclude from this that a type four mechanism is less probable than a type three mechanism; however, its probability is far from insignificant.

**Table 2**  
**Transmitter to generation region statistics**

Transmitter	Kalinlingrad	Moscow	Minsk	Leningrad	Murmansk	Sykttyvkar
Transmitter frequencies and powers	173 kHz 1000 kW	173 kHz 500 kW  263 kHz 2000 kW	281 kHz 500 kW  549 kHz 1000 kW	236 kHz 1000 kW	657 kHz 150 kW	173 kHz 300 kW
Date	Mean distance from transmitter to crossing point, on each day					
Time (UT)	(km)					
22.3.79 19	1309	1279	1351	697	409	1238
26.3.79 19	1302	1280	1347	695	418	1245
27.3.79 20	1350	1321	1397	743	377	1256
29.3.79 22	1608	1736	1743	1136	521	1616
31.3.79 19	1260	1214	1284	630	458	1212
31.3.79 20	1403	1380	1457	805	345	1284
Mean distance to each transmitter (km)	d1 = 1325 ± 54	d2 = 1295 ± 61	d3 = 1367 ± 64	d4 = 714 ± 65	d5 = 401 ± 43	d6 = 1247 ± 26

29.3.79 was omitted in the determination of each mean

## 7 CONCLUSIONS

In this paper we have reviewed data which lead us to believe that Soviet LF and MF broadcast transmissions were demodulated in the high latitude ionosphere and that re-radiation took place at 1 kHz. The transmissions on 173 kHz were identified as the most likely candidates. Further experiments are required to investigate fully this chance discovery, and it may be that the phenomenon could provide a cheap hourly measure of the electrojet latitude over Finland.



## 0 REFERENCES

- Barr, R. and Stubbs, P. ELF and VLF radiation from the polar electrojet antenna, *Radio Sci.*, 19, 4, pp 1111-1122 (1973)
- Buttough, K. and Segredo, J.L. VLF goniometer observations at Halley Bay, Antarctica-1. The equipment and measurement of signal bearing, *Planet. Space Sci.*, 21, pp 899-912 (1973)
- Cannon, P.S. A ground based investigation of high latitude ELF radio signals, Ph.D. Thesis, University of Southampton, UK (1981)
- Cannon, P.S. Ionospheric ELF radio signal generation due to LF and/or MF radio transmissions: Part I Experimental results, *J. Atmos. Terr. Phys.*, 44, pp 819-829 (1982)
- Cannon, P.S., Turunen, T. and Rycroft, M.J. Ionospheric ELF radio signal generation due to LF and/or MF radio transmissions: Part II Interpretation, *J. Atmos. Terr. Phys.*, 44, pp 831-841 (1982)
- Greenwald, R.A., Weiss, W., Nielsen, E. and Thomson, N.R. STARE: A new radar auroral backscatter experiment in Northern Scandinavia, *J. Geophys. Res.*, 13, pp 1021-1039 (1978)
- Rostoker, G. and Kisabeth, J.L. Response of the polar electrojets in the evening sector to polar magnetic substorms. *J. Geophys. Res.*, 78, 5559 (1973)
- Stubbs, P. and Kopka, H. Modulation of the polar electrojet by powerful HF waves, *J. Geophys. Res.*, 82, 16, pp 2319-2325 (1977)
- Turunen, T., Cannon, P.S. and Rycroft, M.J. Generation of ELF radio signals in the auroral ionosphere by non-linear demodulation of LF and/or MF transmissions, *Nature*, 286, pp 375-377 (1980)

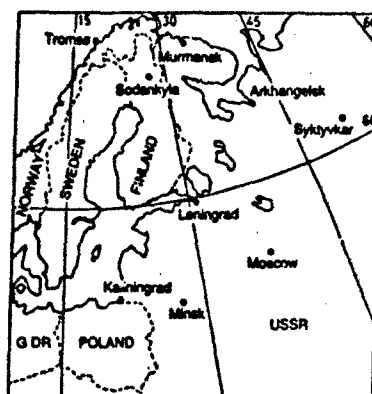


Fig 1 Mercator projection of Scandinavia and North Western USSR showing the major Soviet high power LF and MF broadcast stations within 1500 km of Sodankyla

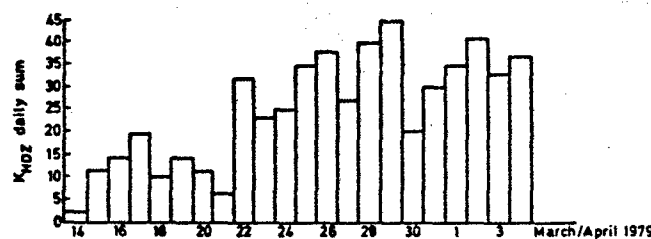
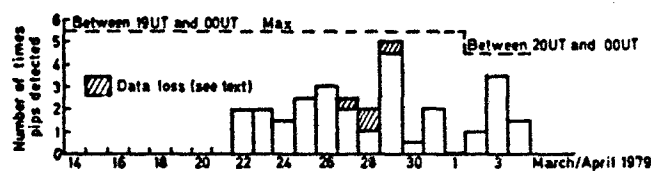


Fig 2 (a) Daily variation of pip occurrence. Shaded areas indicate that data were lost for one or more hours during the day's schedule and show the maximum number of times that pipe might have been detected. (b) Daily geomagnetic activity at Sodankyla

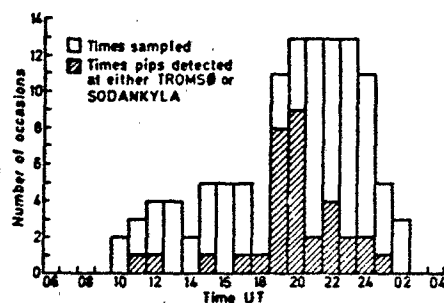


Fig 3 Diurnal variation of pip detection

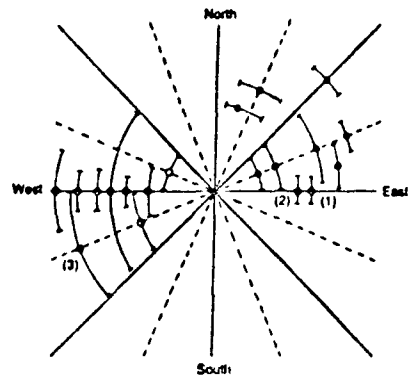


Fig 4 Absence or detection of pips, as a function of the average electrojet direction within the STARE viewing window (geographic coordinates). The radial distance of each point from the intersection of the axes is of no significance.

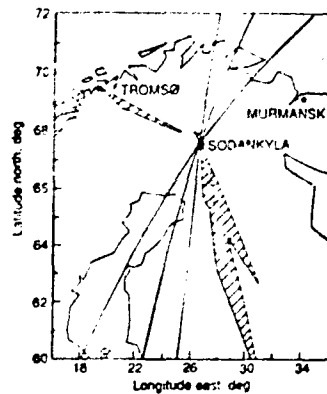


Fig 5 Cartesian projection of Northern Scandinavia showing the positions (O) of the sources in the ionosphere, of the 1 kHz pips together with the worst case error envelope (hatched area). Additionally three bearings from Sodankylä with 180° ambiguity and a typical error of -6° are shown.

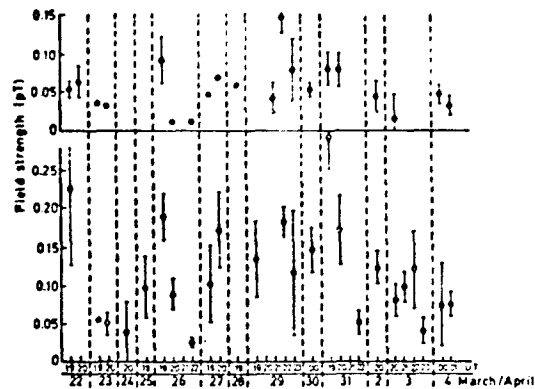


Fig 6 ELF pip field strength at Tromsø (e) and Sodankylä (O)

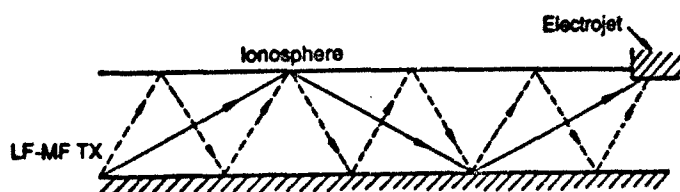


Fig 7 Mechanism two, employing multiply reflected waves

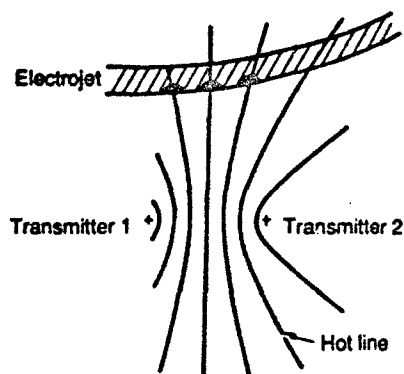


Fig 8 Mechanism three. Ionospheric demodulation occurs in a region (denoted as a) centered on the intersection of a hyperbola, defining the locus of equal phase modulation signals, and the auroral electrojet

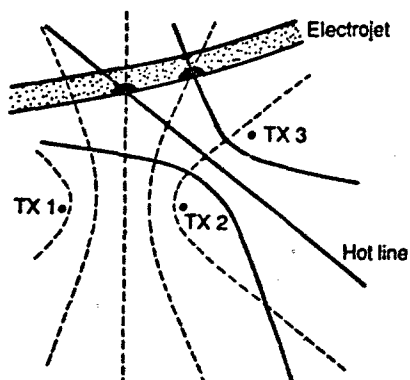


Fig 9 Mechanism four. Ionospheric demodulation occurs where the electrojet flows through a fixed hot region (denoted as a) defined by the intersection of two hyperbolae having equal phase modulation signals

DISCUSSION

M. RIETVELD, MO

Did you examine STARE data to see whether there were enhanced electric fields in the regions you deduced the sources to be?

AUTHOR'S REPLY

We did examine STARE data and found that pips were generated during periods when the electrojet flowed eastward rather than westward. STARE was unfortunately not operational over the whole of the experimental period. Additionally, we must remember that the STARE window lies several degrees to the west of the favored pip generation region.

R. BARR, UK

I was very impressed with this work when it first appeared in JATP, so much so that I have undertaken an extension of your experiment in Lindau, FRG. I am cross correlating the audio modulation signal from a series of powerful HF broadcast transmitters with the VLF signal, assumed to be coming from the ionosphere. I can see clear correlations at non zero time lag which support your claims of a real ionospheric effect rather than an equipment nonlinearity. I should also point out that at Lindau the electric field is probably an order of magnitude smaller than during your experiments.

AUTHOR'S REPLY

I am extremely pleased that you are pursuing further investigations into this phenomenon and I look forward to seeing your results.

U. S. INAN, US

I appreciated your comments concerning LF/MF heating being possibly more efficient than HF, especially in view of our new results concerning D-region heating produced by VLF (30 kHz) that is published in this month's GRL. Did you have any D-region diagnostics (such as VLF) during your experiments?

AUTHOR'S REPLY

No, we didn't. This phenomenon was discovered by chance with an instrumentation set designed for other purposes and no D-region measurement facilities were specifically deployed in association with the experiment. We were able, however, to utilize the Finnish meridional chain of riometers which provided us with much useful information.

## ARTIFICIAL IONOSPHERIC MIRRORS (AIM)

## A. Concept and Issues

Paul A. Kossey and John L. Heckscher  
 Ionospheric Physics Division  
 Geophysics Laboratory  
 Hanscom AFB, MA 01731-5000

Ramy A. Shanny  
 ARCO Power Technologies Inc.  
 1250 24th Street, N.W.  
 Washington, DC 20037

Edward C. Field, Jr.  
 Pacific Sierra Research Corporation  
 12340 Santa Monica Boulevard  
 Los Angeles, CA 90025

Abstract

This paper describes theoretical and experimental research on the creation, maintenance, and control of artificial layers of ionization in the 50-90 km altitude range. The focus of the research is to assess the potential for exploiting such so-called "artificial ionospheric mirrors" (AIM) as scatterers of radio waves to distances well beyond line-of-sight.

The AIM concept is discussed in terms of a specific technical approach, the use of ground-based, very high power, RF waves to breakdown the atmosphere. The concept is described in terms of RF requirements to produce breakdown, electron production and losses, resultant ionization densities, and their lifetimes. In addition, issues concerning the RF reflection properties of artificial patches of ionization in the atmosphere are considered, and the potential of exploiting the AIM concept for practical applications is introduced.

## 1. INTRODUCTION

The concept of the Artificial Ionospheric Mirror (AIM) involves the use of a ground-based radio frequency heater to create localized patches of ionization ("mirrors") in the atmosphere, which could be used as reflectors of radio signals for over-the-horizon (OTH) communication or radar purposes. The concept is revolutionary in that, rather than working within the limitations imposed on conventional systems by the natural ionosphere, it envisions seizing direct control of the propagation environment to insure that it has the electromagnetic wave reflection/scattering properties required to achieve a desired system capability. Many issues associated with the concept have already been defined and investigated, via theoretical research and laboratory chamber experiments, in both the United States and the Soviet Union.

The basic premise for the concept depends on the fact that when free electrons are immersed in an imposed electric field they accelerate. If the electric field is strong enough, or if the electrons can accelerate for a sufficiently long time, the electron velocities can become large enough that subsequent collisions with neutral particles involve energies exceeding the neutral's ionizing potential, thus producing additional free electrons. If the resultant electron production rate exceeds the loss rate, the net electron density increases, i.e., artificial ionization builds-up.

## 2. AIM GENERATION BY CROSSED AND FOCUSED BEAMS

A serious problem that can limit the production of artificial ionization in the atmosphere is self-absorption of the powerful radio wave pulses used to produce the ionization. This effect (often referred to as "tail-erosion") is produced by ionization that is formed along the pulse propagation path, especially at heights below where the desired layer of ionization is intended to be produced. In order to avoid such self-absorption effects, two basic approaches have been receiving attention in recent research efforts; crossed radio beams and focussed beams.

## 2.1. Crossed-Beam Approach

The crossed-beam approach (Figure 1a) has been pioneered by the Soviets since the late 1970's, as described in the seminal papers by Gurevich (1979) and Borisov and Gurevich (1980). The approach is simple: instead of using discrete, powerful radio wave pulses, dual multiple-pulse beams are proposed. Only in the intersecting region of the crossed-beams are the field-strengths sufficient to produce ionization. Thus (in theory), the location and height of the region of artificially produced ionization can be precisely controlled.

In the crossed-beam approach the electric fields of the two beams interfere in the region where they intersect; and, since the ionization rate depends very strongly on the electric field strength, the ionization produced in the intersecting region is intense where the beams interfere constructively and weak where they interfere destructively. The ionization pattern in the intersecting region is illustrated by the dark bands in Figure 1b, where it is assumed that two beams of width  $\Delta$  and wavelength  $\lambda$  intersect at an angle  $\theta$ . The ionization bands are much thinner (approx.  $0.2\lambda/\theta$ ) than the spaces between the bands (approx.  $2\lambda/\theta$ ), because substantial ionization is produced only near the peaks of the constructive interference pattern.

In addition to theoretical work on the crossed-beam approach, extensive laboratory chamber experiments have been conducted in the Soviet Union and the United States to investigate various characteristics of such artificially produced ionization. One such example from the Soviet literature (Vikharev et al., 1984) is illustrated in Figure 2, which shows that the structure of the ionization produced in the beam intersection region depends greatly on atmospheric pressure, i.e., on the altitude at which the AIM layer is to be produced. Such "altitude" issues are further discussed later in this paper.

## 2.2. Focussed Beam Approach

The use of a focussed antenna array (Figure 3), to control the location and altitude of artificially produced ionization in the atmosphere, has been the subject of theoretical and numerical research efforts in the United States. In contrast to an unfocussed array, for which the power density profile from the heater falls off as  $R^{-2}$  with altitude (thereby favoring ionization at lower heights), a focussed array can produce a power density profile which peaks sharply at a desired altitude. To what degree this can be accomplished is illustrated in Figure 4, which illustrates the vertical pattern of a 300 MHz array whose elements have been phased for focussing at 70 km. The array has 200,000 elements and a total width and length of 2000 wavelengths. The peak of the pattern equals that of the  $R^{-2}$  dependence. As shown later, the very sharp rise in the electric field at the ionization altitude creates a high peak density and steep density gradients, which are attractive in terms of radio wave reflection issues.

Whatever approach is taken to produce artificial layers of ionization in the atmosphere, there are many technical and practical issues associated with the AIM concept. For example, what are the heater power requirements, how do they vary with heater frequency and the desired altitude of the patches, what are the resultant electron densities, what are the obtainable patch sizes, lifetimes, and radio wave reflection properties, etc. Theoretical and experimental investigations of many of these issues, being conducted in the United States and the Soviet Union, have not uncovered any physics "show-stoppers" to undermine the basic concept. Nevertheless, more research is needed to properly assess its overall viability in terms of realistic communication and/or radar system applications.

## 3. AIM HEATER POWER REQUIREMENTS

In the scientific literature there seems to be no unique definition of "breakdown". For example, Gurevich's (op.cit.) definition essentially refers to the case when electrons are produced by the incident wave faster than they go away via attachment. On the other hand, most laboratory chamber experiments define breakdown to occur when the incident wave is reflected from the ionization it has created; i.e., the breakdown field is defined to be that which causes the plasma frequency to become equal to the wave frequency during the breakdown pulse's lifetime. Whatever the definition used, however, the power requirements to produce artificial ionization in the atmosphere from ground-based heaters are very large. For example, in his theoretical treatment of the physics of RF breakdown of the atmosphere, Gurevich (op.cit.) illustrates that two-crossed 1 GHz beams, from 11 gigawatt (peak-power) transmitters using 100 m diameter antennas, could produce sufficient ionization at 50 km altitude to reflect a 300 MHz signal. In a later theoretical paper, Novikov and Sergeichev (1982) used focussed 5 GHz crossed-beams to produce sufficient ionization at 70 km to reflect a 1 GHz signal. In their case, "only" 100 MW peak-power was required for each transmitter, but 400 m diameter antennas were specified.

For illustrative purposes, it is of interest to cast the issue in terms of the effective-radiated-power (ERP) required of a heater to produce a desired electron density at a given altitude. Figure 5 does this for a specific set of parameters, assuming a focussed-array approach is used (see Section 2.2) to produce the ionization. Shown are the ERPs required to produce  $1.6 \times 10^{17}$  electrons/cm<sup>3</sup> in 10  $\mu$ sec, as a function of heater frequency and altitude.

Although the curves show that for a given altitude, the ERP requirements decrease with decreasing heater frequency, practical considerations may force the use of much higher heater frequencies to exploit the AIM concept. For example, for 70 km altitude, the ERP required for a 30 MHz heater is about 138 dBW, while the ERP required for a 300 MHz heater is about 153 dBW, 15 dB more. Nevertheless, the use of a 300 MHz heater may be much more practical than the use of a 30 MHz heater. For example, even assuming an antenna gain of 30 dB at 30 MHz (no small achievement itself), a peak transmitter power of 108 dBW would still be required to produce the desired ionization. To put this in some perspective, it should be noted that 60 dBW peak powers are considered very large for HF systems today. At 300 MHz, however, antenna gains of 60 dB or more can be achieved using large arrays, thus leaving a peak power requirement of about 80 dBW (100 MW) to be realized. Although this peak power is still large, the average power requirements for

a communication or radar system may be more on the order of 1-10 MW and thus tolerable. In a like manner, even larger antenna gains are achievable at higher microwave frequencies; and, although the corresponding peak power requirements to achieve breakdown at those frequencies are very large, ongoing advances in high power microwave source development may lead to practical possibilities in achieving them in the foreseeable future.

#### 4. AIM PLASMA FORMATION

Numerical studies have been made of the microwave breakdown of air through avalanche ionization for both the crossed- and focussed-beam approaches discussed above. The result of one such simulation, for a focussed beam, is illustrated in Figure 6. In the example a 300 MHz heater with an ERP of 156 dBW was assumed to be initially focussed at 71 km altitude, and the formation of a one-dimensional ionization profile, made by a 10  $\mu$ sec pulse, was calculated. The result illustrates a long pulse effect, (termed "clamping") that increases the gradient of the ionization layer.

To describe the phenomenon, it is useful to first define a critical power density,  $S_c$ , as the value at which ionization can first occur at a particular altitude. As the long pulse propagates upwards in the atmosphere and ionization takes place, self-absorption of the pulse decreases the field strength in the pulse. Moreover, the areas with the highest induced electron density will absorb more of the pulse. Eventually, the area of peak ionization will absorb so much of the pulse that the remaining power density will fall below  $S_c$ . At this point, further ionization can only occur below and in front of the point of peak electron density. This moves the electron density peak down vertically with time, bringing it closer to the point where the unattenuated power density is  $S_c$ . Figure 6 shows the formation of a one-dimensional profile made by the 10  $\mu$ sec pulse, at 1.5  $\mu$ sec time samples. Also illustrated in the Figure is the reduction in heater power density as the newly created electrons absorb the incident field. Examination of the Figure shows that for this case  $S_c$  is approximately 42 dBW/m<sup>2</sup>. Moreover, when the power density has attenuated below that value, at about 70.5 km, there is no further ionization at that altitude.

The gradient of the electron density profile is dependent on the slope of the heater antenna's array factor near the initial breakdown point and the heater frequency. A steeper slope in power density creates a corresponding sharper electron density gradient along with a higher peak in the electron density profile. Parametric studies show a linear dependence between the power density slope and the resulting electron density slope. Since self-absorption or attenuation goes down as the heater frequency is increased, a higher frequency will produce a greater electron density before the clamping phenomenon occurs and a steeper gradient as well. As shown later, such large gradients are attractive in that they help to reduce the absorption of communication or radar waves reflecting off AIM layers.

#### 5. AIM ALTITUDE CONSIDERATIONS

There are many trade-offs to be considered in choosing the altitude for an artificial ionospheric mirror. In addition to the heater power requirements outlined above, issues associated with the lifetime, stability and radio wave reflection and absorption properties of the ionization must also be considered. Potential communication and/or radar system issues may impact significantly on such considerations, as well. Most Soviet and U.S. AIM research have concentrated on issues associated with ionization produced in the 50-90 km altitude range, for the reasons outlined below.

##### 5.1. AIM Lifetime Issues

At 50 km, since the electron densities that can be practically created are many orders of magnitude less than the neutral density, the formation and evolution of the ionization layers are not expected to be subject to the dynamic motions and plasma instabilities often encountered in plasma physics. The very high electron-neutral collision frequencies at the lower altitudes, however, result in very short electron lifetimes owing to attachment processes. Above about 85 km, the electron lifetimes are much longer but the diffusion of electrons out of the wanted region of ionization may become important, and the potential for triggering the deleterious plasma motions and instabilities mentioned above greatly increases.

Regardless of altitude, one way to insure sufficient AIM lifetimes is to develop techniques to "maintain" the ionization. One possible approach is illustrated in Figure 7, which diagrams the establishment and maintenance of a layer of ionization that always exceeds a minimum density  $N_{MIN}$ , which corresponds to some desired plasma frequency. For purposes of discussion, the amplitudes of the ionizing pulses are kept at a constant level. The first pulse--the "establishment" pulse--is maintained for a time  $\tau_{EST}$ , during which the ionization is raised from its ambient density  $N_0$  to a value  $N_{MAX}$ , which exceeds somewhat the required plasma density  $N_{MIN}$ . After the establishment pulse is turned off, the density drops in a time  $\tau_D$  from  $N_{MAX}$  to  $N_{MIN}$ , at which point a "maintenance" pulse is turned on for the time  $\tau_M$  needed to again achieve the density  $N_{MAX}$ . That cycle of ionization and deionization is repeated to maintain the layer. The deionization time  $\tau_D$  is usually much longer than the maintenance pulse width  $\tau_M$ , so the duty fraction can be very small, and the average power can be much less than the peak power.



Depending on application, it may not be necessary to "maintain" the AIM ionization at all; i.e., the natural lifetime of the AIM ionization may be sufficient that the mirror can be used as a radio wave reflector while the heater is turned off. For example, it is estimated from Lefavrier (1964) that electron lifetimes at altitudes above about 70 km should be greater than 0.5 seconds, which is sufficient time for a number of communication and/or radar applications. The possibility of using AIM ionization as a radio wave reflector while the heater is off also has important implications in terms of signal absorption issues, as discussed below.

## 5.2. AIM Absorption Issues

To illustrate the nature of the absorption losses associated with HF/VHF reflection from AIM layers, reflection coefficients were computed using so-called Epstein profiles to represent derived AIM profiles. The Epstein profiles used for the reflection coefficient calculations are illustrated in Figures 8a and 8b, along with the physically-derived AIM profiles they approximate. The use of the Epstein profiles is a convenience in that closed mathematical expressions can be derived for their reflection coefficients, as described in Budden (1961). Figure 9 summarizes the results of the reflection coefficient calculations, and illustrate dramatically the importance of having the AIM layers at relatively high altitudes. For example, Figure 9a shows that for AIM layers centered at 61 km (heater beam off), the reflectivity is extremely poor; while for layers centered at 72.5 km and 80 km the reflection losses are substantially less, as shown in Figure 9b and Figure 9c, respectively. In the latter case, the losses are really quite small, especially at the more grazing incidence angles.

Figure 10 shows reflection coefficients for heater beam-off and beam-on conditions for the layers of Figure 8b, centered at altitudes of 72.5 km and 90 km. As the graphs illustrate, leaving the heater beam on has a devastating effect on reflectivity, even at an altitude of 90 km. This is due to a very large (factor of 35 or more) increase in the electron-neutral collision frequency compared to beam-off (ambient) conditions (Borisov et al., 1988).

Other investigations indicate that, in order to further minimize signal absorption when AIM layers are used to reflect radio waves, it is important that the heater be capable of producing regions of ionization whose "depth" (i.e., the distance over which the plasma frequency changes from ambient to a sufficient level to reflect the incident wave) is short. In general the depth should be less than about 20-30 signal wavelengths, and the layers should be created at altitudes where the electron-neutral collision frequency is very small compared to the signal frequency. In addition, as shown above, it is also very important to be able to use the AIM layers as reflectors while the heater is off, to avoid catastrophic absorption losses.

As a result of such considerations, AIM layers should be centered in the 70-80 km altitude range in order to be useful for practical communication or radar applications. Even so, there are other issues that must also be resolved before the viability of the AIM concept can be fully investigated. Many of these have to do with factors which affect the structure and stability of the AIM layers, such as those associated with techniques to enlarge and shape AIM layers and by the effects of winds and shears on the resultant ionization.

## 6. ENLARGING AND SHAPING AIM LAYERS

Because of the very high ERPs that would be required to create AIM layers using a ground-based heater, it is certain that the heater antenna(s) would necessarily have very large gains. As such, the initial AIM patch would be very small, most likely much smaller than the size needed to reflect RF beams. For example, an AIM patch at about 60 km altitude would need to have a diameter of the order of 1 km to efficiently redirect an RF signal with a beamwidth of  $1^\circ$ .

The possibility of enlarging or "painting" an AIM patch arises out of the very low duty fraction required of a heater (crossed-beams or focussed array) to produce ionization at practical altitudes. For crossed-beams it is possible by slewing the beams to synthesize a mirror much larger than the beam diameter. The scheme is analogous to the raster used to synthesize television pictures. The layered structure produced by the cross-beam approach (see Figure 1) has prompted suggestions that Bragg reflection might enhance its effectiveness as a radio wave reflector. Although possible in principle, the practical problem of keeping the ionized layers parallel, especially if scanning beams are used to enlarge the ionization region, may be a formidable task. In addition, if the layers are produced and enlarged by antennas that have a limited capacity for movement, the foot-print of the RF reflections may be unduly restricted, much like those associated with RF reflections from meteor trails. Depending on the application, such restricted scattering may limit the usefulness of such AIM-based systems.

Enlarging an AIM patch size by electronically scanning a focussed beam heater array has inherent advantages over crossed-beam approaches. Numerical simulations show, for example, that by scanning such an array over about a 1 degree arc, and by increasing its frequency slightly throughout the scan (thereby effectively moving the focus of the antenna up) an ionization layer can be produced having a length of about 1 km and a tilt of about 45 degrees. Thus, in concept, it should be possible to produce a very large "tilted" mirror by scanning the array both horizontally and laterally as depicted in

Figure 11. Figure 12 shows the results of a simulation of this "frequency chirping" approach in the horizontal direction for the 300 MHz array having an ERP of 156 dBW that was discussed earlier in conjunction with Figure 6. In Figure 12, the heater is initially focussed at 70 km using a frequency of 300 MHz. Then, as the heater frequency is increased to 310 MHz, the location of the peak moves to approximately 71 km. Studies indicate that a full 1 km x 1 km patch could be achieved by the technique in about 100 milliseconds. Similar mirrors could be made in any direction, i.e., over a full 360 degree region above the focussed array using the approach. Such a capability makes it especially attractive for large area communication or radar coverage.

The concept of "painting" an AIM patch to control its size and electron density profile (and hence its RF reflection properties) is a very important one, which requires further investigation. It is certain that such painting will be needed if practical applications of the AIM concept are to be realized. There appears to be a number of painting techniques for generating artificial layers of ionization, depending on such factors as beam step-size, dwell-times, pulse lengths, peak power, single-or-multiple scans, etc. To date, however, relatively few comprehensive numerical details are available which can be used to adequately assess their overall viability. Especially lacking are sensitivity analyses of the numerous interrelated parameters that control patch-ionization characteristics, including whether (ultimately) a "mirror" can be created that will have the necessary spatial and temporal coherence for specific communication or radar applications.

#### 7. AIM PATCH MOTION, WIND SHEAR, AND TURBULENCE EFFECTS

The structure and stability of AIM layers also depend on such factors as winds, shears, and turbulence. The effects of winds on the frequency dependence of the reflections are especially important for radar applications which rely on Doppler processing for clutter rejection. The major factors to be considered include patch motion, wind shear, and turbulence, all driven by motions of the neutral atmosphere. It is not anticipated that motion of the patch, as a whole, will degrade the performance of most AIM-based systems. However, if a wind shear exists at the point where the patch is created, the patch will not only move, but will also be altered in orientation and shape. Because vertical shear is generally more severe than horizontal shear, it is expected to be the dominant source of shear-induced effects. In general, more research is needed to assess how such wind effects will impact the generation and control of artificial layers of ionization in the atmosphere. Needed are wind, shear, and turbulence data in the 70-80 km altitude range, over horizontal and lateral extents well under 1 km, and vertical resolutions of a few tens of meters, or less.

#### 8. AIM ENVIRONMENTAL ISSUES

Because of the very high transmitter powers required to produce artificial layers of ionization in the atmosphere, and because the any motion of atmospheric or ionospheric modification is correctly a sensitive one in general, a number of environmental issues associated with the AIM concept must be addressed. For example, the electromagnetic field strengths in the vicinity of the AIM heater must be assessed. In general, however, because both the crossed-beam and focussed-beam approaches produce very strong fields only at very high altitudes (in the breakdown region around 70 km, for example), it should be possible to insure that the field strengths in the vicinity of the heater(s) are below approved standards. Of course, interference with other RF users would have to be addressed as well. Another issue that has not been adequately addressed is one of the potential for collateral damage to space craft, such as satellites that may be passing above the heater while an AIM plasma cloud is being produced.

Even more important, perhaps, is the way in which the atmospheric breakdown could affect air chemistry. Recent Soviet and U.S. studies indicate, for example, that because of the very high ionization rates that are projected, large amounts of nitric oxide would be produced in the breakdown region of the atmosphere. Since it is established that such molecules act as a catalyst in the destruction of ozone, it is necessary to fully understand the altitude dependence of such effects. For example, what are the effects if the breakdown is produced at 70-80 km, compared to the effects if it is produced at 50 km, etc. To answer such questions comprehensive analyses of the production rates, loss mechanisms, and circulation of the excess nitric oxide from high altitudes down to the ozone layer must be understood and quantified. Although preliminary research shows that nitric-oxide synthesis for an AIM-cloud produced at appropriately high altitudes does not appear to be sufficient to be of environmental concern (Milikh, 1990), more detailed analyses of the issue is already underway in both the Soviet Union and the United States.

#### 9. AIM APPLICATIONS

Potential applications of artificial ionization regions as discussed in the Soviet literature include enhanced long-range communications and radar coverage, secure military communications in the presence of natural or man-made disturbed environments, radio reflectors for improved conventional high-frequency telecommunications, new satellite communications techniques, and controlled ionospheric modification for interference with transmissions through the disturbed region.

Recent U.S. efforts support the technical feasibility of creating artificial patches of ionization in the atmosphere which can be exploited to greatly enhance the capability to detect and track targets having very small radar cross-sections (Figure 13). The focussed beam approach to creating such layers appears especially promising for such applications, in that system configurations can be envisioned providing a capability to detect cruise missiles and other small targets over relatively large coverage areas.

#### 10. AIM PROOF-OF-CONCEPTS FIELD EXPERIMENTS

In some ways, AIM theoretical and numerical research, and laboratory chamber experiments to assess the viability of the AIM concept, are approaching a point of diminishing returns. The logical next step is to construct a prototype ground-based facility for atmospheric ionization research. Such facilities have been proposed and described in some detail in a number of recent Soviet technical articles. However, it is believed that no such facilities currently exist. Such a step would require a considerable investment of technical and financial resources.

Two approaches for field experiments are being investigated in the U.S. One would involve the use of the 300 m radio-telescope antenna at Arecibo, Puerto Rico (Figure 14a); the other would employ an array of as many as 50 twenty-four-meter dish antennas (Figure 14b) to ionize a 12-20 meter diameter spot at 70 km altitude and, with limited scanning, enlarge it ("paint") to about 200 meters in diameter. Neither concept has been fully analyzed, however, to adequately assess their technical merit or implementation costs.

#### 11. SUMMARY

The following summarizes the state of U.S. AIM related research and the direction it may take over the next few years:

- (1) In a general way, the technical feasibility of artificially ionizing the upper atmosphere has been proven.
- (2) Important practical system applications can already be envisioned. For example, in concept, an AIM based radar could be operated at a frequency chosen to optimize target detection, rather than be limited by prevailing ionospheric conditions. This, combined with the possibility of controlling the radar wave polarization to mitigate clutter effects, could result in reliable detection of cruise missiles and other low observable targets.
- (3) Comprehensive theoretical/numerical models, required for the detailed assessment of the AIM concept, have been developed and validated, in part, with experimental data obtained in high power RF experiments conducted in laboratory chambers. These are available to investigate the large number, and a wide variety, of complex interrelated physical and system parameters that must be understood and quantified in order to properly assess the technical feasibility and system desirability of the AIM concept.
- (4) Although there appear to be a number of techniques for generating artificial "mirrors", including the focussed-beam and focussed beam approaches discussed above, relatively few numerical details are available which can be used to adequately assess their overall viability. Especially lacking are sensitivity analyses of the numerous interrelated parameters that control patch-ionization characteristics, including whether (ultimately) a "mirror" can be created that will have the necessary spatial and temporal coherence for specific communication or radar applications.
- (5) In addition to the issues associated with the technical viability of the AIM concept, a number of potential environmental-impact issues have been identified. Although it is thought that these will not prove to be serious, because of the very high altitudes most likely to be associated with the AIM concept (above 70 km), they must be adequately analyzed and resolved before any field experiments of the concept are conducted.
- (6) Although they would require relatively large technical and financial resources, AIM proof-of-concept field experiments could be conducted using available technology.

#### REFERENCES

- Borisov, N.D., and A.V. Gurevich, "High-Frequency Pulsed Air Breakdown in Intersecting Radio Beams," Geomagn. Aeron., 23, 4(1983), 441-444.
- Borisov, N.D., A.V. Gurevich, and G.M. Milikh, Artificial Ionized Region in the Atmosphere, Moscow, 1986.
- Budden, K.G., Radio Waves in the Ionosphere, Cambridge University Press, New York, 1961.
- Gurevich, A.V., "Ionization of the Lower Ionosphere Under the Effect of Strong Radio Pulses," Geomagn. Aeron., 19, 4 (1979), 428-432.

LeVier, R.E., "Determination of the D-Layer Dissociative Recombination Coefficient From a High-Altitude Nuclear Explosion," J. Geophys. Res., 69, 3(1964), 481-485.

Milikh, G.M., private communication, 1990.

Novikov, V.D. and K.F. Sergeichov, "Optimum Conditions for Producing an Artificial Ionized Region in the Atmosphere by Intersecting Microwave Beams," Geomagn. Aeron., 22, 6(1982), 773-776.

Vikharev, A.L., J.A. Ivanov, and A.N. Steranov, "Decay of the Plasma of a Pulsed Microwave Discharge in Intersecting Wave Beams," Sov. J. Plasma Phys., 10, 4(1984), 460-464.

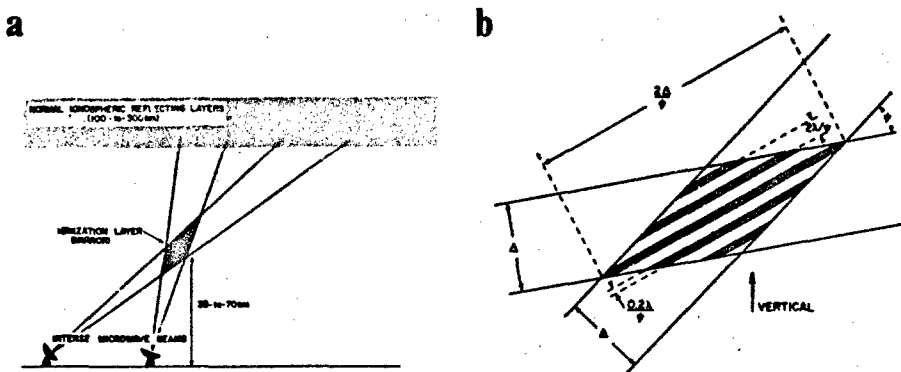
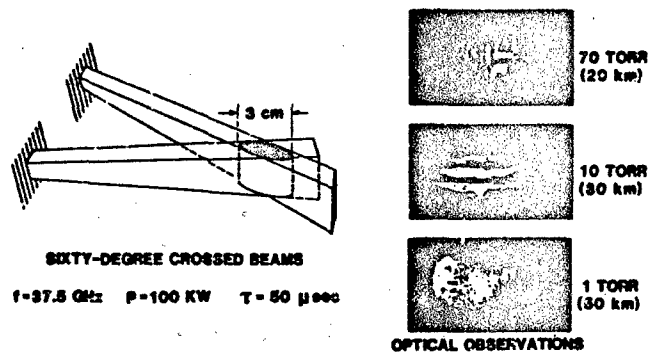


Figure 1. Schematic representation of the crossed-beam approach for generation and maintenance of an artificial ionospheric mirror; (a) concept, (b) layers of ionization resulting from interference pattern produced by intersecting beams.



(ref. VIKHAREV, et al, 1984)

Figure 2. Crossed-beam microwave laboratory chamber experiment.

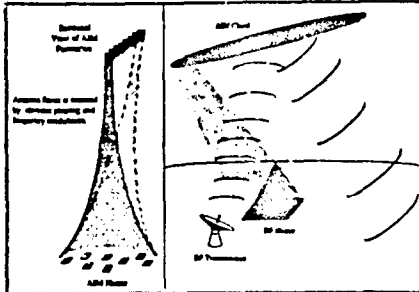


Figure 3. Focussed-beam approach for generating an artificial ionospheric mirror.

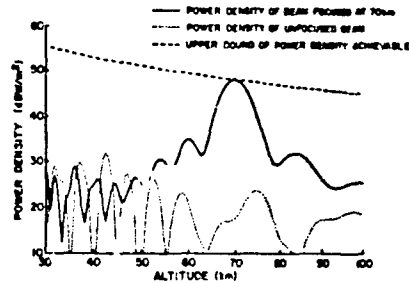


Figure 4. An array focussed at 70 km altitude.

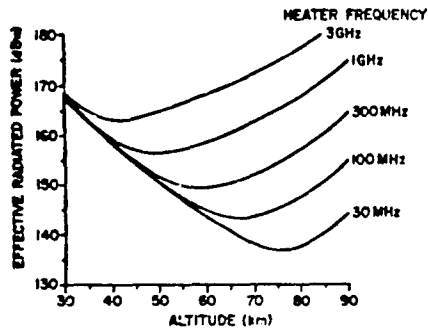


Figure 5. Effective-radiated-power requirements for useful ionization rates.

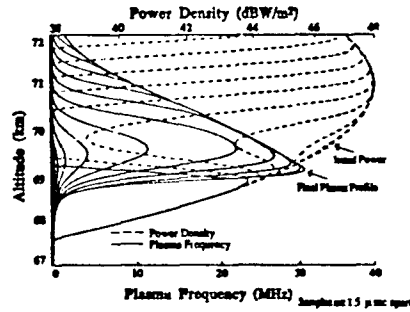


Figure 6. Evolution of an AIM cloud for a 300 MHz heater and a 10 microsecond pulse.

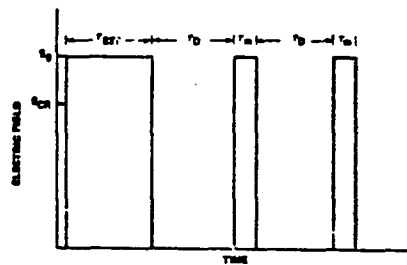
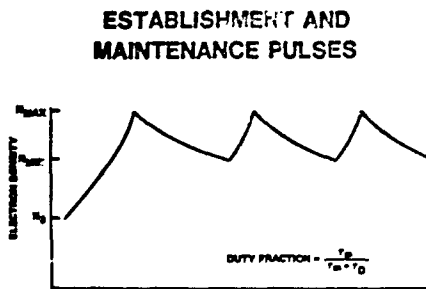


Figure 7. Control of ionization using establishment and maintenance pulses.

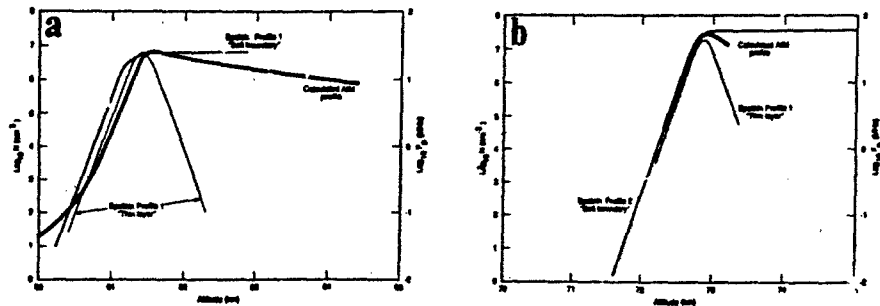


Figure 8. Epstein layers used to approximate calculated AIM profiles; (a) for an AIM layer peaking at an altitude of 61.4 km, (b) for an AIM layer peaking at an altitude of 72.5 km.

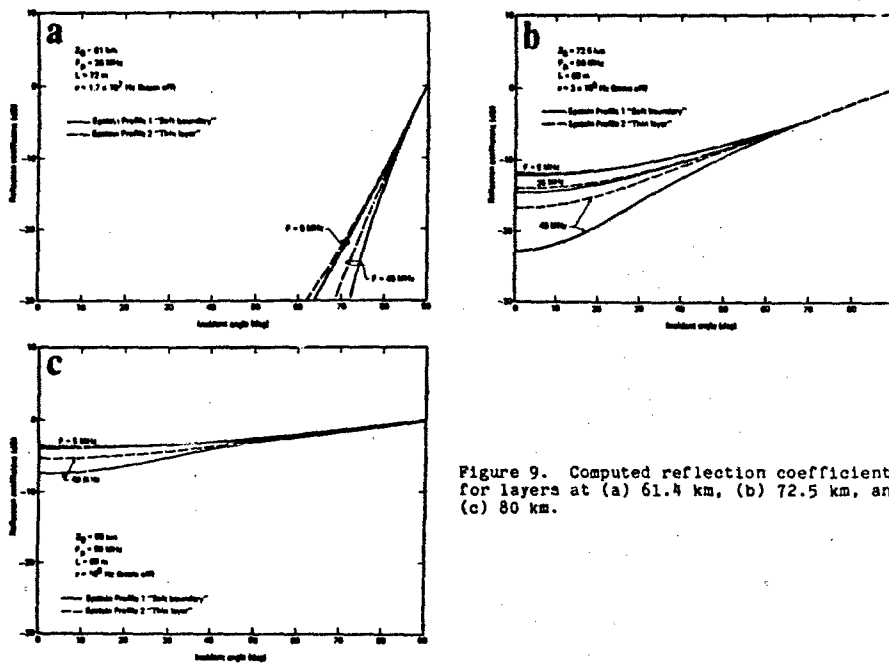


Figure 9. Computed reflection coefficients for layers at (a) 61.4 km, (b) 72.5 km, and (c) 80 km.

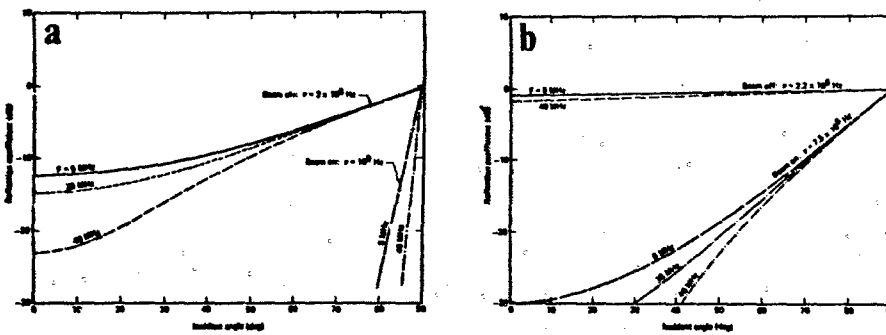


Figure 10. Comparison of reflection coefficients for beam-off and beam-on conditions; Epstein soft boundary model (a) at an altitude of 72.5 km, and (b) at 90 km.

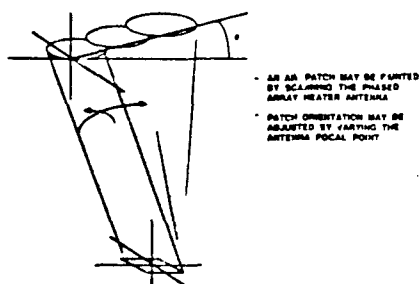


Figure 11. Concept of painting (enlarging) an artificial ionospheric mirror.

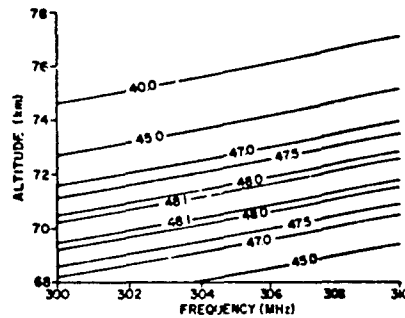


Figure 12. Power density ( $\text{dBW/m}^2$ ) contours of vertical scan with heater frequency.

### OTH RADAR APPLICATIONS

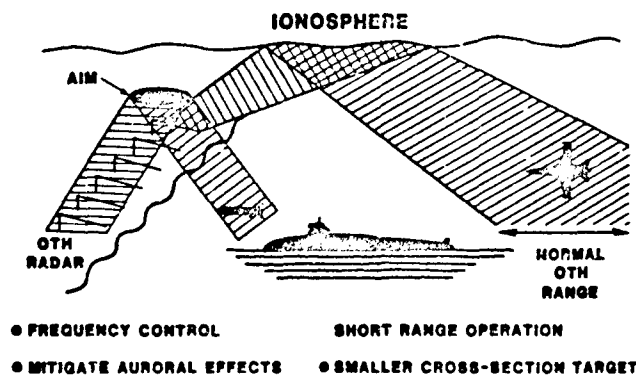


Figure 13. AIM over-the-horizon surveillance concept.

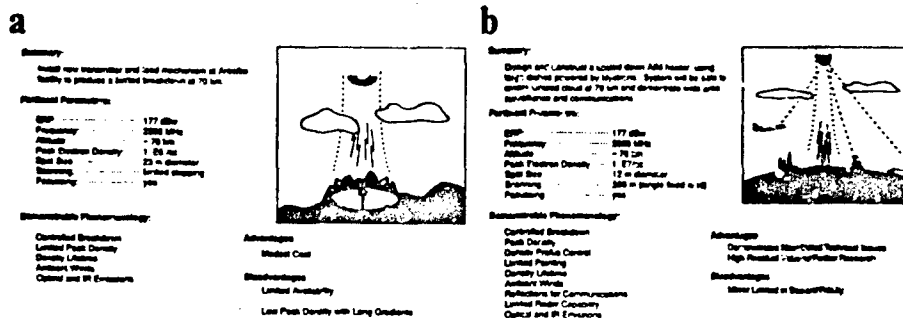


Figure 14. Potential AIM proof-of-concepts experiments; (a) focussed Arecibo dish antenna, (b) s-band array.

## DISCUSSION

A. FRASER-SMITH, US

The altitude range of interest (60-80 km) covers a wide range of electron attachment lifetimes. Above 70 km the lifetimes are measured in seconds, while below 70 km the lifetimes are likely to be measured in milliseconds. This will be an important factor in your choice of altitude for the mirror. What kind of lifetime are you hoping to achieve?

## AUTHOR'S REPLY

The answer has to do with the specific application envisioned. More specifically, however, we have been interested in a surveillance application in which 0.5-1 sec lifetimes are attractive (see paper no. 36). For that reason, the 70-80 km altitude range for the "mirror" is desirable. On the other hand, artificially produced ionization could provide a unique means for investigating ionospheric processes over the 40-90 km altitude range, which is a difficult region to study remotely, from the ground or space. For this application (a geophysical probe), measurements of ionization lifetimes themselves, including their altitude dependence and their temporal and spatial properties, would be of great interest.

J. BELROSE, CA

The speaker's reference to Canadian research requiring high power microwave beam powers is concerned, not with ionospheric/mesospheric breakdown, but with microwave powering of an aircraft for radio relay, flying at 22 km. The comment I wish to make, however, is that an additional item should be added to your list of difficulties associated with AIM, and that is the need to consider environmental effects. For focussed beam powers of 140-170 dBW, power densities outside the beam are also of concern, e.g., to aircraft flying near the microwave transmitter facility.

## AUTHOR'S REPLY

You are correct, and I would have taken a few minutes on environmental issues but for time limitations. Some of those issues have been considered (and they seem to be manageable), but a lot more needs to be done.

W. T. FLOOD, US

Have you considered the effects of tropospheric turbulence on your ability to focus an array of separate dishes? A fixed focus correction will not do it at GHz frequencies if the antennas are well-separated. Oblique incidence increases the path length in the troposphere, making the problem worse than at vertical incidence.

## AUTHOR'S REPLY

We have only begun to look at the problems associated with using an array of dishes for proof-of-concepts experiments. The issue you raise is valid, and must be considered in any detailed assessment of the technical viability of that approach.



# Physics of RF Breakdown for AIM Applications

K. Papadopoulos, T. Wallace, P. Vitello  
R. Shanny, K. Tsang, P. Lallement

ARCO Power Technologies, Inc.  
1250 24th Street, NW  
Washington, DC 20037 (USA)

## Summary

*Both a simple test particle approach and a complete kinetic calculation are used to predict the net electron production rate of an RF signal under conditions appropriate for an Artificial Ionospheric Mirror (AIM) system. These predictions are compared with each other and with experimental data and found to be in good agreement. The test particle based formula is incorporated into a model which calculates the one-dimensional vertical electron density profile created by a ground-based RF heater, and the performance of a baseline heater design is investigated, providing the foundation for the specification of a baseline AIM heater system.*

## 1. Introduction

Many telecommunications and radar surveillance systems rely on ionospheric reflection and refraction of RF signals. As a result, their performance is severely limited by the ambient ionospheric conditions and ionospheric variations. Many ionospheric modification experiments have been performed to develop an understanding of ionospheric behavior during RF heating and its influence on radio wave propagation. It has been found that heating of the ionosphere by high power radio waves results in strong nonlinear and self-action effects which influence the propagation characteristics of the radio waves as well as the state of the ionospheric plasma. The power densities produced in the ionosphere by the present generation of high power RF systems result in electron heating which affects the absorption and propagation of the RF waves by increasing the electron neutral collision frequency and spatially redistributing the electron plasma density (i.e. creating striations). However, the extent of the electron heating is not sufficient to increase the electron density by ionizing the ambient neutrals. The development of new high power RF sources now offers the possibility of controlling the level of ionospheric ionization and therefore its reflective and refractive properties. This is accomplished by initiating at the desired altitude and location a discharge similar to laboratory RF plasma discharges. The region of artificially enhanced ionization which is created is referred to as an Artificial Ionospheric Mirror, or AIM. In assessing the potential uses, engineering requirements, and projected costs of AIM facilities, a thorough understanding of the physical phenomenon of ionospheric breakdown is required. It is the purpose of this paper to present the physical foundations that describe the formation and control of artificial ionospheric mirrors.

## 2. Determination of Ionization Rates

### 2.1. Background

The most critical parameter in the description of breakdown processes is the value of the net ionization rate  $\nu_{net}$ , as a function of the incident RF power density  $S$ , frequency  $\omega$ , ambient neutral density  $N$  and gas composition. Although a large body of theoretical and experimental work exists on the subject of RF breakdown of air, a critical review of the subject (APTI Technical Report 5004, [1]) noted that most of the experimental results and their empirical extrapolations were not appropriate to the parameter range of interest to the AIM program. In fact, erroneous application of the empirical breakdown thresholds and ionization rates resulted in the past in major underestimates of the power requirements and the frequency optimization. On the other hand, analytic efforts by Gurevich and Borisov, et al. [2,3] resulted in substantial errors due to neglect of molecular dissociation processes. A comprehensive numerical kinetic computation was developed to calculate the ionization rates as a function of the local RF power density, frequency, and neutral density for parameters relevant to AIM. The code describes kinetically the electron energization by the incident RF and includes the most current values of cross-sections for elastic and inelastic processes. A brief description of the code is given in section 2.2, a more detailed discussion of the code and of its range of validity can be found in [1]. In section 2.3, the validity of the code is tested against the available experimental evidence. The results of the ionization rate computations are presented in sections 2.4 and

2.5. For concreteness' sake, section 2.3 focuses on the rates for a neutral density value of  $2 \times 10^{15} \text{ cm}^{-3}$ , which corresponds to an altitude of approximately 70 km. The ionization rates are generalized to other altitudes in the form of universal curves with the introduction of scaling parameters in section 2.5. Section 2.6 presents an analytic derivation of the ionization rates based on a test particle approach, compares them with the computational results, and discusses the underlying physics.

## 2.2. Kinetic Modeling

The kinetic calculation is based on the numerical solution of a differential equation for the isotropic portion  $f_0$  of the distribution function  $f(r, v, t)$  of a uniform weakly ionized plasma [2.4]. When the quiver energy is below the energy required for ionization, the isotropic portion of the distribution is responsible for all ionization which occurs; therefore, it is the form of  $f_0$  which determines the ionization rate. At quiver energies below 2-3 eV, the form of the isotropic portion of the distribution also determines the rate of collisions which excite optical resonances and cause dissociation, and the rate of collisions which result in attachment. Since these are the dominant energy and electron loss mechanisms,  $f_0$  may be used to accurately calculate the net rate of electron production. The differential equations governing the time evolution of  $f_0$  are [2]:

$$\frac{\partial f_0}{\partial t} = \frac{1}{2v^2} \frac{\partial}{\partial v} \left[ v^2 \left[ \delta v_m v f_0 + \left( \delta v_m \frac{kT}{m} + \frac{e^2 E_0^2}{3 m^2} \left( \frac{v_m}{v^2 + \omega^2} \right) \right) \frac{\partial f_0}{\partial v} \right] \right] - S_{0in} \quad (2.2.1)$$

$$S_{0in} = S_{0in}^{(1)} + S_{0in}^{(2)} + S_{0in}^{(3)} + S_{0in}^{(4)} + S_{0in}^{(5)} + S_{0in}^{(6)} \quad (2.2.2)$$

$$S_{0in}^{(1)} = -\frac{1}{2v^2} \frac{\partial}{\partial v} \left[ v^2 \left( \sum_k \frac{8 B_k N_k \alpha_k}{m v} \right) \left( v f_0 + \frac{kT}{m} \frac{\partial f_0}{\partial v} \right) \right] \quad (2.2.3)$$

$$S_{0in}^{(2)} = -\frac{2}{m v} \sum_k N_k \left[ (e + \epsilon_k) f(e + \epsilon_k) \sigma_k^{(2)}(e + \epsilon_k^{(2)}) - e f_0(e) \sigma_k^{(2)}(e) \right] \quad (2.2.4)$$

$$S_{0in}^{(3)} = -\frac{2}{m v} \sum_k N_k \left[ (e + \epsilon_k) f(e + \epsilon_k) \sigma_k^{(3)}(e + \epsilon_k^{(3)}) - e f_0(e) \sigma_k^{(3)}(e) \right] \quad (2.2.5)$$

$$S_{0in}^{(4)} = -\frac{2}{m v} \sum_k N_k \left[ (e + \epsilon_k) f(e + \epsilon_k) \sigma_k^{(4)}(e + \epsilon_k^{(4)}) - e f_0(e) \sigma_k^{(4)}(e) \right] \quad (2.2.6)$$

$$S_{0in}^{(5)} = -(N_{O_2} \sigma_{att}(v) + N_{N_2} \sigma_{att}(v)) v f_0 \quad (2.2.7)$$

$$S_{0in}^{(6)} = \sum_k \int_{v_{min}}^{\infty} N_k v^3 F_k(v, v') f_0 \sigma_{ion}(v') dv' \quad (2.2.8)$$

The set of equations (2.2.1-8) above are those which were solved numerically. The major assumptions required in the derivation of these equations are listed below:

- The quiver energy is below the threshold energy for the dominant loss processes, so rates of energy loss and electron production rates are determined by  $f_0$ .
- The plasma is locally uniform, and diffusion operates on much longer timescales than ionization, so transport may be neglected.
- The fractional ionization is low, so electron-electron and electron-ion elastic collisions, as well as electron-ion inelastic processes such as detachment and recombination, may be ignored.
- The number of molecules in excited states is low, so superelastic collisions are unimportant.
- The electric field is rapidly alternating, so the time-averaged field may be used.

In addition, in the implementation of the numerical solution, the neutral atmosphere was assumed to consist of molecular oxygen and nitrogen only, excluding other trace neutral constituents.

To solve the equations for the distribution function numerically, it is necessary to transform them into an equivalent set of equations on discrete time and energy (or velocity) grids. One method for performing this transformation is the finite-difference method; it may be developed very simply from the definition of the derivative. Because the equations to be solved are first-order in time, this will yield an equation for the distribution function at a given timestep in terms of the function at the previous timestep.

Modeling of ionization in the atmosphere is accomplished by setting the distribution function to its initial value, a Maxwellian at the ambient electron temperature, and calculating successive distributions by applying the finite-difference equation repeatedly. This will result in a time history of the distribution function, which may be integrated over velocity to give the electron density, and which may also be used to calculate average collision rates for momentum-transfer, attachment, and ionization.

The set of equations (2.2.1-8) may be approximated by a finite-difference equation of the form

$$\frac{f_0^{n+1} - f_0^n}{\Delta t} = (T + U) f_0^n \quad (2.2.9)$$

Here the continuous function  $f_0$  has been replaced by the vector  $f_0$ , a one-dimensional array which approximates the value of  $f_0$  at discrete energies; the time derivative has been replaced by its difference approximation; and the effects of the electric field and of collisions have been combined into the matrices  $T$  and  $U$ . The matrix  $T$  is a tridiagonal matrix representing the effects of the electric field, elastic collisions, and rotational inelastic collisions, all of which appear in the original equations as terms containing the first and second derivatives of  $f_0$  with respect to  $\epsilon$ . The other inelastic processes cause discontinuous changes in electron energies and cannot be represented in this way; their effects are combined in the upper triangular matrix  $U$ . This is a fully implicit equation because the operators representing the energy derivatives are applied to the value of  $f_0$  at the succeeding timestep; it is unconditionally stable and convergent to the solution of the corresponding differential equation.

A valuable check on the accuracy of the numerical simulation is to compute the energy balance. Because the cross-section for each process is available and the energy loss due to each event is known, the energy absorbed by each process may be computed on each timestep. The energy lost by the electric field may also be computed and compared to the sum of the energies absorbed. Agreement between the two totals was excellent, typically with errors less than 0.1%.

### 2.3. Comparison of Kinetic Computations and Experimental Data

Deriving ionization rates from the experimental observables is, with the exception of one recent experiment (Hays et al. 1987), a convoluted process which involves a great degree of uncertainty. The most relevant data are derived from pulsed experiments [5-9]. In these experiments, the ionization rate is computed by fixing the power density and increasing the pulse length until "breakdown" occurs. Two definitions of breakdown are used:

- when the ratio of the final to the original electron density is:

$$\frac{n_e(t)}{n_e(t_0)} = 10^3 \quad (2.3.1)$$

- when the electron density reaches the critical density (i.e. the plasma frequency equals the wave frequency):

$$n_e(t) = 1.2 \times 10^8 f^2 \quad (2.3.2)$$

The ionization rate  $\nu_{\text{net}}$  is then computed by assuming that over the pulse length the electron transport or other losses are negligible and that the ionization rate is independent of time, so that

$$n_e(t) = n_e(t_0) \exp(\nu_{\text{net}} \tau) \quad (2.3.3a)$$

$$\tau = t - t_0 \quad (2.3.3b)$$

Equation (2.3.3) is often written in the form

$$\frac{v_{\text{net}}}{P} = \frac{1}{P_T} \ln \left( \frac{n_d(t)}{n_d(t_0)} \right) \quad (2.3.4)$$

where  $P$  is the gas pressure. The value of  $v_{\text{net}}/P$  is determined by varying the RF power and pulse length until breakdown, as defined by either of equations (2.3.1) or (2.3.2) occurs. When definition (2.3.2) is used, the initial electron density is either assumed to be  $1 \text{ cm}^{-3}$  or measured in advance. It should be noted that for historical reasons the ionization rates determined from the microwave experiments were presented in a format that makes the interpretation and scaling of the results difficult. Namely, the plots give  $v_{\text{net}}/P$  as a function of  $E_e/P$ , where  $E_e$  is an effective electric field defined by

$$E_e = E_{\text{rms}} \left( \frac{v_T^2}{v_T^2 + \omega^2} \right)^{1/2} \quad (2.3.5a)$$

$$v_T = 5.3 \times 10^8 P \quad (2.3.5b)$$

The confusion and possible pitfalls in using the  $v_{\text{net}}/P$  vs.  $E_e/P$  format will be discussed later. In order to facilitate the comparison of the numerical results with the experimental results, the above format of presentation was maintained.

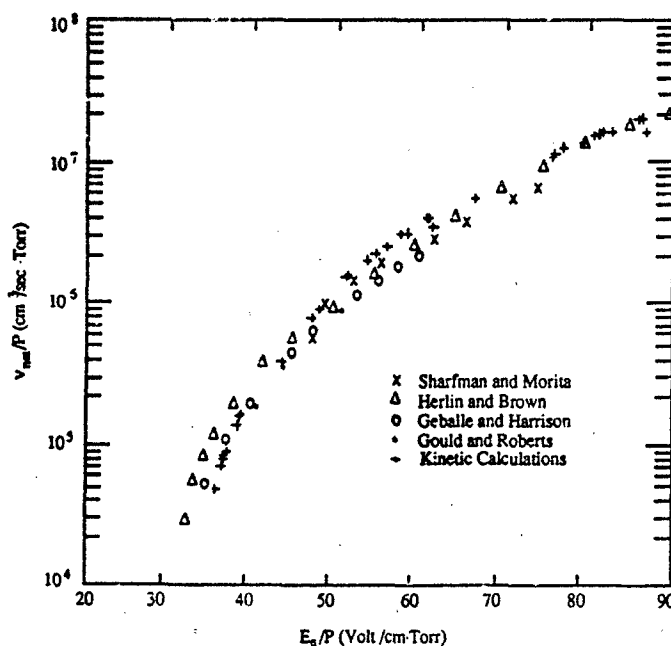


Figure 2.3.1. Comparison of Kinetic Calculations with Experiments

Figure 2.3.1 presents a summary of the early experiments along with the values determined in the numerical work. Given the uncertainties discussed above, the agreement is remarkable. Even more important is the comparison of the numerical results with the recent experiment by Hays et. al. [10], shown in Figure 2.3.2. This experiment was unique in that instead of using equations (2.3.1) - (2.3.3), the ionization rate was monitored as a function of time. It should be noted that the experiment was performed in the presence of a longitudinal magnetic field, and the microwave frequency was adjusted to resonate with the electron gyrofrequency. Under these conditions, the

physics of the electron energization is similar to the one in the presence of a DC electric field with amplitude two times larger than the RF field [10].

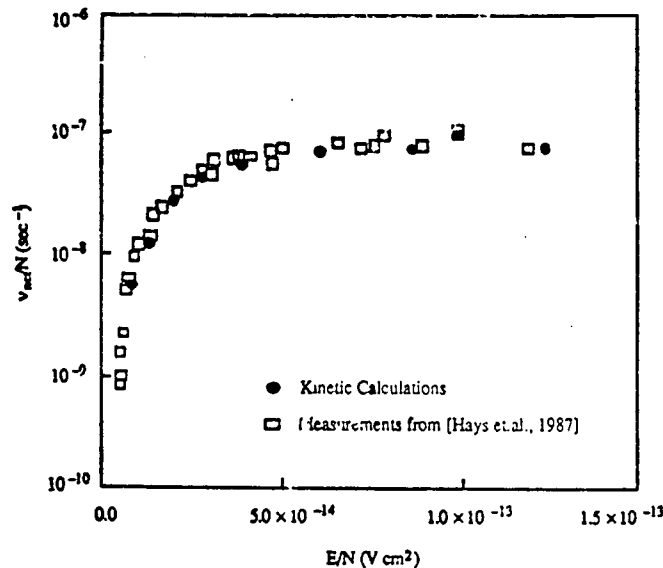


Figure 2.3.2. Comparison With Directly Measured Ionization Rates (Pure  $N_2$ )

#### 2.4. RF Ionization at 70km Altitude

The kinetic equation given in section 2.2 above was numerically solved over a wide range of frequencies, altitudes and power densities. For concreteness, we discuss here results relevant to air density of  $2 \times 10^{15} \text{ cm}^{-3}$ , which corresponds to an altitude of approximately 70 km. Figures 2.4.1 - 3 show the time evolution of the electron distribution function  $f(e)$  at intervals of 200 ns for an incident RF frequency of 300 MHz and powers of 300 W/m<sup>2</sup>, 3 kW/m<sup>2</sup>, and 30 kW/m<sup>2</sup>, respectively.

For the lowest power density case, shown in Figure 2.4.1 below,  $f(e)$  reaches steady state after approximately 2  $\mu\text{s}$ . In this case, the incident power density was below threshold and breakdown did not occur. The energy loss due to the vibrational excitation of molecular  $N_2$  acted as a barrier that prevented generation of significant electron fluxes past 2-3 eV.

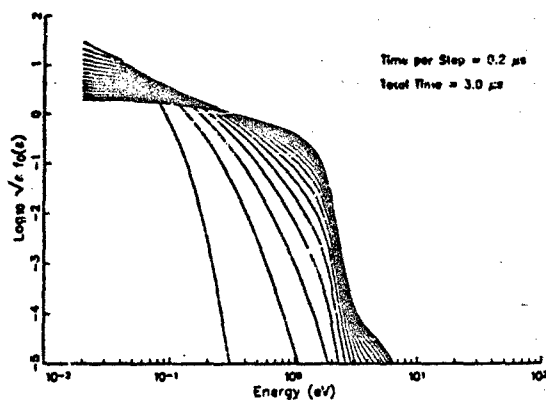


Figure 2.4.1. Evolution of  $f_0$  for Power Density of  $500 \text{ W/m}^2$

Figure 2.4.2 shows  $f(e)$  for  $3 \text{ kW/m}^2$  RF power density. Recent Soviet studies [2-3] predict a threshold power density of  $1.8 \text{ kW/m}^2$  for  $300 \text{ MHz}$  at  $N = 2 \times 10^{15} \text{ cm}^{-3}$ . However, our results indicate that even at  $3 \text{ kW/m}^2$ , although there was significant electron flux above  $5\text{-}6 \text{ eV}$ , few electrons reached ionizing energies. As will be discussed in a future publication, the optimistic results of Borisov et. al. [2] are due to their neglect of  $\text{O}_2$  dissociation.

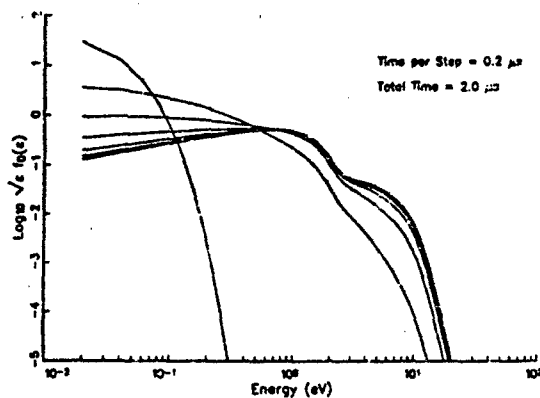


Figure 2.4.2. Evolution of  $f_0$  for Power Density of  $3 \text{ kW/m}^2$

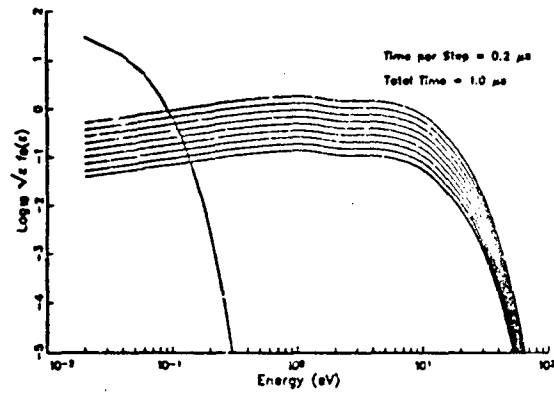


Figure 2.4.3. Evolution of  $f_0$  for Power Density of  $30 \text{ kW/m}^2$

Increasing the power density to  $30 \text{ kW/m}^2$  (Figure 2.4.3) results in significant electron fluxes reaching energies of 20 - 25 eV, ionizing both  $\text{O}_2$  and  $\text{N}_2$  molecules. The evolution of  $f(\epsilon)$  is self similar in energy and only the total electron density  $n_e$  increases with time. The distribution reaches a self similar state in approximately 200 ns.

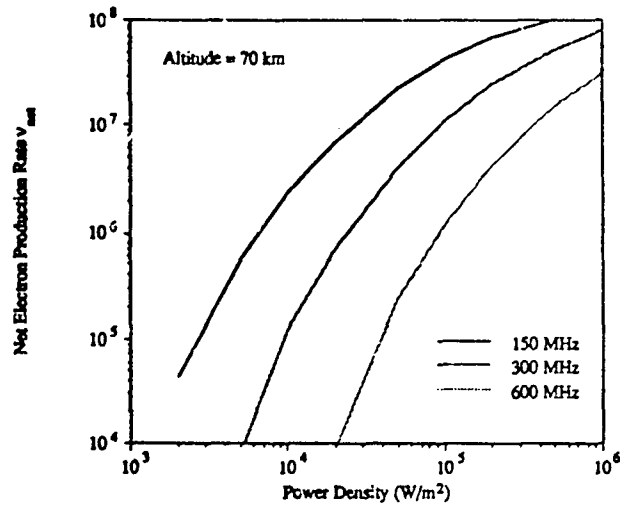


Figure 2.4.4. Net Ionization Rates at 70 km. Altitude

Of primary interest is the rate of ionization as a function of RF frequency and power density. The results of the computations are shown in Figure 2.4.4, for the 70 km altitude case. Figure 2.4.4 indicates a scaling of

$$v_{\text{net}} \propto \frac{S}{\omega^2} \quad (2.4.1)$$

This along with other scaling issues is the subject of the next section.

### 2.5. Ionization Rates and Efficiency Scaling Considerations

Based on the self similarity of  $f(\epsilon)$ , the results of section 2.4 can be generalized to produce universal relations for ionization rates for any combination of  $S$ ,  $\omega$ , and  $N$ . To accomplish this we rewrite equation (2.2.1) in the form

$$\frac{\partial}{\partial t} f_d(\epsilon) = \frac{1}{\sqrt{\epsilon}} \frac{\partial}{\partial \epsilon} \left[ e^{-N} D(\epsilon, \omega, \bar{\epsilon}) \frac{\partial f_d(\epsilon)}{\partial \epsilon} \right] - NL(f_d(\epsilon)) \quad (2.5.1)$$

$$D(\epsilon, \omega, \bar{\epsilon}) = \frac{2}{3} \bar{\epsilon} \frac{v_d(\epsilon)}{1 + \sqrt{\epsilon} \bar{\epsilon} \omega^2} \quad (2.5.2)$$

$$\bar{\epsilon} = \frac{1}{2} m_e \frac{q^2 E^2}{m_e^2 \omega^2} \quad (2.5.3)$$

The elastic electron neutral collision frequency  $v_d(\epsilon)$  has a maximum value  $v_{\text{max}}$  given by

$$v_{\text{max}} = 3 \times 10^{-2} N \quad (2.5.4)$$

This value is reached when  $\epsilon = 20-30$  eV. For the frequencies of interest for AIM, where  $\omega \gg v_{\text{max}}$ , equation (2.5.1) can be written as

$$\frac{\partial}{\partial \tau} f_d(\epsilon) = \frac{2}{3} \bar{\epsilon} \frac{\partial}{\partial \epsilon} \left[ e^{N_d(\epsilon)} \frac{\partial f_d(\epsilon)}{\partial \epsilon} \right] - L_d(f_d(\epsilon)) \quad (2.5.5)$$

$$\tau = v_d t \quad (2.5.6a)$$

$$v_d(\epsilon) = g(\epsilon) v_{\text{max}} \quad (2.5.6b)$$

$$L_d(f_d(\epsilon)) = \frac{1}{3} \times 10^3 L(f_d(\epsilon)) \quad (2.5.6c)$$

Notice that in equation (2.5.5), the altitude dependence enters through the normalized time  $\tau$ , while the RF frequency and power density dependences enter through  $\bar{\epsilon}$ . It is, as a result, expected that the dimensionless ionization rate  $v_{\text{net}}/v_{\text{max}}$  will be only a function of  $\bar{\epsilon}$ . The computational results confirm this conjecture for  $\omega \gg v_{\text{max}}$ , but show a factor of two difference when  $\omega = v_{\text{max}}$ . We will return to this point later on.

### 2.6. Analytic Approximation - A Test Particle Approach

The physics underlying the ionization rates and scaling presented in section 2.5 can be understood by examining the RF acceleration of an electron in the presence of inelastic losses. The energization of a test electron in the presence of RF waves with  $\omega \gg v_{\text{max}}$  can be approximated by

$$\frac{d\epsilon}{dt} = v_d(\epsilon) \bar{\epsilon} \quad (2.6.1)$$

In the presence of only ionization losses, the effective ionization time is the sum of the energization time to ionizing energies  $\tau_e$  and of the time  $\tau_{\text{ion}}$  to make an ionizing collision once the electron energy  $\langle \epsilon \rangle > E_{\text{ion}}$ . For the moderate values of  $\langle \epsilon \rangle$  (i.e.  $\langle \epsilon \rangle < 4-5$  eV) of interest here it is easy to check that  $\tau_e$  is the longest time scale. As a result



$$v_i = \frac{1}{\tau_i(e)} \quad (2.6.2)$$

We approximate the collision frequency by (Kroll and Watson, 1972)

$$v_d(e) = v_{max} g(e) = v_{max} \frac{e+1}{e+5} \quad (2.6.3)$$

where  $e$  is in units of eV. Assuming that ionization occurs near 25 eV energy, as seen in the computations, we find from equations (2.6.1) and (2.6.3)

$$v_{max} \tau_e = \frac{35}{8} \quad (2.6.4)$$

From equations (2.5.2) and (2.6.4),

$$\frac{v_i}{v_{max}} = \frac{7}{35} \quad (2.6.5)$$

The presence of other inelastic losses, shown in Figure 2.6.1, reduces the ionization rate to a great extent. We can compute the effect of inelastic collisions within the test particle theory by noting that from Figure 2.6.2 that there are two main barriers to electron energization. One is between 2-3 eV and is due to  $N_2$  vibrational losses. The second one is between 10-20 eV and is due to molecular dissociation and optical emissions. Ionization losses become dominant near 25 eV. We can account for the inelastic losses by introducing a probability  $P(\bar{e})$  that under the RF action the electron will be accelerated through the loss barriers and undergo an ionization collision. As a result,

$$v_{max} \tau_e = \frac{35}{8 P(\bar{e})} \quad (2.6.6)$$

or,

$$\frac{v_i}{v_{max}} = \frac{7}{35} P(\bar{e}) \quad (2.6.7)$$

On the basis of Figure 2.6.1, we can write

$$P(\bar{e}) = P_{vb}(\bar{e}) P_{opt}(\bar{e}) \quad (2.6.8)$$

where  $P_{vb}(\bar{e})$  refers to the vibrational band and  $P_{opt}(\bar{e})$  to the dissociation-optical excitation band. We calculate first the  $N_2$  vibration effect  $P_{vb}(\bar{e})$ .

Since the band is relatively narrow we can approximate the vibrational excitation rate  $v_{vb}$  by its value at the vibrational peak energy  $\epsilon_{vb}$ . In this range the value of the diffusion coefficient in energy space  $D_E = \langle \Delta \epsilon^2 / \tau \rangle$  is given by

$$D_E(\epsilon_{vb}) = \epsilon_{vb} / \tau(\epsilon_{vb}) \quad (2.6.9)$$

As a result, the energy diffusion time through the width  $\Delta \epsilon_{vb}$  of the vibrational barrier is

$$\tau_{D-vb} = \frac{\Delta \epsilon_{vb}^2}{D_E(\epsilon_{vb})} \quad (2.6.10)$$

If  $\tau_{vb} = 1/v_{vb}$  is the average time to excite vibrational states, then the probability  $P_{vb}(\bar{e})$  that an electron will cross the vibrational barrier is given by

$$P_{vb}(\bar{e}) = \exp \left[ - \left( \frac{\tau_{D-vb}}{\tau_e} \right)^{1/2} \right] \quad (2.6.11)$$

From (2.6.9-11) we find

$$P_{vib}(\bar{\epsilon}) = \exp \left[ - \left( \frac{3}{2} \frac{v_{vib}(\epsilon_{vib})}{v_m(\epsilon_{vib})} \frac{\Delta_{vib}^2}{\bar{\epsilon} \epsilon_{vib}} \right)^{1/2} \right] \quad (2.6.12)$$

From cross-section data we can determine that  $v_{vib}(\epsilon_{vib}) = v_e(\epsilon_{vib})/2$ ,  $\epsilon_{vib} = 2.6$  eV, and  $\Delta_{vib} = 1.0$  eV. Making these substitutions, we find that

$$P_{vib}(\bar{\epsilon}) = \exp \left[ - \sqrt{\frac{29 \text{ eV}}{\bar{\epsilon}}} \right] \quad (2.6.13)$$

The losses in the 5-8 eV range are much smaller and may be ignored. The remaining barrier is due to both optical excitations and dissociation; it occupies the range between 8-20 eV and reaches a maximum near 14 eV. We can find the probability  $P_{opt}(\bar{\epsilon})$  of penetrating this barrier by using an approach similar to the one above. In this case  $v_{opt}(\epsilon_{opt}) = 0.2 v_e(\epsilon_{opt})$ ,  $\epsilon_{opt} = 14$  eV, and  $\Delta_{opt} = 6$  eV. For these values, we find that

$$P_{opt}(\bar{\epsilon}) = \exp \left[ - \sqrt{\frac{77 \text{ eV}}{\bar{\epsilon}}} \right] \quad (2.6.14)$$

The total probability that an electron will cross both barriers and reach the energies necessary to ionize is given by

$$P(\bar{\epsilon}) = P_{vib}(\bar{\epsilon}) P_{opt}(\bar{\epsilon}) = \exp \left[ - \sqrt{\frac{29 \text{ eV}}{\bar{\epsilon}}} \right] \exp \left[ - \sqrt{\frac{77 \text{ eV}}{\bar{\epsilon}}} \right] \quad (2.6.15)$$

From equations (2.6.7) and (2.6.15) we find

$$\frac{v_i}{v_{max}} = 3.0 \times 10^{-2} \bar{\epsilon} \exp \left[ - \sqrt{\frac{29 \text{ eV}}{\bar{\epsilon}}} \right] \exp \left[ - \sqrt{\frac{77 \text{ eV}}{\bar{\epsilon}}} \right] \quad (2.6.16)$$

Substituting the value of  $v_{max}$  from (2.5.4), and realizing that for quiver energies above the ionization threshold  $v_{ion} = v_i$ , we arrive at

$$v_{ion} = 9.0 \times 10^{-7} \bar{\epsilon} \exp \left[ - \sqrt{\frac{29 \text{ eV}}{\bar{\epsilon}}} \right] \exp \left[ - \sqrt{\frac{77 \text{ eV}}{\bar{\epsilon}}} \right] \quad (2.6.17)$$

Figure 2.6.1 compares the prediction of equation (2.6.16) with the kinetically calculated rates presented in section 2.6.5. The agreement is excellent over more than four orders of magnitude in the rate and two in power. The results deviate for  $\bar{\epsilon} > 4.5$  eV. This is expected since at such power densities the energization time becomes smaller than the time for ionizing collisions.

In concluding this section, we should comment on the factor of two differences in the ionization rates between the  $\omega \gg v_{max}$  and  $\omega \sim v_{max}$  situations. To extend the range of validity of the equation toward the  $\omega \sim v_{max}$  regime, observe that the effective quiver energy of an electron at energy  $\epsilon$  is:

$$\bar{\epsilon}_d(\epsilon) = \frac{\bar{\epsilon}}{1 + v_e^2(\epsilon)/\omega^2} \quad (2.6.18)$$

rather than  $\bar{\epsilon}$ . We can conjecture that equation (2.6.17) can be generalized from  $\omega \gg v_{max}$  to the  $\omega \sim v_{max}$  range by substituting the appropriate value of effective quiver energy into each term:

$$v_{ion} = 9.0 \times 10^{-7} \bar{\epsilon}_d(25 \text{ eV}) \exp \left[ - \sqrt{\frac{29 \text{ eV}}{\bar{\epsilon}_d(2.6 \text{ eV})}} \right] \exp \left[ - \sqrt{\frac{77 \text{ eV}}{\bar{\epsilon}_d(14 \text{ eV})}} \right] \quad (2.6.19)$$

From (2.6.3) and (2.6.18):

$$\bar{\epsilon}_d(\epsilon) = \frac{\bar{\epsilon}}{1 + h(\epsilon)v_{ion}^2/\omega^2} \quad (2.6.20)$$

where

$$h(\epsilon) = \left( \frac{\epsilon + 1}{\epsilon + 5} \right)^2 \quad (2.6.21)$$

This extension reproduces the behavior of the numerical results for  $\omega = v_{max}$ . The case of  $\omega < v_{max}$  will be presented elsewhere.

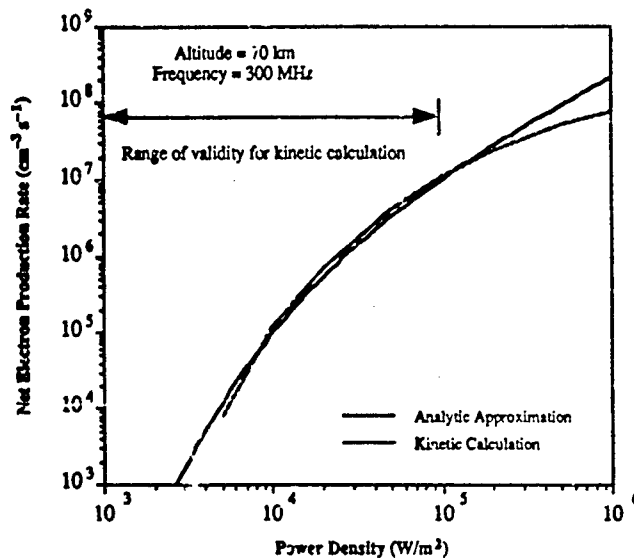


Figure 2.6.1. Comparison of Analytic Approximation and Kinetic Calculations

### 3. AIM Formation Model

The formation of AIM clouds in the ionosphere by ground based RF was studied through the use of a one dimensional simulation. The code models the breakdown and formation of AIM clouds by solving the coupled propagation and ionization equations, including self absorption, for a microwave pulse propagating upwards. The model is a fluid rather than a kinetic one, ignores transport, and uses the ionization rate equation (2.6.17). A detailed description of the mechanics of the one dimensional code can be found in [1].

The need to control the altitude of the AIM cloud requires the use of a focussed heater antenna. If the elements of the heater are spread out over a wider area, the desired location of the AIM cloud is in the near field of the heater, where focusing through phase correction of individual elements is possible. The result is a vertically increasing electric field from the heater antenna at a controlled altitude. This method allows breakdown to occur at higher altitudes, thereby increasing AIM lifetime and decreasing absorption effects. The resulting electron density profiles have a very sharp gradient, which further reduces absorption effects, and fine control over the position of the breakdown is possible.

One dimensional simulations revealed a long pulse effect which increases the gradient of the plasma cloud, thereby reducing the absorption of the radar signal as it reflects from the patch. At each altitude there is a threshold power density  $S_c$ . As a long pulse ( $> 5 \mu\text{sec}$ ) of microwave energy propagates upwards in the atmosphere and ionization takes place, self-absorption of the pulse decreases the field strength in the pulse. Moreover, the areas with the highest induced electron density will absorb more of the pulse. Eventually, the area of peak ionization will absorb so much of the pulse that the remaining power density will fall below  $S_c$ . At this point, further ionization can only occur below and in front of the point of peak electron density. This moves the electron density peak down vertically with time, bringing it closer to the point where the unattenuated power density is  $S_c$ . Figure 3.1 shows the formation of a one-dimensional profile made by a  $10 \mu\text{sec}$  pulse, at  $1.5 \mu\text{sec}$  time samples.

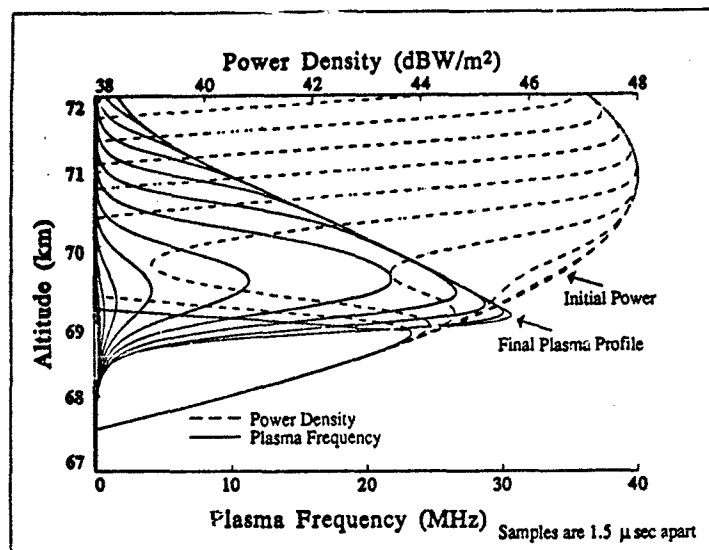


Figure 3.1. Growth Through Time of AIM Cloud with  $f = 300$  MHz,  $\tau = 10 \mu\text{sec}$

The gradient of the electron density profile is dependent on the slope of the heater antenna's array factor near the initial breakdown point and the heater frequency. A steeper slope in power density creates a corresponding sharper electron density gradient along with a higher peak in electron density profile. Parameter studies show a linear dependence between power density slope and resulting electron density slope. Since self-absorption or attenuation goes down as the heater frequency is increased, a higher frequency will achieve a greater electron density before the clamping phenomenon occurs, and subsequently a steeper slope as well.

#### 4. Summary

In this paper, we presented the physical foundations required for the design of an AIM system for radar applications. Ionization rates were computed using a kinetic code that incorporates inelastic losses with the most up to date cross section values. The code reproduces all relevant experimental data. An analytic formula derived by test particle considerations was found in excellent agreement with the numerical results. A one dimensional code was used to study inhomogeneous aspects of the breakdown and plasma formation.

#### References

1. *Physics Studies in Artificial Ionospheric Mirror (AIM) Related Phenomena*. ARCO Power Technologies Technical Report 5004, Washington, DC, 1990.
2. Gurevich, A. V., *Nonlinear Phenomena in the Ionosphere*. New York: Springer-Verlag, 1978.
3. Borisov, N. D., A. V. Gurevich, and G. M. Milikh, *Artificial Ionized Region in the Atmosphere*. U. S. Air Force Foreign Technology Division, 1988. (Translation of *Iskustvennaya Ionizirovannaya Oblast' v Atmosfere*, Moscow, 1986.)
4. Allis, W. P., "Motions of Ions and Electrons", in *Encyclopedia of Physics*, ed. S. Flugge, v. 11, Berlin: Springer-Verlag, 1956.
5. Sharfman, W., and T. Morita, *J. Appl. Physics* 35, 2016 (1964).
6. Sharfman, W., W. Taylor, and T. Morita, *IEEE Trans. AP-12*, 709 (1964).
7. Herlin, M. A., and S. C. Brown, *Phys. Rev.* 74, 291, 74, 1650 (1948).
8. Goulu, L., and L. Roberts, *J. Appl. Physics* 27, 1162 (1956).
9. Geballe, R., and M. Harrison, *Phys. Rev.* 91, 1 (1953).
10. Hays, G., L. Pitchford, J. Gerardo, J. Verdeyen, and Y. Li, *Phys. Rev. A* 36, 2031 (1987).

## DISCUSSION

F. M. BANKS, US

I am curious about the effects of dissociation of  $N_2$  &  $O_2$ . The formation of NO, in particular could offer a means of "conditioning" the mesosphere, opening the way to ionization at lower energies than would be required for "fresh" atmosphere. Also, at low altitudes, where  $N/O \gg 1$  no ionization will occur but N & O will be formed. In this case NO could also be produced in the upper stratosphere, with consequent loss of  $O_3$ . Is this a significant process?

## AUTHOR'S REPLY

Not for our case in which the ionization is only about  $10^{-8}$  (i.e.,  $10^{15}/cm^3$  neutrals and  $10^7/cm^3$  ions) and the ionization occurs in 10-20 ns. Time scales and energetics easily show that NO,  $O_3$ , etc. processes do not play any role.

W. T. ARMSTRONG, US

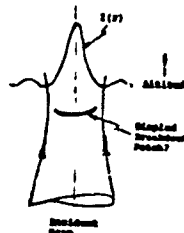
In response to the question by Banks on NO production & threshold reduction, sustinment calculations by Finn indicate - NO levels of  $10^{12}$ , but no significant reduction in power thresholds.

## AUTHOR'S REPLY

This is consistent with our results.

B. RIPIN, US

The focused beam has an intensity profile similar to that in the sketch. Won't the breakdown patch be dimpled due to this profile, and what consequences does this cause?



## AUTHOR'S REPLY

The 2-D profile of the AIM layer is created by superimposing many single beam profiles (i.e., painting, see Fig. 1). Due to clamping as discussed before and by properly painting a smooth layer results. For details see AIM paper on Thursday.



Fig. 1

## Crossed-Microwave-Beam Air Ionization Laboratory Experiments

W. T. Armstrong, R. Karl, M. Kelly, R. Roussel-Dupre,  
M. Buchwald, C. D. Sutherland, J. Zinn  
Los Alamos National Laboratory

R. Alvarez, P. Bolton, G. Sieger, W. Patterson  
Lawrence Livermore National Laboratory

D. Hunton, E. Trzcinski  
Air Force Geophysics Laboratory  
D. Eckstrom, K. Stalder  
SRI Inc.

L. Testerman, T. Tunnell, P. Blain  
EG&G Energy Measurements

## 1. Summary

Detailed laboratory measurements and theoretical modeling relevant to the production, geometrical description and decay of microwave-induced air ionization for an upper atmospheric RF reflecting layer are reported. It is found that breakdown thresholds are adequately predicted by fluid models and simplified scaling models with refinement by kinetic models being important at lower pressures. Repetitive pulse sustainment has been demonstrated to be straightforward with a commensurate reduction in sustainment power levels. However, establishment of a convenient breakdown geometry for specular RF reflections, other than a single layer in a crossed beam geometry, was not obtained. Detailed density decay measurements qualitatively support simple estimates of decay times and indicate ionization dwell times of tens of milliseconds. Chemistry studies indicate three  $N_xO_x$  species will be produced. Further study of these collateral reactions is required to establish whether adverse atmospheric consequences can result. However, large  $N_xO_x$  production does not appear as a concern for relatively small, low repetition rate, proof of concept atmospheric experiments. A realizable proof of concept experiment is found with simple optimization criteria which is corroborated by laboratory measurements and theoretical simulations. Tail-erosion appears as a potentially severe limitation in atmospheric experiments beyond the proof of concept level, suggesting use of multiple-beam systems.

## 2. Introduction

High power microwave radiation is under consideration for use as an ionizing agent to form a radio reflecting region in the stratospheric/mesospheric altitude range. The ionization region is referred to as an Artificial Ionization Mirror (AIM). An AIM could conceivably avoid the following constraints of reflection from the ionosphere: 1) limitation to ~ 30 MHz reflection frequencies, 2) erratic variations due to the ionosphere's natural origin, and 3) reduction of a blind "skip" area for high frequency reflections. Work in this area began in the Soviet Union in the 1970's and continued into the 1980's with a benchmark paper by Gurevich appearing in 1980 [Gurevich, 1980; Borisov and Gurevich, 1980; Vikharev, et al., 1984]. Work in the United States began in 1986. The ultimate utility of the ionizing process is dependent on many issues including: choice of altitude and frequency parameters, atmospheric attenuation, ionization geometry, ionization threshold, and sustainment of the ionization layer. These issues were reviewed by Los Alamos National Laboratory (LANL) and Lawrence Livermore National Laboratory (LLNL) in a report submitted to the Air Force Geophysics Laboratory (AFGL) in 1987 [Armstrong, et al., 1987]. Pursuant to this report an experimental program evolved which consisted of five research campaigns conducted at the LLNL high power microwave laboratory [Byrne, 1986] over the course of two and one-half years. The campaigns consisted of the following:

AIM-I	Jun. 1987	Diagnostic Development & Testing, LANL/LLNL
AIM-II	Jul. 1987	Single Pulse AIM Measurements, LANL/LLNL
AIM-III	Aug. 1988	Repetitive Pulse AIM Measurements, LANL/LLNL
AIM-IV	Apr. 1989	Low Density Decay Measurements, SRI/LLNL
AIM-V	Sep. 1989	Sustainment Chemistry Measurements, AFGL/LLNL

[Armstrong, et al., 1988; Eckstrom and Williams, 1989; Hunton, 1990]. The present paper summarizes the results of these experimental and theoretical research campaigns, with emphasis on AIM-II and III.

The experiment goals of AIM-II were to 1) measure ionization thresholds for single and multiple layer formation, 2) characterize the geometry of layer formation, and 3) determine density and effective collision rates in the ionization layer. The AIM-III research campaign, performed in the same experimental geometry, was dedicated to repetitive pulse operation to explore the issues surrounding prolonged or "sustained" AIM production necessary in many application scenarios. The primary issues to be examined included: 1) reproducibility of breakdown geometry, 2) utility of previous pulses in reducing the power threshold for breakdown by subsequent pulses, and 3) ionization persistence or decay. These two campaigns are described in Section 3. An expanded discussion of ionization decay is presented in Section 4 in the context of AIM-IV low-density measurements. Section 5 contains a discussion of ionization molecular byproducts measured in AIM-V. A discussion of theoretical modeling is given in Section 6. Extrapolation of laboratory measurements and theoretical predictions is made to an atmospheric demonstration experiment in Section 7.

### 3. AIM Characterization and Sustainment

The AIM-II and AIM-III experiments were directed primarily to crossed microwave beams, for localization of the breakdown, in conditions of low pressure air. The experiments typically consisted of a high power (~10 MW) 2.856 GHz microwave pulse focused in a pressure chamber onto a reflecting plate oriented at 45° to the incident beam such that the E-field of the beam was in the plane of the reflector. This geometry simulates two phase-locked microwave beams intersecting at 90° with respect to each other. The resulting air breakdown pattern consisted of ionization layers at surfaces of constructive interference. A diagram of the experimental geometry is shown in Figure 1. The diagnostics employed consisted of: 1) incident and transmitted microwave power from incident directional coupler and magnetic probes in the reflecting plate, 2) sideviewing optical imaging and two color photometry, and 3) cross-layer double-pass x-band interferometry. The parameter space explored included pulse lengths of 75 to 1780 ns, pressures from 0.61 to 3 Torr, and inter-pulse periods from 2 to 30 ms during repetitive pulse operation. Pulse lengths were defined as the 90 % power width, in which the 10-90 % power rise and fall times are typically 55 and 85 ns, respectively. The pressure range was constrained by the desire to operate from the lowest breakdown power threshold, which occurs under matched conditions of microwave frequency comparable to collision frequency, to as low a pressure or equivalently highest altitude as possible with the vacuum and power constraints of the apparatus. We first describe threshold measurements which are compared to previous measurements and discussed in terms of optimization. Breakdown geometry is then described, with a discussion of density and temperature measurements following. Repetitive pulse sustainment discussion concludes this section.

Microwave breakdown is generally described by attainment of plasma densities high enough to affect the driving field -- generally on the order of the critical electron density in laboratory scale experiments. For the cw case, it is expressly defined as the condition where the ionization rate is equal to the effective electron loss rate. For breakdown to occur with microwave pulses of finite length, the ionization rate must not only exceed the loss rate but must exceed it sufficiently that the electron density attains a certain value in a time shorter than the pulse duration. The pulsed breakdown definition is ambiguous as the breakdown density value may be defined differently by different observers. In the present work, threshold is defined by a detectable departure of the transmitted pulse from the incident pulse at the end of the pulse's "flattop". This criterion appears to occur at approximately  $10^{10} \text{ cm}^{-3}$  as indicated from the x-band interferometry. In practice breakdown definitions are less meaningful when the pulse risetime is finite and comparable to the pulse length; i.e., the field amplitude is not constant. In particular, "time to breakdown" for our shortest pulse data of 75 ns is problematic within past definitions.

Typical time histories of data are presented in Figure 2 for conditions of 1 Torr pressure and 75 ns pulse length which show the timing of breakdown, as well as the appearance of light emissions and density buildup. The klystron-produced microwave waveforms and resulting breakdown behavior were observed to be reproducible to within a few percent. However, calibration of the power measurements is known only to about 30 %. A plot of peak power density, inferred at the focal plane for the incident (dark trace) and transmitted (light dotted trace) microwave pulses, is shown in Figure 2a. Note that severe attenuation of the transmitted pulse appears at around 120 ns into the incident pulse in association with the formation of a breakdown layer.

Analysis of the attenuation and phase measurements of the x-band interferometer [Stalder and Eckstrom, 1989] results in the density history displayed in Figure 2b and an

estimate of the peak momentum exchange rate of  $v_m = 1.6 \times 10^{10} \text{ s}^{-1}$ . The density decay inferred from interferometry was measured for different pressures and is presented in Section 3. However, the post-pulse decay measured with the interferometry is much more rapid than the dominant decay found during the extended interpulse period, as discussed below.

High speed (300 ps resolution) photometer measurements of emission in the second positive band system in  $\text{N}_2$  ( $\text{C } ^3\Pi_u \rightarrow \text{B } ^3\Pi_g$ ,  $\lambda = 3371 \text{ \AA}$ ) and the first negative band system in  $\text{N}_2^+$  ( $\text{B } ^2\Sigma_u^+ \rightarrow \text{X } ^2\Sigma_g^+$ ,  $\lambda = 3914 \text{ \AA}$ ) are plotted in Figure 2c. Because the 3914  $\text{\AA}$  line is not pumped significantly during its relaxation because of low electron temperatures, its relaxation rate is a good measure of the sum of the spontaneous emission rate and the quenching rate. The experimental results are in good agreement with the values  $A_{3914} = 1.6 \times 10^7 \text{ s}^{-1}$  and  $Q_{3914} = 5.1 \times 10^{-10} \text{ cm}^3 \text{ s}^{-1}$ . The light emissions data is modeled to provide a characteristic electron energy in Figure 2d [Tunnell, 1989]. The model is based on a three-state coronal approximation in a fluid model [Roussel-Dupre', 1989] which is simplified with a steady-state scaling law [Tunnell, 1990]. The characteristic temperature results from predicted ratios of 3371/3914 emissions, which is generalized as a function of total electron energy,  $E_T = (3/2) kT_e + (1/2)mv_{rms}^2$  to allow for energy dependences both during and after the microwave pulse. This "characteristic energy" represents a best effort attempt to estimate breakdown "temperature" with limited diagnostic information in a transient environment. The restrictions on interpretation and use of these estimates is discussed in the theory section below.

Summary incident power densities and fluences for breakdown thresholds are presented in Figure 3. As expected, minimum power and fluence requirements occur near the matched breakdown condition at  $\sim 1 \text{ Torr}$ , with breakdown powers rising over a factor of 100 for shorter pulses and lower pressures. Lowest power requirements result with the longest pulses and lowest fluence results with the shortest pulses. Breakdown thresholds are replotted in Figure 4 in terms of  $E_{eff}$  for comparison with previous measurements and theoretical predictions at different frequencies.  $E_{eff}$  is defined as  $E_{rms}/(1+\omega^2/v^2)^{1/2}$  where  $v$  is the collision frequency. The calculated thresholds are described further below. The present measurements are found to agree well with previous waveguide measurements of Byrne and August, with some departure of the waveguide measurements at the lower pressures. This departure may be expected due to the large mean free paths of electrons under these low pressure conditions, which could result in collisions with walls. Summary measured median emission ratios are presented in Figure 5. Anomalous behavior of 640 ns data at 0.01 Torr in Figure 5 is suggestive of possible breakdown difficulties associated with energetic electrons escaping the breakdown region and penetrating the anechoic material on the walls of the vacuum vessel.

Figure 6 shows typical variations of breakdown geometry with pressure for single layer formation with 75 ns pulse lengths. It is observed that sharper density gradients and greater inner layer structure occurs at higher pressures with a more diffuse and smooth structure occurring at lower pressures. Figure 7 shows multiple layer formation for a 75 ns pulse at 0.1 Torr and a 400 ns pulse at 3 Torr in which the microwave power is increased in excess of the single layer threshold. Again, greater structure is apparent at the higher pressure, in part due to high reflectivity from initial ionization layers to form a modified interference pattern and additional intermediary ionization layers.

Repetitive pulse experiments from AIM-III were performed in the same experimental geometry as AIM-II. To achieve repetitive pulse operation, the triggering arrangement for the klystron system was modified to allow bursts of microwave pulses with a repetition pulse frequency up to 500 Hz (interpulse period, IPP, down to 2 ms) and sequences up to 100 pulses long, once every 2 seconds. Moreover, there was the ability to step the microwave power an arbitrary amount between any two pulses. This capability allowed the operation in three modes: mode 1 consisted of constant amplitude adjusted to threshold conditions on the first pulse (but in excess of threshold for the subsequent pulses), mode 2 consisted of the first pulse amplitude adjusted to threshold while subsequent pulse amplitudes are reduced to a constant level consistent with repetitive pulse threshold conditions, and mode 3 consisted of constant amplitude reduced to below a single pulse threshold value but consistent with a repetitive pulse threshold conditions, resulting in slow buildup of density to breakdown conditions over several pulses. Emphasis was placed on operation in modes 1 and 2. The most significant change in diagnostic measurements from AIM-II was the incorporation of an array of fast digitizers to record the data from three pulses, arbitrarily chosen, in the fast sequence of repetitive pulses. Typically, the first three pulses were recorded since they exhibited the greatest change in behavior from pulse to



pulse. Comparison of the third and 100<sup>th</sup> pulse found little difference in breakdown parameters.

Mode 1 operation is qualitatively made clear in the images presented in Figure 8 for 0.3 Torr, 640 ns pulse length, and 3 ms IPP operation. Pulse 1 displays a single simple AIM formation typical of threshold conditions. Pulse 2 displays multiple AIM structure typical of power levels above threshold conditions. The structure after pulse 2 then slowly evolves over tens of pulses to that seen in the figure in which a more diverse distribution occurs. This evolution is indicative of high ionization levels driven during the pulse duration which are partially refractive and reflective and lead to more complicated structures than determined by the initial beam geometry. The latent ionization after each pulse resembles this complicated structure and therefore leads to a slowly changing initial condition for each subsequent pulse. However, the most dramatic change occurs between the first and second pulses in which the mean initial ionization level experiences the greatest increase. An anticipated result of mode 1 operation was that the structure would evolve to become diffuse, structureless, and reproducible, so as to offer more utility. This result was not obtained.

A more reproducible breakdown occurs in mode 2 operation, as displayed qualitatively in the images of Figure 9 for 0.3 Torr, 640 ns pulse length, and 10 ms IPP conditions. All AIM structures out to beyond pulse 100 are observed to be composed of simple single layers, with later pulses indicating a more diffuse distribution of ionization associated with an enhanced local ionization distribution.

As indicated above, mode 2 operation constitutes the ability to run at reduced power levels because of the latent ionization from previous pulses reducing the required increase in electron density to reach breakdown conditions. By constructing the ratio of power between the second and first pulse in mode 2 operation, a measure of the effectiveness of repetitive pulsing on power reduction is arrived at for sustainment of an AIM. Figure 10 presents this ratio as a function of several IPPs and pressures. The greatest reduction in sustainment power, a factor of as much as 8 dB, is obtained at lower pressures where ionization decay occurs most slowly. Despite this power reduction, absolute power levels are still significantly higher at lower pressure than at higher pressures near matched conditions (1 to 3 Torr). Hence, even though there is an efficiency improvement with repetitive pulsing at a given pressure, the optimum pressure still appears near the matched pressure condition.

In mode 1 operation a significant change in timing of breakdown occurs between the first and second pulse. This timing difference can be used to infer an average decay rate in the long interpulse period between the pulses and, hence, the ionization density available for AIM applications. By assuming simple repetitive exponential density growth and decay, estimating initial and maximum electron densities, and measuring times to breakdown, we may estimate decay rates and minimum sustainment density. As an example for the conditions of 10 Torr and 3 ms IPP, we infer an interpulse decay time constant of 380  $\mu$ s, and a minimum sustainment density of  $4.3 \times 10^7 \text{ cm}^{-3}$ . Though the growth rate is dependent on power, the decay rate is not. Hence, decay rates inferred in this manner may be compared with other measured decay rates, as is done below for example cases. It is found that these inferred decay rates compare favorably with those measured directly in AIM-IV for low density decay. The change in decay rates from the rapid post-pulse decay to the slower interpulse decay is discussed below in the context of electron attachment and other processes.

#### 4. Ionization Decay

Decay of the ionization after the microwave pulse is of critical interest in assessing the utility of the ionization layer. Three measurements of decay have been performed: 1) direct x-band interferometry of the layers formed in AIM-II and AIM-III in the immediate post-pulse period with a sensitivity range of  $\sim 1 \times 10^{10}$  to  $\sim 1 \times 10^{12} \text{ cm}^{-3}$ , 2) inferred decay rates from changes in breakdown timing during repetitive pulse operation of AIM-III in the extended interpulse period with low accuracy but a large effective range of  $\sim 1 \times 10^5$  to  $\sim 1 \times 10^{10} \text{ cm}^{-3}$ , and 3) direct microwave cavity perturbation measurements of low density decay in AIM-IV which is representative of the interpulse period with a sensitivity of  $2 \times 10^5$  to  $1 \times 10^7 \text{ cm}^{-3}$  and high accuracy. The most substantive of these measurements is the cavity measurements in which a cavity resonant at 329 MHz was placed at the focus of the s-band beam without a reflecting plate. Measurements of the plasma-induced shift in the resonant frequency and Q provided determination of the density and collision frequencies [Eckstrom et al., 1987]. A summary of these measurements and simple estimates of expected

mechanisms contributing to the decay, are shown in Figure 11. The AIM-II post-pulse interferometry results are depicted by a bold upper line, the AIM-III interpulse inferred decays at a few representative high pressures are shown as x's, and the AIM-IV interpulse cavity measurements are depicted by a bold lower line. The large difference of decay rates between the post-pulse period and interpulse period is expected as a result of the change in dominant decay mechanisms with cooling temperature and declining electron density. As seen in Figure 11, 2-body dissociative attachment to  $O_2$  and dissociative recombination appear to dominate at higher pressures during the post-pulse period. During the interpulse period, it is observed that 3-body attachment and detachment contributes strongly to the decay rate at high pressures with diffusion dominating at the low pressures. As inferred from the more precise cavity measurements, the useful plasma lifetimes during the interpulse period are in the range of 20 to 40 ms at the lower pressure ranges of the AIM experiments, decreasing to about 1 ms at 30 Torr.

### 5. Sustainment Chemistry

Changes in the air constituents during and after AIM breakdown are of interest for two areas: 1) contributions to variation in the threshold for breakdown, and 2) contributions to nitric oxides which would contribute to catalytic depletion of ozone at lower altitudes. The first concern is mitigated by the expectation that upper atmospheric winds and breakdown induced turbulence would replenish the breakdown volume with a standard air mixture. The second concern has a potential environmental impact that must be carefully resolved by a combination of laboratory measurements and modeling of ion production rates, as well as comprehensive global atmospheric convection modeling. In AIM-V, chemistry measurements of high repetition breakdown in a small volume waveguide configuration were performed with both mass spectroscopy and optical absorbancy (Huntton, 1990). The repetition rate of breakdown was typically 315 Hz with 1  $\mu$ s pulse lengths and working pressures varying from 0.3 to 200 Torr. Previous optical absorbancy work (Askarjan, et al., 1988) had indicated substantial production of  $NO_2$  at similar energy deposition rates, but over a limited pressure range above 100 Torr. The present measurements corroborated previous high pressure work, but extended to examine additional chemical products under more appropriate conditions for AIMS: lower pressures, lower microwave frequencies, and higher repetition frequencies. Indeed, the present absorbancy measurements proved insensitive below about 20 Torr which required the spectroscopy measurements to examine the AIM pressure range of interest which typically extends from about 3 Torr to below 0.1 Torr. Three primary gaseous products were found in the spectroscopy measurements:  $NO$ ,  $NO_2$  and  $N_2O$ . In Figure 12, time history results of  $NO_2$  formation are shown from simultaneous absorbancy and spectroscopy measurements. The typical experimental cycle is shown as consisting of a 10 minute repetitive discharge period followed by a 10 minute inactive period during which the microwaves are turned off. Mass spectra were recorded once every minute. A summary of all three species formed under different conditions is presented in Figure 13. Whereas  $NO_2$  is formed predominantly at higher pressures,  $N_2O$  is formed at lower pressures while  $NO$  is formed under all conditions. Though the mechanisms leading to  $NO$  and  $NO_2$  are well documented, the formation mechanism for  $N_2O$  is somewhat uncertain. However, the appearance of  $N_2O$  at low pressures is suggestive of a dependence on the energetic electrons present in low pressure microwave air breakdown.

### 6. Theoretical Modeling

The ordering of theoretical review associated with AIM laboratory experiments progresses here from the simplest and most tractable models to the sophisticated and most detailed modeling: steady-state scaling laws, fluid time-dependent simulations, kinetic time-dependent simulations and, finally, inclusion of extensive chemical reaction sets.

Steady-state scaling laws for breakdown parameters, (e.g., ionization rate, momentum exchange rate, electron kinetic energy or drift velocity, and electron thermal energy) are desirable in reducing the complicated coupled dependence of the parameters in the equations describing breakdown. Steady-state scaling laws are arrived at by first refining the scaling dependence of breakdown parameters on  $E_{eff}/P$  to include the electric field dependence in collision rates, and then by repeated running of the fluid model for constant rms microwave field values to arrive at steady-state parameter dependence. Since  $E_{eff}$  is dependent on the collision frequency, implementation of this new universal scaling law is less convenient than previous simpler scaling laws, necessitating an iterative tabular interpolation. However, the results shown in Figure 14 of frequency insensitivity

substantiate the applicability of this new scaling. The resulting scaling laws for breakdown parameters are usable with square pulse envelopes for rapid solution of microwave propagation and breakdown over large propagation paths associated with AIM scenarios, as seen in the example of the next section, or for rapid survey of parameter space for obtaining optimum conditions for particular experiments. Caveats implicit in the use of these scaling laws include: 1) the assumptions of a steady-state and a square pulse require transient effects associated with finite rise times to be explicitly modeled; 2) the use of an effective field assumes that  $\omega \geq \nu$  in order for the rms electric field to enter into the scaling; at high pressures when  $\nu \gg \omega$  the instantaneous electric field defines the plasma properties; hence, an average rate must be calculated to characterize the time to breakdown accurately; and 3) kinetic effects are generally important in predicting breakdown thresholds particularly at high field strengths and/or low pressures and low field strengths and/or high pressures. Figure 15 displays an example of kinetic effects influencing the ionization rate.

Time-dependent fluid models were used to investigate the mean properties of the breakdown plasma produced in the laboratory experiments. Both 1-D and 2-D models were utilized [Roussel-Dupre' and Armstrong, 1988; Mayhall, et al., 1988]. The 1-D model results are briefly described here. The fluid equations are derived from the Boltzmann equation assuming a shifted Maxwellian for the electron velocity distribution function. Appropriate moments of the Boltzmann equation are performed to obtain equations for particle, momentum and energy conservation. In each case, the collision integrals which incorporate elastic, inelastic and ionization processes through energy dependent cross-sections reduce to rate coefficients. Electron spatial diffusion and ponderomotive effects are neglected. These equations advance the local fluid parameters in time with  $E$  being determined from a 1-D wave equation which describes field propagation through the fluid. Introducing an area factor into the wave equation that changes along the path of propagation and making use of Poynting's theorem results in discrete terms which provide the effects of reflection, propagation, focusing and fluid coupling. The fields are advanced in time and space with the current density being determined from the fluid equations. In the present experimental simulation a distinction between propagation directions in the equation is included by the introduction of left and right propagating components of the wave field and corresponding area factors. The area factors are obtained from measurements taken along the 2-D propagation path and folded into an equivalent 1-D simulation. Optical emissions in the  $N_2$  3371 Å and  $N_2^+$  3914 Å bands are calculated as described above.

Detailed results from 1 Torr calculations, based on the incident waveform of Figure 2, are shown in Figure 16. Figure 16a shows the time history of the microwave pulse at a quarter wavelength from the reflecting surface. This waveform corresponds directly to the transmitted pulse in the experiment. Note that severe attenuation occurs at approximately 150 ns into the pulse in rough agreement to the value of 120 ns measured in the experiments. An additional feature is the existence of a significant tail on the transmitted pulse, in qualitative agreement with the data. Plots of electron density, mean kinetic energy and thermal energy vs. time are also shown in Figures 16b and 16d. The calculated ionization and momentum exchange rates are  $\nu_i = 3.1 \times 10^8 \text{ s}^{-1}$  and  $\nu_m = 2.0 \times 10^{10} \text{ s}^{-1}$ , respectively. Plots of the volume emissivity are shown in Figure 17c. Note that the normalized peak of 3914 Å preceeds that of 3371 Å by about 15 ns, compared with the measured value of 23 ns. In absolute magnitude the 3914 Å emissivity is calculated to be about a factor of 87 less than that of 3371 Å while measurements yield ratios of from 2.5 - 6.6.

At this point in the analysis of data we find that the fluid calculations of the breakdown times (ionization rates) are in good agreement with the experiments at 1 Torr. In other simulations at 3 Torr the agreement is less satisfactory while substantial discrepancies exist at the lower pressures. This trend is supported by previous microwave breakdown measurements as well. Figure 4 illustrates this fact quite clearly. Note the significant scatter in the data taken at low pressures (data above 200 V/cm/Torr were generally taken at pressures < 1 Torr). Note also that the kinetic results are, on average, in better agreement with the breakdown times at low pressure. The transmitted pulse shapes decay at a rate faster than predicted at 1.0 and 0.1 Torr, suggesting that the collisionality of the plasma is higher than predicted -- perhaps due to the existence of anomalous wave particle interactions. The decay at 0.03 Torr is less than predicted by fluid theory, a result that could be explained by kinetic effects (see below).

The photometer measurements often yield intensity ratios significantly different from theory. We believe that this discrepancy reflects our inability to completely model the temperature relaxation of the plasma accurately with a fluid model. Both emission pulses

are in good agreement with the simulations in terms of the rise in intensity, the time of the peak intensity, and the decay of the pulse (maximum discrepancies of 30-50 %). The observed delay in peak emission is consistent with a 60 ns life time for the 3914 Å transition. In both experiment and theory the decay for 3914 Å is consistent with quenching and spontaneous decay rates. However, for 3371 Å the decay rate is less than expected and suggests the existence of additional heating or enhanced excitation. In general, it appears that 3371 Å emission is very sensitive to the evolution of the electron energy tail which may be influenced by conduction or diffusion effects not included in the simulation.

Kinetic effects were studied through detailed solutions of the Boltzmann equation for air breakdown, which yielded highly non-Maxwellian distribution functions under some conditions. As an example of kinetic effects the calculated ionization rate is shown in Figure 15. For energies less than 7.5 eV the ionization rate is higher for kinetic calculations due to the presence of a high-energy tail while for greater energies the ionization rate is less due to runaway depletion of the tail of the distribution function. The fact that the computed ionization rate at 3 Torr (electron energy of 5.7 eV) is less than the measured rate and higher than that measured at pressures less than 1 Torr (electron energies greater than 10 eV) is evidence for these effects. Similar results are apparent in Figure 4 where the agreement between experiment and kinetic theory is better than with fluid theory at low pressure. To the extent that the excitation ratios shown in Figure 16 are indicative of the relative line ratios, kinetic theory would predict a lower ratio below 20 eV and a higher one above 20 eV than fluid theory, in qualitative agreement with the experimental results.

Finally, air chemistry computations have been performed for various AIM geometries which take into account 55 chemical species [Zinn, 1989]. For the conditions of 120 ns pulses separated by 1 ms focused to result in critical density breakdown at an altitude of approximately 45 km, it is first found that the neutral gas is heated to temperatures exceeding 5000 °K. These high temperatures would lead to strong turbulent mixing of the air. Local NO production rates are found to be  $\sim 6 \times 10^{13} \text{ cm}^{-3} \text{ s}^{-1}$  at this altitude. This rate is significant with respect to detectable local ozone depletion if the breakdown volume approaches  $\sim 10^4 \text{ m}^3$ . Figure 17 shows calculated NO concentration evolution over the first few seconds of sustained breakdown. Under conditions of low pulse rate operation in this altitude range or high pulse rate operation at higher altitudes,  $\text{NO}_x$  concentration enhancements appear negligible. These results are preliminary and require further refinement with global atmospheric convective models to confidently resolve existence of collateral atmospheric hazards.

## 7. Atmospheric Experiment Implications

The laboratory experiments and theoretical modeling provide the groundwork for rudimentary design of an atmospheric experiment, given an optimization criteria. Several optimization criteria are available depending on the application and availability of resources: frequency selection, pulse duration, power density, pressure (altitude), fluence, or breakdown size. Cost is chosen here as the driving factor, which is assumed to relate to breakdown cross sectional size and required fluence. We first make use of the scaling relationships referred to above in establishing optimization criteria for minimized fluence, check the criteria with the laboratory measurements, and then combine the criteria with electro/mechanical constraints of existing resources to arrive at a minimum proof-of-concept experiment. Finally, a simulation of the approximate optimal conditions is performed to include self-action phenomena.

Fluence optimization begins with rewriting the simple relationship of fluence,  $F = (E_{\text{rms}}^2/377) \tau_{\text{BD}}$ , in terms of the breakdown parameters  $E_{\text{eff}}/P$  and  $v_m/\omega$ , and optimizing with respect to these parameters. All other breakdown parameters are then obtainable from the scaling laws. The breakdown time,  $\tau_{\text{BD}}$ , is arrived at by assuming a breakdown criteria of  $10^8$  electron density gain, and using an empirical formula for ionization rate derived from experiments [Ali, 1988]. The rms field is rewritten as the effective field. Optimization of fluence with respect to the breakdown parameters obtains the matched condition described earlier,  $\omega = v_m$ , and the primary optimization criteria of  $E_{\text{eff}}/P = 0.029 \text{ (V/nl/T)}$ . A summary of optimization criteria may be written as:

$$\begin{aligned} P(\text{T}) &= 0.75 \text{ f(GHz)} \\ E_{\text{eff}}(\text{V/m}) &= 0.029 P(\text{T}) \\ F(\text{J/m}^2) &= 0.4 P(\text{T}) \\ \tau_{\text{BD}}(\text{ns}) &= 132.0/P(\text{T}) \end{aligned}$$

Reduction of the breakdown area to minimal size requires maximizing antenna gain; i.e., maximizing antenna size and minimizing wavelength. Though there is a tradeoff here with respect to the expense of production of energy at different frequencies, review of available resources suggests minimal equipment development if use of the Arecibo Observatory 300 m antenna dish in a single beam system and the Stanford Linear Accelerator (SLAC) 2.856 GHz klystrons are utilized. Choosing  $f = 2.856$  GHz results in  $P = 2$  T,  $E_{eff} = 52$  kV/m ( $14$  MW/m<sup>2</sup>),  $F = 0.9$  J/m<sup>2</sup>, and  $\tau_{BD} = 60$  ns. Checking with the measured optimum conditions for fluence in Figure 3 verifies these parameters (where the single beam fluence for a two beam system must be multiplied by four to obtain a single beam system equivalent fluence). The diffraction limited spot size of the 300 m dish with this frequency, focused at 60 km is 22 m, located at  $\sim 45$  km altitude. This results in a required radiated pulse energy of  $\sim 340$  J, or  $\sim 0.9$  kJ initial pulse energy assuming  $\sim 40\%$  efficiency in pulse compression and transmission. Current SLAC klystrons produce 30 MW in 10  $\mu$ s pulses, or  $\sim 300$  J. Hence, a minimum system would consist of 3 ea klystrons with pulse compression. Different pulse compression techniques are available, but the maximum compression demonstrated in experiments is  $\sim \times 100$  [Alvarez, 1986; Alvarez, et al., 1986]. Hence, 100 ns pulses should be obtainable, as an approximate match to the above optimization. Thus, a minimum proof-of-concept AIM atmospheric experiment might consist of 3 klystrons, the Arecibo dish focused to give a 22 m spot size with 3.6 GW pulses lasting 100 ns. Alternatively, a 430 MHz frequency choice (an established radar frequency at Arecibo Observatory) results in a higher altitude and lower fluence requirement, but a  $\times 10$  increase in energy due to the reduced antenna gain. Further power conditioning development appears required to employ UHF frequencies in an Arecibo-based demonstration experiment.

To examine this scenario in greater detail, a simulation was performed with a simplified version of the 1-D fluid code in which the high frequency limit ( $\omega_e \ll \omega_c$ ) for the plasma dielectric constant was assumed. The results are presented in Figure 18 showing the fluence enhancement, or gain factor, over initial 300 m aperture fluence, both without (dashed line) and with (solid line) breakdown. The enhancement without breakdown represents the near field focus from the 300 m dish down to the 22 m focus spot. The truncated enhancement with breakdown represents the attenuation of the tail of the pulse ("tail erosion") by the electron density buildup resulting from the front of the pulse. This phenomenon is similar to the pulse attenuation seen in laboratory data of Figure 3, but is associated with long path lengths and low densities only found in atmospheric experiments. Even with the indicated severe tail-erosion, density gain is observed to be  $\sim 10^7$ , a satisfactory value for initial experiments. Electron temperatures rose to  $\sim 12$  eV. A four klystron simulation was also run to attempt additional density enhancement. However, only a factor of  $\times 2$  increase in density was obtained as a result of even earlier onset of tail erosion. Hence, tail-erosion is observed to be a strong limitation in single-beam systems.

## 8. Conclusions

Laboratory measurements and supporting theoretical modeling described here have demonstrated the feasibility of producing and maintaining a microwave-induced ionization layer under upper atmospheric conditions within existing technology constraints. However, critical issues of tail-erosion of the microwave pulse over long atmospheric paths, control of the ionization geometry for specular RF reflection, and management of collateral environmental, biological and electronic hazards, require further review in the context of specific atmospheric experiment designs.

## REFERENCES

- Ali, A. W., *Laser and Particle Beams* 6, No. 1, p. 105, 1988.  
 Alvarez, R. A., et al., *Rev. Sci. Instr.* 57, p. 2475, 1986.  
 Alvarez, R. A., *Rev. Sci. Instr.* 57, p. 2481, 1986.  
 Armstrong, W. T., and R. A. Roussel-Dupre', private communication, 1987.  
 Armstrong, et al., *Lecture Notes Second Suzdal URSI Symposium* (Tromsø, Norway, 19-23 Sept. 1988), 1988.  
 Askarjan, G. A., et al., *Proc. Academy of Sciences USSR, Geophysics* 302, No. 3, p. 566, 1988.  
 Borisov, N. D., and A. V. Gurevich, *Geomagnetism and Aeronomy* 20, p. 587, 1980.  
 Byrne, D. P., "Intense Microwave Pulse Propagation Through Gas Breakdown Plasmas in a Waveguide", Ph. D. Thesis, U. of Cal. Davis, 1986.  
 Eckstrom, D. J., et al., *Rev. Sci. Instrum.* 58, p. 2244, 1987.  
 Eckstrom, D. J., and M. S. Williams, private communication, 1989.  
 Gurevich, A. V., *Sov. Phys. Usp.* 23, 862, 1980.  
 Hutton, D. E., private communication, 1990.  
 Mayhall, D. J., et al., *Laser Interactions and Related Phenomena* (Plenum Publishing) 8, p. 121, 1988.  
 Roussel-Dupre', R. A., and W. T. Armstrong, *Proc. 1988 IEEE Conf. Plasma Science* (6-8 June 1988), p. 82, 1988.  
 Roussel-Dupre', R. A., et al., *Proc. XIX Int. Conf. on Phen. in Ionized Gases* 1, p. 200, 1989.  
 Stalder, K. R., and D. J. Eckstrom, private communication, 1989.  
 Tunnell, T., private communication, 1989.  
 Tunnell, T., private communication, 1990.  
 Vikharev, A. L., et al., *Sov. J. Plasma Phys.* 10, 96, 1984.  
 Zinn, J., private communication, 1989.

## FIGURES

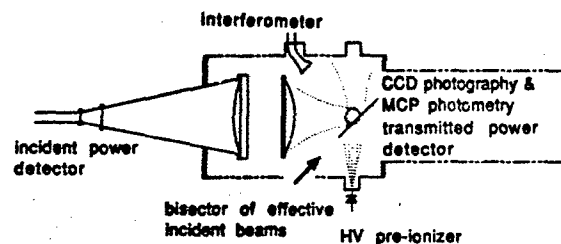


Figure 1. Experiment schematic for AIM-II and III research campaigns.

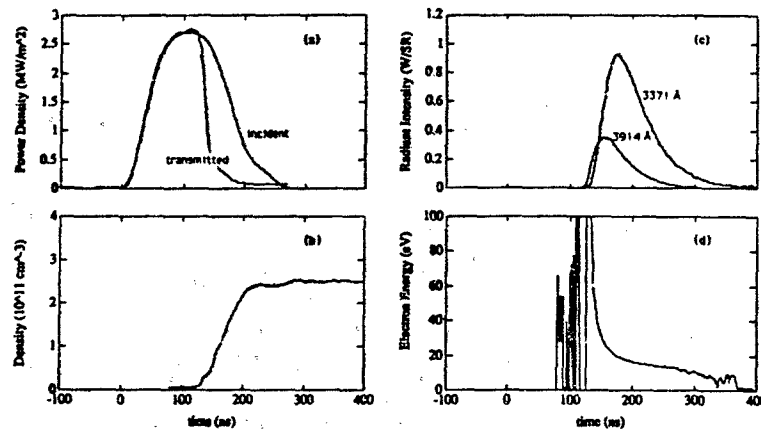


Figure 2. Example experimental data time histories for AIM-II 1 Torr conditions.

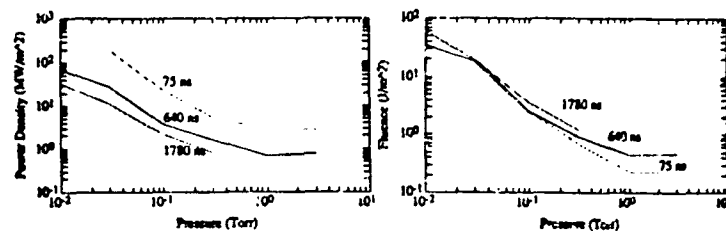


Figure 3. Power density and fluences for present breakdown threshold data.

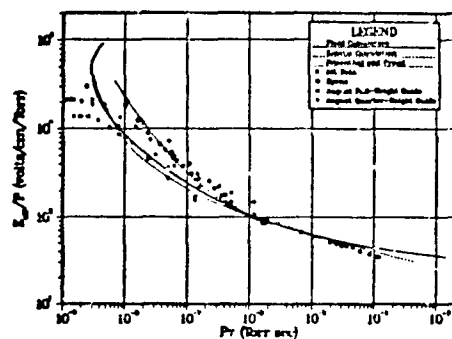


Figure 4. Field thresholds from present and past data, and modeling.

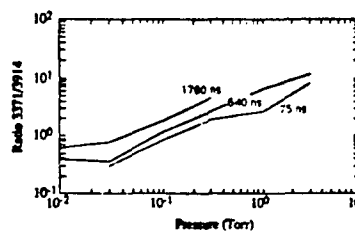


Figure 5. Summary emission ratios.

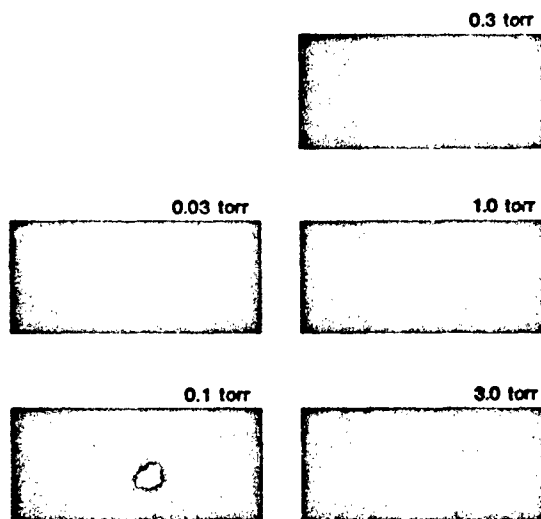


Figure 6. Pressure variation of single layer breakdown geometry.

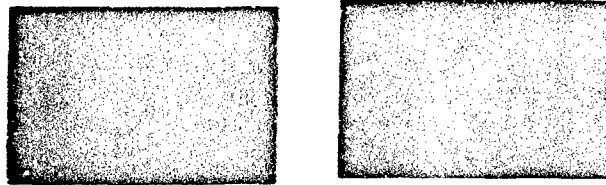


Figure 7. Multiple layer breakdown geometry for 0.1 Torr (left) and 3 Torr (right).

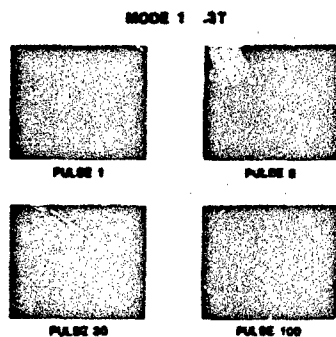


Figure 8. Mode-1 breakdown evolution.

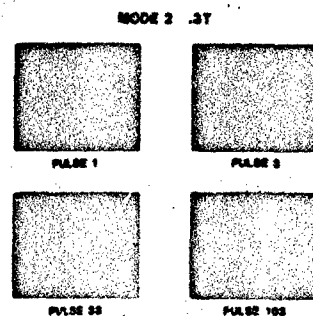


Figure 9. Mode-2 breakdown evolution.

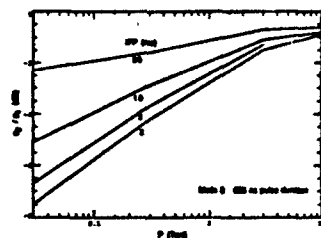


Figure 10. Repetitive pulse reduction of sustainment power.

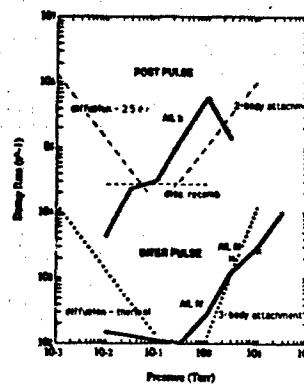


Figure 11. Ionization decay rate summary.

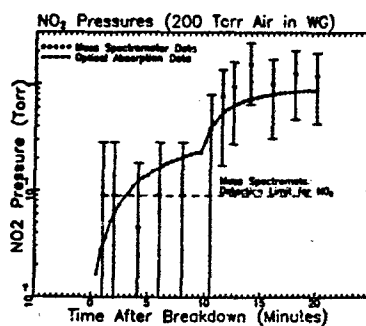


Figure 12. NO<sub>2</sub> rise from light absorptancy and mass spectroscopy.

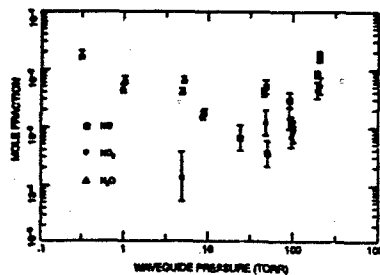


Figure 13. Mole fractions of N<sub>x</sub>O<sub>x</sub> products from mass spectroscopy.



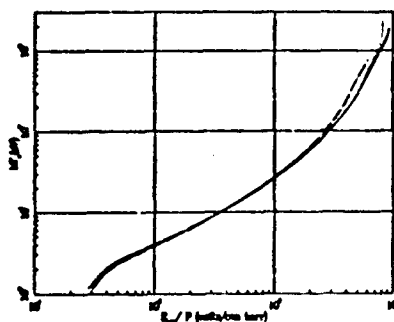


Figure 14. Steady state scaling of  $T_e$  vs  $E/P$  for frequencies from DC to 10 GHz.

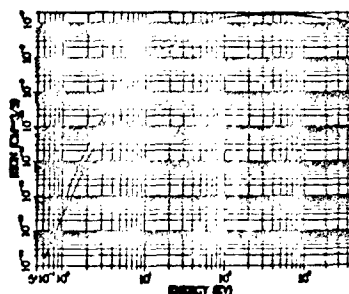


Figure 15. Predicted kinetic ionization rate (solid) and fluid model result.

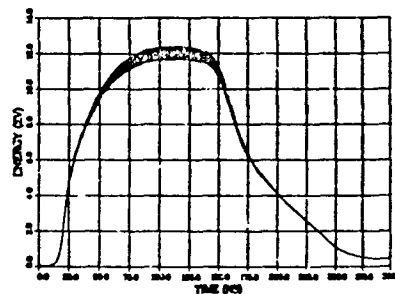
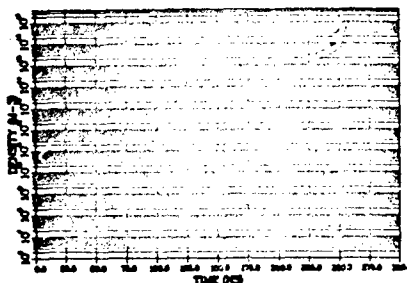
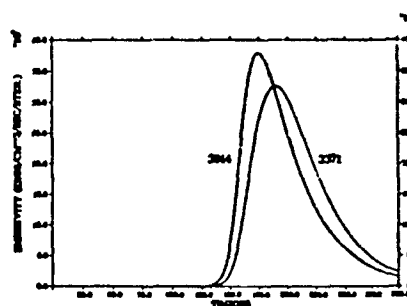
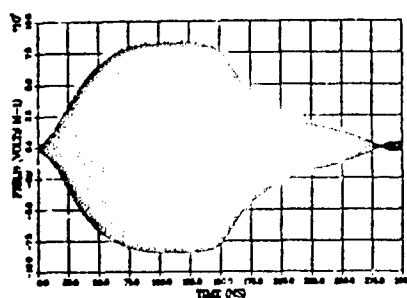


Figure 16. Fluid simulations at 1 Torr.

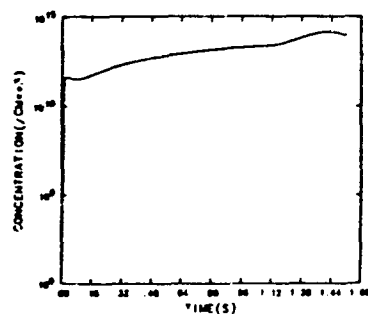


Figure 17. Calculated concentration of NO produced by sustained AIM operation at  $-45$  km altitude.

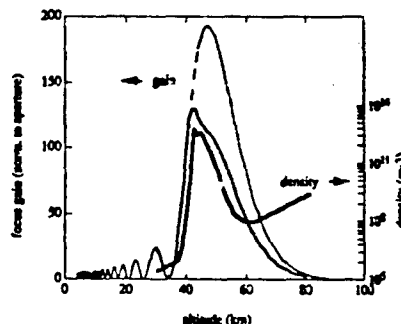


Figure 18. Arecibo Observatory proof of concept experiment simulation.

## DISCUSSION

D. PAPADOPOULOS, US

I would comment that I view tail erosion as one of the beneficial items, since it allows us to control the shape of the layer and avoid reaching critical frequency with its associated uncontrollable structure.

## AUTHOR'S REPLY

Tail erosion within the conditions discussed in this paper, occurs at densities of  $10^8$ - $10^9$  cm<sup>-3</sup>. This effect prevents access to densities of  $10^9$ - $10^{10}$  cm<sup>-3</sup> which are of interest in maximizing ionization lifetimes and accessing higher reflecting frequencies. These densities are still well below the critical density of  $10^{11}$  cm<sup>-3</sup> for conditions considered in this paper. Tail erosion contribution to the shape of the layer depends on the specific system design, but appears to necessitate multiple beams or extremely large apertures for higher frequency systems.

## ON THE FEASIBILITY OF MICROWAVE PRODUCED BRAGG REFLECTOR: EXAMINED BY THE CHAMBER EXPERIMENT

S. P. Kao and Y. S. Zhang

Weber Research Institute, Polytechnic University,  
Route 110, Farmingdale, NY 11735, U. S. A.

Paul Kosey

Air Force Geophysics Laboratory  
Hanscom AFB, MA 01731, U. S. A.

Robert J. Barker

Air Force Office of Scientific Research  
Bolling AFB DC 20332-6448 U. S. A.

### ABSTRACT

A set of parallel plasma layers is generated by two intersecting microwave pulses in a chamber containing dry air at a pressure comparable to the upper atmosphere. The dependencies of breakdown conditions on the pressure and pulse length are examined. The results are shown to be consistent with the appearance of tail erosion of microwave pulse caused by air breakdown. A Bragg scattering experiment, using the plasma layers as a Bragg reflector is then performed. Both time domain and frequency domain measurements of wave scattering are conducted. The experiment results are found to agree very well with the theory. Moreover, the time domain measurement of wave scattering provides an unambiguous way for determining the temporal evolution of electron density during the first 100  $\mu$ s period. A Langmuir double probe is also used to determine the decay rate of electron density during a later time interval (1 ms to 1.1 ms). The propagation of high power microwave pulses through the air is also studied experimentally. The mechanisms responsible for two different degree of tail erosion have been identified. The optimum amplitude of an 1.1  $\mu$ s pulse for maximum energy transfer through the air has been determined.

### 1. INTRODUCTION:

It is a well known fact that conventional line of sight radars are limited by their range of detection. This limitation is removed, however, by over-the-horizon (OTH) radars<sup>1</sup>. OTH radars use ionospheric plasma to reflect obliquely incident radar pulses back to the ground a distance away from the radar site. The range of detection is, in general, from 1000 to 4000 km which is far outside the range of line of sight (about 400 km). Since the radar pulses are coming down from the ionosphere, moving targets can be detected, in principle, at any altitude. The extended range of detection of OTH radars can also be used to monitor ships and oceans from a land base. Moreover, OTH radar can also be used for air traffic control in areas where the simple line of sight radars can not reach. The above mentioned attractive applications of the OTH radar in turn generate a great deal of concern on how to improve the sensitivity of the OTH radar.

It is believed that the sensitivity of an OTH radar can be improved if the capability of the OTH radar can be extended with respect to three major factors. The first one regards the range of the radar. In order to avoid cluttering in the radar return, a large clearance region which is proportional to the height of the ionospheric reflector is required. The next concerns the resolution of the radar which depends strongly on the radar frequency. The last concern is on the stability of the ionosphere, which varies from day to night. This variation will affect the performance and reliability of the radar.

These concerns may be resolved if a reflector can be positioned at a much lower altitude which is able to reflect radar pulses of much high frequency. In addition, if the reflector is made artificially, its stability and location are controllable. Two schemes have been proposed. Both schemes use a high power RF breakdown approach for plasma generation<sup>2-5</sup>. The RF pulses used for air breakdown and plasma maintenance will be transmitted by ground based phased array antennas. In the first scheme, only a single focused RF beam will be employed to produce an ionization patch in the D region of the ionosphere. The RF beam is required to be focused because the altitude is well above the altitude of minimum breakdown threshold. Consequently, the cross section of the beam at the patch altitude will be too small in comparison with the Fresnel size, and a scanning process must be incorporated in the operation of the RF beam in order to enlarge and tilt the ionization patch. The density of the patch is expected to be only slightly higher than that of the F-peak (i.e.  $n_e \approx 10^{16} \text{ cm}^{-3}$ ). The schematic arrangement of this scheme is shown in Figure 1. The radar resolution may still be improved since the reflector is located at a much lower height.

The second scheme can, however, remedy these difficulties. Two crossed beams are proposed<sup>5</sup> to be used for plasma generation in their interaction region, at an altitude between 30 and 60 km<sup>1,2</sup>. The interference between the fields of the two beams enhances the peak field amplitude and, thus, reduces the required power level of each RF beam. This, in turn, helps to reduce the propagation loss to pulse energy before the two beams intersect. In fact, more energy will be delivered to the destination because the pulse tail erosion problem can be almost completely suppressed, especially when the intersection altitude is chosen to be near 50 km (1 torr pressure<sup>6,7</sup> where the breakdown threshold is minimum (so that the most effective ionization patch can be achieved)). Such a low altitude can be used because the ionization patch will be tilted automatically to a large angle (the average of the propagation angles of the two beams). Moreover, the ionization patch consists of a set of parallel plasma layers which are the consequence of interference between the fields of two beams<sup>6,7</sup>. In the intersection region, field amplitude varies periodically in space in the direction perpendicular to the plane bisecting the two beams. Using Bragg reflection to replace conventional plasma cutoff reflection, the supplemental radar may be possible to operate at much high frequency. Using this scheme, the location of the ionization layers can also be fixed easily. A schematic of the scheme is shown in Figure 2.

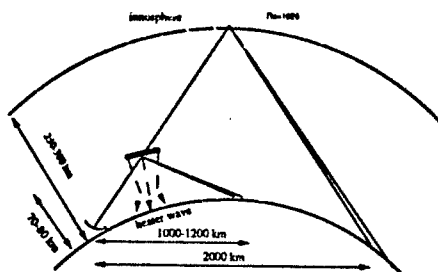


Fig. 1. OTH radar using artificial plasma patches as a mirror

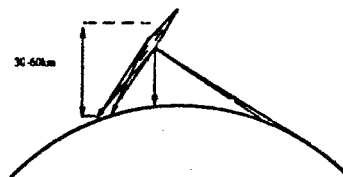


Fig. 2. Two crossed beams scheme

We have conducted a chamber experiment to examine the scientific feasibility of the second scheme. In order to achieve a meaningful simulation of the scheme, three major issues will be addressed by our chamber experiments. These include 1) the effectiveness of the plasma layers as a Bragg reflector, 2) the propagation of high power microwave pulse (HMP), and 3) the lifetime of the plasma.

The organization of this paper is as follows. The experimental set-up is described in Sec. II. The results of an experiment determining the characteristics of air breakdown by microwave pulses are also presented. The Bragg scattering experiment is reported in Sec. III. Measurements in both time domain and frequency domain on scattering are performed and compared with the theory. In Sec. IV the propagation of high power microwave pulses through the chamber is studied. Two different tail erosion mechanisms are identified experimentally. The optimum pulse amplitude for maximum energy transfer through the air is also determined. Described in Sec. V is the measurement of Langmuir probe on the density and temperature of plasma electrons. These results together with those extracted from the Bragg Scattering measurement are used to determine the lifetime of plasma electrons. This work is summarized and discussed in Sec. VI.

## II. EXPERIMENTAL SET-UP AND AIR BREAKDOWN BY MICROWAVE PULSES

Experiments are conducted in a large chamber<sup>8</sup> made of 2 foot cube of Plexiglass and filled with dry air at a pressure corresponding to the simulated altitude. The microwave power is generated by a single magnetron tube (OKH1448) driven by a soft tube modulator. The magnetron delivers 1 megawatt peak output power at a center frequency of 3.27 GHz. The modulator uses a pulse forming network having a pulse width which can be varied from 1.1  $\mu$ s to 3.3  $\mu$ s with respective repetition rates from 60 to 20 Hz. Two microwave beams are fed into the cube, with parallel polarization direction, by two S-band microwave horns placed at right angles to the adjacent sides. The plasma layers are then generated in the central region of the chamber where the two beams intersect. Shown in Fig. 3 is a photo of the plasma layers which are manifested by the enhancement of airglow from the corresponding locations. A maximum of eight layers can be generated, though only seven of them are shown in the photo. Shown in Fig. 4(a) is the typical envelope of a 1.1  $\mu$ s pulse used for plasma generation. Using a focusing lens to localize the enhanced airglow, its temporal evolution between the two consecutive pulses is then recorded on the oscilloscope through a photomultiplier tube. A typical result is shown in Fig. 4(b), which shows the growth and decay of the enhanced airglow. Breakdown of air<sup>8</sup> was detected either visually, as the first sign of a glow in the chamber, or as the distortion in the shape of the pulse received by the horn placed at the opposite side of the chamber. The dependence of the breakdown threshold field as a function of the pressure

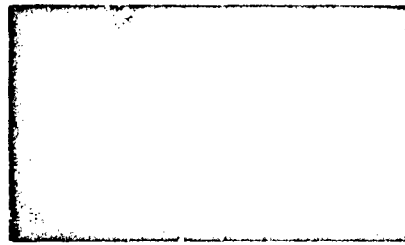
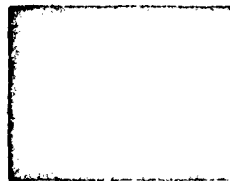


Fig. 3. Plasma Layer Produced by crossed microwave beams



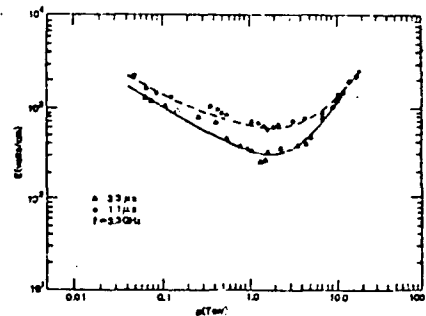
(a)



(b)

Fig. 4. The optical measurement of the airglow from a plasma generated by two intersecting 1.1  $\mu$ s microwave pulse (a) Envelope of 1.1  $\mu$ s microwave pulse the horizontal axis is 200 ns/division 4(b) growth and decay of the enhanced airglow

is then measured. The microwave field is measured by a microwave probe which has been calibrated by a known waveguide field. Shown in Fig. 5 are the Paschen breakdown curves for the cases of 1.1  $\mu$ s and 3.3  $\mu$ s pulses. Since a shorter pulse requires a larger ionization rate in order to generate the same amount of electrons, the threshold field is, therefore, accordingly increased. This tendency is clearly demonstrated in Fig. 5. It shows that the breakdown threshold field for 1.1  $\mu$ s pulse is always larger than that for a 3.3  $\mu$ s pulse. The results also show that in both cases, the breakdown threshold field decreases with a decrease in air pressure and reaches a minimum in the 2 to 1 torr region where  $\omega \approx \nu_c$ ;  $\omega$  and  $\nu_c$  are the microwave frequency and the electron-neutral collision frequency, respectively. With a further decrease in the pressure, the breakdown threshold field increases again. The increase of the threshold field happens also because the wave is in the pulse mode. The ionization frequency and collision frequency are proportional to the neutral density; lower pressure requires a larger field in order to maintain the ionization frequency.

Fig. 5. Dependence of the air breakdown threshold field on the pressure for two pulse lengths breakdown curve for 1.1  $\mu$ s and 3.3  $\mu$ s pulses

The dependence of the breakdown threshold field on the pressure is also manifested by a similar dependence of the degree of attenuation in the tail portion of a single transmitted pulse through the chamber. The experiment is performed by reducing the chamber pressure consecutively from 8 torr to 50 m torr, while the incident pulse is fixed at constant amplitude. A series of snap shots demonstrating this behavior is presented in Fig. 6. In the high pressure region ( $\geq 8$  torr), the breakdown threshold field is higher than that of the incident pulse, and therefore, very little ionization can occur; thus, the pulse can pass through the chamber almost without any distortion (Fig. 6(a)).

However, as the pressure drops, the breakdown threshold also decreases before reaching the minimum, and hence, more ionization occurs and so does more distortion to the pulse (Fig. 6(b)). The distortion always starts from the tail portion of the pulse (i.e. tail erosion) because it takes finite time for the plasma to build up and thus, maximum absorption of pulse energy by the generated electrons always appears in the tail of the pulse. Consequently, the leading edge of the pulse is not affected. Between 2 to 1 torr, the pulse appears to suffer maximum tail erosion and hence only the very narrow leading edge of the pulse can pass through the chamber (Fig. 6(c)). The tail erosion becomes weak again for a further decrease in the pressure (Fig. 6(d)) and eventually vanishes (Fig. 6(e)) once the pressure becomes so low ( $\leq 0.05$  torr) that the breakdown threshold power exceeds the peak power of the incident pulse.

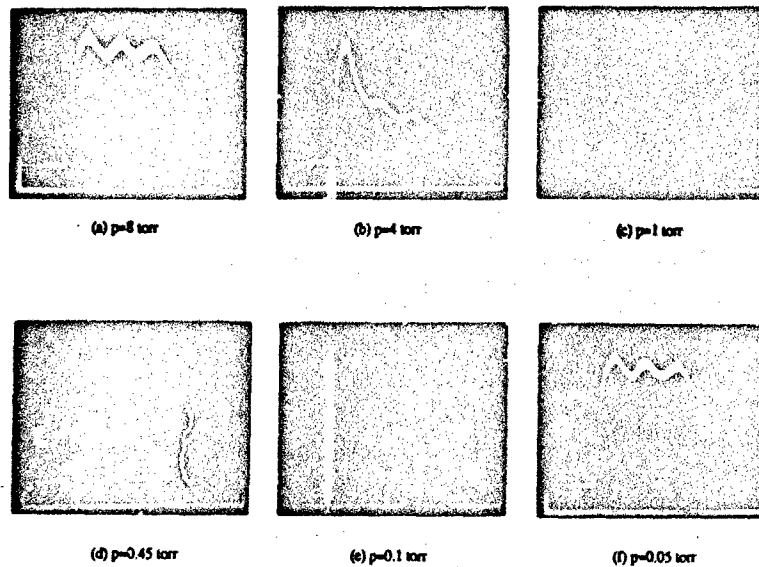


Fig. 6. Pulse propagating through chamber at different air pressure at different pressure

### III. BRAGG SCATTERING

The plasma layers generated by the two crossed microwave pulses are used for the Bragg scattering study<sup>6</sup>. The spatial distribution of the plasma layers is first measured with a Langmuir double probe. This is done by using a microwave phase shifter to move the plasma layers across the probe. The peak density distribution for a spatial period is thus obtained and presented in Fig.7. The result shows that we have indeed produced very sharp plasma layers with very good spatial periodicity. A Bragg scattering experiment has then been conducted and described as follows.

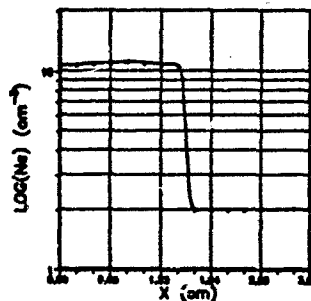


Fig. 7. Probe measurement of the plasma peak density distribution along the direction transverse in the plasma layers. Measurement is from the central point  $x=0$  of one layer to the midpoint  $x=3.24$  of the next layer

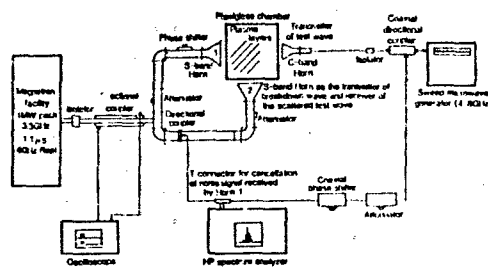


Fig. 8. Microwave Bragg scattering experiment setup

Presented in Fig. 8 is a block diagram of the experiment setup. In addition to the facility used for plasma generation (located to the left of the Plexiglas chamber), a sweep microwave generator (4-8 GHz) is used to generate a test wave which is incident into the chamber through a C-band horn. The incident angle of the test wave with respect to the normal of the plasma layers is 45 degrees. Hence, the S-band horn #2 located at a right angle in the adjacent side can be used as the receiver of the Bragg scattering test wave. In order to separate the Bragg coherent reflection mechanism from the cutoff reflection mechanism, the test wave is swept in a frequency range much higher than the plasma cutoff frequency. Consequently, the test wave will be received by the S-band horn #1 even while the plasma is present. The amplitude of this undesired signal is reduced by using a directional coupler; nevertheless, it represents a large noise to the real scattering signal. To resolve this problem, a standard noise cancellation technique is used. The microwave components used for noise cancellation are shown in the diagram (Fig. 8). An HP spectrum analyzer (8569B) is used for recording the scattering signal. It is noted that the attenuation of the directional coupler is frequency dependent. Only test waves with frequencies leading to more than 15 db attenuation of the directional coupler are used in the experiment. Consequently, the perturbations of the noise signal due to the presence of the plasma, which in principle is in the same intensity level as the scattering signal, is reduced by 15 or more db and will not affect the measurement of the Bragg scattering signal.

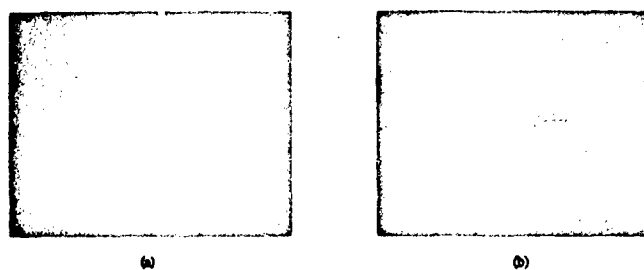


Fig. 9. Spectrum analyzer CRT display. (a) No signal is received when the plasma is off. (b) The spectrum of scattered signal detected when plasma layers are present.

Presented in Fig. 9 are the outputs of the spectrum analyzers for two cases. Fig. 9(a) shows that no signal is received when there is no plasma. However, an appreciable scattering signal is detected, as shown in Fig. 9(b) whenever the plasma layers are produced. The frequency of the test wave is 4.01 GHz, which is much higher than the cutoff frequency. A clear signature of Bragg scattering has been demonstrated. The temporal evolution of the scattering signal has also been measured. The result for a test wave with frequency 6.6 GHz is presented in Fig. 10(a). For comparison, one of the two microwave pulses (both are 1.1 μs) used for plasma generation is shown in Fig. 10(b). As one can see, the scattering signal continues to persist for about 100 μs after the breakdown pulses are turned off. This result indicates that the coherent scattering process can be very effective even when the plasma is well below ( $\approx 2$  order of magnitude) the cutoff frequency of the test wave.

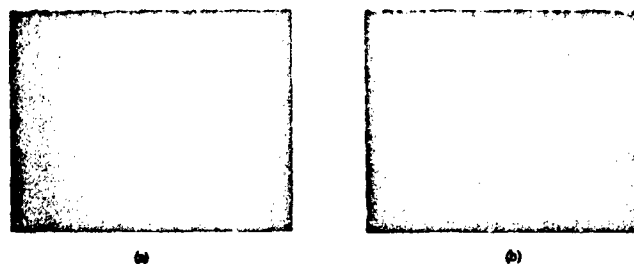


Fig. 10. The time domain measurement of the scattered signal and the microwave pulse used for plasma generation. 10 μs/division. (a) Growth and decay of the scattered signal over a 100 μs time interval. (b) 1.1 μs pulse envelope shown at the same time scale.

The next question is how the experimental results compare with the theory. Considering a set of  $N$  parallel plasma slabs with thickness  $\delta$  and separation  $d$ , and using the Bragg condition  $2d \sin \theta = n\lambda$ , where  $\theta$  is the angle of Bragg scattering,  $\lambda$  is the wavelength of the scattered wave, and  $n$  is a positive integer, the scattering (reflection) coefficient  $S$  of wave intensity is derived analytically and expressed as

$$S = |E_r/E_i|^2 = \left[ k_0^2 \alpha / 2 \right]^2 \sin^2 (n\pi\delta/d) (n\pi/d)^2 \sin^2 N\theta / \sin^2 \theta \quad (1)$$

where  $E_t$  and  $E_r$  are the field amplitude of test wave and scattering wave, respectively,  $\omega = \omega_0 \sqrt{1 + \nu^2}$ ;  $k$  and  $\omega_0$  are the wave number and frequency of test wave, and  $\sin(\omega_0 - \omega) \sin \theta/c$  and  $\omega_0 = 2\pi c/\lambda_0$ . This reflection coefficient is then plotted as a function of the test wave frequency in Fig. 11. By sweeping the test wave frequency, such a dependence is also determined experimentally in a relatively small frequency range (4.3 GHz to 7.8 GHz) and presented in Fig. 11 for comparison. The frequency dependencies of output intensity of the sweep generator and the antenna gain of the receiving horn (S-band horn/2) have been examined and taken into account in calibrating the intensity of the scattering signals. Though a maximum eight layers can be produced, only three of them have significant overlap along a line of sight. Therefore, only these layers can significantly contribute to the Bragg scattering process. Besides an uncalibrated absolute magnitude, the two functional dependencies are shown to agree with each other very well. It is noted that the separation  $d$  between the two adjacent plasma layers is related to the wavelength  $\lambda_0$  of the microwave pulse and the angle  $\theta$  between the propagation directions of the two intersecting pulses, with the relationship  $d = \lambda_0/2 \sin(\theta/2)$ . Using the Bragg condition  $2d \sin \theta = n\lambda_0$ , the optimum frequency for Bragg scattering is given by

$$f_b = n f_0 \sin(\theta/2) / \sin \theta \quad (2)$$

In the present experiment,  $\theta = 90^\circ$ , and thus  $f_b = n f_0$ . This indicates that the frequency of the test wave, which satisfies the Bragg condition for the current experimental arrangement, is equal to the frequency and its harmonics of the breakdown pulses. Consequently, the breakdown wave can not be filtered out and represent a very strong noise, which prevents any meaningful test of Bragg scattering at these frequencies, and in fact, also in the neighborhood frequency regions. Although the optimum frequency region for Bragg scattering is not examined, nevertheless the consistency between prediction and experimental results may lead us to conclude, based on the maximum theoretical reflection coefficient, that plasma layers can indeed be an effective Bragg reflector, especially if more layers can be produced for scattering purposes.

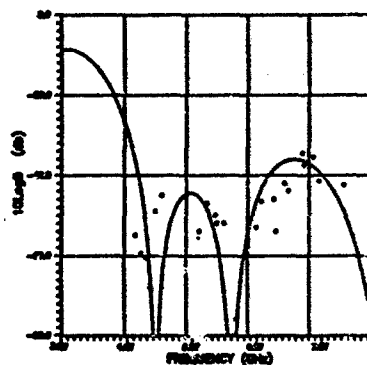


Fig. 11. The dependence of the reflectivity  $S$  of plasma layers on wave frequency. Experimental and theoretical results. The 0dB on the vertical axis is an arbitrary reference

#### IV. PROPAGATION OF HIGH POWER MICROWAVE PULSES THROUGH THE CHAMBER

The propagation of high power microwave pulses through the atmosphere has been a subject with considerable scientific interest.<sup>3-8</sup> This is because air breakdown produces ionization phenomena that can radically modify wave propagation. Ionization gives rise to a space-time dependent plasma which attenuates the tail of the pulse but hardly affects the leading edge because of the finite time for the plasma to build up. A mechanism which is called "tail erosion" plays the primary role in limiting transmission of pulse.<sup>9-11,14</sup> Moreover, the nonlinear and non-local effects brought about by the space-time dependent plasma also play important roles in determining the propagation characteristic of the pulses.<sup>13</sup> Therefore, any meaningful theoretical effort requires a self-consistent description of the propagation process. Consequently, an experimental effort could be more relevant and useful.

Basically, there are two fundamental issues to be addressed. One concerns the optimum pulse characteristic for maximum energy transfer through the atmosphere by the pulse. The second concern is maximizing the ionizations in the plasma trail following the pulse. In general, these two concerns are interrelated and must be considered together. This is because in order to minimize the energy loss in the pulse before reaching the destination, one has to prevent the occurrence of excessive ionization in the background air. Otherwise, the overdense plasma can cutoff the propagation of the remaining part of the pulse and cause the tail of the pulse to be eroded via the reflection process. This process is believed to be far more severe in causing tail erosion than the normal process attributed to ionization and heating. Once this process occurs, the remaining pulse will become too narrow to ionize dense enough plasma.



The purpose of our experimental effort is to understand the fundamental behavior of tail erosion and address the question of how energy loss depends on basic parameters such as pulse intensity and background pressure. The experimental data can then be incorporated for the development of an useful theoretical model for a self-consistent derivation of pulse propagation.

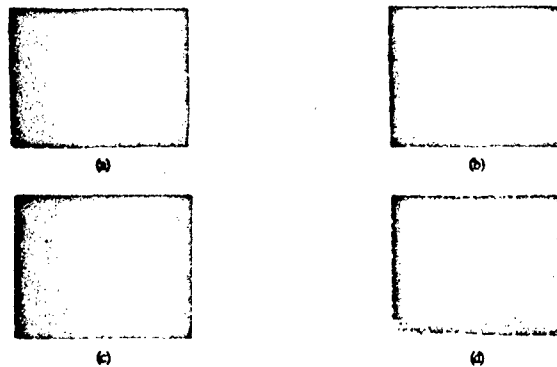


Fig. 12. Tail erosion of microwave pulses of four consecutively increasing amplitudes  $A_0 - A_3$  after propagating through the chamber with 1 Torr background pressure (a) Amplitude  $A_0$  below the breakdown threshold and no erosion. (b)  $A_1 = 1.5A_0$ . (c)  $A_2 = 2A_0$ . (d)  $A_3 = 3A_0$

Tail erosion phenomenon is demonstrated by the snap shots presented in Figure 12, where 1.1  $\mu$ s pulses, with four consecutively increasing amplitude, are transmitted into the chamber of 1 torr pressure from one side and received from the opposite side. The first pulse has amplitude below the breakdown threshold, and hence, nothing is expected to happen. Consequently, the received pulse shape (Fig. 12(a)) is undistorted from that of transmitted pulse. Once the amplitude exceeds the breakdown threshold, more tail erosion occurred to the larger amplitude pulses, as is observed by the subsequent three snap shots (Figs. 12(b)-12(d)). This is because the increase of the ionization rate with field allows more electrons, which attenuate the pulse, so build up. Now let's focus on the last two pictures (Figs. 12(c) and 12(d)). Pulses have been eroded strongly in both cases. However, a clear distinction between the two cases is noticed. In one case corresponding to the third picture (Fig. 12(c)), the erosion to the tail of the pulse is not complete. In other words, the received pulse width extends to the original width. In the other case (Fig. 12(d)), a large portion of the pulse is more or less eroded completely during the finite propagation period. Obviously it is a different mechanism responsible for the second case. The ionization frequency becomes so large in the second case that the electron density exceeds the cutoff density of the wave before the whole pulse passes through. The overdense plasma screen reflects the remaining portion of the pulse and causes even more severe tail erosion. In summary, two mechanisms responsible for the tail erosion are identified. One is due to attenuation by the self-generated underdense plasma. The other one is caused through reflection by the self-generated overdense plasma screen. These two processes are also verified by the reflected power level measured for each case. As shown in Figure 13, the snap shots (Figs. 13(b) and 13(d)) presented on the RHS of the Figure are the reflected pulse shape corresponding to each received pulse on the left (Figs. 13(a) and 13(c)). As shown by the last set of pictures (Figs. 13(c) and 13(d)), strong reflection and complete erosion are observed consistently.

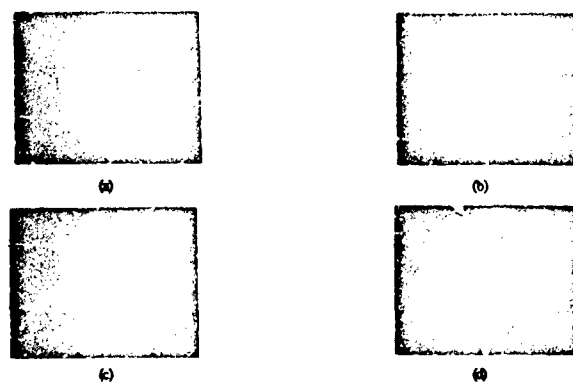


Fig. 13. Received pulses and corresponding reflected pulses. (a) Envelope of received pulse. (b) Reflected pulse corresponding to case (a). (c) received pulse with larger incident amplitude than that of case (a). (d) Reflected pulse corresponding to case (c).

In order to avoid cut off reflection, the power of the pulse should be lower than a critical power  $P_r$  which is defined as the minimum required power for generating an overdense plasma screen. When an overdense plasma screen is formed the shape of the reflected pulse changes drastically and can be monitored easily. Thus, the critical power  $P_r$  can be determined. This critical power varies in general with the pressure. Measurements are made to determine its functional dependency on the pressure  $p$ , shown in Figure 14, where  $P=P_r/P_c$  is the critical power normalized to the breakdown threshold power  $P_c$  whose dependencies on the pressure and pulse width are shown in Fig. 5. Due to the limitation on the power of our microwave facility, only region of 0.2 to 10 torr for the critical power is examined. Nevertheless, this is the pressure region of main concern because air breakdown has its lowest threshold.

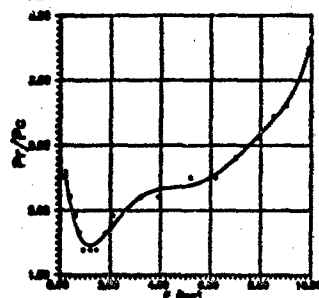


Fig. 14. The dependence of the normalized critical power  $P=P_r/P_c$  on pressure for 1.1  $\mu$ s pulse.

Our study indicates that an increase of pulse amplitude may not help to increase the energy transfer by the pulse. This is because two tail erosion mechanisms are at play to degrade the energy transfer. A demonstration is presented in Figure 15, where the growth and decay of airglow enhanced by electrons through air breakdown by 3.3  $\mu$ s pulse are recorded for two different power levels. In Figure 15(a) the power level is below the critical power and the airglow grows for the entire 3.3  $\mu$ s period of the initial pulse width. As power is increased beyond the critical value, the initial growth of the airglow becomes faster as shown in Figure 15(b). However, it is also shown in Figure 15(b) that the airglow saturates at about the same level as that of Figure 15(a). Moreover, the airglow already starts to decay even before the 3.3  $\mu$ s period. In other words, cutoff reflection happening in the second case limits the energy transfer by the pulse. The additional energy added to the pulse is wasted by reflection. The way to solve the problem is either to lower the amplitude of the pulse or to narrow the pulse width so that the propagation loss can be minimized.

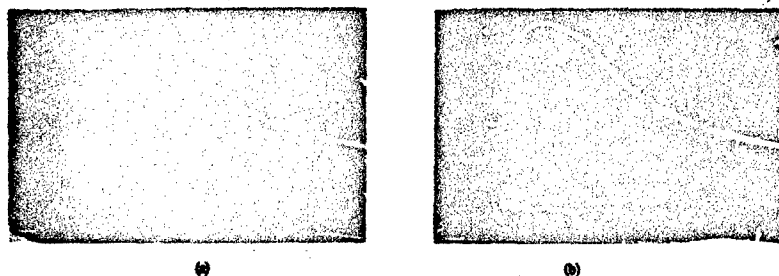


Fig. 15. The growth decay of enhanced airglow (upper trace). Pulses of 3.3  $\mu$ s duration and at two different levels  $P_1$  for (a) and  $P_2$  for (b) are used for causing air breakdowns, where  $P_2/P_1 = 1.32$ . The lower trace of each photo represents the time dependence of the microwave pulse. The horizontal scales are 1  $\mu$ s/div.

#### V. LIFETIME OF ELECTRONS

For practical purpose, the lifetime of plasma generated by microwave pulses is interested. Since in the application, e.g. use of plasma as a reflector of OTH radar, One would require that the plasma is sustained at or above certain electron density level (e.g.  $10^{17} \text{ cm}^{-3}$  one order of magnitude higher than that of the F peak) for long enough time (e.g. about 1 sec of the operation time of the radar), it could be done by using repetitive pulses. However, if plasma decays very fast, one would have to increase the duty cycle of microwave facility (i.e. the repetition rate of the pulse). It implies that more power is needed in the operation. This is then translated as that more expensive microwave facility will be required and more running cost will be resulted. On the other hand, if plasma is shown to have desired long lifetime, the current technology is already ready for required specifications. The design of the system becomes straightforward and more important, the whole system can be justified to be economically feasible and competitive.

In general, there are three processes that work together to cause the decay of the plasma. They are electron diffusion, electron-ion recombination, and attachment of electrons to the neutral molecules. For the case of 1 torr background pressure, electron-neutral collision frequency is about GHz. The free electron diffusion coefficient  $D$  is estimated to be about  $3 \times 10^4 \text{ cm}^2/\text{sec}$ . Thus, the diffusion time for free electron to walk randomly from the center of the chamber to the side walls is calculated to be about 20 ms. If the ambipolar effect is taken into account, the diffusion time becomes even larger and is in the order of seconds. Therefore, we simply ignore the diffusion effect on the electron decay rate in the present study. Since the carrier frequency of microwave pulses is 3.27 GHz, the peak electron density ionized by the microwave pulses is in the order of  $10^{11} \text{ cm}^{-3}$ . Thus, the electron-ion recombination rate is always smaller than the electron attachment rate whose maximum value at 1 torr pressure of air is about  $1.4 \times 10^5 \text{ cm}^{-3}\text{sec}^{-1}$ . We therefore expect that the initial decay rate (i.e. the maximum decay rate) of the electrons is determined by the electron attachment rate and is somewhat bounded by this value  $1.4 \times 10^5 \text{ sec}^{-1}$ .

As given by (1), Bragg scattering coefficient  $S$  of wave intensity is directly proportional to  $n_e^2$ . Hence, the Bragg scattering experiment with the produced plasma layers described in sec.III also provides a way for a non-destructive measurement on the temporal evolution of plasma electron density. Using the result, shown in Fig. 10(a), of the temporal evolution of the scattering signal from a test wave, the electron decay rate after the breakdown pulses have passed through (i.e. the initial decay rate) is evaluated to be  $6 \times 10^4 \text{ sec}^{-1}$ , which is consistent with the dissociative attachment rate. It also shows that the electron density after 70  $\mu\text{s}$  is reduced by a factor of about 30. Similarly, the electron decay rate is also reduced over a factor of 10 from the initial decay rate. In this density level ( $\approx 3 \times 10^9 \text{ cm}^{-3}$ ) the decay rate is consistent with the recombination loss rate. This is realized by the fact that when enough negative molecule ions are produced through the electron attachment process, the detachment rate for electron regeneration is increased and eventually balances out the electron attachment loss rate. Thus, the dominant electron loss mechanism is shifted to the recombination process. On the other hand, the attachment process also plays the role to reduce the recombination and diffusion losses of electrons. Through the attachment process, the excess of free electrons is first stored by attaching themselves to the low mobility neutral molecules and then released to be the source of free electrons of the system whenever there is a need for the balance among all the process involved. When such a balance is reached (e.g. 70  $\mu\text{s}$  point of Fig. 10(a)), free electron density will only decay at a relatively slow rate determined by the recombination process and the ambipolar diffusion process.

With the available power ( $\approx 10 \text{ mW}$ ) of sweep microwave generator and the detecting facility (HP spectrum analyzer 8569B), the Bragg scattering measurement is no longer sensitive to the electron density at the level after 100  $\mu\text{s}$  decay from its peak (i.e. Fig. 10(a)). The evolution of electron density at later time is then determined by a Langmuir double probe. The main purpose of Langmuir probe measurement is to confirm that the decay of electron density after the balance of process is reached is indeed caused mainly by the recombination process. As an additional payoff, the probe measurement can also provide the information on electron temperature. The difficulty with Langmuir probe measurement lies on the presence of negatively charged molecules so that the ion density is not quite the same as the electron density. The presence of negatively charged molecules also complicates the relationships among the electron density, electron temperature, and ion density etc. inside a sheath. For instance, the sheath potential changes its sign when the density of negatively charged molecules becomes much larger than that of free electrons. It can be monitored experimentally by the direction of current flow through a grounded single probe. We, therefore, report only the results in the time interval in which the percentage of negatively charged molecules is effectively low. Shown in Fig. 16 is the Langmuir double probe measurement of temporal evolution of electron temperature  $T_e(t)$  during the first 18  $\mu\text{s}$  right after the passing through of the microwave pulses. It shows that electron temperature is heated by the microwave pulses to about 1 eV and decreases quickly after the microwave is turned off. The decay rate is about  $10^5 \text{ sec}^{-1}$  which is consistent with the electron energy loss rate via electron-neutral collision. The corresponding evolution of electron density can be drawn from the result of Fig. 10(a).

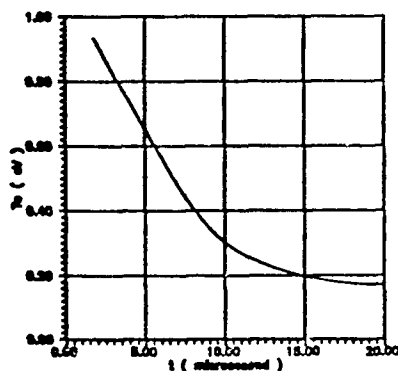


Fig. 16. Langmuir double probe measurement of temporal evolution of electron temperature  $T_e(t)$

We next report the measurement for 100 $\mu$ s period starting at 1ms after turning off the microwave. The V-I characteristics of the Langmuir double probe at four different times are presented in Fig. 17. These curves having a same slope at  $I_p=0$  indicate that all the species of the gas have already reached thermal equilibrium and have a temperature  $\approx 300^\circ\text{K}$ . However, these curves saturate at different current levels. It indicates that ion density still varies with time. Based on the saturation levels of these curves, the evolution of ion density with time is determined. In this time interval (1ms, 1.1ms) electron density can be assumed to be in the same order of magnitude as the ion density. The evolution of electron density is thus determined and plotted in Fig. 18. The decay rate of  $500\text{ sec}^{-1}$  is indeed consistent with the recombination rate at this density level.

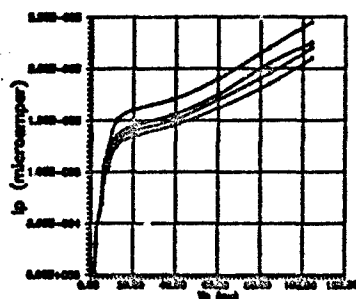


Fig. 17. The V-I characteristics of the Langmuir double probe at four different times

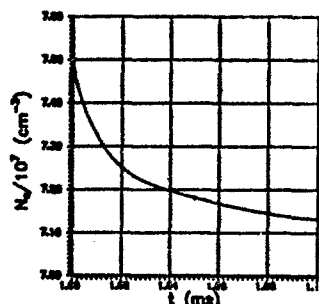


Fig. 18. The evolution of electron density in time interval (1ms, 1.1ms)

We have shown that in the density region of interest the decay rate of electron density is governed by the electron-ion recombination rate. Based on this decay rate, repetitive pulses with a repetition rate about  $250\text{ sec}^{-1}$  will suffice for maintaining the electron density to a level ( $\approx 10^7\text{ cm}^{-3}$ ), which is high enough for the OTH radar applications. Moreover, the pulses used for maintaining the plasma can be much shorter than the first pair of triggering pulses which have to start the ionization from relatively low background electron density. Therefore, the required microwave power and energy for plasma generation and its sustenance can be shown to be within the state of the art of current technology.

## VI. SUMMARY AND DISCUSSION

Plasma layers generated by two intersecting microwave pulses are used for the study of Bragg scattering. The experiment is conducted in a large chamber with a microwave absorber so that the microwave reflection from the wall can be minimized. Hence, the experiment can be considered to be a laboratory simulation of conceptualized plasma layers generated by high power radio waves in the upper atmosphere, as investigated theoretically by Gurevich.

We first determine the characteristic of air breakdown by powerful microwave pulse. This is mainly because the plasma generated near the wall adjacent to the microwave horn causes erosion of the tail of the incident pulse and the pulse becomes too short, by the time it reaches the central region of the chamber, to cause appreciable ionization. However, this problem is easily overcome when the scheme of two intersecting pulses is used for plasma generation. In this approach, each pulse has its field amplitude below the breakdown threshold to avoid the tail erosion. However, the fields in the intersecting region can add up and exceed the breakdown threshold. This scheme is most effective when the two pulses have the same polarization and are coherent. In this case, the wave fields form a standing wave pattern in the intersecting region in the direction perpendicular to the bisecting line of the angle  $\phi$  between the intersecting pulses. Thus, parallel plasma layers with a separation  $\phi/\lambda \approx (0)$  can be generated. This result is shown in Fig. 1.

Since there are no electrodes involved in the current experiment of air breakdown, we can determine the breakdown threshold field as a function of the air pressure within the accuracy of microwave probe measurement. Two Paschen breakdown curves for the cases of 1.1 and 3.3 $\mu$ s pulses are determined as shown in Fig. 5. The appearance of a Paschen minimum can be explained as the result of breakdown by a short pulse which is equivalent to a dc discharge with short separation between electrodes (i.e. short electron transit time). The result that the breakdown threshold by a longer pulse (3.3 $\mu$ s) is lower than that by shorter pulse (1.1 $\mu$ s) agrees with the explanation. The characteristic of the curves is also confirmed phenomenologically by the various degrees of tail erosion of the same pulse passing through the chamber at different pressure, as shown in Fig. 6.

An optical probe has been used to monitor the growth and decay of airglow enhanced by microwave generated electrons. Two processes are, in general, responsible for the airglow. One is through the electron-ion recombination and the other one is through impact

excitation of natural gas. Since only weakly ionized plasma is generated, the second process is believed to be dominant. However, the second process requires that the electron energy exceed 2eV. Therefore, the decay rate of airglow intensity shown in Fig. 4(b) accounts for not only the decay of the electron density caused by the dissociative attachment loss but also for the decay of electron temperature caused by energy loss to the neutrals and the loss of fast electrons.

We then conducted the Bragg scattering experiment with the produced plasma layers. Both temporal evolution of the scattering signal from a test wave and the spectral dependence of the scattering coefficient have been examined. Good agreement between theoretical and experimental results on the spectral dependence of the scattering coefficient has been achieved (Fig. 11). It should be noted that, due to the dimension of the chamber and microwave beams, only three plasma layers have significant overlap along a central line of sight used as the incident path of the test wave for Bragg scattering. Nevertheless, a remarkable effectiveness of Bragg scattering has been demonstrated by the chamber experiment. It is further realized that more layers and much larger cross sectional area for each layer will be produced in the actual installation. One would expect that much more plasma layers can be incorporated for Bragg scattering. Since the scattering coefficient is proportional to the square of the number of layers at play, effective Bragg scattering can still be achieved at even much lower plasma density ( $\sim 10^7 \text{ cm}^{-3}$  for practical application) than that of current experiment ( $\sim 10^9 \text{ cm}^{-3}$ ), where the radar frequency is also more than one order of magnitude lower than that of the test wave used in the current experiment.

An experiment investigating the propagation of high power microwave pulses through the air is also performed. We have identified two mechanisms which are responsible for two different degree of tail erosion. One is attributed to absorption by the self-generated underdense plasma. The other one is caused by reflection by the self-generated overdense plasma screen. Our study indicates that an increase of pulse amplitude may not help to increase the energy transfer by the pulse. This is because the two identified tail erosion mechanisms are at play to degrade the energy transfer. A demonstration is presented in Figure 15, where the growth and decay of airglow enhanced by electrons through air breakdown by 3.3  $\mu\text{s}$  pulse are recorded for two different power levels. In Figure 15(a) the power level is below the critical power and the airglow grows for the entire 3.3  $\mu\text{s}$  period of the initial pulse width. As power is increased beyond the critical value, the initial growth of the airglow becomes faster as shown in Figure 15(b). However, it is also shown in Figure 15(b) that the airglow saturates at about the same level as that of Figure 15(a). Moreover, the airglow already starts to decay even before the 3.3  $\mu\text{s}$  period. In other words, cutoff reflection happening in the second case limits the energy transfer by the pulse. The additional energy added to the pulse is wasted by reflection. The way to solve the problem is either to lower the amplitude of the pulse or to narrow the pulse width so that the propagation loss can be minimized. The optimum pulse amplitude for maximum energy transfer through the air has been determined for 1.1  $\mu\text{s}$  pulse used in the present experiment. Since the effect of pressure gradient and large propagation distance can not be incorporated in chamber experiment, the determination of optimum parameters of the pulses for achieving the most effective plasma generation is deferred until a practical theoretical model developed under the guide of present study is established.

A practical issue concerning the applicability of present study to the OTH radar is the lifetime of plasma electrons generated by the microwave pulses. The theoretical result (1) shows that the scattering coefficient is proportional to the square of the electron density and insensitive to the electron temperature. Therefore, the electron decay rate after the breakdown pulses have passed through can be evaluated from Fig. 10(a). It shows that the initial decay rate is about  $6 \times 10^4 \text{ sec}^{-1}$  which is consistent with the dissociative attachment rate. It also shows that the electron density after 70  $\mu\text{s}$  is reduced by a factor of about 30. Similarly, the electron decay rate is also reduced over a factor of 10 from the initial decay rate. In this region the decay rate is consistent with the recombination loss rate. This is realized by the fact when enough negative molecule ions are produced through the electron attachment process, the detachment rate for electron regeneration is increased and eventually balances out the electron attachment loss rate. Thus the dominant electron loss mechanism is shifted to the recombination process. Using Bragg scattering, the evolution of electron density can be measured only for 100  $\mu\text{s}$ . In order to be sure that the loss of electrons is indeed caused mainly by the recombination process which has acceptable low rate, a Langmuir double probe is used to measure the evolution of electron density at much later time (i.e. 1 ms to 1.1 ms). The result of probe measurement confirms the conclusion of Bragg scattering measurement.

Based on the results of our chamber experiments, it seems to us that the implementation of a Bragg reflector in the upper atmosphere ( $\sim 50 \text{ km}$ ) by two intersecting microwave pulses transmitting from ground for potential OTH radar applications is technically feasible.

#### ACKNOWLEDGEMENT

This work is being supported by the Air Force Geophysical Laboratory through NASA Grant No. NAG 5-1051 and by the Air Force Office of Scientific Research Grant No. AFOSR-85-0316. Useful discussion with Dr. M.C. Lee is appreciated.

#### REFERENCES

1. J. M. Hadrick, M. I. Skolnik, Proceedings of The IEEE Vol. 62 No. 6 June 1974
2. A. V. Gurevich, Geomag. Aeronom 12, 631 (1972).

3. A. V. Gurevich, *Geomag. Aeronoma* 19, 428 (1979).
4. N. D. Borisov, and A. V. Gurevich, *Geomag. Aeronoma* 20, 841 (1980).
5. A. V. Gurevich, *Sov. Phys. Usp.* 23, 862 (1981).
6. S.P. Kao and Y.S. Zhang, *Phys. Fluids B*, 2(3), 667-673, 1990.
7. A. L. Vikharev, V. B. Gifdenburg, O. A. Ivanov, and A. N. Stepanov, *Sov. J. Plasma Phys.* 10, 96 (1984); A. L. Vikharev, O.A. Ivanov, and A. N. Stepanov, *Sov. J. Plasma Phys.*, 10, 460 (1985).
8. A. D. MacDonald, D. U. Gaskill, and H. N. Ginzman, *Phys. Rev.*, 5, 1841 (1963).
9. W. M. Bolka, C. L. Yee, A. W. Ah, M. J. Nagurney, and M. E. Read, *J. Appl. Phys.* 54, 101 (1983); C. L. Yee, A. W. Ah, and W. M. Bolka, *J. Appl. Phys.*, 54, 1278 (1983).
10. J. H. Yee, R. A. Alvarez, D. J. Mayhall, N. K. Madsen, and H. S. Cabayan, *J. Radiation Effects Res. and Eng.*, 3, 152 (1984).
11. B. Goldstein and C. Longmire, *J. Radiation Effects Res. and Eng.*, 3, 1626 (1984).
12. Wee Woo and J. S. DeGroot, *Phys. Fluids*, 27, 475 (1984).
13. J. H. Yee, R. A. Alvarez, D. J. Mayhall, D. P. Byrnes, and J. DeGroot, *Phys. Fluids*, 29, 1238 (1986).
14. S. P. Kao, Y. S. Zhang, and P. Kossey, *J. Applied Phys.*, 67(6), 2762-2766, 1990.

## DISCUSSION

L. DUNCAN, UF

I don't quite understand your equating of tail erosion with formation of a critical density layer. After forming an artificial reflecting layer, why does the experiment just not assume a geometry similar to the one discussed in the preceding paper? In this case the interference pattern would clearly be very dynamic, but this would not be equivalent to traditional descriptions of tail erosion.

AUTHOR'S REPLY

In our case, when cutoff layer is formed, the reflected pulse has different characteristics from that by an inserted conducting plane discussed in the preceding paper. The differences are

1. Plasma cutoff layer is not equivalent to a conductor; in the layer, the electric field is maximum instead of zero.
2. The reflected pulse has shorter pulse length than the incident pulse because the leading part of the pulse can always penetrate through the layer.
3. The cutoff layer has a size equal or smaller than the pulse's cross section. Therefore, the edge effect can significantly deteriorate the shape of the reflected pulse.
4. Experimental evidence: when cutoff layer is formed (as indicated by the anomalous reflection), the breakdown induced plasma loses the expected interference pattern.

## OVERVIEW OF IONOSPHERIC MODIFICATION FROM SPACE PLATFORMS

Peter M. Banks  
 Space, Telecommunications and Radioscience Laboratory  
 Department of Electrical Engineering  
 Stanford University  
 Stanford, CA 94305 USA

## Abstract

This paper discusses space-borne, non-electromagnetic methods of modifying the E- and F-regions of the terrestrial ionosphere. Of these, the most well-understood is the direct injection of chemical vapors into the ambient medium. The first injection of barium clouds into the upper atmosphere over two decades ago has led to evolution of understanding of complex electrodynamic processes acting in the ionosphere and spawned extensive studies of small-scale plasma instabilities. Modification to the ionosphere can last for up to hours from such injections. Other vapors have also been released, including water vapor,  $\text{SF}_6$  and more noxious gases, in successful efforts to alter the chemistry of the ionosphere. In another direction, injections of high amu gases from orbiting spacecraft have been made in attempts to understand the non-classical ionization processes involved in the critical ionization velocity (CIV) concept. The results seem to indicate that for CIV to act in space, large quantities of injected gas are required to achieve a minimum interaction volume density. However, in these and other experiments, it has been found that the potential CIV effects are supplemented by a variety of associated classical processes also acting for these same gases. For example, plasma disturbances are associated with neutral gas releases when charge exchange to ambient ions occurs. This leads to the formation of electrostatically polarized plasma clouds around the neutral gas-emitting space platform and these create large disturbances in the ionosphere.

Direct modification of the ionosphere via energetic electron beams has also been undertaken from rocket and satellite platforms. Results indicate that the process of electron energy deposition is much more complex than previously thought as a consequence of the need to take into account charging of the launching platform, the retarding effects of substantial electric fields near the beam, and atmospheric scattering in the ionosphere. Other forms of ionospheric modification via ion beams, energetic neutral particle beams, x-ray sources and MeV particle beams have also been proposed, but several of these remain to be consummated with experiments.

## DISCUSSION

J. S. BELROSE, CA

Clearly your calculations of the electron densities that your high energy beam might produce at low heights (<50 km) have not taken account of electron loss rates, since you did mention lifetimes of milliseconds. I think it might be useful if you could relate what you might do to what nature can do. During very large solar proton events the electron densities at say 45 km do not exceed  $10^{10} \text{ cm}^{-3}$ . Your speculated instantaneously produced densities were  $10^{10}$  to  $10^{11} \text{ m}^{-3}$ . At 40 km I suspect that electrons will disappear almost as fast as you produce them (lifetimes  $\ll 1 \text{ ms}$ ). Can you comment?

## AUTHOR'S REPLY

The high initial electron densities are quickly reduced by electron attachment to  $\text{O}_2$ . The  $\text{O}_2$ ,  $\text{N}_2$ ,  $\text{O}_2^+$  plasma then decays via dissociative recombination over a period of  $10^{-6}$  to  $10^{-7}$  seconds. Natural solar proton fluxes, in contrast, are in quasi-equilibrium so that production = loss. In this situation the densities of  $\sim 10^{10} \text{ cm}^{-3}$  indicate production rates of  $\sim 1 \text{ cm}^{-3} \text{ sec}^{-1}$ .

R. F. BENSON, US

Concerning ionospheric modification resulting from transmitters in space, the high frequency portion of the space shuttle Waves in Space Plasma (WISP) experiment is scheduled to fly on the Orbital Manoeuvring Vehicle (OMV) test flight in 1995. There has been renewed interest in this field using data from the Alouette and ISIS topside sounders stimulated by the new theoretical approach introduced by V. Osharovich [J. Geophys. Res., 22, 316, 1987; 24, 5530, 1989].

## AUTHOR'S REPLY

Thank you for the added information.

19-2

M. J. RYCROFT, UK

Pursuing J. Belrose's comment, A. von Biel, in a paper published in the August 1989 issue of Planetary and Space Science, reported some unusual radar echoes from heights of 45 to 50 km at Scott Base, Antarctica. Such phenomena, which might be due to solar protons, could, perhaps, be used to cross-calibrate some of your predictions of middle atmosphere ionization profiles.

AUTHOR'S REPLY

We appreciate this information.

B. RIPIN, US

A plasma ejected at orbital velocity can either continue to  $E \times B$  drift in the original direction and speed, or, perhaps, the internal polarization fields can be shorted out due to connection to lower layers of the ionosphere by the B-field. The question is, what actually does occur in these types of releases?

AUTHOR'S REPLY

Both processes occur with erosion at the outer edges of the plasma cloud & forward motion continuing within the core.



# PLASMA DENSITY MODIFICATION BY MEANS OF PULSED BEAM CIV IN THE IONOSPHERE

by

Shu T. Lai  
Space Physics Division, Geophysics Laboratory,  
Hanscom AFB, MA 01731, USA

William J. McNeil  
Rader Inc., Bedford, MA 01730, USA

Edmond Murad  
Space Physics Division, Geophysics Laboratory,  
Hanscom AFB, MA 01731, USA

## SUMMARY

Alfvén's critical ionization velocity (CIV) discharge gives rise to rapid increase in electron density. The existence of CIV has been proven in the laboratory. If CIV occurs in space, there would be important consequences. Not only would electromagnetic wave propagation be affected by the enhanced plasma density, but there would also be important implications in spacecraft contamination. In attempts to prove CIV in space, many researchers used the barium shaped charge explosion method. The results have been mostly negative with two exceptions. We propose a modified CIV space experiment by means of a multiple pulse beam (MPB) of neutral atoms. We use the 'particle-in-cell' method to simulate CIV in a MPB under ionospheric conditions. A single or MPB neutral beam with seed ionization develops the modified two-stream instability which energizes the electrons. When the electrons become hot enough, they ionize the neutrals in the beam. Numerical simulation results of single and multiple pulse cases are compared, revealing the enhanced ionization for the MPB case.

## PREFACE

Alfvén [1954, 1960] proposed the idea of critical ionization velocity (CIV). It suggests that when the relative velocity  $V$  between a neutral gas and a magnetized plasma exceeds a critical velocity  $V_c$ , rapid ionization occurs. The critical velocity [Alfvén, 1960] is given by equating the kinetic energy of the neutrals with their ionization energy:

$$V_c = \sqrt{2e\phi/M} \quad (1)$$

where  $e\phi$  is the ionization energy and  $M$  the mass of the neutral gas molecules. The existence of CIV has been proved repeatedly in the laboratory [Alfvén, 1960; Fahlsson, 1961; Danielsson, 1973; Brenning, 1982]. Indeed, the critical velocity observed in laboratory experiments is very near or slightly above that predicted by Eq(1). Furthermore, nearly 100% ionization has been reported [Alfvén, 1960].

If CIV occurs in the ionosphere, there would be important consequences. As a result of rapid ionization in a CIV discharge, the plasma density in the vicinity of the discharge region would increase rapidly. Enhanced plasma density in the ionosphere may affect electromagnetic wave propagation. In addition, there are important implications of CIV in spacecraft contamination. Under appropriate conditions [Lai and Murad, 1987], spacecraft exhausts may undergo CIV ionization, which may result in chemical modification of the molecular species in the spacecraft environment, and in generation of radiation signatures. In addition, CIV may affect the transport of ion species in the ionosphere.

In recent years, there have been many attempts to prove the existence of CIV in space [see, for example, Newell, 1985; Torbert, 1988; Hallinan, 1988]. All have reported negative or puzzling results so far, with the exception of Porcupine [Macraed, 1982] and CRITZ [Torbert, 1989; Stenflo-Nielsen, et al, 1989; Westcott et al, 1992] experiments which reported about 20% and 4% critical velocity ionization of the barium cloud respectively. All of these space experiments have employed practically the same method, namely, shaped charge explosion of barium (or strontium) in the ionosphere (Fig. 1).

In this paper, we propose a new CIV experiment designed with a better space condition for CIV to occur. The proposed experiment differs from the conventional ones in that instead of using a shaped charge barium explosion, we propose to use multiple pulses. Under these conditions, we hope to be able to initiate CIV in space and to achieve a higher level of ionization when a CIV discharge occurs.

## 1. PULSED BEAM

In the space CIV experiments using shaped charge explosions of barium or strontium, the neutral gas beam is ejected in a single pulse manner. The neutral gas density drops rapidly as the beam expands. When the neutral density is low, so is the probability of ionization. Thus, if CIV is to occur, it must take place in the high density region near the explosion point. On the other hand, the pulse duration is also short in this region. Since electrons are accelerated mainly along magnetic field lines, the electron heating time is limited by the root-mean-square time of the pulse with a given magnetic field line. Since the line is essentially stationary, the contact time equals the pulse duration approximately. This means that when the pulse is too short, electrons do not have enough time to be energized, and therefore CIV can not occur. To improve the beam experiment design, we propose using multiple pulses separated by gaps.

To sustain ionization in a CIV discharge, it is necessary to satisfy Townsend's criterion [Brenning, 1982]:

$$\tau_a \geq \tau_i \quad (2)$$

where  $\tau_a$  is the transit time of a hot electron across the beam. The ionization time  $\tau_i$  is given by

$$\tau_i(x) = 1/[n(x)\sigma(v_e)v_e] \quad (3)$$

where  $n(x)$  is the neutral density at distance  $x$  from the explosion point,  $\sigma$  is the ionization cross section and  $v_e$  the velocity of a hot electron. Assuming that a neutral beam has a conical shape,  $n(x)$  drops as  $x^{-2}$ .

$$n(x) = N_0/[V\pi x^2 \tan^2(\theta/2)] \quad (4)$$

where  $N_0$  is the release rate,  $V$  the beam velocity, and  $\theta$  the cone angle. On the other hand,  $r_e(x)$  increases linearly with  $x$  because of the increasing beam dimension.

$$r_e(x) = 2xv \tan(\theta/2) \quad (5)$$

Therefore, there must exist a critical distance ( $x=x_c$ ) beyond which Eq(2) is not satisfied.

For example, consider a neutral beam of full cone angle  $\theta = 30^\circ$ , release rate  $N_0 = 3$  kg in 300 ms, and a beam velocity  $V = 5$  km/s, and assume a cross section  $\sigma$  of  $10^{-18}$  cm<sup>2</sup>. The critical distance  $x_c$  given by the equality Eq(4) is near and above 1 km. Beyond this distance the beam density is too low to sustain ionization. Thus, if CIV is to occur, the distance  $x$  that the pulse has traveled must be shorter than  $x_c$ .

On the other hand, the pulse duration  $\tau_D$  is also too short at small  $x$ . In order to sustain CIV ionization, it is necessary to satisfy another Townsend's criterion:

$$\tau_D \nu_H^{-1} \geq 1 \quad (6)$$

which is simply a requirement that the interaction time be long enough for hot electrons to be energized. For example, the neutral density curves [Torbert, 1986] of the Star of Lima experiment indicate that the pulse duration  $\tau_D$  is less than 50 ms at distance  $x$  shorter than 0.25 km. The duration  $\tau_D$  is of the order of magnitude of electron heating time  $\tau_H$  in the ionosphere [Tanaka and Papadopoulos, 1982; Murad et al, 1986]. This leads one to suspect that the finite nature of the pulse could affect the outcome of the experiment.

Our results therefore impose two critical distances, one ( $x_c$ ) being governed by the first Townsend's criterion (Eq.2) and another ( $x_h$ ) by the second Townsend's criterion (Eq.6). The CIV domain lies in between the two critical distances. The length ( $L=x_h-x_c$ ) of the domain could be an important factor affecting the outcome of the experiment. If the length is zero, CIV can not occur; if it is too short, the ionization level achieved would be too low even if CIV occurs.

With multiple pulses separated by gaps, the disadvantage of insufficient electron energization time ( $\tau_D < \tau_H$ ) can be overcome. For the succeeding pulses may continue the heating process left behind by the preceding pulses. Ions slowing down and falling behind a pulse may continue to energize electrons in the following gap, albeit the energy supply will fade away for long gaps.

## 2. SIMULATION

We have performed computer simulations on CIV in single and multiple pulse beams [Lai et al, 1990]. The technique, which we used for these simulations is essentially a particle simulation code [Birdsall and Langdon, 1983; Machida and Goertz, 1986], has been described earlier [McNeil et al, 1990]. In these simulations, the collisional processes considered are charge exchange and ground state ionization. Both electrons and ions are initially stationary and ions are energized through charge exchange. The electrons and ions are represented by "clouds of charge" which can move through one another in response to electric field created by charge separation. The simulation is one-dimensional in the displacement, allowing an electric field in only one direction. A magnetic field is applied in a direction almost perpendicular to the electric field, with a small angle  $\theta = \sqrt{m/M}$ , where  $m$  and  $M$  are the electron and ion masses respectively. This angle is chosen to allow for maximum growth rate of the modified two-stream instability. The simulation parameters are shown in Table 1.

TABLE 1. SIMULATION PARAMETERS

Parameter	Value
Initial Number of Particles	$N_0 = 8192$
Number of Cells	$N_c = 512$
Time step	$\Delta t_{step} = 0.2$
Initial Debye Length / Cell Size	$\lambda_D / \Delta x = 1$
Ion Mass / Electron Mass	$M_i/m_e = 100$
Initial Plasma Frequency / Electron Gyrofrequency	$\omega_{pe}/\Omega_e = 1$
Reference Collision Rate	$\nu_H/\nu_{Te} = 0.04$
Tilt Angle of Magnetic Field	$\theta = 6^\circ$
Beam Width / System Width	$\delta/L = .03, .015, .01$
Beam Velocity / Critical Velocity	$V/V_c = 1.5$

Typical results are shown in Figures 2. Ion (upper panels) and electron (lower panels) velocities are plotted as functions of distance. The neutral beams travel from left to right. The total beam width is the same in all four panels. Electrons in a pulse are gaining energy as the ions transfer energy to them via plasma waves. When the electron energy reaches the ionization energy  $\phi_0$ , ionization of the neutrals begins to occur. The new electrons are of low energy when created and they are being energized to higher velocities. As a result, a spread in electron energy occurs.

Figure 3 shows the ionization rates (slopes) of the four cases in Figure 2. In the multiple-beam cases, ionization rate increases faster and get off the ground earlier than in the one beam case. Notice that the asymptotic ionization rates in all three cases seem about the same. This means that MPBs may be most valuable in initiating a CIV discharge.

Figure 4 shows the phase space of the newly created electrons. Electron heating occurs even between the pulses because some ions lagging behind a pulse still have energy to energize electrons. Succeeding pulses continue the heating process left behind by the preceding pulses. In Figure 4, notice that most of the new electrons are created by the third pulse. This means that if the third pulse were absent, the electrons energized by previous pulses would not have any beam neutral to ionize.

## 3. DISCUSSION

We have suggested using MPB to improve the condition in CIV space experiments. MPB is better than a single pulse beam because of more efficient use of hot electrons. For some beam atom species, such as barium, with substantial line excitation properties [Newell and Torbert, 1985], the use of pulses with gaps may help the electrons, which are being energized, to survive the excitation window energy range [McNeil et al, 1990; Papadopoulos, 1990] so that electron ionization energy may be reached in a succeeding pulse. Furthermore, a pulse beam allows more beam fronts. The MPB method applies only to the high density regime near the explosion point.

## 4. REFERENCES

- Alfvén, H., *On the Origin of the Solar System*, Oxford University Press, Oxford, 1954.
- Alfvén, H., Collision between a non-ionized gas and a magnetized plasma, *Rev. Mod. Phys.*, 32, 710, 1960.
- Birdsall, C.K., and B.G. Langdon, *Plasma Physics via Computer Simulation*, New York:McGraw-Hill Book Co., 1983.
- Bresling, N., Review of impact experiments on CIV, Rep. TRITA-EPP-82-14, Roy. Inst. Tech., Stockholm, 1982.
- Deschamps, L., Review of the Critical Velocity of Gas Plasma Interaction. I. Experimental Observation, *Astrophys. Space Sci.*, 24, 459, 1973.
- Fahlsson, U. V., Experiments with Plasma Moving Through Neutral Gas, *Phys. Fluids*, Vol.4, 123, 1961.
- Haerendel, G., Alfvén's Critical Velocity Effect Tested in Space, *Z. Naturforsch.*, 37A, 728, 1982.
- Hallinan, T.J., Observed rate of ionization in shaped-charge releases of barium in the ionosphere, *J. Geophys. Res.*, A93, 8705, 1988.
- Lai, S.T., W.J. McNeil, E. Murad, Amplification of critical velocity ionization by a pulsed neutral beam, *Geophys. Res. Lett.*, in press, 1990.
- Lai, S.T. and E. Murad, Critical ionization velocity experiments in space, *Planet. Space Sci.*, Vol.37, No.7, pp.865-872, 1989.
- Machida, S., and C.K. Goertz, A simulation study of the critical ionization velocity process, *J. Geophys. Res.*, 91, 11965, 1986.
- McNeil, W.J., S.T. Lai, and E. Murad, Interplay between collective and collisional processes in critical velocity ionization, *J. Geophys. Res.*, in press, 1990.
- Murad, E., S.T. Lai, A.T. Stalf, An experiment to study the critical ionization velocity theory in space, *J. Geophys. Res.*, Vol.91, No.A9, pp.10188-10192, 1986.
- Newell, P.T., Review of critical ionization velocity effect in space, *Rev. Geophys.*, 23, 93, 1985.
- Newell, P.T., and Torbert, R. B., Competing atomic processes in Ba and Sr injection critical velocity experiments, *Geophys. Res. Lett.*, Vol.12, 835, 1985.
- Papadopoulos, K., A comprehensive analysis of Ba injection critical velocity experiments, preprint, 1990.
- Stenback-Nielsen, H.C., E.M. Wescott, G. Haerendel, A. Vainavets, CRIT II: Optical observations of critical velocity ionization ions (abstract), *EOS*, Vol.70, No.43, p.1277, 1989.
- Tsutsui, M., and K. Papadopoulos, Creation of High-Energy Electron Tails by Means of the Modified Two-Stream Instability, *Phys. Fluids*, Vol.26, 1697, 1983.
- Torbert, R.B., Critical velocity experiments in space, *Adv. Space Res.*, Vol.8, p.39, 1988.
- Torbert, R.B., An overview of the CRIT II experiment (abstract), *EOS*, Vol.70, No.43, p.1277, 1989.
- Wescott, E.M., H.C. Stenback-Nielsen, and R. Torbert, CRIT II: Observations and consequences of non-illuminated emissions at 4354A and 6300A from the neutral barium jets (abstract), *EOS*, 70, No.43, p.1278, 1989.

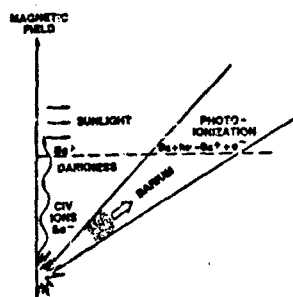
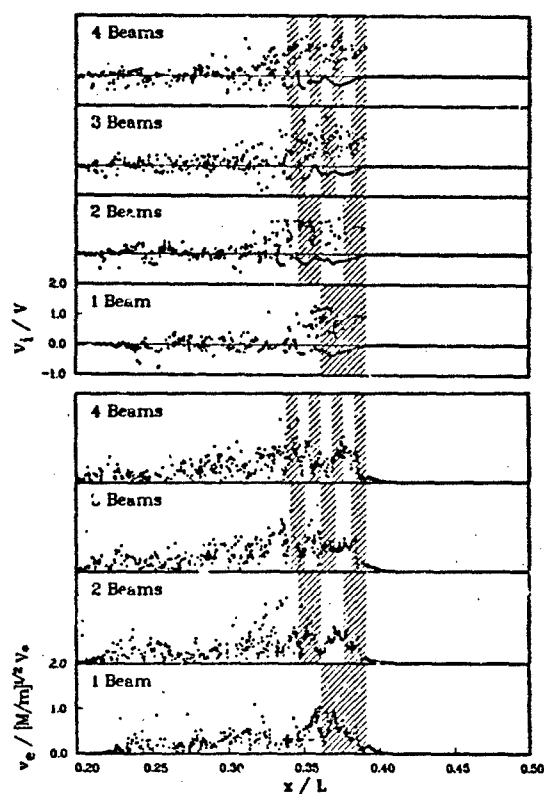


FIGURE 1. Barium beam generated by means of shaped charge explosion.

FIGURE 2. Ion (upper panels) and electron (lower panels) phase space plots for one, two, three, and four pulses. The ion velocity is normalized to the beam velocity  $V$ . The electron velocity  $v_e$  is normalized to that at which an electron would have kinetic energy equal to the ionization potential.

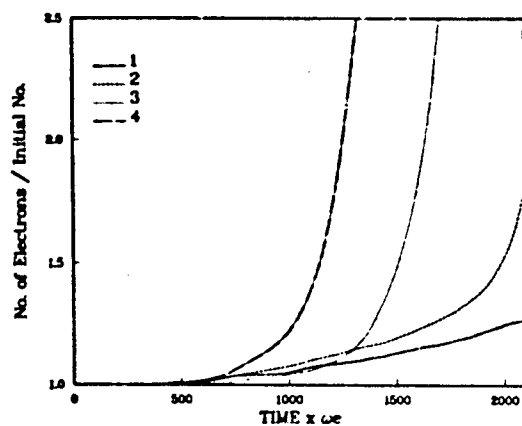


FIGURE 3. Plasma density for one, two, and three pulse cases for a fixed gap length with about equal to the pulse length itself.

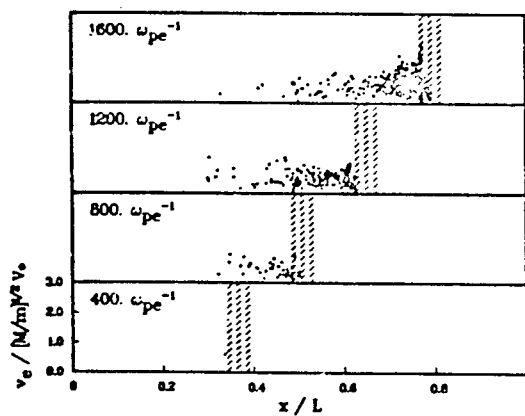


FIGURE 4. Phase space of newly created electrons.

DISCUSSION

D. PAPADOPOULOS, US

I have two comments and a question: (i) The results of the Ba experiments are consistent with our theoretical understanding of CIV, which requires  $2 \times 10^{15}/\text{cm}^3$  for low altitude Ba experiments; and (ii) The Soviet ACTIVE program observed Xe CIV at 1500 km altitude. The question is: How with a 1-D code can you describe the proper evolution of field aligned FAICS which requires a 2-D dense  $E_z$  spectrum.

AUTHOR'S REPLY

Our code is 1-D in position and 3-D in velocity. It is similar to Machida and Goertz's.

W. BURKE, US

Did simulations include self-consistent electric fields in the code?

AUTHOR'S REPLY

Yes.

## Plasma Density Enhancements Created by the Ionization of the Earth's Upper Atmosphere by Artificial Electron Beams

TOASTEN NEUBERT AND PETER M. BANKS

Specs, Telecommunications, and Radioscience Laboratory, Stanford University, Stanford, CA 94305-4055

**Abstract.** We present analytical calculations and experimental observations relating to the interaction with the Earth's upper atmosphere of electron beams emitted from low altitude spacecraft. The problem is described by two coupled non-linear differential equations in the up-going (along a magnetic field line) and down-going differential energy flux. The equations are solved numerically, using the ISIS atmospheric model and the IRI ionospheric model. The results from the model compare well with recent observations from the CHARGE 2 sounding rocket experiment. Two aspects of the beam-neutral atmosphere interaction are discussed: First we investigate the limits on the electron beam current that can be emitted from a spacecraft without substantial spacecraft charging. This question is important because the charging of the spacecraft to positive potentials limits the current and the escape energy of the beam electrons and thereby limits the ionization of the neutral atmosphere. As an example we find from CHARGE 2 observations and from the model calculations that below about 180 km, secondary electrons generated through the ionization of the neutral atmosphere by 1-10 keV electron beams from sounding rockets, completely balance the beam current, thereby allowing the emission of very high beam currents. Second, the amount of plasma production in the beam-streak is discussed. Results are shown for selected values of the beam energy, spacecraft velocity, and spacecraft altitude.

### 1. Introduction

The return current to an electron beam-emitting spacecraft will, in general, have two components arising from completely different processes. The first component is the "drift" current that flows from the ambient plasma to a charged conductor, which we will refer to as the passive current [Langmuir and Blodgett, 1924; Beard and Johnson, 1961; Parker and Murphy, 1967]. The second component, the active current, relies on the electron beam or the charged spacecraft as a generator of return current electrons. Experiments performed from the space shuttle [Waterman et al., 1953] and rockets [Winckler et al., 1975; Myers et al., 1982] have pointed out the importance of this component. The active current may be generated by a Beam-Plasma Interaction (BPI), a Beam-Plasma Discharge (BPD), a Beam-Atmosphere Interaction (BAI), or a Penning type discharge (PD). For a review see Linson [1982].

The CHARGE 2 tethered rocket experiment has provided the first direct measurements allowing to differentiate between the active and passive components of the return current, at least for the altitude range from 160 - 260 km [Myers et al., 1989; Gulchrist et al., 1990]. One important result was the observation that at altitudes below about 180 km, the active component of the return current was able to completely balance the beam current. The observations indicated to us that the BAI was a likely candidate for the generation mechanism of the active current. As we will show below, the BAI return current is directly proportional to the beam current. As a consequence, below 180 km very large currents can be emitted with relatively little charging of the spacecraft. The limit on the current that will escape a spacecraft is in this case more likely to be spacecharge effects in the beam as discussed in recent computer simulations [Winglee, 1990].

This paper presents a summary of the results presented at the AGARD conference held in Bergen in May, 1990. Part of the material relating to the CHARGE 2 results is given in more detail in Neubert et al. [1989]. The following section describes briefly the CHARGE 2 experiment and the observations of the return current to the spacecraft during electron beam emissions. Then follows a description of the method developed to study electron fluxes generated by artificial electron beams. The BAI return current is estimated for the conditions of the CHARGE 2 experiment and found in good agreement with observed values. Finally we determine the plasma density enhancement created by the emission of an electron beam emitted at 200 km altitude from a moving space platform.

### 2. The CHARGE 2 Experiment

The CHARGE 2 payload consisted of two sections, a mother and a daughter section, which were electrically connected by an insulated tether. The experiment was designed to study phenomena related to electron beam emissions from spacecraft as well as the electrodynamic interaction of a tethered system with ambient ionospheric plasmas [Sasaki et al., 1988]. During the flight, the two sections drifted apart in a direction roughly perpendicular to the spacecraft velocity and to the earth's magnetic field. Apogee was at 261 km altitude and the maximum separation distance of the two payloads was 426 m, reached at the end of the flight.

A schematic drawing of the CHARGE 2 payload is shown in Figure 1. The mother carried an electron beam accelerator emitting beams with electron energies of 1 keV and currents up to 48 mA. Return currents were collected by both the mother ( $I_M$ ) and the daughter ( $I_D$ ) during beam injections. The electron beam current ( $I_{beam}$ ) was measured by a Rogowski coil and the tether current ( $I_{tether}$ ) was measured by a tether current monitor. Assuming that the beam escaped the mother payload, we have  $I_D = I_{tether}$  and  $I_M = I_{beam} - I_{tether}$ .

The tether impedance was relatively low (4 k $\Omega$ ) in certain experimental sequences and the tether current was typically less than 6 mA. As a consequence, the potential difference between the two payloads was less than 24 V and small compared to the potentials of 200-500 V reached by the mother payload. Thus the two payloads were at almost the same potential during these particular sequences. Since the daughter was separated by up to several hundred meters from the mother in the direction perpendicular to the Earth's magnetic field and therefore was well outside of the disturbed region around the beam column, the daughter return current represents a measurement of the passive return current. The return current to the mother contains both a passive and an active component.

Figure 2 shows the fraction of the beam current collected by the daughter as a function of altitude. The labels SQ2 through SQ6 mark the beam emission sequences performed during the flight numbered in time-sequential order. Also indicated is the ratio of the daughter collecting area to the collecting area of both payloads,  $A_D/A_{total}$ . At high altitudes, around 250 km,

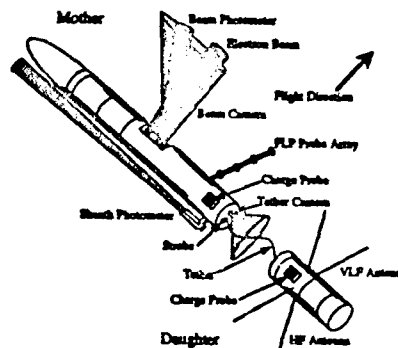


Figure 1. Configuration of the CHARGE 2 payload and the electron current system around the payload during electron beam emissions.  $I_{beam}$  is the emitted beam electron current,  $I_{tether}$  is the electron current in the tether,  $I_M$  is the return current to the mother and  $I_D$  is the return current to the daughter.

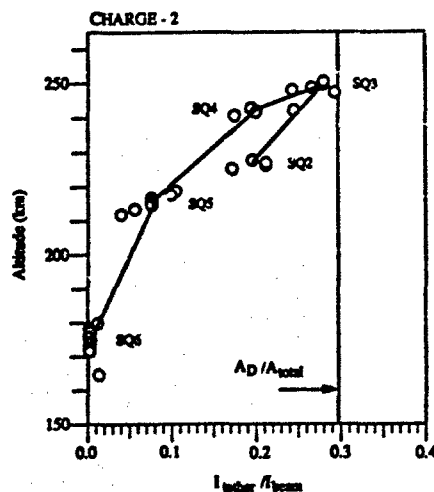


Figure 2. Tether to beam current ratio,  $I_{\text{tether}}/I_{\text{beam}}$ , as a function of altitude. SQ2 through SQ6 marks in time-sequential order the experimental sequences performed during the flight. Also indicated is the ratio of the daughter collecting area to the total collecting area of Mother and daughter,  $A_D/A_{\text{total}}$ .

the tether current approaches 0.3 times the beam current. This value is close to  $A_D/A_{\text{total}}$ , indicating that the two payloads collect return currents roughly in proportion to their areas, which is to be expected for passive current-collection. Thus at high altitudes, where the ambient plasma density is large and the neutral density is low, the payloads mainly collect currents from the ambient plasma. The return currents and corresponding spacecraft potentials observed around apogee have been found in accordance with the model of Parker and Murphy [Myers et al., 1989; Mandell et al., 1990].

As the altitude decreases, the current collected by the daughter decreases such that by an altitude of 180 km and below almost no current is collected by the daughter. Assuming that the beam escapes the near environment of the mother payload, we conclude that the active component of the return current, which flows directly to the mother, increases with decreasing altitude. Since the ambient neutral atmospheric density also increases with decreasing altitude, such an altitude dependence is suggestive of a BAI process. In the following section we describe the method developed to quantify the fluxes generated by BAI.

### 3. The Beam-Atmosphere Interaction Model

The code developed to study the interaction of an electron beam with the Earth's upper atmosphere solves two coupled first order non-linear differential equations in the forward and the backward flux of electrons streaming in the direction of the ambient magnetic field. The equations coupling the forward differential energy flux,  $\Phi^+$ , and the backward flux,  $\Phi^-$ , are given by

$$\begin{aligned} \frac{d\Phi^+(z, E)}{dz} = & -\sigma_2(z, E)\Phi^+(z, E) \\ & +\sigma_1(z, E)\Phi^-(z, E) + Q^+(z, E) - L(E)\Phi^+(z, E) \end{aligned} \quad (1)$$

$$\begin{aligned} \frac{d\Phi^-(z, E)}{dz} = & \sigma_2(z, E)\Phi^-(z, E) \\ & -\sigma_1(z, E)\Phi^+(z, E) - Q^-(z, E) + L(E)\Phi^-(z, E) \end{aligned} \quad (2)$$

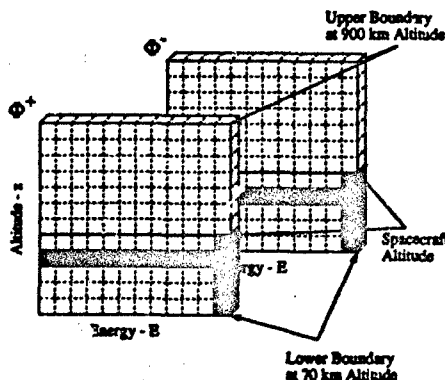


Figure 3. The iteration scheme used to solve the two coupled non-linear differential equations of the counter-streaming fluxes.

Here  $\sigma_2(z, E)$  is the cross section describing the loss of flux in the energy range  $E$  to  $E + dE$ ,  $\sigma_1(z, E)$  is the cross section describing the elastic back-scattering of electrons,  $Q^+(z, E)$  is the electron production rate in the range  $E$  to  $E + dE$  due to ionization processes and cascading of electrons down in energy from higher energy bins, and  $L(E)$  describes the losses due to a finite spacecraft velocity. The cross sections take into account ionization of the atmospheric neutral species, backscatter of electrons by neutral and charged particles, elastic and inelastic collisions, cascading of electrons down in energy etc. The coordinate system is chosen such that the  $z$ -axis is along the magnetic field with  $\Phi^+$  streaming in the positive direction. To account for pitch angle effects, an average pitch angle of  $54.7^\circ$  is used. The equations in their detailed form, excluding the term describing losses due to finite spacecraft velocities, are discussed in detail in Beaks et al. [1974], where the equations were solved for the case of auroral electron beams interacting with the Earth's upper atmosphere.

The scheme adopted to solve the two coupled differential equations is shown in Figure 3. The altitude domain is divided into two regions: one is between the lower altitude boundary (70 km) and the spacecraft altitude, and the other is between the spacecraft altitude and the upper altitude boundary (900 km). First, the differential electron flux of a beam emitted from the spacecraft is assumed at the spacecraft altitude. The beam may be emitted either up or down, but let us assume in the following that the beam is emitted down. The fluxes are then determined in the region between the lower boundary and the spacecraft altitude in the same way as was done for the case of auroral electron fluxes. Next, the upward return flux found at the spacecraft altitude is emitted upwards, and the flux

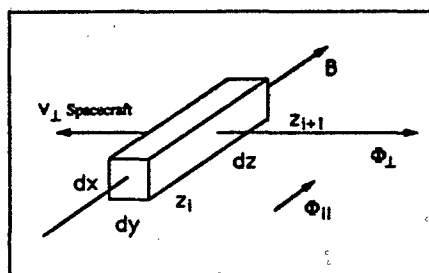


Figure 4. Illustration of the loss of electrons due to a finite spacecraft velocity perpendicular to the magnetic field.



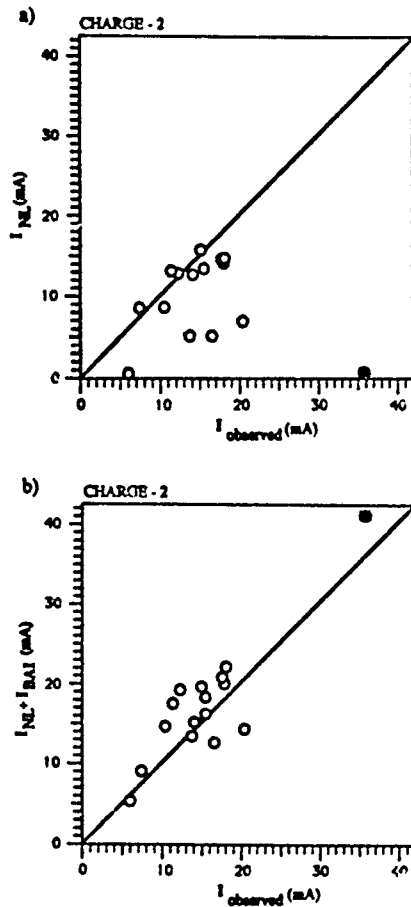


Figure 7. Model estimates of the return current to the mother vs. observed return current. a) The model assumes passive current collection only (NASCAP/LEO estimates). b) The model includes passive and BAI return currents.

upwards and in the opposite direction to the beam it will observe a flux corresponding to the value of the upper branch of  $\Phi_{\text{beam}}$  at the spacecraft altitude. The downward flux shown in Figure 6b is continuous because no beam electrons are emitted at 10 eV.

As can be seen from Figures 6a and 6b, energetic electron fluxes are generated along the magnetic field out to considerable distances from the spacecraft. At low altitudes the electron fluxes approach zero and become omnidirectional because of scattering in the dense atmosphere. The upward flux decreases relatively slowly with altitude. This effect is caused by a decrease in the ambient neutral density or an increase in the mean free path which allow the electrons to escape almost freely. Similarly, the downward electron flux increases from essentially zero at high altitudes to large values at lower altitudes. The creation of electron fluxes extending along the direction of the magnetic field both above and below the payload to distances far beyond the payload potential sheath region is in qualitative agreement with optical observations made during the Exedre 2 [O'Neil et al., 1978] and the Echo 7 [Winckler et al., 1989] sounding rocket experiments.

The current densities,  $J^{\text{BAI}}(z_0)$ , at the spacecraft location,  $z_0$ , can be found by integrating the return fluxes from both

hemispheres over energy. Since the fluxes and thereby the BAI return currents are proportional to the emitted beam current it is convenient to define the gain factor  $A$  as the sum of the current densities from both directions normalized to the emitted beam current density,

$$A(z_0) = \frac{J^{\text{BAI}}_{\text{down}}(z_0) + J^{\text{BAI}}_{\text{up}}(z_0)}{J_{\text{beam}}} \quad (4)$$

The passive return current to the mother estimated by the NASCAP/LEO code [Mandell et al., 1990] is shown in Figure 7a as a function of the observed return current. For most of the values the model current is lower than the observed current. Extreme differences can be seen, especially for the data point marked with an asterisk. This observation was performed at a low altitude during the downleg. Here the model current is less than 1 mA while the observed return current was 36 mA.

Figure 7b shows an estimate of the return current when the BAI current is added to the passive current. The BAI current has been found from the relation

$$I_{\text{BAI}} = I_{\text{beam}} \cdot A \cdot \frac{A}{dxy} \quad (5)$$

where  $A$  is the sheath area. As can be seen from Figure 7b, the agreement between this new model estimate of the return current and the observed return current is much better. The data point marked with an asterisk is now lifted to a value slightly larger than the observed value.

The values shown in Figures 5-7 have been calculated assuming that only a small fraction of the flux is collected by the spacecraft. As discussed in Neubert et al. [1989] the sheath area of the mother is about 12.8 m<sup>2</sup> when charged to 400 V. With the assumption that the flux-tube cross-sectional area is 100 m<sup>2</sup>, the payload actually collects about 13% of the electrons in the flux-tube and thus the values shown in Figures 3-5 are slightly overestimated.

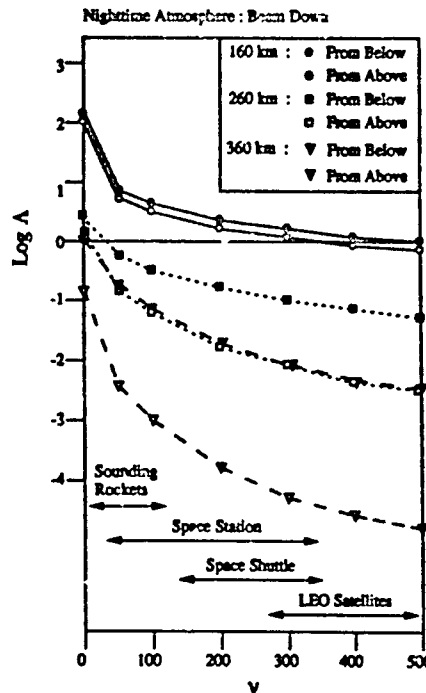


Figure 8. The BAI gain factor  $A$  as a function of the spacecraft parameter  $\nu$ .

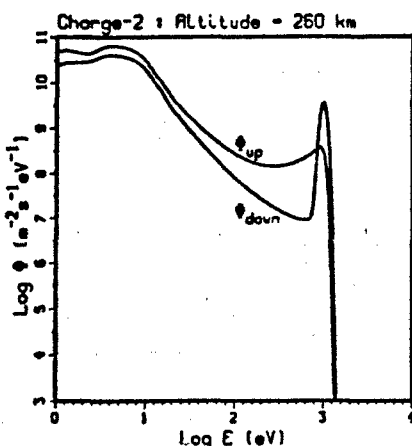


Figure 5. The upward and the downward differential electron flux as a function of energy at the spacecraft altitude (260 km). The beam is emitted downward with an energy of 1 keV and a current of 100 mA (the fluxes scale linearly with the beam current). The primary beam is seen as the peak at 1 keV in the downward flux.

equations are solved in the region from the spacecraft altitude and to the upper boundary. The downward flux generated at the spacecraft altitude is added to the beam flux and the procedure is repeated until satisfactory convergence is reached.

The equations are solved for the highest energy bin first and progressing downwards in energy, because ionization and inelastic scattering leads to source terms in lower-energy bins. The various cross-sections are read by the code from a large file containing the cross-sections in tabulated form. The energy range covered is from 0.25 eV to 44 keV.

The effect of a finite spacecraft velocity has been approximated by the inclusion of the loss term  $L(E)$  in equations (1) and (2). The loss term can be determined from the following considerations illustrated in Figure 4: The beam is assumed to fill a volume with the dimensions  $dx, dy$  perpendicular to the magnetic field. The spacecraft velocity component perpendicular to the magnetic field,  $v_{\perp}$ , gives rise to a perpendicular flux  $\Phi_{\perp}$  through the area element  $dx dy$  as seen in the spacecraft reference system. This flux is lost to the beam flux-tube and the loss term can be expressed as

$$L(E) = \frac{v_{\perp}}{\eta dy} \quad (3)$$

where  $\eta$  is the particle velocity along the field.

The electron beam flux is modelled by a Gaussian distribution in energy centered around 1 keV and with an energy width of 10%. For the CHARGE 2 simulations, the beam is assumed to fill a flux-tube with a dimension perpendicular to the magnetic field of 10 m x 10 m, which corresponds to about 4 beam electron gyro-radii (for 90 deg pitch angle). This choice of beam column width is in accordance with observations obtained in the Spacelab-2 experiment flown on the space shuttle [Frank et al., 1989] and in the ECHO-7 sounding rocket experiment [Wahlster et al., 1989]. The beam is emitted downwards for the range of spacecraft altitudes and corresponding perpendicular velocities obtained in the CHARGE 2 experiment and it is assumed that the mother collects only a small fraction of the return fluxes. The MSIS/86 model [Hedin, 1987] is used for the neutral atmosphere ( $N_2, O_2$  and  $O$ ) and the IRI model [Bilitza, 1986] is used for the ionosphere. The models are those corresponding to the local time, season, geographic location etc. of the launch. The IRI model of electron densities compares well with the electron densities observed during the flight [Myers, 1989].

#### 4. CHARGE 2 Model Calculations

An example of the differential energy flux spectrum obtained at the location of the mother platform when located at an altitude of 260 km is shown in Figure 5. The two components of the fluxes shown are the flux streaming in the direction of the beam (down) and the flux streaming counter to the beam (up). The downward flux consists of two contributions, the primary electron beam which is seen with a peak at the beam energy, and the flux incident from above the spacecraft, seen at lower energies.

The fluxes as a function of altitude and for fixed energies are shown in Figure 6a for the 1-keV electron beam energy and in Figure 6b for 10-eV electrons. The spacecraft altitude is again 260 km as indicated on the figures and the beam is emitted downwards. The downward flux shown in Figure 6a is discontinuous at the spacecraft altitude. This fact simply reflects the location of the beam source at this altitude. If aimed downwards, a spectrometer mounted on the spacecraft will observe a value of the back-scattered flux corresponding to  $\Phi_{up}$  at the spacecraft altitude. If the spectrometer is aimed

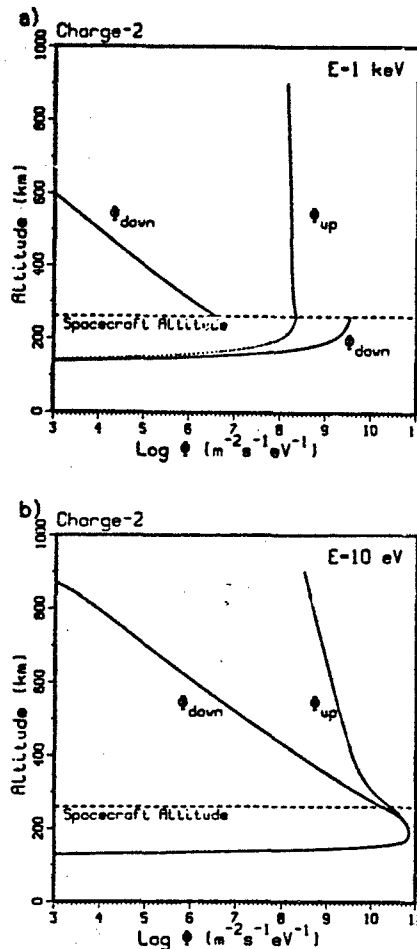


Figure 6. The differential electron fluxes as a function of altitude for the same parameters used in Figure 5. (a) 1-keV electrons and (b) 10-eV electrons.

### 5. Plasma Density Enhancements

From the discussion in the previous section it is clear that the BAI return current collected by an ionospheric spacecraft depends on the size of the current collecting area around the spacecraft as well as the velocity of the spacecraft. In general, we expect the faster moving orbiting spacecraft like the space shuttle, the planned US space station Freedom, and low Earth orbiting (LEO) satellites to collect less BAI currents than the slower moving sounding rocket payloads. On the other hand, both the space station and the shuttle have very large current collecting areas. Both of these effects are contained in the equation for the loss term (eq. (3)), and can be described by a single parameter  $\nu$ ,

$$\nu = \frac{v_A}{dy} \quad (6)$$

In Figure 8 is shown the gain factor  $A$  as a function of  $\nu$  for three different altitudes. In this case, the gain factor is separated into two parts describing the fluxes returning from above and below the spacecraft. As expected, when  $\nu$  becomes large,  $A$  decreases. Similarly, when the altitude increases,  $A$  decreases. At the bottom of the figure is indicated the range in  $\nu$  that can potentially be covered by the various ionospheric spacecraft. An array of 10 electron guns along the space station may for instance result in a large value of  $dy$ , say 100 m. The ionospheric orbital velocity is typically  $7 \text{ km s}^{-1}$  with perpendicular velocities (to B) down to  $3.5 \text{ km s}^{-1}$ . The minimum of  $\nu$  is then  $35 \text{ s}^{-1}$ .

In order for the BAI current to balance the beam current  $A$  must be somewhat larger than 1. From Figure 8 we estimate that at 200 km altitude, a spacecraft with a  $\nu$  of  $50 \text{ s}^{-1}$  will just be able to collect the complete return current from the BAI. The plasma density enhancement in the beam column resulting from beam emissions from such a spacecraft is shown in Figures 9. The beam current is 1 A, and the beam energy is 1 keV (9a) and 10 keV (9b). The cross-sectional area of the beam flux-tube is scaled with the energy in order to maintain a beam radius that is 3.5 beam electron Larmor radii. Also shown for reference with a thin line is the background ionospheric density. The model atmosphere is the same as the one used for the CHARGE 2 simulation, which is a model for local midnight at  $32^\circ$  latitude.

As can be seen from Figure 9, substantial enhancements of the plasma density is created by the beam. This beam-produced density enhancement will decay first to  $\text{NO}^+$  through rapid reactions of  $\text{N}^+$ ,  $\text{O}^+$ , and  $\text{O}^+$  with the neutral constituents  $\text{N}_2$ ,  $\text{O}_2$ , and  $\text{O}$ , then  $\text{NO}^+$  is lost via a dissociative recombination reaction of the form



Using the dissociative recombination rate,  $\alpha_D$ , to represent the rate of the decay of the density enhancement, an approximate density dependant time constant is

$$\tau_D \approx 1/\alpha_D n_e \quad (8)$$

or  $\tau_D \approx 7.7 \times 10^8/n_e$  seconds, with  $n_e$  given in units of electrons/cm<sup>3</sup> [Banks and Gulkrist, 1985]. The time constant is about 7.7 second for the maximum density enhancement seen in Figure 9b for a 10 keV beam. When the density has decayed to  $10^3 \text{ cm}^{-3}$ , the time constant is about one minute. This density is still a factor 100 larger than the background density around 110 km altitude.

### 6. Summary

Under the simple assumption that the beam flux-tube has a cross-sectional area of  $100 \text{ m}^2$ , the observed active return current to the CHARGE 2 mother payload is found to be in good agreement with the BAI model. This supports our assumption that the BAI is the dominant process generating the active component of the return current at these altitudes and reinforces our trust in the BAI model. We find that the predictions from the model of electron fluxes extending to large distances in the direction of the emitted beam as well as in the opposite direction is in qualitative agreement with optical observations performed in past experiments [O'Neil et al, 1978; Winckler et al, 1982]. Similarly, the prediction of elec-

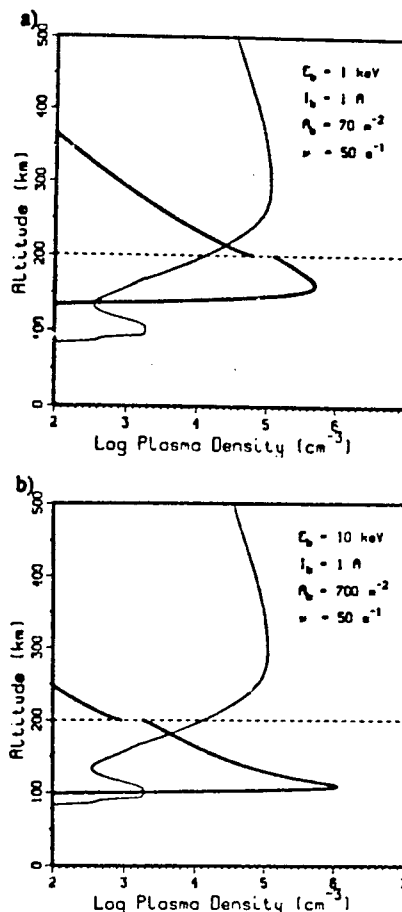


Figure 9. The plasma density enhancement created by a beam emitted from 200 km altitude. The beam current is 1 A and the beam energy 1 keV (a) and 10 keV (b).

tron fluxes incident on the spacecraft from both hemispheres is in qualitative agreement with observations [Winckler et al, 1975].

One of the main shortcomings of the model is the uncertainty of the cross-sectional area of the beam flux-tube and the variation of the electron fluxes across this area. A more rigorous treatment of the problem would involve Monte Carlo techniques to determine the dimension and the distribution of electrons across the flux-tube.

We have shown that the BAI process, below altitudes of about 180-200 km altitude, may supply a return current to a spacecraft, which completely balances the beam current. In this case, very large currents may be emitted without disruptive charging of the spacecraft. This allows for the generation of substantial plasma density enhancements at ionospheric E-region altitudes. The decay of these through recombination have a density dependent time scale. For a plasma density enhancement two orders of magnitude larger than the background E-region plasma density, the time scale is of the order of one minute.

**Acknowledgments.** The experimental work was sponsored by NASA and the Air Force Geophysical Laboratory under NASA grant NAGW-1566, by NASA under contracts NAS8-35350 and NAGS-607, and by RADAC under contract F19628-89-K-0040.

## References

- Banks, P. M., C. R. Chappell, and A. F. Nagy, A new model for the interaction of auroral electron beams with the atmosphere: spectral degradation, backscatter, optical emission, and ionisation, *J. Geophys. Res.*, **79**, 1459, 1974.
- Banks, P. M., and B. E. Gilchrist, Artificial plasma density structures produced by energetic electron beams from rockets and spacecraft, *Geophys. Res. Lett.*, **12**, 175, 1985.
- Beard, D. B., and F. S. Johnson, Ionospheric limitations on attainable satellite potential, *J. Geophys. Res.*, **66**, 4113, 1961.
- Bilitza, D., International reference ionosphere: Recent developments, *Radio Sci.*, **21**, 313, 1986.
- Frauk, L. A., W. R. Paterson, M. Ashour-Abdalla, D. Schreiver, W. S. Kurth, D. A. Gornett, N. Omidi, P. M. Banks, R. I. Bush, and W. J. Raitt, Electron velocity distributions and plasma waves associated with the injection of an electron beam into the ionosphere, *J. Geophys. Res.*, **94**, 6995, 1989.
- Gilchrist, B. E., P. M. Banks, T. Neubert, P. R. Williamson, N. B. Myers, W. J. Raitt, and S. Sasaki, Electron collection enhancement arising from neutral gas jets on a charged vehicle in the ionosphere, *J. Geophys. Res.*, **95**, 2469, 1990.
- Hedin, A. E., MSIS-86 thermospheric model, *J. Geophys. Res.*, **92**, 4649, 1987.
- Langmuir, I., and K. B. Blodgett, Current limited by space charge flow between concentric spheres, *Phys. Rev.*, **24**, 49-59, 1924.
- Lisaco, L. M., Charge neutralization as studied experimentally and theoretically, in *Artificial Particle Beams in Space Plasma Studies*, edited by B. Grandal, p. 573, Plenum Press, New York, 1982.
- Mandel, M. J., J. R. Lilley, Jr., L. Katz, T. Neubert, and N. B. Myers, Computer modelling of current collection by the CHARGE 2 Mother payload, *Geophys. Res. Lett.*, **17**, 135, 1990.
- Myers, N. B., W. J. Raitt, B. E. Gilchrist, P. M. Banks, T. Neubert, P. R. Williamson, and S. Sasaki, A comparison of current-voltage relationships of collectors in the ionosphere with and without electron beam emission, *Geophys. Res. Lett.*, **16**, 365-368, 1989.
- Myers, N. B., Studies of the system-environment interaction by electron beam emission from a sounding rocket payload in the ionosphere, *Ph.D. Dissertation*, Utah State University, Center for Atmospheric and Space Sciences, Logan, Utah, 1989.
- Neubert, T., P. M. Banks, B. E. Gilchrist, A. C. Fraser-Smith, P. R. Williamson, W. J. Raitt, N. B. Myers, and S. Sasaki, The interaction of an artificial electron beam with the earth's upper atmosphere: Effects on spacecraft charging and the near-plasma environment, submitted to *J. Geophys. Res.*, 1989.
- O'Neil, R. R., O. Shepherd, W. P. Reidy, J. W. Carpenter, T. N. Davis, D. Newell, J. C. Ulwick, and A. T. Stair, Jr., Exceeds 2 test, an artificial auroral experiment: Ground-based optical measurements, *J. Geophys. Res.*, **83**, 3281, 1978.
- Parker, L. W., and B. L. Murphy, Potential buildup on an electron-emitting satellite in the ionosphere, *J. Geophys. Res.*, **74**, 1631-1636, 1967.
- Sasaki, S., K. I. Oyama, N. Kawashima, T. Obayashi, K. Hiras, W. J. Raitt, N. B. Myers, P. R. Williamson, P. M. Banks, and W. F. Sharp, Tethered rocket experiment (Charge 2): Initial results on electrodynamics, *Radio Sci.*, **23**, 975-988, 1988.
- Waterman, J., K. Wilhelm, K. M. Torkar, and W. Riedler, Space shuttle charging or beam-plasma discharge: what can electron spectrometer observations contribute to solving the question?, *J. Geophys. Res.*, **93**, 4134, 1988.
- Winckler, J. R., R. L. Arnoldy, and R. A. Hendrickson, Echo 2: A study of electron beams injected into the high-latitude ionosphere from a large sounding rocket, *J. Geophys. Res.*, **80**, 2083, 1975.
- Winckler, J. R., P. R. Malcolm, R. L. Arnoldy, W. J. Burke, K. N. Erickson, J. Ernstmeier, R. C. Frans, T. J. Hallinan, P. J. Kellogg, S. J. Monson, K. A. Lynch, G. Murphy, and R. J. Nemzek, ECHO 7 An electron beam experiment in the Magnetosphere, *EOS*, **70**, 657, 1989.
- Winglee, R. M., Electron beam injection during active experiments 2. Collision effects, *J. Geophys. Res.*, **95**, 4167, 1990.

## DISCUSSION

B. N. MAERLUM, NO

Did you observe any enhancements in the background plasma density during electron beam injections on the CHARGE rocket?

## AUTHOR'S REPLY

The instrument capable of making these observations refused to cooperate and we have no information, unfortunately.

D. PAPADOPOULOS, US

All the spectra you showed are consistent with what was observed in the JSC chamber and ELJEDE as well other experiments under beam plasma instability and BPD conditions which clearly invalidate single particle dynamics. How do you justify the analysis?

## AUTHOR'S REPLY

We see no evidence for BPD in the CHARGE-II experiments. The return current variation with altitude is well explained by classical electron scattering in the atmosphere. BPD is not required for current balance.

W. BURKE, US

In the ECHO 7 experiment, 36 keV electrons were emitted both up and down. The vehicle charging was greater than 5 kV in both cases. I suspect that a 36 keV beam stops at 95 km where the scale height is small differs from Neubert's 1 keV beam that stops near 160 km where the scale height is long.

## AUTHOR'S REPLY

Calculation of the ECHO-7 results should be made.

## IONOSPHERIC MODIFICATION USING RELATIVISTIC ELECTRON BEAMS

P. M. BANKS, A. C. FRASER-SMITH, AND B. E. GILCHRIST

Space, Telecommunications and Radioscience Laboratory  
Stanford University  
Stanford, California 94305, U.S.A.

### SUMMARY

The recent development of comparatively small electron linear accelerators (linacs) now makes possible a new class of ionospheric modification experiments using beams of relativistic electrons. These experiments can potentially provide much new information about the interactions of natural relativistic electrons with other particles in the upper atmosphere, and it may also make possible new forms of ionization structures extending down from the lower ionosphere into the largely unionized upper atmosphere. In this paper we investigate the consequences of firing a pulsed 1 A, 5 MeV electron beam downwards into the upper atmosphere. If a small pitch angle with respect to the ambient geomagnetic field is selected, the beam produces a narrow column of substantial ionization extending down from the source altitude to altitudes of ~ 40 to 45 km. This column is immediately polarized by the natural middle atmosphere fair weather electric field and an increasingly large potential difference is established between the column and the surrounding atmosphere. In the regions between 40 to 60 km, this potential can amount to many tens of kilovolts and the associated electric field can be greater than the field required for breakdown and discharge. Under these conditions, it may be possible to initiate lightning discharges along the initial ionization channel. Filamentation may also occur at the lower end to drive further currents in the partially ionized gases of the stratosphere. Such discharges would derive their energy from the earth-ionosphere electrical system and would be sustained until plasma depletion and/or electric field reduction brought the discharge under control. It is likely that this artificially-triggered lightning would produce measurable low-frequency radiation.

### 1. INTRODUCTION

Previous experiments with electron beams in space have been limited by practical considerations to relatively low particle energies. To the best of our knowledge the maximum electron energy yet used in a conventional space experiment is of the order of 40 keV. The motivation for the present study has come from a realization that linac electron accelerators have reached a state of technology permitting relatively small units to be mounted in payloads suitable for spacecraft. Thus, it is now worth considering the full range of consequences of using such a beam for a variety of purposes, including the creating of plasma density irregularities in the lower ionosphere and the probing of electrodynamic regions of the middle atmosphere.

In the following sections we describe the possible consequences of operating a moderately powerful (~ 5 MW peak power), relativistic (~ 5 MeV) electron accelerator from a satellite or rocket platform. In such an experiment, a beam of relativistic electrons fired downwards from space will create, by means of electron impact ionization, an ionized column whose length and cross sectional area will be set by electron energy loss and scattering. As discussed later, owing to the relatively small cross section for electron interaction with matter at relativistic energies, a single pulse from such a beam will penetrate to the lower mesosphere and upper stratosphere, creating a dense column of free electrons and positive ions. At mesospheric/stratospheric altitudes the electrons are rapidly lost via attachment reactions with  $O_2$  to form  $O_2^-$ . While the column is composed largely of free electrons, it can scatter electromagnetic radiation and, surprisingly, may even initiate an intense upward traveling electrical discharge similar to lightning.

Before passing to the calculations of beam interactions, however, it is informative to compare the ionizing effects of electrons and photons. Generally speaking, electrons in the energy range 1 to 5 MeV have appreciably smaller interaction cross sections with matter than easily obtainable EUV photons or X-rays. Even hard X-rays, for which there are as yet no convenient space payload sources, only penetrate to the altitude range of 50 to 60 km. Thus, if there is a need to produce appreciable ionization as deep as the upper stratosphere, relativistic electrons are the logical choice.

Another factor relates to the net energy flux carried by electron beams. Unlike high energy photon sources, which have a generally broad beam divergence and accompanying  $r^{-2}$  energy diminution with distance from the source, electron beams are constrained to remain geometrically confined, varying in intensity only in response to changes in the strength of the magnetic field and transverse spreading associated with scattering by atmospheric particles. Thus, it can be expected that a relativistic electron beam, if injected at a small pitch angle with respect to the geomagnetic field (and assuming adequate space charge neutralization), will remain confined until it has lost a substantial fraction of its initial kinetic energy. Furthermore, a surprisingly large fraction (~ 20%) of the initial beam energy will be expended in producing atmospheric ionization along the path of the beam.

We now describe the physical processes which accompany the firing of a pulsed relativistic electron beam downwards along a magnetic field line into the middle atmosphere. Consideration is given to the resulting altitude profile of ionization, the conversion of the initial atmospheric positive ions and free electrons into an end product state of positive ions, electrons, and negative ions, and the possibility that the resulting beam column of ionization may lead to a high voltage breakdown condition mimicking, to some extent, natural lightning.

### 2. IONIZATION COLUMN DYNAMICS

#### 2.1. Ionization Production Rates

Consider a relativistic electron beam of current  $I$  composed of monoenergetic electrons of velocity  $v$  fired parallel to the

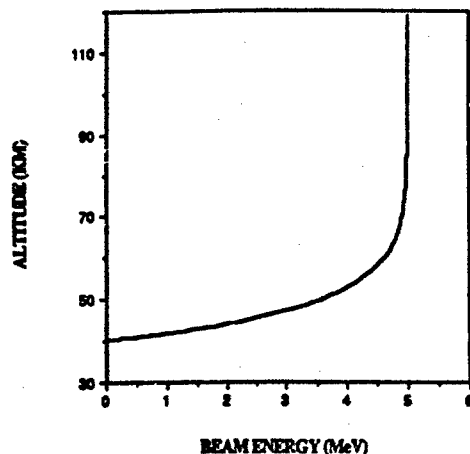


Figure 1. Average energy per particle of a 5 MeV electron beam penetrating vertically into the middle atmosphere. Details of the calculation are given in Appendix A.

local geomagnetic field. We assume that the beam emerges from an aperture of area  $A_0$  and expands slowly with distance along the magnetic field such that the area of the beam is  $A_s$  at a distance  $s$  from the source. The beam current is assumed to be pulsed with an "on" period of  $t$  seconds each pulsing cycle. As the beam travels downwards along the magnetic field, ionization is produced through electron impact.

Following the treatment of [1], the number of ionization pairs per unit path length in air at STP produced for each incident electron is approximated by the ionization formula

$$\frac{dN}{ds} \approx \frac{45}{\beta^2} \frac{\text{ion pairs}}{\text{air-cm}} \quad (1)$$

where the distance  $s$  is measured along the local geomagnetic field and  $\beta = v/c$  is the ratio of particle velocity,  $v$ , to the speed of light,  $c$ . Equations of greater detail also exist and are discussed in Appendix A.

As the electron beam moves downwards into the atmosphere, each electron of the beam gradually loses kinetic energy as a consequence of inelastic collisions with the atmospheric gases. This effect is shown in Figure 1, and it is based on the equations in Appendix A. The figure gives the average energy per particle of the incident beam as a function of altitude. For altitudes down to about 70 km there is little energy loss. Below this point, however, the exponentially increasing density of the atmosphere, coupled with the rise of energy loss rate with decreasing electron energy, dictates a progressively greater decrease in beam particle energy. By the time that the beam has reached 40 km, virtually all of the original beam energy has been deposited in the atmosphere.

Using the results of Appendix A, it is possible to compute the local rate of energy loss per unit distance of beam travel as a function of altitude. The typical profile of energy deposition is shown here as Figure 2. The interesting result is that the rate of energy deposition is generally proportional to the neutral gas concentration and that a large amount of energy is deposited in the atmosphere at the end of the beam penetration. This arises because of the large increase in beam energy loss rate at low electron energies. The consequence is that there can be a substantial increase in local electron density in the terminus zone of beam penetration. This general effect is discussed in more detail following a discussion of the effects of beam scattering.

For a beam of current,  $I$ , and projected area,  $A_s$ , normal to the magnetic field, the local rate of production of electrons and ions per  $\text{cm}^3$  per second,  $q$ , is given by the expression

$$q = \frac{45}{\beta^2} \left( \frac{I}{c A_s} \right) \left( \frac{n}{n_0} \right) \text{ cm}^{-3} \text{ sec}^{-1} \quad (2)$$

where  $n$  is the neutral gas concentration at the observation point and  $n_0$  is the concentration of the atmosphere at STP ( $n_0 = 2.67 \times 10^{19} \text{ molecules cm}^{-3}$ ).

Knowledge of the area,  $A_s$ , of the beam at any point in the trajectory is an important part of calculating the local ionization production rate. As individual electrons pass through matter, minute deflections occur as a consequence of Coulomb interactions with atmospheric atoms and molecules. These deflections are equivalent to the introduction of perpendicular (to the local magnetic field) velocity components to the beam electrons and small displacements of their gyrocenters so that after many collisions there can be appreciable spread of the beam. This effect can spread the total ionization production over a significant area, lowering the local enhancement of the electron and ion density.

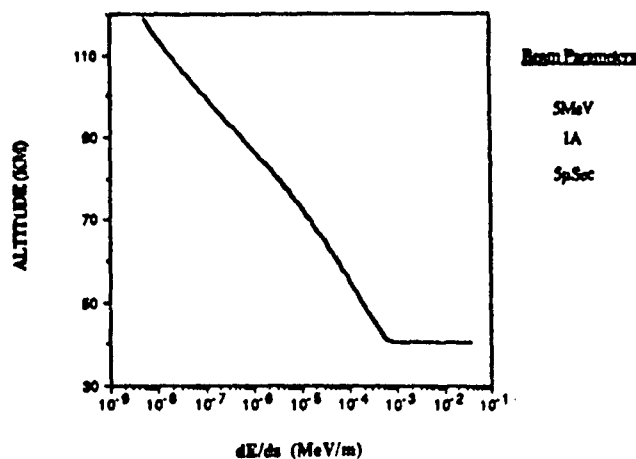


Figure 2. Relativistic electron beam energy loss rate shown as a function of altitude in the middle atmosphere. The peak deposition at the end of the path is due to the rapid rise in energy loss which occurs at low electron energies. Details of the calculation are given in Appendix A.

There is extensive knowledge of electron scattering in various materials, including air; e.g., [2]. Using standard approaches, it is even possible to compute the angular scatter effects of low density materials where perpendicular transit is an important part of the final beam area distribution. However, up to the present time we have been unable to discover any method which adequately takes into account the confining effect of a magnetic field on a strongly peaked (energy and angle) electron beam. Figure 3 illustrates this situation by following the trajectory of a single electron. As it leaves the source the electron initially travels directly down the magnetic field. At some point, however, it suffers a scattering collision which changes its pitch angle. Such scattering interactions continue with increasing frequency until the electron has lost all of its initial energy. As a consequence of the accumulated angular scattering, the electron may be substantially deflected in a lateral direction with respect to the original magnetic field line trajectory. This behavior is indicated in Figure 3 by showing hypothetical scattering collisions and the envelope of an electron's helical motion.

In this situation, we find that the traditional calculations of electron beam spreading are incorrect since they ignore the confining effects of the geomagnetic field. Walt *et al.* [3] have attacked this problem for the case of a non-peaked relativistic electron beam, and they derived analytic expressions for the ionization rate as a function of altitude, but the results may not be accurate for the case at hand.

Calculations for the highly peaked distributions considered here could be made in a guiding center formalism which would take into account the gradual outward diffusion of electrons resulting from scattering. However, this new work has not been practical within the limits of the present study. Instead, we use three approximations to the electron beam area: An area which corresponds to no scattering by the atmosphere ( $A_0 = \pi/4 \text{ m}^2$ ), an area which corresponds to the gyroradius of the relativistic electrons at the energy of the source ( $A_1 = 602^2 \pi \text{ m}^2$ ), and the full scattering predicted from non-magnetic, conventional scattering equations ( $A_2 = 10^9 \text{ m}^2$  at 50 km altitude). In addition, we simply assume that at the very end of the beam penetration there is a substantial spatial blooming of the beam as scattering assumes great importance in the last few kilometers of beam travel.

The result of these assumptions is to give the model of the region of electron beam ionization enhancement shown in Figure 4. The overall shape of the ionization region produced by the beam can be compared with that of a mushroom anchor: A long, increasingly thick column of ionization eventually meets a thick, radially broad cap, a consequence of electron scattering.

We now return to quantitative calculations. Using the energy loss rate, altitude profiles of the plasma produced by single pulses from an electron source can be made taking into account the full range of energy degradation process. Since charged particle recombination operates on time scales of many milliseconds, a beam pulsed with relatively short, microsecond bursts will give a net production of new ionization equal to the product of the local production rate and the beam on time. The newly introduced charged particles then decay according to recombination and other ionic and electronic reactions with the gases of the middle atmosphere.

Figure 5 shows ionization production rate as a function of altitude calculated for a 1 A, 5 MeV electron beam pulsed on for 5  $\mu\text{sec}$  with different assumptions about the beam area. The production is proportional to the neutral gas number density for most of the path, but large ionization rates obtained near the end of the beam show where scattering is important with consequent large lateral dispersions.

The initial burst of new ionization from a relativistic electron beam can have a high "contrast" with respect to the pre-existing, background plasma. Figure 6 shows typical day and night electron densities for the middle atmospheric regions. Also included is the new density calculated above for a single 5  $\mu\text{sec}$  burst. It can be seen that the beam-associated ionization can be much larger than the ambient ionization for altitudes depending on the particular beam cross sectional area.

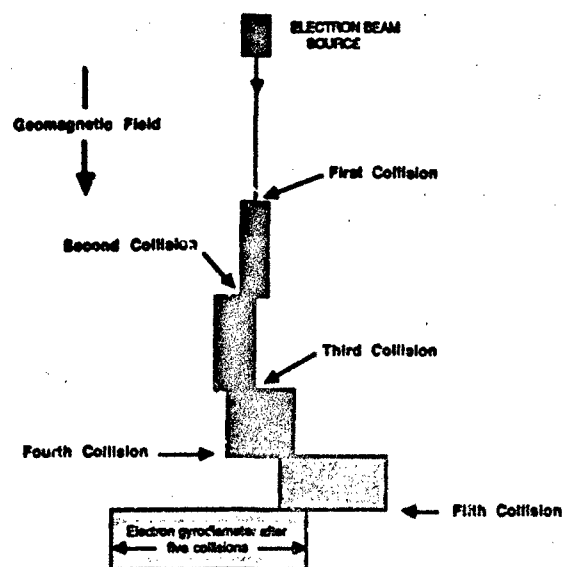


Figure 3. Schematic view of the effects of small angle scattering on the pitch angle and lateral deflection of an energetic electron initially moving parallel to the local magnetic field. Each collision enlarges the gyroradius and moves the gyroradius defining the electron motion.

More complete analyses of electron beam penetration must take into account beam divergence arising from the finite range of pitch angles at the beam source, the confining feature of the magnetic field, and the important effects of electron scattering which accompany traversal through the atmosphere. A description of these is given in Appendix A, which provides the basis for the ionization production rate discussion of this section.

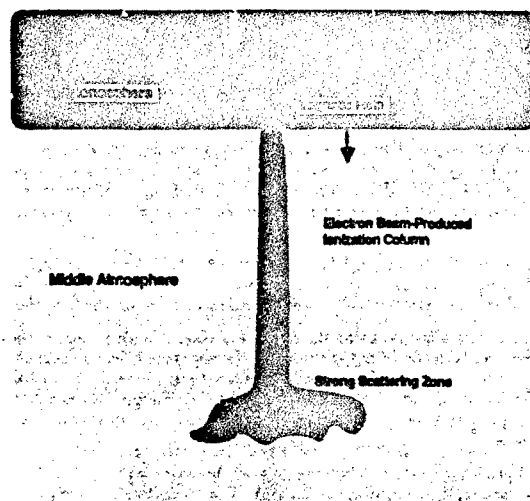


Figure 4. Illustrating the penetration of the electron beam into the middle atmosphere. The plasma density of the beam-produced ionization column will be much greater than the ambient ionospheric density. In addition, owing to strong scattering at the end of the trajectory, we expect a substantial "blooming" of the ionization structure. It is assumed that the beam is launched parallel to the local magnetic field.



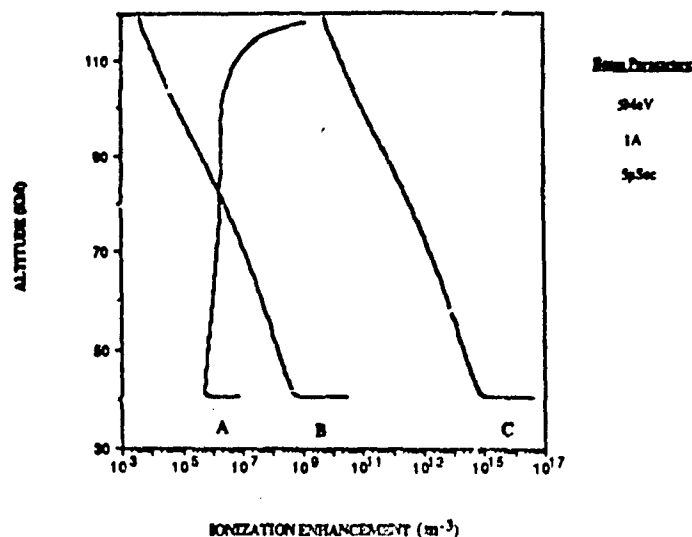


Figure 5. Ionization production as a function of altitude for a 5  $\mu$ second, 5 MeV, 1 A, electron beam for three different beam cross sections. Contour A is for a variable beam cross section due to atmospheric scattering without a magnetic field. Curve B and C assumes constant cross section radii of 602 and 0.5 meters, respectively. The 602 m radius represents the relativistic gyroradius of a 5 MeV beam.

## 2.2. Plasma Chemistry

The initial ionization created by the pulsed electron beam consists of positive atmospheric ions ( $O_2^+$ ,  $N_2^+$ ) and free secondary electrons. Once created, the positive ions will undergo reactions with the ambient gases of the atmosphere, resulting in a variety of final positive ion products which can be computed using atmosphere chemistry codes. Typically, large cluster positive ions will begin to form in competition with dissociative recombination, a process which is rapid at the high plasma densities of the narrower models of the ionization column.

The secondary electrons, in contrast, undergo two more stages of activity. First, those having significant energies will have subsequent additional energy losses, including optical excitation and impact ionization of atmospheric gases. Electrons of lower energy will cool to atmospheric temperature by means of various inelastic collisions with atmospheric gases and, thereby, become part of the background D-region and upper stratospheric plasma.

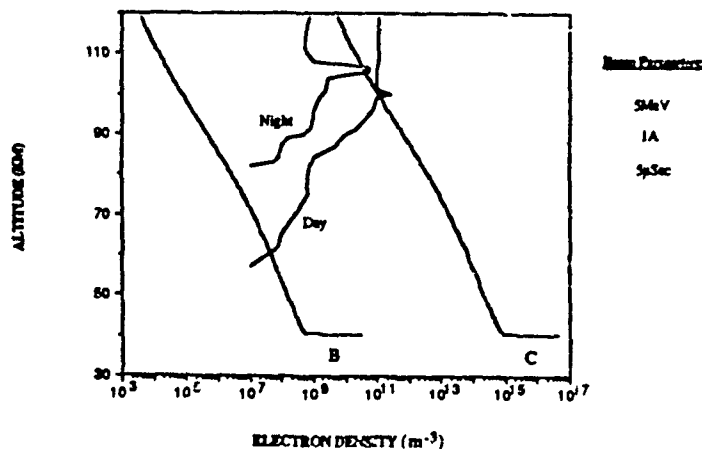


Figure 6. Comparison of initial ionization enhancement produced per unit volume with the average ambient density of the E- and D-regions for day and night conditions. Curves B and C are defined in Figure 5.

Since it is the electrons that interact most strongly with electromagnetic radiation, it is important to understand the various processes which affect their density decay. On the one hand, recombination with ions occurs at a certain rate in proportion to the ion concentration. The time constant for this is set by the dissociative recombination coefficient,  $\alpha$ , and the density of ambient ions. A useful expression for the time constant for dissociative recombination is given by

$$\tau_D = \frac{1}{\alpha_D n_e} \quad (3)$$

where  $\alpha_D$  is the dissociative recombination rate, given by

$$\alpha_D = 3 \times 10^{-7} \left( \frac{300}{T} \right)^{\frac{1}{2}} \text{ cm}^3 \text{ sec}^{-1} \quad (4)$$

where  $T$  is the electron temperature. Typical plasma densities of  $10^4$  to  $10^6 \text{ cm}^{-3}$  within the beam-produced ionization column give dissociative recombination decay times of seconds or more.

A more important loss process for cold electrons is attachment to neutral  $O_2$  to form  $O_2^-$  ions. This three-body reaction progresses according to the reaction



which has a rate coefficient [4] given by

$$k = 1.5 \times 10^{-29} \left( \frac{300}{T} \right) e^{-(600/T)} n^2(O_2) \text{ sec}^{-1} \quad (6)$$

where  $T$  is the temperature of the background neutral atmosphere and  $n(O_2)$  is the molecular oxygen density. Calculations show that such attachment of free electrons becomes a very important process below about 70 km altitude in the mesosphere. As shown below, it is the primary limitation on the lifetime of free electron densities arising from the relativistic electron beam experiment.

To understand this effect, we must consider the overall balance between electrons and  $O_2^-$  ions. While electron attachment removes the free electrons, there are several reactions serving to liberate them, including photodetachment (in sunlight) and reactions of  $O_2^-$  with  $O_3$  and  $O$ . For the present models, it seems reasonable to ignore these last two reactions: The  $O$  and  $O_3$  densities are sufficiently low in the regions between 40 km and 70 km for their detachment reactions with  $O_2^-$  to be ignored. Thus, to model the time-dependent electron density in the beam column, we can approximate the real situation by considering only electron attachment to  $O_2$  and photodetachment in sunlight.

The photodetachment of electrons from  $O_2^-$  is expressed as:



where the rate coefficient  $J = 0.3 \text{ sec}^{-1}$  at zero optical depth [4].

**Table 1. Electron-Negative Ion Equilibrium Time Constant.**

Height (km)	Time Constant (sec)
30	$1.2 \times 10^{-4}$
40	$1.9 \times 10^{-3}$
50	$2.3 \times 10^{-2}$
60	$2.5 \times 10^{-1}$
70	$1.9 \times 10^0$
80	$3.3 \times 10^0$

Competition between electron attachment and photodetachment can be studied by a simple time dependent model of ionization loss which ignores recombination. If there is an initial electron density,  $N_0$ , at time  $t = 0$ , the electron density at a later time is given by the expression

$$\frac{n_e}{N_0} = [1 - \tau k(1 - e^{-t/\tau})] \quad (8)$$

where  $\tau$  is a time constant for reaching equilibrium conditions, given by the expression

$$\tau = \frac{1}{(J + k)} \quad (9)$$

$k$  is the attachment rate for equation (5), and  $J$  is the zero optical depth photodetachment rate for  $O_2^-$ . Values of  $r$  as a function of altitude are given in Table 1.

Figure 7 shows the time history of the equilibrium ratio of electron density to initial ion density,  $\gamma$ , at several altitudes. It is clear that even in daylight electrons at low altitudes will quickly be transformed to negative ions.

From the foregoing we can conclude that an appreciable concentration of free electrons can be created by an initial pulse of relativistic electrons. However, these will disappear by two major processes: (i) attachment with  $O_2$  and, at a slower pace, by (ii) recombination with positive ions. At altitudes above 70 km the lifetime of the electrons is long, measured in terms of seconds. Below 70 km, attachment becomes increasingly important, such that at altitudes of 50 km free electron lifetimes are measured in terms of milliseconds, even in daytime.

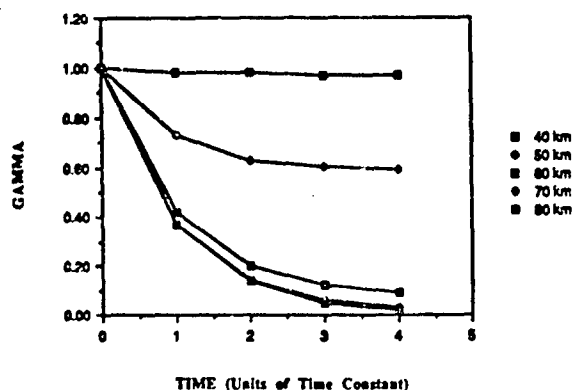


Figure 7. Showing the ratio of equilibrium electron to initial ion density,  $\gamma$ , as a function of altitude. These results demonstrate the idea that free electrons are rapidly converted to negative ions at low altitudes.

### 8. ELECTRODYNAMICS OF AN IONIZATION COLUMN IN THE MIDDLE ATMOSPHERE

It is well known that the middle atmosphere plays an active part in global electrodynamics, serving as a conducting medium for the spatially dispersed currents arising from thunderstorm activity throughout the world. Although the largest values for the atmospheric electric fields are found within the troposphere near the earth's surface, *in situ* observations indicate that substantial potential drops are still possible in the upper stratosphere and mesosphere. Using several different measuring methods, Maynard and Hale and their co-workers have found, on occasion, electric fields on the order of volts per meter in the D-region, implying that there may be total potential drops on the order of 10's of kilovolts over distances of 10's of kilometers [5, 6].

Within the context of the present study it is appropriate to investigate the interactions that might occur between a transient, highly conducting ionization column and ambient electric fields of the middle atmosphere. This is done in the following way. First, we assume that the ionization column is produced instantaneously with a certain altitude profile of electron density and beam area. Next, under the action of the existing atmospheric electric fields, currents will be established in the column, leading it to charge at a certain rate to the potential of the highly conducting ionosphere lying above. At each point along the column the potential difference between the column and the surrounding atmosphere will also rise. At some point it may be the case that the associated electric fields are sufficiently large to accelerate ambient and ionization column electrons to sufficiently large energies to cause additional ionization; i.e., breakdown will occur. In this situation, a discharge would be initiated with the possibility of subsequent large currents occurring in the ambient medium and the conducting ionization column. Such a discharge, the equivalent of lightning, would continue until the ionization column-associated electric field is reduced below the breakdown level of the atmosphere.

To proceed, we first compute the resistivity and charging time of the beam-produced ionization column. This time is shown, for typical parameters, to be somewhat less than the time for loss of the electrons due to attachment. Next, a computation is made of the breakdown electric field for conditions within the middle atmosphere. Using a model for the distribution of electric potential along the ionization column and typical values of middle atmosphere electric fields, it is shown that it is likely that some portion of the ionization column will establish electric fields which exceed the threshold for breakdown. This then leads to discussion of subsequent effects which are important to the magnitude and duration of the discharge current.

#### 8.1. Resistance and Charging of the Ionization Column.

We consider a simple model where the ambient electric field,  $E$ , is parallel to the vertical ionization column.

When the ionization column is created, current will pass along it with a magnitude set by the resistivity of the column and the magnitude of the external electric field. Owing to its high conductivity, however, the interior electric field will quickly change, introducing a net potential difference between the column and the exterior atmosphere. If the column were perfectly conducting, it would achieve the same, uniform potential as the ionosphere. Figure 8 illustrates this situation in terms of equipotential contours in the vicinity of the column. Owing to the high electrical conductivity of the column, the local contours of electrostatic potential are altered, producing large potential gradients in the vicinity of the column.

To begin the computation of the resistivity of the ionization column, the relationship between the local vertical current density,  $j$ , and the vertical component of the local electric field,  $E$ , is given by

$$j = \sigma E \quad (10)$$

where  $\sigma$  is the ordinary Pedersen conductivity of the ionospheric medium. If we then assume that a current  $I$  passes through an area  $A$  of the column, we have

$$I = (\sigma A) E \quad (11)$$

Next, we adopt the standard expression for the conductivity:

$$\sigma = \frac{n_e e^2}{m_e \nu_{en}} \quad (12)$$

where  $n_e$  is the ambient electron density,  $\nu_{en}$  is the electron-neutral collision frequency,  $m_e$  is the electron mass, and  $e$  is the magnitude of the electron charge.

Further progress can be made by noting that the electron-neutral collision frequency and the initial electron density created by the beam electrons are both proportional to the neutral gas density. Thus, if we normalize our results to the values of initial electron density  $n_e^0$  and collision frequency  $\nu_{en}^0$  at some reference altitude, we can write the relation between column current and electric field as

$$I = \left[ \frac{n_e^0 e^2 A}{m_e \nu_{en}^0} \right] E \quad (13)$$

To obtain the resistivity of a column of length  $L$ , we note that if there is a voltage  $V$  present over a distance  $L$ , Eqn. (13) becomes

$$V = \left[ \frac{m_e \nu_{en}^0 L}{n_e^0 e^2 A} \right] I \quad (14)$$

so that the column resistance per unit length,  $r$ , can be written as

$$r = \frac{m_e \nu_{en}^0}{n_e^0 e^2 A} \quad (15)$$

Values for the collision frequency can be obtained from the CIRA reference atmosphere [11]. Normalizing to 50 km altitude, using these values and the electron density from Figure 5 gives a resistance per unit length of

$$r = 35 \Omega \text{m}^{-1} \quad (16)$$

or, for a total length of, say, 40 km, a total column resistance of 1.4 M $\Omega$ .

From this, we find that the resistance of the ionization column is substantial and that a potential drop of about 20 kV will result in a current of tens of milliamperes. In this situation, the time constant for charging of the column does not follow from the usual transmission line equations of electrical charging: They apply only to cases where the resistance per unit length is a small part of the line impedance provided by the capacitance and inductance per unit length. In this instance another approach is needed, and this is discussed in Appendix B in terms of a diffusion-controlled electric field. The result applicable to the present circumstances is that the time constant for the beam column charging,  $\tau_c$ , can be approximated by the expression

$$\tau_c \approx \frac{\nu_{en}}{\omega_p^2} \quad (17)$$

where  $\nu_{en}$  is the electron-neutral collision frequency and  $\omega_p$  is the plasma frequency. For the situation outlined here, the time constant for charging of the column is on the order of 10's of  $\mu$ seconds. Thus, as seen from an attachment time scale of 10's of milliseconds, the ionization column rises to the ionospheric potential very quickly, leading to the electrical model shown in Figure 8.

As a consequence of these calculations, we see that not only does the electron beam pulse create a channel of highly conductive plasma, albeit for a relatively short time of 10's of milliseconds at low altitudes, but also that the ambient electric fields of the middle atmosphere will drive current within this structure, bringing it quickly (on time scales of 10's of  $\mu$ seconds) to the potential of the overlying ionosphere.

### 3.2. Electric Discharge of the Beam Column

As the potential of the beam column rises with respect to the background, an electric field is generated within the surrounding medium. This situation was illustrated in Figure 8, where we showed the equipotential contours of the middle atmosphere as they have responded to the increasing potential of the beam-induced plasma column. The concentration of potential contours near the lower tip of the column indicates the increasing electric field there, and opens the question of the possibility of creating the conditions necessary for an electrical discharge.

To resolve this possibility, two separate issues must be investigated: (1) the magnitude of the breakdown electric field in the middle atmosphere, and (2) the magnitude of the electric field in the vicinity of the beam structure. Each of these is presented in the following sections.

**1. The Breakdown Electric Field.** Electrical breakdown occurs in a partially ionized gas when the local electric field is sufficiently large to accelerate ambient electrons to ionizing energies, typically of the order of 15 eV. The tendency of electric field accelerated electrons to rise in energy towards breakdown energies is opposed by electron collisions with the ambient neutral gas. In each energetic electron-neutral collision the energy imparted to the electron by the electric field is largely lost. The problem in its simplest form, then, is to compute the energy of an individual electron under combined effects of the accelerating electric field and the momentum lost in electron-neutral collisions. In fact, more accurate theories of breakdown would include the distribution of velocities of the electrons, and the fact that it is the high energy portions of the electron velocity distribution function that lead to the initial avalanche ionizations that result in electrical breakdown. However, for this discussion, the simple model of breakdown is probably sufficiently accurate to indicate the magnitudes of fields needed.

We wish to compute the energy acquired by an electron between collisions with neutral gas particles. If there is an ambient electric field of magnitude  $E$ , the velocity,  $v$ , after a time,  $t$ , has elapsed since the last collision is

$$v = \left( \frac{eEt}{m_e} \right) \quad (18)$$

where  $e$  is the magnitude of electron charge and  $m_e$  is the electron mass. The electron energy,  $\epsilon$ , then follows as

$$\epsilon = \frac{1}{2} m_e \left( \frac{eE}{m_e} \right)^2 t^2 \quad (19)$$

If  $\nu_{en}$  is the collision frequency for electron-neutral gas collisions, the time,  $T$ , between collisions is  $T = 1/\nu_{en}$  and the relation between electron energy and collision frequency becomes

$$\epsilon = \frac{e^2 E^2}{2 m_e \nu_{en}^2} \quad (20)$$

If we adopt a value of 10 eV as the mean energy of the electron gas to acquire between collisions to initiate the ionizations necessary for breakdown, we arrive at the desired relation between breakdown electric field,  $E_b$ , and the collision frequency between electrons and neutrals:

$$E_b \approx \frac{1.1 \times 10^{-8}}{\nu_{en}} \quad (\text{volt m}^{-1}) \quad (21)$$

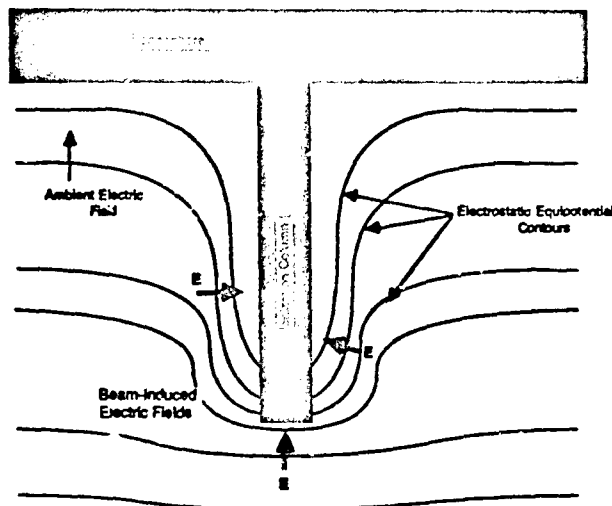


Figure 8. Electrostatic effect of introducing a conducting plasma column into the ambient middle atmosphere. It is assumed here that the ambient electric field is uniform and vertical. Note the large electric fields which surround the region near the surface of the ionization column.

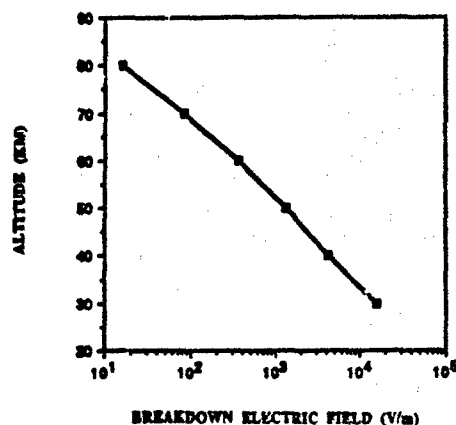


Figure 9. Showing the dc breakdown electric field strength as a function of altitude in the middle atmosphere.

Figure 9 plots values of  $E_b$  as a function of altitude in the middle atmosphere. The results indicate that relatively small fields of 100-1000 V/m will initiate electrical discharge in the regions between 50 km and 70 km altitude, the zone of principal interest in this study.

**2. Electric Fields Near the Plasma Column.** Figure 8 shows the general situation of electric equipotential contours near the beam column. Up to this point we have assumed that the beam has a geometry set by the initial pulse of high energy electrons; i.e., that a long, thin structure is created with the diameter set by atmospheric scattering. Furthermore, we have been able to show that this plasma structure will rapidly charge itself towards the potential of the overlying ionosphere, yielding progressively larger radial potential differences between the plasma column and the ambient ionosphere as one progresses downwards. Now, however, a difficult problem arises; namely, how to estimate the local electric field. If the potential changes rapidly with distance, then a large electric field will be present and the conditions required for electrical breakdown may be present. If, on the other hand, the potential is distributed over a large radial distance, only weak fields will occur and no cataclysmic breakdown effects can be expected.

The core structure of the ionization column is determined by atmospheric scattering. In the absence of accurate numerical results in the literature, we have estimated that the beam will achieve a diameter that is much larger than the source area,  $A_s$ , but substantially less than one gyrodiameter (600 meters for a 10 MeV electron). In fact, the column will not be uniform in radial dimension. Consequently, the potential of the core of the beam will be higher than even the outside edges, indicating that the correct calculation for the distribution of electric potential must include not only the time-dependent effects, but also the dimensionality of the electron distribution in the radial direction. This difficult task lies beyond the scope of the present work. Instead, we can indicate the possible values based on typical potentials and characteristic radii of the ionization column.

For example, if the core of the column has a diameter of 20 m, and if there is a 20 kV potential drop, then it might be possible to have a radial electric field of 1 kV/m within this extended zone. According to Figure 9, this would be sufficient to create breakdown above 50 km. On the other hand, if the diameter is 200 meters and the potential drop only 10 kV, then the radial electric field will be on the order of 50 V/m, which is probably too low to meet the requirements for breakdown except above 74 km altitude.

At this time, lacking knowledge about the actual distribution of electric fields in the middle atmosphere and about the redistribution of fields which will accompany the establishment of a conducting column of ionization in the same region, we cannot state categorically that electrical discharge is an inevitable consequence of the relativistic electron beam experiment. Part of this uncertainty can be removed by more thorough calculations of the electrodynamics of the column. But, in the face of poor information about the spatial and temporal variability of middle atmosphere electric fields, it will probably not be possible to have full confidence in the breakdown hypothesis: A suitable *in situ* experiment will be needed to test all of the complex factors.

### 3.3. Consequences of a Discharge.

It is interesting to speculate what might happen if, indeed, it is possible to initiate an electrical breakdown at some point in the column. In this situation, we first expect that additional electrons will be liberated to carry current. This might occur through the formation of filaments or leaders which would extend away from the column into the surrounding gases. The subsequent rush of free electrons would produce an electromagnetic pulse whose principal frequencies would be determined by both the duration of the breakdown and any characteristic oscillations that might accompany the formation and decay of leaders in the gas.

The general effect of the discharge would be to transport electric charge along the column. With sufficient fields, such a discharge could conceivably extend the full length of the beam. Heating of the atmosphere would be a slight consequence, and optical emissions would provide a way of seeing the development of the discharge process.

The decay of the discharge would be determined by the change in local potential and electric fields. As the region of enhanced density grows in size, the potential drop will become spread out, lowering the electric field strength until it falls below that required for breakdown. However, since this threshold depends on altitude, a complicated pattern of discharge might result, with prolonged discharge occurring at higher altitudes along the beam column. Countering this would be the diminution of the local fields with altitude as one approaches the conducting regions of the D-layer.

#### 4. A PROPOSED EXPERIMENT

As stated in the Introduction, current technology is available for a rocket-borne relativistic electron beam experiment. The goal of such an experiment should be to assess a variety of phenomena associated with firing a high energy beam into the atmosphere. These include: (1) the formation of a highly ionized column of ionization extending downwards to the upper stratosphere, (2) the formation of a large lateral cap of ionization at the end of the beam travel, as implied by Figure 4, (3) the time dependent decay of the free electrons in the column, (4) the possibility of creating a large scale electrical discharge in the middle atmosphere, and (5) understanding the physics of the interaction of the energetic particles with the atmosphere, as seen in the geometry of the beam and the character of energetic particles reflected back into space.

The most suitable experiments would be done with the nighttime launch of a recoverable rocket payload at White Sands Missile Range. The rocket trajectory could be chosen to minimize the cross-magnetic field velocity, permitting the accelerator to fire many pulses into the same general region of the atmosphere. The payload would consist of the accelerator and various on-board detectors, including those related to measuring the performance of the pulsed beam, the electrical charging of the rocket, and high energy particle detectors capable of measuring the fast backscatter of electrons from the atmosphere. Other remote diagnostic devices could also be flown on the rocket to permit characterization of the ionization column, as seen from immediately above. These could be optical and UV detectors capable of seeing by product radiation arising from beam interactions with the atmosphere and broadband radio receivers.

Coordinated ground observations would be essential. Optical imagers would be needed to provide information about the geometry of the beam, while radars of various frequencies could probe the extent to which the column ionization interacts with the incident radiation. Broad-band radio receivers would also help to assess the emission of any initial electromagnetic radiation (expected to be weak) and the possible stronger emissions following from an electrical discharge.

A schematic view of the experimental situation is given in Figure 10.

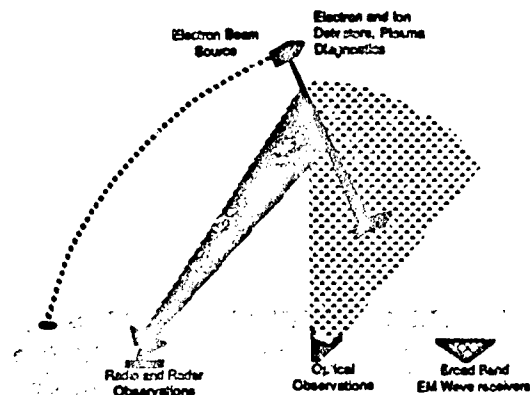


Figure 10. Illustrating the geometry of a relativistic electron beam rocket experiment. Ground sites provide optical, radar, and radio measurements of the beam characteristics, while diagnostics of the rocket measure vehicle charging, backscattered electron and ion fluxes, and image photon emission from the underlying ionization structure.

#### 5. CONCLUSION

There are many interesting features of relativistic electron beam experiments in space. Here, we have focused on problems relating to the interaction of the beam with the atmosphere to produce ionization enhancements. It is seen that the high energy of the beam electrons means that interaction with the middle atmosphere is possible, and that there are a number of subsidiary phenomena which may come into play. In the face of substantial theoretical uncertainties, firm understanding of the physical consequences will require an experimental program involving, at the least, several rocket flights with supporting ground and space observations. This should be done in connection with an extensive theoretical analysis of the important features of beam production, scattering, and electrodynamic consequences.

## 6. APPENDIX A: IONIZATION PRODUCED BY THE BEAM

The process of calculating the ionization produced by a relativistic electron beam in the atmosphere can be divided into two parts. First, the energy loss of the electron beam per unit distance ( $dE/ds$ ) as it penetrates through the atmosphere is calculated. It is assumed that most of this energy loss is caused by impact ionization of the neutral background of the plasma. An immediate result of this calculation is the penetration depth of the beam and also the ionization per unit length as a function of distance. The second part of the process is the estimation of the lateral extent (i.e., the extent perpendicular to the local geomagnetic field) of the primary beam, which enables us to derive the resulting incident primary electron flux,  $\Phi(s)$ . Both sets of calculations are necessary to estimate the ionization densities that are to result for the relativistic electron beam.

Given the above, it is straightforward to estimate the ionization rate,  $q$ , at any given altitude from

$$q = \frac{dE \Phi(s)}{ds \Delta \epsilon} \quad (A.1)$$

where  $\Delta \epsilon$  is the required average ionization energy, which is assumed here to have a value of 35 eV [4]. Assuming a short duration pulse, the value of  $q$  in (A.1) can be multiplied by the "on" time of the beam pulse to estimate the additional ionization or ionization enhancement that is created by the relativistic electron beam.

In the following, the two parts to the ionization calculation will be discussed separately, but it should be kept in mind that both are necessary to provide the final predictions of electron densities as a function of penetration. The results presented are intended for use with relativistic beam energy levels up to approximately 5 MeV, although it may be satisfactory for some applications for the energy to extend up to the 10 MeV level.

### A.1. Energy Loss and Ionization Rate Per Unit Length, $dE/ds$

The penetration of energetic electron beams through the atmosphere and the ionization produced by such beams can be straightforwardly calculated for non-relativistic electrons with energies greater than 1 keV. For example, Rees [7] used experimentally verified energy distribution functions to calculate the penetration and ionization deposition versus altitude. These results are useful for first order calculations in the lower energy ranges (1-300 keV). For beam energies above about 0.5 MeV, where the electron kinetic energy is approximately equal to the electron rest mass, it is necessary to include relativistic effects in these calculations.

Both ionization and penetration calculations start by estimating the electron beam energy loss per unit path length and assuming that all of the energy loss goes into ionization at that altitude. A form of the Bethe equation that accounts for relativistic effects can therefore be used [1], where

$$\frac{dE}{ds} = 4\pi r_0^2 \frac{m_0 c^2}{\beta^2} N Z \left\{ \ln \left[ \beta \frac{E + m_0 c^2}{I} \sqrt{\frac{E}{m_0 c^2}} \right] - \frac{1}{2} \beta^2 \right\} \text{ MeV/m} \quad (A.2)$$

and where  $E$  is the incident electron beam kinetic energy (MeV),  $r_0$  is the classical electron radius,  $NZ$  is the number of atomic electrons per  $\text{m}^3$  ( $Z$  is the atomic number and  $N$  is the number of atoms per  $\text{m}^3$ ),  $m_0 c^2$  is the rest energy of the electron (0.51 MeV),  $\beta^2 = (v/c)^2 = 1 - [(E/m_0 c^2) + 1]^{-2}$ , and  $I \approx (11 \pm 3/Z) \text{ eV}$ .

The original Bethe equation is basically a summary of detailed quantum mechanical calculations of soft collision energy loss between an energetic particle and bound electrons (by soft or, conversely, hard, we are referring to whether the struck electrons are initially considered bound or free). This was later extended to include relativistic effects. Although the Bethe equation is calculated assuming soft collisions only, it has been found to be an adequate first order estimate of total energy loss from both hard and soft collisions when it is extended to cover all energy losses up to the maximum possible loss per collision of  $E/2$ . This has been done in (A.2).

The use of (A.2) to estimate  $dE/ds$  ignores contributions to energy loss from bremsstrahlung radiation and straggling effects. However, for electron beam energies up through 10 MeV, radiative losses remain at least an order of magnitude lower [1]. Also ignored in (A.2), is the effect of electron back-scattering, which would decrease the incident flux at any given altitude but which would represent an additional ionizing electron flux contribution in the reverse direction. The effect from back-scattering is not expected to be significant except near the end of the electron beam path. Figure 2 shows the variation of  $dE/ds$  as a function of altitude for a 5 MeV beam, while Figure 1 shows the actual energy of the 5 MeV beam as it penetrates the atmosphere.

### A.2. Primary Beam Electron Flux, $\Phi(s)$

While the loss of electron beam energy, as the beam penetrates the atmosphere, plays the principal role in determining penetration depth and ionization per unit length, it is the radial expansion of the primary beam that sets the enhancement densities that are ultimately achieved within the ionization column. Factors that can play a role in determining radial expansion include initial beam source divergence, confining magnetic field forces, and electron scattering from interactions with the neutral atmosphere. How these effects interact becomes a very significant physical and computational problem, especially for the case of narrow energetic beam source. Walt *et al.* [3] used a formulation of the Fokker-Planck diffusion equation to, in part, predict radial expansion of auroral flux. Their method was not considered to be easily applied to distributions that were strongly peaked in either energy or angle; precisely the situation under consideration here. Another complimentary approach integrates the diffusion equations using Monte Carlo techniques, as in [8] and [3]. It is implicitly assumed that the primary beam and secondary flux electrons all behave independently, following single particle motions, and interact only with neutral atmosphere particles and the earth's magnetic field.

The work of Walt *et al.* [3] indicates that typical perpendicular-to-B diffusion of an auroral (non-relativistic) flux with broad energy and angular spread is on the order of an electron gyroradius; a result that is indicative of the confining effect of the geomagnetic field. That the magnetic field should still be necessary to confine the radial expansion of a narrow relativistic



monoenergetic electron beam launched nearly parallel to the field in a tenuous atmosphere is not necessarily obvious. After all, as beam energy increases the scattering cross-sections decrease [10] and highly focused relativistic beam generators are available. As will be shown, even in tenuous atmospheric conditions present for upper stratospheric and higher altitudes (neutral atmosphere molecular densities are at least three to seven orders lower than STP density levels), the relativistic electron-neutral elastic scattering collisions still can cause substantial radial beam diffusion without the presence of the geomagnetic field.

To demonstrate this fact, standard equations collected and published by the International Commission on Radiation Units and Measurements (ICRU) can be utilized to predict radial beam expansion [2] in a reference atmosphere [11] due to small angle scattering. Small angle scattering assumes that any large angle scattering events are relatively infrequent and can therefore be ignored. Fundamental to small angle scattering calculations is the fact that the mean square angular scatter for each electron-neutral collision is statistically independent and therefore additive [12]. This fact can be used to estimate the mean square radius of a narrow Gaussian electron beam as a function of penetration depth,  $s$ , given by

$$\overline{r^2}(s) = \overline{r_0^2} + 2\overline{r_0\theta}s + \overline{\theta^2}s^2 + \int_0^s (s-u)^2 T(u) du \quad (A.3)$$

where  $\overline{r_0^2}$  is the initial mean square radial spread of the beam,  $\overline{r_0\theta}$  is the initial covariance of the simultaneous radial and angular distribution,  $\overline{\theta^2}$  is the initial mean square angular spread of the beam, and  $T(u)$  is the change in mean square angle of scattering per unit length,  $u$ , given by

$$T(u) = \sum_i d \frac{\overline{\theta^2}}{du} = \sum_i 4\pi r_0^2 N_i \left( \frac{Z_i}{(\tau+1)\beta^2} \right)^2 \left\{ \ln[1 + (\theta_{mi}/\theta_{si})^2] + 1 + [1 + (\theta_{mi}/\theta_{si})^2]^{-1} \right\} \quad (A.4)$$

where

$$\theta_{mi} = \frac{2A_i^{-1/2}}{\alpha\beta(\tau+1)}, \text{ or } 1, \text{ whichever is smaller} \quad (A.5)$$

and

$$\theta_{si} = 1.130 \frac{\alpha Z_i^{-1/2}}{\beta(\tau+1)} \quad (A.6)$$

and where  $A_i$  is the nucleon number,  $\alpha$  is the fine structure constant ( $1/137$ ),  $\theta_{mi}$  is the cut-off angle due to the finite size of the nucleus, given by the ratio of the reduced de Broglie wavelength of the electron to the nuclear radius, and  $\theta_{si}$  is the screening angle due to the screening of the nucleus by the orbital electrons and is given by the ratio of the reduced de Broglie wavelength to the atomic radius.

As indicated in (A.4),  $T(u)$  is the sum of the mean square angle scattering contributions from each neutral atmospheric constituent. Mean square angle scattering for each constituent is proportional to its respective density and the square of the nucleus charge number. For a narrow, well focused beam, the integral in (A.3) completely dominates radial expansion and need be the only term considered. The integral weights scattering that occurs early along the path of the beam more heavily than scattering occurring near the end of the integration path.

Figure A.1 shows the predicted rms beam radius, assuming an initially narrow (1 cm radius) 5 MeV beam focused at infinity with no magnetic field, as it traverses vertically down from an altitude of 119 km. As seen, the beam spread due to elastic scattering would be substantial; well beyond the gyroradius for 5 MeV electrons (502 m). The somewhat surprising result here is that significant beam spread is predicted to occur even due to the scattering levels present in the highest altitude portion of the beam path where collisions are the most infrequent. For example, in transitioning from 119 to 118 km,  $T(u)$  has the average value

$$T(u) = T_0 = 1.26 \times 10^{-9} \text{ rad}^2/\text{m} \quad (A.7)$$

In transitioning one kilometer the rms angular spread of an initially columnar beam would thus increase to approximately 1 milliradian. Without any additional scattering collisions, this angular spread would cause the average beam radius to increase to approximately 80 m after penetrating down to a depth near 40 km; substantially less than a gyroradius. If instead,  $T(u)$  was maintained at the value in (A.7), the integral in (A.3) could be straightforwardly solved resulting in an approximate mean square radius of

$$\overline{r^2}(s) = \frac{1}{3}s^2 T_0 \quad (A.8)$$

which when evaluated at maximum range gives an rms radius of 460 m. However, since the beam must penetrate at least ten scale heights down to 40 km (for a 5 MeV beam),  $T(u)$  will increase correspondingly and so would the rms radius as shown in Figure A.1, without the presence of the magnetic field. Placement of the beam source at higher or lower altitudes would modify the integrated mean square scattering and therefore the resulting radial spread shown in Figure A.1.

Even with the reduced scattering cross-section of a relativistic electron beam, each primary electron experiences many elastic small angle scattering events as it penetrates through the atmosphere [10]. This will cause substantial spread in the angular distribution function describing the primary beam flux, even for the case of a focused narrow beam, directed down the magnetic field. Therefore, without the presence of the magnetic field, it would not be possible to keep a narrow, focused relativistic electron beam from having significant radial diffusion as it penetrated the atmosphere.

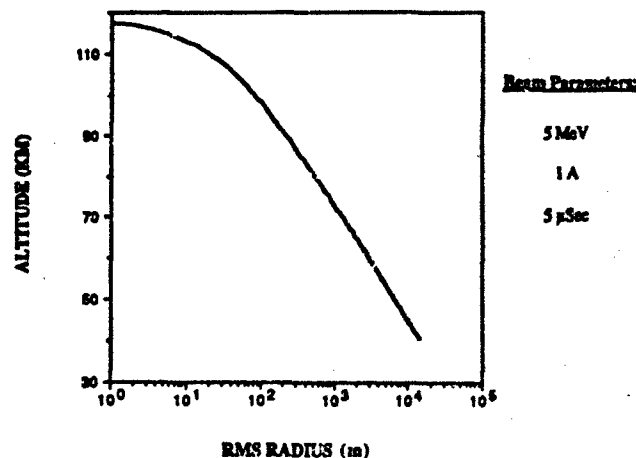


Figure A.1. Predicted rms beam radius versus altitude for a 5 MeV electron beam with an initial 1 cm radius. It is assumed that no magnetic field is present.

The problem of specifically including the confining effect of the magnetic field's Lorentz force with the statistical behavior of the electrons, due to elastic and inelastic collisions, is much more complicated, most likely requiring the methods of [3], [5], or [9]. However, it is probably safe to assume that the electron beam will not spread much more than a gyroradius, following the results of [3], at least until the beam penetrates sufficiently deeply into the atmosphere to an altitude where large angle scattering collisions become significant.

There are several assumptions that have been made in generating the above. For example, straggling and reflection effects have not been included (although most reflections tend to come from deep along the electron path [3, 10]). In the above analysis it has been implicitly assumed that the primary electrons, having identical initial conditions, all penetrate to the same final altitude. In actuality, different primary electrons in the beam will penetrate to different altitudes and possibly be reflected based on their unique collision history. This would have the effect of spreading out the very pronounced peaks that occur at the end of the beam penetration in Figure 5 over several kilometers or to reduce the incident flux somewhat.

We have also assumed that all secondary electrons produced, which on the average have sufficient energy to produce approximately two additional ion-electron pairs, will stay within the same location where they were initially generated. However they can easily move along the geomagnetic field lines within a mean free path before generating additional ionization. This will also have the tendency to reduce and broaden the pronounced peak observed at beam termination in Figure 5.

Finally, under certain conditions it is predicted that the mean square scattering angle will reach an equilibrium value, so that much beyond 0.3 to 0.5 of the mass weighted range the electrons will reach a state of full diffusion and a rms value of approximately 45 [2]. The explanation for this is that electrons scattered over larger angles are rapidly lost from the beam so that the largest depths are only reached by electrons with nearly straight paths. However, for the case under consideration here, the stated mass weighted range is only reached at approximately the last atmospheric scale height. Further, the effect of a confining magnetic field was apparently not considered, which should prevent large-angle scattered electrons from moving more than a gyroradius away and leaving the beam.

To summarize, the neutral atmospheric densities in the mesospheric and stratospheric altitudes under consideration here are sufficient to cause enough angular spread, on an initially narrow electron beam, such that without the presence of the magnetic field there would be substantial radial diffusion of the beam flux. The elastic collisional effect can be thought of as random walk of the primary electron guiding center. Therefore, for a first order estimate of the column ionization density, we would propose to use the initial beam energy gyroradius to set the primary electron flux and further assume that the flux is uniformly distributed within this gyroradius. This is the gyroradius curve (curve B) of Figure 5 where a much narrower column radius (0.5 m) is also included (curve C). In practice we would expect to see the actual ionization enhancement start with values near the 0.5 m curve and then move towards the gyroradius curve as the beam penetrated into the atmosphere. At the end of beam penetration, it may also be that the primary electron beam will diffuse slightly beyond a gyroradius, causing the resulting ionization density to dip below the gyroradius curve. Finally, we would expect that a variety of effects, such as electron straggling, will tend to broaden and reduce the peak levels of ionization predicted at the end of beam penetration in Figure 5.

## 7. APPENDIX B: RELAXATION OF AN IONIZED COLUMN TO UNIFORM POTENTIAL

Consider the ionized column shown in Figure B.1 with the initial ambient potential profile in Figure B.2.

The electromagnetic equations governing electron motion in the column are

$$\nabla \cdot \mathbf{E} = -ne/\epsilon_0 \quad (B.1)$$

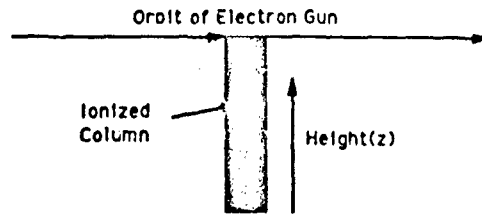


Figure B.1. Ionized column in the lower ionosphere and upper atmosphere produced by a relativistic electron beam fired downwards from within the ionosphere.

$$\frac{\partial n}{\partial t} = -\nabla \cdot n\mathbf{v} \quad (B.2)$$

where  $\epsilon_0$  is the permittivity of free space,  $-e$  is the electron charge,  $m$  is the electron mass, and  $n$  and  $\mathbf{v}$  are the electron density and velocity, respectively, and

$$\frac{\partial \mathbf{v}}{\partial t} = -\frac{e\mathbf{E}}{m} - \frac{kT\nabla n}{nm} - \nu\mathbf{v} = 0 \quad (B.3)$$

In this last equation  $\nu$  is the electron collision frequency and  $k$  is Boltzmann's constant.

We will derive two solutions to the above set of equations, first using an approximate approach and then a more general approach.

#### B.1. Solution for High Electron Collision Frequency

When  $\nu$  is very much greater than the plasma frequency the left hand side of (B.3) can be ignored. Rearrangement of the remaining equation gives

$$n\mathbf{v} = -\frac{ne\mathbf{E}}{\nu m} - \frac{kT\nabla n}{\nu m} \quad (B.4)$$

Substituting this into (B.2) gives

$$\frac{\partial n}{\partial t} = \nabla \cdot \frac{ne\mathbf{E}}{\nu m} + \frac{kT}{\nu m} \nabla^2 n \quad (B.5)$$

which, when we substitute for  $n$  from (B.1), gives

$$-\frac{\partial}{\partial t} \left( \frac{\epsilon_0}{c} \nabla \cdot \mathbf{E} \right) = \nabla \cdot \frac{ne\mathbf{E}}{\nu m} - \frac{kT}{\nu m} \nabla^2 \left( \frac{\epsilon_0}{c} \nabla \cdot \mathbf{E} \right) \quad (B.6)$$

Rearranging this latter equation gives

$$\nabla \cdot \left[ \frac{\partial \mathbf{E}}{\partial t} + \frac{\omega_p^2}{\nu} \mathbf{E} - \frac{v_e^2}{\nu} \nabla^2 \mathbf{E} \right] = 0 \quad (B.7)$$

where  $\omega_p = (ne^2/\epsilon_0 m)$  is the plasma frequency and  $v_e$  is the electron drift velocity. One possible solution of this last equation is

$$\frac{\partial \mathbf{E}}{\partial t} = -\frac{\omega_p^2}{\nu} \mathbf{E} + \frac{v_e^2}{\nu} \nabla^2 \mathbf{E} = 0 \quad (B.8)$$

Let us now assume a one-dimensional solution in the vertical, or  $z$ , direction, so that we have

$$\frac{\partial E_z}{\partial t} = -\frac{\omega_p^2}{\nu} E_z + \frac{v_e^2}{\nu} \frac{\partial^2 E_z}{\partial z^2} = 0 \quad (B.9)$$

Then, given an initial constant value of  $E_z$ , or  $E_{z0}$ , in the column, the solution to (B.9) is

$$E_z = E_{z0} \exp[-\omega_p^2 t / \nu] \quad (B.10)$$

In other words, the  $E_z$  field relaxes to zero in a characteristic time,  $t_0$ , equal to  $\nu/\omega_p^2$ . If we take  $\nu = 10^5 \text{ sec}^{-1}$  and  $\omega_p = 10^4 \text{ sec}^{-1}$ , we have

$$t_0 = \frac{\nu}{\omega_p^2} = 10^{-7} \text{ sec}$$

## B.2. Solution for the General Case

In the general case the governing equations are

$$\nabla \cdot \mathbf{E} = -ne/\epsilon_0 \quad (B.11)$$

$$\frac{\partial n}{\partial t} = -n_0 \nabla \cdot \mathbf{v} \quad (B.12)$$

where  $n_0$  is the electron density, and

$$n_0 \frac{\partial \mathbf{v}}{\partial t} = -\frac{en_0 \mathbf{E}}{m} - \frac{kT}{m} \nabla n - n_0 \nu \mathbf{v} \quad (B.13)$$

Taking the divergence of (B.13) gives

$$n_0 \frac{\partial}{\partial t} (\nabla \cdot \mathbf{v}) = -\frac{en_0 \nabla \cdot \mathbf{E}}{m} - \frac{kT}{m} \nabla^2 n - n_0 \nu \nabla \cdot \mathbf{v} \quad (B.14)$$

Writing (B.11) in the form

$$n = -(e_0/\epsilon) \nabla \cdot \mathbf{E} \quad (B.15)$$

and substituting for  $n$  in (B.12) gives

$$\nabla \cdot \mathbf{v} = -\frac{1}{n_0} \frac{\partial n}{\partial t} = -\frac{1}{n_0} \frac{\partial}{\partial t} \left( -\frac{e_0}{\epsilon} \right) \nabla \cdot \mathbf{E} = \frac{e_0}{en_0} \frac{\partial}{\partial t} \nabla \cdot \mathbf{E} \quad (B.16)$$

If we now substitute (B.15) and (B.16) into (B.14) and simplify, we obtain

$$\frac{\partial^2 \mathbf{E}}{\partial t^2} + \nu \frac{\partial \mathbf{E}}{\partial t} = -\omega_p^2 \mathbf{E} + v_s^2 \nabla^2 \mathbf{E} \quad (B.17)$$

We now write  $\mathbf{E} = E(t)\hat{z}$ , where  $\hat{z}$  is a unit vector in the  $z$ -direction, upon which (B.17) becomes

$$\frac{\partial^2 E}{\partial t^2} + \nu \frac{\partial E}{\partial t} + \omega_p^2 E = 0 \quad (B.18)$$

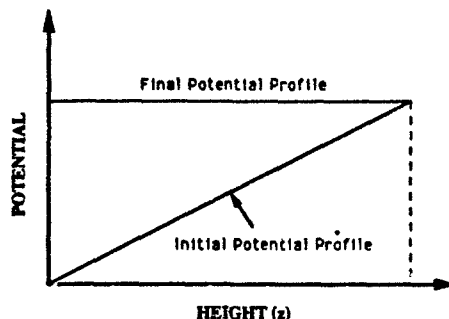


Figure B.2. Initial and final potential profiles within the ionized column shown in Figure B.1.

which has the solution

$$E(t) = E(0) \exp \left[ -\left( \nu + \sqrt{\nu^2 - 4\omega_p^2} \right) t/2 \right] \quad (B.19)$$

If  $\nu < 2\omega_p$ , the solution becomes

$$E(t) = E(0) \exp[-\nu t/2] \exp \left[ -i \left( \sqrt{4\omega_p^2 - \nu^2} \right) t/2 \right] \quad (B.20)$$

and if  $\nu > 2\omega_p$ ,

$$E(t) = E(0) \exp[-\omega_p^2 t/\nu] \quad (B.21)$$

where this latter equation corresponds to (B.10) derived previously under less general conditions.

## 8. REFERENCES

- [1] Evans, Robley D., *The Atomic Nucleus*, McGraw-Hill, New York, 1955.
- [2] ICRU Report No. 35, Radiation dosimetry: Electron beams with energies between 1 and 50 MeV, International Commission on Radiation Units and Measurement, Bethesda, Maryland, 15 September 1984.
- [3] Walt, M., W. M. MacDonald, and W. E. Franci, Penetration of auroral electrons into the atmosphere, in *Physics of the Magnetosphere*, (Ed. R. L. Carovillano, J. F. McClay, and R. R. Radoski), Reidel, Dordrecht, p. 534, 1967.
- [4] Banks, P. M., and G. Kochar's, *Aeronomy, Vol. A and B*, Academic Press, New York, 1973.
- [5] Maynard, N. C., C. L. Croskey, J. D. Mitchell, L. C. Hale, Measurement of volt/meter vertical electrical fields in the middle atmosphere, *Geophys. Res. Lett.*, **8**(8), 923, August 1981.
- [6] Hale, L. C., C. L. Croskey, J. D. Mitchell, Measurements of middle-atmosphere electric fields and associated electrical conductivities, *Geophys. Res. Lett.*, **8**(8), 927, August 1981.
- [7] Rees, M. H., Auroral ionization and excitation by incident energetic electrons, *Planet. Space Sci.*, **11**, 1209, 1963.
- [8] Wedde, T., Internal Report E-162, Norwegian Defense Research Establishment, 1970.
- [9] Maeda, K., Diffusion of auroral electrons in the atmosphere, NASA TN D-2612, 1965.
- [10] Mørhøj, B. N., Particle precipitation: Scattering and absorption, in *Cosmical Geophysics*, (Ed. A. Egeland, O. Holter, and A. Omholt), Universitetsforlaget, Oslo, Norway, p. 211, 1970.
- [11] *Cospar International Reference Atmosphere (CIRA) - 1965*, North Holland Publishing, Amsterdam, 1965.
- [12] Rossi, B., *High-Energy Particles*, Prentice-Hall, Englewood Cliff, NJ, 1952.

## 9. ACKNOWLEDGEMENTS

Our special thanks to Dr. K. J. Harker, now at SRI International, for his work on the relaxation of the ionization column, which forms the basis of Appendix B. We also thank Dr. P. A. Kossey of the Air Force Geophysics Laboratory, and Dr. J. Haimson of Haimson Research Corporation for assistance and helpful advice. Support for this work was provided by the Air Force Geophysics Laboratory through an augmentation of NASA Grant No. NAGW 235 to Stanford University.

22-18

DISCUSSION

T. JONES, UK

Is there any physical reason why the experiment you described could not be done from a balloon with the beam directed upwards? Clearly there would be some advantages (power capability, etc.) in doing it this way around.

AUTHOR'S REPLY

We welcome a balloon experiment. It would enable us to carry a large number of batteries for power and would enable us to study almost all the beam/atmosphere interactions if the balloon could be flown high enough.

U. S. INAN, US

Tony, have you computed any light emission levels that would be generated by these types of beams? What types of optical signatures do you expect?

AUTHOR'S REPLY

We have only made some informal computations -- estimates would be a better word -- of the light emissions. It appears that practically all of the known emissions will be stimulated. In my discussion today I largely ignored the role played by secondary electrons and one of their roles is to stimulate light emissions.

D. PAPADOPOULOS, US

A key problem with REB injection in a low density plasma is the issue of establishing equilibrium with respect to beam self fields, pinching,  $dB/dt$  induced currents, etc. Have you looked at these conditions and what they imply with respect to the type of currents and energies that can be stably injected?

AUTHOR'S REPLY

We have looked at all these conditions, but only briefly. We found no indication that any of them would affect the stability of the beam under the conditions I discussed today. Please note that the pulses were restricted to about 5  $\mu$ sec in duration.

## Electron gyro-harmonics generated by spaceborne artificial electron beam

D. Mourenas and C. Béghin

Laboratoire de Physique et Chimie de l'Environnement, 45071 Orléans Cedex 2, France

### ABSTRACT

Results on high-frequency waves generated by the PICPAB (Phenomena Induced by Charged Particle Beams) experiment flown on the Spacelab-1 shuttle mission are presented. Then we propose an interpretation for the wave generation mechanism associated with such an experiment.

This experiment comprised both electron and ion accelerators of a few keV energy installed on board the space shuttle and associated with nearby diagnostic instruments such as plasma and wave analysers. First, the observations are compared to previous results obtained in similar conditions and they are discussed in the frame of various beam-plasma interactions models. The main features are electron cyclotron harmonics which appear modulated in amplitude with maxima occurring near the harmonics of the upper hybrid resonance. An interaction between the return flux electrons and the ambient plasma is thought to have generated the first cyclotron harmonics close to  $f_{UH}$  and, after non-linear saturation and trapping processes, the entire spectrum. By means of a non-linear single-wave model, developed analytically and solved numerically, we finally recover most of the experimental features.

### INTRODUCTION

Numerous active experiments aimed at studying charged particle beam-plasma interactions have been conducted in the past 20 years [Suszczewicz, 1985]. They had first been carried out on rockets, but the shuttle era opened new opportunities, allowing in particular the investigation of wave production during electron beam injection for a wide range of plasma conditions [Shawhan *et al.*, 1984].

The major scientific objective of PICPAB (Phenomena Induced by Charged Particle Beams) experiment, which was launched on board the space shuttle on November 28, 1983 as a part of the SPACELAB-1 payload, was the study of the interaction of an artificial beam of energetic electrons (8 keV, 100 mA) with the ionosphere [Béghin *et al.*, 1984].

According to many previous experiments, we were expecting to observe wave emissions near the plasma frequency  $f_p$  or the upper hybrid  $f_{UH}$  which are very close to each other in middle latitude F-region, and possibly some electron cyclotron harmonics  $nf_{ce}$ . Nevertheless, a careful examination of the data led us to the discovery that most of our spectra were made of cyclotron harmonic series of a kind we had never heard before [Mourenas *et al.*, 1989] with the noticeable exception of Kellog *et al.* [1982], who reported a partly alike observation in a laboratory experiment. That puzzling kind of spectrum can be described as follows. Several successive cyclotron harmonics are gathered together, appearing in periodic packets of decreasing amplitude, with successive maxima occurring near the plasma frequency and its harmonics. Cyclotron harmonics and  $f_p$  harmonics have often been observed independently of each other in the past. However, both features had never been reported simultaneously. A tentative explanation raised from the fact that these waves are electrostatic in nature, and are thought to propagate inside an extremely narrow region at the edge of the primary beam column. Therefore, this kind of emission could be observed solely close to the beam path. Furthermore, a very good frequency resolution has been revealed to be needed to pick out the cyclotron harmonic structure from the packets near  $f_p$  and  $nf_{ce}$ , as well as a wide frequency

range of analysis to cover high harmonics of the plasma frequency (up to 4 or 5).

This paper is an attempt to describe the generation mechanism which we think is responsible for the observed waves.

In the forthcoming section, we give a brief description of the experimental conditions. Then, we present the main observations, along with some considerations leading to a single model of wave production. This linear model is developed and applied to the observational conditions. Finally, a non-linear model is shown to explain most of the remaining results, namely the harmonics generation and power law.

### EXPERIMENTAL CONDITIONS

Spacelab-1 was launched on November 28, 1983 in its nominal 57° inclination orbit at an altitude of about 240 km.

The PICPAE experiment comprised three packages (fig. 1). The accelerator package was installed on the pallet. The diagnostic package, deployed in the scientific airlock about 60 cm above the Spacelab pressurized module was instrumented with a magnetic and an electric antenna and associated receivers for covering two frequency ranges (SFL and SFH), respectively 0.2 to 11.4 MHz and 2 to 92 MHz, in 144 equally spaced steps. Both packages were controlled by a processor unit installed in a rack inside the pressurized module. The electron accelerator could be operated either in low current (10 mA) or high current (100 mA) mode. The accelerators could be operated in the so-called pulse mode (pulse on during 20 ms) or modulated mode (pulse on during 40 ms, modulated at 500 Hz), with rate of  $3.75 \text{ s}^{-1}$  in both cases.

The interaction of the shuttle with the ambient ionospheric plasma, at a velocity of about 8 km/s, is known to create a region of depleted plasma density, extending in a wake-like structure at distances as large as 250 m downstream of the spacecraft [e.g. Gurnett *et al.*, 1988]. The plasma conditions encountered by the beam were therefore depending on the spacecraft attitude: when injected upstream of the shuttle, the beam encountered an almost homogeneous medium, but when emitted at 90° or more with respect to the shuttle velocity vector, it first had to cross a low density region before entering the background ionospheric plasma. The different methods used to determine the value of the background plasma density are detailed in Mourenas *et al.* [1989].

### HIGH-FREQUENCY WAVE OBSERVATIONS

#### Results

As noted above, we can classify the wave data in two major categories, depending upon whether the plasma density is homogeneous or not along the beam trajectory.

In the following, we shall refer to the spectrum of the HF electric field displayed in figure 2, which is one of the most significant ones, obtained in the homogeneous case [Mourenas *et al.*, 1989]. The wrapping curve, which was obtained with a frequency resolution of 660 kHz, shows the  $pf_{ce}$  harmonics, while the sharp spikes occurring very near  $nf_{ce}$  forming the actual spectrum, are displayed with a better resolution (82 kHz). The character of the emissions has been determined to be electrostatic, with the noticeable exception of the fundamental electron gyrofrequency, whose magnetic component cannot be neglected. Here, the plasma frequency was well above the gyrofrequency ( $f_{pe} = 3.4 f_{ce}$ ). In the remaining of the paper, we shall call  $F_0$ , such as  $F_0 = Nf_{ce}$  the "fundamental frequency", closest to  $f_{ce}$ , whose harmonics are observed.

After careful analysis of the data, we have concluded that these lines could not be produced inside the electronics itself. Indeed, sometimes the intensity of the harmonic lines  $pf_0$  is higher than that of the fundamental, a fact which



cannot be explained by a non-linear effect inside the electronics. Moreover, the level reached by fundamental lines is often lower than the required level to produce harmonics by nonlinearity in the electronics. We conclude that these harmonics are really produced in the medium. In most cases, their amplitude - which reaches 0.8 V/m near  $f_{ce}$  when the angle between the electric antenna and the Earth magnetic field is close to  $90^\circ$  - is decreasing when the ambient plasma density is increasing. We have found that the amplitude of individual  $pF_e$  emissions follows a power law  $E(pF_e) \propto p^{2.5}$  (fig. 3).

#### Interpretation

In fact, the type of waves we measured seems to be intimately linked to the shuttle neutralization process. Indeed, a vehicle emitting an electron beam of 100 mA into vacuum would charge up to the acceleration voltage. Here, the ambient thermal plasma provides a return current proportional to the effective collecting area of the shuttle. Part of it is made of suprathermal electrons accelerated by the charging mechanisms. Recent results [Frank *et al.*, 1989] indicated that a return current could also be produced by an ion acoustic instability driven by the primary beam. These return current electrons would be more efficient than the primary beam electrons in interacting with slow plasma waves, because of their somewhat smaller velocity.

Young *et al.* [1973] have shown that emissions very close to  $n f_{ce}$  can only be excited by means of an interaction between ionospheric electrons and a less dense electron beam, whose distribution function has to exhibit some kind of anisotropy. Namely, either a temperature anisotropy or a loss-cone like anisotropy is necessary. However, in the peculiar case of the PICFAB experiment, as well for the primary beam as for the return current, vehicle charging favors  $T_{\perp} > T_{\parallel}$ , in which case cyclotron instability cannot be triggered by temperature anisotropy [Mikhailovskii, 1974]. Thus, we came to assume the existence of a loss-cone like distribution. Besides, after-effects in both wave and return flux measurements showed that emissions could be observed up to one millisecond after the beam was shut down, well correlated with neutralization return fluxes, at a time when the primary beam had travelled a few tens kilometers away from the shuttle. This is another strong argument in favor of a wave generation mechanism associated with the secondary beam of returning electrons. This assumption is also supported by the observation of the same waves during beam injection parallel to the  $B_0$  field, in which case it would be unlikely that the primary beam could exhibit a loss-cone structure at a so short distance from the accelerator.

It should be noted that Belmont [1981] has already reported some simulations with a hot ring distribution, showing the occurrence of instabilities in the vicinity of gyroharmonics for a parameter range very close to ours. The non-Maxwellian perpendicular velocity distribution needed for a pronounced loss-cone like distribution, such as a helical beam, could have been achieved by the effect of the radial electric field, due to the unneutralized primary beam, acting on the return flux's electrons which are supposed to flow at the edge of the primary beam column. Indeed, according to the review by Linson and Papadopoulos [1990], transverse fields of the order of several volts per meter could be expected with beam intensity similar to that of PICFAB.

In the peculiar conditions of the PICFAB experiment, such a wave generation mechanism occurring in the vicinity of the primary beam column edge could lead to an explanation of the lack of previous observation of the fine structure in  $f_{ce}$  harmonics. Indeed, due to the strong plasma inhomogeneity at the edge of the column, these waves won't be able to travel on a long distance perpendicularly to the magnetic field, being rapidly and strongly cyclotron damped as Bernstein modes are. In fact, if the wave normal of Bernstein modes is known to be restricted to directions quasi-perpendicular to  $B_0$  field, the wave energy propagates longitudinally as cylindrical waves around the source [Gonsalves and Béghin, 1973], in a direction where the density of suprathermal electrons is supposed to be homogeneous. Furthermore, one must remember that the space shuttle is flying through the ionosphere with a velocity of about 7 km/s when emitting the primary electron beam. Then, to be detected on board the same moving orbiter, waves have to suit a certain "rendezvous" condition. In fact, the perpendicular component of their group

velocity must be equal to the perpendicular component of the shuttle velocity.

Moreover, it is always assumed that for beam-plasma experiments in the ionosphere, the interaction region can be considered as homogeneous over a great distance (few hundred meters) along the magnetic field line, whereas sharp inhomogeneities can be observed transversely within a short distance (less than the Larmor radius of the primary beam). Here, it is worth noting that if the "rendez-vous" condition can be met, the wave amplitude will be bounded by the parallel interaction length alone. In such a case, we would get rid of eventual damping caused by perpendicular inhomogeneities of the medium, and the whole beam-return current-waves system would be motionless in the perpendicular direction in the shuttle frame. This would infer that unless being very close to the beam column, no fine structure in  $f_{\omega}$  harmonics could be detected.

#### WAVE FOLLOWER MODEL

##### Dispersion equation

We aim here at recovering the generation of the very first part of the spectrum, i.e. only the first cyclotron harmonics modulated in amplitude around the plasma frequency. The next section will treat the subsequent non-linear evolution of the same kind of instability, leading to the generation of harmonics of this first packet, in a way similar to that adopted by O'Neil *et al.* [1971] to explain  $f_{\omega}$  harmonics generation.

In the present model, we consider a helicoidal electron beam travelling through an uniform magnetic field in an infinite homogeneous plasma. Ion motion can be neglected, since we aim at studying high-frequency emissions. The perturbations are assumed quasistatic and in the form of plane waves:  $\exp(-i[\omega t - k_{\perp}x - k_{\parallel}z])$ , where  $x$  and  $z$  are perpendicular and parallel directions with respect to the  $B_0$  field, respectively.

We shall consider either (i) complex  $\omega$  and real  $k$  (CWRK) to determine the branches  $(\omega, k)$  of instability and their growth rate  $\gamma = \text{Im}(\omega)/|\omega|$ , or (ii) real  $\omega, k_{\parallel}$  and complex  $k_{\perp}$  (RWCK), in order to find out whether the instabilities are absolute or convective and then, in case of convective waves, to evaluate their group velocity  $v_g$  and to obtain the spatial growth rate  $\text{Im}(k_{\perp})$ .

We start from the usual quasistatic dispersion equation

$$1 + \epsilon_p + \epsilon_b = 0 \quad (1)$$

where  $\epsilon_p$  and  $\epsilon_b$  are the plasma and beam susceptibilities, as defined by Harris [1961]. With the further assumption of a Maxwellian distribution for the plasma electrons, we get:

$$\epsilon_p = \frac{2\omega_{pe}^2}{k^2 v_{te}^2} \left[ 1 + \frac{\omega}{|k_{\parallel}| v_{te}} \sum_{n=-\infty}^{+\infty} Z\left(\frac{\omega - n\omega_{ce}}{|k_{\parallel}| v_{te}}\right) \exp(-\lambda) I_n(\lambda) \right] \quad (2)$$

with  $\lambda = k_{\perp}^2 v_{te}^2 / 2\omega_{ce}^2$ , where  $v_{te}$  is the background plasma thermal velocity.

$I_n(\lambda)$  are modified Bessel function of the first kind and  $Z(\zeta)$  is the plasma dispersion function [Fried and Conte, 1961]. The return-beam distribution function is chosen as

$$f_b = n_b f_1(v_{\perp}) (1/\pi v_b)^2 \exp(-[v_{\parallel} - U]^2 / v_b^2) \quad (3)$$

where  $U$  is the directed beam velocity along  $B_0$  and the transverse velocity distribution is assumed to be of the loss-cone kind, in the form of the Dory-Guest-Harris function

$$f_1(v_{\perp}) = f_{\text{sp}}^{(1)}(v_{\perp}) = (1/\pi V_d^2) (v_{\perp}/V_d)^2 \exp(-[v_{\perp}/V_d]^2) \quad (4)$$

Making use of the formalism adopted by Seidl [1970], it follows that

$$\epsilon_0 = \frac{2\omega_p^2}{k^2 v_e^2} \sum_n \left\{ S_n + \left( S_n \frac{\omega - m\omega_n - k_{||}U}{|k_{||}|v_e} + T_n \frac{mk_{\perp}^2 v_e}{2|k_{||}|\omega_n} \right) Z\left(\frac{\omega - m\omega_n - k_{||}U}{|k_{||}|v_e}\right) \right\} \quad (5)$$

$$\begin{aligned} \text{where } S_n &= \exp(-\nu) [I_n(\nu)(1-\nu+m) + \nu I_{n+1}(\nu)] \\ T_n &= \exp(-\nu) [I_{n+1}(\nu) + I_n(\nu)(m/\nu-1)] \\ \nu &= k_{\perp}^2 V_e^2 / 2\omega_n^2 \end{aligned}$$

Though extensive work had been done in this field, our particular parameter range had not yet been investigated in detail. Indeed, the previous numerical calculations have been done for a ratio of beam density over plasma density  $n_b/n_p$ , greater than one, what leads to  $(n+1/2)f_{ce}$  emissions [Ashour-Abdalla and Kennel, 1973]. We shall see below that the lower expected ratio (0.01) in our case will help also to move the instability region from the usual  $(n+1/2)f_{ce}$  to near  $n f_{ce}$ . This could have been expected from the work by Young *et al.* [1973], at least when  $k_{||}$  is sufficiently small, or from the careful study of experimental results in space and laboratory [Koons and Cohen, 1982; Bernstein *et al.*, 1975].

Equation (1) has been solved for  $n_b/n_p = 0.01$  and  $V_b/V_e = 30$ , which are values close to those of the experimental conditions. Indeed, the secondary beam density and temperature have been grossly estimated to lie in the range [Mourenas *et al.*, 1989]. The ratio  $f_{pe}/f_{ce} = 3.5$  has been selected to agree with the conditions generally encountered along the shuttle orbit. Finally, we took  $V_e = v_e/2$  and  $U = 0$  for most of the simulation runs. As for  $\theta$ , it can be shown that in case of cyclotron harmonics, it has to lie inside a narrow band close to  $90^\circ$ . The lower limit for  $\theta$  can be described in terms of cyclotron damping due to the cold plasma electrons. Similarly, an upper limit can be determined by noting that small  $k_{||}$  are linked by the resonant conditions to high beam electron velocities. Thus, the lower  $k_{||}$ , the lower the number of resonant particles.

#### Comparison of the model with the experiments

First, we have drawn the dispersion curves for the above defined parameters. It appeared that the emissions were effectively Bernstein modes, whose growth rate was significant in the vicinity of  $n f_{ce}$  and negligible near the half-harmonics. Now, as the waves fitting the "rendezvous condition" are the only ones which should be detected, it is of considerable interest to find out whether  $v_{e1}$  can effectively fit  $v_{e1}$ . As the angle between the shuttle velocity vector and the geomagnetic field was observed to vary from  $30^\circ$  to  $87^\circ$  during the mission, we get  $3.7 < v_{e1} < 7.5$  km/s. Measurements provided by the electron temperature probe [Ingroy *et al.*, 1986] indicate that  $v_e$  was lying between about 145 and 175 km/s. Thus, we must look for  $v_{e1}$  values such as

$$1/40 < v_{e1}/v_e < 1/20 \quad (6)$$

In a further attempt to try our model, we consider the whole spectrum as it can be predicted in the experimental parameter range. We aim in particular at recovering a growth rate modulation similar to the amplitude modulation observed in the data (figure 2). In addition to the parameters which have been already determined, we maintain  $|v_{e1}|$  fixed by the rendezvous condition ( $|v_{e1}| = 0.04 v_e$ ) and determine the growth rate for each cyclotron harmonic. That is shown in figure 4, where  $\gamma$  is plotted as a function of the ratio  $f_{pe}/f_{ce}$ . We can notice there that each mode of order  $n$ , with the sole exception of mode 3, reaches its maximum growth rate and rises upon all others when  $(n-1)f_{ce} < f_{pe} < n f_{ce}$  then otherwise decreases. Thus, according to the present model, it is expected that, for instance, the wave near  $4 f_{ce}$  should dominate the spectrum when  $3.5 < f_{pe}/f_{ce} < 4.3$ , accompanied by smaller amplitude waves near  $3 f_{ce}$  and  $5 f_{ce}$ .

#### Interaction length

To complete this work, we have to find out whether these cyclotron modes could eventually reach growth rates

high enough to lead to some subsequent non-linear generation of (at least) the largest among them. Examining the resonance close to  $4f_m$  as observed in figure 2, with  $f_p/f_m = 3.5$ ,  $v_a = 147$  km/s and  $v_{a1} = v_{a2} = 0.044 v_a$ , we obtain a solution at  $f = 4.00465 f_m$  with  $k_{\perp} v_a = 0.6075 \omega_m$ ,  $\gamma = 7.310^\circ$  and  $\text{Im}(k) v_a = 6.6 \cdot 10^{-3} \omega_m$  (we have in addition  $f_m = 1$  MHz).

The time needed by the wave to grow from the noise level and to reach the non-linear regime corresponds to about 10 e-foldings periods. That is, the growth time  $t_g$  required for the  $n = 4$  mode to enable the production of its harmonics ( $8 f_m$ ,  $12 f_m$ , ...) is about 5.4 ms. At that time, the parallel distance covered by the wave is  $D_{//} = v_{a1} t_g = v_a t_g / \tan(\gamma, B_0)$ . Here we have  $(\gamma, B_0) = 8^\circ$ , thus we get  $D_{//} = 250$  m.

The above values are consistent with the experimental conditions. Indeed, first a gun pulse lasts 20.8 ms and the entire frequency range analysis needs 19 ms to be performed. Therefore, one can expect to observe the mode 4, which is considered here, within one single pulse, as it occurs. Second, a longitudinal growth length of about 250 m is reasonably supported by measurements made by several rocket experiments. For example, *Jacobsen* [1982], with the rocket experiment Polar 5, reported some observations related to high energy beam injection in the F-region, showing that the suprathermal region extended up to one hundred meters up and down the accelerator along the geomagnetic field line.

Thus, at least for the linear step of wave generation mechanism, i.e. production of the first cyclotron harmonics around  $f_m$ , the agreement between theory and experiment appears to be quite good.

#### NON-LINEAR EVOLUTION

##### Model

In the previous sections we have underlined that the instability was growing in time and not in space, in the shuttle reference frame, in the perpendicular direction with respect to the magnetic field. We shall therefore consider in the following an absolute instability. Intrinsically, our work is an extension of the single-wave model previously developed by *O'Neil et al.* [1971] in case of a linear instability non-linearly saturated by trapping. However, the work of these authors, as well as subsequent experimental and theoretical works [*Seidl et al.*, 1976] were restricted to either strictly or grossly one-dimensional problems, therefore excluding any magnetic field effect. It is obvious that this cannot be a proper approach to our problem, since we wish to consider cyclotron Bernstein waves. Consequently, we have developed a new analytical model which can apply to a two- or three-dimensional problem.

We consider a simple model of particle in cell, which must be solved numerically. The cold plasma is treated like an infinite homogeneous fluid, while the beam consists of  $N$  discrete charges which are initially uniformly distributed in space. To facilitate forthcoming calculations, we assume that the beam exhibits a ring distribution, i.e., a Dirac distribution in perpendicular velocity what represents the limiting case of a Dory-Guest-Harris function. We take care that the condition  $\nabla_{\perp} \cdot \Sigma v_{\perp} = 0$  be satisfied, given that the steady magnetic field  $B_0$  is aligned with the  $z$  axis. It means that we shall have an isotropic or quasi-isotropic velocity distribution. We shall hereafter consider a system with a  $2\pi/k_z$  periodicity imposed by the fact that we write the potential in the form  $\Phi(r) \sim \exp(ik_z \cdot r)$ , with  $k_z = (k_{\perp}, 0, k_{//})$  as before. Thus, we get a  $2\pi/k_{\perp}$  periodicity in the plane perpendicular to  $B_0$  and a  $2\pi/k_{//}$  periodicity along the  $z$ -axis. The beam is distributed uniformly on a layer perpendicular to the  $z$ -axis. Similarly, we could have chosen a uniform distribution along the  $B_0$ -field line. However, the interaction of a beam with a single wave in this direction leads to the case studied by *O'Neil et al.* [1971] in one dimension. Accordingly, we should observe beam particle trapping, the limiting case consisting in a delta function charge density  $\rho(z) = \delta(z)$ . In the present case, as we are working in the limit  $\lambda_{\perp} \ll \lambda_{//}$  (where  $\lambda = 2\pi/k$  and  $k \sim k_{\perp}$ ), we can expect the much faster perpendicular trapping to dominate the dynamics and insure non-linear saturation of the wave amplitude before that any motion of the electrons along  $z$  becomes perceptible. Moreover, it has been shown [*Mourenas*, 1989] that taking into account either one or  $L$  perpendicular beam-particles layers does not make any difference in the linear growth-rate calculation. Therefore, we chose to use a one-layer beam configuration.

The beam plasma system evolution can be described as follows. Initially, it exhibits a finite number of resonances, which grow exponentially from the thermal noise level. The fastest growing wave will rapidly exceed its neighbors amplitude, and will dominate the interaction dynamics. However, after a first period of linear growth, the beam electrons will be trapped and begin to oscillate in the waves troughs. Indeed, when the wave amplitude is large enough, the linear growth rate  $\gamma$  becomes of the same order of magnitude as the beam electrons trapping frequency  $\omega_r$ , and the wave profile does not undergo many variations while an important part of the beam particles change their direction, therefore losing their ability to exchange energy with the wave. A general stabilization criteria reads [Marheimer, 1971]

$$\gamma = \alpha \omega_r \quad (7)$$

where  $\alpha \sim 1$ .

During trapping, the beam-electrons orbits become very non-linear. The particles bunch in space periodically, what induces the harmonic generation.

Some time after the stabilization of the fastest-growing wave amplitude, other excited waves will reach the same level. Thus, the problem involves many waves and a proper description would make use of a quasilinear theory. The present model is only valid for the initial stage of the non-linear evolution, but it is sufficient to provide an appropriate description of the growth, saturation and harmonic production mechanisms.

#### Basic equations

First, we have to formulate the non-linear Poisson equation to obtain an expression of the temporal evolution of the wave potential  $\Phi(t)$  for the frequency  $\omega_s$  and the wave vector  $k_s$ . To this end, we expand the background plasma contribution terms around the solution  $(\omega_s, k_s)$  of the linear equation (i.e. Poisson equation without the beam charge-density term) under the assumption  $\text{Im}(\omega) < \omega_s$ . Details of the calculations can be found in Mourenas [1989]. Then, we get for the plasma charge-density the following expression

$$\rho^p(k_s) = (2n_e e^2 / m_e v_{th}^2) \exp(-\lambda) \Sigma I_n(\lambda) [A_n(\omega_s) + (\omega - \omega_s)(\partial A_n / \partial \omega)] \Phi(k_s \omega) \quad (8)$$

where  $\lambda = (k_s v_{th} / \omega_s)^2$  and  $A_n(\omega) = 1 + (\omega / k_{Te} v_{th}) Z[(\omega - n \omega_{ce}) / k_{Te} v_{th}]$  and using usual notations.

Then, to calculate  $\Phi(t)$ , we need to apply the inverse Laplace transform. To this end, we take for the potential a formulation similar to that of equation (2) of O'Neil *et al.* [1971] in case of Cerenkov emission, in one dimension, except that we work in a coordinate system moving both along and around the  $B_0$ -field line, with the initial parallel and radial beam velocities. In this reference frame,  $\Phi(t)$  can be expressed [Mourenas, 1989] as

$$\Phi(t) = \Sigma \Phi_n(0) \exp(-i \int_0^t (\omega - k_{Te} v_{Te} - m \omega_{ce}) d\tau) \quad (9)$$

Then, we set  $\omega_s = k_{Te} v_{Te}(0) + p \omega_{ce} - p \omega_{ce}$  what corresponds both to the previous linear theory and to experimental results. In terms of the following dimensionless variables

$$T = \omega_{ce} t ; \quad \Omega_m = (\omega_s - n \omega_{ce}) / k_{Te} v_{Te} \\ \Omega_s = \omega_s / k_{Te} v_{Te} ; \quad \Omega_n = \omega_n / k_{Te} v_{Te}$$

the plasma charge-density can be rewritten as

$$\rho^p(T) = [2 e^2 \exp(-\lambda) n_e / m_e v_{th}^2] \Sigma I_n(\lambda) \{ -i [\partial \Phi / \partial T] \Omega_n + \\ + \Phi(T) \cos(T) k_{Te} v_{Te}(0) / k_{Te} v_{Te} \} [2 \Omega_s + Z(\Omega_m) (-1 + 2 \Omega_m \Omega_s)] \\ + \Phi(T) [1 + 2 p \Omega_s \Omega_m + Z(\Omega_m) (\Omega_m + \Omega_n [n - p + 2 p \Omega_s \Omega_m])] \} \quad (10)$$

To complete the Poisson equation, we have to determine the beam charge-density  $\rho^b(T)$ . Assuming the above-mentioned distribution, we get

$$\rho^b(k, T) = (en_b/N) \sum \exp(-ik_x X_j(T) - ik_y Y_j(T)) \quad (11)$$

where  $n_b$  is the beam density,  $N$  is the total number of charges introduced in the simulation box and  $X_j, Y_j, Z_j$  are the coordinates of individual beam particles in the new reference frame. Finally, from equations (10) and (11), we can express the potential evolution in the form

$$\partial \Phi / \partial T = [A + B \cos(T)] \Phi(T) + C \sum \exp(-i[k_x X_j(T) + k_y Y_j(T)]) \quad (12)$$

where  $A, B$  and  $C$  are constants which can be easily deduced from (10) and (11). This is simply a power balance equation. The energy gained by the wave equals the energy lost by the beam (last right-hand side term), minus the energy dissipated by cyclotron damping (first right-hand side term). To describe correctly the beam-plasma system evolution, we further add the  $3N$  equations of motion of the  $N$  beam charges, what we formulate as follows

$$\begin{aligned} \partial^2 X_j / \partial T^2 &= -i(ek_x / 2m_e \omega_{ce}) \Phi(R, T) + C.C. - \partial Y_j / \partial T \\ \partial^2 Y_j / \partial T^2 &= \partial X_j / \partial T \\ \partial^2 Z_j / \partial T^2 &= -i(ek_z / 2m_e \omega_{ce}) \Phi(R, T) + C.C. \end{aligned} \quad (13)$$

where we have used the fact that  $\Phi$  can be written as  $\Phi(R, T) = \exp(i k_x X(T) + i k_y Y(T)) \Phi(T)$ . For now on, we shall impose  $V_{||}(0) = 0$ . However, we could have considered a finite positive value. The only difference would have consisted in the appearance of some new oscillating term with no significant influence on the potential amplitude evolution.

#### Numerical calculations

##### Fundamental wave amplitude evolution

The four differential equations of first and second order derived above (i.e. Eq. (12), (13)) have been rewritten in the laboratory reference frame in the form of seven first order differential equations involving  $X, \partial X / \partial T, Y, \partial Y / \partial T, Z, \partial Z / \partial T$  and  $\Phi$ . These seven equations have to be solved simultaneously for each of the  $N$  beam electrons, for the one single wavelength system with periodic boundary conditions as described above. To this end, we have used the Hamming predictor-corrector integration scheme [Carnahan et al., 1969], which represents a good compromise between stability and precision.

To initiate the program, we assume that the wave amplitude has already grown linearly from a very small value. The integration start when  $\Phi$  is still within the linear range ( $\Phi(0) \sim 10^{-2} \Phi_{sat}$ ), but with an amplitude large enough so that the program is not overcome by significant errors before the saturation is reached. During each run, the momentum was conserved to better than 0.1 %, all along the 2000 to 20000 time steps. The program has been written for a SUN MS-1306 work-station, and the integration time for one step was about 4 seconds. To keep the running time from being too prohibitive while maintaining the required accuracy, no simulation was run for more than 20000 steps. Moreover, we have checked the exactness of the initial portion of each curve by carefully performing the same calculations with a time step ten times smaller.

We have performed a simulation in a case corresponding grossly to the experimental conditions. We chose  $n_b/n_p = 0.23$ ,  $k_x v_{th}/\omega_{ce} = 0.5$ ,  $\lambda_1 = 0.3$  m,  $\theta = 89.90$ ,  $\omega_{pe} \sim 3.5 \omega_{ce}$  and we have considered  $\omega_{pe}$  in the vicinity of  $4\omega_{ce}$ . The ratio  $V_1(0)/v_{th} = 11.3$  was chosen so as to ensure an initial growth of the wave amplitude [Crawford et al., 1970]. The potential evolution is displayed on figure 5. The linear growth rate as well as the saturation amplitude agree quite well with analytical estimations. For instance, we read in figure 5 that  $e\phi_{sat}/m_e \sim 7 \cdot 10^{11}$  m<sup>2</sup> s<sup>-2</sup>, while we can calculate

$$e\phi_{SAT}/m_e = k_e^{-2} [(\gamma/\alpha)^2 + 2\omega_{ce} \gamma/\alpha] \quad (14)$$

which gives  $e\phi_{SAT}/m_e \sim 10^{11} (0.22/\alpha^2 + 1/2)$ .

Thus, taking  $\alpha \sim 0.3$  gives a good estimate. One can see on figure 6 that  $\gamma$  is proportional to  $(n_b/n_e)^{1/2}$ , while the evolution of the beam charge-density, which describes the trapping of the beam electrons, is plotted in figure 7. It would take the value of unity if the beam electrons were concentrated on one single  $X$  value, and would be zero if they were uniformly distributed over one perpendicular wavelength. In figure 7, it appears that the electrons, initially smoothly distributed, are slowly trapped together as the wave amplitude grows exponentially. But their cyclotronic motion detraps them, causing oscillations in the beam charge-density, which nevertheless remains at a high value, while the wave reaches the saturation. From equations (20) and (21), we find that the ratio  $\omega_{r2}/\omega_{ce}$  would lie between 1/15 and 1/4 for  $n_b/n_e$  varying between  $2 \cdot 10^{-3}$  and  $10^{-2}$ . Such small values seem to be compatible with cyclotron wave generation. Indeed, it means that trapping effects would take place over a much greater time scale than the cyclotron motion, thus appearing only as perturbation effects on the closed orbits of beam particles.

#### Harmonics generation

During the trapping process, the anharmonicities in the beam particles orbits cause the growth of the harmonics  $(n\omega_e, nk_e)$  of the beam charge-density. Indeed, the periodicity of the system implies that there can exist only harmonics of the fundamental wavenumber, and the cyclotron resonance condition for the beam electrons  $\omega - q\omega_e = k_{\parallel}/n$  implies that  $\omega/\omega_e = k/k_e = n$  for the harmonics. From the Laplace transform of Poisson equation, we get

$$\epsilon_e (nk_e)^2 \Phi(nk_e) = \rho^b(nk_e) + \rho^b(nk_e) \quad (15)$$

In order to determine the ratio  $\Phi(nk_e)/\Phi(k_e)$ , we need first to know the variation of the charge density  $\rho^b(nk_e)$  as a function of  $n$ . Using equation (11), we have computed this quantity, in the same case study as in figure 4. We observe that  $\rho^b(nk_e)$  follows roughly a power law  $\propto n^\mu$  with  $\mu$  evolving from 5, when trapping is still small ( $T = 0.5$ ), to 1 when saturation of the fundamental wave amplitude is reached. This can be explained as follows. Before that trapping occurs, the beam charge-density can be calculated by mean of a power expansion of the fundamental electric field. Consequently,  $\rho^b(nk_e)$  must decrease exponentially with  $n$ . On the contrary, when trapping cannot be neglected any more, the expansion is no longer valid. In the limit where  $\rho^b(X) = \delta(X)$ , the charge density would even become independent of  $n$ . Thus, the decrease in the exponent corresponds to increasing trapping effects.

Next, we calculate  $\Phi(nk_e)$ . To begin, we take  $n = 2$  and we solve (15) with  $\rho^b(2k_e) = \rho^b(k_e)/2$  (i.e.  $\rho^b(nk_e) \propto n^{-1}$  as estimated numerically near the saturation) and  $\rho^b(2k_e) = G(2k_e)\Phi(2k_e)$ , where the function  $G(k)$  includes terms of equation (12) which are independent of  $\Phi$  and have been numerically determined for  $(2\omega_e, 2k_e)$ . In the small beam density case ( $n_b/n_e = 0.23$ ), we have obtained  $\Phi(2k_e)/\Phi(k_e) = 0.02$ . Furthermore, we have observed that the contribution of the background plasma to the harmonics could be neglected. This last result can be easily understood when noting that the main wave frequency is taken to lie very close to an unperturbed Bernstein branch, while harmonics  $(n\omega_e, nk_e)$  are not. Thus, the plasma can be considered as non-resonant for the harmonics. Finally, repeating this procedure for any integer  $n$ , we have obtained the following power law for the considered case study

$$|E(nk_e)| \sim 0.16 n^{-2} |E(k_e)| \quad (16)$$

## CONCLUSION

Measurements of high-frequency were made on board SPACELAB-1 during artificial electron beam injection from the shuttle bay. The most unusual kind of spectrum is considered here, i.e., packets of electron cyclotron waves occurring at successive harmonics of a frequency  $F_0$  close to the plasma frequency.

We have shown that the first electron gyrofrequency harmonics modulated in amplitude, with a maximum near  $f_{pe}$  could be explained in terms of an interaction between the ambient Maxwellian plasma and a neutralization beam whose distribution function must be of a loss-cone kind.

A numerical resolution of the dispersion equation has been undertaken, with the experimental constraint that the waves have to fit the "rendezvous" condition with the instruments flying on board the orbiter. The observed electron cyclotron emissions, as well as their amplitude modulation around the fundamental of the plasma frequency, are found to be easily explained by such a linear theory.

However, the observation of successive harmonic packets around  $pF_0$  remained to be interpreted. To this end, a two-dimensional ring-wave model of the non-linear interaction between a finite size ring beam and an infinite homogeneous magnetized plasma is presented. A system of scaled equations is developed, and then solved numerically. The solution shows that the considered single  $F_0$  wave grows exponentially at the linear growth rate, then the wave potential saturates due to beam electron trapping, while producing a power law spectrum of the higher  $pF_0$  harmonics of the electric field, very similar to what was observed experimentally.

## REFERENCES

- Ashour-Abdalla, M., and C.F. Kennel, Non-convective and convective electron cyclotron harmonic instabilities, *J. Geophys. Res.*, **83**, 1531-1543, 1978.
- Bégin, C., J.P. Lebreton, B.N. Machlum, J. Troim, P. Ingsoy, J.L. Michau, Phenomena induced by charged particle beams, *Science*, **225**, 188-191, 1984.
- Belmont, G., Characteristic frequencies of a non-maxwellian plasma : A method for localizing the exact frequencies of magnetospheric intense natural waves near  $f_{pe}$ , *Planet. Space Sci.*, **29**, 1251-1266, 1981.
- Bernstein, W., J. Leinbach, H. Cohen, P.S. Wilson, T.N. Davies, T. Hallinan, B. Baker, J. Martz, R. Zeimke, and W.J. Huber, Laboratory observations of RF emissions at  $\omega_{pe}$  and  $(n+1/2)\omega_{pe}$  in electron beam-plasma and beam-beam interaction, *J. Geophys. Res.*, **80**, 4375-4379, 1975.
- Carsahan, B., H.A. Luther and J.O. Wilkes, *Applied Numerical Methods*, John Wiley and Sons Inc. Editors, 1969.
- Crawford, F.W., J.C. Lee and J.A. Tataronis, *Plasma waves in space and laboratory*, Thomas and Landmark Editors, Vol.2, 447-460, 1970.
- Frank, L.A., W.R. Paterson, M. Ashour-Abdalla, D. Shriver, W.S. Kurth, D.A. Gurnett, N. Omid, P.M. Banks, R.I. Bush, and W.J. Raitt, Electron velocity distribution and plasma waves associated with the injection of an electron beam into the Ionosphere, *J. Geophys. Res.*, **69**, 6995-7002, 1969.
- Fried, B.D., and S.D. Conte, *The plasma dispersion function*, Academic Press Inc. Editor, 1, 1961.
- Gonfalonc, A., and C. Bégin, Excitation of quasicylindrical waves connected with electron Bernstein modes, *Phys. Rev. Lett.*, **31**, 886-870, 1973.
- Gurnett, D.A., W.S. Kurth, J.T. Steinberg, and S.D. Shawhan, Plasma wave turbulence around the shuttle : results from the Spacelab-2 flight, *Geophys. Res. Lett.*, **15**, 760-763, 1988.
- Harris, E.G., Unstable plasma oscillations in a magnetic field, *Phys. Rev. Lett.*, **2**, 34-36, 1959.
- Ingsoy, P., B. Machlum, J. Troim, and J.P. Lebreton, Plasma energization in the shuttle wake region during beam injection from Spacelab-1, *Planet. Space Sci.*, **34**, 555-562, 1986.
- Jacobsen, T.A., Observations of plasma heating effects in the ionosphere by a rocket borne electron accelerator, in *Artificial particle beams in space plasma studies*, B. Grandal Editor, 175-197, 1982.



- Kaiser, K.S., J.D. Gaffey, Jr., C.P. Price, X.W. Hu, and G.C. Zhou, Nonlinear wave interaction and evolution of a ring-beam distribution of energetic electrons, *Phys. Fluids*, 31, 2233-2248, 1988.
- Kellog, P.J., H.R. Anderson, W. Bernstein, T.J. Hallinan, R.H. Holtzworth, R.J. Jost, H. Leinbach, and E.P. Smaczewicz, Laboratory simulation of injection of particle beams in the Ionosphere, in *Artificial particle beams in space plasma studies*, B. Grandal Editor, 289-329, 1982.
- Koons, M.C., and H.A. Cohen, Plasma waves and electrical discharges stimulated by beam operation on a high altitude satellite, in *Artificial particle beams in space plasma studies*, B. Grandal Editor, 111-120, 1982.
- Linson, L.M., and K. Papadopoulos, Review of the status of theory and experiment for injection of energetic electron beams in space, *Tech. Report n° Laps 69*, Laboratory for applied plasma studies, La Jolla, California, 1980.
- Manheimer, W.M., Strong turbulence theory of nonlinear stabilization and harmonic generation, *Phys. Fluids*, 14, 579-590, 1971.
- Mikhailovskii, A.B. Theory of plasmas instabilities, *Consultant Bureau Editor*, 1974.
- Mourenas, D., *Etude des mecanismes de generation d'ondes cyclotron electroniques par un faisceau artificiel d'electrons*, Doctoral Thesis, Université d'Orléans, 1989.
- Mourenas, D., C. Béghin and J.P. Lebreton, Electron cyclotron and upper hybrid harmonics produced by electron beam injection on Spacelab 1, *Ann. Geophys.*, 7, 5, 519-530, 1989.
- O'Neil, T.M., J.H. Winfrey, and J.H. Malmberg, Nonlinear interaction of a small cold beam and a plasma, *Phys. Fluids*, 14, 1204-1212, 1971.
- Shawhan, S.D., G.B. Murphy, P.M. Banks, P.R. Williamson and W.J. Raitt, Waves emissions from dc and modulated electron beams on STS-3, *Radio Sci.*, 19, 471-486, 1984.
- Seidl, M., W. Carr, D. Boyd and R. Jones, Nonlinear development of absolute and convective instabilities, *Phys. Fluids*, 19, 78-92, 1976.
- Smaczewicz, E.P., controlled electron beam experiments in space and supporting laboratory experiments : a review, *J. Atmos. Terr. Phys.*, 47, 1189-1210, 1985.
- Watermann, J., K. Wilhelm, K.M. Torkar, and W. Riedler, Space shuttle charging or beam-plasma discharge : what can electron spectrometer observations contribute to solving the question ?, *J. Geophys. Res.*, 93, 4134-4140, 1988.
- Young, T.S.T., J.D. Calfee, and J.E. McCune, High-frequency electrostatic waves in the magnetosphere, *J. Geophys. Res.*, 78, 1082-1099, 1973.

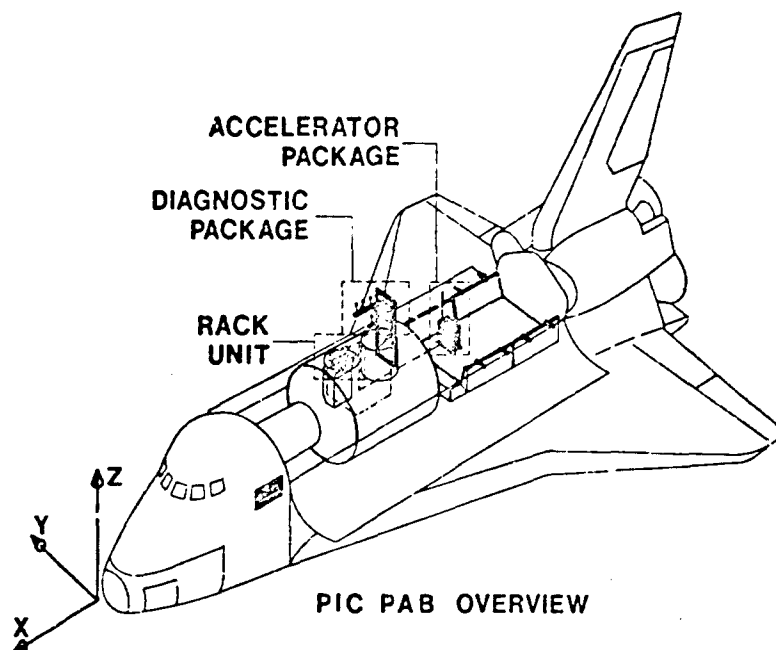


Fig. 1. Configuration of the PICPAR instruments on the shuttle.

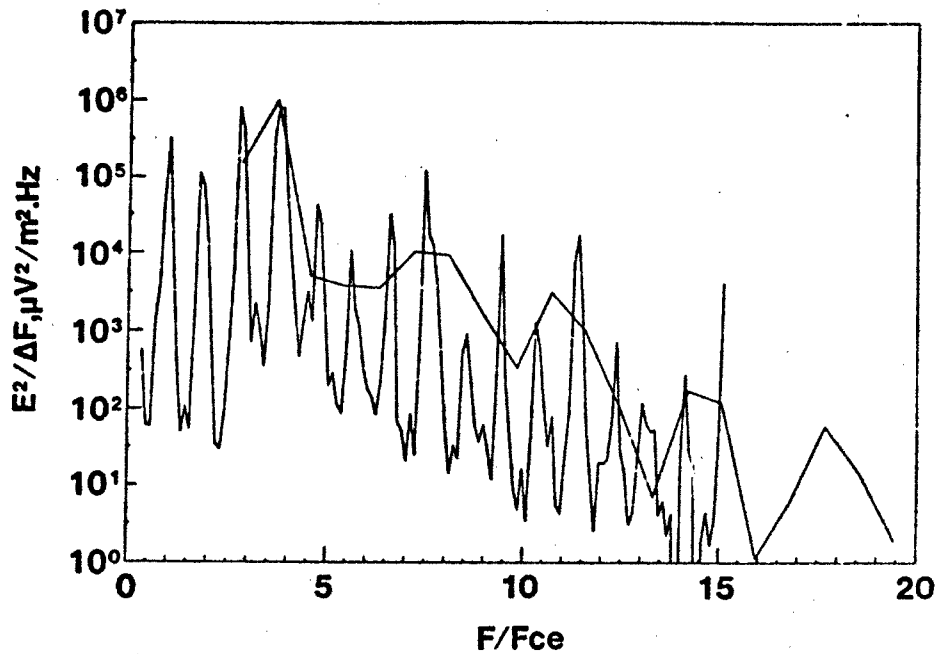


Fig. 2. Plot of the spectral density of the electric field for  $f_p \sim 3.4 f_{ce}$ . The frequency is normalized with respect to a modeled value of  $f_{ce}$ . The envelope curve is provided by a large band analyzer (0-90 MHz, resolution 0.66 MHz). The full resolution of the spectrum is given by a narrow band analyzer (0-11.5 MHz, resolution 0.082 MHz). Here,  $I(\text{beam}) = 100 \text{ mA}$ ,  $E(\text{beam}) = 8 \text{ KeV}$ .

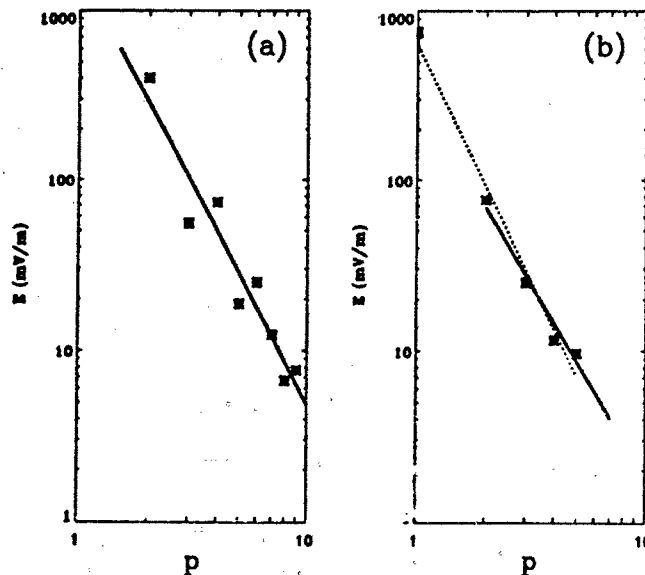


Fig. 3. Plot of the electric field amplitude for the harmonics  $pF_p$ :

a) Sequence 28, least-square root drawing for  $p = 2$  to 9, giving a law  $\propto p^{-2.5}$ .

b) Sequence 53; dotted line: least-square root drawing for  $p = 1$  to 5, solid line: least-square root drawing for  $p = 2$  to 5 leading to  $p^{-2.25}$ .

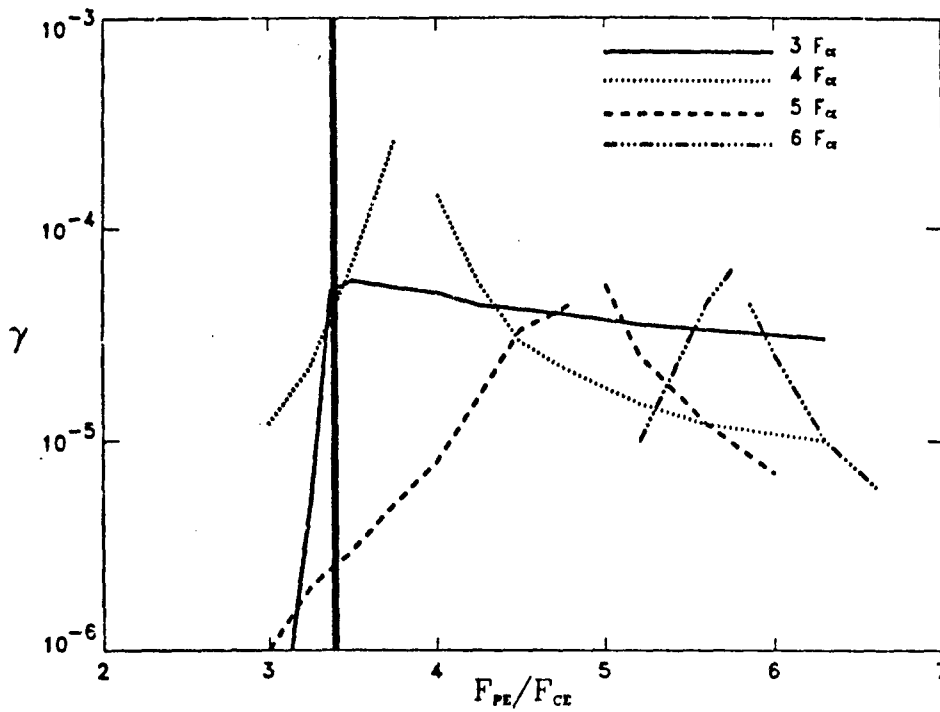


Fig. 4. Evolution of the growth rate for different  $n/\alpha$  modes against the plasma frequency with  $\theta = 89.9^\circ$  and  $v_{\alpha} = 0.04 v_A$  for a distribution  $f_0 = f_{\alpha}^{(0)}$ .

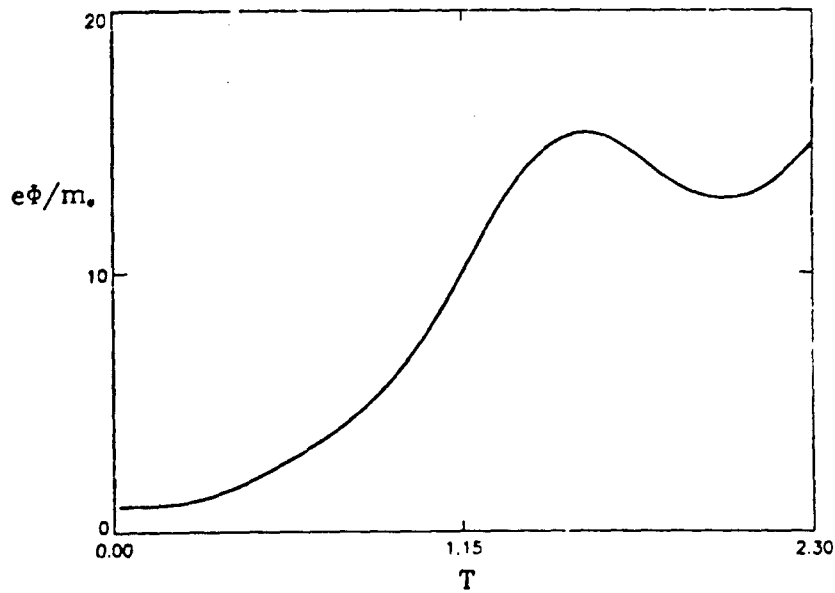


Fig. 5. Evolution of the wave potential, normalized to its initial value,  $e\Phi(0)/m_e = 4 \cdot 10^{10} \text{ m}^2 \text{ s}^{-2}$ , for  $V_A(0)/v_A = 1.13$  and  $n_e/n_i = 0.23$ .

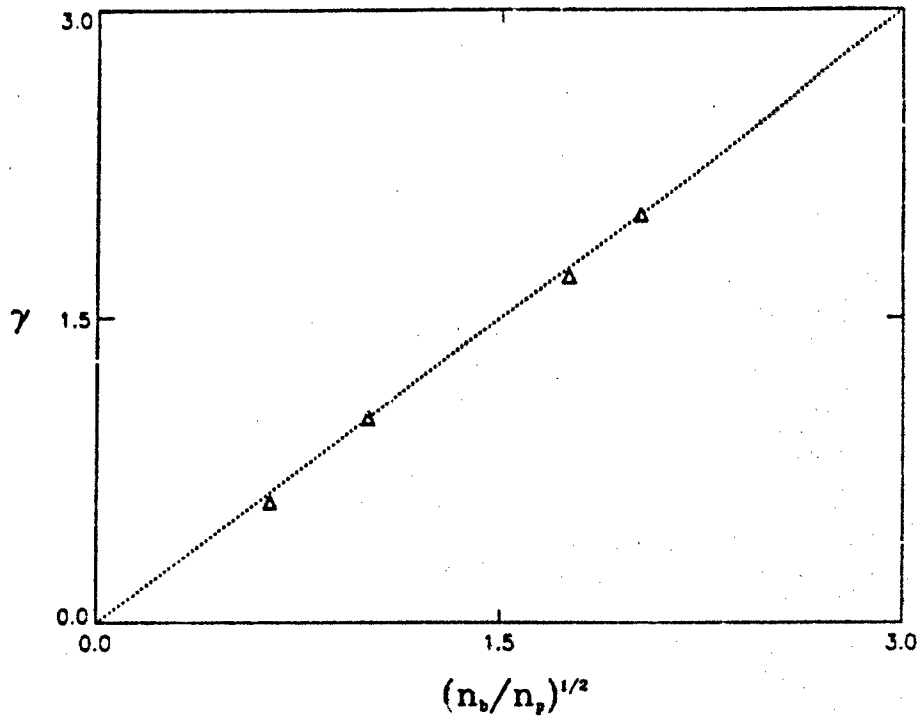


Fig. 5. Variation of the growth rate as a function of the ratio  $(n_b/n_p)^{1/2}$ , both normalized to the values of figure 4.

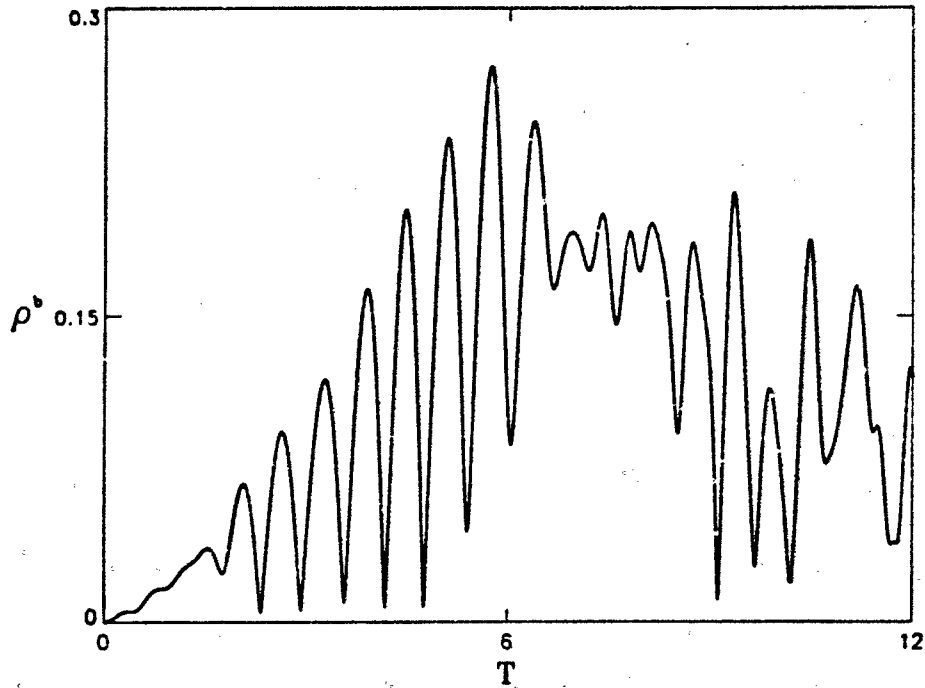


Fig. 7. Evolution of the beam charge density in the case study of figure 4.

PAPER NO. 23

## DISCUSSION

R. F. BENSON, US

What range of plasma to gyro frequency values were covered by your experimental conditions and what was the value corresponding to the results presented? Also, how different are the frequencies of these waves from the peak frequencies of the Bernstein modes -- called the Q resonances on Alouette and ISIS topside sounder ionograms?

## AUTHOR'S REPLY

While the ratio ( $f_{pe}/f_{ce}$ ) varied between about 1 and 9, the results presented here were for 3.4, and the kind of waves we observed was similar in the range 1 to 9. When this ratio was about 1, different kinds of emissions occurred, depending on the background plasma density level and inhomogeneity. The frequencies of the reported waves were exact harmonics of the electron gyrofrequency, thus very different from the Q resonances, at least for the first ones (in particular,  $4f_{ce}$  and  $5f_{ce}$ ).

## VEHICLE CHARGING IN LOW DENSITY PLASMAS

B N Machlum and J Troim  
Norwegian Defence Research Est  
P O Box 25, 2007 KJELLER, Norway

### INTRODUCTION

Studies of electrical charging of space vehicles have been reported in a number of papers in the last ten years. These studies are based on charging due to onboard electron and ion accelerators as well as charging due to thermal and energetic electrically charged particles impinging on the surface of the vehicle. In spite of this significant effort made in the field both theoretically and experimentally, the vehicle charging problem is far from being completely understood.

Part of the problem relates to the effects of the plasma disturbances created by the beam. Several attempts have been made with a varying degree of success to simulate space plasma processes in large plasma chambers. The celebrated studies in the large chamber at Johnson Space Center in Houston by Bernstein and collaborators (1) show that the plasma may be very disturbed in the presence of a beam of fast electrons by a "BPD" process ("Beam Plasma Discharge"). This process was expected also to explain phenomena observed in the upper atmosphere and possibly various aspects of the vehicle charging. However, there are still some doubts as to whether the BPD really occurs in space, and the significance of the laboratory simulation experiments conducted in the past remains obscure.

In this paper we present a number of high vehicle charging generated by electron beams and discuss how this charging depends on the characteristics of the plasma environment. Also, some results from a simulation study of these problems conducted in the NDRE plasma chamber are reviewed.

### ELECTRICAL CHARGING OF SPACE VEHICLES

By early rocket-borne electron accelerators, such as Hess' artificial aurora experiment (2) and Winckler's first ECHO rockets (3) there was a general fear for an excessive vehicle charging associated with the electron injection into the plasma, and large sails were installed on the vehicle to enhance the return current area. However, neither of these spacecrafts nor a series of consecutive rocket and satellite payloads in the ionospheric F layer displayed any excessive charging. In fact, in most cases the payload potential was limited to a few per cent of the accelerator energy (4).

The unexpected low potential of these payloads was never really properly explained. The various types of return currents from the environment which contribute to the neutralization of the vehicle include (i) electron and ion currents from the undisturbed thermal plasma, (ii) secondary electrons generated by the beam, (iii) background electrons energized by the beam and the charged vehicle and finally, (iv) secondary electrons generated on the spacecraft surface when it is bombarded by energetic particles.

If the thermal, undisturbed plasma environment played an important role in the neutralization, we would anticipate that the vehicle potential varied with the density and temperature of these electrons. The thermal return current to a satellite surface  $A'$  may be derived from the following formula (5):

$$I_r = (10^{-11} N_e) (T_e/1600)^{1/2} A' \quad (\text{mA})$$

For a background plasma density  $N_e = 10^{11} \text{ m}^{-3}$ , and temperature  $T_e = 1600 \text{ K}$  the total current amounts to only 1 mA on a return surface of  $1 \text{ m}^2$ . It is difficult to envisage how this low current could possibly contribute significantly to the neutralization for beam currents greater than say 10 mA. Therefore, for many years it was assumed that the vehicle is neutralized by a current carried by newly generated secondary electrons or heated background electrons rather than the thermal electrons in the plasma.

Unfortunately, simple formulas are not available for calculating the return currents from plasmas ionized and heated by the particle beams. This plasma may not have a thermal (6) or isotropic distribution. Furthermore, the relation between the plasma density enhancement and the beam current and energy has not yet been established in regions where the atmospheric density is so low that ionization produced by non-elastic collisions between the beam particles and atmospheric atoms can be neglected.

The question is now whether the disturbed plasma environment is always capable of neutralizing an electrically charged space vehicle. The answer is negative. In fact, the first spacecraft to obtain an excessive charging due to on-board particle accelerators was the SCATHA satellite (7). Later, the SPACELAB 1 payload on STS was reported to reach a potential similar to the beam energy during the electron accelerator operation of the Japanese/US experiment SEPAC (7).

More recently, the USSR accelerator rocket Gruzia-Sput electric field monitors indicated that the potential of the payload exceeded the electron beam energy during part of the flight (9). This effect, which at first appeared as some sort of a "perpetual motion" and explained as an experimental error, has later been referred to as "supercharging" and treated in several experimental and theoretical papers, some of which we return to later.

Why some of the electron accelerator carrying vehicles show high charging, whereas others are charged to moderate potentials is still an unsolved question, although certain clarifications have emerged from recent theoretical studies.

The highest spacecraft potential up to now was observed by the tethered Mother-Daughter rocket MAIMIK. For beam currents higher than 80 mA and electron beam energies equal to 8 keV the accelerator carrying Daughter payload was charged to more than 12 kV (Figure 1). This measurement was based on several diagnostics instruments, including a tether voltage monitor, several return current spectrometers and electric field probes.

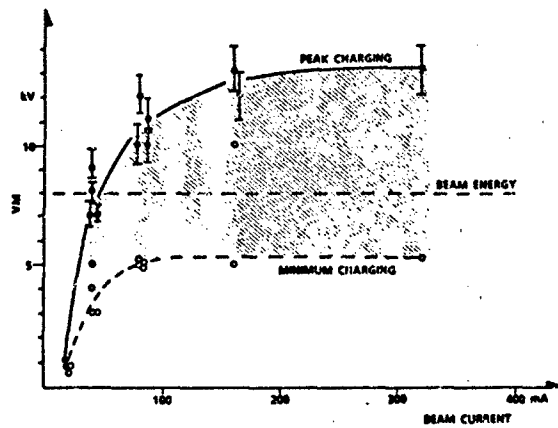


Figure 1 Observed potential of the MAIMIK rocket vs the electron accelerator beam current (10)

The MAIMIK rocket data have been thoroughly studied, and it was concluded that the high charging may have been caused by the exceptionally low density of the plasma environment (10). In fact, the density was only  $10^{10} \text{ m}^{-3}$ . This conclusion is very significant, since most of the previous studies have assumed that the return current from the undisturbed plasma is too low anyhow, and hence of less importance for the neutralization process.



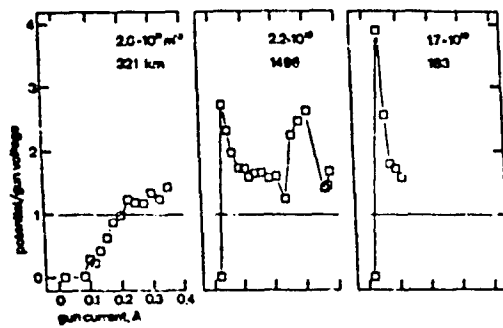


Figure 2 Observed potential of the accelerator rocket Gruzia-Sput vs beam current for three different background plasma densities. (11)

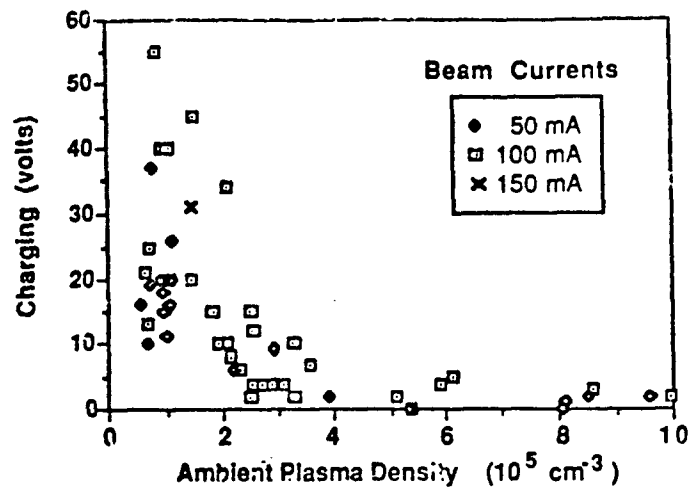


Figure 3 Observed potential of STS as a function of background plasma density during injection of electron beams from the spacecraft. (12)

More recently several workers have discussed how the background plasma density affects the vehicle neutralization. Managadze et al (11) have analyzed how the Gruzia-Sput rocket is charged in different plasma densities, and indeed found that the highest potentials occur in the most tenuous plasmas (Figure 2). Also, in his PhD thesis Hawkins (12) demonstrates how the charging of Spacelab 2 varies with the density of the environmental plasma based on the VCAP experiment (Figure 3). He finds that the potential of this fairly large vehicle was increased significantly when the background density was reduced below some  $2 \times 10^{11} \text{ m}^{-3}$ .

If the space vehicle potential really is reaching a value which exceeds the beam energy, one would like to ask two relevant questions:

- 1 Which physical processes in the plasma allow the potential to exceed the beam energy? Is this result based on an erroneous interpretation of the observations, or is it real?
- 2 How is the plasma around a highly charged vehicle modified during "super charging" events?

The supercharging problem was first treated by Wingley and Pritchett (13), who utilized the "Virtual Cathode" concept originally proposed by Langmuir in the 1930-s. They found that an electron emitting body in a plasma may indeed be charged to a potential which is slightly higher than the beam energy. More recently Mancini and Katz (14) have proposed another model based on the assumption of an energy spreading of the beam under the influence of electrostatic waves set up by the beam itself. Therefore, there are several ways to approach this problem, but the final solution is not yet reached.

Remote effects of the high vehicle charging on the environmental electric fields was measured on the Mother payload of MAIMIK up to several tens of meters from the Daughter payload for beam currents greater than 80 mA (15). It is interesting to see how the field built up during the first milliseconds, when the shielding was being created. Later in the pulse the charged Daughter was screened by the plasma. Hence, the Debye shielding distance does not really have any meaning during the initial part of the pulse.

Another interesting effect of the plasma screening is seen in the temperature disturbances in the remote plasma. Examples of the observed temperature enhancements at distances of 15 - 25 m normal to the local geomagnetic field vector during electron beam injections are given in Figure 4 (16). For beam currents less than 80 mA the temperature increases with increasing current. For higher currents the electron temperature is almost unaffected by the beam. For these currents the Daughter payload is supercharged (Ref Figure 1), and the plasma near the payload probably screens the Daughter potential, which means that little energy "leaks out" to the surrounding plasma.

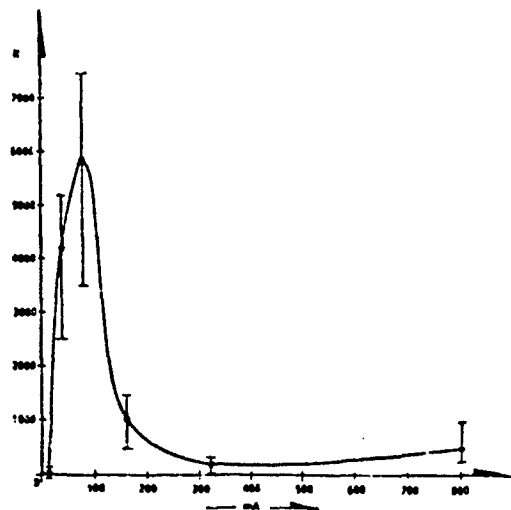


Figure 4 Observed temperature enhancements in the electron plasma at distances from 15 to 25 m from the accelerator rocket MAIMIK as a function of beam current (16)

Up to now I have discussed how the plasma environment influences the vehicle charging in the upper part of the ionosphere. Further down, in the E region the interaction between the beam of fast particles and the neutral atoms plays a much more important role. The effect of the background density of the neutral atmosphere is clearly seen in Figure 5. Here the Daughter potential is presented for various beam currents as a function of altitude. The results are based on an eight channel Retarding Potential Analyzer of the energy distribution in the return current. Above 150 km the vehicle potential exceeds 3.2 keV for beam currents greater than 0.32 A, whereas a 20 mA pulse charges the payload only to a potential of less than 85 V even at 180 km. On the other hand, below 120 km the neutral atmosphere is sufficiently dense to allow an adequate production of secondary electrons for neutralizing the accelerator payload even for the highest beam current, which amount to 0.8 A.

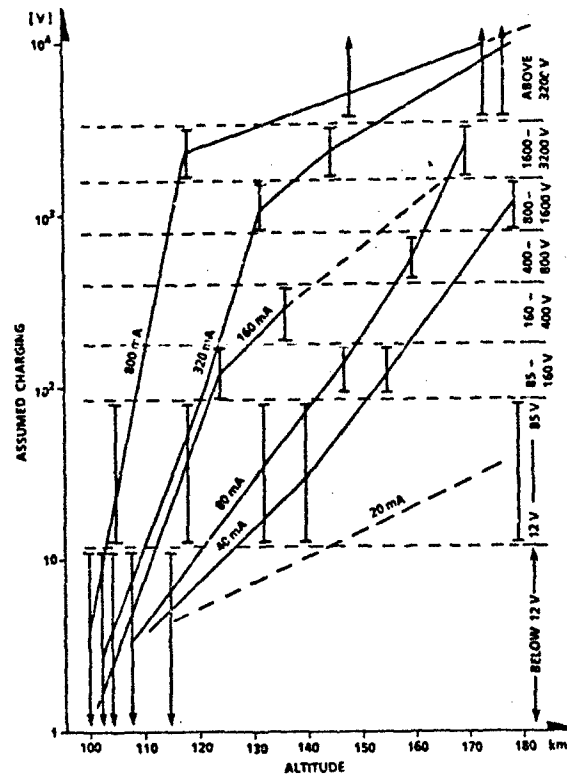


Figure 5 Observed height variation of the MAIMIK potential during injection of beam currents from 20 to 800 mA. The results are based on an array of eight Retarding Potential Analyzers with fixed energies between 12 and 3200 eV

In the previous paragraphs we have discussed the charging of a space vehicle which are emitting fast electrons. The reciprocal problem has also been investigated, i.e. charging of a vehicle which is bombarded by beams of fast (auroral) electrons. Gussenhoven and collaborators (17) showed that a satellite may be charged to several hundred volts in polar region when the background plasma density was sufficiently low (See Figure 6). This finding is in excellent agreement with results from electron beam experiments on rockets.

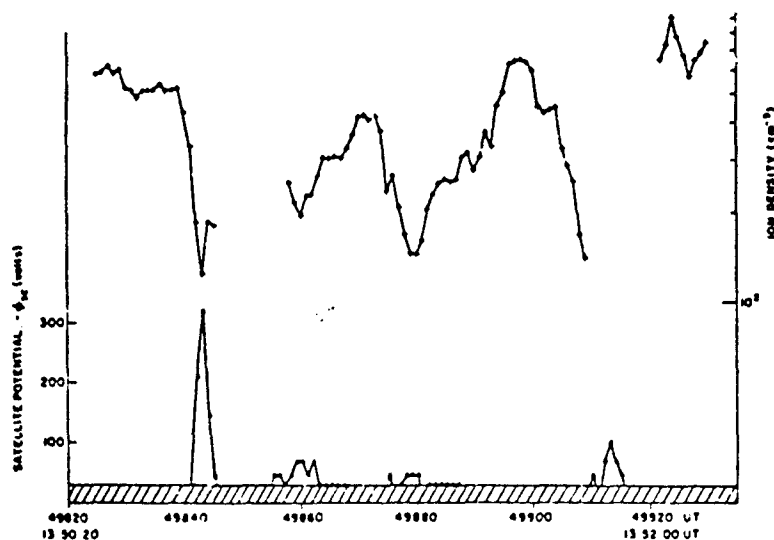


Figure 6 Observed variations in the potential of the DMSP F7 satellite (lower curve) and the background plasma density (upper curve) (17)

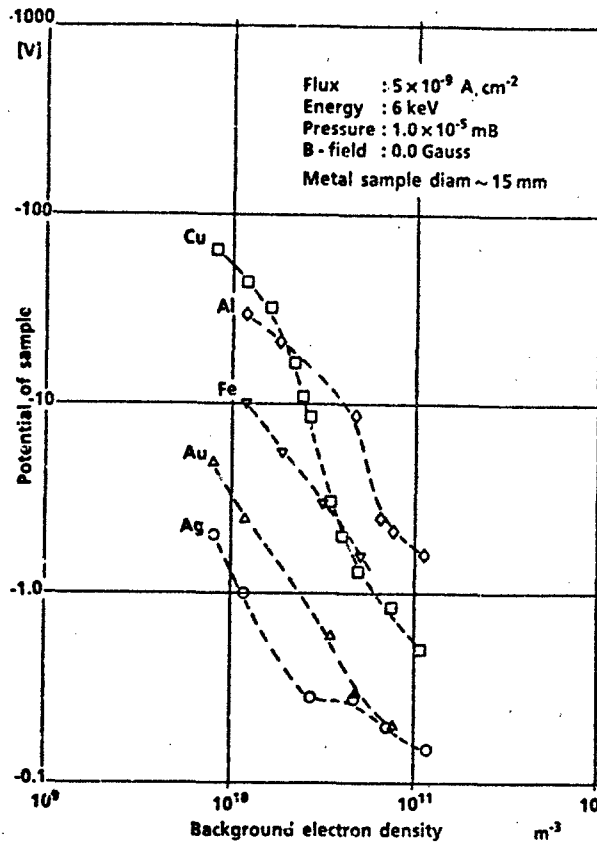
#### LABORATORY SIMULATION OF VEHICLE CHARGING

In order to investigate Gussenhovens et al's results in more details a laboratory study has recently been started at the NDRE to simulate how an object embedded in a beam of fast electrons is charged for various background plasma densities. I will comment very briefly on some preliminary results from this study.

The plasma chamber consists of a cylinder with a cross-section of 80 cm and a total length of some 2 m, and the background plasma density can be varied between  $10^9$  and  $10^{12} \text{ m}^{-3}$  by an Argon Kauffman plasma source. Helmholtz coils are installed around the chamber to vary the magnetic field between 0 and 1 Gauss.

Small objects (10 – 20 mm in diameter) of different materials are installed in the chamber and bombarded by fast electrons with energies between 1 and 20 keV and a current density of a few  $\text{nA/cm}^2$ . The beam is emitted in a direction parallel to the cylinder axis, and the potentials of the objects are monitored as function of the beam current and energy, background plasma density, magnetic field intensity and object material.

The first results from these studies indicate that the object charging depends critically on the background plasma density and the material of the charging object (Figure 7). For background plasma densities higher than  $10^{11} \text{ m}^{-3}$  all the objects are almost completely neutralized when exposed to a 6 keV beam of electrons with a current density of  $5 \text{ nA/cm}^2$ .



**Figure 7** Relation between the charging of metal objects (15mm diameter) and the surrounding plasma density. The objects, which are produced from different metals, are exposed to a beam of 6 keV electrons with a current density of  $5 \text{ nA/cm}^2$

When the density is decreased below  $10^{11} \text{ m}^{-3}$ , the potential increases rapidly, and the aluminum and copper objects are charged to potentials up to 100 V negative for the same

density. For other materials like silver and gold the potentials are significantly lower for a given plasma density. For a background plasma density between  $10^{10}$  and  $10^{11} \text{ m}^{-3}$  the aluminum object is charged to a potential which is almost 100 times higher than that consisting of silver. We interpret the difference in terms of material-dependent secondary electron production of the objects. Hence, vehicle charging problems may be reduced by selecting the right metal surface.

We believe that these studies may prove to be a valuable tool for understanding how the electron beam density and energy and the background plasma parameters control the vehicle charging, and we expect to publish the first detailed results from these studies early next year.

## REFERENCES

- 1 Bernstein, W, H Leinbach, P J Kellogg, S J Monson and T Hallinan: Further Laboratory Measurements of the Beam-Plasma Discharge, *J Geophys Res*, 84, 7271, 1979
- 2 Hess W et al : Artificial auroral experiment, experiment and principal results, *J Geophys Res*, 76, 6067, 1871
- 3 Hendrickson, R A: The Electron Echo Experiment Observations of the Charge Neutralization of the Rocket and Analysis of the Echoes from Electron Artificially Injected into the Magnetosphere, PhD Thesis, Univ of Minnesota. 1972
- 4 Machlum, B N: Beam-Plasma Experiments, *Computer Physics Comm*, 49, 119, 1988
- 5 Linson, L M and K Papadopoulos: Review of the Status of Theory and Experiments for Injection of Energetic Electron Beams in Space, Report No LAPS 69, SAI-023-80-459-LJ, Science Appl Inc, 1980
- 6 Jacobsen, T A: Observations of Plasma Heating Effects in the Ionosphere by a Rocket Borne Electron Accelerator, In *Artificial Particle Beams in Space Plasma Studies* (ed B Grandal), Plenum Press, 1982
- 7 Cohen, H A et al: P78-2 Satellite and Payload Response to Electron Beam operation on March 30 1979, *Spacecraft Charging Technology 1980*, NAS Conference Publ 2182, AFGL-TR-0270, 1981
- 8 Sasaki, S, N Kawashima, K Kuriki, M Yanagisawa and T Obayashi: Vehicle Charging Observed in SEPAC Spacelab-1 Experiment, *J Spacecraft and Rockets*, 23, 194, 1986
- 9 Managadze, G G: Active Experiments in Space, *ESA SP-195* (ed G Haerendel), p 161, 1983
- 10 Machlum, B N et al: MAIMIK A High Current Electron Beam Experiment on a Sounding Rocket from Andoya Rocket Range, *Proc of the 8th ESA Symposium on European Rocket and Balloon Programmes and Related Research*, Sunne Sweden, ESA SP-270, 1987
- 11 Managadze et al: Potential Observations of an Electron-Emitting Rocket Payload and Other Related Plasma Measurements, *Planet Space Sci*, 36, 399, 1988

- 12 Hawkins, J G: Vehicle Charging and Return Current Measurements during Electron Beam Emission Experiments from the Shuttle Orbiter, PhD thesis, Stanford University, 1988
- 13 Winglee, R M and L Pritchett: Comparative Studies of Cross-Field and Field-Aligned Electron Beams in Active Experiments, J Geophys Res, 93 5823, 1988
- 14 Mandell, M S and I Katz: Dynamics of Spacecraft Charging by Electron Beams. To appear in Proceedings from the Space Charging Conference 1989
- 15 Denig, W F, N C Maynard, W J Burke and B N M'chum: Electric Field Measurements During Supercharging Events on the MAIMIK Rocket Experiment, submitted for publication in J Geophys Res, 1990.
- 16 Svenes, K, J Troim, M Friedrich, K M Torkar and G Holmgren: Ionospheric Plasma Measurements from the Accelerator Rocket MAIMIK, Planet Space Sci, 36, 1509, 1988
- 17 Gussenhoven, M S, D A Hardy, F Rich, W J Burke and H-C Yeh: High Level Spacecraft Charging in the Low-Altitude Environment, J Geophys Res, 90, 11009, 1985

#### DISCUSSION

W. BURKE, US

In conducting the laboratory experiments, the beam energy should be varied. The efficiency of secondary electron production depends on both the surface characteristics and the beam energy. Below about 7 keV the secondary production exceeds unity and the DMSP and SCATHA satellites never charged. Above this electron energy severe charging was always found.

AUTHOR'S REPLY

Yes.



## PLANNING FOR COORDINATED SPACE AND GROUND-BASED IONOSPHERIC MODIFICATION EXPERIMENTS

M. C. Lee  
Plasma Fusion Center  
Massachusetts Institute of Technology  
Cambridge, Massachusetts 02139, U.S.A.

W.J. Burke, H.C. Carlson, J.L. Heckacher, P.A. Kossey, E.J. Weber  
USAF Geophysics Laboratory  
Hanscom AFB, Massachusetts 01731, U.S.A.

S.P. Kuo  
Weber Research Institute  
Polytechnic University  
Farmingdale, New York 11735, U.S.A.

### ABSTRACT

The planning and conducting of coordinated space and ground-based ionospheric modification experiments are discussed. The purpose of these experiments is to investigate (1) the nonlinear VLF wave interaction with the ionospheric plasmas, and (2) the nonlinear propagation of VLF waves in the HF modified ionosphere. It is expected that the HF-induced ionospheric density striations can render the nonlinear mode conversion of VLF waves into lower hybrid waves. Lower hybrid waves can also be excited parametrically by the VLF waves in the absence of the density striations if the VLF waves are intense enough. Laboratory experiments are planned for crosschecking the results obtained from the field experiments.

#### 1. Introduction

The abstract of this paper was submitted about one year ago, responding to the announcement for the AGARD Conference in Bergen, Norway. At that time we were proposing coordinated space and ground-based ionospheric heating experiments at Arecibo, Puerto Rico using the Soviet ACTIVE satellite. This is a joint U.S.-Soviet Space Plasma Physics Program sponsored by NASA in the United States. The ACTIVE satellite, placed in a high inclination orbit with its perigee at the altitude of 500 km and its apogee at 2,500 km, carries a VLF transmitter operated at frequencies near 10 KHz.

Since December 17, 1989 we have carried out several experiments at Arecibo when the ACTIVE satellite reached its perigee position. The dates of our experiments are: 17, 22, 28 December, 1989 and 12, 20 March, 1990. Our Arecibo experiments involve the following groups: M.C. Lee of MIT and his three graduate students: K.M. Groves, K.L. Koh, and C. Yoo; USAF scientists: W.J. Burke, H.C. Carlson, J.L. Heckacher, P.A. Kossey, and E.J. Weber at the Geophysics Laboratory; S.P. Kuo of the Polytechnic University; L.M. Duncan and his graduate student: K. Dighe from the Clemson University; F.T. Djuth of the Aerospace Corporation; M.P. Sulzer of the Arecibo Observatory; and U.S. Inan of the Stanford University.

We will first describe the setup and scientific goals of the experiments. Then, the theoretical background and the diagnostics for the proposed experiments will be discussed. Comments on the experiments will be followed by a brief description of the planned laboratory simulation of field experiments at MIT. A summary will be finally given.

#### 2. Active Experiments with the ACTIVE Satellite

Delineated in Figure 1 is the scenario of active experiments with the ACTIVE satellite at Arecibo, Puerto Rico. The Arecibo HF Heater first transmits radio waves vertically at a frequency (say, 8 MHz) less than the peak plasma frequency in the F region. Short-scale (typically, meter-scale) ionospheric density striations can be excited in a second, while large-scale (typically, hundreds of meters and kilometer-scale) density striations are generated in tens of seconds. Then, a VLF wave is launched from the transmitter onboard the ACTIVE satellite, propagating through the HF modified ionospheric region. The scientific goals of these experiments are to study the nonlinear VLF propagation through the HF-heated ionospheric region and to investigate experimentally the possible nonlinear interactions of VLF waves with ionospheric plasmas. Active VLF wave injection experiments have been conducted with ground-based transmitters for the study of VLF wave interaction with energetic charged particles in the magnetosphere [see, e.g., Hellwiel, 1983 and references therein]. The possible interaction between VLF waves and the ionospheric plasmas received little attention. However, it is shown theoretically that intense lower hybrid waves and

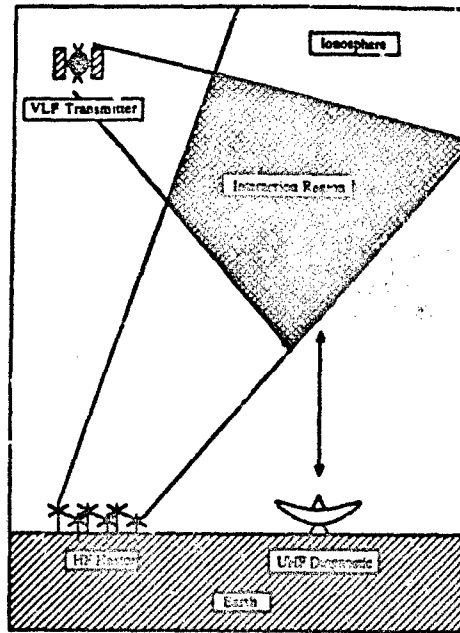


Figure 1. Coordinated space and ground-based ionospheric heating experiments

plasma density striations can be favorably excited by either injected or lightning-induced VLF waves [Lee and Kuo, 1984]. The wavelengths of the excited lower hybrid waves (or field-aligned density striations) are found to be a few meters in the lower ionosphere, a few tens of meters in the upper ionosphere, and a few hundreds of meters in the magnetosphere at  $L=4$  [Lee and Kuo, 1984]. Observations of VLF wave-excited lower hybrid waves in the ionosphere were actually indicated in the experiments of the Franco-Soviet ARCAD 3 satellite [Berthelier et al., 1982; L. R. O. Storey and P. Lefevre, personal communication, 1984] and others [e.g., Chmyrev et al., 1976 & 1986].

### 3. Theoretical Background

Distinct VLF propagation effects in the HF heater modified ionosphere depend on the scale lengths of the HF-induced ionospheric density striations. As elaborated below, the nonlinear scattering of VLF waves is most effective by short-scale (meter-scale) density striations [Lee et al., 1987; Groves et al., 1988]. It is also our intent to study the VLF wave propagation in the presence of large-scale density striations whose scale lengths are comparable to the VLF wavelength (~ a few hundreds of meters in the F region).

For simplicity, the VLF wave transmitted from the ACTIVE satellite is assumed to propagate along the Earth's magnetic field in a ducted whistler mode, whose wave electric field is represented by

$$\vec{E}_0 = (\hat{x} + i\hat{y})E_0 \exp[i(k_0 z - \omega_0 t)] \quad (1)$$

The HF heater-induced ionospheric density striations are denoted by

$$\delta n = \delta n \exp(-ky) \quad (2)$$

After solving the equation for whistler propagation in the presence of density striations, the scattered wave field is found to change from a circularly polarized into an elliptically polarized polarization, viz.,

$$\vec{E}_s = \{(\hat{x} + i\hat{y})E_{cp} + \hat{y}E_{lp}\} \exp[i(k_0 z - \omega_0 t)] \quad (3)$$

where  $E_{cp}$  and  $E_{lp}$  designate, respectively, the field intensity of the circularly polarized component and that of the linearly polarized component; they are related by

$$E_{cp} = 2 \left( \frac{\lambda}{\lambda_0} \right)^2 E_{lp} = 2E_0 \left( \frac{\delta n}{N_0} \right) \left( \frac{\lambda}{\lambda_0} \right)^2 \quad (4)$$

where  $\lambda$  and  $\lambda_0$  are the scale length of the ionospheric density striations and the wavelength of the whistler wave, respectively;  $\frac{\delta n}{N_0}$  is the fractional density fluctuations caused by the HF heater.

We can see from (4) that  $E_{sp}$  is negligible when  $\lambda \ll \lambda_0$ , leading to a nonlinear mode conversion of electromagnetic waves into electrostatic mode waves. The wavelengths of whistlers are of order (a few hundreds of meters in the ionosphere). Hence, the HF heater-induced various, especially, the small-scale density striations can effectively render the nonlinear mode conversion of a VLF (whistler) wave into an electrostatic (lower hybrid) wave. Then, the scattered wave carries a large perpendicular wave vector introduced by the short-scale density striations. It is expected that in situ measurements with the satellite-borne sensors will detect significant spectral broadening of the scattered wave with a single-peaked spectrum centered at the carrier frequency [Groves et al., 1988]. The spectral broadening of injected monochromatic VLF waves was reported in Bell et al. [1983] and Inan and Bell [1985]. Prominent ionospheric effects are associated with the appearance of lower hybrid waves. The lower hybrid waves can accelerate electrons effectively along the Earth's magnetic field. This process causes the impact excitation of neutral particles and Langmuir waves, leading to intense airglow and a broad height distribution of enhanced plasma lines. These expected ionospheric effects can be monitored by radars and an all sky imager.

We are also interested in the VLF (whistler) propagation in the disturbed ionosphere having large-scale density striations. To distinguish it from the above said nonlinear scattering process, the HF heater should be operated in CW mode long enough to excite the large-scale density striations. Then, turn off the heater to let the short scale density striations decay for a few seconds. The position of the ACTIVE satellite can be distant from the HF modified ionospheric region. However, we should make sure that the VLF signal, after its transionospheric propagation to reach the ground, is detectable above the background VLF noise. Several VLF receivers will be deployed on the ground at the estimated footprints of the transmitted VLF (whistler) signals.

In addition to the nonlinear scattering process, the lower hybrid waves can be produced by parametric instabilities if the incident whistler waves are intense enough [Lee and Kuo, 1984]. The concerned physical process involves a four wave interaction described by the following wave frequency ( $\omega$ ) and wave vector ( $\vec{k}$ ) matching relations:

$$\begin{aligned}\omega_+ &= \omega_0 + \omega_s = \omega_- + \omega_0^* \\ \vec{k}_+ &= \vec{k}_0 + \vec{k}_s = \vec{k}_- + \vec{k}_0^*\end{aligned}$$

where the subscripts 0, +/− and s represent the incident whistler wave, the Stokes/anti-Stokes components of the lower hybrid sidebands and the concomitantly excited field-aligned zero-frequency mode, respectively. The parametric instability is characterized by a two dimensional process and the excited low-frequency mode is a purely growing mode. Hence, both the Stokes and anti-Stokes components of the lower hybrid waves have to be taken into account in the analysis of the instability. Further, whistler propagation along the geomagnetic field provides the most favorable symmetric configuration for the four-wave interaction process to occur.

The concerned instability is driven additively by two types of nonlinear effect which are predominant in different frequency domains of the whistler (VLF) waves:

(a) Frequency domain 1:

$$\omega_{LH} \left( 1 + \frac{M v_{Te}^2 \omega_{pe}^2}{m c^2 \Omega_e^2} \right)^{1/2} < \omega_0 < \omega_{pe} \quad (5)$$

wherein the non-oscillatory beating current is to be the dominant nonlinear effect. Here  $M(m)$ ,  $v_{Te}$ ,  $c$ ,  $\omega_{pe}$  ( $\omega_{pi}$ ),  $\Omega_e$ ,  $\omega_{LH}$  are the ion (electron) mass, electron thermal velocity, speed of light, electron (ion) plasma frequency, electron cyclotron frequency and lower hybrid resonance frequency, respectively. The threshold field for exciting the parametric instability in this frequency domain is found to be

$$E_{th} = 1.2(m/e)\nu_e v_{Te} |\eta|^{1/2} \quad (6)$$

where  $\eta$  is defined by  $[1 + (M/m)(k_0/k_s)^2]/[1 - (M/m)(k_0/k_s)^2(\omega_0/\omega_{pe})^2]$ .

(b) Frequency domain 2:

$$\omega_{pe} < \omega_0$$

wherein the thermal pressure force is to be the dominant nonlinear effect. The corresponding threshold field has the following form:

$$E_{th} = 0.85(k_s^2 v_{Te}^3 / \Omega_e)(m/e)[1 + (1 + 4\Omega_e^2 \nu_e^2 / k_s^4 v_{Te}^4)^{1/2}]^{1/2} / |\eta|^{1/2} \quad (7)$$

The growth rates of the instability are given by

$$\begin{aligned}\gamma &\sim 0.5(\nu_e k_s^2 v_{Te}^2 / \Omega_e^2)[E_R^2 - 1] \quad \text{for } E_R^2 \ll 10 \\ \gamma &\sim 1.4(\nu_e k_s^2 v_{Te}^2 / \Omega_e^2)E_R \quad \text{for } E_R^2 \gg 10\end{aligned} \quad (8)$$

where  $E_R$  is the incident field intensity of the whistler wave normalized by the threshold field of the instability. Based on these characteristics of the parametric instability, the following predictions can be made for the experimental corroboration.

First of all, since both Stokes and anti-Stokes components of lower hybrid waves are excited, we expect that in situ measurements will detect a spectrally broadened signal with peaks at a discrete set of frequencies  $\omega$  both sides of the nominal carrier frequency [Groves et al., 1988]. Secondly, from (6):  $E_{th} \propto [1 + (M/m)(k_0/k_s)^2] / [1 - (M/m)(k_0/k_s)^2(\Omega_e/\omega_{pe})^2]$  and (9a & 9b):  $\gamma \propto k_s^2$ , it is clear that the excitation of plasma modes with larger wave number,  $k_s$  (i.e., small scale lengths,  $\lambda_s$ ) requires lower thresholds; consequently, the short-scale modes can be quickly excited. In the upper ionosphere, the threshold fields are typically less than 1 mV/m and the growth rates are about 1 Hz for  $E_R \sim 30$ .

The excited lower hybrid waves have a zero perpendicular phase velocity, because both the Stokes and anti-Stokes components of lower hybrid waves are excited simultaneously by the parametric instability, leading to the formation of a standing wave pattern across the Earth's magnetic field. However, the excited lower hybrid waves can propagate along the Earth's magnetic field. From the dispersion relations of lower hybrid waves and whistlers, we find the group velocity of the lower hybrid waves is related to that of whistlers by

$$\left(\frac{d\omega_0}{dk_0}\right)_{lh} = \frac{1}{2} \left[ \frac{(M/m)(k_0/k_s)^2}{1 + (M/m)(k_0/k_s)^2} \right] \left(\frac{d\omega_0}{dk_0}\right)_{whistlers} \quad (9)$$

If the in-situ measurements of VLF waves are carried out, it is expected that a significant delay exists in detection of the whistler wave and the excited lower hybrid waves. We note that a strong emission line at the lower hybrid resonance frequency ( $\Omega_{lh}$ ) was detected and the expected delay between the excited mode waves and the whistler pump wave was indeed observed in the rocket experiments during lightning storms [Kelley et al., 1985; Liac et al., 1989].

It is expected that the field intensities of lower hybrid waves excited by the parametric instability are much greater than those produced by the nonlinear (mode conversion) scattering process. Strong electron acceleration by lower hybrid waves in this case may yield intense airglow [Chemmyrev et al., 1976 & 1986]. Consequently, a very broad height distribution of enhanced plasma lines can be detected by radars [Carlson et al., 1982]. The growth time of the instability can be determined by varying the pulse duration and monitoring the intensities of VLF waves, airglow, and plasma lines recorded on the ground.

#### 4. Comments on Planning and Conducting of Experiments

Based on the nominal orbital information provided in the Research Announcement on the ACTIVE Space Plasma Physics Program distributed by NASA, an analysis of the ACTIVE satellite's orbital characteristics was carried out to determine the frequency of favorable observing periods at Arecibo. The satellite performs about 12.5 revolutions per day, giving approximately 25 passes when both ascending and descending nodes are considered. Every five days, after some 62 revolutions, the orbital ground track has drifted  $\sim 3^\circ$  east and repeats the cycle. The result is a fine sampling of longitudes by ACTIVE in a relatively short time period. The orbit simulation predicts that 59 passes would occur over Arecibo ( $18.3^\circ$  N. lat.,  $293.4^\circ$  long.) at elevations greater than  $45^\circ$  in a 60 day period, for an average of about one favorable pass per day. 16 passes were found to be less than  $15^\circ$  from zenith over that period; 12 of these were concentrated in a 20 day subset of the 60 day simulation.

The simulations show a relatively large number of passes in the near vicinity of the experimental site of interest. However, the optimum conditions for our experiments require the satellite to reach its perigee position and overpass the Arecibo 430 MHz radar beam. Therefore, we only found a few days appropriate for experiments in the past December (1989) and March (1990). The coordination for the experiments was very difficult, stemming from the following fact: the orbits of the ACTIVE satellite are easily affected by the solar activities during this solar maximum period. The satellite ephemeris has been carefully monitored. Nevertheless, we were not certain if the day was good for experiments or not until, sometimes, a couple days before. Yet, a nine-day's notice was required for scheduling the dates for the experiments.

Ground-based optical imaging measurements with the AFGL All Sky Imaging Photometer (ASIP II) were proposed as part of the coordinated diagnostics during the RF transmissions from the ACTIVE satellite. Fast electrons accelerated during these transmissions can cause impact excitation of various spectral species. Optical emissions (artificial auroras) from these species can then be detected by sensitive imaging systems to yield information on the location, intensity and energy of the electron fluxes. For instance, the excitations of the  $O(^1D$  and  $^1S)$  states of atomic oxygen are produced by fluxes of electrons with energies exceeding 1.96 and 4.17 eV, respectively, and lead to optical emissions at  $6300\text{\AA}$  and  $5577\text{\AA}$ . Other possible processes include excitation of the  $O(^3P^3P)$  (threshold energy of  $\sim 9.6$  eV and radiation of  $7774\text{\AA}$ ) and  $N_2^+$  (ING) (threshold  $\sim 18.7$  eV and radiation at  $4278\text{\AA}$ ). Thus, optical measurements at multiple wavelengths can be used to detect characteristics of the spectrum of accelerated electrons, at least in the sense that several threshold energies have been exceeded.

The ASIP employs a variable field of view with interchangeable lenses covering  $180^\circ$ ,  $90^\circ$ ,  $40^\circ$ ,  $20^\circ$ , and  $12^\circ$  full field. A filter wheel rotates up to four interference filters into the optical axis of the images by successive exposures. An image intensifier is used to increase the gain followed by a  $512 \times 512$  CCD (charge-coupled device) for signal detection. Some unique aspects of detection of optical emission features from a moving satellite must be considered, as compared to detection of these same features generated

by a fixed ground-based transmitter. The main difference is related to exposure time. For a moving satellite the factor limiting the exposure time is the motion of the satellite (the motion of the beam of accelerated electrons) across the ASIF II detector. For a satellite at 500 km perigee, with a nominal velocity of 7 km/sec, the satellite will change zenith angle at a rate of  $.15^\circ/\text{sec}$  near the horizon and up to  $\sim .30^\circ/\text{sec}$  near the zenith. Assuming a  $40^\circ$  field of view lens and that 500 CCD pixels are available for the image, maximum exposure times are only .01 sec/pixel near the zenith and .33 sec/pixel near the horizon. For  $180^\circ$  field of view lens, these times increase to .45 sec/pixel and 2.4 sec/pixel, respectively. Thus, spatial resolution is sacrificed for longer exposure times with the  $180^\circ$  lens. A dark background is needed for the optical measurements of RF induced ionospheric effects. Unfortunately, most satellite passes for experiments at Arecibo occurred in late afternoon or early evening when the sky was still quite bright.

Ground-based VLF receivers were used to monitor the signal transmitted from the orbiting ACTIVE satellite. Doppler shifting of the signal frequency due to the orbital velocity (of the order of 7600 m/s) and inclination ( $83^\circ$ ) is small (of the order of  $\pm 0.25$  Hz) and depends on the direction of the observer relative to the satellite motion. Thus, the receiver should have a bandwidth of at least 400 Hz in order to record the transmitted signals. Ideally, a receiving system might consist of two orthogonal loop antennas, each feeding a low-noise, 400 Hz bandwidth amplifier/receiver whose output voltage is downconverted to baseband; the two output voltages are sampled simultaneously (both in-phase and quadrature phase) and digitally stored in computer memory at a rate sufficient to insure no aliasing occurs ( $> 800$  Hz). The crossed-loops allow the determination of direction of arrival of the signals (but have  $\pm 180^\circ$  ambiguity). In two seconds, 1600 samples will have been recorded, so an 800 point discrete Fourier transform (DFT) can be calculated for the 400 Hz band, each point separated by 0.5 Hz. In effect, the two second integration has narrowed the bandwidth from 400 Hz to 0.5 Hz and improved the SNR by 22 dB. Should a greater SNR be required, longer integration times could be used, but the time resolution of the satellite signals would be correspondingly coarser.

The portable FFT computing spectrum analyzers (Nicolet Model 446), deployed at Arecibo to monitor the transmitted VLF waves, provide digital sampling of the VLF signals. These spectrum analyzers have selectable bands of 10, 50, 100, 500, 1K, 2K, 10K, or 20K Hz wide. They calculate a 400 point spectrum from 1024 time samples. The nominal bandwidth is 1/400 of the frequency range; for example, if the 500 Hz band is chosen, each spectral point is separated by  $500/400$  Hz = 1.25 Hz. Other instrument features include several averaging modes, such as selection of number of spectra averaged, and various digital outputs.

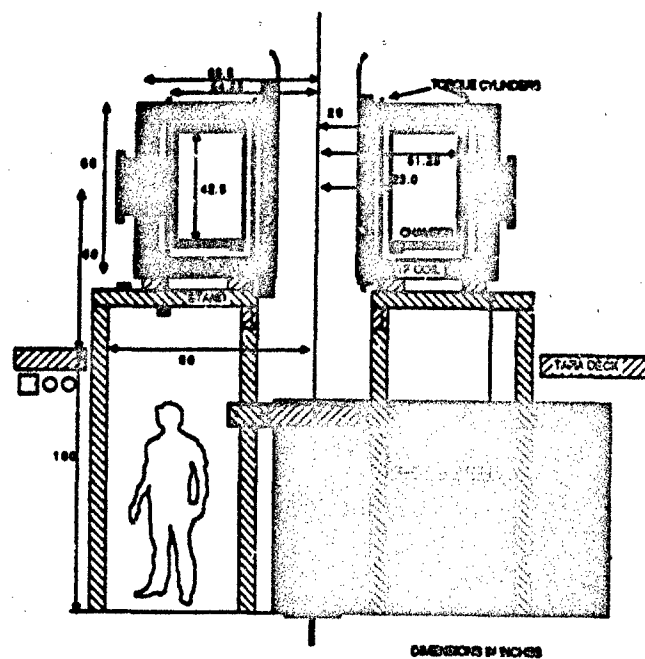
We have not succeeded in recording transmitted VLF signals yet. The satellite-borne transmitter was operated in one-second on and one-second off mode for the experiments. It took about half a second for the satellite to move across the radar beam. It was likely that the signals happened to be not transmitted when the satellite passed over Arecibo. Another possibility was that the transmitted signals were so weak that they could not be distinguished from the background noise. This possibility arises from the fact that the ACTIVE satellite is unfortunately not working as originally planned. The power input to the antenna, planned to be 10 kW (with 80 A of current into the antenna), was reduced by two orders of magnitude.

It seems unlikely to produce nonlinear ionospheric effects with this weak VLF transmitter. We have planned different schemes to conduct Arecibo experiments. In our recent experiments performed in late May and early June (1990), we concentrated on the radar diagnosis of the near field effects of the VLF transmitter. Some interesting phenomena were observed and the data are currently being analysed by the three MIT graduate students: K.M. Groves, K.L. Koh, and C. Yoo. The results will be reported somewhere else later.

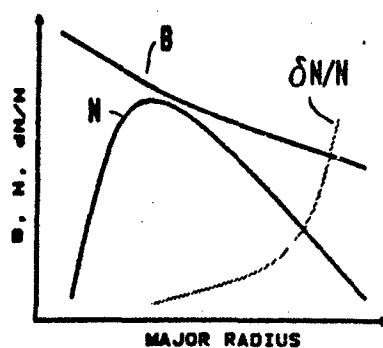
### 8. Planned Laboratory Simulation

A large experimental plasma device called the Versatile Toroidal Facility (VTF) is currently under construction at the MIT Plasma Fusion Center. The construction materials have been taken from the discontinued MIT Tora mirror machine and the ISX-B fusion device of the Oak Ridge National Laboratory. It is a student-powered project in the sense that its construction involves five graduate students and twenty undergraduate students. Shown in Figure 2 is the cross-sectional view of the VTF device. This plasma device has 18 toroidal field (TF) coils and 48 large side, top and bottom ports providing access for probes throughout the plasma volume for measurements of turbulent density fluctuations, plasma waves, and bulk parameters such as electron temperature and density. The construction of the VTF is near completion and the first plasmas will be produced shortly. The main purpose of constructing this VTF device is to conduct laboratory study of nonlinear wave propagation and interaction with magnetoplasmas, simulating field experiments [Lee and Parker, 1990].

The VTF device can generate steady-state plasmas which are radially inhomogeneous but quite uniform along the axial direction. It is projected that preliminary experiments to characterize the plasmas will be carried out this summer. Schematically illustrated in Figure 3 are plasma density ( $N_e$ ), magnetic field intensity ( $B_z$ ), and the fractional density fluctuation ( $\frac{\Delta N_e}{N_e}$ ) as a function of radius ( $R$ ) in VTF. The plasma density profile is controlled by variation of location of the cyclotron resonance layer. The magnetic field decreases inversely with radius. The plasma density fluctuations remain approximately



**Figure 2. Cross sectional view of VTF**



**Figure 3.** Plasma density( $N$ ), magnetic field intensity( $B$ ), and fractional density fluctuations( $\delta N/N$ ) as a function of radius in VTF.

constant throughout the device. However, since plasma density drops sharply near the wall, the fractional density fluctuations range from a few percent at the center to nearly fifty percent near the wall. These laboratory plasmas with inherent density fluctuations can simulate the disturbed ionospheric plasmas for the concerned nonlinear wave propagation and interactions. Further, the near field effects of the VLF transmitter can be conveniently studied with this large plasma device.

## 6. Summary

### Planning and conducting of coordinated space and ground-based ionospheric modification experi-

ments at Arecibo, Puerto Rico are discussed. Although several experiments were carried out at Arecibo in the past December (1989) and March (1990), we have not got significant results yet. We realize that the ACTIVE satellite is not working as originally planned. Therefore, we have already planned alternative schemes for the proposed experiments. Some interesting phenomena were seen in the May-June (1990) experiments. The results will be reported after we accomplish the data analysis and interpretation. Laboratory simulation of the field experiments will be conducted with the new Versatile Toroidal Facility (VTF) at MIT. The crosscheck of the results obtained from the laboratory and field experiments will be conducive to the understanding of the concerned nonlinear wave-plasma interactions.

**Acknowledgments.** The work at the Massachusetts Institute of Technology is supported by the NASA grants NAG 5-1336 and NAG 5-1055, that at the Polytechnic University by the NASA grant NAG 5-1051.

#### References

#### References

- Bell, T. F., H. G. James, U. S. Inan, and J. P. Katsufakis, The apparent spectral broadening of VLF transmitter signals during transionospheric propagation, *J. Geophys. Res.*, **88**, 4813, 1983.
- Burthaler, J. J. et al., Measurements of the VLF electric and magnetic components of waves and dc electric field on board the AUREOL-3 spacecraft: The TBF-ONCH experiment, *Ann. Geophys.*, **38**, 643, 1982.
- Carlson, H. C., V. B. Vickwar, and G. P. Mantas, Observation of fluxes of suprathermal electrons accelerated by HF excited instabilities, *J. Atmos. Terr. Phys.*, **44**, 1039, 1982.
- Chmyrev, V. M. et al., Artificial injection of very low frequency waves into the ionosphere and the magnetosphere of the Earth, *JSTP Lett.*, **23**, 409, 1976.
- Chmyrev, V. M. et al., Particle precipitation, optical emissions, and VLF noises in the mid-latitude ionosphere stimulated by ground-based VLF transmitters, *Proceedings of the International Symposium on "Modification of the ionosphere by powerful radio waves"*, Suzdal/Moscow, U.S.S.R., 8-12 September, 1986.
- Groves, K. M., M. C. Lee, and S. P. Kuo, Spectral broadening of VLF radio signals traversing the ionosphere, *J. Geophys. Res.*, **93**, 14583, 1988.
- Hellivell, R. A., Controlled stimulation of VLF emissions from Siple Station, Antarctica, *Radio Sci.*, **18**, 801, 1983.
- Inan, U. S., and T. F. Bell, Spectral broadening of VLF transmitter signals observed on DE 1: A quasi-electrostatic phenomena?, *J. Geophys. Res.*, **90**, 1771, 1985.
- Lee, M. C. and S. P. Kuo, Production of lower hybrid waves and field-aligned plasma density striations by whistlers, *J. Geophys. Res.*, **89**, 10873, 1984.
- Lee, M. C., K. M. Groves, C. P. Liao, D. R. Rivas, and S. P. Kuo, Combined operation of two ground transmitters for enhanced ionospheric heating, *J. Geomag. Geoelectr.*, **40**, 1141, 1988.
- Liao, C. P., J. P. Friedberg, and M. C. Lee, Explosive spread F caused by the lightning induced electromagnetic effects, Accepted for publication in the *J. Atmos. Terr. Phys.*, 1989.

## DISCUSSION

U. S. INAM, US

1) Ionospheric electric field amplitudes of 1-5 mV/m are not unreasonable overhead major VLF transmitters, having 1MW radiated power.

2) As far as the AXTIV satellite is concerned, the power input to the antenna was planned to be 10 kW, with 80 A of current into the antenna. The physical fact is that the current is down by a factor of 10 to 5 A. Nobody really knows what the radiation efficiency is, so it does not make too much sense to talk about radiated power.

## AUTHOR'S REPLY

1) Yes, we expect that powerful ground-based VLF transmitters can excite lower hybrid waves via the proposed instability mechanism.

2) Thank you for this comment to clarify Dr. Balrose's questions regarding the input power to the antenna and the radiated power.

MJS/LNUS, NO

Is the VLF wave tuned to nearly the local LH frequency of the perturbed bottom-side ionospheric plasma?

## AUTHOR'S REPLY

No, the wave frequency of the incident VLF wave is 10 kHz, while the lower hybrid resonance frequency in the ionosphere is 5 kHz or so. However, the VLF wave frequency is within the wave-frequency range of the lower hybrid waves. Hence, if the VLF wave is intense enough, lower hybrid waves can be parametrically excited.



## WAVE-PARTICLE INTERACTIONS ASSOCIATED WITH VLF TRANSMITTERS.

François Lefeuve

Laboratoire de Physique et Chimie de l'Environnement,  
45071 Orléans, France.

### SUMMARY

Wave-particle and wave-wave interactions associated with VLF ground-based transmitters are reviewed. The topics covered include: particle precipitation, amplification and triggering of new emissions, and excitation of resonant frequencies.

### 1. INTRODUCTION

Numerous VLF ground-based transmitters, operated between 3 and 20 kHz, have been set up all over the world, mainly for the purpose of radio-navigation. They are known to induce wave-particle and wave-wave interactions within the ionosphere and the magnetosphere. The aim of the present paper is to give a short overview of those interactions.

Many advances in the understanding and in the discovering of new phenomena are due to controlled wave-injection experiments. Most of them have been conducted from the Siple antenna [1 and references therein], but other active experiments have also produced key results [2 - 8]. At the present time, a set of new phenomena is induced by the powerful Alpha transmitters located in the USSR [9 - 11].

In the following the phenomena are gathered into three classes: particle precipitation, amplification and triggering of new emissions, and excitation of resonant frequencies in the medium. Phenomena such as the quenching of natural emissions by a VLF transmitter are excluded from the present review.

### 2. PARTICLE PRECIPITATION

#### 2.1 OBSERVATIONS

##### *Electron precipitation*

Some of the first indications of wave-induced precipitations of radiation-belt electrons were obtained by observing secondary effects of electron precipitations, such as X rays, enhanced D-region ionization and optical radiation [12, 13].

Direct evidence of particle interactions with man-made waves was provided by observations of the energy spectra of electrons in the drift-loss cone [14 - 16]. Observations of modulated precipitations of electrons in the bounce-loss cone were made during Stimulated Emission of Energetic Particles (SEEP) experiments [17, 18]. Two main features characterize the energy spectra of precipitating electrons. First, peaks have central energies that decrease with increasing L shell (electrons above 100 Kev at  $L \leq 2$  and below 1 Kev at  $L > 2.5$ ). Second, the width of those peaks is very narrow (less than 10% of the central energy).

### Proton precipitation

Few observations of protons precipitations by man-made waves have been reported [20 - 21; 27]. They concern the energy range 50 - 530 Kev.

### 2.2 Basic mechanism

The Doppler-shifted resonance of a whistler-mode VLF wave is generally considered as being responsible for the precipitation of energetic particles [28]. The mechanism is known to work with non-coherent (ELF/VLF hiss) as well as with coherent (whistlers, ELF/VLF chorus) natural emissions. There is no fundamental difference with artificially injected coherent waves.

The gyroresonance condition is written

$$\omega + K V = N \Omega \quad (1)$$

where  $\omega$  is the Doppler-shifted frequency of the wave,  $K$  is the wave-normal vector,  $V$  is the electron-resonant velocity,  $N$  is an integer and  $\Omega$  is the particle gyrofrequency.

In the case of electrons,  $\Omega$  is equal to the electron gyrofrequency  $\Omega_e$ . Most authors consider that the only active resonance is the first-order cyclotron resonance ( $N = 1$ ), which is known to be more efficient in the equatorial region and for  $K$  vectors parallel to the earth magnetic field  $B_e$ . A ducting of the wave requires  $\omega < \Omega_e/2$  all along the field line; then equation (1) implies that resonant electrons move opposite to the wave-propagation direction.

As a result of the interaction a pitch-angle change is induced by the wave. The electrons are moved into the bounce-loss cone. After one or several bounces, depending on the characteristic parameters of the particle and of the altitude of the mirror points, the electrons are precipitated.

One generally uses equation (1) to estimate which resonant electrons may interact with a given wave frequency at given  $L$  value. It allows for instance to show an  $L$  dependency that is in agreement with most experimental observations. An exception was noted by Kovrazkin et al., [20, 21] on AUREOL-3 data. For those particular observations, the authors suggest a Landau (or Cerenkov) resonance, obtained by setting  $N=0$  in equation (1). Such a resonance could be more efficient out of the equatorial plane [29].

At first sight the problem of the VLF-wave-induced precipitation of protons is more difficult to solve. It seems impossible for a VLF frequency to match the proton gyrofrequency. Now, Shkylar [30] made two very important remarks. First, wave propagation at large  $\theta$  values (with  $\theta = (K, B_e)$ ) allows equalities of the form  $\omega \approx \Omega_p \cos\theta$ , with  $\Omega_p$  the proton gyrofrequency. Second, as distances in velocity space between different resonance modes (different  $N$  values) are very small, multiple resonances may be taken into account.

### 2.3 NUMERICAL SIMULATION

A complete understanding of the electron precipitations requires understanding of the following points:

- (a) the  $L$  dependency of the energy spectra of the precipitating electrons in the drift loss cone;
- (b) the relationship between the flux of precipitated particles and the power of the transmitted VLF waves;
- (c) the narrowness of the peaks in energy.

Several simulations of the first-order cyclotron resonant interaction of energetic electrons and coherent VLF waves were carried out, based on motion of a resonant electron into the potential trough of a wave. The motion is established by superimposing the adiabatic motion of the particle in the absence of the wave to the Lorentz force equation. It is written [31].

$$\frac{dV_{\parallel}}{dt} = \left( \frac{e B_w}{m} \right) V_{\perp} \sin \psi - \frac{V_{\perp}^2}{2\Omega_e} \frac{\partial \Omega_e}{\partial z} \quad (2-a)$$

$$\frac{dV_{\perp}}{dt} = - \left( \frac{e B_w}{m} \right) \left( V_{\parallel} + \frac{u}{K} \right) \sin \psi + \frac{V_{\perp} V_{\parallel}}{2\Omega_e} \frac{\partial \Omega_e}{\partial z} \quad (2-b)$$

$$\frac{d\psi}{dt} = \Omega_e - u - K V_{\parallel} - \left( \frac{e B_w}{m} \right) \left( V_{\parallel} + \frac{u}{K} \right) \frac{\cos \psi}{V_{\perp}} \quad (2-c)$$

with  $V_{\parallel}$  and  $V_{\perp}$  the parallel and perpendicular electron velocities,  $e$  and  $m$  the charge and mass of the electron,  $B_w$  the modulus of the wave magnetic-field vector, and  $\psi$  the complement of the angle between the electron's perpendicular velocity ( $V_{\perp}$ ) and  $B_w$ . A flux of precipitated electrons is obtained by computing for a full distribution of particles the wave-induced changes  $\Delta V_{\parallel}$  and  $\Delta V_{\perp}$ , and so the pitch-angle scattering over the time intervals where the resonance condition (1) is satisfied.

The computer simulation approach used by Inan et al. [32] is based on the approximation of the full distribution of particles by test electrons appropriately distributed in energy and pitch angle. It was extended by Chang and Inan [33] to the quasi-relativistic electrons ( $> 50$  Kev). The results are in agreement with the measured energy spectra of the precipitated electrons.

An important concept developed by Besselov and Trakhtengerts [34] and Trakhtengerts [35] has been recently reviewed by Villalon et al. [36]. It supposes that a maser instability is produced by the interaction of a hot-electron population ( $> 40$  Kev) with first-order cyclotron waves near equatorial regions, and that diffusion occurs over time scales that are longer than particle bounce times and the group-time delays of the waves. The resonant part of the energetic particle's distribution functions is described within the framework of a quasilinear theory. The equatorially generated waves may be partially trapped between the two hemispheres, the reflection coefficients at the top of the ionosphere being possibly increased by heating the foot of the flux tube.

A full distribution test-particle simulation was carried out to determine the precipitated electron flux that would be induced by a Landau resonance interaction [37]. It is shown that for typical parameters the resulting precipitation fluxes are much smaller than those induced in a gyroresonance interaction.

### 3. AMPLIFICATION AND TRIGGERING OF NEW EMISSIONS

#### 3.1 OBSERVATIONS

The existence of triggered emissions was discovered accidentally by Helliwell et al. [38] during the examination of natural events. New emissions (risers, fallers and hooks) were triggered by dashes in man-made Morse code signals, transmitted from the NPG (18.6 kHz) and NAA (14.7 kHz) stations. A few years later, Kimura [39] discovered that new emissions were also triggered by the omega (10.2 kHz) signals, although much less power was transmitted (100 W instead of 1 MW for NAA). Some of those new emissions were preceded by intensification in the signal, but amplification of the order of 10 dB was observed in the absence of triggering. Since that time numerous observations have been

made, particularly from the Siple controlled-VLF-wave-injection experiment [1, 41, 42]. Signal growth was observed to be as much as 30 dB. A triggering occurs above a given threshold. Reviews of the observations can be found in [1, 39, 42, 43, 44]. Surprisingly, similar phenomena have never been detected in laboratory plasmas.

### 3.2 BASIC MECHANISM

The basic physics were reviewed by Matsumoto [45]. The motion of an electron in a whistler wave is given by the set of equation (2). Due to the mirror force,  $|V_{\parallel}|$  increases as the electron travels along the geomagnetic field toward the equator. At a given point, called the first resonance point, it satisfies  $|V_{\parallel}| = |V_{\phi}|$ . Then, depending on its initial phase value, it may be trapped. Here, a trapping means that the phase oscillation of the electron is bounded. Under certain conditions, established by Helliwell and reformulated by Nunn, a trapped electron can stay in resonance even in an inhomogeneous magnetic field. A detrapping occurs when the electron moves away from the equator and encounters the second resonance point where  $|V_{\parallel}| = |V_{\phi}|$ . An untrapped electron continues to be accelerated by the mirror force till it meets the equatorial plane, beyond which it decelerates. Such behaviour is easily understood from computer simulation studies [46]. When many resonant electrons are taken into account, several of them may be phase bunched around a certain angle. The phase-bunching concept has been used for a calculation of a nonlinear current in many works [45 and references therein, 47, 54]

Several theories have been proposed to explain the triggered emissions. Many authors refer to instabilities caused by a distorted velocity-distribution function of resonant-electrons after the interaction. As an example Roux and Pellat [54] suggested that a hole or a beam in the spatially averaged velocity distribution is created by the presence of untrapped and suddenly detrapped electrons at the end of the interaction zone. Other authors stressed the importance of the nonlinear current associated with the phase bunching. In order to explain a self-sustaining exponential growth of triggered emissions, Helliwell and Crystal [47] and later Helliwell and Inan [48] proposed to include a feedback effect between the simulated emissions and the incoming resonant electron. They constructed a model where the interaction region is treated like an unstable feedback amplifier with a delay line.

### 3.3 NUMERICAL SIMULATION

A list of features of artificially stimulated emissions that theory should explain is given in [45]. It has been recently rephrased and completed in [52]. To summarize, numerical simulation studies may be consistent with:

- (a) the observed triggering signals (narrow bandwidth, duration, threshold)
- (b) the observed growth rate and the conditions for the termination
- (c) the observed triggered signal (frequency/time variations)
- (d) the geomagnetic periods of most active triggering.

At the moment, no simulation has been able to reproduce all the above characteristics. However, each one brings new items of information. As examples, three studies will be considered.

In a computer simulation based on the interaction of a coherent wave propagating along an homogeneous magnetic field and counter-streaming high-energy electrons, Omura and Matsumoto [49] demonstrated that a rising tone is caused by detrapping of phase-bunched electrons.

A kinetic theory has been used by Molvig et al. [52] to simulate the triggering of whistler emissions but only fallerz are produced. The emission process requires an inverted population in the

perpendicular velocity-distribution function, sufficient amplitude for trapping in the trapping signal, and sufficient density in the resonant portion of the distribution function such that the driven current can offset convection.

Numerical simulations were recently performed by Nunn [53] using a Vlasov hybrid simulation technique. The particle population is described as a continuous Vlasov fluid in phase space. It was found that, provided the linear growth rate exceeds a minimum of about 80 dB/s any initial pulse that is long enough and reaches nonlinear amplitudes by the time it reaches the equator will trigger a riser with the same sweep rate. For a narrow-band emission the rate of change in frequency is due to an active term corresponding to the detrapping of electrons and to an inhomogeneous term. For a broader bandwidth the frequency appears to rise due to successive generation of the next upper sideband.

## 4. EXCITATION OF RESONANT FREQUENCIES

### 4.1 OBSERVATIONS

Signals injected from ground-based VLF transmitters, operated between 10 and 15 kHz, are commonly observed to broaden as they traverse the ionosphere [55, 58, 10] and the magnetosphere [59] at L values smaller than 3. The expansion of the bandwidth, which results in a proportional increase in signal-to-noise ratio, may be as large as 1% of the carrier frequency. The transmitted frequency seems to be always above the local lower hybrid frequency. The nature of the broadening is thought to be electrostatic.

From time to time, sidebands at  $\omega_{\perp}$  and  $\omega_{\perp+1}$  are observed around the transmitted frequency  $\omega_{\perp}$  [10, 60] with similar amplitudes. Bicoherence analyses performed on several observations made by the AUREOL-3 satellite have demonstrated that phase relationships existed between the transmitted frequency  $\sim 12$  kHz, each side band, and a natural emission observed at  $\omega_{\perp} \sim 500$  Hz. The last is the frequency distance between the transmitted frequency and each side-band [10, 11].

Acceleration of  $H^+$ ,  $He^+$  and  $O^+$  ions, accompanied by enhancement of natural VLF emissions (around 4 kHz), have been observed on COSMOS-1809 in association with injections of a coherent wave from a powerful VLF transmitter operated at 19.1 kHz [9]. A possible interpretation consists in a parametric decay of the transmitted wave into a lower-hybrid frequency and electrostatic ion-cyclotron waves; the two produced waves are generally considered as good candidates to accelerate ions [61].

Other observations suggest stimulations of geomagnetic pulsations in the 0.008 - 1.0 Hz range [62], and enhancements of ELF/VLF waves [63] from powerful VLF ground-transmitters.

### 4.2 BASIC MECHANISM

The common denominator of the above observations is the excitation of a resonance frequency, and more specifically of the lower-hybrid frequency.

Several authors [55, 60, 64] suggest that high-amplitude electrostatic waves, with a lower frequency cut-off at the lower hybrid resonance, are excited by electromagnetic VLF whistler-mode waves propagating through regions of the ionosphere and magnetosphere where magnetic-field-aligned plasma-density irregularities exist. A theoretical model, based upon passive linear scattering in a cold magnetoplasma, has been developed by Bell and Ngo [64] while Groves et al. [65] proposed a nonlinear scattering. Several hypotheses were put forward on the origin of the plasma-density irregularities, but those irregularities have never been seen at the L values where the interactions take place, and particularly by the AUREOL-3 high-time-resolution plasma measurements [66].

Independently of any experimental data, Riggall and Kelley [67] suggested that VLF ground-transmitters could produce an instability, considered as a three-wave interaction, in which the transmitted wave decays into a lower hybrid wave and an ion acoustic type of oscillation. If the transmitted wave has a frequency  $\omega_0$  and wave number  $K_0$ , then conservation of energy and momentum requires that the decay waves obey:

$$\omega_0 = \omega_1 + \omega_2 \quad (3-a)$$

$$K_0 = K_1 + K_2 \quad (3-b)$$

A similar model was used by Chmyrev et al. [61] to explain the COSMOS-1809 observations. However Lee and Kuo [68] and Groves et al. [65] have shown that a four-wave parametric instability is more likely, since it has a lower threshold and is more consistent with the symmetric side-bands observed on satellites.

In the two cases, the lower hybrid waves so excited have large wave vectors. A broadening is the result of the Doppler effect produced by the movement of the satellite in the medium.

AUREOL-3 sidebands being produced at frequencies much higher than the lower hybrid-resonance, a model has been developed by Sotnikov et al. [69] based on the excitation of sidebands due to non-linear coupling between a VLF transmitter signal and a natural ELF emission.

At the present time no numerical simulation is available.

## REFERENCES

- [1] Helliwell, R.A., VLF wave stimulation experiments in the magnetosphere from Siple Station, Antarctica, *Rev. Geophys.*, 26, 351, 1988.
- [2] Likhter, Y.I., O.A. Molchanov, V.M. Chmyrev, Modulation of spectrum and amplitude of low-frequency signals in the magnetosphere, *Pisma Zh. Teor. Fiz. (JETP Lett.)*, 14, 475, 1971.
- [3] Koons, H.C., and M.H. Dazey, Transportable VLF transmitter, in *ELF-VLF Radio Wave Propagation*, edited by J. Heltet, D. Reidel, Hingham, Mass., 1975.
- [4] Chmyrev, V.M., V.K. Roldugin, I.A. Zhulin, M.M. Mogilevsky, V.I. Di, V.K. Koshelevsky, V.A. Brushmarin, and O.M. Raspopov, Artificial injection of very low frequency (VLF) waves into the ionosphere and the magnetosphere of the Earth, *JETP Lett.*, 23, 409, 1976.
- [5] Dowden, P.L., A.C. McKey, L.E.S. Amon, H.C. Koons, and M.H. Dazey, Linear and nonlinear amplification in the magnetosphere during a 6.6-kHz transmission, *J. Geophys. Res.*, 83, 169, 1978.
- [6] Koons, H.C., B.C. Edgar, and A.L. Vampola, Precipitation of inner zone electrons by whistler mode waves from the VLF transmitters UMS and NWC, *J. Geophys. Res.*, 86, 640, 1981.
- [7] Dazey, M.H., and H.C. Koons, Characteristics of a power line used as a VLF antenna, *Radio Science*, 17, 589, 1982.
- [8] Garnier, M., G. Girolami, H.C. Koons, and M.H. Dazey, Stimulated wave-particle interactions during high-latitude ELF wave injection experiments, *J. Geophys. Res.*, 87, 2347, 1982.
- [9] Dzordzhio, N.V., M.M. Mogilevski, V.M. Chmyrev, R.A. Kovrazhkin, O.A. Molchanov, Y.I. Galperin, J.M. Boske, and J.L. Roche, Acceleration of ions in the plasma environment of the Earth by the radiation from a low-frequency transmitter on the ground, *JETP Lett.*, 46, 405, 1987.
- [10] Tanaka, Y., D. Lagoutte, M. Hayakawa, F. Lefeuvre, and S. Tajima, Spectral broadening of VLF transmitter signals and sideband structure observed on AUREOL-3 satellite at middle latitudes, *J. Geophys. Res.*, 92, 7551, 1987.
- [11] Lagoutte, D., F. Lefeuvre, and J. Hanasz, Application of biocoherence analysis in study of wave interaction in space plasma, *J. Geophys. Res.*, 94, 435, 1989.
- [12] Rosenberg, T.J., R.A. Helliwell, and J.P. Katsufakis, Electron precipitation associated with discrete very-low-frequency emissions, *J. Geophys. Res.*, 76, 8445, 1971.
- [13] Helliwell, R.A., S.B. Mende, J.H. Doolittle, W.C. Armstrong, and D.L. Carpenter, Correlations between 4278 optical emissions and VLF wave events observed at L-4 in the Antarctic, *J. Geophys. Res.*, 85, 3376, 1980.
- [14] Imhof, W.L., E.E. Gaines, and J.B. Resgan, Evidence for the resonance precipitation of energetic electrons from the slot region of the radiation belts, *J. Geophys. Res.*, 79, 3141, 1974.
- [15] Vampola, A.L., VLF transmission-induced slot electron precipitation, *Geophys. Res. Lett.*, 4, 569, 1977.

- [16] Imhof, W.L., R.R. Anderson, J.B. Reagan, and E.E. Gaines, The significance of VLF transmitters in the precipitation of inner belt electrons, *J. Geophys. Res.*, **86**, 11225, 1981.
- [17] Imhof, W.L., J.B. Reagan, H.D. Voss, E.E. Gaines, D.W. Datlowe, J. Mobilia, R.A. Helliwell, U.S. Inan, and J.P. Katsufakis, Direct observation of radiation belt electrons precipitated by the controlled injection of VLF signals from a ground-based transmitter, *Geophys. Res. Lett.*, **10**, 361, 1983a.
- [18] Imhof, W.L., J.B. Reagan, H.D. Voss, E.E. Gaines, D.W. Datlowe, J. Mobilia, R.A. Helliwell, U.S. Inan, and J.P. Katsufakis, The modulated precipitation of radiation belt electrons by controlled signals from VLF transmitters, *Geophys. Res. Lett.*, **10**, 615, 1983b.
- [19] Vampola, A.L., Observations of VLF transmitter-induced depletions of inner zone electrons, *Geophys. Res. Lett.*, **10**, 619, 1983.
- [20] Kovrazhkin, R.A., M.M. Mogilevsky, J.M. Bosqued, Y.I. Galperin, N.V. Dzhordzhio, Y.V. Lissakov, O.A. Molchanov and A. Reme, Observation of particle precipitation from the ring-current zone stimulated by powerful ground-based VLF transmitter, *JETP Lett.*, **38**, 397, 1983.
- [21] Kovrazhkin, R.A., M.M. Mogilevsky, O.A. Molchanov, Y.I. Galperin, N.V. Dzhordzhio, Y.V. Lissakov, J.M. Bosquel, H. Reme, Direct detection of the precipitation of ring current electrons and protons stimulated by artificial VLF emission, *Geophys. Res. Lett.*, **11**, 705, 1984.
- [22] Imhof, W.L., T.J. Rosenberg, L.J. Lanzerotti, J.B. Reagan, H.D. Voss, D.W. Datlowe, J.R. Kilner, E.E. Gaines, J. Mobilia, and R.G. Joiner, A coordinated satellite and ground-based study of an intense electron precipitation spike over the southern polar cap, *J. Geophys. Res.*, **10**, 837, 1984.
- [23] Vampola, A.L., Electron precipitation in the vicinity of a VLF transmitter, *J. Geophys. Res.*, **92**, 4525, 1987.
- [24] Vampola, A.L., and G.A. Kuck, Induced precipitations of inner zone electrons, 1, observations, *J. Geophys. Res.*, **83**, 2543, 1978.
- [25] Vampola, A.L., and C.D. Adams, Outer zone electron precipitation produced by a VLF transmitter, *J. Geophys. Res.*, **93**, 1849, 1988.
- [26] Arnoldy, R.L., and P. Kintner, Rocket observations of the precipitation of electrons by ground VLF transmitters, *J. Geophys. Res.*, **94**, 6825, 1989.
- [27] Koons, H.C., Proton precipitation by a whistler-mode wave from a VLF transmitter, *Geophys. Res. Lett.*, **2**, 281, 1975.
- [28] Kennel, C.F., and H.E. Petschek, Limit on stably trapped particles fluxes, *J. Geophys. Res.*, **71**, 1, 1966.
- [29] Pinto, O.Jr., and W.D. Gonzalez, The rule of Landau resonance in energetic electron precipitation from the inner radiation belt, *J. Geophys. Res.*, **94**, 12,027, 1989.
- [30] Shklyar, D.R., Particle interaction with an electrostatic VLF wave in the magnetosphere with an application to proton precipitation, *Planet. Space. Sci.*, **34**, 1091, 1971.
- [31] Dysthe, K.B., Some studies of triggered whistler emissions, *J. Geophys. Res.*, **76** (26), 6915, 1971.



- [32] Inan, U.S., T.F. Bell, and R.A. Helliwell, Nonlinear pitch angle scattering of energetic electrons by coherent VLF waves in the magnetosphere, *J. Geophys. Res.*, **83**, 3235, 1978.
- [33] Chang, H.C., and U.S. Inan, Quasi-relativistic electron precipitation due to interactions with coherent VLF waves in the magnetosphere, *J. Geophys. Res.*, **88**, 318, 1983.
- [34] Beslanov, P.A., and V. Y. Trakhtengerts, Cyclotron instability of earth radiation belts, *Rev. Plasma Phys.*, **10**, 84, 1980.
- [35] Trakhtengerts, V. Y., Alfvén masers in active experiments in space, *Eur. Space Agency Spec. Publ.*, ESA SP 195, 67, 1983.
- [36] Villalon, E., W.J. Burke, P. Rothwell, and M.B. Gilevitch, Quasi-linear wave-particle interactions in the earth's radiation belts, *J. Geophys. Res.*, **94**, 15,243, 1989.
- [37] Tkalcevic, S., U.S. Inan, and R.A. Helliwell, Nonlinear pitch angle scattering and trapping of energetic particles during Landau resonance interactions with whistler mode waves, *J. Geophys. Res.*, **89**, 9857, 1984.
- [38] Helliwell, R.A., J.P. Katsufakis, M. Trimpi, and N. Brice, Artificially stimulated very-low-frequency radiation from the ionosphere, *J. Geophys. Res.*, **69**, 2391, 1964.
- [39] Kimura, I., On observations and theories of the VLF emissions, *Planet. Space Sci.*, **15**, 1427, 1967.
- [40] Matsumoto, H., and Y. Omura, Computer simulation studies of VLF triggered emissions; deformation of distribution function by trapping and detrapping, *J. Geophys. Res.*, **10**, 607, 1983.
- [41] Helliwell, R.A., and J.P. Katsufakis, VLF wave-injection into the magnetosphere from Siple Station, Antarctica, *J. Geophys. Res.*, **79**, 2511, 1974.
- [42] Helliwell, R.A., Controlled stimulation of VLF emissions from Siple Station, Antarctica, *Radio Sci.*, **6**, 801, 1983.
- [43] Helliwell, R.A., Whistlers and related ionospheric phenomena, *Stanford University Press, Stanford, Calif.*, 1965.
- [44] Gendrin, R., Waves and wave-particle interactions in the magnetosphere: a review, *Space Sci. Rev.*, **18**, 145, 1975.
- [45] Matsumoto, H., Nonlinear whistler mode interaction and triggered emissions in the magnetosphere: a review, in *Wave Instabilities in Space Plasma*, edited by P.J. Palmadesso and K. Papadopoulos, *D. Reidel, Pub. Co.*, 163, 1979.
- [46] Omura, Y., and H. Matsumoto, Computer simulations of basic processes of coherent whistler wave-particle interactions in the magnetosphere, *J. Geophys. Res.*, **87**, 4435, 1982.
- [47] Helliwell, R.A., and T.L. Crystal, A feedback model of cyclotron interaction between whistler-mode waves and energetic electrons in the magnetosphere, *J. Geophys. Res.*, **78**, 7357, 1973.
- [48] Helliwell, R.A., and U.S. Inan, VLF wave growth and discrete emission triggering in the magnetosphere: A feedback model, *J. Geophys. Res.*, **87**, 3537, 1982.
- [49] Omura, Y., and H. Matsumoto, Simulation study of frequency variations of VLF triggered emission in a homogeneous field, *J. Geomag. Geoelectr.*, **37**, 829, 1985.

- [50] Nunn, D., A self-consistent theory of triggered VLF emissions, *J. Geophys. Res.*, 22, 349, 1974.
- [51] Nunn, D., The quasi static theory of triggered VLF emissions, *Planet. Space Sci.*, 32, 325, 1984.
- [52] Molvig, K., G. Holfer, R.H. Miller, and J. Myczkowski, Self-consistent theory of triggered whistler emissions, *J. Geophys. Res.*, 93, 5665, 1988.
- [53] Nunn, D., The numerical simulation of VLF nonlinear wave-particle interactions in collision-free plasmas using the VLASOV hybrid simulation technique, *Comput. Phys. Comm.*, to be published.
- [54] Roux, A., and R. Pellat, A theory of triggered emissions, *J. Geophys. Res.*, 83, 1433, 1978.
- [55] Bell, T.F., H.G. James, U.S. Inan, and J.P. Katsufakis, The apparent spectral broadening of VLF transmitter signals during trans-ionospheric propagation, *J. Geophys. Res.*, 88, 4813, 1983.
- [56] Titova, E.E., V.I. Di, V.E. Yurov, O.M. Raspopov, V.Y. Trakhtengertz, F. Jiricek, and P. Triska, Interaction between VLF waves and the turbulent ionosphere, *J. Geophys. Res.*, 11, 323, 1984.
- [57] Titova, E.E., V. Yurov, A. Perlikov, O. Raspopov, V.Y. Trakhtengertz, O. Maltseva, O.A. Molchanov, and Y. Golperin, On the spectral broadening of ground transmitter VLF-signals in the high latitude ionosphere observed from INTERCOSMOS-19 and AUREOL-3 satellites, Results of the ARCAD 3 project and the recent programmes in the magnetospheric and ionospheric physics, *CEPADUES Ed., Toulouse*, 627, 1975.
- [58] Inan, U.S., and T.F. Bell, Spectral broadening of VLF transmitter signals observed on DE-1: A quasi-electrostatic phenomenon?, *J. Geophys. Res.*, 90, 1771, 1985.
- [59] Bell, T.F., and H.D. Ngo, Electrostatic waves stimulated by coherent VLF signals propagating in and near the inner radiation belt, *J. Geophys. Res.*, 93, 2599, 1988.
- [60] Bell, T.F., High amplitude VLF transmitter signals and associated sidebands observed near the magnetic equatorial plane on the ISEE-1 satellite, *J. Geophys. Res.*, 90, 2792, 1985.
- [61] Chmyrev, V.M., M.M. Mogilevsky, O.A. Molchanov, Y.P. Sobolev, E.E. Titova, T.A. Yakhina, R.N. Sunchelev, V.A. Gladyshev, N.V. Baranets, N.V. Dzhordzhio, Y.I. Galperin, and A.V. Streltsov, Parametric excitation of ELF waves and acceleration of ions during the injection of strong VLF waves into the ionosphere, *Kosmicheskie Issledovaniia (Sov. Phys. Space Res.)*, 27, 249, 1989.
- [62] Molchanov, O.A., M.M. Mogilevsky, Y.A. Kopytenko, Non-linear effects of injection of very-low-frequency waves into the magnetosphere, *Adv. Space Res.*, 1, 229, 1981.
- [63] Parrot, M., World map of ELF/VLF emissions observed by a low-orbiting satellite, *Ann. Geophys.*, 8, 135, 1990.
- [64] Bell, T.F., and H.D. Ngo, Electrostatic lower hybrid waves excited by electromagnetic whistler mode waves scattering from planar magnetic-field-aligned plasma density irregularities, *J. Geophys. Res.*, 95, 149, 1990.
- [65] Groves, K.M., M.C. Lee, and S.P. Kuo, Spectral broadening of VLF radio signals traversing the ionosphere, *J. Geophys. Res.*, 93, 14683, 1988.

- [66] Beghin, C., J.F. Karczewski, B. Poirier, R. Debris, and N. Massevitch, The ARCAD-3 ISOPROBE experiment for high time resolution thermal plasma measurements, *Ann. Geophys.*, **33**, 615, 1982.
- [67] Riggin, D., and M.C. Kelley, The possible production of lower hybrid parametric instabilities by VLF ground transmitters and by natural emissions, *J. Geophys. Res.*, **87**, 2545, 1982.
- [68] Lee, M.C., and S.P. Kuo, Production of lower hybrid waves and field-aligned plasma density striations by whistlers, *J. Geophys. Res.*, **89**, 10373, 1984.
- [69] Sotnikov, V.I., V. Fiala, F. Lefevre, D. Lagoutte, and M. Mogilevski, Excitation of sidebands due to non-linear coupling between a VLF transmitter signal and a natural ELF emission, in preparation.

PAPER NO. 26

#### DISCUSSION

U. S. IMAN, US

The irregularities required by the linear mode coupling model can be as small as tens of meters or smaller. Does ARCAD-3 have the time resolution to measure such irregularities?

AUTHOR'S REPLY

Very high resolution measurements are performed by the ISOPROBE experiment embarked on ARCAD-3. There is an operation mode with a time resolution of 1 ms, which means a spatial resolution better than 20 m. Irregularities of the size of tens of meters are found in the light ion trough region (see Beghin et al., *Adv. Space Res.*, **2**, 229, 1985). But they are never observed in the high plasma density region, even at the lowest ARCAD-3 altitude (400 km).

**Causes and effects of interactions between energetic electrons and whistler-mode waves in the coupled magnetosphere-ionosphere-atmosphere system**

M J Rycroft

Head, College of Aeronautics,  
Cranfield Institute of Technology,  
Cranfield,  
Bedford MK43 0AL,  
U.K.

**Summary**

The physical mechanism of a cyclotron resonance interaction between trapped energetic electrons and whistler-mode waves in the magnetosphere is discussed. Not only do the electrons have their pitch angles reduced in this interaction, so that they may be precipitated into the upper atmosphere, but also the waves can be amplified. Such a flux of precipitating electrons can, either by direct ionisation or via bremsstrahlung radiation, cause a pulse to be produced on the bottom of the ionosphere. That can significantly modify the amplitude and/or phase of very low frequency radio signals propagating in the Earth-ionosphere waveguide. Various experimental observations that demonstrate the reality of such effects are presented.

**1. Background**

Cornwall (1964) and Dungey (1963) considered theoretically the interaction between whistler-mode (electromagnetic) waves and energetic electrons trapped in the Earth's magnetosphere, the van Allen radiation belts. Price (1964), in a paper full of physical insight, discussed the energetics of this cyclotron resonance interaction. He showed that the whistler-mode waves can be amplified considerably by taking a little energy from the transverse motion of the electrons. This reduces the pitch angles of the electrons, such that some of them might be lost from the radiation belts and precipitated into the upper atmosphere.

Electromagnetic waves in the ELF (< 3 kHz) and VLF (3 to 30 kHz) bands are radiated by man-made transmitters and by lightning. These radio signals - and atmospheric (or spherics for short) - propagate several thousand km in the Earth-ionosphere waveguide. They can also penetrate the lower ionosphere to propagate in the whistler-mode along geomagnetic field-aligned ducts of enhanced plasma density, from one hemisphere to the other. As they propagate through the magnetosphere, they are dispersed. This accounts for the characteristic curved dynamic spectrum (frequency vs time) of a natural whistler. The dispersion is used to find the electron density in the equatorial plane (Park 1972; Tarceal et al., 1989).

**2. Cyclotron resonance interactions between energetic electrons and whistler-mode waves.**

Energetic electrons, gyrating about geomagnetic field lines, bouncing back and forth from one hemisphere to the other, and drifting eastwards in longitude (Hess, 1968), can interact with whistler-mode waves. This wave-particle interaction is explained by a cyclotron resonance interaction, in which the waves are amplified (perhaps by 30 dB, Melliwell 1983); simultaneously, the electrons have their pitch angles reduced. The equatorial plane is generally a preferred interaction region since there waves will resonate with the lowest energy electrons (Rycroft, 1979; Goldberg et al., 1987).

Rycroft (1973) presented the first direct experimental evidence for such an interaction. Fig.1 shows even-numbered whistlers, recorded on the ground at South Uist, Scotland, and a burst of electrons of >45 keV recorded aboard a rocket launched from South Uist. The interaction occurs on the L=3.3 field line. (The L shell of a geomagnetic field line is approximately the distance from the centre of the Earth at which the field line crosses the equatorial plane, measured in Earth radii.)

Fig.2 shows diagrammatically the interpretation of this observation in terms of a half hop whistler interacting in the equatorial plane, causing the pitch angle of > 45 keV electrons to be decreased such that they are precipitated over South Uist. In the process, the half hop whistler is amplified, is reflected in the southern hemisphere and received at South Uist as a two hop whistler; further multiple even hop whistlers are evident. The gyroresonance condition in the equatorial plane is, for a dipole representation of the geomagnetic field (Rycroft 1974, 1976), with  $W$  in keV,  $N$  in  $\text{cm}^{-3}$  and wave frequency and cyclotron frequency ( $f$  and  $f_{ce}$ ) in kHz,

$$W/N_{eq} = 3.16 (f_{ce} - f)^2 / f \text{ keV cm}^{-3}.$$

This relation is shown graphically in Fig. 3 taken from Mergaueves (1979). Fig. 3 shows  $W_{eq}$  as a function of L-value for different wave frequencies  $f$ . With the model equatorial plane plasma distribution given in Fig. 3b, for either normal or magnetically disturbed conditions,  $W_{eq}$  is found as a function of L-value and shown in Fig. 3c at a wave frequency  $f = 3$  kHz. Considering that the whistler shown in Fig. 1 interacted at 3 kHz on the  $L = 3.3$  flux tube, with an equatorial plane electron density of  $330 \text{ cm}^{-3}$ ,  $W_{eq} = 25 \text{ keV}$ . Alternatively, at 1 kHz,  $W_{eq} = 100 \text{ keV}$ . The highest energy electrons are precipitated either just outside the plasmapause or in the inner magnetosphere.

Fig. 4 shows that electrons of 25 keV penetrate down through the upper atmosphere reaching 83 km altitude (Thorne, 1977), whereas 100 keV electrons reach down further, to 75 km. There they can create extra ionisation, making a pimple on the bottom of the ionosphere. Alternatively, they produce bremsstrahlung radiation which penetrates deeper into the middle atmosphere before producing ionisation.

The gyroresonance interaction has been generalised by Resh et al. (1984). Fig. 5b shows essentially the same physical situation as Fig. 2, but with the lightning in the South and the wave receiver in the southern hemisphere rather than in the North. Fig. 5a shows the situation for a southern observer in which the gyroresonant and pitch angle scattered electrons are reflected in the northern hemisphere, where the magnetic mirror field strength is greater, and precipitated in the southern hemisphere, in association with whistler-mode waves from a lightning discharge in the North that have propagated a half hop after the gyroresonant interaction.

Resh et al. (1984) provide useful results on the difference in arrival time between the whistler mode waves and the energetic electrons for these two cases occurring on the  $L = 4$  flux tube. Fig. 6 shows the travel time difference  $\Delta t$ , a positive value of which indicates that the whistler-mode waves arrive earlier than the electrons, for different densities in the equatorial plane at  $L = 4$ . On the left a diffusive equilibrium plasma distribution model for the plasmasphere is assumed, whereas on the right an  $L^{-4}$  distribution is taken: a) and b) are as in Fig. 5a) and b). The main result is that the waves and the electrons will arrive essentially simultaneously at a certain frequency which for a) is near 1 or 2 kHz, but for b) is near 7 or 8 kHz. Gyroresonance at frequencies other than these will give a time delay between the electrons and waves that have interacted, such that a time difference of the order of a few seconds may be interpreted to give the gyroresonance energy,  $W_{eq}$ , if the equatorial plane electron density,  $N_{eq}$ , is known from whistlers.

### 3. Recent observational evidence of cyclotron resonance interactions in the magnetosphere

A manifestation of the precipitation of energetic electrons by whistlers is the so-called Trimpl effect (Inan and Carpenter, 1967). A lightning flash in the North (see Fig. 7a) is ducted through the magnetosphere (see Fig. 7b) and precipitates electrons in the North and South. Such a localised precipitation region changes the mode structure for VLF waves propagating in the Earth-ionosphere waveguide. Signals from a transmitter  $T_1$  to a receiver  $R_1$ , or from  $T_2$  to  $R_2$ , would be affected, whereas those from  $T_2$  to  $R_1$  would not. Such Trimpl effects are made manifest as changes in the amplitude and/or the phase of VLF signals from transmitters on the Earth's surface that are received at other ground stations. Such effects have been modelled by Tolstoy et al. (1986).

Fig. 8 considers the situation with the VLF transmitter at Siple, Antarctica, transmitting at 3.79 kHz on 15 July 1982. Signals propagate in the Earth-ionosphere waveguide to Halley at  $L=4.3$ . Signals propagating a similar distance either to Palmer or South Pole cross L-shells. The amplitude of the Siple signal received at Halley, shown in Fig. 9b, increases at 1930:35 UT, about 2 seconds after a whistler (whose spectrogram is shown in Fig. 9d) was received at Halley (Hurren et al., 1986). This explains the increased amplitude of the natural 0.5 to 2.5 kHz signal at Halley (Fig. 9c). The recovery time after the transient ( $\sim 10$ s, as is evident in Fig. 9b) is typical for the D region.

Inan et al. (1988a) have investigated Trimpl events at lower L-shells between 1.8 and  $\sim 3$ , caused by more energetic electrons ( $\sim \text{MeV}$ ). They have also considered the geographic variation of Trimpl events, explaining them in terms of preferred precipitation on the western edge of the region conjugate to the South Atlantic Geomagnetic Anomaly. This effect is illustrated in Fig. 10, due to Sheldon et al. (1988), in which the equatorial pitch angle,  $\theta_{eq}$ , of electrons is plotted against longitude. As electrons drift eastwards, they are preferentially precipitated at geographic longitudes between  $270^\circ$  and  $360^\circ$  E.

Inan et al. (1988 b) present further evidence for whistler-electron interactions near  $L=1.8$ , having located the positions of the causative cloud-to-ground lightning discharges, as shown in Fig. 11 by crosses. These are close to the great circle path of the diagnostic VLF transmitter signal at 28.5 kHz, and near its mid-point. The initial recovery time is only  $\sim 1$ s, indicating more energetic ( $\sim \text{MeV}$ ) precipitation to deeper into the denser atmosphere, followed by recovery on a 10s time scale.

Ionisation profiles and amplitudes of the diagnostic VLF transmitter signal have been successfully modelled (see Fig. 12) at different L-shells. Profiles are shown at the time of the precipitating electron burst ( $t=0$ ), and at 1, 5, 20 and 100 seconds thereafter.

#### 4. Effects related to whistlers

LeSalle (1988a) has considered violet light flashes lasting a millisecond from the upper atmosphere at  $L=1.6$  as being due to lightning in the conjugate region triggering precipitation of  $\sim 1$  MeV electrons from the inner radiation belt. Short duration bursts of precipitating energetic electrons have been observed at  $L=2.2$  by Voss et al. (1984). Successive bursts correspond to the bouncing motion (period  $\sim 0.4$  seconds) of a bunch of electrons. Vampola (1988) has argued against this interpretation based on an interaction in the equatorial plane, using concepts discussed by Reah et al. (1984) amongst others. LeSalle (1988b) counters this criticism by suggesting that lightning from the southern hemisphere causes a wave-particle interaction in the northern topside ionosphere and then the millisecond light flash.

Voss et al. (1984) presented satellite observations of bursts of electrons  $>100$  keV (upper curve in Fig. 13, for trapped electrons) and  $>45$  keV (lower curve in Fig. 13, for precipitating electrons) near  $L=2.3$ . Simultaneously with this, whistlers were received at Palmer Station, Antarctica, also at  $L=2.3$ . These satellite/ground observations confirmed the rocket/ground data obtained by Rycroft (1973) one solar cycle earlier.

Such satellite data show bursts of electrons bouncing back and forth between the northern and southern hemispheres. These occur just after a whistler, and the precipitating energetic electrons cause a pimple on the bottomside ionosphere which explains the Trimpf effect observed.

Lohrey and Kaiser (1979) and Dowden and Adams (1988 a,b) received at Dunedin, in New Zealand, 22.3 kHz radio signals from North West Cape (NWC) in Australia, 5750 km away. They explain some Trimpf events as slight departures from great circle propagation in the Earth-ionosphere waveguide, and then forward scatter, with a characteristic polar diagram, from the pimple. This weak scattered signal interferes with the great circle path signal, which leads to both increases and decreases of amplitude and phase.

The interference between the direct and pimple-scattered signals is shown in another way in Fig. 14, E being the phasor of the direct signal and e that of the scattered signal. Because the latter may have any phase with respect to the former, its tip traces out a circle.

Fig. 15 shows two nighttime Trimpf events, A and B, with very different amplitude and phase characteristics, as expected from this phasor model. Systematic changes over the night indicate that the precipitation region drifts polewards by about 4 km/hour.

A model for the pimple has been constructed, as a two-dimensional Gaussian height perturbation on the bottom of the ionosphere. This was placed 1200 km from Dunedin. It causes amplitude and phase perturbations of the right size, their sign depending on the pimple's lateral displacement from the great circle path;  $+$  indicates a range of displacements for which the phase change is positive and the amplitude change is negative, etc. There is some indication that a perturbation region stretched along an L-shell may be better at explaining the results than a region of circular cross section.

Armstrong (1987) has made the case that one whistler triggers another about 5 seconds later. How could this be? A possible mechanism, illustrated in Fig. 16, is (1) that a northern hemisphere lightning discharge (2) launches whistler-mode waves into the magnetosphere, (3) electrons cyclotron resonate with the wave, and have their pitch angles reduced, (4) the one hop whistler is reflected in the South and the bunch of electrons which interacted near the northern atmosphere, and (5) they create ionisation in the atmosphere. This could reduce the resistance of the air column above the thundercloud, causing a lightning discharge to the ionosphere when the two hop whistler is received (Rycroft, 1987). This triggered lightning discharge then produces more whistlers.

Armstrong (1987) has published the spectrogram (see Fig. 17) of a whistler W which generates echoes with a 4 second periodicity and which evolve into bursts of almost constant frequency.  $T_2$  triggers whistler  $W_2$  at the same time as emission  $E_2$  (not labelled). There is a 1 second delay associated with the triggering process.

### 5. Closing Remarks

Attention has been concentrated here on the effects of electron precipitation triggered by impulsive lightning, a powerful source of broad-band whistler-mode radiation. A man-made ELF/VLF radio transmitter (Koons et al., 1981; Vampola, 1983) or power line harmonic radiation (Tatnell et al., 1983; Bullough, 1988) each producing narrow-band whistler mode radiation could cause the precipitation of energetic electrons. It is not yet clear whether a natural whistler is more, or less, effective than a short (or long) pulse of narrow-band whistler-mode radiation, of constant frequency, or of slowly changing frequency. Neither is it known whether a man-made pulse of ELF (though not VLF, from energy considerations) whistler-mode radiation could cause >100 keV electron precipitation to generate energetic bremsstrahlung radiation or avalanche effects above a thundercloud and trigger a lightning discharge to the ionosphere. (D'Angelo (1987) has considered bremsstrahlung X-ray generation in the atmosphere from >100 keV electrons produced by lightning.) Also, natural whistler-mode radiation termed chorus (Olliver and Gurnett, 1968) can cause energetic electron precipitation effects (Rosenberg et al., 1971). Clark and Smith (1990) have reported the Trimpf effect caused by quasi-periodic VLF emissions. Thus there is scope for further experimental studies as well as for theoretical and numerical modelling investigations.

### References

- Armstrong, W.C. 1987. *Nature* **327**, 405.  
 Brice, N.M. 1964. *Journal of Geophysical Research*, **69**, 4515.  
 Bullough, K. 1988. Proceedings of the International Symposium at Wroclaw, Poland, on Electromagnetic Compatibility.  
 Clark, T.D.G. and Smith, A.J. 1990. *Journal of Atmospheric and Terrestrial Physics*, in press.  
 Cornwell, J.M. 1964. *Journal of Geophysical Research*, **69**, 125.  
 D'Angelo, N. *Annales Geophysicae*, **82**, 119.  
 Dowden, R.L. and Adams, C.D.D. 1988 a. *Journal of Geophysical Research*, **93**, 11543.  
 Dowden, R.L. and Adams, C.D.D. 1988 b. *Journal of Geophysical Research*, **93**, 11543.  
 Duney, J.W. 1963. *Planet Space Science*, **11**, 391.  
 Goldberg, R.A., Curtis, S.A. and Barcus, J.R. 1987. *Journal of Geophysical Research*, **92**, 2505.  
 Hargreaves, J.K. 1979. *The Upper Atmosphere and Solar-Terrestrial Relations*, Van Nostrand Reinhold Company.  
 Helliwell, R.A. 1983. *Radio Science*, **18**, 801.  
 Hess, W.N. 1968. *The Radiation Belt and Magnetosphere*, Blaisdell.  
 Murrin, P.J., Smith, A.J., Carpenter, D.L. and Inan U.S. 1986. *Annales Geophysicae*, **4**, 311.  
 Inan, U.S. and Carpenter, D.L. 1987. *Journal of Geophysical Research*, **92**, 3293.  
 Inan, U.S., Burgess, Wolf, Shefer, Orville, 1988a. *Geophysical Research Letters* **15**, 172.  
 Inan, U.S., Wolf, Carpenter 1988b. *Journal of Geophysical Research*, **93**, 9841.  
 Koons, H.C., Edgar, B.C. and Vampola A.L. *Journal of Geophysical Research*, **88**, 640.  
 LaBelle, J. 1988 a. *Geophysical Research Letters*, **15**, 279.  
 LaBelle, J. 1988 b. *Geophysical Research Letters*, **15**, 279.  
 Lohrey, B. and Kaiser A.B. 1979. *Journal of Geophysical Research*, **84**, 5122.  
 Olliver and Gurnett, D.A. 1968. *Journal of Geophysical Research* **73**, 2355.  
 Park, C. 1972. Stanford University Technical Report 34454-1.  
 Rish, J.P.S., Scourfield, M.W.J. and Dougherty M.K. 1984. *South African Journal of Physics*, **2**, 116.  
 Rosenberg, T.J., Helliwell R.A. and Katsufakis, J.P. 1971. *Journal of Geophysical Research*, **76**, 8445.  
 Rycroft, M.J. 1973. *Planet Space Science*, **21**, 239.  
 Rycroft, M.J. 1974. *ELF-VLF Radio Wave Propagation*, ed. J. Holtet, 317.  
 Rycroft, M.J. 1976. *Journal of Atmospheric and Terrestrial Physics*, **38**, 1211.  
 Rycroft, M.J. 1987. *Nature* **327**, 368.  
 Sheldon, W.R. et al. 1988. *Journal of Atmospheric and Terrestrial Physics*, **50**, 1019.  
 Tarsel, Gy. et. a. 1989. *Journal of Atmospheric and Terrestrial Physics*, **51**, 249.  
 Tatnell, A.R.L. Matthews, J.P. Bullough K. and Kaiser, T.R. 1983. *Space Science Reviews*, **35**, 139.  
 Thorne, R.M. 1977. *Science*, **195**, 287.  
 Tointoy, A., Rosenberg, T.J., Inan, U.S. and Carpenter D.L. 1986. *Journal of Geophysical Research*, **91**, 13473.  
 Vampola, A.L. 1983. *Geophysical Research Letters*, **10**, 619.  
 Vampola, A.L. 1988. *Geophysical Research Letters*, **15**, 633.  
 Voss, H. et al. 1984. *Nature* **312**, 740.

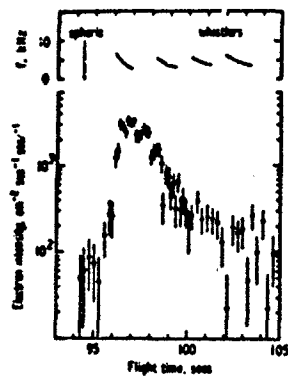


Fig. 1. Diagram showing the intensity of precipitating electrons of  $>45$  keV observed near 100km altitude at the time of some even-numbered hop whistlers (from Rycroft, 1973).

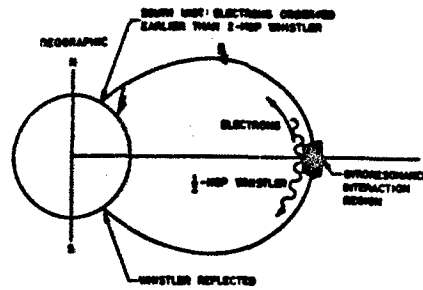


Fig. 2. Diagram illustrating the gyroresonance interaction in the equatorial plane between energetic electrons and a half hop whistler (from Rycroft, 1973).

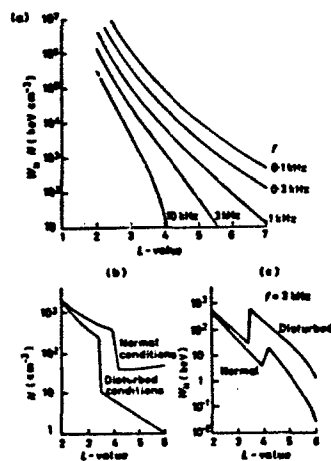


Fig. 3. (a) Plot of  $W_e N$  (see text) versus L-value for a gyroresonance interaction in the equatorial plane. (b) Model plasmaspheric electron density distribution. (c) Derived parallel energy of gyroresonant electrons (from Hargreaves, 1979).

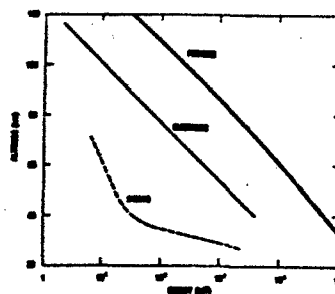


Fig. 4. Plot of altitude reached by precipitating protons, electrons and X-rays of different energies (from Thorne, 1977).



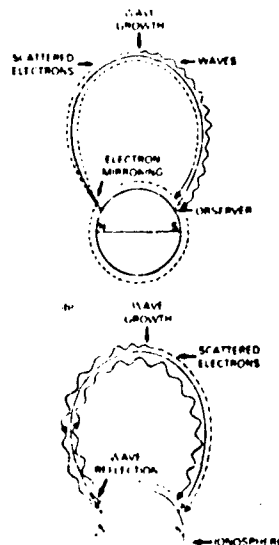


Fig. 5. Diagram similar to Fig. 2, but with the whistler receiver in the southern hemisphere - see text (from Rash et al., 1984). In (a) the lightning discharge is in the North and in (b) it is in the South.

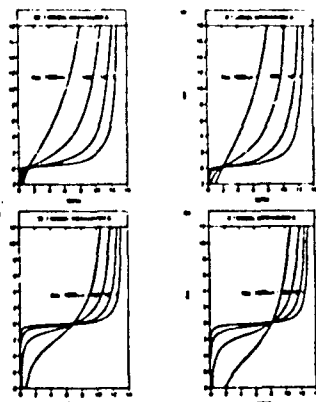


Fig. 6. Differences in arrival time,  $\Delta t$ , for whistlers and energetic electrons that have undergone a gyroresonant interaction in the equatorial plane (where the electron density is  $N_{eq}$ ) at  $L=6$ , for different values of the whistler wave frequency  $f$ . (a) or A and (b) or B refer, respectively, to (a) and (b) in Fig. 5 (from Rash et al., 1984).

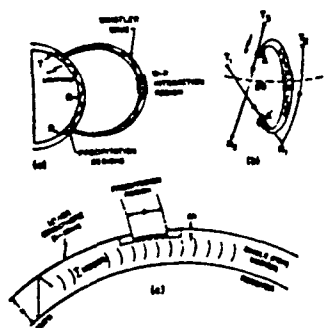


Fig. 7. Diagram from Inan and Carpenter (1987), showing (a) a diagram similar to Fig. 2, and also showing the signal from a VLF transmitter T in the North propagating to a receiver R in the South, (b) a perspective diagram showing precipitation at A' causing a Trimpl event on the signal from T, to R, and (c) a diagram showing how the waveguide propagation is perturbed by a precipitation region of size d.

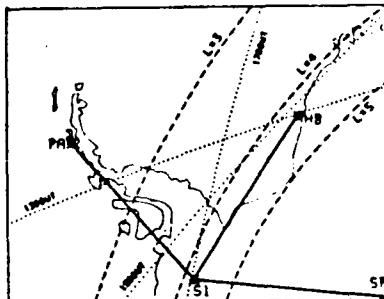


Fig. 8. Map, from Hurren et al. (1986), showing propagation of a VLF signal from the Siple transmitter parallel to L-shells to Halley Bay (HB), and across L-shells either to South Pole (SP) or to Palmer (PA).

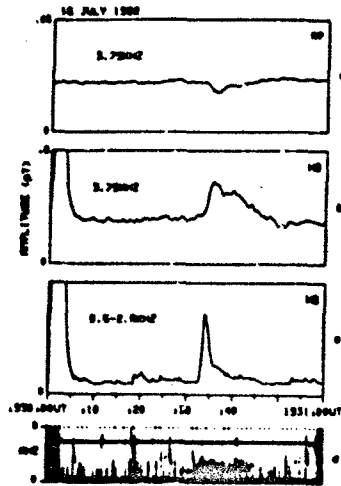


Fig. 9. Amplified Siple transmitter signal at 3.79 kHz received at (a) South Pole and (b) Halley Bay. A scintillation at 1930:33UT on 15 July 1982, evident on the spectrogram (d), causes not only the enhanced 0.5-2.5 kHz signal recorded at Halley Bay but also the Trimpl event evident in (b) at 1930:35UT (from Murren et al., 1986).

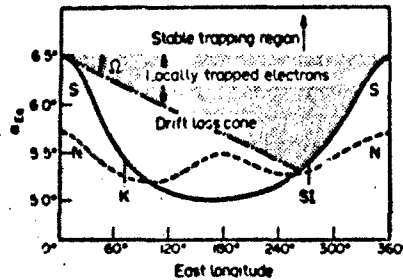


Fig. 10. Diagram illustrating the longitudinal variation of the loss cone pitch angle in the equatorial plane,  $\theta_{eq}$ . Electrons drifting eastwards at  $L=4$  are preferentially precipitate from 270°E to 360°E geographic, in the southern hemisphere (from Sheldon et al., 1988).

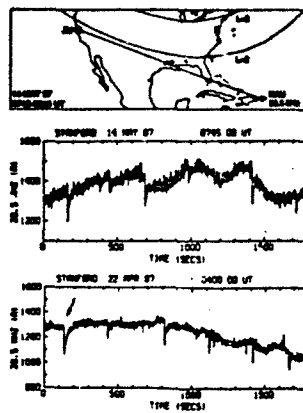


Fig. 11. Diagram illustrating Trimpl events at  $L=1.8$  observed on the Puerto Rico to Stanford University path on two days in 1987 (from Inan et al., 1988b).

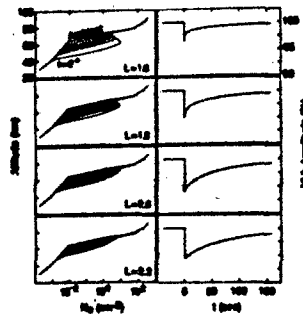


Fig. 12. Modelled D region profiles (left) and Trimpl event signatures (right) at different  $L$  values and times after a burst of precipitating electrons - see text (from Inan et al., 1988b).

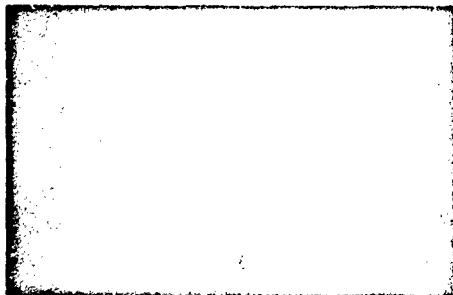


Fig. 13. Observations by Voss et al. (1984) of bursts of electrons associated with whistlers observed at Palmer - see text.

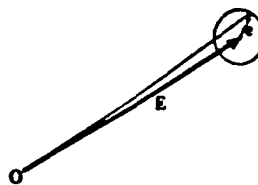


Fig. 14. Diagram, from Dowden and Adams (1988a) illustrating the change, in amplitude and phase, of a waveguide signal (E) due to scattering from a pimple on the bottom of the ionosphere (a).

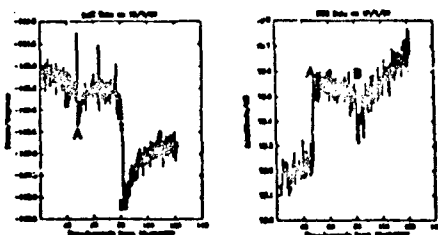


Fig. 15. Phase (left) and amplitude (R) of waveguide signals from MWC in Australia received at Dunedin, New Zealand, associated with Trimpl events (from Dowden and Adams, 1988a).

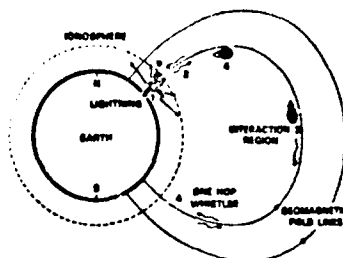


Fig. 16. Diagram, from Rycroft (1987) illustrating how precipitating energetic electrons due to a gyroresonant interaction with a half hop whistler may trigger an upward propagating lightning discharge.

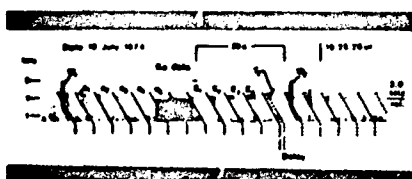


Fig. 17. Experimental evidence, from Armstrong (1987), for one whistler triggering another.

PAPER NO. 27

## DISCUSSION

L. DUNCAN, US

I have a question regarding the suggested feedback process by which lightning produces ducted VLF whistlers which in turn induces particle precipitation or directly interacts with the lower ionosphere, which then may trigger a subsequent lightning event. If I understood correctly, the lightning source needs only to be within about 1000 km of the duct insertion location. The subsequent ionospheric disturbance, either from the one-hop VLF or precipitating particles, is rather small, on the order of 50 km or less, and may be far removed from the initiating lightning storm. Thus one would expect such feedback events to be quite rare, and at least from this simplistic model, an unlikely explanation for the frontal chain of lightning events mentioned by Dr. Banks.

## AUTHOR'S REPLY

It is generally believed that the lightning needs to be within 1000 km or so of the magnetospheric duct for whistler excitation. Also, the perturbed region is likely to be of the order of only 50 km. For these reasons and, perhaps, others too, such feedback events are extremely rare. I believe that more experiments are needed above thunderclouds when the whistler propagation path is along a geomagnetic flux tube whose ionospheric footprint is above the thundercloud.

P. M. BANKS, US

Paul Weitz, a Space Shuttle pilot, has reported visual sightings of multiple lightning discharges over distances of several hundred kilometers. Could this be related to the progressive precipitation of energetic particles and stimulation of subsequent discharges?

## AUTHOR'S REPLY

You have made a most interesting suggestion. My initial reaction is that could be the explanation if the interval between the discharges were a few seconds, and if the magnetic latitude of the phenomena were appropriate for very energetic electron precipitation. However, the explanation may also lie in the natural progression of discharges from different charge centers within a thundercloud.

P. KOSSEY, US

Might some of the observations be attributed to VLF heating of the D-region, leading to changes in the effective recombination rate, and hence  $\Delta N_e$  effects?

## AUTHOR'S REPLY

See reply by Inan.

U. S. INAN, US (In response to a question by Paul Kossey.)

There are basically two classes of ionospheric disturbances associated with lightning discharges. The larger class of events exhibit a distinct delay of a fraction of a second between the signature of lightning and the onset of the ionospheric disturbance event. In such cases, the whistler-induced precipitation mechanism is consistent. In a smaller set of events, the ionospheric disturbance appears to occur within few tens of ns of the lightning discharge. Such events could very well be due to heating of the lower ionosphere, as suggested in my paper in the May 1990 issue of GRL. At this meeting, I also learned that  $\Delta n$  can result due to  $\Delta \nu$  resulting from heating. This, I believe, means that the lightning associated events in the latter category can be explained as a consequence of heating of the lower ionosphere by lightning discharges.

## AUTHOR'S REPLY

No reply needed.

# IONOSPHERIC HEATING FOR RADIATION BELT CONTROL\*

William J. Burke

Geophysics Laboratory  
Hanscom AFB, MA 01731

Klena Villalon

Northeastern University  
Boston, MA 02115

## SUMMARY

Pitch-angle scattering interactions of electromagnetic waves in the ELF/VLF bands with trapped electrons, as formulated by Kennel and Petschek [1], describe the dynamics of the freshly filled radiation belts flux tubes. The natural existence of a "slot" region with electron fluxes below the Kennel-Petschek limit requires non-local wave sources. We describe a set of planned, active experiments in which VLF radiation will be injected from ground and space based transmitters in conjunction with the CROES satellite in the radiation belts. These experiments will measure the intensity of waves driving pitch-angle diffusion and the electron energies in gyroresonance with the waves. An ability to reduce the flux of energetic particles trapped in the radiation belts by artificial means could improve the reliability of microelectronic components on earth-observing satellites in middle-altitude orbits.

## LIST OF SYMBOLS

$B$	Magnetic Field
$c$	Speed of Light
$E_{0,i}$	Resonant Energy for Electrons, Ions
$E_A$	Magnetic Energy per Particle
$k$	Wave Vector
$L$	Magnetic Shell Number
$m_{e,i}$	Mass of Electrons, Ions
$n$	Plasma Density
$N$	Harmonic Number
$\epsilon_0$	Permittivity of Free Space
$\mu_0$	Permeability of Free Space
$\omega$	Wave Frequency
$\omega_{UH}$	Lower Hybrid Frequency
$\omega_{pe}$	Electron Plasma Frequency
$\Omega_{ce,i}$	Electron, Ion Cyclotron Frequency

## INTRODUCTION

One of space physics major success stories of the 1960's was the development of the theory of pitch-angle scattering of energetic electrons trapped in the earth's radiation belts by ELF/VLF radiation [1]. This theoretical model postulates that energetic electrons moving along magnetic field lines near the equatorial plane of the magnetosphere see low-frequency waves Doppler shifted to their local gyrofrequencies. In consequence, gyroresonant interactions particles diffuse in pitch angle along surfaces of constant phase velocity. Particles diffusing toward the loss cone give up small amounts of energy to wave growth. The model is self consistent in the sense that waves responsible for pitch-angle scattering grow from background fluctuation levels due to the free energy contained in the anisotropic pitch-angle distributions of trapped particles. If the anisotropy of the trapped distribution falls below a critical level growth ceases.

During magnetic storms the radiation belts fill up with trapped, energetic particles from about  $L = 8$  to  $L = 1.5$ . In the weeks following storms the flux of trapped electrons in the slot between  $L = 2$  to  $L = 3.5$  fall to the thresholds of detector sensitivity, well below the stable trapping limit of Kennel and Petschek. Trapped protons do not show slot-like distributions. Lyons and coworkers [2] recognized that waves responsible for the pitch-angle scattering of slot electrons need not grow self consistently from background fluctuation levels. Rather, they can be injected from non-local sources and still pitch-angle scatter trapped electrons into the atmospheric loss cone.

The sources of ELF/VLF waves are multiple and their relative importance for magnetospheric particle distributions is the subject of an ongoing research. The waves envisaged by Kennel and Potchek arise naturally out of background fluctuations by selective amplification. Atmospheric lightning produces broad-band ELF/VLF emissions. Part of the radiation propagates in the earth-ionosphere waveguide and part accesses the magnetosphere in field-aligned ducts. Studies of lightning induced precipitation abound in the literature [3 - 5]. The Stanford group has pioneered techniques for monitoring lightning induced dumping of the radiation belts using the SUNY Albany network.

Another major source of VLF is man-made radiation. The Stanford group has made numerous studies of magnetospheric effects of ELF/VLF transmissions from the Siple station in Antarctica to magnetic conjugate points in Canada [7]. The intensities of waves emitted from Siple have been measured directly by the wave detector experiment on satellites near the equatorial plane of the magnetosphere [8]. A series of successful experiments were conducted in the early 1980's in which time-coded VLF emissions from US Navy transmitters were compared with electron precipitation events simultaneously detected by the SEEP satellite [9]. Vampola [10] investigated the effects of a powerful VLF transmitter at Gorky on radiation belt electrons and suggested that it maintains the inner reaches of the slot.

The purpose of this paper is to describe a group of active experiments that will be conducted by Geophysics Laboratory scientists after the launch of the CRRES satellite this summer. In these experiments, low-frequency waves will be injected into the magnetosphere by several different methods. Instrumentation on CRRES will monitor: (1) the intensity and interactions of the injected waves, and (2) the dynamics of electrons and protons near the loss cone. The object of these experiments is to establish the feasibility of using active techniques to control the fluxes of energetic particles in the slot. A human ability to accelerate or maintain slot depletion would allow earth observing satellites to fly in orbits now considered too hazardous [11]. Space Based Radar would profit from this capability [12].

In the following sections we first review criteria for pitch-angle scattering trapped particles. After summarizing the capabilities of CRRES instrumentation for measuring wave-particle interactions, we describe three methods of wave injection using ground-based VLF and HF transmitters, and VLF transmissions from the Soviet ACTIVE satellite.

#### WAVE-PARTICLE INTERACTIONS

To understand slot dynamics it is necessary to consider whistler mode propagation in the radiation belts and its interactions with energetic particles. The waves of interest are in the ELF-VLF (0.3-30 kHz) bands. Two empirical facts are used in our simple models: (a) The earth's magnetic field  $B$  is approximately dipolar, and at the magnetic equator is given by

$$(1) \quad B(\text{mT}) = 3.1 \cdot 10^4 \cdot L^{-3}$$

where  $L$  is the standard magnetic shell number. (b) The background plasma is dominated by cold particles whose density is approximated [13]

$$(2) \quad n(\text{cm}^{-3}) = 3 \cdot 10^3 \cdot (2/L)^4$$

The high-energy particles have densities that are  $< 1 \text{ cm}^{-3}$ . Thus, wave propagation is well described in the magnetized, cold plasma limit. The whistler wave is a right hand mode that propagates along the magnetic field if its frequency  $\omega$  is less than the electron cyclotron  $\Omega_{ce}$  and greater than the lower-hybrid  $\omega_{LH}$  frequencies at all points.

As illustrated in Figure 1, whistler waves in the radiation belts in two distinct modes called ducted and unducted [14]. Ducted waves propagate along magnetic field-aligned plasma irregularities as in waveguides. Waves injected into a duct can propagate from one hemisphere to its conjugate and back many times [15]. Unducted waves observed in the magnetosphere never make it to the ground. Ray-tracing studies [16] show that as the waves propagate away from the equatorial region the contributions of ions to the dielectric coefficient grow in importance. As unducted waves propagate to locations along magnetic field lines where their frequencies approach  $\omega_{LH}$  their wave vectors turn and reflect back toward the equator. The process is analogous to total internal reflection at optical frequencies. Not being confined to propagate in a single magnetic shell these waves suffuse throughout the plasmasphere as a broadband hiss.

For waves and particles to interact strongly they must satisfy a resonance condition

$$(3) \quad \omega - kv + N\Omega_{ce,i} = 0$$

where  $N$  is an integer,  $v$  the component of particle motion along the magnetic field,  $\omega$  and  $k$  are the wave frequency (in radians per second) and the wave vector. In the nonrelativistic limit the cyclotron frequency for electrons (e) and ions (i) is  $\Omega_{ce,i} = |e|B/m_{ce,i}$  where  $e$  represents the elemental unit of charge,  $B$  the magnetic field and  $m$  the mass of an electron or ion. A particle must see the wave Doppler-shifted in to some harmonic of its gyrofrequency. Figure 2 depicts whistler interactions with electrons and protons. Electron interactions occur at the  $N = -1, -2, \dots$  harmonics and require that they travel in opposite directions to the waves. Proton interactions occur for positive values of  $N$  with the protons traveling in the same direction and overtaking the waves.

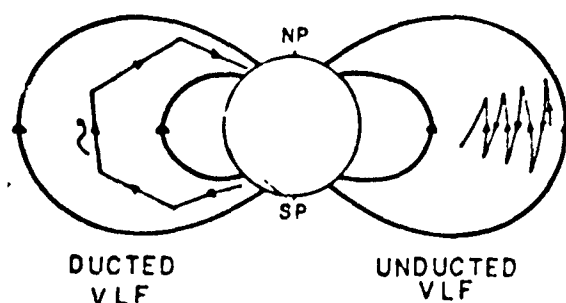


Fig. 1. Ducted and unducted whistler waves in the magnetosphere.

The dispersion relation for whistler waves propagating along the magnetic field near the equatorial plane is approximately

$$(4) \quad \frac{c^2 k^2}{\omega^2} = \frac{\omega_{pe}^2}{\omega(\Omega_{ce} - \omega)}$$

where  $\omega_{pe} = [n e^2 / m_e \epsilon_0]^{1/2}$  is the electron plasma frequency and  $\epsilon_0$  is the permittivity of free space. Combining equations (3) and (4) shows that the energy of resonant electrons is

$$(5) \quad E_e = E_A N^2 \left[ \frac{\Omega_{ce}}{\omega} \right] \left[ 1 - \frac{\omega}{\Omega_{ce}} \right] \left[ 1 + \frac{\omega}{N \Omega_{ce}} \right]^2$$

For protons the resonant energy is

$$(6) \quad E_p = E_A N^2 \left[ \frac{\Omega_{ci}}{\omega} \right] \left[ 1 - \frac{\omega}{\Omega_{ci}} \right] \left[ 1 + \frac{\omega}{N \Omega_{ci}} \right]^2$$

where  $E_A = 3^2 / 2 \mu_0 n$  is the magnetic energy per particle and  $\mu_0$  is the permeability of free space. In planning active experiments in the radiation belts we estimate  $E_A$  using the dipolar magnetic fields and the cold plasma densities given in equations (1) and (2). To study pitch-angle scattering in a given energy range the only free parameters that remain are the wave frequency and the resonance harmonic number  $N$ .

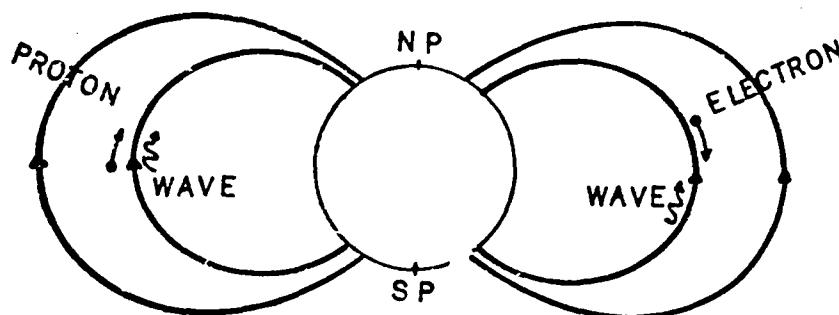


Fig. 2. Resonant interactions of whistlers with protons and electrons.

## CRRES INSTRUMENTATION

CRRES (Combined Release Radiation Effects Satellite) is scheduled to be launched in June 1990 into a 17° inclination, geostationary transfer orbit. As its name suggests, CRRES has two mission objectives: to study the effects of chemical releases at high altitudes, and to understand the interactions of advanced microelectronics components with natural radiation environments. Detailed descriptions of the comprehensive scientific payload on CRRES have been compiled by Gussenhoven and coworkers [17]. For the studies discussed below three instruments are germane and are described briefly. These are the Low Energy Plasma Analyser (LEPA), the Plasma Wave Experiment and a Langmuir Probe.

The LEPA experiment was designed to measure the three dimensional distribution function of ions and electrons with energies between 10 eV and 30 keV. The particle distribution functions are measured by two 260° spherical electrostatic analyzers. Each sensor consists of two concentric spherical plates. On one edge the space between the plates is closed off except for a 5.6° by 128° aperture. A microchannel plate is placed at the other edge. The energy analysis is achieved by changing the electrostatic potential between the plates. The instrument focusing is such that particle pitch angles are imaged on the microchannel plate to an accuracy of better than 1 degree. The particle positions are divided into sixteen 80 bin can be resolved into eight 1° zones. Because the limited telemetry does not allow the full data set to be transmitted to ground, a microprocessor has been programmed to select desired sampling patterns.

Particles that are in resonance with a given wave mode can be identified by means of a correlator device [18] that measures the time of arrival of electrons or ions in an 8° sector with a high-frequency clock. The microprocessor then performs autocorrelations to identify bunching of the particles. During active experiments the microprocessor will select the bin closest to the direction of the local magnetic field to study the dynamics of particles in and near the atmospheric loss cone and identify the wave modes responsible for resonant pitch-angle scattering.

The Passive Wave Experiment was designed by the University of Iowa to measure electric and magnetic fluctuations over a dynamic range of 100 dB using a 100 m tip-to-tip dipole and a search coil magnetometer. The instruments will operate in swept frequency and fixed-filter modes. The swept frequency analyzer covers the range from 100 Hz to 400 kHz in 128 steps. For wave frequencies in the VLF band both electric and magnetic spectra be compiled every 15 s. The fixed filters will be used to compile a 14 point spectrum with center frequencies between 5.6 Hz and 10 kHz eight times per second.

The Langmuir probe experiment consists of a 100 m tip-to-tip dipole that uses spherical sensors each containing a preamplifier with a 1 MHz bandwidth. The instrument can be used in either a low-impedance mode to measure the plasma density or a high-impedance mode to measure electric fields. It contains two microprocessors, one controls ordinary operations and the other a "burst memory" device. The burst memory holds 192 kbytes and can be filled with data from the Plasma Wave and/or Langmuir Probe Experiments at rates up to 50 kHz. The measured parameters and collection rates are controlled by ground command. Data of the desired kind will be continually fed through the burst memory as a buffer. When the microprocessor recognizes some specified event, it will save a small amount of pre-event data and proceed to fill the burst memory. A rapid increase in the wave activity measured near the central frequency of a fixed-filter channels will probably be used to trigger burst memory data collections during the experiments described below. After the memory is filled, data will be slowly leaked to the main tape recorder for later transmission to ground.

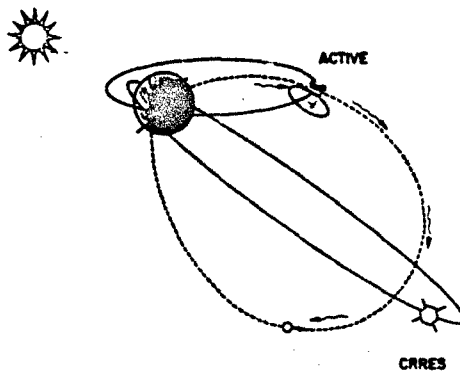


Fig. 3. Wave injection experiments from ACTIVE to CRRES.



## VLF WAVE-INJECTION EXPERIMENTS

In this section we discuss a number of active techniques for injecting and diagnosing whistler waves in the radiation belts. The experiment concept is illustrated schematically in Figure 3. The antennas used to transmit energy into the radiation belts may operate in either the VLF or HF ranges and may be either ground or space based. For simplicity we first consider the case of transmissions from the polar orbiting ACTIVE satellite. This allows us to illustrate the principles that apply to experiment planning and easily extend to ground-based transmissions.

The ACTIVE satellite was launched on 28 September 1989, into polar orbit with an apogee, perigee and inclination of 2500 km, 500 km and 83°, respectively. The prime experiment is a VLF generator that powers a single turn loop antenna of 20 m diameter. The emitted frequency falls in the range from 9.0 to 10.5 kHz and is controlled by ground command. There are eight preprogrammed on/off emission sequences that may be selected. Because the loop antenna failed to deploy properly the emitted power from ACTIVE is well below its planned 10 kW value.

The rates of orbital precession for the ACTIVE and CRRES satellites are  $\sim 1.65$  and  $0.67$  degrees per day. This implies that within a few months of launch the orbital planes of the two spacecraft will overlap favorably for conducting experiments in which VLF radiation can be emitted from ACTIVE and received by CRRES. Since ACTIVE changes magnetic latitude quite rapidly relative to the near equatorial CRRES, it is necessary to determine the useful locations for conducting transmission and pitch-angle scattering experiments. Figure 4 plots the equatorial cyclotron and plasma frequencies derived for the magnetic field and plasma densities given in equations (1) and (2) as functions of  $L$ . We also indicate ACTIVE's emission band. The figure indicates that this radiation can only propagate to the equator for  $L$  shells less than 4. At greater distances ACTIVE's radiation cannot reach CRRES.

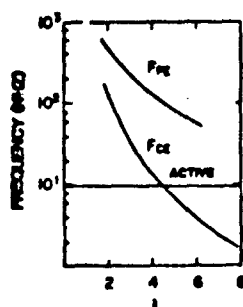


Fig. 4. Electron cyclotron and plasma frequencies at the magnetic equator.



Fig. 5. Energies of electrons resonant with ACTIVE emissions for  $N = -1$  and  $-2$ , at the magnetic equator as functions of  $L$ .

Using equations (1) and (2) we calculate that the magnetic energy per particle is  $50 \text{ keV}/L^2$ . With an emission frequency from ACTIVE of 9.6 kHz, the ratios  $\Omega_{ce}/\omega$  and  $\Omega_{ci}/\omega$  are  $90.4/L^3$  and  $0.31/L^3$ , respectively. In Figure 5 we have plotted the energies of electrons that are resonant with 9.6 kHz waves at the equator using equation (5) for the first two harmonics. At distances  $L > 2.3$  ( $> 3$ ) the energy of resonant electrons is in range of LEPA's sensitivity for the  $N = -1$  ( $-2$ ) harmonic interaction. Higher harmonic interactions can be detected by high-energy detectors but with coarser pitch-angle resolution than LEPA. At off equatorial latitudes the magnetic energy per particle increases leading to higher energies for resonant interactions. Note that CRRES can detect resonant interactions resulting from directly injected waves only if the two spacecraft are in opposite hemispheres. Resonant interactions can occur at the location of CRRES with the satellites in the same hemisphere if the waves undergo internal magnetospheric reflections. Protons interacting with whistler waves emitted by ACTIVE at the first harmonic must have energies  $> 1 \text{ MeV}$ . Higher harmonic interactions take place at lower energies.

There are two methods for injecting VLF waves into the magnetosphere from the ground, directly from VLF transmitters or indirectly from HF ionospheric heaters. Many direct VLF injections have already been cited. The Siple transmitter had flexibility in its emitted frequencies. However, Siple was closed when Antarctic ice crushed the station. Inhof and coworkers carried out experiments using VLF transmitters at a number of fixed frequencies used by the U.S. Navy. These can be repeated with CRRES. Consistent with SEEP measurements [9], frequencies  $> 20 \text{ kHz}$  will interact with electrons in LEPA's energy range at  $L > 2$ .

Indirect injections of VLF waves into the radiation belts can be accomplished by two methods. The first is through modulation of ionospheric currents and the second through beat waves. Ionospheric current modulations have been achieved by a modulated heating of the D region of the ionosphere [19-20]. The basic concept is that the HF waves heat the ionospheric electrons and thus increase the ionospheric conductivity. If the amplitude of the heater is modulated at VLF frequencies the ionospheric currents are also modulated, turning them into a virtual antenna in space. Trakhtengerts [21]

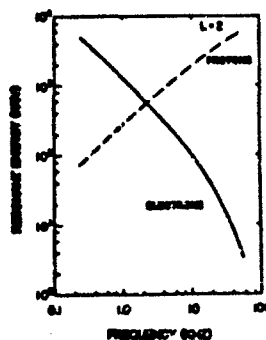


Fig. 6. Energies of electrons and protons resonant at the first harmonic with whistlers at  $L=2$ .

suggested that this technique can be adopted to turn whole flux tubes into a maser-like device in which injected waves grow to large amplitudes. Quantitative conditions required for growth with parallel wave propagation have been explored by Villalón and coworkers [22]. Ionospheric current modulation techniques have the advantage of flexibility over fixed frequency transmitters. However, while waves emitted from virtual ionospheric antennas have been detected at the ground, little is known about the efficiency with which they transmit across the ionosphere into deep space. The wave detectors on CRES will reduce this uncertainty.

A second method for indirect VLF injection involves the use of beat waves. Different sectors of the Arecibo antenna can radiate at selected frequencies whose difference lies in the VLF range. This also provides flexibility for studying resonant interactions in LEPA's energy range near  $L=2$ . The HF heater also provides a means for enhancing the efficiency of wave injections. If the ionosphere is heated for about ten minutes prior to VLF turn-on, it develops field-aligned thermal striations [23]. Induced irregularities can enhance VLF transmission through the ionosphere either along artificially created ducts or off strategically located scattering centers. Figure 6 plots the resonant energy of electrons and protons at the first harmonic at  $L=2$  as a function of frequency. Resonant electrons in LEPA's range of sensitivity require injected wave frequencies  $> 20$  kHz.

#### REFERENCES

- [1]. Kennel, C.F. and H.E. Petschek, Limit on stably trapped particle fluxes, *J. Geophys. Res.*, 71, 1 - 28, 1966.
- [2]. Lyons, L.R., R.M. Thorne and C.F. Kennel, Pitch-angle diffusion of radiation belt electrons within the plasmasphere., *J. Geophys. Res.*, 77, 3455 - 3474, 1972.
- [3]. Chong, H.C. and U.S. Inan, Lightning-induced electron precipitation from the magnetosphere, *J. Geophys. Res.*, 90, 1531 - 1541, 1985.
- [4]. Inan, U.S. and D.L. Carpenter, Lightning-induced electron precipitation events observed at  $L=2.4$  as phase and amplitude perturbations on subionospheric VLF signals, *J. Geophys. Res.*, 92, 3293-3303, 1987.
- [5]. Inan, U.S., W.C. Burgess, T.G. Wolf, D.C. Shater and R.E. Orville, Lightning-associated precipitation of MeV electrons from the inner radiation belt, *Geophys. Res. Lett.*, 15, 172 - 175, 1988.
- [6]. Bycroft, M.J., Strange new whistlers, *Nature*, 327, 368 - 369, 1987.
- [7]. Helliwell, R.A., Controlled stimulation of VLF emissions from Siple Station, Antarctica, *Radio Sci.*, 18, 801 - 814, 1983.
- [8]. Inan, U.S., T.F. Bell, D.L. Carpenter and R.R. Anderson, Explorer 45 and Imp 6 observations in the magnetosphere of injected waves from the Siple VLF transmitter, *J. Geophys. Res.*, 82, 1177 - 1187, 1977.
- [9]. Bahof, W.L., J.B. Reagan, H.D. Voss, J.E. Gaines, D.W. Dattlow, J. Mobilis, R.A. Helliwell, U.S. Inan, J. Katsoufrakis and R.G. Joiner, The modulated precipitation of radiation belt electrons by controlled signals from VLF transmitters, *Geophys. Res. Lett.*, 10, 615 - 618, 1983.
- [10]. Vampola, A.L., Electron precipitation in the vicinity of a VLF transmitter, *J. Geophys. Res.*, 92, 4525 - 4532, 1987.
- [11]. Burke, W.J. and R.C. Sagalyn, Active space experiments and international treaty obligations, *ISOSM*, (in press) 1990.
- [12]. Tsandoulas, G.W., Space Based Radar, *Science*, 237, 257 - 262, 1987.
- [13]. Chappell, C.R., K.K. Harris and G.W. Sharp, A study of the influence of magnetic activity on the location of the plasma pauses as measured by OGO 5, *J. Geophys. Res.*, 75, 50 - 56, 1970.
- [14]. Smith, R.L. and J.J. Arpersaai, Magnetospheric properties deduced from OGO 1 observations of ducted and nonducted whistlers, *J. Geophys. Res.*, 73, 1 - 20, 1968.
- [15]. Helliwell, R.A., Whistlers and VLF emissions, in *Physics of the Magnetosphere*, ed. by R.L. Carovillano, J.F. McClay and H.N. Dadoaki, D. Reidel Co., Dordrecht, 106 - 146, 1968.
- [16]. Akura, I., Effects of ions on whistler-mode ray tracing, *Radio Sci.*, 1, 269 - 283, 1966.

- [17]. Quackenbush, M.S., E.G. Mullen and R.C. Sagalyn, CRRES-SPACERAO experiment descriptions, AFCE-85-0017, 1985.
- [18]. Gough, M.P. and A. Urban, Auroral beam/plasma interaction observed directly, *Planet. Sp. Sci.*, 31, 873 - 883, 1983.
- [19]. Lunnan, R.J., A.J. Ferraro, M.C. Lee, R. Allshouse, K. Carroll, D. Werner and T.W. Collins, Detection of local and long-path VLF/ELF radiation from modulated ionospheric current systems, *Radio Sci.*, 20, 553 - 563, 1985.
- [20]. Stubbe, P., M. Kopka, M.T. Rietveld, A. Frey, P. Hoeg, M. Kohl, E. Nielsen, G. Rose, C. LaHoz, E. Barr, M. Deblon, A. Hedberg, B. Thidé, T.B. Jones, T. Robinson, A. Brekke, T. Hansen and O. Holt, Ionospheric modification experiments with the Tromsø heating facility, *J. Atmos. Terr. Phys.*, 47, 1151 - 1163, 1985.
- [21]. Trakhtengerts, V. Yu., Alfvén Masers, in *Active Experiments in Space*, ESA SP-195, 67 - 74, 1983.
- [22]. Villalón, E., W.J. Burke, P.L. Rothwell and M.B. Silevitch, Quasi-linear wave-particle interactions in the earth radiation belts, *J. Geophys. Res.*, 94, 15,243 - 15256, 1989.
- [23]. Lee, M.C. and S.P. Rao, Ionospheric irregularities and geomagnetic fluctuations due to ionospheric heating, in *Active Experiments in Space*, ESA SP-195, 81 - 89, 1983.

#### ACKNOWLEDGMENTS

This work was supported in part by USAF Contract No. F19628-89-K-0014 with Northeastern University and by AFOSR Tr-4 2311G6.

PAPER NO. 28

#### DISCUSSION

P. LEFEUVRE, FR

In a paper you co-authored with Dr. Villalón you suggested to heat the foot of the flux tube where the interaction takes place. Do you plan to do it in your CRRES experiment?

AUTHOR'S REPLY

The CRRES experiments are designed for single-hop whistlers. To heat the conjugate point for the Alfvén maser would require a two-hop whistler. If it happens, CRRES could see it.

# MODIFICATION OF THE LOWER IONOSPHERE IN LIGHTNING-INDUCED ELECTRON PRECIPITATION EVENTS AND THROUGH VLF HEATING

by

Umaru S. Inan  
STAR Laboratory, Stanford University  
Stanford, CA 94305  
USA

## SUMMARY

Different mechanisms by which VLF waves from ground-based sources modify the nighttime lower ionosphere (D-region) are discussed. One process by which the ionosphere is regularly disturbed involves the precipitation of short (<2s) bursts of energetic (>40 keV) electrons out of the radiation belts in gyroresonant interactions with whistler waves launched by lightning discharges. A second process involves direct upward coupling of lightning electric fields to the lower ionosphere leading to intense electric fields and ionization enhancements. A third process is the heating of the lower ionosphere by upgoing VLF waves from ground-based transmitters and lightning, leading to up to 100% increase in electron temperature at 80-90 km altitudes [1].

## 1. IONOSPHERIC MODIFICATION IN LIGHTNING-INDUCED ELECTRON PRECIPITATION (LEP) EVENTS

A substantial body of evidence has recently emerged indicating that the nighttime lower ionosphere is regularly disturbed by energetic (>40 keV) electron bursts that are precipitated out of their trapped radiation belt orbits in gyroresonant interactions with lightning-generated whistlers. While electron precipitation bursts have been observed on satellites [2] and on rockets [3,4], the overwhelming evidence for the occurrence characteristics and geographic distribution of LEP events, and the causative association of the observed ionospheric signatures with whistlers and lightning, have been obtained by means of ground-based VLF remote sensing of the nighttime D-region [5, 6, 7, 8, 9, 10, 11, 12, 13, 14]. Examples of ground-based signatures of LEP events are shown in Figure 1, together with the locations of causative lightning that was available for that case [11]. The characteristic VLF signatures of these events are commonly referred to as *Trimpi* events and involve a rapid (< 2 s) onset followed by a relatively longer (10-100 s) recovery, representing the recombination and/or attachment of the enhanced secondary ionization produced by the energetic electrons. The typical density profiles of ionospheric disturbances in events observed at mid latitudes ( $2 < L < 3$ ) are believed to be as shown in Figure 2 [15]. Both amplitude and phase of the subionospheric signal exhibits basically similar signatures as shown in Figure 3, with differences in the amplitude and phase responses reflecting the altitude profile of enhanced ionization [16].

In the past few years, Stanford University has developed a network of VLF/LF remote sensing observations in the northern hemisphere, distributed across the continental United States, and at Palmer Station, Antarctica, as shown in Figure 4. Observations at 5 locations in the north of signals from 6 different VLF transmitters (see Table 1) is used to monitor ionospheric disturbances occurring on or near a crisscrossing set of subionospheric paths, with the potential for 'imaging' the location and structure of the disturbed ionospheric regions.

An example illustrating the possible use VLF data for such imaging is shown in Figure 5. Here, the top panel shows a 30-minute sequence of events observed on the 48.5-SA path on 10 October 1987. The events are clearly identifiable on the basis of their known characteristic signature mentioned above. The simultaneous record of the NAA-SU signal (lower panel), shows a perturbation at about the same time with the first and largest event on the 48.5-SA path occurring at  $t \sim 180$ s. (The drop in the NAA signal level between  $\sim 280$ -310 s was recorded at all stations and is attributed to interruption of the transmission at the source.)

The simultaneity of the two events at higher resolution is illustrated in Figure 6. The left hand panels show a 200-s data record of the 48.5-SA and NAA-SU signals, as well as the amplitude of the  $48.5 \pm 0.15$  kHz channel as observed at Stanford (48.5-SU signal). While no characteristic amplitude changes are observed on the 48.5-SU path, this channel is useful as a means of identifying causative radio atmospherics superimposed on the relatively weak transmitter signal. In the case shown, a clear isolated spike in the 48.5-SU channel is apparently coincident with the Trimpi events on the upper two panels. The panels on the right show a further expanded version of the data. In this 10-s record displaying the raw data with no time averaging, the radio atmospheric is clearly visible in the 48.5-SU, 48.5-SA, and NAA-SU channels. The Trimpi event in the 48.5-SA channel displays all the classical features, including a  $\sim 1.2$  s delay between causative atmospheric and event onset, as well as an  $\sim 0.5$  s risetime indicative of the duration of the precipitation burst, consistent with the predictions of theoretical models of whistler-induced pitch angle scattering and precipitation of electrons [17]. The simultaneous Trimpi event in the NAA-SU channel is less well defined, but basically has the same temporal characteristics as the 48.5-SA event.

The association of radio atmospherics with Trimpi event onsets is generally established on the basis of repeatability of the signatures. Similar cyberic signatures (sharp peaks preceding the event onsets by  $\sim 1$  s) were observed in at least one or more of the receiver channels for all the events observed on the 48.5-SA signal that are displayed in the upper panel of Figure 5.

The simultaneity of the events observed on the 48.5-SA and NAA-SU is consistent with an ionospheric disturbance in the vicinity of the crossing point of these two paths, subject to certain assumptions as discussed in [18]. Equally important in this consideration is the absence of events on any of the other VLF paths that were observed on SU and SA on this day (no data was available from LM for 10 Oct 1987) and HU and AR observations had not yet started in 1987.

The association of observed events with ducted whistlers from the magnetosphere is shown in Figure 7. Here, a 25 minute sequence of Trimpi events observed on the 48.5 kHz signal at Huntsville (HU) are shown on the top panel. The first two of these are shown in the lower panel at higher resolution together with the associated ducted whistlers (middle panel) observed at Palmer Station, Antarctica. The Trimpi events are very well defined amplitude changes of up to 20%. For the case shown, the whistler data was only available during synoptic periods of 1-minute out of every five.

The potential use of subionospheric VLF data extract information concerning the shape (altitude profile) of the secondary ionization in the disturbed region is shown in Figure 8. The top panel shows a series of events on the 48.5-HU signal consisting of negative amplitude changes, except for one event which exhibits a positive change in amplitude as well as an unusual recovery signature. The second and third panels show this event at two different resolutions, better illustrating the overall recovery as well as the sharp initial

recovery portion that takes place within the first second after the amplitude change. Such exceptionally rapid recoveries have in the past been interpreted as being due to MeV electrons that penetrate to and create ionization at altitudes as low as 50-70 km [11]. The bottom two panels show the 48.5 kHz signal observed at Arecibo (AR), with striking differences in signature. The amplitude change at AR is negative, followed by a typical exponential recovery. The differences in signatures between AR and HU are interpreted to be due to the high energy (deep penetrating) component of the precipitation burst, which produces ionization at low altitudes and selectively perturbs the higher order waveguide modes. These modes add up to produce a positive amplitude change at HU. By the time the signal reaches AR, the higher order modes are attenuated and the signal consists of lower order modes which are not as sensitive to ionization at the lower altitudes. It appears that the diversity of waveguide modes available on these relatively short VLF paths may reveal such information concerning the energy spectrum of the precipitation, especially when used in connection with quantitative models of VLF propagation in the earth-ionosphere waveguide [15].

## 2. SUBIONOSPHERIC VLF EVIDENCE OF DIRECT UPWARD COUPLING OF LIGHTNING TO THE IONOSPHERE

While many Trimp events display the temporal features (onset delay and duration) consistent with that expected on the basis of a high altitude whistler-particle interaction [17], either early (onset delay < 50 ms) or fast (onset duration < 50 ms) events have been reported [11, 12]. While the quantitative mechanisms for such phenomena are not yet known, they may be a manifestation of ionospheric heating produced by the VLF energy from lightning [1] together with other types of direct coupling of lightning energy up to the lower ionosphere. In this subsection, we present two examples of such events.

Figure 9 shows three of a sequence of events observed on 13 May 1987 that were previously reported [12]. The caption is self explanatory and more details are provided in the original paper.

Figure 10 shows a composite illustration of an isolated event at both low and high time resolution as well as a map showing only the perturbed subionospheric paths. The left hand panels show 300-s records illustrating the perturbations on the NSS-LM, NAA-SA, NAA-SU, and NAU-LM paths. Superimposed on the latter signal is an intense impulse, i.e., a radio atmospheric, that stands out clearly among other, weaker impulses. A small amplitude increase is nevertheless clearly visible. The association of this atmospheric with the NSS-LM event onset at high resolution is shown in the right hand panels, together with the output of a 2.4 kHz peak detector (used specifically for detecting spherics) at LM, which also registers the intense radio atmospheric. While the initial part of the response on the NSS-LM signal is probably the interference of the spheric energy in this channel, the delay between the peak of the radio atmospheric and the event onset could at most be as long as the duration of the spheric, or < 200ms. We note that the onset delay predicted by theoretical models on the basis of whistler-electron scattering for the L-shell of the presumed perturbed region is  $\sim 1.5$  s [17]. On this basis, this perturbation event is not likely to be caused by whistler-induced pitch angle scattering in the magnetosphere, but is more likely to be another example of direct coupling of lightning energy up to the ionosphere. Because of the interference from the spheric, we cannot determine whether the risetime of the event onset is unusually 'fast'. However, the event does appear to fit the category of 'early' events as reported before [11].

The event illustrated in Figure 10 was an isolated one, with no similar amplitude changes registered on the NSS-LM signal (or on any of the other three signals shown) during the 0500-0600 UT period on this day. In spite of this, the likelihood of the event being a chance coincidence between the spheric and VLF changes is small, since the observed spheric was by far the most intense during this same period. Furthermore the SUNY-Albany east coast lightning detection network measured isolated cloud-to-ground lightning activity within the 200x200 km region encompassed by the paths during this hour [19]. The data appears to indicate that a  $\sim 200 \times 200$  km region of the ionosphere encompassed by these four signals is directly perturbed in an individual event. While examples of such direct coupling observed on individual VLF paths have been previously reported, this result is our first glimpse of the size of the regions that may be affected.

## 3. IONOSPHERIC MODIFICATION THROUGH VLF HEATING

A controlled wave-injection experiment with a 28.5 kHz transmitter having a radiated power of 100 kW has recently revealed evidence of ionospheric heating by the VLF waves [1]. The ionospheric disturbance caused by the injected VLF signal was detected by means of the transfer of its modulation to a second VLF signal in the same manner as the Luxembourg effect [19]. Calculations indicate that the observed effect can be attributed to result in a 30% enhancement in the electron temperature at 85 km. This process also represents a new means of direct coupling of lightning energy to the lower ionosphere. In this paper we briefly summarize this recently reported result [1] and also present an example of data not previously shown.

The VLF wave-injection experiment was carried out during Spring and Fall 1989 in order to stimulate the precipitation of electrons from the inner radiation belt. It was found that the amplitude of the 24.0 kHz NAA transmitter (Maine) signal observed at Palmer Station (PA), Antarctica exhibited the modulation pattern of the 23.5 kHz NAU transmitter (Agua de Dios, Puerto Rico), which was being keyed nightly for 0335-0350 UT and 0735-0750 UT with a 5-s periodic format (3s ON/2s OFF). The NAA-PA great-circle path crossed within <50 km of the ionosphere above NAU (Figure 11).

Superposed-epoch and spectral analyses of the various signal amplitudes received at Palmer were conducted to search for effects of the 5-s periodicity and the results for 21 Oct 89 are shown in Figure 12. Here, the NAA-PA signal clearly exhibits the 3s ON/2s OFF pattern in terms of a decrease (0.07 dB) simultaneous (analysis indicates <20 ms) with the keying OFF of the NAU signal at  $t = 3s$ . The NSS-PA, as well as other transmitter signals observed at Palmer, did not show any evidence of 3s ON/2s OFF keying.

The spectral analysis as shown in the bottom panel shows the 5-s periodicity as a clear (>10 dB above background) peak at 0.2 Hz. Data from other 15-min periods both before and after the period shown were similarly analyzed, and no evidence of spectral peaks (>3 dB above background) were found. Similar analysis on the amplitude of the NSS-PA signal did not show any signatures of the NAU keying.

Analysis of the data from the two 6-week periods of keying experiments in Spring and Fall of 1989 indicate that spectral peaks >5 dB above background at 0.2 Hz were observed on the NAA-PA on the average about 1-2 times a week. It is not clear whether lack of a spectral signature is due to the absence of heating or the relative insensitivity of the NAA-PA signal to a localized disturbance relatively far away from the receiver.

The frequency dependence of heating is shown in Figure 13 [1]. We note that the perturbation at 85 km is maximum for 50-60 kHz, with heating decreasing rapidly beyond 60 kHz to <10% for >300 kHz. There is a broader maximum for the 80 km altitude with the change in collision frequency  $\Delta\nu \approx 20\%$  for 4-90 kHz.

Theoretical work on HF heating of the D-region typically considered cases with the wave frequency being much smaller than the electron collision frequency ( $\omega \gg \nu$ ) [20]. In our work, we consider the full magneto-ionic expression that does not require  $\omega \gg \nu$ . For the VLF range, we find  $\Delta \nu$  comparable to  $\nu$ , indicating that the heating effect is more significant than for  $>200$  kHz [1].

The amplitude of the heating wave near 85 km for the case in Figure 12 is estimated to be  $\sim 12$  mV/m. Since transient electric fields from lightning of up to 50 mV/m have been observed in the ionosphere [21], localized enhancements in  $\nu$  should be readily produced in association with lightning discharges, representing a new means of direct modification of the lower ionospheric plasma by lightning. Lightning-associated conductivity changes observed on rockets and balloons [22] can thus be due to the localized heating effects, and some of the observed rapid changes in subionospheric signal amplitudes as shown in Figures 9 and 10 may be caused by modification of the earth-ionosphere waveguide mode structure due to the enhanced  $\nu$ . However, effects involving slow (10-100 s) recovery are likely to involve other mechanisms (leading to generation of ionization enhancements) operating in conjunction with heating. One such possibility that needs to be further investigated is the modification of the effective recombination rate during heating, which may lead to an enhanced density [24].

The ability to substantially heat the lower ionosphere with VLF signals could lead to a new set of controlled experiments to evaluate the effects of ionospheric disturbances of known configuration. Comprehensive [ground-(radars) and rocket-based] measurements are now needed in order to fully understand the extent of the effect. Conductivity changes resulting from the heating could possibly be utilized to generate ULF waves. Powerful VLF transmitters and thunderstorm centers may be a continuous source of heating for the overhead ionospheric regions. The possibility of D-region heating by VLF transmitters or lightning leading to the formation of whistler ducts needs to be evaluated. New experiments are now planned with more powerful transmitters such as the NAA facility in Cutler, Maine.

**Acknowledgement.** This research at Stanford University was supported by NSF grants DPP86-11623 and ATM88-04273 and by ONR grant N00014-82-K-0489. The NAU keying experiments were arranged by R. G. Joiner of ONR courtesy of the U. S. Navy.

TABLE 1. VLF/LF Transmitters.

Call Sign	Transmitter	Frequency	Latitude	Longitude
NSS	USN Maryland	21.4 kHz	39°N	76°W
NPM	USN Hawaii	23.4 kHz	21°N	158°W
NAU	USN Puerto Rico	28.5 kHz	18°N	67°W
NAA	USN Maine	24.0 kHz	45°N	67°W
NLK	USN Washington	24.8 kHz	48°N	122°W
	USAF Nebraska	48.5 kHz	42°N	98°W

#### REFERENCES

- [1] Inan, U.S., VLF heating of the lower ionosphere, *Geophys. Res. Lett.*, 17, 259, 1990.
- [2] Voss, H.D., W.L. Imhof, J. Mobilia, E.E. Gaines, M. Walt, U.S. Inan, R.A. Helliwell, D.L. Carpenter, J.P. Katsufakis, H.C. Chang, Lightning induced electron precipitation, *Nature*, 312, 740, 1984.
- [3] Rycroft, M.J., Enhanced energetic electron intensities at 100 km altitude and a whistler propagating through the plasmasphere, *Planet. Space Sci.*, 21, 239, 1973.
- [4] Goldberg, R.A., J.R. Barcus, L.C. Hale, and S.A. Curtis, Direct observation of magnetospheric electron precipitation stimulated by lightning, *J. Atmos. Terr. Phys.*, 48, 293, 1986.
- [5] Carpenter, D.L., and J. W. LaBelle, A study of whistlers correlated with bursts of electron precipitation near  $L = 2$ , *J. Geophys. Res.*, 84, 4427, 1982.
- [6] Inan, U.S., H.C. Chang, R.A. Helliwell, J.P. Katsufakis, W.L. Imhof, J.B. Reagan, M. Walt, D.W. Dailowe, and J. Mobilia, Wave-induced precipitation as a loss process for radiation belt particles, *Adv. Space Rev.*, 5, 243, 1985.
- [7] Inan, U.S., and D.L. Carpenter, On the correlation of whistlers and associated subionospheric VLF/LF perturbations, *J. Geophys. Res.*, 91, 3106, 1986.
- [8] Inan, U.S., and D.L. Carpenter, Lightning-induced electron precipitation events observed at  $L \approx 2.4$  as phase and amplitude perturbations on subionospheric VLF signals, *J. Geophys. Res.*, 92, 3293, 1987.
- [9] Carpenter, D.L., and U.S. Inan, Seasonal, Latitudinal and Diurnal distribution of whistler-induced precipitation events at low latitudes, *J. Geophys. Res.*, 92, 3429, 1987.
- [10] Inan, U.S., W.C. Burgess, T.G. Wolf, D.C. Shafer, and R.E. Orville, Lightning-associated precipitation of MeV electrons from the inner radiation belt, *Geophys. Res. Lett.*, 15, 172, 1988a.
- [11] Inan, U.S., T.G. Wolf, and D.L. Carpenter, Geographic distribution of lightning induced electron precipitation observed as VLF/LF perturbation events, *J. Geophys. Res.*, 93, 9841, 1988b.
- [12] Inan, U.S., D.C. Shafer, W.Y. Yip, and R.E. Orville, Subionospheric VLF signatures of nighttime D-region perturbations in the vicinity of lightning discharges, *J. Geophys. Res.*, 93, 11455, 1988c.
- [13] Dowden, R., and C.D.D. Adams, Modal effects on amplitude perturbations on subionospheric signals (Trimpis) deduced from two-frequency measurements, *J. Geophys. Res.*, 94, 1515, 1989.
- [14] Dowden, R.L., and C.D.D. Adams, Location of lightning-induced electron precipitation from measurement of VLF phase and amplitude perturbations on spaced antennas and on two frequencies, *J. Geophys. Res.*, 95, 4135, 1990.
- [15] Poulsen, W.L., T.F. Bell, and U.S. Inan, 3-D modeling of subionospheric VLF propagation in the presence of localized D-region perturbations associated with lightning, *J. Geophys. Res.*, 95, 2355, 1990.
- [16] Wolf, T.G., and U.S. Inan, Path dependent properties of subionospheric VLF amplitude and phase perturbations associated with lightning, *J. Geophys. Res.*, (in review) 1990.
- [17] Chang, H.C., and U.S. Inan, Lightning-induced electron precipitation from the magnetosphere, *J. Geophys. Res.*, 90, 1531, 1985.
- [18] Inan, U.S., F.A. Knifsend, and J.Oh, Subionospheric VLF 'Imaging' of lightning-induced electron precipitation from the magnetosphere, *J. Geophys. Res.*, (in press) 1990.
- [19] Orville, R.E., Private communication.
- [20] Tellegen, B.D.H., Interaction between radio waves, *Nature, Lond.*, 131, 840, 1933.

- [21.] Showen, R.L., Artificial heating of the lower ionosphere, *J. Geophys. Res.*, 77, 1923, 1972.  
 [22.] Kelley, M.C., C.L. Siefing, R.F. Pfaff, P.M. Kintner, M.Larsen, R.Green, R.H. Holzworth, L.C. Hale, J.D. Mitchell, and D.Le Vine, Electrical measurements in the atmosphere and ionosphere over an active thunderstorm, I. Campaign overview and initial ionospheric results, *J. Geophys. Res.*, 90, 9815, 1985.  
 [23.] Holzworth, R.H., and K.W. Norville, P.M. Kintner, and S.P. Powell, Stratospheric Conductivity Variations Over Thunderstorms, *J. Geophys. Res.*, 91, 13257, 1986.  
 [23.] Jones, T., Paper #1 in this proceedings.

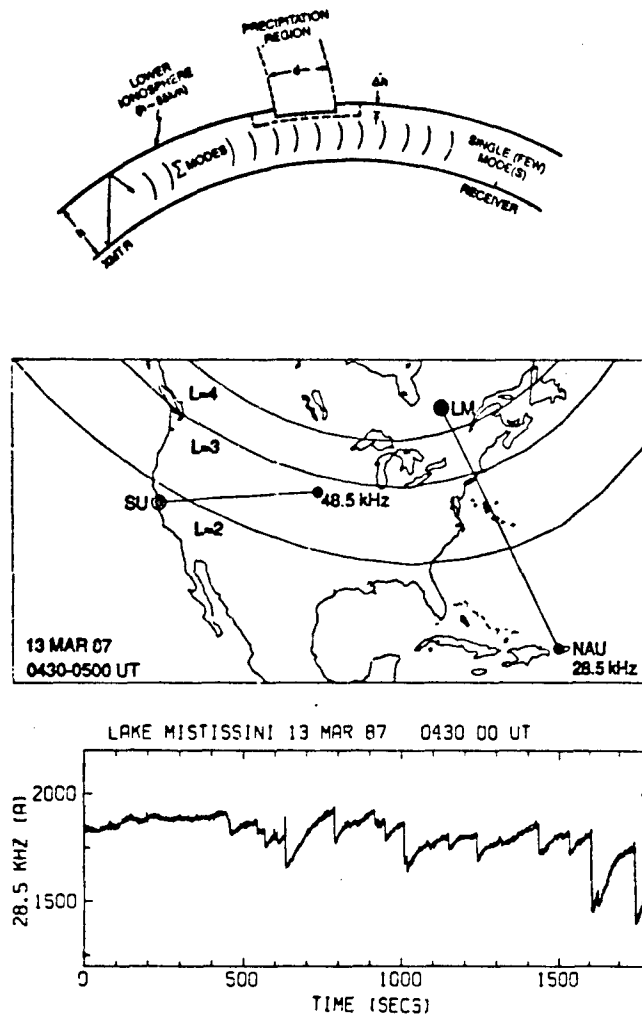


Figure 1: Illustration of the subionospheric VLF remote sensing technique for measurement of ionospheric density variations at altitudes of 85 km or below. The top panel depicts the effect on a subionospheric path of a localized ionospheric 'depression'. The lowest panel shows reception at Lake Mistissini, Quebec of the 28.5 kHz signal from the NAU transmitter in Puerto Rico. The vertical scale shows signal amplitude  $A$  on a linear scale with arbitrary units, with  $A = 0$  representing absence of signal. The time  $T = 0$  corresponds to the UT time given in the upper right corner. The '+'s on the map are locations of cloud-to-ground lightning flashes that occurred during the 0430-0500 UT period shown. The characteristic VLF perturbations (rapid decreases followed by slow recoveries) were found to be causatively associated with individual lightning flashes [12].

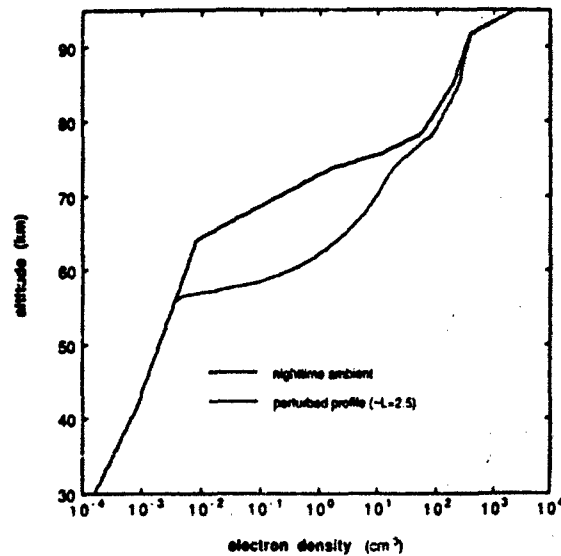


Figure 2: Plot of an ambient nighttime electron density distribution and a typical ionospheric disturbance profile corresponding to electron precipitation bursts produced by lightning-generated whistlers propagating at  $L = 2.5$ . A typical value of 200 ms was assumed for the duration of the precipitation burst at a peak energy flux level of  $10^{-2}$  ergs/cm<sup>2</sup>-s [17].

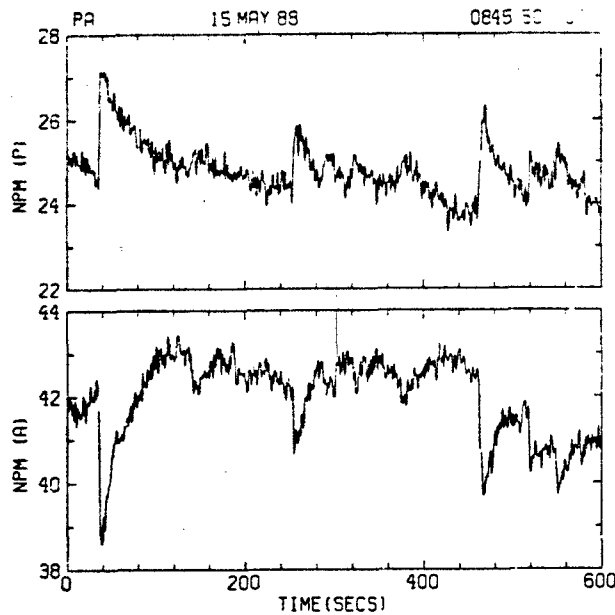


Figure 3: Illustration of the observation geometry and event examples at Palmer Station, Antarctica. The two panels show the phase (upper panel) and amplitude (lower panel) of the signal from the 23.4 kHz NPM transmitter in Hawaii as observed at Palmer. The characteristic variations are clearly seen and are nearly always associated with magnetospheric whistlers, also observed at Palmer station [7, 8]. The amplitude scale for the lower panel is linear in arbitrary units, showing signal amplitude  $A$ , with  $A = 0$  representing the absence of signal. The vertical axis in the upper panel shows signal phase on a linear scale with arbitrary units. For the scale shown, a phase change from about 24 to about 27 units corresponds to  $3^\circ$ .



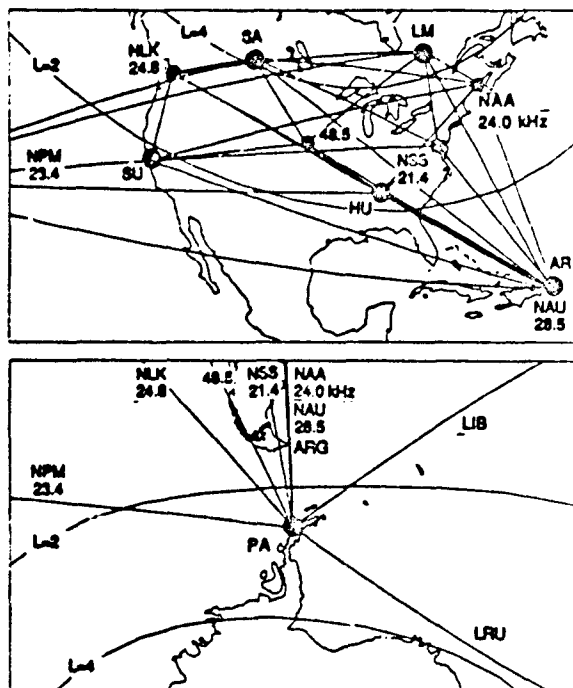


Figure 4: Stanford University VLF network observation sites and signal paths. The sites are Saskatoon (SA), Lake Mistissini (LM), Quebec, Arecibo (AR), Puerto Rico, Stanford (SU), California, and Huntsville (HU), Alabama. At each site signals from multiple transmitters are monitored and amplitude and phase information is stored with 50/20 Hz resolution. Recordings are generally made for the 0000-1200 UT period where most of the monitored paths are propagating under a nighttime ionosphere. Summary plot data is produced at the end of each night.

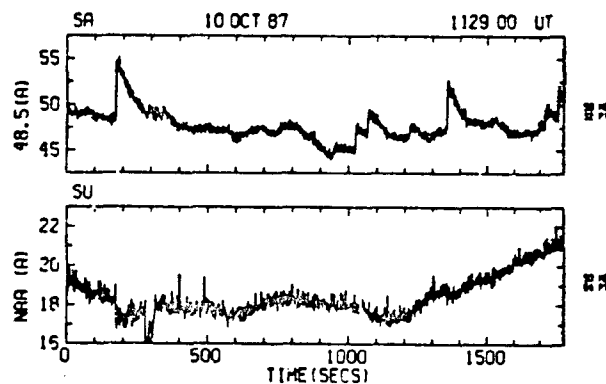


Figure 5: The top panel shows a 30-minute sequence of events on the 48.5-SA path together with the NAA signal amplitude as observed at Stanford (NAA-SU) shown in the lower panel. The drop in the NAA-SU signal  $\sim 1134$  UT ( $t \approx 300$  s) is due to transmitter interruption (recorded also at SA). The vertical scale is linear, showing signal amplitude ( $A$ ) in arbitrary units, with  $A = 0$  representing absence of signal. The numbers shown on the y-axis correspond to the percentage of full scale. Thus, the first event at 1132 UT (top panel) represents an amplitude change of 5 units on top of an ambient level of 50 units, i.e., a 10% event. The data in the top and bottom panels represent detected amplitude time averaged over 0.64 s and 1.28 s, respectively [18].

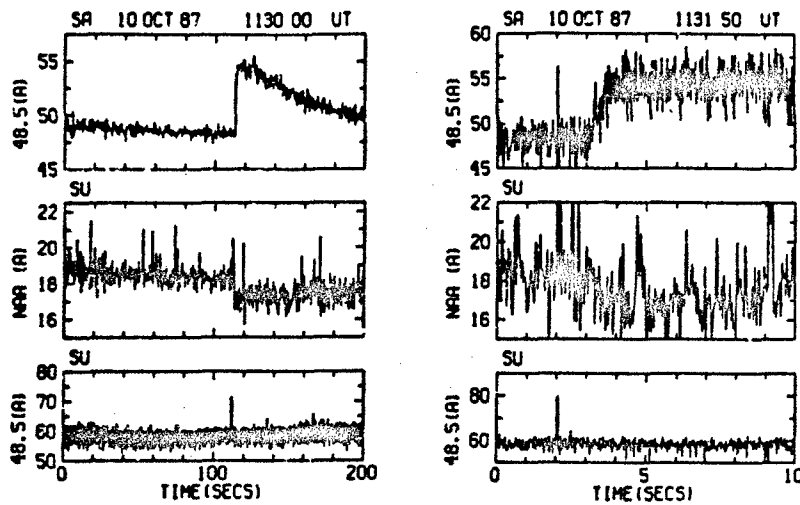


Figure 6: High resolution displays of the largest event shown in Figure 5. The format of the data displays is similar to that of Figure 5. The panels on the right show the 20 ms samples without averaging, while the panels on the left are time averaged over 0.32 s (top), 0.16 s (middle) and 0.04 s (lower). The causative spheric and the negative perturbation simultaneous with the well-defined event at 48.5-SA are both apparent on the NAA-SU signal. The absence of other spherics of comparable amplitude on the 48.5-SU signal make the causative spheric easily identifiable. The panels on the right show the same event at higher resolution. The causative spheric precedes the event by  $\sim 1.2$  seconds, consistent with theoretical predictions [17].

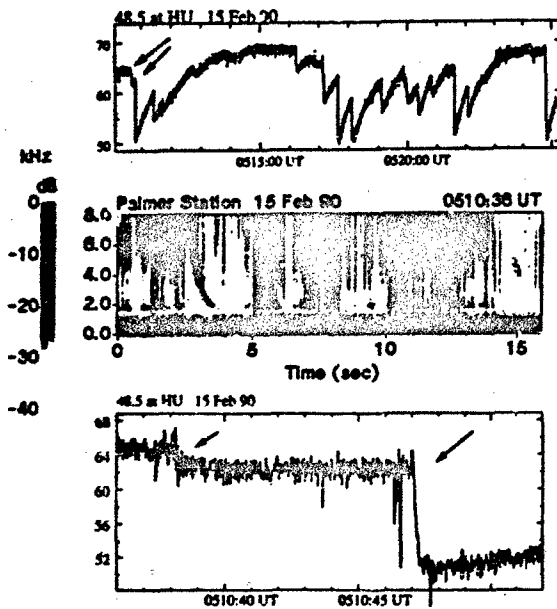


Figure 7: Whistlers observed at Palmer correlated with VLF perturbations on the 48.5 kHz signal observed at Huntsville (HU). The top panel shows a 25-min sequence of unusually well defined events observed on the 48.5 kHz signal observed at Huntsville (HU) shown in a format similar to that of the data panels in Figure 5. The first two successive events (indicated by arrows) from the top panel are shown on an expanded scale in the lower panel. The middle panel shows the broadband (0-8 kHz) spectra observed at Palmer showing two whistlers in succession, time correlated with two negative amplitude changes on the 48.5-HU signal. The broadband data was only available on a synoptic basis (1 minute of every five).

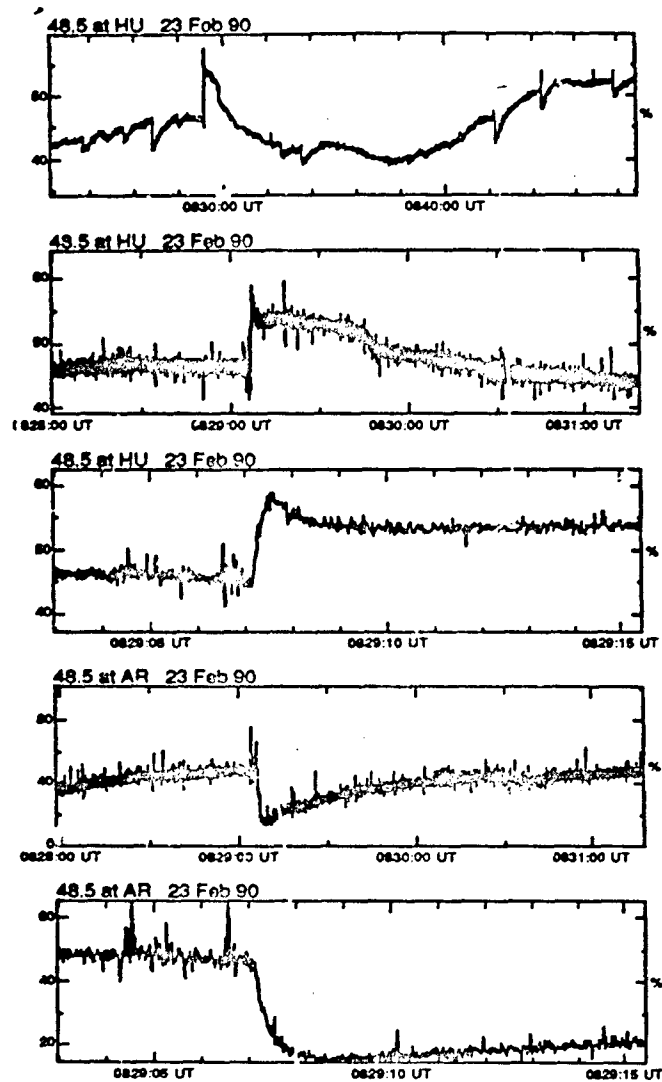


Figure 8: Possible evidence of selective excitation of different earth-ionosphere waveguide modes by an unusually large ionospheric disturbance. The top three panels show the 48.5 signal at Huntsville (HU) illustrating an unusual event at different resolutions. The format of the amplitude records are similar to that for Figure 5. The illustrated event is a positive amplitude change occurring in the midst of smaller amplitude decreases and also exhibits a distinctly different recovery signature. The 48.5 kHz signal observed at Arecibo (AR) does not display any of the unusual features. The 48.5-HU and 48.5-AR signal paths are colinear as can be seen from Figure 4.

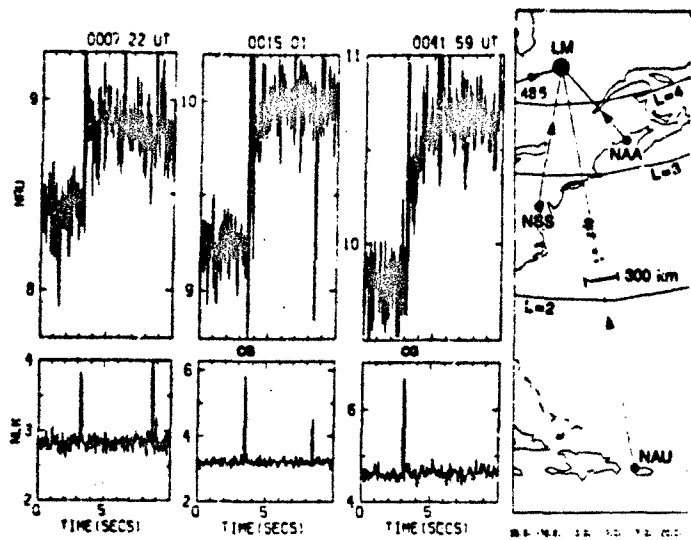


Figure 9: Examples of direct upward coupling between lightning and the lower ionosphere. The observations shown were made during an isolated thunderstorm off the east coast of the United States, as represented by the cloud-to-ground (CG) lightning discharges shown as +'. The lightning data was recorded by the SUNY-Albany lightning detection network. The data displays on top show individual perturbation events on the 28.5 kHz NAU signal received at Lake Madsen (LM), Quebec, with time  $t=0$  in each panel corresponding to the UT time given on the upper right corner. The vertical axes show signal strength ( $A$ ) in linear arbitrary units, with  $A=0$  representing absence of signal. The lower panels show the signal intensity in the 24.8 kHz (NLK) channel, which shows the signature of the impulsive radio atmospheric from lightning discharges. The 1-s periods during which a network CG flash were detected are so indicated. The absence of measurable delay between the lightning discharge and the onset of the VLF perturbations indicates that these events are not likely to be a manifestation of lightning-induced electron precipitation from the magnetosphere (Figure from [12]).

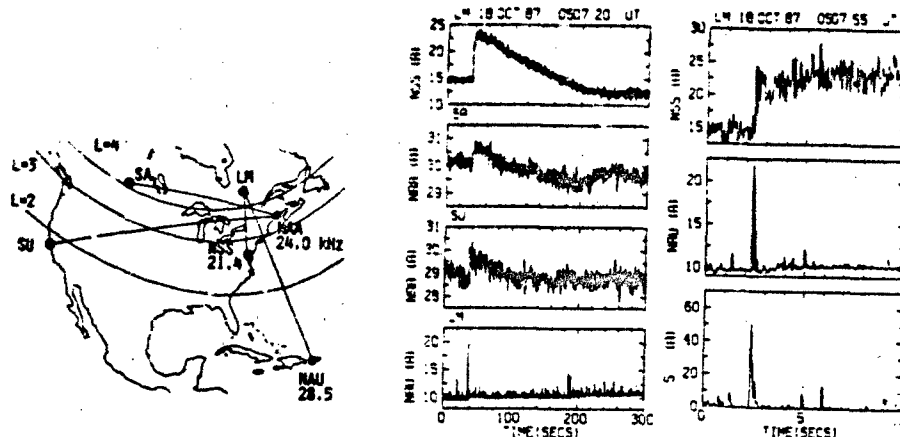


Figure 10: An unusual VLF event observed simultaneously at three stations on four different signals as shown in the left hand panels. The signal paths corresponding to the data displays are illustrated on the map above. The format of the amplitude records is similar to that for Figure 5. The perturbation (amplitude increase) is smallest in the NAU-LM channel but is still clearly identifiable. Also seen in this channel is an intense radio atmospheric from the causative lightning discharge. The panels on the right show the NSS-LM signal and the associated spheric channels at higher resolution. With the 50 ms resolution of the measurement, there is no time delay between the causative atmospheric and the VLF perturbation onset. Such events are believed to represent a new type of direct upward coupling between the troposphere and the lower ionosphere.

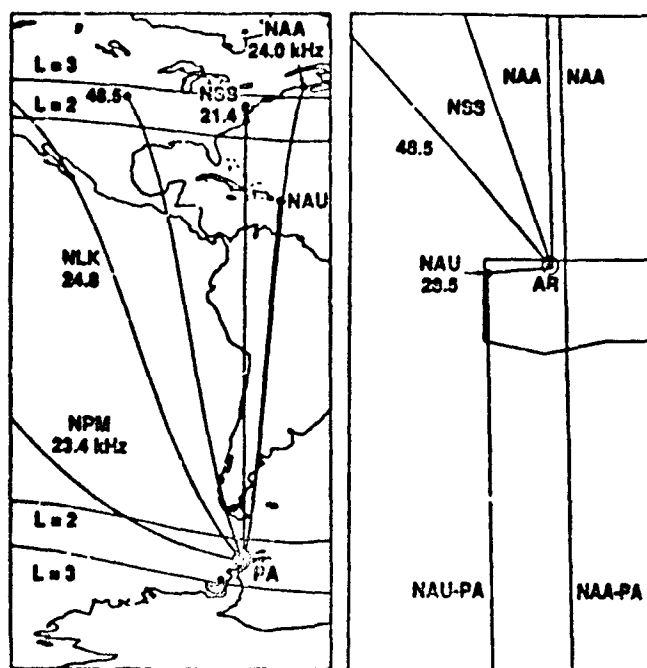


Figure 11: Observation geometry at Arecibo (AR), Puerto Rico (right) and at Palmer (PA) Station, Antarctica (left). At both sites, signals from 6-10 VLF transmitters are routinely observed although only selected propagation paths are shown above. The NAA-PA path crosses within <50 km of the NAU transmitter as seen in the right hand panel. The loci of the foot of the  $L = 2$  and  $L = 3$  field lines at 100 km altitude is also shown for reference. The NLK and the NPM transmitters are located respectively at (48°N, 122°W) and (21°N, 158°W). The number associated with each transmitter is the operation frequency in kHz (Figure from [1]).

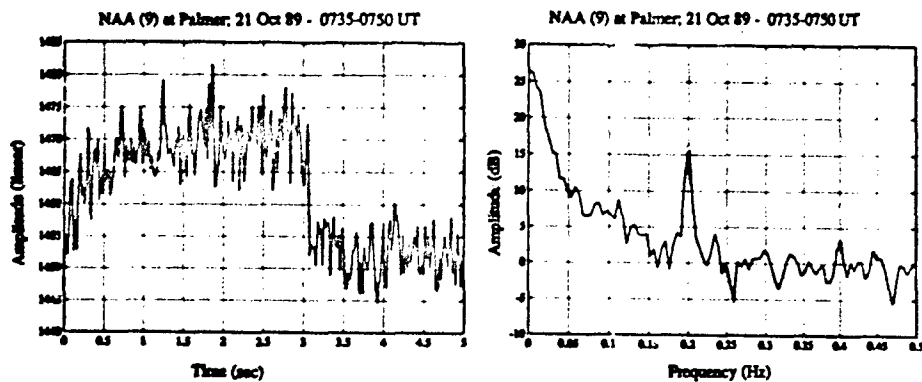


Figure 12: (a) The top panel shows superposition of 180 5-s segments from the 0735-0750 UT period on 21 Oct 89 for NAA-PA signal. The vertical axis shows amplitude ( $A$ ) in linear arbitrary units, with  $A = 0$  being absence of signal. (b) The lower panel shows power spectra of the 15-min data for the period 0735-0750 UT for NAA-PA signal.

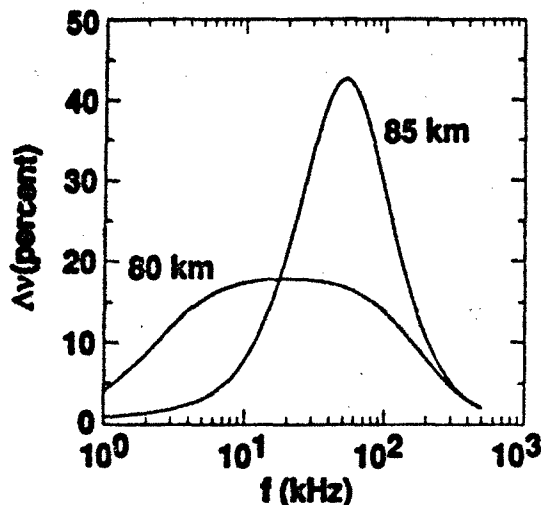


Figure 13: Frequency dependence of heating at 80 and 85 km altitudes. The percentage change in collision frequency ( $\nu$ ) is shown for 80 and 85 km altitudes for the ordinary component for  $2.5 \times 10^{-4} \text{ W/m}^2$  input wave power density at 70 km altitude (corresponding to 100 kW radiated power) and a typical nighttime exponential ambient density profile. (Figure from [1]).

#### DISCUSSION

J. S. BELROSE, CA

Your association of sharp onset events seen in VLF transmissions with lightning is very interesting. I question, however, your interpretation that this event is due to heating. At the higher USA/lower Canadian latitudes ( $L = 2.5$  to  $4$  say), Canadian VLF propagation data over paths of near to  $L = 4-6$ , for those paths where we had a 30 MHz riometer near mid path, showed that all events were associated with riometer absorption. This would suggest that the lightning induced events are associated with particle precipitation rather than heating.

#### AUTHOR'S REPLY

I believe that the larger subset of the events we see are indeed due to induced electron precipitation as evidenced by the distinct time delay between lightning and the event onset. However, the events that do not exhibit this delay are likely not due to precipitation, as I discussed in my talk. The  $L = 4-6$  events that you speak of are most likely occurring outside the plasmapause, where both whistler-triggered and spontaneous ELF/VLF chorus emissions are known to precipitate electron bursts.

M. C. LEE, US

I would like to point out that observations of VLF wave-excited lower hybrid waves in the ionosphere were indicated in the Franco-Soviet ARCAD 3 satellite experiments (Berthelier et al., 1982; L. R. O. Storey and F. Lefeuvre, personal communication, 1984). Lower hybrid waves were detected when the satellite passed over VLF transmitters. Further, enhanced airglow was measured (Chayrev et al., 1976; Chayrev et al., 1988).

G. SALES, US

I noticed that you placed the perturbation near the location of the mode interference for your simulations. Is this a coincidence or are you saying that this is the only location that produces a significant event?

#### AUTHOR'S REPLY

The range of flux levels in precipitation events is quite large so that I think detectable VLF perturbations would occur even when the disturbed region is near a signal maximum along the path. However, modeling clearly shows that the largest amplitudes are observed where the disturbance is near a minimum.

R. SHOWN, US

For the lightning induced effects on VLF propagation, are you postulating a change in electron temperature or electron density? Can the measured recovery time constants help determine the cause?

AUTHOR'S REPLY

For lightning-induced electron precipitation effects, we believe that a change in electron density (generation of secondary ionization) is involved. For direct effects of the RF fields from lightning, I suggested in my paper (GRL, May 1990) that a change in collision frequency (i.e., in temperature) was involved. However, at this meeting, I learned in Dr. Jones' tutorial talk that change in temperature leads to change in density because the recombination rate is altered. Thus, it occurred to me that lightning would also cause electron density changes which would then be consistent with observed recovery rates. After talking to some of my colleagues (Duncan, Kossy, Field), I am further convinced that lightning-induced heating is the mechanism for these VLF events without delay.

P. KOSSEY, US

Have you compared the effects of the events on VLF phase, as well as amplitude? Is one a more sensitive "detector" than the other?

AUTHOR'S REPLY

We conduct phase measurements on a selected number of our stations and the results are contained in a PhD thesis that was completed by T. Wolf in Jan 1990. Basically, observations in the southern hemisphere indicate that phase may be as much as 10 dB more sensitive than amplitude in response to a given ionospheric disturbance. However, in the northern hemisphere, for reasons not yet well understood, we find that amplitude may be just as (if not more) sensitive as phase.

# IONOSPHERIC CHEMICAL RELEASES

P. A. BERNHARDT, V. A. SCALES  
SPACE PLASMA BRANCH, PLASMA PHYSICS DIVISION  
NAVAL RESEARCH LABORATORY  
WASHINGTON, DC 20375-5000

## SUMMARY

Ionospheric plasma density irregularities can be produced by chemical releases into the upper atmosphere. F-region plasma modification occurs by (1) chemically enhancing the electron number density, (2) chemically reducing the electron population, or (3) physically convecting the plasma from one region to another. The three processes (production, loss, and transport) determine the effectiveness of ionospheric chemical releases in subtle and surprising ways. Initially, a chemical release produces a localized change in plasma density. Subsequent processes, however, can lead to enhanced transport in chemically modified regions. Ionospheric modification by chemical releases excites artificial enhancements in airglow intensities by exothermic chemical reactions between the newly created plasma species. Numerical models have been developed to describe the creation and evolution of large scale (>1 km) density irregularities and airglow clouds generated by artificial means. Experimental data compares favorably with these models. In general, we find that chemical releases produce transient, large amplitude perturbations in electron density which can evolve into fine scale irregularities via nonlinear transport processes.

## 1. INTRODUCTION

The ionosphere is the primary medium for radio wave propagation. Natural irregularities can degrade a communication channel by inducing amplitude or phase fluctuations as a result of multipath mixing or scattering. Artificial modification of the F-region can be used to generate artificial density structures, control existing irregularities or to study processes which govern their evolution.

Artificial ionospheric irregularities can be generated by the release of neutral substances into the F-region. The generation of localized density perturbations can be understood in terms of the electron and ion continuity equations

$$\frac{dn_j}{dt} + \nabla \cdot (n_j \mathbf{v}_j) = P_j - L_j \quad (1)$$

where the subscript "j" refers to electrons or ions,  $n_j$  is the concentration,  $\mathbf{v}_j$  is the velocity,  $P_j$  is the production rate and  $L_j$  is the loss rate for the plasma species. Chemical releases can directly affect the right side of the continuity equation by enhancing the production by photo or collisional ionization of neutral vapors. Or chemical releases can accelerate losses through electron attachment or dissociative recombination processes.

Immediately following a neutral gas release, the dense neutral cloud "snowplows" the background plasma. This coupling to the plasma occurs by modifying the transport term  $[\nabla \cdot (n_j \mathbf{v}_j)]$  in the continuity equations for electrons and ions. The velocity of each plasma species is determined by the equation of motion:

$$\frac{d\mathbf{v}_j}{dt} + (\mathbf{v}_j \cdot \nabla) \mathbf{v}_j = - \frac{\nabla P_j}{\rho_j} + \frac{q_j}{m_j} (\mathbf{E} + \mathbf{v}_j \times \mathbf{B}) + \mathbf{g} - \nu_{jn} (\mathbf{v}_j - \mathbf{U}) - \nu_{ji} (\mathbf{v}_j - \mathbf{v}_i) \quad (2)$$

where  $P_j = n_j k T_j$  is pressure,  $\rho_j = n_j m_j$  is mass density,  $T_j$  is electron or ion temperature,  $m_j$  is mass,  $q_j$  is charge,  $\mathbf{E}$  is electric field,  $\mathbf{B}$  is ambient magnetic flux density,  $\mathbf{g}$  is gravitational acceleration,  $\nu_{jn}$  is the electron- (or ion-) neutral collision frequency,  $\mathbf{U}$  is the velocity of the neutrals,  $\nu_{ji}$  is the electron- (or ion-) ion collision frequency, and  $\mathbf{v}_i$  is the velocity of the other plasma species. Most of the terms on the right side of (2) can be artificially changed by a chemical release. Heating of the plasma can occur by several processes including collisional interactions with the neutrals and energy dissipation by plasma waves in the interaction regions. The resulting increase in plasma pressure will affect the flow. Polarization electric fields at the edge of expanding clouds accelerate the ambient electrons and ions resulting in nonuniform flows.

This paper is an overview of the relative effects of production, loss and transport on large scale ionospheric modification by chemical releases. The next three sections discuss chemical mechanisms, parallel and perpendicular transport, and the effects of injection velocities on the interactions. The results from computer simulations are compared with experimental observations when possible. The last section summarizes the relative effectiveness of various chemical releases for production of ionospheric irregularities.

## 2. CHEMISTRY OF CHEMICAL RELEASES

The chemistry of ionospheric depletion chemicals has been discussed in detail by Bernhardt [1987]. Here a simple comparison of the chemical processes is made to illustrate the relative strengths and weaknesses of the different classes of chemical modification in the ionosphere.



There are four classes of initial reactions in the upper atmosphere following a neutral gas release. The first class is oxidation. Atomic oxygen is the most abundant species between about 250 and 600 km altitude. It can react rapidly with the released material to yield substances which may be less effective as ionospheric modifiers. This reaction has the form

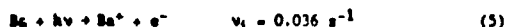


where XY represents the injected substance and  $XO^+$  is the product of the reaction which may be left in an excited state. Airglow emissions from the excited states may interfere with other light emissions which are related to the ion-electron chemistry. From the point of view of ionospheric modification, the Class I neutral reactions are unwanted because they reduce the efficiency for ionospheric modification and they produce airglow emissions which contaminate emissions used to diagnose plasma chemistry.

The second class of reaction in the upper atmosphere is photoionization. This reaction is generically represented as



When easily ionizable materials such as barium, cesium, sodium, europium, etc. are released in sunlight, photoionization yields enhanced ion and electron concentrations. Optical diagnosis of these releases is possible if the parent neutral and/or the product ion fluoresce in sunlight. The reaction for barium is



The primary disadvantage for the Class II reactions is that sunlight is required to produce the ionospheric modification.

The third class of ionospheric modification reaction is the positive-ion, molecule charge transfer. This reaction takes the form



where  $XO^+$  is a positive molecular ion which can rapidly recombine with electrons. The dissociative recombination reaction is

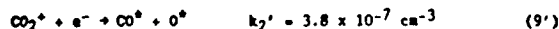
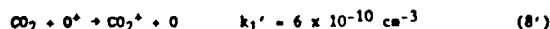


where  $X^*$  and  $O^+$  are excited states. The sequence of reactions for a  $CO_2$  release at thermal speeds is



where  $O(^1D)$  is the lowest excited state of atomic oxygen which yields red-line emissions upon transition to the ground  $O(^3P)$  state. Class III reactions eventually lead to electron density reductions after the molecular ions ( $XO^+$ ) has recombined. The primary limitation of this class of reaction is that at two step process [reaction (6) followed by (7)] are required to produce electron density reductions.

At orbital velocities, reaction rates can change because of the added energy of injection. For kinetic energies on the order of 3 eV, the  $CO_2$  reactions are

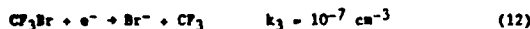


Optical emissions from excited states of carbon monoxide, which will not be excited for low energy releases, can provide experimental verification of the importance of reactions (8') and (9') for  $CO_2$  releases from orbiting vehicles.

The fourth class of reaction directly depletes the electron concentration by dissociative electron attachment. The form of this reaction is



where  $X^-$  is the negative ion dissociation product. The reaction with tri-fluoromethylbromide is



Comparing reactions (8) and (12), we see that the initial electron attachment reactions can be one hundred times more rapid than the initial ion-molecule reactions. Complications arise from the temperature dependence of the electron attachment reactions. Below the activation energy of reaction, the reaction rates decrease rapidly with temperature. The activation energy for (12) is 0.065 eV. The negative ion created by the Class IV reactions either reacts with the atomic oxygen ion



or becomes photo dissociated



The mutual neutralization between  $Br^-$  and  $O^+$  is thought to proceed as follows:



The photodetachment reaction from solar illumination for the bromine anion from (12) is



The primary limitation for ionospheric modification from electron attachment reactions is that they must be conducted in darkness for long lived effects. Enhanced airglow from the excited states in (13) and (15) can provide a diagnostic of the chemical and physical processes in the modified plasma.

### 3. PARALLEL TRANSPORT

The motion of the plasma following a chemical release can be considered in terms of parallel and perpendicular transport relative to  $B$ . The two directions tend to be uncoupled owing to the relatively large parallel conductivity which makes the magnitude of the ambipolar electric fields oriented parallel to  $B$  much less than the magnitude of the polarization fields across the magnetic field lines.

The details of the numerical model of parallel transport is described by Bernhardt [1990]. The distribution of ionized species along magnetic field lines is computed from the equations of continuity (1) and momentum (2). Only variation along the magnetic field direction is considered. The inertial terms on the right side of (2) are dropped. The spatial distributions of the ambient species ( $e^-$  and  $O^+$ ) and the chemically produced species ( $Br^-$  or  $X^-$ ) are computed self consistently with chemical reactions and transport. The ambipolar electric field ( $E$ ) is calculated assuming constant current density along  $B$ .

Simulations have been carried out for the ionospheric modification with Class II, III, and IV chemical reactions for releases at 300 km altitude into an F-region plasma with an undisturbed density of  $3 \times 10^{15} \text{ cm}^{-3}$ . To illustrate a Class II reaction, the release of  $10^{26}$  atoms (23 kg) of barium vapor was simulated (Figure 1). The production and loss terms for the continuity equation (1) are

$$P_1 = n[Ba] \nu_1, \quad L_1 = 0 \quad (17)$$

$$P_2 = 0, \quad L_2 = 0 \quad (18)$$

$$P_3 = n[Ba] \nu_1, \quad L_3 = 0 \quad (19)$$

where the subscript 1, 2, and 3 refer to electrons,  $O^+$ , and  $Ba^+$  ions, respectively,  $n[Ba]$  is the barium neutral concentration, and  $\nu_1 = 0.036 \text{ s}^{-1}$  is the ionization rate due to sunlight. The barium ion concentration reaches a maximum of  $5.8 \times 10^{16} \text{ cm}^{-3}$  at the center of the cloud. The diffusion along the magnetic field line causes the  $Ba^+$  ions to extend 70 kilometers from the release point 9 minutes after the release. The  $O^+$  ions are excluded from the center of the barium cloud and are compressed at the sides. The electron concentration is the sum of the positive ion concentrations.

The  $O^+$  depression at the center of the barium cloud is a result of the ambipolar electric fields at the edges of the cloud. These fields reach a maximum of 8  $\mu\text{V/m}$  and are oriented to keep the mobile electrons from escaping from the region of high density barium. These same fields will exclude the positively charged  $O^+$  ions from entering the barium region. This process is called the electrostatic snowplow [Schunk and Szuszczewicz, 1988]. The fluxes of all species are directed outward from the center of the cloud because the  $O^+$  ions are being carried along with the expanding barium plasma. Figure 1 also shows a 40% increase in the parallel conductivity at the center of the cloud which is much smaller than the 20-fold increase in electron density. Electron-ion collisions limit the magnitude of this conductivity.

The electrostatic snow-plow of ambient  $NO^+$  ions during the Placer barium release is shown in Figure 2 [Marsini and Szuszczewicz, 1983]. The enhancement of  $NO^+$  of about 50% at 149 km altitude (designated by the arrow in Figure 2) can be attributed to ambipolar electric fields at the edge of the barium cloud.

The Class III reactions initially reduce the  $O^+$  density. The production and loss terms in (1) for the release of carbon dioxide at low velocity have the form

$$P_1 = 0, \quad L_1 = k_2 n_3 n_1 \quad (20)$$

$$P_2 = 0, \quad L_2 = k_1 n[CO_2] n_2 \quad (21)$$

$$P_3 = k_1 n[CO_2] n_2, \quad L_3 = k_2 n_3 n_1 \quad (22)$$

where the subscripts 1, 2, and 3 refer to the electron,  $O^+$ , and  $O_2^+$  ion concentrations, respectively;  $n[CO_2]$  is the neutral carbon dioxide concentration;  $k_1$  and  $k_2$  are the reaction rates given in (8) and (9). The ionospheric modification 12.8 seconds after the release of  $10^{26}$

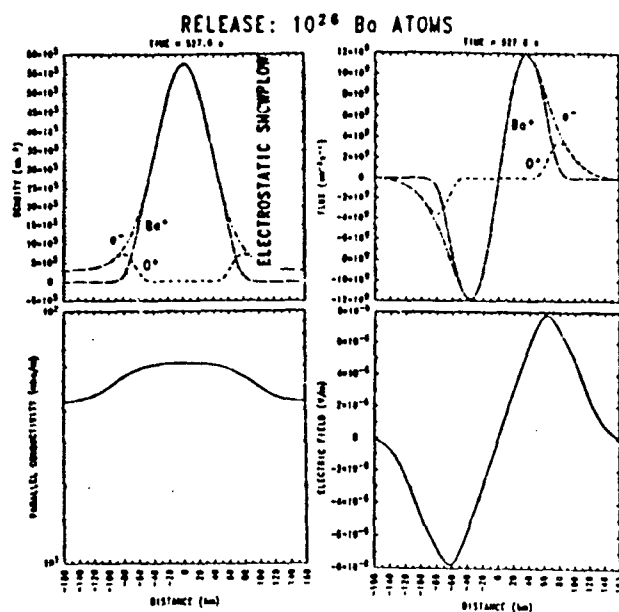


Figure 1. Computed densities, fluxes, conductivities, and ambipolar electric fields for a solar-illuminated barium release in the ionosphere.

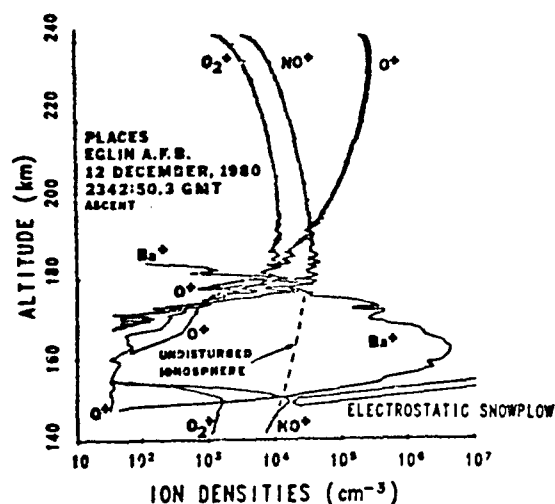


Figure 2. Ion mass spectrometer measurement of  $\text{NO}^+$  density showing the effects of ambipolar electric fields.

$\text{CO}_2$  molecules at 300 km altitude is illustrated in Figure 3. At the center of the cloud, most of the  $\text{O}^+$  ions have been converted into  $\text{O}_2^+$  ions. Recombination of the diatomic ion with electrons produces a 15% reduction in the electron density. The hole is being replenished by field aligned fluxes of  $\text{O}^+$  and  $e^-$  toward the center of the depletion. The molecular ion concentration is reduced by both chemistry and by outward fluxes. The parallel conductivity perturbation from this release is negligible and the ambipolar electric fields are relatively weak (less than 4  $\mu\text{V/m}$ ).

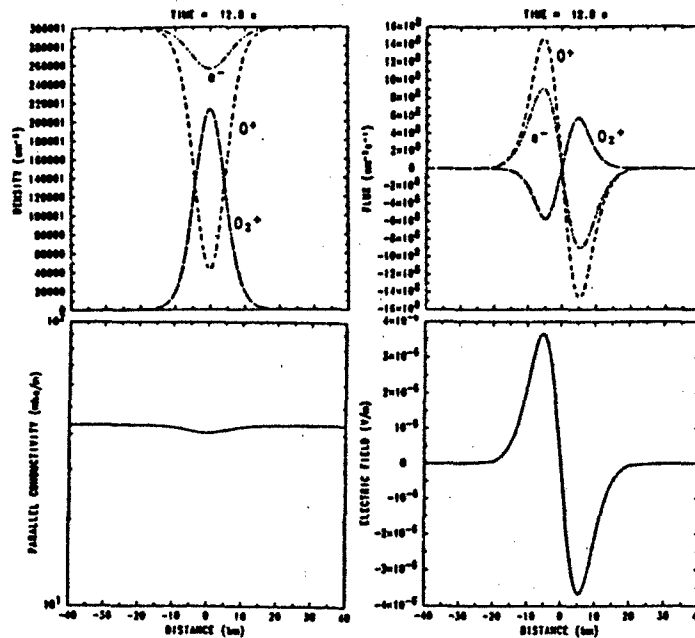
RELEASE:  $10^{26}$   $\text{CO}_2$  MOLECULES

Figure 3. Computed densities, fluxes, conductivities and ambipolar electric fields for a  $\text{CO}_2$  release into a uniform ionosphere.

During the NASA sponsored Spacelab II experiment, the Space Shuttle Orbital Maneuvering Subsystem (OMS) engines were used to deposit 280 kg of  $\text{CO}_2$ ,  $\text{H}_2\text{O}$ ,  $\text{H}_2$ ,  $\text{CO}$ , and  $\text{N}_2$  molecules into the F-layer over Arecibo, Puerto Rico. Figure 4 shows the evolution of the localized depletion near the peak of the layer as measured with the Arecibo incoherent scatter radar. The observed density depression is consistent with the numerical models involving Class III reactions and ambipolar diffusion. The initial density enhancements at the sides of the hole are a result of the collisional "snowplow" which is not included in Figure 3 but has been described by Bernhardt et al. [1988 a,b].

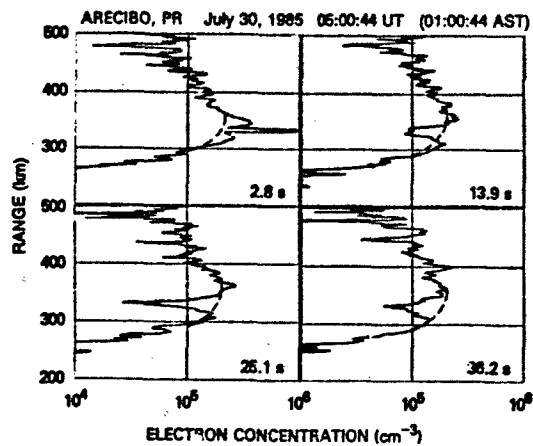


Figure 4. Ionospheric profiles showing the evolution of the hole produced by the Space Shuttle OMS engine burn over Arecibo, Puerto Rico.

The class IV reactions produce much larger perturbations in electron density, plasma fluxes, parallel conductivity, and electric fields (Figure 5). The loss terms in the continuity equation for the electron attachment releases are

$$P_1 = 0, \quad L_1 = k_3 n[\text{CF}_3\text{Br}] n_1 \quad (23)$$

$$P_2 = 0, \quad L_2 = k_4 n_3 n_2 \quad (24)$$

$$P_3 = k_3 n[\text{CF}_3\text{Br}] n_1, \quad L_3 = k_4 n_3 n_2 \quad (25)$$

where  $k_3$  and  $k_4$  are the reaction rates in (12) and (15), respectively. Nine seconds after the release of  $10^{26}$  molecules of  $\text{CF}_3\text{Br}$ , nearly all electrons within a seven kilometer radius are attached to form  $\text{Br}^-$  ions. The ambipolar electric field strength is  $130 \text{ kV/m}$  with a polarity that inhibits electrons from flowing into the center. These fields compress the ambient  $\text{O}^+$  ions toward the center as shown in Figure 5. The steep gradients at the edge of the modified region produce electron fluxes that are a factor ten greater than in the previous examples.

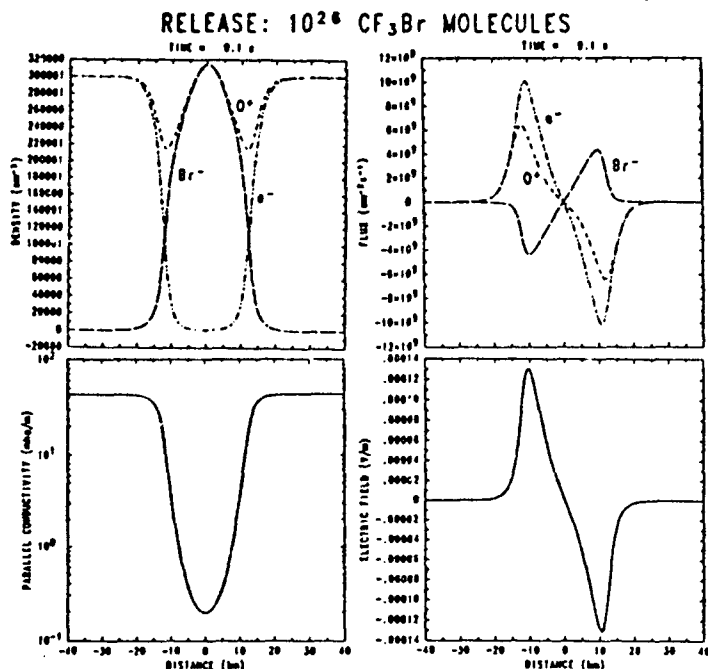


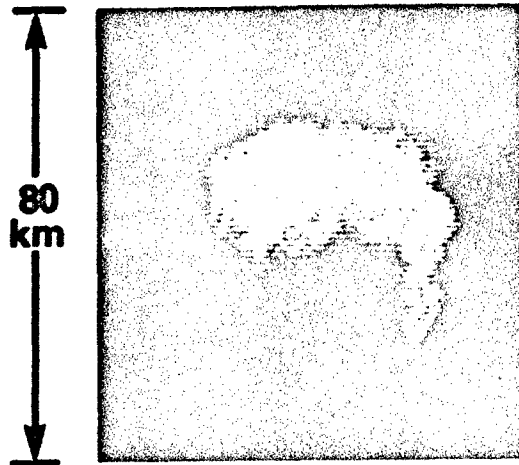
Figure 5. Simulation of the release of an electron attachment material in a uniform plasma.

Near the release point, the electron concentration is reduced to the point that ions are only carriers of electric current. This limits the parallel conductivity reduction to two orders of magnitude. The class IV reactions are preferred for experiments which need the maximum changes in longitudinal conductivity. In situ measurements were made with the NRL Langmuir probe flying through the ionospheric hole created by the release of 30 kg of  $\text{CF}_3\text{Br}$  during the NASA sponsored NICARE-1 experiment. The electron concentration was reduced from  $3 \times 10^5 \text{ cm}^{-3}$  to less than  $15 \text{ cm}^{-3}$  in a radius greater than 15 km [P. Rodriguez and C. S. Lin, private communication, 1990].

As illustrated by reactions (13) and (15), mutual neutralization of the negative and positive ions leaves the products in excited states. This can produce airglow that can be recorded from the ground. We do not have any images of airglow excited by a  $\text{CF}_3\text{Br}$  release but we do have data acquired by an intensified CCD camera for an  $\text{SF}_6$  release. Figure 6 is an image of the airglow cloud produced by the  $\text{SF}_6$  release which occurred during the NASA/Boston University SPINEX-2 experiment [Pulford et al., 1987]. Negative ions are created and destroyed according to the following reactions with  $\text{SF}_6$  in the F-region.



Mutual neutralization of  $\text{SF}_6^-$  and  $\text{O}^+$  ions by reaction (26) yields excited  $\text{O}(^3\text{P})$  states and 777.4 nm airglow [Bernhardt et al., 1986]. The airglow cloud fills the region initially depleted by the electron attachment reactions.



02:01:40 UT

Figure 6. 777.4 nm airglow emissions for a nighttime, 40 kg release of  $\text{SF}_6$  at 252 km altitude during the 28 April 1986 SPINEX-2 experiment. The maximum intensity is 160 Rayleighs.

At night, field aligned plasma flow provides the recovery mechanism for ionospheric holes produced by the  $\text{CO}_2$  and  $\text{CF}_3\text{Br}$  releases. Ten minutes after the  $\text{CO}_2$  release, the computed plasma depression has a full width at half maximum of 92 km with a maximum reduction of 28%. Ten minutes after the  $\text{CF}_3\text{Br}$  release, the diameter of the hole is 120 km and the maximum reduction is 65%. In general, electron attachment substances are more effective ionospheric modification agents than are those which initially react with  $\text{O}^+$ .

#### 4. PERPENDICULAR TRANSPORT

Chemically produced density irregularities become polarized by collisions with neutrals that are moving across magnetic field lines. The resulting electric fields cause  $\mathbf{E} \times \mathbf{B}$  drifts of the ions and electrons and produce a distortion of the cross-section of the modified region. The cross-field motion of ionization enhancements from Class II reactions has been extensively studied [e.g., Scannapieco et al., 1974]. Two dimensional simulations of this flow have been studied for chemical modification produced by electron attachment (Class IV reactions) by Bernhardt [1988] using a numerical model. These simulations included the effects of electron attachment and mutual neutralization chemistry, self-consistent electric fields, and three-species plasma transport but ion and electron inertia [i.e., the right side of (2)] were neglected.

The results of these previous studies are briefly summarized as follows: Pedersen conductivity enhancements such as barium ion clouds and positive-ion, negative-ion clouds become polarized by neutral winds. The polarization fields cause motion of the clouds in the direction of the neutral wind. The down wind side of the enhancement steepens and eventually splits (bifurcates) into field aligned irregularities. In contrast, the polarization direction is reversed for Pedersen conductivity depressions such as initially produced by class III reactions or by Class IV reactions after the positive and negative ions have mutually neutralized. The plasma cavity drifts across  $\mathbf{B}$  in the direction opposing the neutral wind.

A computer simulation of the ionospheric hole 30 minutes after the release of 30 kg of  $\text{SF}_6$  into the F-region is shown in Figure 7, reproduced from Bernhardt [1988]. Contours of the field-line-integrated Pedersen conductivity are shown as a function of the coordinate axis perpendicular to  $\mathbf{B}$ . The ambient neutral wind is taken to be 200 m/s in the x-direction. Plasma drifts up to 45 m/s are found inside the hole. This causes distortion and bifurcation of the originally smooth contours. This  $\mathbf{E} \times \mathbf{B}$  Gradient Drift Instability produces irregularities on the upwind edge of the cavity.

We will now present several new results from a study of the release of electron attachment chemicals (see class IV reactions) directed at orbital velocities across the ambient magnetic field. A similar study for the injection of materials which photoionize (see class II reactions) has been studied by Mitchell et al. [1985].

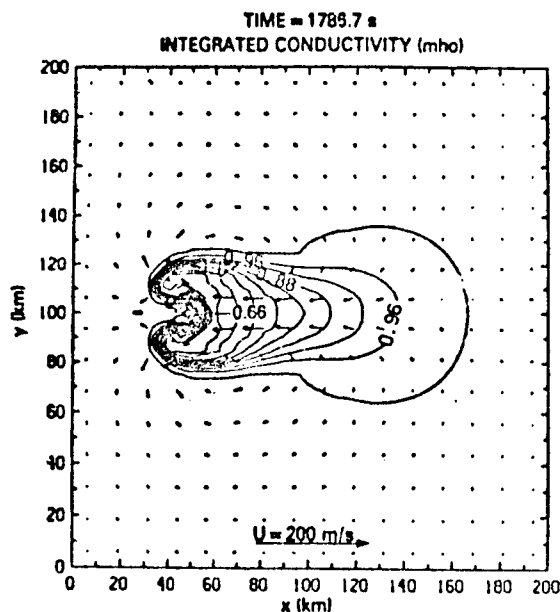


Figure 7. Computed contours of integrated Pedersen conductivity for a plasma hole created by the release of 30 kg of  $\text{SF}_6$  into the F-region. After 30 minutes, the ambient neutral wind parallels the cloud, steepens the upwind side and causes it to bifurcate.

The neutral cloud moving perpendicular to  $\mathbf{B}$  begins to attach electrons to form a negative-ion positive-ion plasma cloud. Because the negative-ions are created with initial cross-field momentum, they become polarized. An electric field is set up across the plasma cloud that causes it to  $\mathbf{E} \times \mathbf{B}$  drift in the direction of the neutral cloud. The distance the cloud moves across the magnetic field is an important aspect of the "skidding" process. Collisions with the background neutral particles will cause the neutral cloud as well as the plasma cloud to eventually slow down and stop. The radial expansion of the clouds initially depends on the release temperature and, as collisional interaction with the background becomes important, on the temperature of the atmosphere.

To study these processes, we have developed a two-dimensional plasma simulation. It is an extension of the one described by Bernhardt [1988] which was limited to low speed flow where the neutral wind dominated. In this simulation code the effects of the ion inertia on the right hand side of (7) have been included. Inertial effects become important at sufficiently high altitudes in the rarefied atmosphere where the ion neutral collision frequency becomes small. Generally, when the time between ion and the background neutral collisions becomes on the order of or larger than characteristic time scales of the phenomena under investigation, these effects must be incorporated into the theoretical model. Inertial terms in continuity equation introduce an effective inertial capacitance that causes (1) the initial potential to decay at a slower rate and (2) the region of highest potential to lag further behind the neutral cloud.

Figures 8, 9, and 10 show the results of the simulations with and without the effects of ion inertia for the release of an electron attachment material at 7 km/s across the magnetic field. In the figures, the magnetic field  $\mathbf{B}$  is directed out of the page. The background plasma density (composed of  $\text{O}^+$  and  $\text{e}^-$ ) is assumed to be  $4 \times 10^5 \text{ cm}^{-3}$  while the background neutral density is  $4 \times 10^8 \text{ cm}^{-3}$ . The positive and negative ion-neutral collision frequencies are 0.61 and  $0.14 \text{ s}^{-1}$ , respectively. The left sides of the figures show (1) contours of the plasma Pedersen conductivity which are proportional to the ion densities and (2) the plasma flow vectors that are determined from the  $\mathbf{E} \times \mathbf{B}$  velocity. The right sides contain contours of the electrostatic potential.

Figure 8 illustrates the evolution of the conductivity and potential after 1 second in the simulation. The material is released at the point (0,0) in the simulation box. Initially we see that the neutral cloud attaches electrons and forms negative ions. This produces an enhancement in the conductivity of the plasma and leads to the generation of an electrostatic potential. Figure 9 shows the collision dominated case where ion inertia has been neglected. After 16.7 seconds in the simulation, we see that the plasma cloud has expanded causing a significant enhancement in the plasma conductivity and has moved roughly 30 km. At this time, the plasma velocity is less than 100 m/s so the plasma cloud has essentially stopped moving with respect to the neutrals. The maximum potential has decayed significantly from the initial value of about 200 volts. From the neutral cloud contours (not shown) we determine that the region of largest conductivity is essentially collocated with the region of largest neutral cloud density. This is true in the inertial simulation as well.

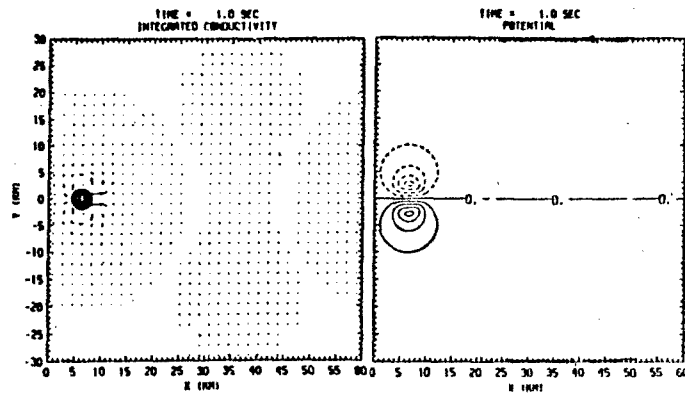


Figure 8. Field-line integrated Pedersen conductivity (mho), velocity field (km/s) and electrostatic potential (V) from the initial injection of an electron attachment vapor at orbital velocity (7 km/s). One second after release, the maximum plasma velocity has a magnitude of 3 km/s. The electric potential reaches 200 V inside the negative-ion cloud.

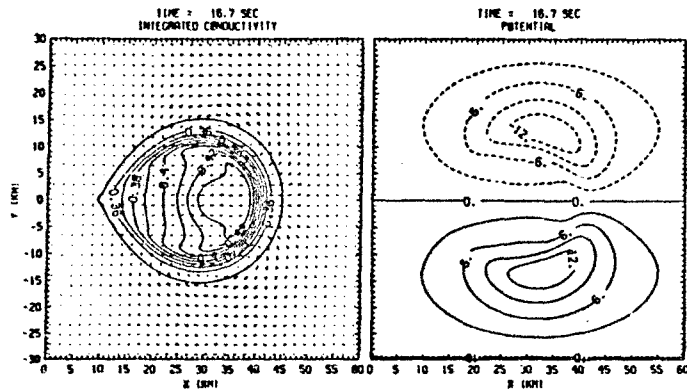


Figure 9. Integrated Pedersen conductivity (mho), plasma drift velocities (km/s) and electric potential (V) for a simulation without ion inertia. Sixteen seconds after release, the maximum flow vector has a magnitude of 0.82 km/s. The peak electric potential is 12 V.

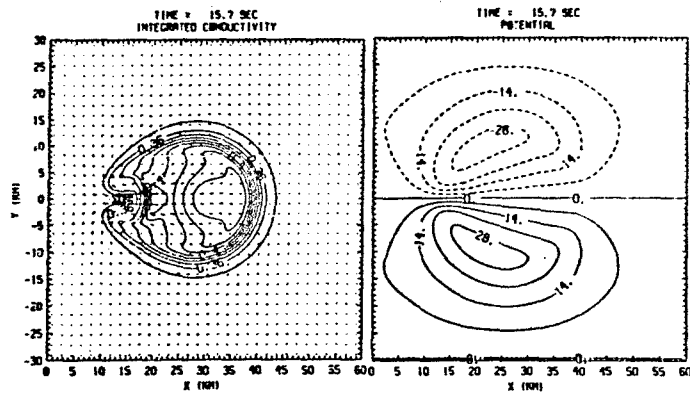


Figure 10. Integrated Pedersen conductivity (mho), plasma flow velocities (km/s) and electric potential (V) for a simulation which includes ion inertia. Sixteen seconds after release, the maximum flow velocity has a magnitude of 3.1 km/s. The peak electric potential is 30 V.



Figure 10 illustrates the evolution of the plasma cloud including the effects of ion inertia, 15.7 seconds after the release. The main differences between this and Figure 8 are that the potential has decayed with a significantly slower rate and the region of the strongest potential lags behind the region of highest conductivity. Due to relatively strong electric fields at the back, a shear in the  $E \times B$  velocity causes the cloud to bifurcate. This behavior should be observable in experiments. In general both the inertial and noninertial simulation runs show that a plasma cloud created by injection of electron attachment materials at orbital velocities may skid several 10's of km across the magnetic field.

#### 6. CONCLUSIONS

Ionspheric modification by chemical releases provides the means to generate large scale plasma irregularities. Chemicals produce localized density gradients either by enhancing or reducing the electron concentrations. The magnitudes of the density changes are determined by both chemical processes (i.e., photoionization, photodetachment, electron attachment, ion-molecule reactions, and dissociative recombination) and transport processes (i.e., inertia, diffusion, and  $E \times B$  convection). Ambient neutral winds and electric fields will transport modified region away from the release location. Nonuniform velocity gradients can steepen the density gradients and may eventually yield small scale structures. Releases from orbiting satellites may be different from low speed releases for two reasons. First, chemical reaction rates and reaction products are dependent on the chemical injection speeds. Second, the injection velocity can stimulate velocity-shear (i.e., Kelvin-Helmholtz) instabilities which yield irregularities in the modified ionosphere.

#### ACKNOWLEDGEMENTS

This work is supported by the NASA CRRES Projects Office and the Office of Naval Research.

#### REFERENCES

- Bernhardt, P. A., E. J. Weber, J. G. Moore, J. Baumgardner, and M. Mendillo, "Excitation of oxygen permitted line emissions by  $Si_6$  injection into the F region", *J. Geophys. Res.*, **91**, 8937-8946, 1986.
- Bernhardt, P. A., "A critical comparison of ionospheric depletion chemicals," *J. Geophys. Res.*, **92**, 4617, 1987.
- Bernhardt, P. A., "Cross-B convection of artificially-created negative-ion clouds and plasma-depressions: low speed flow," *J. Geophys. Res.*, **93**, 8696-8704, 1988.
- Bernhardt, P. A., B. A. Kashiva, C. A. Tepley, and S. T. Noble, "Spacelab 2 upper atmospheric modification experiment over Arecibo, 1, neutral gas dynamics," *Astrophys. Lett. and Comm.*, **7**, 169-182, 1988a.
- Bernhardt, P. A., W. E. Schwartz, M. C. Kelley, M. P. Sulzer, S. T. Noble, "Spacelab 2 upper atmospheric modification experiment over Arecibo, 2, plasma dynamics," *Astrophys. Lett. and Comm.*, **7**, 183-198, 1988b.
- Bernhardt, P. A., "Parallel-to-B dynamics of chemically induced perturbations to the ionosphere, submitted to *J. Geophys. Res.*, 1990.
- Pulford, J. A., J. V. MacDougall, P. A. Forsyth, M. Mendillo, and P. A. Bernhardt, "Ionospheric electron content measurements during the second space-plasma negative-ion experiment (SPINEX-2), *Canadian J. Phys.*, **65**, 403, 1987.
- Mitchell, H. G., J. A. Fadder, J. D. Hubs, and S. T. Zalesak, "Transverse motion of high-speed barium clouds in the ionosphere," *J. Geophys. Res.*, **90**, 11091-11095, 1985.
- Marcisi, R. S., and E. P. Szuszczewicz, "Plasma composition and structure characterization of an ionospheric barium cloud, *Active Experiments in Space*, pp. 299-304, Alpbach, Austria, 24-28 May 1983.
- Scannapieco, A. J., S. L. Ossakov, D. L. Book, B. E. McDonald, and S. R. Goldman, "Conductivity ratio effects on the drift and deformation of F region barium clouds coupled to the E region ionosphere," *J. Geophys. Res.*, **79**, 2913, 1974.
- Schunk, R. W., and E. P. Szuszczewicz, "Early time plasma expansion characteristic of ionized clouds in the ionosphere," *J. Geophys. Res.*, **93**, 12901-12915, 1988.

#### DISCUSSION

RYCROFT, UK

In your interesting simulation of the disruption of field-aligned currents in the auroral region, at what altitude is the  $CF_3Br$  released? How do the effects expected vary with the altitude of the release?

AUTHOR'S REPLY

The release of  $CF_3Br$  should occur in the F-region near the peak. If the release occurs above ~ 400 km, the gas will expand too rapidly for chemical reactions to be effective. Releases below 130 km would yield localized changes in both parallel and perpendicular (Podersen and Hall) conductivities. Chemical deposition on discrete Birkeland current paths is most easily accomplished for releases between 200 and 300 km altitude.

OBSERVATIONS DE PERTURBATIONS PRODUITES  
PAR DES EXPLOSIONS CHIMIQUES PUISSANTES  
DANS L'IONOSPHERE

Elisabeth Blanc  
Commissariat à l'Energie Atomique  
Laboratoire de Détection et de Géophysique  
BP 12, 91680 BRUYERES-LE-CHATEL, FRANCE

Abram B. Jacobson  
Mail Stop D 466  
Los Alamos National Laboratory  
LOS ALAMOS - N.M. 87545 - U.S.A.

RESUME

Cet article décrit des observations par sondage ionosphérique HF de perturbations produites par des explosions chimiques puissantes (plusieurs KT). Ces expériences ont été effectuées à des distances de l'ordre de 30 à 40 km du point d'explosion. A cause de l'amplification due à la décroissance de densité atmosphérique lorsque l'altitude augmente, les ondes acoustiques issues de telles explosions sont caractérisées par des propriétés d'ondes de choc lorsqu'elles atteignent l'ionosphère. L'évolution de la perturbation a été étudiée de la région E inférieure jusqu'à la région F2 en utilisant 8 fréquences de sondage. On montre qu'une couche E sporadique occultante subit des fluctuations de petite échelle et devient semi-transparente après le passage de la perturbation. Plusieurs fronts d'onde avec des caractéristiques différentes ont été suivis jusqu'en région F1. Dans la région E inférieure, la perturbation produit des stratifications sur lesquelles les ondes radio sont partiellement réfléchies. Les échos de région E subissent une modulation d'amplitude avec une période de l'ordre de 2 secondes persistant environ 30 minutes. Les variations de la hauteur de réflexion et de l'effet Doppler sont les plus importantes en région F1. L'onde perd son caractère d'onde de choc en région F2, et la signature de la perturbation est alors celle d'une onde pseudo-sinusoidale avec une longueur d'onde de plusieurs dizaines de kilomètres.

ABSTRACT •

This paper describes observations by HF ionospheric sounding of disturbances produced by powerful chemical explosions (several KT). These experiments were performed at distances of about 30-40 km from the explosion point. Because of the amplification due to the atmospheric density decrease with increasing altitude, the acoustic waves from such explosions are characterized by shock wave features when they reach the ionosphere. The development of the disturbance has been studied from the lower E region up to the F2 region by using 8 sounding frequencies. We show that a blanketing sporadic E layer undergoes small scale fluctuations and becomes semi-transparent after the passage of the disturbance. Several wave fronts with different properties are followed up to the F1 region. In the lower E region, the wave induced stratifications on which the radio waves are partially reflected. The echoes totally reflected in the E region undergo an amplitude modulation with a period of about 2 seconds, persisting about 30 minutes. The variations of the total reflection height and of the Doppler frequency shift are most noticeable in the F1 region. The wave loses its shock wave feature in the F2 region and the disturbance signature is then that of a pseudo-sinusoidal wave with a wave length of several tens of kilometers.

1. INTRODUCTION

Les effets des ondes acoustiques issues de sources explosives puissantes au sol ont fait l'objet d'études intensives dans les années 1960-1970. Ces ondes sont amplifiées lors de leur propagation verticale et ont des caractéristiques d'onde de choc lorsqu'elles atteignent l'ionosphère. Ces sources peuvent produire des systèmes d'ondes itinérantes qui perturbent l'ionosphère sur une échelle de distance aussi importante que celle de la circonférence terrestre (voir les articles synthèses de Yeh et Liu, 1974, et de Francis, 1975). Les différentes sources acoustiques capables de perturber l'ionosphère ont été décrites par Blanc (1985).

Un intérêt nouveau s'est manifesté lorsqu'il a été suggéré que ces sources puissent perturber le système atmosphère-ionosphère-magnétosphère dans son ensemble. Une variation importante du champ électromagnétique observée par satellite au-dessus d'une explosion de 250 T, a été interprétée comme résultant d'une onde de Alfvén excitée en région 3 par l'onde acoustique issue de l'explosion (Gokhberg, 1984). Les modèles ont confirmé la possibilité de tels effets (Jacobson et Bernhardt, 1985, Jacobson 1986).

• A. English version of this text is available (contact the authors).

Les mesures des effets ionosphériques en zone proche sont peu nombreuses et se limitent souvent à l'étude des effets des ondes de choc directes (Barry et al. 1966, Jones et Spracklen, 1974, Pittevey et al. 1985).

Le but de la présente communication est d'effectuer une synthèse des résultats de deux expériences de sondage ionosphérique vertical réalisées en zone proche d'explosions chimiques puissantes pour étudier, d'une manière très détaillée, les effets directs et indirects de l'onde de choc au niveau des différentes régions de l'ionosphère.

## 2. RESULTATS EXPERIMENTAUX

### 2.1 Description des expériences

Deux expériences ont été réalisées dans le cadre d'un programme de collaboration du Laboratoire de Détection et de Géophysique du Commissariat à l'Energie Atomique (France) et de l'Atmospheric Science Group du Los Alamos National Laboratory (USA). Les explosions (approximativement 5 KT d'ANFO - ammonium nitrate fuel oil -), appelées Minor Scale et Misty Picture ont eu lieu à White Sand Missile Range, New Mexico (USA) le 27 Juin 1985 et le 14 Mai 1987.

Les résultats présentés dans ce rapport sont ceux qui ont été obtenus par une expérience de sondage ionosphérique vertical effectuée à une distance du point source de l'ordre de 30 à 38 km. Le but de l'expérience était d'étudier la structure fine du milieu ionisé à partir du sondeur RHF fonctionnant simultanément sur 6 fréquences de sondage, choisies en fonction des conditions ionosphériques fournies par des ionogrammes (Herbreteau, 1979). D'autres détails expérimentaux ont été fournis par ailleurs (Blanc et Rickel, 1977, Blanc et Jacobson, 1989).

Les résultats d'autres expériences de sondages ionosphériques effectuées à plus grande distance pour ces deux mêmes explosions ont été décrites par Jacobson et al. (1986, 1988) et Fitzgerald (1986).

### 2.2 Interaction en présence d'une couche Es occultante

Lors de la première expérience (à 18:20:00 TU), les conditions ionosphériques n'étaient pas favorables parce qu'une couche E sporadique (Es) intense ne permettait pas d'obtenir des réflexions au niveau de la région F.

La figure 1 présente l'amplitude d'un écho obtenu à la fréquence de sondage 4,590 MHz et correspondant à une réflexion au niveau de la couche Es. Avant le passage de la perturbation, on observe un écho stable obtenu par réflexion verticale sur la base de la couche Es et, à plus haute altitude, des irrégularités de faible amplitude, dont l'intensité décroît lorsque l'altitude augmente. Ces irrégularités subissent des fluctuations temporelles et spatiales sur des échelles de plusieurs secondes et de 5 à 10 km. Ces échos se produisent sur la base pseudo-ondulatoire et irrégulière de la couche Es, l'absence de directivité des antennes permettant d'obtenir des réflexions obliques jusqu'à des angles de l'ordre de 50 degrés de part et d'autre de la verticale.

Le passage de la perturbation se traduit par deux effets :

- au niveau de la couche Es elle-même, deux diminutions brusques de l'amplitude de l'écho produites par le passage des fronts avant et arrière de l'onde ; la couche Es reste semi-transparente après le passage de l'onde.
- au niveau des irrégularités il se produit un changement de la structure irrégulière du milieu au niveau d'un front d'onde qui apparaît à 18:25:30 TU. Ce front peut être suivi pendant environ une minute sur une vingtaine de kilomètres. Sa vitesse apparente, déterminée par les variations de hauteur de réflexion par unité de temps est de l'ordre de 500 m/s (figure 2). Les irrégularités apparaissant à la suite de ce front sont caractérisées par des échelles temporelles et spatiales de l'ordre de 1-2 s et 1-4 km.

Afin de déterminer les caractéristiques de cette structure, des analyses spectrales de l'amplitude de ces irrégularités échantillonnées à trois hauteurs de réflexion différentes (115, 120 et 125 km) ont été effectuées. La figure 3 compare les spectres avant le passage du front d'onde (18:25:00 TU) et après le passage du front (18:25:30 à 115 km et 18:26:00 à 125 km). Les différents spectres n'ont pas été normalisés, le spectre de référence représentant les conditions non perturbées a été superposé sur chaque spectre en trait fin. Les caractéristiques des spectres semblent proches de spectres de turbulences, et il n'apparaît pas de pics à des fréquences bien déterminées ; la densité spectrale est plus importante après le passage du choc dans la bande fréquentielle considérée.

A 115 km à 18:26:30, un signal haute fréquence ( $\sim 7$  Hz) apparaît ; il s'agit d'un résidu de l'effet Doppler d'un trajet supplémentaire (figure 4). Une analyse détaillée de ce trajet (Blanc et Rickel, 1989) a montré qu'il s'agit probablement du front d'onde qui avait été observé à plus grande distance par Jacobson et al. (1987), et qui se propageait à une vitesse supersonique (500 m/s) à base de la couche Es.

### 2.3 Interaction dans des conditions ionosphériques normales

Lors de la deuxième expérience (16:00:00), les conditions ionosphériques étaient normales et les différentes fréquences du sondeur ont été choisies de façon à observer les effets de la perturbation dans les différentes régions de l'ionosphère.

#### \* Interaction au niveau d'une couche Es non occultante

La figure 5 présente les variations de l'amplitude des échos au niveau d'une couche Es non occultante, qui présentait des fluctuations irrégulières au moment de l'expérience. La fréquence de sondage utilisée (4,130 MHz) se réfléchissait partiellement sur cette couche, le niveau de réflexion totale se situait en région F à 270 km.

Une perturbation importante apparaît à 16:06:30 TU, différents trajets grossièrement parallèles se superposent au trajet principal ; un écho se forme ensuite à basse altitude ( $\sim 90$  km) et persiste un peu plus d'une minute à une hauteur presque constante. Les caractéristiques de cet écho sont différentes de celles des échos des couches E habituellement observées dans l'ionosphère inférieure ; altitude inférieure à celle des échos des couches E, vitesse importante ; ces réflexions sont issues de stratifications produites par le choc acoustique ; une analyse plus détaillée a été publiée par ailleurs (Blanc et Rickel, 1989).

La figure 8 présente les résultats d'une analyse de la perturbation de l'écho principal, les deux diagrammes hauteur de réflexion-temps montrent respectivement :

- la puissance spectrale avec un seuil en amplitude éliminant le bruit, dans un filtre spectral limité à des fréquences Doppler de -1 à +9 Hz (partie inférieure de la figure).
- la fréquence Doppler avec un seuil et un filtrage similaire ; le niveau de gris le plus intense représente des fréquences Doppler de +9 Hz, le niveau le plus faible des fréquences de -1 Hz (partie supérieure de la figure).

Deux trajets différents, correspondant à des vitesses apparentes de l'ordre de 450 et 200 m/s apparaissent ; le trajet observé le dernier est caractérisé par les fréquences Doppler les plus importantes.

Pour mieux séparer les différents trajets, une analyse similaire a été effectuée avec 4 filtres spectraux différents de -1 - 3, -3 - 5, -5 - 7 et -7 - 9 Hz (figures 7 et 8). Les trajets ont des caractéristiques différentes :

- le dernier trajet apparaissant est celui qui a la vitesse apparente la moins élevée et la fréquence Doppler la plus importante ( $\sim -8$  à  $-7$  Hz).
- le trajet qui apparaissait avant sur la figure 6, de vitesse apparente la plus grande est caractérisé par une fréquence Doppler moins importante ( $\sim -5$  Hz).

Ces remarques indiquent que le premier trajet correspond probablement à une réflexion sur un front d'onde qui pénètre en région F1. La plus faible valeur de la fréquence Doppler est le signe d'une valeur plus faible de l'indice de réfraction ; le second trajet est probablement obtenu par réflexion partielle oblique sur un front qui se propage à plus basse altitude, la fréquence Doppler détermine alors la vitesse du front, l'indice de réfraction étant proche de l'unité.

#### • Interaction en région E

La figure 9 présente les variations de la hauteur de réflexion d'un écho de région E obtenu pour la même expérience.

La partie supérieure de la figure représente le passage de l'onde de choc, en distingue, de la même manière que précédemment, différents trajets.

La partie inférieure représente le même signal, avec des échelles différentes de manière à visualiser plus largement les phénomènes précédant et suivant le passage de la perturbation. Cette figure montre un changement de la structure de l'écho au moment du passage du front d'onde, il subit des fluctuations d'amplitude avec des périodicités de l'ordre de 2 secondes. Ces fluctuations persistent plusieurs dizaines de minutes. Une analyse publiée par ailleurs (Blanc et Jacobson, 1989) a montré une déformation bilatérale des spectres de l'effet Doppler correspondant à cet effet.

#### • Interaction en région F

Les figures 10, 11, 12 représentent les échos obtenus pour la même expérience à plus haute altitude sur les fréquences de sondage 4.130 MHz, 4.700 MHz, 6.410 MHz.

Sur la première de ces fréquences, on distingue une décroissance brusque du niveau de réflexion puis un signal complexe, composé d'un mélange d'une oscillation de grande amplitude et de différents trajets similaires aux trajets de région E. Ce signal est suivi d'une oscillation de période de l'ordre de 10 secondes qui se prolonge pendant environ 10 minutes.

Les effets sont extrêmement complexes sur la fréquence 4.700 MHz. On distingue deux augmentations brusques de la hauteur de réflexion des échos pouvant être produites par le passage des fronts avant et arrière de la perturbation ; la présence d'une vallée d'ionisation au passage de chacun de ces fronts peut produire une augmentation très rapide de la hauteur, de la même manière que les vallées d'ionisation au niveau des fréquences critiques des régions E ou F1 sur un ionogramme. Ce signal est suivi d'une oscillation de période de plusieurs dizaines de secondes. A des hauteurs de réflexion très importantes, de l'ordre de 500 km, un trajet supplémentaire apparaît, qui pourrait être expliqué par une réflexion oblique, mais l'origine du réflecteur, front d'onde, irrégularités, instabilités, n'a pas été identifiée.

Sur la fréquence 6.410 MHz, le signal est différent. Sous l'effet du filtrage de l'atmosphère, la perturbation à plus haute altitude est plus simple ; elle se compose de deux augmentations brusques de la hauteur de réflexion et la perturbation est modélisable par une ride d'ionisation pseudo-sinusoidale (Blanc, 1984, Pittevey et al., 1985) ; sa longueur d'onde est de l'ordre de 54 km si on suppose une vitesse de propagation égale à 600 m/s.

#### REMERCIEMENTS

Les auteurs remercient les différentes personnes du LDG qui ont participé aux expériences et au traitement des données, spécialement L. Herbreteau, D. Raoux, A. Le Roy, B. Rascalou et D. Giraud.

## REFERENCES

- G.M. Barry, L.J. Griffiths, J.C. Tenser "HF radio measurements of high altitude acoustic waves from a ground level explosion" *J. Geophys. Res.*, 71, 4173, 1966.
- E. Blanc "Interaction of an acoustic wave of artificial origin with the ionosphere as observed by vertical HF sounding at total reflection levels" *Radio Sci.* 19, 653-664, 1984.
- E. Blanc "Observations in the upper atmosphere of infrasonic waves from natural or artificial sources : a summary" *Ann. Geophysicae*, 3, 6, 673-687, 1985.
- E. Blanc, A.R. Jacobson "Observations of ionospheric disturbance following a 5 kiloton chemical explosion II stratifications and long term anomalies in the lower ionosphere after shock passage" *Radio Sci.* 24, 6, 733-746, 1989.
- E. Blanc, D. Rickel "Non linear wave fronts and ionospheric irregularities observed by HF sounding over a powerful acoustic wave" *Radio Sci.* 24, 3, 279-288, 1989.
- J. Fitzgerald "Bistatic phase sounding in the ionosphere above Minor Scale explosion". Report LAMP, LA-10657-MS, UC-35, 1986.
- S.W. Francis "Global propagation of atmospheric gravity waves : a review", *J. Atmos. Terr. Phys.*, 37, 1011-1054, 1975.
- N.B. Gokberg "Strong acoustic wave action, active experiments in space" Alpbach, ESA, SP-195, 99-110, 1983.
- L. Herbretes "Etude et réalisation d'une ionosonde de hautes performances : application à l'étude de la propagation d'ondes acoustiques dans l'ionosphère" Thèse d'Université, Univ. Paris VI, 1979.
- A.R. Jacobson "A model for conjugate coupling from ionospheric dynamos in the acoustic frequency range" *J. Geophys. Res.*, 91, 4404-4412, 1986.
- A.R. Jacobson, P.A. Bernhardt "Electrostatic effects in the coupling of upper atmospheric waves to ionospheric plasma" *J. Geophys. Res.*, 90, 6533-6541, 1985.
- A.R. Jacobson, R. Carlos, E. Blanc "Observations of ionospheric disturbance following a 5 kiloton chemical explosion : I persistent oscillation in lower thermosphere after shock passage" *Radio Sci.* 23, 5, 820-830, 1988.
- A.R. Jacobson, R.C. Carlos, P.E. Argo, D.G. Rickel "Radio wave diffraction during the passage of an acoustic shock through a sporadic E layer" *Radio Sci.*, 21, 4, 752-760, 1986.
- T.B. Jones, C.T. Spracklen "Ionospheric effects of the Flixborough explosion" *Nature*, 250, 719, 1974.
- M.L.V. Pitteway, D.G. Rickel, J.W. Wright, M.M. Al-Jarrah "Modelling the ionospheric disturbance caused by an explosion on the ground" *Ann. Geophysicae*, 3, 6, 695-704, 1985.
- K.C. Yeh, C.H. Liu "Acoustic gravity waves in the upper atmosphere" *Rev. Geophys. Space Phys.* 12, 2, 193-216, 1974.

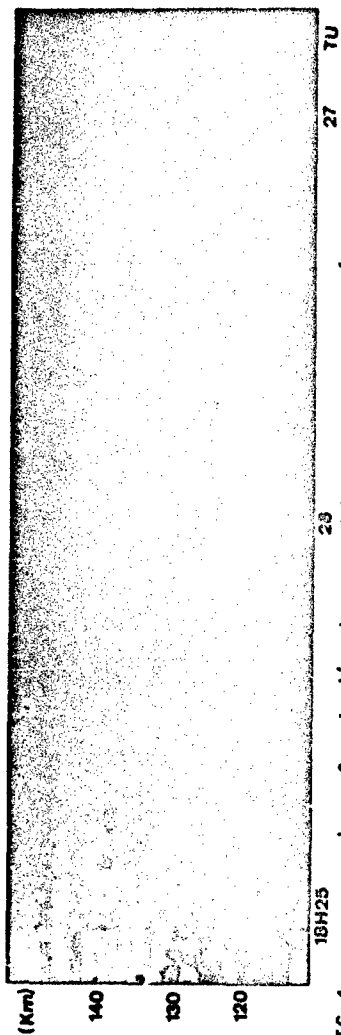


FIG 1 passage d'un front d'onde acoustique au niveau d'une couche Es

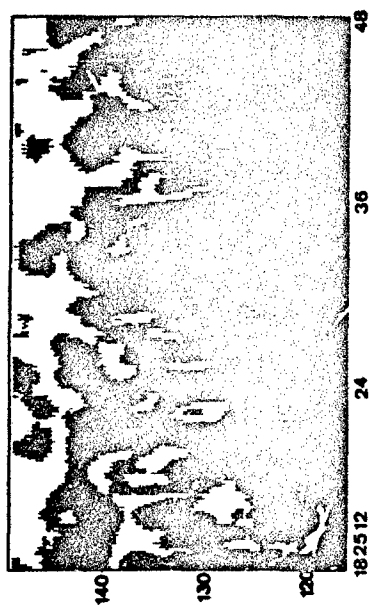


FIG 2 détails de la figure 1

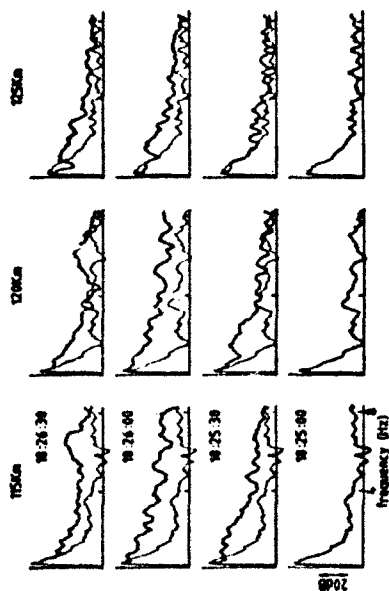


FIG 3 spectres à 115 , 120 , 125 km

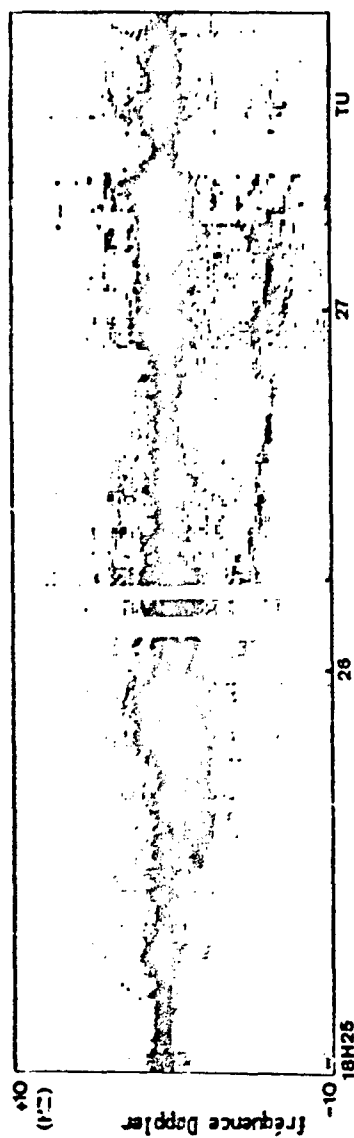


FIG 4 fréquence Doppler au niveau de l'écho principal sur la couche Es au moment du passage de l'onde acoustique, un trajet supplémentaire apparaît à 18:26:30 TU

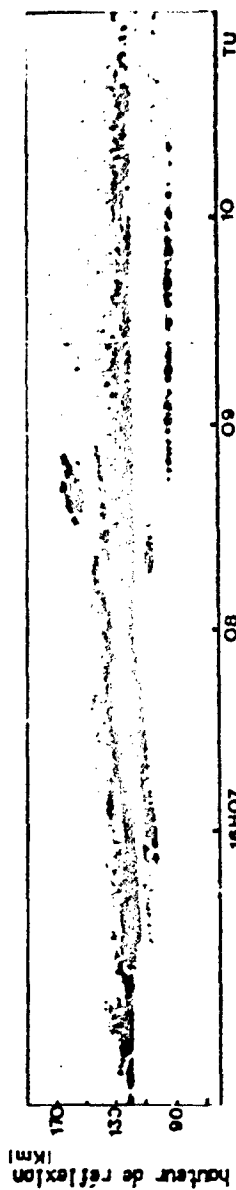


FIG 5 diagramme hauteur de réflexion-temps montrant des réflexions multiples sur différents fronts d'onde, des réflexions partielles à basse altitude apparaissent après le passage du choc

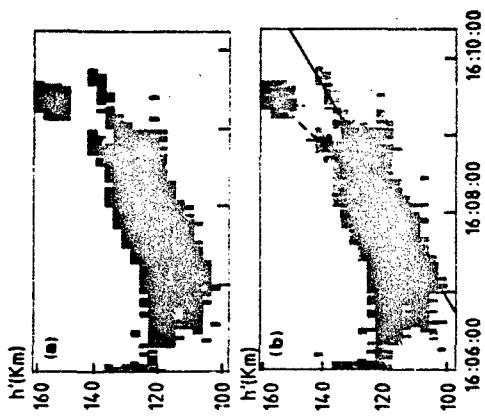


FIG 6 diagrammes hauteur de reflexion  
 temps lors du passage de la perturbation  
 en region E  
 (a) puissance spectrale dans un filtre  
 -1 -9 HZ  
 (b) frequences Doppler correspondantes

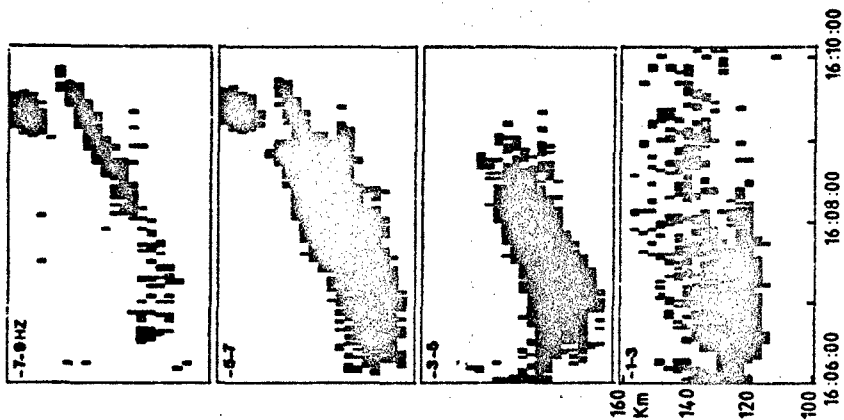


FIG 7 puissance spectrale dans les bandes  
 spectrales -1 -3 , -3 -5 , -5 -7 , -7 -9 HZ

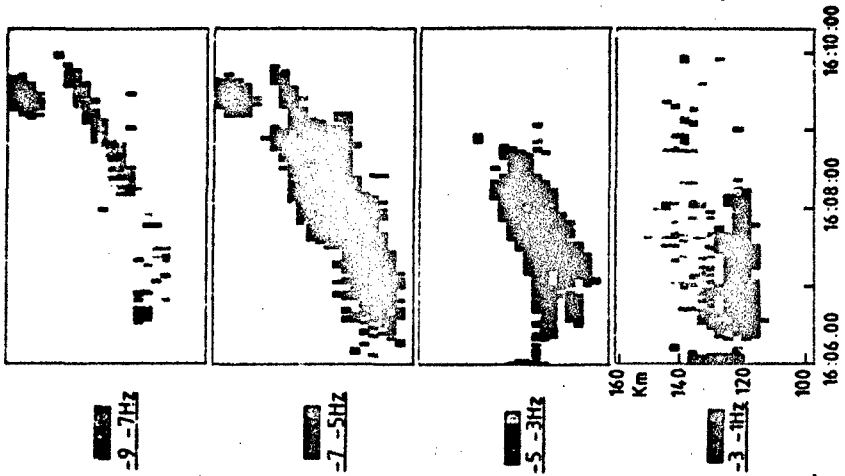


FIG 8 frequences Doppler  
 correspondantes



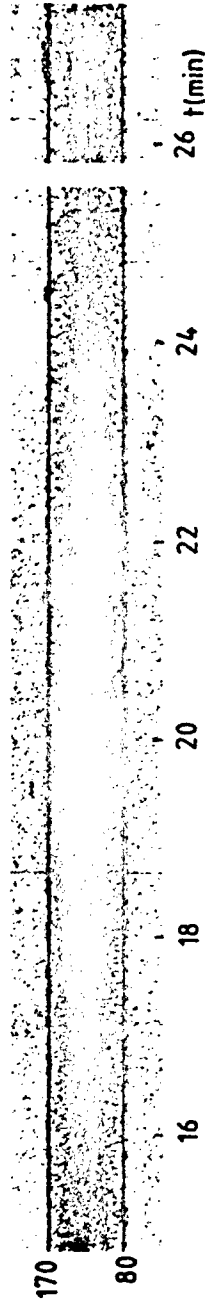
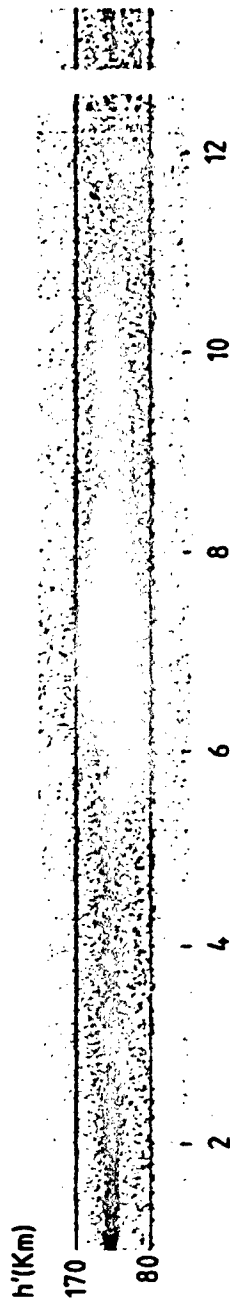
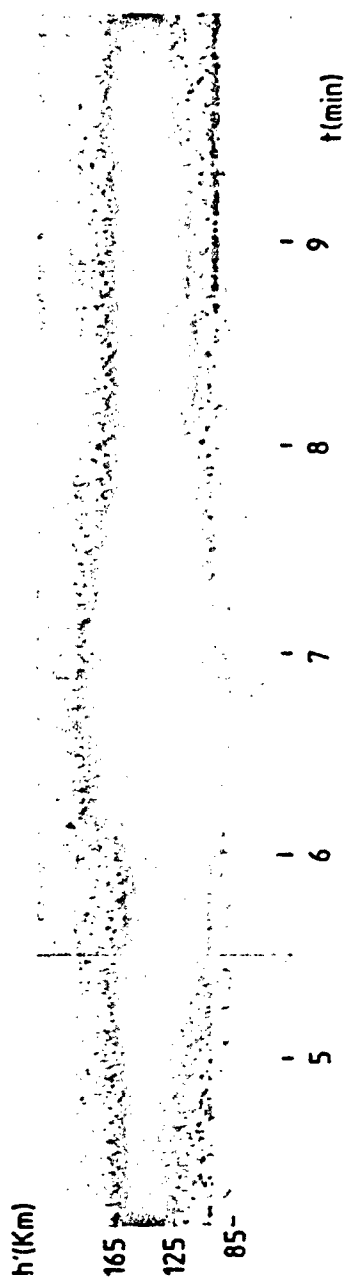


FIG9 exemple d interaction en region E (frequence 3.290 MHz)

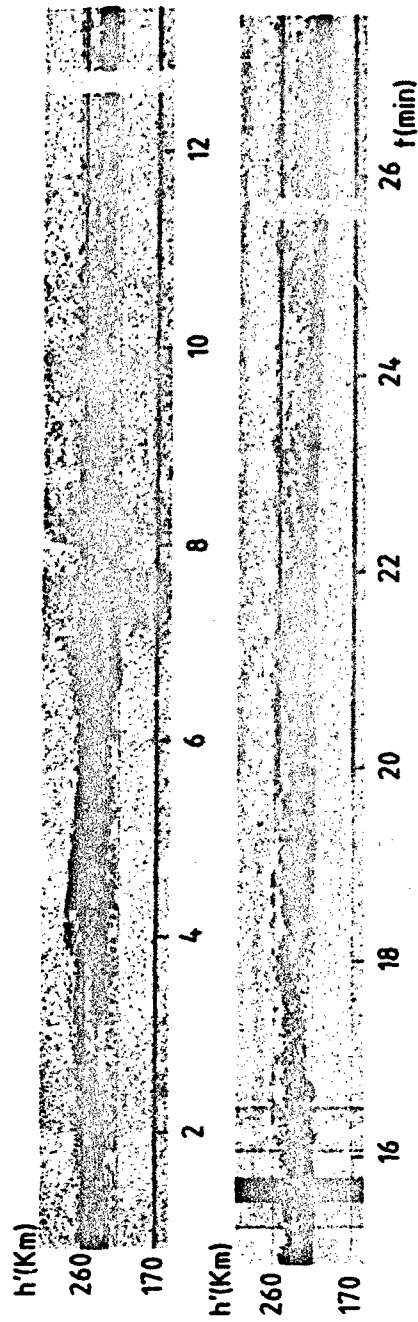


FIG10 interaction en region F1 (frequence 4,138 MHz)

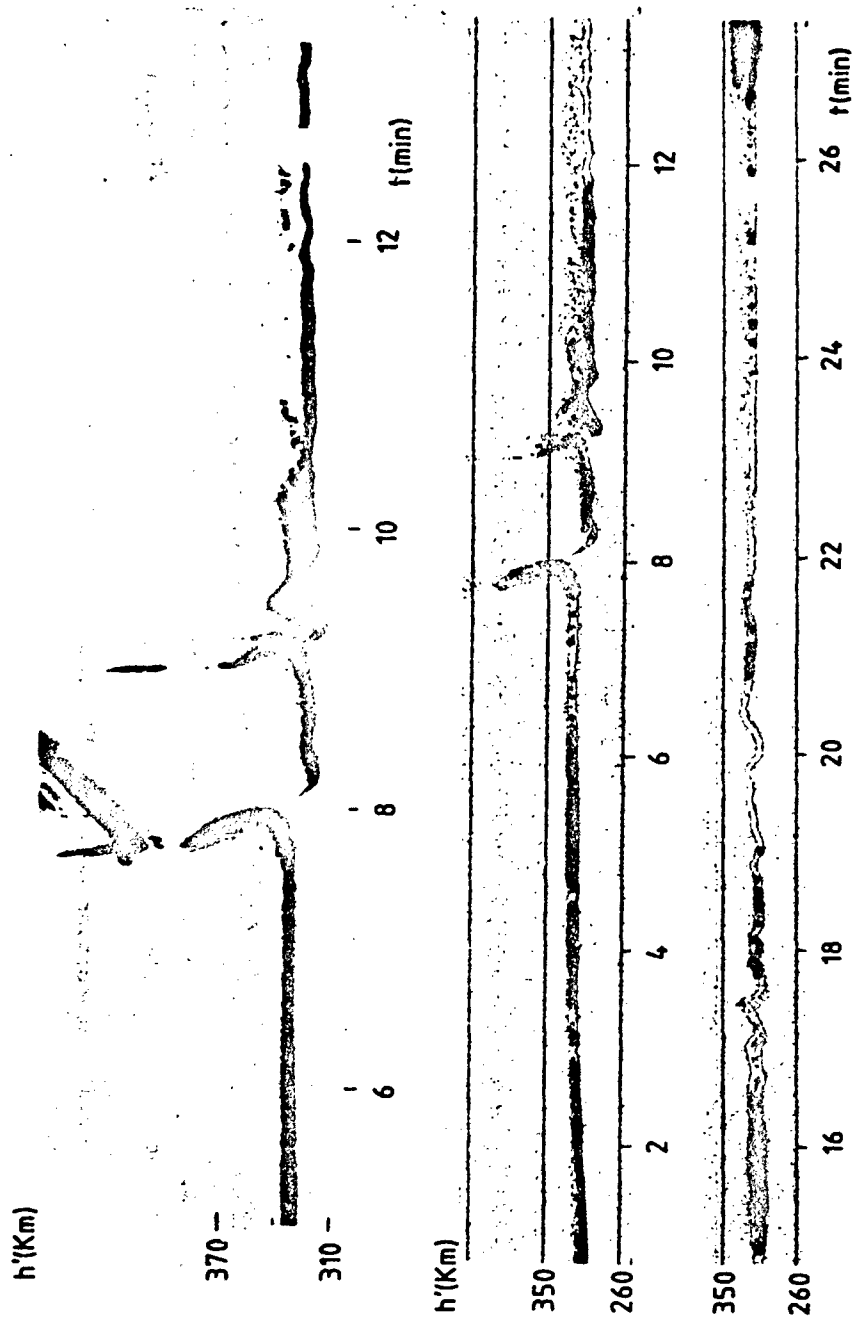


FIG11 Interaction en region F1 (frequence 4,700 MHz)

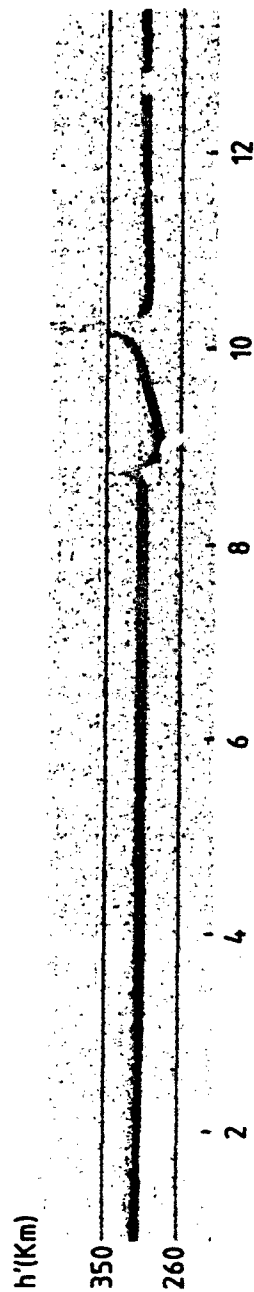
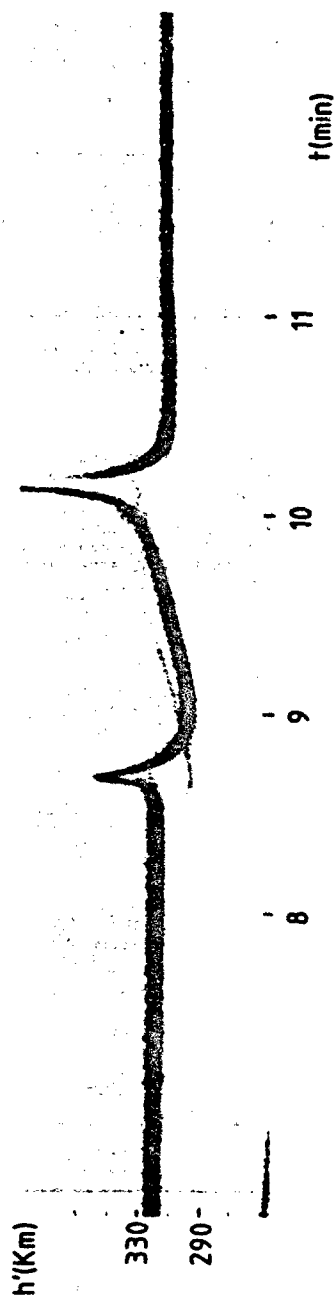


FIG 12 interaction en region F2 (frequency 6,410 MHz)

## DISCUSSION

T. JONES, UK

We saw very similar ionospheric events following an explosion at a chemical factory in the UK (published in Nature 1972). There were acoustic waves of large amplitude but we did not observe the generation of gravity waves with periods greater than the Burnt Viscaia period. We found the HF Doppler technique to be more sensitive to transient events such as these explosions than the conventional  $h'(t)$  method (i.e., phase height changes rather than group height changes).

## AUTHOR'S REPLY

For the first part of the question there is probably a threshold: the yield of the explosion has to be high enough to excite gravity waves. For the second part, phase measurements are indeed more sensitive, but it is necessary to thoroughly study the disturbances and the wave forms to have both phase and amplitude data.

J. S. BEIROSE, CA

You have certainly showed very clear and complex effects of grand level, powerful chemical explosions on traditional  $h'(t)$  records, similar to those used by many early researchers to study traveling ionospheric disturbances and other naturally occurring phenomena. My question concerns what new physics can be learned about such observations?

## AUTHOR'S REPLY

The wave form deformation when the altitude increases can be used for studying the filtering effect of the atmosphere, but it would be more interesting to study the secondary effects. The long duration spectral anomalies and the formation of stratifications in the lower ionosphere are not understood. Their explanation needs new theoretical approaches. These experiments can yield also useful data to study the formation and the propagation of acoustic gravity waves which can propagate over large distances. Jacobson (1967) observed a gravity wave with another experiment of CW ionospheric sounding at 250 km from the explosion point.

# LABORATORY SIMULATION OF HIGH-ALTITUDE DISRUPTIVE EFFECTS\*

B. H. Ripin, J. Grun, C. K. Manka, J. A. Stamper,<sup>a</sup>  
E. A. McLean, J. Resnick,<sup>b</sup> R. Burris,<sup>c</sup> J. Crawford<sup>d</sup>, J. D. Huba and G. Ganguli

Space Plasma Branch  
Plasma Physics Division  
Naval Research Laboratory  
Washington, DC 20375-5000  
USA

## SUMMARY

Disturbed ionospheric and space conditions are simulated and studied with laser-produced plasmas in the Naval Research Laboratory PHAROS Laser Facility. Intense laser pulses, containing up to 1500 Joules in 3 ns, produce plasma energy densities over 1 Gigajoule/gm, comparable to those occurring in nuclear detonations. The expansion of these plasmas through a background ambient magnetized plasma simulate high-altitude nuclear explosion (HANE) effects, as well as supernova shock and other energetic space plasma conditions. In this paper we focus on effects, such as blast-waves and plasma instabilities leading to nonuniform and disturbed space environments that can affect space-based communications and sensor systems. The laser experiment is useful for investigation of mechanisms accompanying less energetic active space experiments also, such as chemical releases and particle beam injections. In this connection, we describe laboratory experiments demonstrating the existence of the large Larmor radius (LLR) instability which caused the plasma structuring observed in the 1985 magnetospheric AMPTE-barium release experiment. Extensions of the LLR-instability experiment into the nonlinear regime and towards parameters scaled to model very high-altitude nuclear explosions (VHANEs) and several CRRES chemical releases are outlined. We also discuss space related laboratory experiments on blast-waves, plasma jetting, MHD turbulence. Finally, the NRL Space Chamber program is described.

## INTRODUCTION

Laser-produced plasmas provide a unique laboratory test bed for investigation of energetic space plasma processes. These can range from natural phenomena, such as supernova shocks, solar wind interactions with comets and planetary magnetospheres, to man-made disturbances, such as active space experiments like chemical releases, space particle beams injections, and high altitude nuclear explosions. Laser-produced plasmas can be formed with energy-densities that range from nuclear-detonation-like ( $\sim 10^9$  J/cc) at the high end, down to strong coupled plasma whose kinetic energy falls below its interparticle potential energy; plasma  $\beta$ 's ( $\beta$  = kinetic energy/magnetic energy density) can be made with values less than unity to several hundred; plasma temperatures span the range from 1 eV to multi-keVs, and directed velocities from zero to over  $10^8$  cm/s. These conditions can be generally achieved with good control, reproducibility, and diagnosability.

Because of the great versatility of laser-produced plasmas, many ionospheric, space, and HANE-related phenomena can be studied best in the laboratory. We discuss several experiments which, hopefully, will bring some insight to these processes. Here, we briefly discuss: sub-Alfvénic plasma expansions across magnetic fields (such as the large Larmor radius instability), blast-waves, cross-field plasma jetting and plasmoid formation, MHD turbulence, and strong coupled plasma production.

## PLASMA PROPERTIES

Several distinct plasma components are generated in laser-target interactions that are useful for space plasma investigations; these include: Ablation plasma; Ambient plasma (magnetized or unmagnetized); Highly-accelerated solid targets; Shocked target plasma; Strong coupled plasma. A schematic of sources of these plasma components is shown in Figure 1.

Ablation plasma is generated directly in the laser-solid target interaction. Laser energy is absorbed in the plasma on the front of the target near the critical density ( $10^{21}$  e/cc for 1.05  $\mu$ m Nd-laser light). At high incident laser irradiances, e.g., above  $10^{13}$  W/cm<sup>2</sup> the ablation plasma has the highest specific energy density material achievable in the laboratory, of the same order as in nuclear weapon detonations. It is the high yield to mass ratio which allows early-time HANE phenomena to be simulated in the laboratory. Of course, since the amount of material involved in the laboratory is of order micrograms compared to megagrams for a nuclear device the laboratory explosion is vastly miniaturized. We will describe the scaling between HANEs and the laboratory simulations in a later section. The ablation plasma subsequently streams away from the focal region with velocities ranging from  $10^6$  to over  $10^8$  cm/s, depending upon irradiation conditions.<sup>1,2</sup> Ablation plasmas become wind-like,<sup>3</sup> in which most energy resides in a relatively cold (few-eV), but energetic (multi-keV) ion component after expanding a few

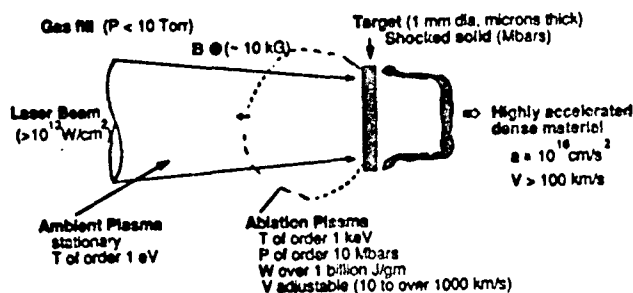


Figure 1. Schematics of laser-target-plasma interactions. Regions of formation of ablation, ambient, accelerated, and shock generated plasma components are indicated.

millimeters from the focal spot. Ablation plasma has many characteristics of nuclear weapon expansions and the solar wind<sup>4</sup> except that it is much smaller in size.

Ambient background plasma can be formed simultaneously with the energetic ablation component by bleeding gas into the chamber at pressures up to 10 Torr; the gas becomes photoionized by laser-target interaction radiation in the vicinity of the target<sup>5</sup> or, over a larger volume, by means of a preionizer device. Ambient plasma is typically cold (about 1 eV) with no net velocity. The ablation plasma streams into the ambient media and causes interactions that emulate many magnetospheric and ionospheric HANE processes that can be studied in the laboratory. At low ambient plasma densities, collisionless coupling instabilities can be examined while at high pressures collisional phenomena, such as blast-waves,<sup>6</sup> can be generated.

The expansion of the ablation plasma puts tremendous pressure (tens of Megabars) on the remaining target material, acting much like a rocket exhaust. These high pressures can accelerate the remaining nearly solid-density target-foil to speeds over 100 km/s.<sup>7</sup> Such targets undergo accelerations of  $10^{16}$  cm/s<sup>2</sup> or more at high density and are susceptible to hydrodynamic instabilities, such as Rayleigh-Taylor.<sup>8</sup> Device components and casings undergo a similar magnitude acceleration during detonation; we are attempting to understand whether and by how much these disassembly instability nonuniformities seed later-time structure. This dense plasma/target component is also being used to generate and study high Mach number MHD turbulence similar in appearance to that seen in the Fish-bowl high-altitude test series.

Shock waves set up in the target interior by the high-pressure laser/plasma impulse can create still another distinct plasma component. The shocked material is dense and of low temperature. It expands towards the laser like the ablation plasma, but is denser and slower ( $V < 10^6$  cm/s). The amount of shocked plasma generated can be controlled by adjusting the target foil thickness or by using special target geometries such as cylinders. The HANE analog to this shocked-plasma occurs when there is excess mass present in the vicinity of the detonation, such as rocket casings or RV materials. Shocked-plasma has been especially useful in our studies of moderate- $\beta$  plasma jets. Plasma jets are clumps of plasma which can travel many gyro-radii across magnetic fields; they may be involved in HANE cross-field jetting such as observed in STARFISH and other high-altitude tests. Jetting is a phenomena common to asymmetric expansions.

At the other extreme, an especially low energy-density plasma (strong-coupled) can also be made using lasers.<sup>9</sup> Strong coupled plasmas have the property that the particle kinetic energy is less than the interparticle potentials. Strong coupled plasmas occur in Jupiter's core, planetary nebulae, railgun plasma armatures, and in aspects of conventional and nuclear explosive detonations, to name a few.

#### SCALING FROM HANE TO LABORATORY

There are obvious differences in length, time, and density scales between HANEs, space plasmas and laboratory plasmas. First, it should be understood that there is no universal scaling law that will guarantee faithfully reproduction of all details of a HANE event in the laboratory; scaling must be specific to the phenomenon under investigation. For collisional or collisionless dominated plasma effects, scaling laws are obtained by casting the appropriate governing equations (eg., MHD, Vlasov equations) in dimensionless form; the dimensionless variables then define the scaling relations.

For situations where binary collisions dominate the expansion, such as occurs at altitudes below 150 km, scaling parameters fall naturally out of the dimensionless equation for a strong shock wave.<sup>10</sup> Longmire<sup>11</sup> showed that if the debris velocity is held fixed (to minimize velocity dependences of collisional cross sections) then most parameters scale with the energy ratio of the field-to-laboratory explosions, i.e.,  $Y = E_f/E_l$ . Debris mass scales as  $Y^{-1}$ , length and time scales as  $Y^{1/2}$ , and ambient background density scales like  $Y^{1/2}$ . Kohlberg derived the generalized collisional scaling relation that applies for arbitrary velocity ratio and showed that this same scaling held for

Rayleigh-Taylor instability driven turbulence processes occurring in collision dominated expansions.<sup>12</sup> For collisionless processes, the appropriate scaling relations stem from the dimensionless Vlasov equation or dispersion relations for the relevant instabilities. Longmire also derived a number of these scaling laws in Reference 11.

Sometimes, it is often difficult to satisfy all of the scaling laws simultaneously and an educated compromise is then needed. Dominant parameters for the phenomenon are picked for accurate scaling and the less crucial variables are allowed to deviate from exactitude, as long as they are still in the proper regime. One example of this is scaling of the magnetic field strength from the field case to the laboratory. On one hand,  $B$  can be scaled such that the Larmor radii scale proportionally with lengths (e.g.,  $Y^{1/2}$ ), or, alternately,  $B$  can be scaled so that the magnetic energy density scales with the plasma energy density (e.g.,  $Y^{1/4}$ ); the former requirement mandates megagauss field strengths while the latter case only kilogauss fields for proper scaling. Both can not be satisfied simultaneously. Thus, judgement is used to choose between them. In another example, radiative lifetimes are fixed and do not scale with the collisional scaling rules. If radiation is important to a particular problem then it must be given special treatment. For instance, we have seeded the ambient gas with high-Z constituents, such as Xe gas, or used mixtures of gases to increase radiation loss for specialized cases. A beneficial feature of laboratory experiment is that individual parameters can be widely varied and scaling assumptions can be reliably verified. In practice, parameters can be chosen that provide good simulations for most needs.<sup>6</sup>

### LARGE LARMOR RADIUS INSTABILITY

The large Larmor radius (LLR) instability is a good example of a space (and, very high-altitude nuclear explosion (VHANE)) phenomena that was scaled to the laboratory. This instability was first observed in the March 1985 AMPTE barium release experiment in the tail of the magnetosphere (about 12 earth radii away).<sup>13</sup> Marked striations appeared as the barium plasma expanded to its maximum radius (radius at which the excluded magnetic field equaled the plasma kinetic energy) even though the barium ion Larmor radius was very large (about equal to the magnetic confinement diameter). Huba and Hassam developed a MHD-like theory<sup>14,15</sup> for sub-Alfvenic expansions in the large Larmor radius (LLR) limit. In this theory, the electrons are treated as being magnetized since their orbits are quite small, but the ions are considered unmagnetized since they have Larmor radii large compared to wavelength and density gradient length dimensions and because the time scales of interest are faster than an ion cyclotron period. The LLR instability is the analog to the conventional MHD Rayleigh-Taylor (interchange) instability but has a much faster growth rate, i.e.,

$$\gamma_{LLR} = k L_n \gamma_{MHD}, \quad (1)$$

where the MHD growth rate is  $\gamma_{MHD} = [g/L_n]^{1/2}$ ,  $k$  is the instability wave number, and  $L_n$  is the density gradient length in the expanding plasma leading edge. Dominant unstable wavelengths are slightly less than  $L_n$  yielding LLR instability growth rates factors an order of magnitude higher than  $\gamma_{MHD}$ . A laser-plasma experiment was launched at NRL to verify the existence and properties of this new instability using the ablation plasma expanding into across a magnetic field (up to 10 kG).<sup>16,17</sup> Figure 2 shows two examples of the unstable plasma structure; the photo on the left is an example of structure near the end of the linear phase showing the well-developed flute structure, and the photo on the right is an example of the very unusual structure seen later, in the nonlinear stage. The nonlinear structure does not really saturate, but rather it continues to expand outward at approximately the original plasma speed even though it is well beyond the magnetic stopping distance. Eventually, the flutes take on an erratic structure and even appear to bifurcate. It appears like each flute tip is acting like an independent plasma jet.

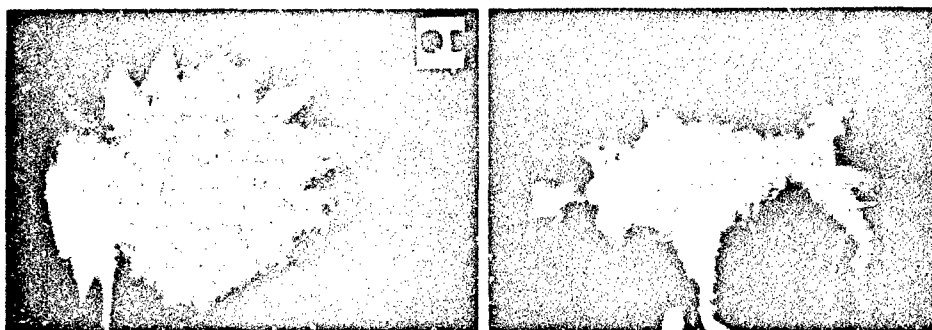


Figure 2. Two examples of the LLR instability seen in the NRL experiment. Left side shows instability near the end of its linear stage (10 kG, 376 J, 99 ns). The right side shows some fascinating bifurcation-like structure appearing in the nonlinear stage (10 kG, 30 J, 90 ns).



LLR instability, or its relatives, can have large potential impact upon systems operating in the VHANE regime. Several SDIO engagement scenarios occur between 1500 and 3000 km altitude. If instability occurs here, it represents a mechanism through which nuclear debris would be thrown many times the magnetic confinement radius from the burst point in a very structured manner. Material would be injected into a host of L-shells which could affect remote satellites as well as precipitating into the atmosphere over a much wider area than predicted with conventional MHD codes. Injection of nuclear decay betas are conjectured to be particularly dangerous to satellites.<sup>18</sup> The scaling of the LLR instability into the VHANE regime is somewhat uncertain at this point. Two criteria for instability are that: 1) the Larmor radius to density scale length ratio must be greater than unity, and 2) the magnetic confinement radius,  $R_b$ , needs to be greater than the density scale length and the critical radius for onset,  $R_c$ . A critical radius was first noticed in the experiment where it was observed that the LLR instability only appeared beyond a specific expansion distance ( $\sim 2.5 - 3$  cm) which was relatively independent of magnetic field. An expression for the critical radius,  $R_c$ , is

$$R_c = \frac{eZ}{m_i c} \sqrt{\frac{L_n M}{2}} \quad (2)$$

where  $M$  is the total plasma mass,  $m_i$  is the ion mass, and  $Z$  is the ion charge state. These criteria are clearly met for VHANEs above 7000 km or, potentially, in multiburst situations. A note of caution, these onset criteria are not yet firmly established for all LLR situations and even when not satisfied, the usual MHD Rayleigh-Taylor interchange mode may well still be unstable. It is still an open question whether single or multiple VHANE bursts will be unstable since VHANEs are in the 1500 to 3000 km altitude range. Since Larmor radii are small compared to magnetic confinement radii here ( $\rho_i/R_b < 0.1$ ), both the theory and experiment needs to be extended into the finite Larmor radius regime. The most important parameter appears to be the ratio of the expanding debris-shell front density gradient,  $L_n$ , to the ion Larmor radius,  $\rho_i$ ; if  $\rho_i/L_n$  ratio is large then the VHANE may be unstable even though  $\rho_i/R_b < 1$ . Parameters in the NRL experiment are being adjusted to explore this regime currently.

Further details of the linear growth and nonlinear development of this experiment can be found in References 16 and 17.

#### HIGH MACH NUMBER SHOCKS

When an ambient plasma is introduced, the Mach number of the ablation plasma goes from sub-sonic (or sub-Alfvénic when  $B > 0$ ) to super-sonic. Mach numbers of hundreds are easily produced. Additionally, when the ambient gas pressure is above 0.5 Torr (for  $V_d = 5 \times 10^7$  cm/s) collisional blast-waves are formed. A good example of the variety of phenomena that can appear under these circumstances is shown in the dual-time, dark-field shadowgram (backlit with laser pulses at the indicated times) shown in Figure 3. Very strong, thin, energy and momentum conserving shocks are seen in the laser side of the target as the ablation plasma sweeps up the ambient media.<sup>6</sup> These shocks behave much like ideal VonNeumann-Sedov shocks<sup>10</sup> but do exhibit significant deviations from the simple theory. At least four important unresolved areas remain which affect HANE interpretations. First, the role of radiation loss from the blast wave/bubble system has been briefly studied previously, but is deserving of a concerted effort; it was found that radiation transport can indeed affect the energy balance and stability in blast-wave expansions. Second, the agreement between theory and experiment on the transition into the collisional regime (between 0.1 and 1.0 Torr) is good.<sup>19,20</sup> But, coupling efficiency in the transition regime is found to be very sensitive to assumptions in quantities such as the ionization state of the debris and background media as well as the shape of the velocity distributions and more detailed measurements are needed to remove ambiguities. Third, the temperature of the material within the bubble region has been ambiguous; in some measurements it has been high, as expected in ideal blast-waves, and in other measurements it has appeared much cooler (eg., few eV). Since the bubble interior of a  $\gamma = 1.2$  blast-wave can contain up to 80% of the total particle energy, the concern is not just academic. A hypothesis that fits these observations is that the prompt hot ablation plasma forms the blast-wave structure and that slow cold dense material spewed from the shocked portion of the target fills the bubble later. Fourth, the general question of under what circumstances blast-waves are hydrodynamically stable or unstable has not been answered. Ideal blast-waves in uniform media are inherently stable. But, theory and simulation of ideal self-similar blast-waves suggest that hydrodynamic instability sets in if the ambient density falls off with radius faster than  $r^\alpha$ , where  $\alpha > 3$ , and/or if the effective ratio of specific heats is below some value (eg., 1.3).<sup>21,22</sup> Non-ideal blast-waves are also susceptible to hydrodynamic instability if, for instance, radiation loss rates from the blast-wave front are sufficient to create an adverse (Rayleigh-Taylor unstable) pressure/density gradient profile, or if non-negligible debris mass is present to form a pusher region behind the shock front. Gross instability and turbulence has indeed been found in the NRL experiment in the region behind the target;<sup>5,6</sup> this will be discussed further below and in Reference 23. In addition, the front-side blast-waves have been induced to go unstable by forming them in high-Z (highly radiative) gases, such as Xe.<sup>24</sup>

More work needs to be done in this area since knowledge of blast-wave instability physics is needed to explain the highly structured photographs of HANEs taken in the Fishbowl series as well as to explain highly structured supernova remnants, such as the Crab Nebula, seen in optical and radio telescope images.

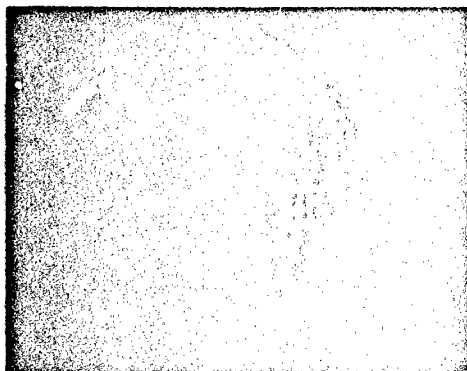


Figure 3. Features of a laser-plasma ambient media interaction in the collisional regime. Note the sharp blast-fronts, regions of turbulence, and the aneurism. The laser is incident from the left (36 J, 5 Torr  $N_2$ , Al 1.5  $\mu$ m thick target,  $B = 800$  G,  $t = 55$  ns and 155 ns).

Note the small scale-length turbulence formed behind the blast wave shocks (hazy region just inside the bubbles) and the gross large scale-length turbulence formed behind the target. Finally, one type of 'aneurism' feature has been shown to result from a cylindrical shock caused by laser beam warming of a channel<sup>25</sup> or by jetting target material.

#### TURBULENCE

In this Section the nature of the large scale turbulence that appears behind the target (e.g., Fig. 3) is briefly described. A much more complete discussion can be found in Reference 23. Turbulence (or turbulent appearing structure) is seen in a wide variety of HANE, natural space, and laboratory situations.

The turbulent structure is most visible in the laboratory when optical diagnostics sensitive to small light deflections, such as dark-field and phase contrast shadowgraphy and holographic interferometry are employed. Structure is also observed in the natural optical emission image of the turbulent region, but the shorter wavelength components tend to wash out.

The turbulent plasma is generated when the highly accelerated target foil ( $a \sim 10^{16}$  cm/s<sup>2</sup>) pushes into the ambient background gas/plasma. The accelerated material has high Mach number and speed ( $M \sim 100$ ,  $V_t \sim 100$  km/s) with respect to the ambient media. Turbulence is not observed when the target foil is accelerated under high vacuum conditions, nor when the gas density is low (i.e., under collisionless conditions). Even though the accelerated foil is known to undergo Rayleigh-Taylor hydrodynamic instability during acceleration,<sup>8</sup> the turbulence seen at late times ( $>100$  ns) does not appear highly correlated with the initial target Rayleigh-Taylor structure. This was demonstrated by comparing results from otherwise similar smooth and pregrooved accelerated targets. The turbulence persists for long periods of time ( $\sim$  microseconds) compared to transit times of the debris through the background gas; Figure 4 shows a time sequence of the turbulence taken on separate shots. Observations, such as recorded in Figure 3 and 4, are densitometered, digitized, corrected for film response, and Fourier analyzed to obtain the turbulence power spectral density function. A typical one-dimensional spatial power spectrum shown in Figure 5, has a  $k^{-2.1}$  scaling (equivalent to a  $k^{-3.2}$  two-dimensional k-space power spectrum dependence) in the inertial range between an outer scale length of 1 mm and an inner scale length of less than 20  $\mu$ m (true inner scale length is not resolvable).<sup>23</sup> For sake of comparison, Kolmogorov turbulence [big eddies decaying into smaller eddies] is characterized by a  $k^{-5/3}$  power-law spectrum between the inner and outer scale lengths. Eventually, we hope to completely characterize the nature and cause of this turbulence and apply the findings to relevant space situations, such as supernova remnant observations.

#### PLASMA CROSS-FIELD JETTING

It is possible for plasmas to propagate large distances across magnetic fields, distances much greater than the magnetic confinement radius or ion gyro-radius, in many space and laboratory situations. This cross field motion isn't possible for isolated charged particles which are constrained to their gyro orbits, but plasma clumps can act collectively to circumvent the applied magnetic field force. The  $V_0 \times B_0$  force on a plasma moving across magnetic field  $B_0$  with speed  $V_0$  causes a polarization electric field  $E_p$  to form inside the plasma. The plasma then responds to the  $E_p \times B_0 = V_0$  force and the plasma can continue forward at its original velocity. Charge is continually depleted at the boundaries in this process due to the decrease of  $E_p$  in the boundary layer, and the cross field motion will eventually stop when insufficient plasma is left to polarize.<sup>26</sup> But, plasma depletion rates are generally low and the plasma can travel great distances across B.

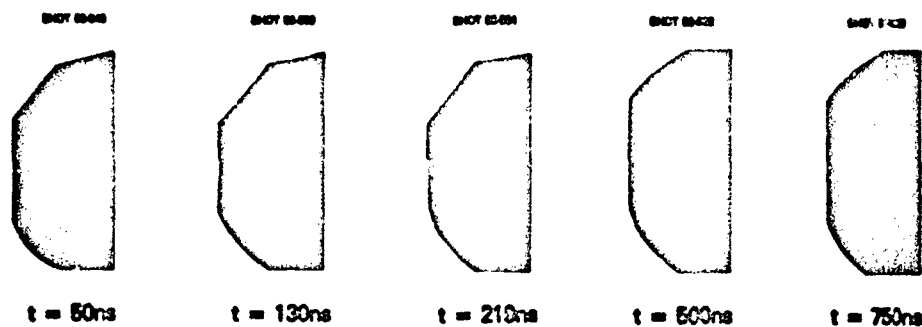


Figure 4. Sample phase-contrast (top) and bright-field (bottom) time sequence of the turbulent region. The target is a 20  $\mu\text{m}$  CH foil, laser energy is about 300 J, and the background gas is 5 Torr of nitrogen.

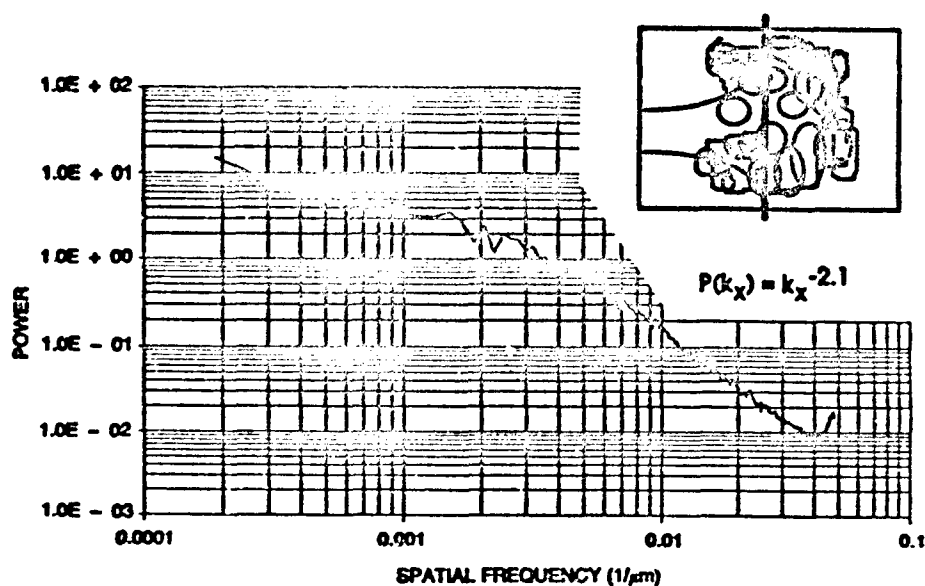


Figure 5. One-dimensional power spectrum of the turbulent region in a typical shot.

Figure 6 shows several examples of cross-field jetting observed in our experiments.<sup>27-30</sup> The top left image is a time-resolved ( $\sim 1$  ns shutter time) photograph of a high- $\beta$  jet produced simply by aperturing the ablation plasma with a cylindrical mask to allow plasma sectors to flow across the magnetic field. The top right image is another time-resolved photograph of a moderate- $\beta$  jet produced by firing the laser beams into the ends of a small glass cylinder and allowing an asymmetric plasma to squirt out its ends across the magnetic field. Finally, the middle and bottom photographs are resonant dye laser shadowgrams showing a low- $\beta$  barium plasma jet squirting across the B-field and structuring along the magnetic field.

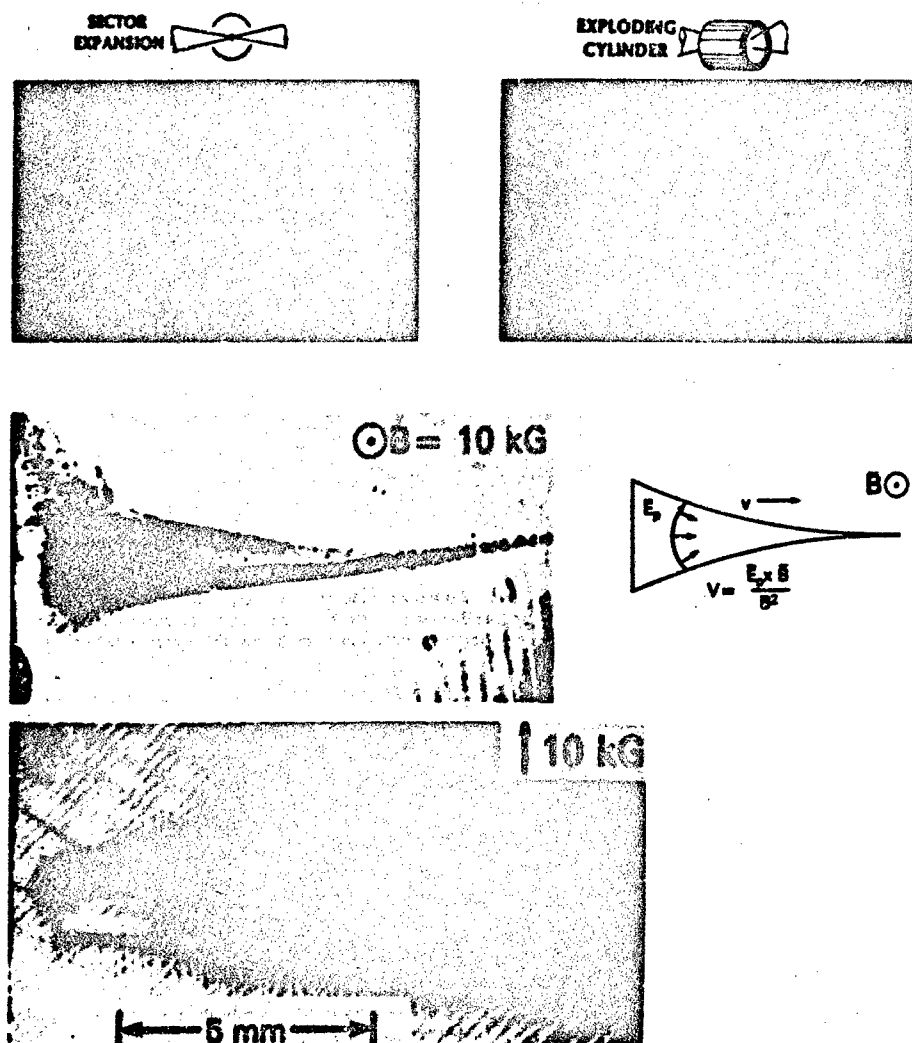


Figure 6. Three examples of cross-field plasma jetting. Top left: High- $\beta$  ( $>10$ ) ablation plasma jets (aperture plasma) with  $V_0 \sim 5 \times 10^7$  cm/s, 10 kG, 90 ns. Top right: Moderate- $\beta$  ( $\sim 1$ ) cylindrical target jet,  $V_0 \sim 5 \times 10^6$  cm/s, 10 kG, 1000 ns. Middle left: Low- $\beta$  ( $\sim 0.05$ ) Barium-jet with  $V_0 \sim 10^6$  cm/s, 10 kG,  $\sim 1000$  ns. Middle right: Schematic of polarization electric field configuration leading to cross-field jetting. Bottom: Same as middle left except that view is now from the top, i.e., cross-B view; note the fine scale B-field aligned structure.

There are several notable features of our laboratory jets: 1) They occur if the plasma has an asymmetric expansion. 2) They propagate great distances across the magnetic field at nearly their initial speed. 3) They tend to pinch down at their leading edge, probably due to curvature of the internal polarization electric field. 4) They often form field-aligned structure near their boundaries, as can be seen in Figure 6, which is a result of instability. The instability seen in the low- $\beta$  Barium jet case (bottom Fig. 6 and Reference 29) is consistent with one of a recently discovered new class of instability, nonlocal velocity shear types,<sup>31</sup> at the lower hybrid frequency.<sup>32</sup> Figure 7 shows the configuration of the instability. This experiment is the first observation of the new instability.<sup>29</sup> The structuring is obviously robust and is expected to occur in many natural and disturbed space situations where there are velocity shears. The phenomena occurs not only near the lower hybrid frequency, but at other plasma frequencies as well. For instance, nonlocal velocity shear instability may explain the enhanced broadband noise in the ion cyclotron range in the auroral ionosphere<sup>33</sup> in the absence of sufficient relative drift velocity to cross the Drummond-Rosenbluth current driven ion cyclotron instability threshold criteria. The instability seen around the periphery of the cylindrical jets (moderate- $\beta$  cases) has a much longer wavelength than that of the low- $\beta$  case, but can also be explained by the lower hybrid nonlocal velocity shear instability or, possibly, by the related Kelvin-Helmholtz instability.<sup>34</sup>

Conditions allowing gross plasma jetting to occur appear in many natural and disturbed space situations. This obviously applies to HANEs and must be taken into account to properly predict where the debris will travel and how it will structure.

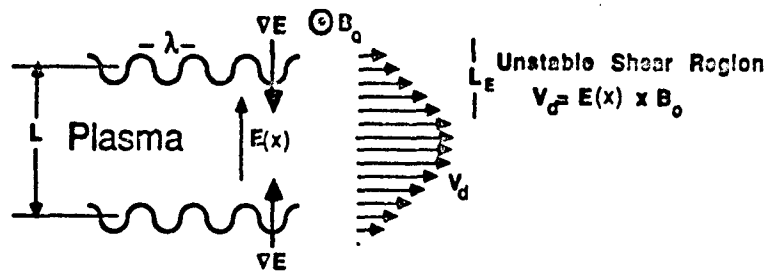


Figure 7. Nonlocal velocity shear instability geometry. An electric field gradient perpendicular to the applied magnetic field causes a sheared plasma velocity perpendicular to both the electric field and magnetic field in response to the  $E \times B$  plasma drift. The shear velocity instability develops in the shear region with wave numbers of order  $kL_E < 1$ .

#### NRL SPACE PLASMA CHAMBER PROGRAM

The Space Plasma Branch at NRL is building up a new large volume space chamber facility. The Space Chamber will incorporate a large (up to 1.8m x 5m) low-energy density plasma ( $T_e = 0.1 - 10$  eV,  $n_e = 10^3 - 10^{10}$  e/cc,  $B_0 < 1000$  Gauss) for experiments requiring much lower densities and larger dimensions than the NRL Pharos Laser Facility. Space Chamber experiments can be run in either steady-state or pulsed mode (where magnetic fields of  $\sim 1$  kG can be imposed on the volume). The large size of the Space Chamber plasma enables investigations of space phenomena without the interference of boundary effects, it permits detailed diagnosis of wave phenomena using probing techniques, and it allows *in situ* testing of space instrumentation before launch.

Figure 8 shows a schematic of an experimental arrangement designed to study the nonlocal velocity shear instability near the ion cyclotron frequency. The experiment consists of a large magnetized plasma with an electric field gradient imposed perpendicular to  $B$ . The gradient scale length,  $L_E$  must be  $10\rho$  or less, where  $\rho$  is the appropriate gyroradius ( $\rho_i$  for ion cyclotron-like modes, and  $\rho_e$  for lower-hybrid modes). The particular configuration shown in Fig. 8 with concentric biased rings to setup the radial electric field gradient, would drive the instability in cylindrical geometry. The magnetic field strengths required are only 50 gauss for ion modes ( $H^+$  at 1eV) and much less for the lower-hybrid modes. The potential difference in the shear layer need only be of order 10 volts for the parameters assumed here. Weak collisions with neutrals would be tolerable, and even useful, for ionospheric simulations. A variable axial current can also be imposed. The plasma parameters needed can be easily achieved in the Space Chamber.

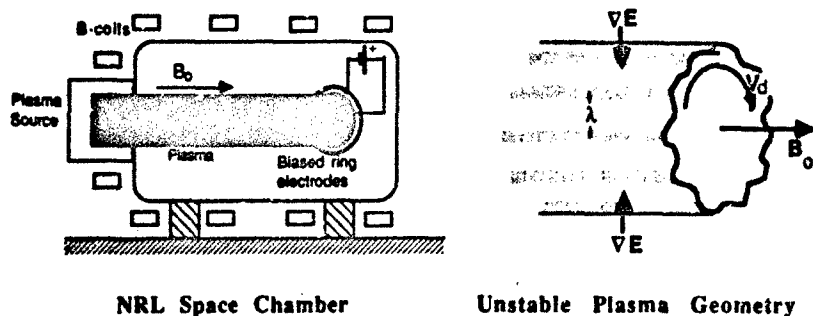


Figure 8. Possible experimental arrangement for driving a velocity shear instability in cylindrical geometry. Left, the Space Chamber with plasma source, axial magnetic field, and bias ring to create the electric field gradient. Right, the plasma geometry undergoing instability.

In addition to the above traditional types of space chamber studies, we plan to direct one or more beams from the Pharos laser into the Space Chamber to permit study of high-energy plasmas in a large volume space-like setting. One investigation anticipated is to examine the physics of the formation of artificial or disturbed radiation belts. HANE induced-belt formation and evolution is undoubtedly a complex dynamic process. Consequently, it is important that modeling efforts be guided and validated wherever possible by experiment. Some features can, in principle, be tested with active space-based experiments; but these are risky, expensive and infrequent endeavors. Laboratory experiments, on the other hand, can provide relevant information in a relatively inexpensive and flexible test-bed. Figure 9 shows a possible experimental arrangement to study radiation belt phenomena. A beam from the high-power (~1TW) Pharos Nd-laser is focused onto a small (mm diameter) target suspended at an appropriate point (latitude and altitude) in a dipole magnetic field inside the NRL Space Chamber. This creates a burst of plasma, with nuclear-like energy density, that scales much like a miniature HANE, with comparable debris velocities, blast-wave formation, magnetic bubble formation, temperatures, and disturbed 'nuclear' conditions to a real HANE. Suprathermal electrons with energies of several hundred keV generated when the laser beam is focused to over  $10^{14}$  W/cm<sup>2</sup> has many of the salient properties of HANE fission  $\beta$ -particles. The ambient magnetic field can be adjusted and scaled to other characteristic dimensions, such as the magnetic containment radius  $R_b$  and radius of curvature of the magnetic field. For instance, HANE- $\beta$ s have  $p_e \sim 100$  m and  $R_b \sim 350$  km giving  $p_e/R_b \sim$

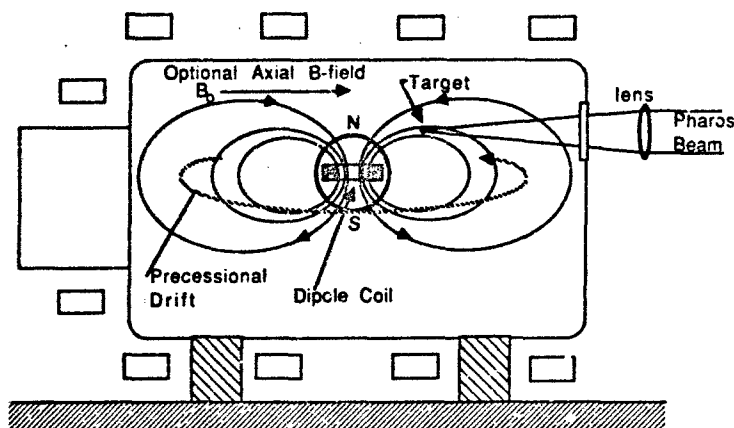


Figure 9. Experimental arrangement for study of radiation belt phenomena. The large dimensions of the space chamber ensure that boundaries do not dominate the physics while the energetic laser-produced plasma provides populations for the dipole-field (mock radiation belt region) with large Larmor radii.

few  $\times 10^{-4}$  in a 10 kG field; this ratio is comparable to the laser case where  $R_b \sim 3$  cm and  $p_e \sim 20$  mm (10 kG). The ratio of  $R_b$  to the dipole field dimensions (eg., to the earth radius  $R_e$ ) can also be comparable; eg.,  $R_b/R_e \sim 5 \times 10^{-7}$  for HANEs and  $\sim 10^{-1}$  for the laboratory case if  $R_{lab} \sim 30$  cm is chosen. Scaling can be made even more precise if we fabricate a stronger magnet. The large dimensions of the NRL Space Chamber (1.8m x 5m) are necessary to isolate the artificial belt magnetic field lines from the walls and to minimize boundary effects. The chamber can be operated either under high vacuum,  $\sim 10^{-7}$  Torr, to emulate the pressure in the radiation belt region, or with gas bled in to provide neutral collisions characteristic of lower altitudes. In addition, axial magnetic fields and external plasma sources (solar wind simulation) are also planned for the facility and can be utilized if needed. Initially the experiment will be used to investigate single-burst events, but eventually, multi-burst scenarios can be examined when a second Pharos beam is brought into the Facility (Pharos has 3 high-power beams). An extensive array of diagnostic equipment is available in the Pharos Facility to make detailed measurements of the artificial belt formation and evolution; these diagnostics include: optical and X-ray streak cameras, multi-frame fast (100 ps) intensified framing cameras, multi-frame laser schlieren shadowgraphy, holographic interferometry, dye laser resonant and nonresonant probing beam, space and time resolving IR, optical, UV and X-ray spectrographs/OMAs, ion and electron particle detectors, magnetic field probes, 6-GHz oscilloscope, etc..

The Space Chamber should be completed in FY90 and available for initial experiments early in FY91. Experiments using one Pharos beam in the Space Chamber Facility could commence later in FY91.

### SUMMARY AND CONCLUSIONS

Laser-produced plasmas can be made with parameters of HANE. Aspects of early-time HANE shocks, and some jet-like features can be emulated in the laboratory. The interactions of these plasmas with magnetic fields and other plasma components produce many phenomena which resemble those observed in the Fishbowl series of atmospheric tests. Although it is naive to believe that our experiments are miniature simulations of HANE phenomena, laboratory investigations certainly aid in their understanding.

### ACKNOWLEDGEMENTS

We thank the following persons for their assistance in this work: L. Daniels, J. Ford, N. Nocerino, T. Peyser, C. Brown, H. Griem, A. Ali, and S. Obenshain. This work has been supported by the US Defense Nuclear Agency and ONR.

### REFERENCES

- a) Laser Plasma Branch, Naval Research Laboratory.
- b) Science Applications International Corp., McLean, VA.
- c) Physical Sciences Inc., Alexandria, VA.
- d) SW Texas State University, San Marcos, TX USA.
- 1) Ripin, B. H., et al., "Laser-Plasma Interaction and Ablative Acceleration of Thin Foils at  $10^{12}$ - $10^{15}$  W/cm<sup>2</sup>," *Phys. Fluids* **23**, 1012 (1980).
- 2) Grun, J., et al., "Ablative Acceleration of Planar Targets to High Velocities," *Phys. Fluids* **26**, 588 (1983).
- 3) Grun, J., R. Stellingwerf, and E. H. Ripin, "Control of Ion-Velocity Distributions in Laser-Target Interaction Experiments," *Phys. Fluids* **29**, 3390 (1986).
- 4) Brandt, J. C., *Introduction to the Solar Wind*, (Freeman, San Francisco, 1970).
- 5) Ripin, B. H., et al., "Structuring Processes in Expanding Laser-Produced Plasmas," in *Laser Interaction and Related Plasma Phenomena*, Vol. 8, pp. 417-433 (Plenum Press, 1988, eds., H. Hora and G. Miley).
- 6) Ripin, B. H., et al., "Physics of Laser-Produced Interstreaming Plasmas," in *Laser Interaction and Related Plasma Phenomena*, Vol. 7, pp. 857-877 (Plenum, NY, 1986), ed. H. Hora and G. Miley.
- 7) Obenshain, S. E., et al., "Uniform Ablative Acceleration of Targets by Laser Irradiation at  $10^{14}$  W/cm<sup>2</sup>," *Phys. Rev. Lett.* **50**, 44 (1983).
- 8) Grun, J., et al., "Rayleigh-Taylor Instability Growth Rates in Targets Accelerated with a Laser Beam Smoothed by Induced Spatial Incoherence," *Phys. Rev. Lett.* **58**, 2672 (1987).
- 9) Mostovych, A. N. and B. H. Ripin, private communications (1987).
- 10) Sedov, L. I., *Similarity and Dimensional Methods in Mechanics*, (Academic Press, NY, 1959).
- 11) Longmire, C., MRC Report AMRC-R-338 (1981).
- 12) Kohlberg, I., "Scaling of Middle Altitude Nuclear-Produced Shock Waves with Applications to IR Detection of Boosters," *ETHANL* **9**, 74 (1989).
- 13) Bernhardt, P. A., et al., "Observations and Theory of the AMPTE Barium Releases," *J. Geophys. Res.* **92**, 5777 (1987).
- 14) Hassam, A. B. and J.D. Huba, "Structuring of the AMPTE Magnetotail Barium Release," *Geophys. Res. Lett.* **14**, 60 (1987).

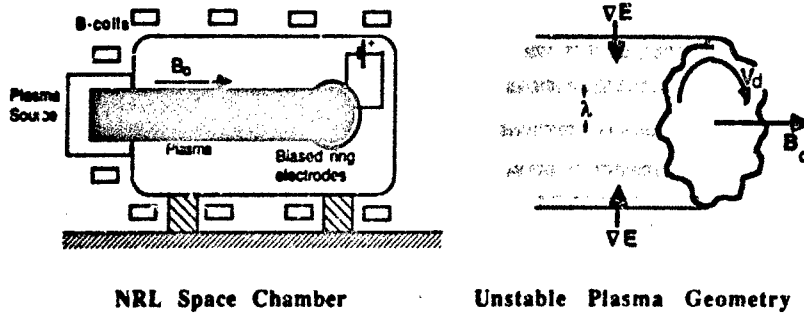


Figure 8. Possible experimental arrangement for driving a velocity shear instability in cylindrical geometry. Left, the Space Chamber with plasma source, axial magnetic field, and bias ring to create the electric field gradient. Right, the plasma geometry undergoing instability.

In addition to the above traditional types of space chamber studies, we plan to direct one or more beams from the Pharos laser into the Space Chamber to permit study of high-energy plasmas in a large volume space-like setting. One investigation anticipated is to examine the physics of the formation of artificial or disturbed radiation belts. HANE induced-belt formation and evolution is undoubtedly a complex dynamic process. Consequently, it is important that modeling efforts be guided and validated wherever possible by experiment. Some features can, in principle, be tested with active space-based experiments; but these are risky, expensive and infrequent endeavors. Laboratory experiments, on the other hand, can provide relevant information in a relatively inexpensive and flexible test-bed. Figure 9 shows a possible experimental arrangement to study radiation belt phenomena. A beam from the high-power (~1TW) Pharos Nd-laser is focused onto a small (mm diameter) target suspended at an appropriate point (latitude and altitude) in a dipole magnetic field inside the NRL Space Chamber. This creates a burst of plasma, with nuclear-like energy density, that scales much like a miniature HANE, with comparable debris velocities, blast-wave formation, magnetic bubble formation, temperatures, and disturbed 'nuclear' conditions to a real HANE. Suprathermal electrons with energies of several hundred keV generated when the laser beam is focused to over  $10^{14}$  W/cm<sup>2</sup> has many of the salient properties of HANE fission  $\beta$ -particles. The ambient magnetic field can be adjusted and scaled to other characteristic dimensions, such as the magnetic containment radius  $R_0$  and radius of curvature of the magnetic field. For instance, HANE- $\beta$ s have  $\rho_c \sim 100$  m and  $R_0 \sim 350$  km giving  $\rho_c/R_0 \sim$

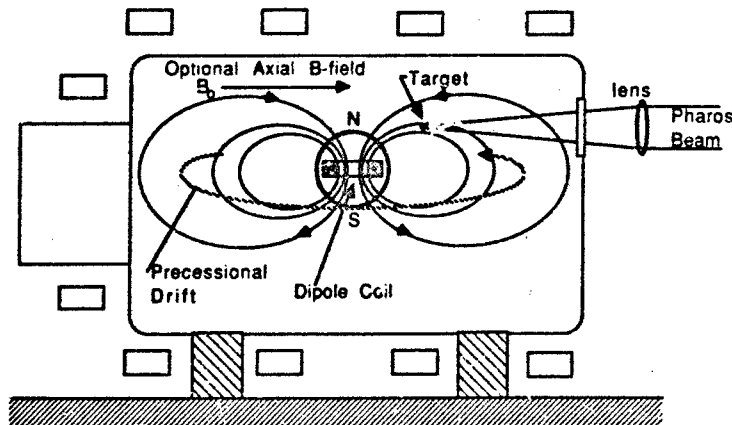


Figure 9. Experimental arrangement for study of radiation belt phenomena. The large dimensions of the space chamber ensure that boundaries do not dominate the physics while the energetic laser-produced plasma provides populations for the dipole-field (mock radiation belt region) with large Larmor radii.



- 15) Huba, J. D., J. G. Lyon, and A. B. Hassam, "Theory and Simulation of the Rayleigh-Taylor Instability in the Limit of Large Larmor Radius," *Phys. Rev. Letters* **59**, 2971 (1987).
- 16) Ripin, B. H., et al., "Large Larmor Radius Interchange Instability," *Phys. Rev. Lett.* **59**, 2299 (1987).
- 17) Ripin, B. H., et al., "Large Larmor Radius Instability," to be published (1990).
- 18) Fedder, J. A. and B. H. Ripin, "Injection of Beta Particles by HANES: A New Conceptual Model and Experimental Verification," (unpublished 1990).
- 19) J. J. MacFarlane, G. A. Moses, and R. R. Peterson, "Energy Deposition and Shock Wave Evolution from Laser-Generated Plasma Expansions," *Phys. Fluids B* **1**, 635 (1989).
- 20) J. L. Giuliani Jr., M. Mulbrandon, and E. Hyman, "Numerical Simulation of Laser-Target Interaction and Blast-Wave Formation," *Phys. Fluids B* **1**, 1463 (1989).
- 21) Kohlberg, L., "Blast-Wave Stability Theory," KAINRL02-89 (1989) and references therein.
- 22) Stellingwerf, R. F., "Blast Wave Stability: A review with Models," *ETHANL* **9**, 345 (1989); and "Blast Wave Stability in Nuclear Explosions I. Stability of Adiabatic Blast Waves," MRC Report MRC/ABQ-R-1254 (1990).
- 23) Grun, J., J. Stamper, J. Crawford, C. Manka, and B. H. Ripin, "Turbulence in Very-High Mach Number Laser-Accelerated Material," in *Laser Interaction and Related Plasma Phenomena, Vol. 9*, (in press, Plenum Press, 1990, eds. H. Hora and G. Miley).
- 24) Ripin, B. H., et al., "Progress of the DNA-NRL Laser Plasma Early-Time Experiment," *ETHANL* **6**, 29 (1985) and J. Grun, et al., to be published.
- 25) Stamper, J. A., et al., "Aneurisms in Laser-Driven Blast-Waves," *Phys. Fluids* **31**, 3353 (1988).
- 26) Schmidt, G., "Plasma Motion Across Magnetic Fields," *Phys. Fluids* **3**, 961 (1960); and Borovsky, J., "Limits on the Cross-Field Propagation of Streams of Cold Plasma," *Phys. Fluids* **30**, 2518 (1987).
- 27) Ripin, B. H., et al., "Laboratory Laser-Produced Astrophysical Plasmas," in *Laser Interaction with Matter*, pp. 196-199 (World Scientific, Singapore, 1989) eds. G. Velarde, E. Minguez, and J. Perlado.
- 28) Manka, C. K., et al., "Jets in Laser-Produced Plasmas," in *Laser Interaction with Matter*, pp. 401-404 (World Scientific, Singapore, 1989) eds. G. Velarde, E. Minguez, and J. Perlado.
- 29) Mostovych, A. N., B. H. Ripin, and J. A. Stamper, "Laser-Produced Plasma Jets: Collimation and Instability in Strong Transverse Magnetic Fields," *Phys. Rev. Letters* **62**, 2837 (1989).
- 30) Mostovych, A. N., B. H. Ripin, and J. A. Stamper, "Resonant Diagnostics of Laser-Produced Barium Plasmas," *Rev. Sci. Instr.* **59**, 1497 (1988) and **60**, 807 (1990).
- 31) Ganguli, G., Y. C. Lee and P. J. Palmadesso, "Electrostatic Ion Cyclotron Instability due to Nonuniform Electric Field Perpendicular to the External Magnetic Field," *Phys. Fluids* **28**, 761 (1985); and Ganguli, G., Y. C. Lee, and P. J. Palmadesso, "Kinetic Theory for Electrostatic Waves due to Transverse Velocity Shears," *Phys. Fluids* **31**, 825 (1988).
- 32) Ganguli, G., Y. C. Lee and P. J. Palmadesso, "Kinetic Theory for Electrostatic Waves due to Transverse Velocity Shears," *Phys. Fluids* **31**, 823 (1988).
- 33) Basu, S., et al., "Simultaneous Density and Electric Field Fluctuation Spectra Associated with Velocity Shears in the Auroral Oval," *J. Geophys. Res.* **93**, 115 (1988); Earle, G. D., M. C. Kelley, and G. Ganguli, "Large Velocity Shears and Associated Electrostatic Waves and Turbulence in the Auroral F Region," *J. Geophys. Res.* **94**, 321 (1989); Nishikawa, K.-I., et al., "Simulation of Ion-Cyclotron-like Modes in a Magnetoplasma with Transverse Inhomogeneous Electric Field," *Phys. Fluids* **31**, 1568 (1988).
- 34) Peyser, T., C. K. Manka, and B. H. Ripin, "Cylindrically-Collimated Laser-Produced Plasma Expansion Across Magnetic Fields," (to be published 1990).

#### DISCUSSION

U. S. INAN, US

I am very interested in your dipole-like field configuration to simulate the radiation belts. Are you implying that the gyro radii of the particles produced by the laser burst is much smaller than the chamber dimensions? What would the estimated lifetime of such particles be?

#### AUTHOR'S REPLY

Yes. The ion gyro radii range upward from ~ 1 cm with 10 kG magnetic fields; they can, of course, be made arbitrarily large by decreasing the field. This is to be compared to the chamber dimensions of about 2 m x 5 m and typical radii of curvature of the dipole field lines of 10's of centimeters. Thus, we should be able to dial the system in and out of adiabatic invariant preserving conditions. It will be interesting to see if we can configure the experiment to test whether VLF-like RF can precipitate out the energetic plasma trapped in the dipole field, as suggested by your paper and others in the conference, such as Burke's.

The lifetime of the particles in the dipole field should be long compared to the longitudinal and azimuthal invariant time scales if we can achieve the desired base pressure of the chamber,  $\leq 10^{-7}$  torr. Crudely, mean free paths for ion-neutral collisions should be 10's of kilometers. On the other hand, the charge exchange process may be stronger, with cross-sections perhaps up to  $10^{-14}$  cm<sup>2</sup>. If so, the mean free path for a charge exchange event may be as short as 100 m and the corresponding mean collision time for charge exchange is of the order of 1 ns.

P. A. BERNHARDT, US

Is there any evidence of coupling between 1) E-region disturbances, and 2) the F-region or the magnetosphere?

AUTHOR'S REPLY

We have no data in the magnetosphere. But Gokhberg (1983) published an observation of an Alfvén wave in the magnetosphere with the satellite Aureol 3 above a 250 T explosion. Unfortunately, it has not been possible to make correlations with satellite data for our experiments because the time of the explosion is chosen according to the meteorological conditions.

R. SCHWEICHER, EE

How does the time scale (rise time, fall time) of your laser produced explosions compare with the time scale of EMP (electromagnetic pulses)?

AUTHOR'S REPLY

We observe two types of electromagnetic pulses in our experiments. The first occurs from the dynamics of the laser-produced plasma formation which has a time scale comparable to the laser pulse duration, i.e., with nanosecond rise and fall times; this would correspond to a prompt EMP caused by the time varying thermo-electric currents in the explosion. The second type of disturbance we see corresponds to the hydrodynamics of the expansion of the plasma distorting the ambient magnetic field, an analog to MHD-EMP, which occurs on tens of nanosecond time scales. We do not generate TREE or system EMP effects induced in satellites in this experiment.

## Modification of Tropospheric Propagation Conditions

H. Jeske

Meteorological Institute of Hamburg University  
Bundesstrasse 55, 2000 Hamburg 13, F.R.G.

### Summary:

The propagation mechanisms of ultra short radio waves and microwaves (10 m - 1 mm) are governed by the composition of the troposphere and their space-time structure of the refractive index field. After a short discussion of the natural environmental parameters, condensed in the complex refractive index, some ideas and examples of man-made changes of the propagation properties of the lower atmosphere are given.

Useful effects are obtained by chaff clouds concerning communication channels, masking of targets or meteorological research. A wide field of possibilities seems to be within the scope of weather modification experiments. But due to the huge variability of cloud and rain parameters only minor propagation changes are to be expected.

A successful application of remotely determining atmospheric temperature profiles is the modulation of the atmospheric refractive index field by sound waves and tracking the acoustic wave fronts by an Doppler radar (Radio Acoustic Sounding System - RASS).

Oil and alga slicks on water surfaces may change the reflection, scattering and emission properties for radar waves. They also suppress evaporation which may influence the development of tropical storms but just so evaporation duct propagation of microwaves.

### 1. Introduction

This paper will give a review of attempts or founded possibilities to modify the non-ionized atmosphere (troposphere, lower stratosphere). These lower layers of the atmosphere are responsible for the most propagation effects of ultra short radio waves and microwaves (wave lengths between 10 m and 1 mm or frequencies between 30 GHz and 300 GHz). In contrast to the wide ionospheric modification researches, here no special coordinated research programs are running. But it is a very interesting field and there are a lot of possibilities for radio propagation purposes, some of which are well established, others are only ideas or theoretical proposals. In this lecture only the general directions can be touched, two points will be discussed a little bit more: Modulation of the atmosphere by sound waves and the effects of slick covered water surfaces (research themes at Hamburg University).

### 2. Microwave propagation in the non-ionized atmosphere

#### 2.1 Characterization of the medium

The propagation properties of electromagnetic waves for the medium "atmosphere" are mostly described by the refractive index  $n$ . Hence the analysis of transmission (loss of signal amplitude and variation in transit time) over a given path is commonly performed by describing the medium influence with a transfer function defined by

$$t = \exp \left[ i \left( \frac{2\pi}{\lambda_0} \right) \int_0^L n(z) dz \right] = \exp \left[ i \left( \frac{2\pi}{\lambda_0} \right) \int_0^L n(z) dz \right] \quad (1)$$

for propagation of plane-wave radiation with frequency  $\nu$  over the distance  $L$  ( $c$  is the speed of the light and  $\lambda_0$  the vacuum wavelength). The dimensionless, generally complex, refractive index is written as

$$n = n' + i n'' \quad (2)$$

or reduced for air to a refractivity  $N$  in units of parts per million (or N-units), because the refractive index of air is only slightly greater than unity

$$N = (n - 1) \cdot 10^6 = (n' - 1) \cdot 10^6 + i n'' \cdot 10^6 = N' + i N'' \quad (3)$$

For non-ionized air, the refractivity consist of three components

$$N = N_0 + dN(\nu) + i N''(\nu) \quad (4)$$

namely, a frequency-independent refractivity  $N_0$  (valid for  $\nu < 10$  GHz) plus various spectra of refractive dispersion  $dN(\nu)$ , and absorption effects  $N''(\nu)$  due to resonances of oxygen and water vapor within the microwave domain. As well-known, the frequency-independent first term is given by half-empirical formulas (e.g. from Smith and Weintraub, 1953) and can be calculated in a straightforward manner by aid of available meteorological parameters ( $p$  total pressure in mb,  $T$  temperature in K,  $e$  water vapor pressure in mb),

$$N_0 = \frac{77.6 p}{T} - \frac{6 e}{T} - \frac{3.75 \cdot 10^5 e}{T^2} \quad (5)$$

The first two terms are the result of induced molecular polarization of air and water vapor, respectively; the third term represents the effects of the permanent dipole moment of the water vapor molecule (Debye-term). Included in the composition of dry air are 0.03 % carbon dioxide.

The sensitivity to atmospheric parameters, under the assumption of the ICAO Standard Atmosphere, may be read from

$$\Delta N = 0.27 \Delta p - 1.27 \Delta T + 4.5 \Delta z \quad \text{linear (the surface)} \quad (5a)$$

$$\Delta N = 0.30 \Delta p - 0.50 \Delta T + 7.5 \Delta z \quad \text{lat 10 km} \quad (5b)$$

The next equation gives the surface conditions for optical waves. Note here the very small influence of water vapor (omission of the Debye-term)

$$\Delta N_{\text{opt}} = 0.27 \Delta p - 0.95 \Delta T - 0.04 \Delta z \quad (5c)$$

The overall error using Eq. (5) at sea level amounts to 0.5 %. The error for an improved equation (Thayer, 1974) will range from 0.02 % for dry air to about 0.05 % for extremely moist air.

The effect of the most present trace gas carbon dioxide, constantly increasing, may be estimated by the additional term (Thayer, 1974)

$$N(\text{CO}_2) = \frac{133 p_{\text{CO}_2}}{T} \quad \text{or} \quad \Delta N(\text{CO}_2) = 0.48 \Delta p_{\text{CO}_2} \quad (6)$$

A doubling of the actual value of 350 ppm ( $p_{\text{CO}_2} = 0.354 \text{ mb}$ ) results in an increase of  $N$  by 0.16 N-units (= 0.05 %). A short-term variation by an order of magnitude corresponds to 1.5 N-units.

The absorption and dispersion effects for frequencies > 10 GHz (up to 1000 GHz) are contributions from several lines of water vapor - (29) and oxygen - (44) resonances and may be formulated as (Liebe et al., 1977, 1978, Liebe, 1981)

$$dN(\nu) = \sum (SF^+)_i \quad \text{in ppm and} \quad N'' = \sum (SF^-)_i \quad \text{in ppm} \quad (7)$$

where  $S$  is the line strength and  $F^+$  or  $F^-$  are shape factors. The  $N''$ -term has to be completed by some corrections due to wing terms or cluster effects. Liebe (1981) has given a computer program to evaluate the dispersion and absorption effects. Some examples of  $dN(\nu)$  and  $N''(\nu)$  for three different humidities and two temperatures as functions of frequency are given in Fig. 1. Absorption bands and window regions are recognizable. Within the absorption bands anomalous dispersion occurs.

The refractive index of air may be changed by admixed particles or hydrometeors (water drops in clouds, fog, or rain). From a two-phase mixing formula for spheres (water) within a host material (air) (Ullaby et al., 1986)

$$n_m = n_a \left( 1 + 3V \frac{n_w^2 - n_a^2}{n_w^2 + 2n_a^2} \right) \quad (8)$$

where  $n_m$ ,  $n_a$ ,  $n_w$  are the relative dielectric constants of the mixture, air (host) and water, respectively, and  $V_w$  is the water-inclusion volume fraction, follows (approximately) for the contribution of droplets to the refractivity  $N$

$$(n_m - 1)10^6 = N_m = \frac{10^6 3rV}{2} \frac{n_w^2 - 1}{n_w^2 + 2} \quad (9)$$

Here  $n$  is the refractive index of water,  $r$  the number density of droplets per unit volume of air, and  $V$  the volume of an individual droplet. The real part of the complex index (water is a lossy medium) is shown in Fig. 2 for different rain rates as function of frequency. The contribution may reach some N-units for very intense rain. The shown refractive index curves are determined by the frequency behaviour of water.

Plasma refractive effects can be ignored within the lower atmosphere. Apart from lightning channels with an electron concentration up to  $10^{18} \text{ cm}^{-3}$ , the tropospheric air contains a number of positive and negative (so-called) small ions (cluster ions) built up by hydration (for instance,  $\text{H}_3\text{O}^+ (\text{H}_2\text{O})_n$  or  $\text{O}_3^- (\text{H}_2\text{O})_n$ ,  $n$  up to about 10). The number density near land surfaces amounts to  $10^3 \text{ cm}^{-3}$  and to  $10^2 \text{ cm}^{-3}$  over the oceans. The contribution to refractivity (real part) may be determined by (Hartmann et al., 1984)

$$N_j = - \frac{r_j e^2}{\epsilon_0 m_j 2 \pi \nu^2} 10^6 \quad \text{with} \quad j = 1, 2, 3 \quad (10)$$

where  $j = 1$  corresponds to electrons,  $j = 2$  to positive ions, and  $j = 3$  to negative ions,  $r$  is the number density,  $e$  electron charge,  $\epsilon_0$  dielectric constant of free space, and  $\nu$  the frequency. Using SI-units for the physical constants it follows from Eq. (10)

$$N_1 = -40.3 \cdot 10^6 \frac{r_1}{\nu^2} \quad \text{for electrons, and} \quad (10a)$$

$$N_{2,3} = - \frac{180 r_{2,3}}{\nu^2} \quad \text{for pos. and neg. ions} \quad (10b)$$

For the mass of the ions 122 amu was assumed, the density is in  $\text{m}^{-3}$  and  $\nu$  in Hz. The contribution of the ions ( $r_{2,3} = 1000 \text{ cm}^{-3}$ ) amounts for a frequency of 1 GHz to  $-2 \cdot 10^{-7}$  N-units (-0.08 N-units for the same number of electrons), that is to say, the correction is only of academic interest.

For completeness, also a term for nonlinear (i.e. intensity-dependent) refractive index contributions may be given (Martin et al., 1988)

$$N_{\text{non}} = N \cdot 10^6 \sum_i \chi_i I_i \quad (11)$$

where  $\chi_i$  is the density of each gas ( $\text{m}^3$ ),  $I$  the intensity of the source ( $\text{GW}/\text{m}^2$ ) and  $\chi_i(I)$  is the nonlinear index coefficient. These effects are relevant for high peak power laser or maser propagation through the atmosphere. Since, for instance, the intensity in the center of a (Gaussian) beam is higher than at the border, a beam-induced refractive index gradient may lead to self-focussing phenomena.

## 2.2 Tropospheric propagation mechanisms

The composition of the air and the prevailing structure of the tropospheric refractive index field (mean and fluctuating components) in space and time determine the propagation mechanisms as refraction, scintillation, ducting, reflection, multi-path propagation, scattering, and absorption (Fig. 3).

Each type of propagation has its special loss of signal amplitude, change of polarization, variation in transit time or phase shift, all dependent from the generally complex and frequency-dependent refractive index. To modify the propagation medium one has to change the refractive index either by changing the composition of the air or by altering its structure. An essential role may also have the refractive index and the structure (smooth, rough, layered) of the underlying surface of the earth.

## 3. Modification of the refractive index of air

### 3.1 Changes of the real refractive index of air

The natural variations of the radio refractive index of the atmosphere is extremely large as well in space (s. world charts of N. Bean et al., 1968) as in time (diurnal and annual variations up to 60 N-units). Special topographical-induced effects on the meteorological environment, travelling weather systems with strong frontal lines, or other storm types provide for the ever alternating refractive index field and its propagation effects. So an artificial change of the environmental refractivity of the air by changing the temperature, or the humidity, or the suspension content is a hopeless operation.

Only a horrible scenario as the nuclear winter following a major nuclear exchange (1000 - 10 000 Mt nominal) would lead to a decisive modification of microwave propagation due to the new refractive index structure of the troposphere and land surfaces. Tremendous amounts of smoke particles (say 200 million tons) and dust (say up to 1000 million tons) would be injected into the troposphere and lower stratosphere of the Northern Hemisphere (among other things) and encircle the earth. From numerous "sensitivity experiments", modelers (s. Pittock et al., 1985) found a cooling of the surface of mid continental regions of 10 - 40 degrees down to absolute values of -25° C within 1 or 2 weeks after the exchange (Fig. 4a). An analogous cooling occurs in the lower atmosphere; above about 5 km, on the other hand, a strong warming sets in (Fig. 4b). Temperatures in the Northern Hemisphere's 10 - 20 km altitude range will have increased by 80° C or more. A very stable atmosphere is the consequence with strong vertical refractivity gradients. This would be the hotbed for multiple path propagation due to ducting and reflecting (top of the clouds) effects. Also the change of surface properties with frozen and perhaps snow-covered ground (persisting for several months) influences the propagation conditions considerably.

### 3.2 Nonlinear effects

The propagation of high-energy laser or maser beams through the atmosphere is subjected to a wide variety of effects (Martin et al. 1988, Zuev et al. 1985). Besides the well known linear phenomena, such as absorption, scattering, and diffraction from density-dependent refractive index gradients several nonlinear, i.e. intensity-dependent, processes set in. Worth mentioning are nonlinear thermal blooming, self-focusing (self-trapping) of laser beams, stimulated scattering, air and aerosol induced breakdown effects or beam induced plasma.

Some practical applications seem imaginable. The vaporization of fog or cloud droplets by high-power beams may create a communication channel or may open the possibility of clearing areas from fog or water hazes in the atmosphere. Opto-acoustic sensing of atmospheric parameters analysing the shock wave following the optical breakdown of the air has been proposed. But the most possibilities are yet in the theoretical and experimental stage.

## 4. Absorption and emission of the atmosphere (noise)

### 4.1 Natural effects

Microwave absorption and emission in the troposphere is dominated by oxygen and water vapor. Other atmospheric gases and pollutants as  $\text{O}_3$ ,  $\text{SO}_2$ ,  $\text{N}_2\text{O}$ ,  $\text{NO}_2$ ,  $\text{CO}$ ,  $\text{CH}_4$ ,  $\text{NH}_3$ ,  $\text{OH}$ ,  $\text{HNO}_3$ ,  $\text{ClO}$ , among others have also several absorption lines in the microwave region. But due to their small concentration at sea level and the large pressure-broadening effect by the major gases contributions to the microwave absorption spectrum are negligible in comparison to oxygen and water vapor. The situation is demonstrated in Fig. 5.

On the other hand, however, the strong attenuation within the absorption bands of oxygen or water vapor (say near 60 GHz, 118 GHz, 183 GHz, 325 GHz) allows controlled communication links for small distances.

The atmospheric attenuation increases essentially if clouds, fog, snow, or rain are present. An impression may give Fig. 6. The prediction of rain attenuation in space and time is an important, but very difficult, task for all radio link operators.

The absorption properties are also responsible for the generation of atmospheric radio noise. The noise effect plays sometimes a larger role in degrading signal-to-noise level for low-noise systems than does absorption itself. At frequencies above 1 GHz the emission from the gaseous atmosphere ( $\text{H}_2\text{O}$ ,  $\text{O}_2$ ) is a significant source of external noise limiting low-noise communication or navigation systems (see Fig. 7a). Again clouds and precipitation enhance the environmental (thermal) noise of the atmosphere (see Fig. 7b). For very high rain rates the noise temperature corresponds to the environmental temperature. Below 500 MHz other radio noise sources begin to dominate as galactic noise, man-made noise, or atmospheric noise generated by statics, which are wide band pulses radiated by lightning strokes.

## 4.2 Modification possibilities

The increase of minor constituents of the atmosphere (e.g. CO<sub>2</sub> problem) by human activities is a relevant problem for questions of climatic change because most trace gases belong to the greenhouse gases. But the influence on microwave attenuation or noise generation ooze away within the effects of the natural turbulent environment.

Short-term propagation experiments with an artificial injection of absorbing gases into the rather turbulent lower atmosphere promise no success. Perhaps a method of laser weapon counter measure by placing strong absorbing gases in the laser path producing so thermal blooming may be considered.

At a first sight, experiments which change the cloud and precipitation conditions of the atmosphere may appear promising for propagation questions due to the strong interaction of microwaves and hydrometeors. This topic is close connected with the wide and complex field of weather modifications. With few exceptions, weather modification refers to the artificial modification of clouds. Experiments in cloud modification consist of seeding the clouds with some material, and are usually undertaken with one of following goals in mind: (1) to stimulate precipitation (rain or snow), (2) to dissipate fog or clouds, and (3) to suppress hail. The activities are worldwide. Varying degrees of success have been reported for each type of experiment. However, it is very often difficult to obtain convincing evidence that an experiment was successful because of the large variability that characterizes clouds. Nevertheless, evidence is emerging from a few carefully regulated experiments that, under the appropriate conditions, modest changes in cloud structure and precipitation can be effected by seeding. Due to these general uncertainties and the wide natural variations of cloud or precipitation parameters in space and time an utilization of these results for radiowave propagation appeared not necessary up to now. Eventually the steady increasing employment of mm- and sub-mm-waves may alter this situation. From Fig. 8 may be deduced how small the modification of attenuation (for different wavelengths) will be, if the rain rate is changed by a moderate (say 30%) amount what may be expected by weather modification efforts. The effect on noise temperature may be seen from Fig. 7b.

## 5. Admixture of chaff

Chaff - a cloud of many dipoles or thin aluminum foil or metallized glass strips released into the air - was used for the first time (in World War II) to produce large reflecting areas for radar waves. In this way the radar cross section of a target (aircraft) behind the cloud can be reduced. But with chaff also communication channels, especially for over-the-horizon links, can be established via scattering processes at the chaff cloud. Today the theoretical and practical experiences are sufficient to use a chaff channel when there is only a short-time need for a communication purpose and the meteorological situation is unfavourable for a troposcatter link (Lampert, 1976).

For remote sensing of the vertical wind speed within the upwind tube of thunderstorms disposed chaff may be tracked by Doppler radars.

## 6. Modulation of the atmosphere by sound waves

A special preparation of the atmosphere is carried out for a remote sensing technique to get temperature profiles of the atmosphere. This method is a combination of radar and acoustics and has been given the acronym RASS: Radio Acoustic Sounding System (Marshall et al. 1972, Peters et al. 1983). Briefly, a sound packet directed vertically into the atmosphere is tracked by a Doppler radar, and the speed of the acoustic packet provides the environmental air temperature. An acoustic wave travelling through the atmosphere may be viewed as a local condensation of the air followed by a rarefaction. Their density variations cause a change in the refractive index of air that scatters back a small part of the electromagnetic energy. The sound speed is related mainly to the (virtual) temperature  $T$  which can, therefore, be derived from the Doppler shift of the scattered signal.

$$v_s = \frac{f_D \lambda_r}{2} = \left( \gamma \frac{RT}{M} \right)^{1/2} \approx 20.047 T^{1/2} \quad (12)$$

where  $v_s$  is the sound speed (m/s),  $f_D$  the Doppler frequency (Hz),  $\lambda_r$  the radar wavelength (m),  $R$  the gas constant,  $\gamma$  the ratio of specific heats of air ( $\approx 1.4$ ),  $M$  the mean molecular weight of the constituents of the medium.

Acoustic sources with wavelengths ranging from 1.5 cm to 4 m have been used. Also different modes of RASS operation has been tried, i.e. pulsed or continuous acoustic sources and/or pulsed or continuous wave Doppler radars (Peters et al. 1983). The method makes use of the enhancement in the backscattering by matching the acoustic wavelength to half of the radar wavelength (Bragg scattering condition) and by making use of the focusing effect of the spherical wave fronts. But the horizontal winds displace the acoustic wavefronts. Thereby the focusing effect is negated causing a limitation in altitude (lower boundary layer, say 1 km). Aligning the antennas in wind direction with a movable radar receiving antenna on the leeward (for instance, mounted on a rotary system as in Hamburg) may enlarge the height range a little bit. Large aperture antennas or arrays of antennas and low-noise receivers may also be effective. Experiments in Japan (Mazuda, 1988) with steerable radar beams to allow for the effect of the horizontal displacement of the acoustic radiation by wind get temperature profiles up to 22 km.

Acoustic sources with wavelengths ranging from 1.5 cm to 4 m have been used. Also different modes of RASS operation has been tried, i.e. pulsed or continuous acoustic sources and/or pulsed or continuous wave Doppler radars (Peters et al. 1983). The method makes use of the enhancement in the backscattering by matching the acoustic wavelength to half of the radar wavelength (Bragg scattering condition) and by making use of the focusing effect of the spherical wave fronts. But the horizontal winds displace the acoustic wavefronts. Thereby the focusing effect is negated causing a limitation in altitude (lower boundary layer, say 1 km). Aligning the antennas in wind direction with a movable radar receiving antenna on the leeward (for instance, mounted on a rotary system as in Hamburg) may enlarge the height range a little bit. Large aperture antennas or arrays of antennas and low-noise receivers may also be effective. Experiments in Japan (Mazuda, 1988) with steerable radar beams to allow for the effect of the horizontal displacement of the acoustic radiation by wind get temperature profiles up to 22 km.

Some examples of measurements may demonstrate the eminent efficiency of the method. Fig. 9 shows a time series in a fixed height measured simultaneously by RASS and an electric thermometer. In Fig. 10 a, a RASS-temperature profile is compared with a radiosonde and in Fig. 10 b with a profile determined by a 58 GHz - radiometer (angle scanning mode). With modern systems a height resolution down to 10 m may be achieved and accuracies up to 0.1 K (Peters et al. 1988). Also atmospheric systems, as developing or dissolving temperature inversions or weather fronts

may be observed continuously and analysed in detail. Fig. 11 gives the passage of a cold front. In Fig. 12 a profile up to 22 km (Masuda, 1988) is shown gained with a high-power monostatic VHF-radar ( $\lambda = 3.4$  m) with a steerable beam and a high-power acoustic source.

## 7. Surface films on water surfaces

### 7.1 General remarks

The presence of oil layers or monomolecular films of organic or artificial material may effect the properties of the sea surface in several ways. The emission of electromagnetic radiation and the scattering of radar waves are changed and a modification of air-sea interaction processes (as evaporation) sets in. There are three types of layers to distinguish. Whereas thick mineral oil patches normally are a consequence of tanker accidents, natural monomolecular films produced by plankton and fish occur very often in coastal regions of high biological productivity, and artificial monolayers formed by oleyl alcohol films are used for scientific experiments. The monolayers have a thickness of the order of  $3 \cdot 10^{-6}$  nm, so that the amount of film material floating on a sea surface of 1 km<sup>2</sup> area is less than 2 liters. Oil slicks are typically several mm thick.

### 7.2 Emission of the surface (brightness temperature)

The brightness temperature is proportional to the emissivity of the surface material and its physical temperature. The emissivity of a smooth surface is (as the reflectivity) a function of the complex dielectric constant of the emitting surface. Generally, the dielectric constant of an oil layer is much smaller than that of sea water, and the emissivity and so the brightness temperature consequently greater. However, because of multiple reflections at the air-film and film-sea interfaces, standing waves can be set up resulting in an brightness temperature variation having a strong dependence on the layer thickness (Fig. 13). So measurements of microwave radiometers installed at airplanes or satellites can be used not only to detect the presence of oil slicks, but also to estimate its thickness (if using two or more frequencies).

The influence of monolayers is somewhat different compared to the thicker oil films. As mentioned, the brightness temperature is a function of the complex dielectric constant of the upper layer of the ocean. However, the thickness of the efficacious layer is of the order of the penetration depth, which, for sea water, varies between 1 cm and 1 mm if the frequency increases from 1 GHz (30 cm) to 20 GHz (1.5 cm). That means, the microwave brightness temperature should normally not be effected by a monomolecular film. But experimental investigations with airborne radiometers at 1.43 and 2.65 GHz yield a somewhat surprising result (Alpers et al. 1982). The measurements show (s. example in Fig. 14) that at 1.43 GHz the brightness temperature drops down by several tens of degrees, whereas the brightness temperature at 2.65 GHz is not effected. This implies that at 1.43 GHz (21 cm) the emissivity of the film-covered sea (i. e. oleyl alcohol) is extremely small, similar to a metallic layer. The effect was interpreted as a re-onant-type phenomenon, that means the film-water layer is polarized and exhibits an anomalous dielectric relaxation regime ( $\tau = 5 \cdot 10^{-4}$ ) centered at a frequency close to 1.43 GHz. The wind speed during the experiment (North Sea near Sylt) was between 12 and 16 knots.

Additionally to the influence of the surface material, the surface roughness increases the brightness temperature of a clean surface due to Bragg-scattering effects of the rough surface and foam formation. The damping out of the wave structure by oil films or other films reduces the increase of brightness temperature because the film-covered surface becomes smoother. Calculations of the difference in antenna temperature (proportional to brightness temperature) between oil-covered and oil-free surfaces gives Fig. 15. An additional decrease of the brightness temperature is due to the fact that the film inhibits the generation of foam and white caps which is also controlled by the wind speed. According to the last figure the wind-related effects of a film on the brightness temperature can be ignored for frequencies below 30 GHz if the wind speed is below 10 m/s ( $\Delta T < 4$  K). At higher wind speeds the oil slicks breaks up into small patches and become ineffective. Then a radiometer cannot work as an oil-slick monitor.

### 7.3 Radar backscattering effects

Surface films of oil or biological or artificial material influence the scattering effects of a rough surface by damping out the ocean waves. So the detection and monitoring of oil spills or other slicks at the sea surface by radar is possible (De Loor et al., 1978). Experiments were conducted with artificial monolayer in wind wave tanks and over the open sea. Fig. 16 shows radar cross sections for a 9.8 GHz radar of a clean water surface compared with a film-covered surface carried through in the wind wave tank in Hamburg (Feindt, 1985). Below a wind speed of 13 m/s a depression of the scattered energy by the film is observed, at 13 m/s the radar cross sections for the clean and slick-covered surfaces become equal. At this wind speed the slick is "washed down" by breaking waves. Open ocean experiments confirm the depression of radar cross sections. The maximum measured difference between a slick-covered area and a non-slick-covered area during airborne experiments over the North Sea at a frequency at 13.9 GHz (Hühnerfuß et al., 1978) was  $7.3 \pm 3.5$  dB, which implies that about 80 % of the energy of the surface wave component with a wavelength corresponding to the Bragg condition is lost by damping effects. These smoothing effects may become important for the interpretation of remote sensing results or surveillance of polluted ocean surfaces.

### 7.4 Retardation of evaporation

A surface slick not only damps small surface waves but modifies essentially air-sea interaction parameters as dynamic roughness length  $z_0$ , the turbulent fluxes of momentum, sensible heat, latent heat, and other exchange processes. Of some importance is the retardation of evaporation  $E$  (the suppression of the latent heat flux). Practical interest exists in the field of hurricane abatement, conversion of water in larger water reservoirs or lakes, and reduction of duct propagation through the evaporation duct above the sea. Experiments on Lake Hefner with monolayers result in a reduction of evaporation of about 65 % (Mansfield et al., 1973). From this, 55 % are due to molecular barrier effects of the film and 10 % to wave damping effects which decrease the roughness parameter  $z_0$ . The bulk aerodynamic method of the meteorological boundary layer theory gives for  $E$

$$E = -\rho z_0^2 u_* \left( \frac{q_1 - q_2}{\ln \frac{z_1}{z_2}} \right) \quad (13)$$

where  $E$  is the rate of evaporation per unit area and time,  $\rho$  the density of air,  $\kappa$  the v. Karman's constant,  $u_1$  the mean wind velocity at a level  $z_1$  near the surface (say 10 m),  $z_0$  the roughness length (typically 0.018 cm),  $q_1$  the specific humidity at  $z_1$ , and  $q_0$  the saturation value of specific humidity for the surface temperature. Using typical values of  $z_0$  and  $u_1$  from an experiment with artificial sea slicks on the open oceans (Barger et al., 1970), one can confirm with materials that modify wave parameters only (no barrier effect), the expected 10 % reduction of evaporation. The main effect is given by films that act as a barrier to molecular transfer and reduce the gradient of moisture ( $q_1 - q_0$ ).

The flux of moisture determines the refractive index gradient (via the moisture gradient) above the sea (s. Eq. 5a). The thickness of the evaporation duct  $z$ , which controls the propagation (at low elevation angle) of radar and microwaves above the sea in about 80 % of time may be approximated by (neutral conditions)

$$z = \frac{N_0 - N_1}{(10^6/r_0)} \frac{1}{\ln(z_1/z_0)} \quad (15)$$

where  $N_1 - N_0$  is the refractivity difference between the measuring height  $z_1$  and the (saturated) surface, and  $1/r_0$  is the curvature of the earth ( $= 0.157 \cdot 10^{-6} \text{ m}^{-1}$ ). The thickness varies generally between 0 and 40 m in temperate and subarctic latitudes. Superdetection ranges or field strength enhancements for microwaves (up to the multiple free-space level) are possible (s. Fig. 17), but also, especially within the horizon, very low field strength levels (so-called radio holes) may occur. Under neutral conditions ( $T_1 - T_0 = 0$ ) a retardation of evaporation of 60 % by a monolayer reduces also the thickness of the evaporation duct by 60 %; for non-neutral conditions a smaller temperature effect (s. Eq. 5 a) has to be regarded. In Fig. 17, a 50 % reduction of the duct thickness would compress the whole scatter diagram between a thickness of 0 and 10 m and a field strength between -5 and 50 dB $\mu$ . For radar or communication systems in coastal regions of high biological productivity, natural monolayers may disturb the propagation conditions in a noteworthy way if microwaves are used.

### 8. Concluding remarks

Summing up it is to say that in the field of modifying microwave propagation in the non-ionized atmosphere, there are a lot of ideas but there are only a few realistic applications. These may be the admixture of chaff, modulation of the atmosphere by sound waves, or the utilization of surface films (for instance within the scope of monitoring ocean surfaces). An influence on tropospheric propagation could be better attained by the methods of Electronic Counter Measures.

### 9. References

- Alpers, W., et al., The effect of monomolecular surface films on the microwave brightness temperature of the sea surface, *Int. J. Remote Sensing*, 3 (4), 1982, 457 - 474
- Barger, W. R., et al., Effects of an artificial sea slick upon the atmosphere and the ocean, *J. Appl. Meteor.*, 9, 1970, 396 - 400
- Bean, B. R., Dutton, E. J., *Radio Meteorology*, New York, Dover Publ., 1968
- De Loor, G. P., van Hulten, H. W., Microwave measurements over the North Sea, *Boundary Layer Meteor.*, 13, 1978, 119 - 131
- Feindt, F., Radar-Rückstreuexperimente im Wind-Wellen-Kanal bei sauberer und filmbedeckter Wasseroberfläche im X-Band, *Hamb. Geophys. Einzelschr.*, A 75, 1985, 224 pp.
- Flock, W. L., Slobin, S. D., Smith, E. K., Propagation effects on radio range and noise in earth-space telecommunications, *Radio Sci.*, 17 (6), 1982, 1411 - 1424
- Hartmann, G. K., Leitinger, R., Range errors due to ionospheric and tropospheric effects for signal frequencies above 100 MHz, *Bull. Geod.*, 58, 1984, 109 - 136
- Hollinger, J. P., The determination of oil slick thickness by means of multifrequency passive microwave technique, Dept. of Transportation Rept. No. CG-D-31-75, 1974, US Coast Guard Office, Washington, D.C.
- Hühnerfuss, H., Alpers, W., Jones, W. L., Measurements at 13.9 GHz of the radar backscattering cross section of the North Sea covered with an artificial surface film, *Radio Sci.*, 13, 1978, 979 - 983
- Jeske, H., Wellenleitereinflüsse über See auf die Ausbreitung im mm- und cm-Band, *Kleinheubacher Berichte*, 14, 1971, 13 - 18, Deutsche Bundespost, FTZ, Darmstadt
- Lampert, E., Review on communication aspects of chaff-produced scatter propagation, AGARD-Conf. Proc. No. 192, 1976, 3-1-3-10
- Liebe, H. J., Gimmestad, G. G., Hopponen, J. D., Atmospheric Microwave Spectrum Experiment versus Theory, *IEEE Ant. and Prop. Ap-25* (3), 1977, 327 - 335
- Liebe, H. J., Gimmestad, G. G., Calculation of clear air EHF refractivity, *Radio Sci.*, 13 (2), 1978, 245 - 251
- Liebe, H. J., Modelling attenuation and phase of radio waves in air at frequencies below 1000 GHz, *Radio Sci.*, 10 (6), 1981, 1183 - 1199
- Mansfield, D. M., Mickelson, Th. P., Experiments with monomolecular films on the surface of the open sea, *J. Phys. Ocean.*, 3, 1973, 328 - 336
- Marshall, J. M., Peterson, A. M., Barnes, A. A., Combined radar-acoustic sounding system, *Appl. Opt.*, 11, 1972, 108 - 112
- Martin, W. E., Winfield, R. J., Nonlinear effects on pulsed laser propagation in the atmosphere, *Appl. Opt.*, 27 (3), 1988, 567 - 577
- Masuda, Y., Influence of wind and temperature on the height limit of a radio acoustic sounding system, *Radio Sci.*, 23 (4), 1988, 647 - 654
- Mondre, E., Atmospheric effects of mm-wave communication channels, NASA Goddard Space Flight Center, Rept. X-733-70-250, March, 1970
- Peters, G., Trummermann, H., Minzpeter, H., Temperature sounding in the planetary boundary layer by RASS-system, *Int. J. Remote Sensing*, 4, 1983, 49 - 63
- Peters, G., Minzpeter, H., Baumann, G., Measurements of heat flux in the atmospheric boundary layer by SO-DAR and RASS, *Radio Sci.*, 20, 1985, 1555 - 1564
- Peters, G., Hasselmann, D., Pang, S., Radio acoustic sounding of the atmosphere using FM CW radar, *Radio Sci.*, 23 (4), 1988, 640 - 646



- Pittock, A. B., et al., Environmental consequences of nuclear war (Vol. I), New York, J. Wiley & sons, 1986
- Richter, B., Atmospheric microwave thermal emission in presence of precipitating clouds at 9, 33, and 94 GHz, Beitr. Phys. Atm., 54, 1981, 123 - 135
- Setzer, D. E., Computed transmission through rain at microwave and visible frequencies, Bell Syst. Tech. J., Oct. 1970
- Smith, E. K., Centimeter and millimeter wave attenuation and brightness temperature due to atmospheric oxygen and water vapor, Radio Sci., 17 (6), 1982, 1455 - 1464
- Smith, E. K., Kohntraub, S., The constants in the equation for atmospheric refractive index at radio frequencies, Proc. IRE, 41, 1953, 1035 - 1037
- Thayer, G. D., An improved equation for the radio refractive index of air, Radio Sci., 9 (10), 1974, 803 - 807
- Thrane, E. V., Media effects on systems in the high latitude region, AGARD-Conf. Proc. No 382, 1985, 1.2-1.2-16
- Turco, R. P., et al., Nuclear Winter: Global consequences of multiple nuclear explosions, Science, 222, No 4630, 1983, 1283 - 1292
- Ulaby, F. T., Moore, R. K., Fung, A. K., Microwave remote sensing, Vol. I, London, Addison-Wesley Publ. Comp., 1981
- Ulaby, F. T., Moore, R. K., Fung, A. K., Microwave remote sensing, Vol. III, 610 Washington St., Artech House, Inc., 1986
- Zuev, V. E., et al., High-power laser radiation in atmospheric aerosols, Dordrecht, Reidel Publ. Comp., 1985

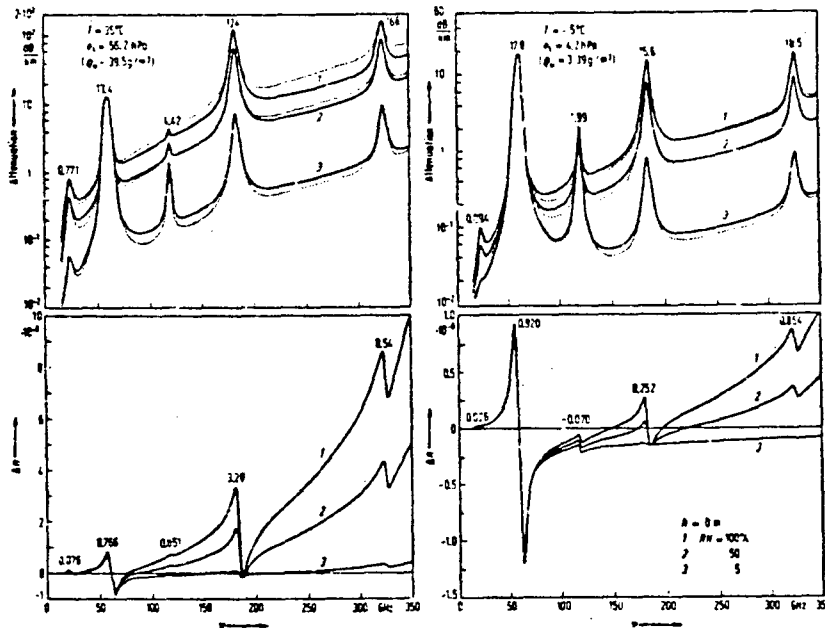


Fig. 1: Attenuation and refractive dispersion  $\Delta n$  (deviation of  $n$  from the frequency-independent term) of 3: dry (RH = 5%), 2: humid (RH = 50%) and 1: saturated (RH = 100%) air at sea level for temperatures of -5°C and 35°C over the frequency range of 15 ... 350 GHz ( $\lambda$ : 20 ... 0.86 mm) after Liebe, 1981;  $p_s$ : saturation pressure;  $p_w$ : absolute humidity; solid and dotted curves refer to two different models of the additional contributions of the continuum spectrum.

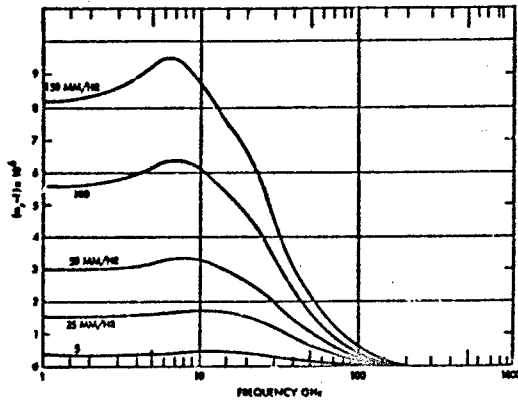


Fig. 2: Real part of complex refractivity of a medium consisting of water drops at 20°C in vacuum (s. Flock et al., 1982)

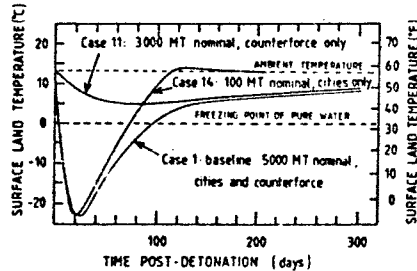


Fig. 4 a: Surface land temperatures as function of time after detonation, as calculated by Turco et al. (1983) for nuclear war scenarios. Values apply to mid-continental regions and do not take into account buffering of temperature changes by oceanic heat capacity.

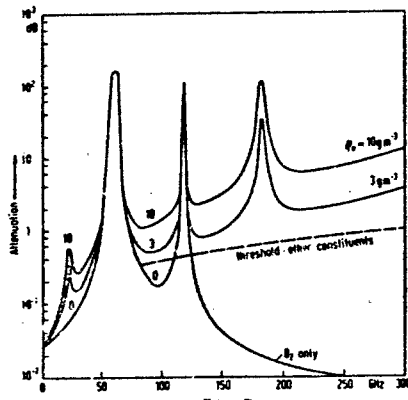


Fig. 5: Absorption properties of the atmosphere: Total one-way zenith attenuation as function of frequency (U.S. Standard Atmosphere) (Smith, 1982).

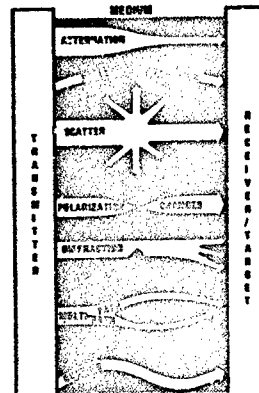


Fig. 3: Schematic illustration of tropospheric propagation effects (Thrane, 1985).

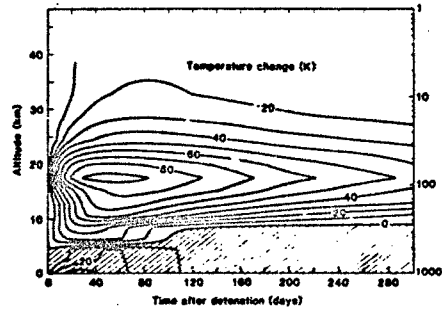


Fig. 4 b: Northern Hemisphere troposphere and stratosphere temperature perturbations (in Kelvins) after the baseline nuclear exchange (case 1). The hatched area indicates cooling.

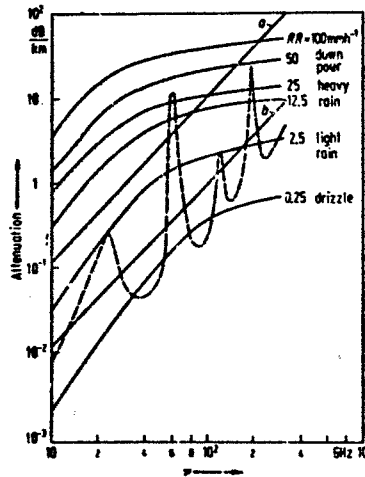


Fig. 6: Comparison of attenuation per distance by atmospheric gases, fog, and rain as function of frequency. Dashed curve: atmospheric gases (standard atmosphere); solid curves: rain of various strengths  $RR$ ; straight lines: fog and mist ( $T = 18^\circ\text{C}$ ); a: visibility = 30 m,  $e_w = 2.3 \text{ gm}^{-3}$ ; b: visibility = 150 m,  $e_w = 0.25 \text{ gm}^{-3}$  (Mondre, 1970).

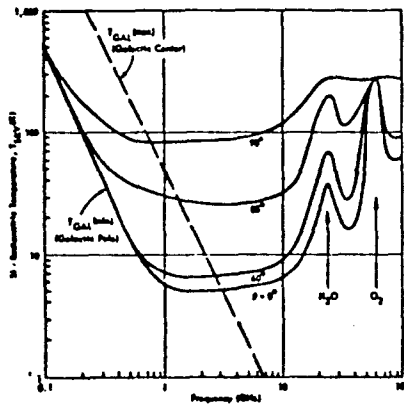


Fig. 7 a: Calculated sky radiometric temperature for several zenith angles in the 0.1 - 100 GHz region (Standard Atmosphere with  $7.5 \text{ g m}^{-3}$  absolute humidity) (s. Ulaby et al., 1981).

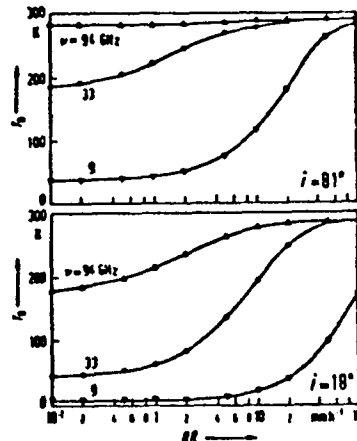


Fig. 7 b: Brightness temperature  $T_B$  of raining clouds as function of rain fall rate  $RR$  at three frequencies and two zenith angles  $i$ . Rain (Marshall-Palmer distribution) is combined with a cumulus cloud, cloud top 3 km (Richter, 1981).

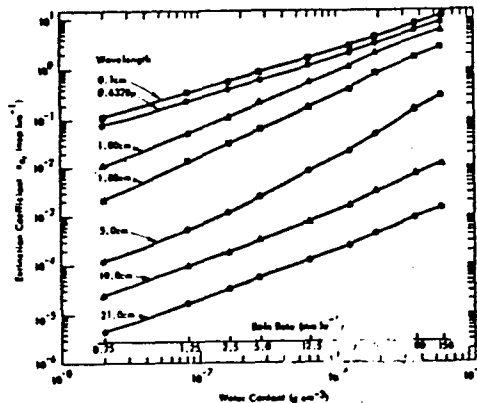


Fig. 8: Rain attenuation coefficient as function of rain rate or water content (Setzer, 1970).

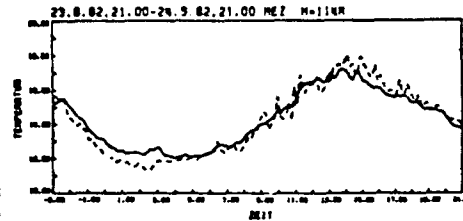


Fig. 9: Comparison of RASS and directly measured (Pt 100) temperatures (height: 114 m, 2.5 min averages) (Peters et al., 1983).

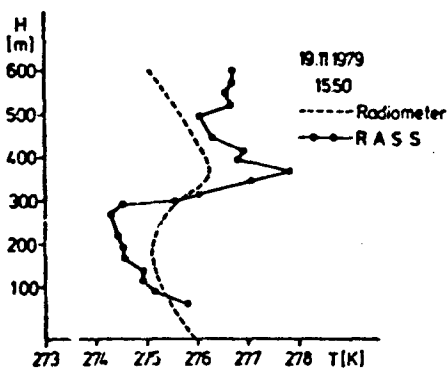


Fig. 10 b: Comparison of a RASS temperature profile and a 58 GHz radiometer profile (Peters et al., 1983).

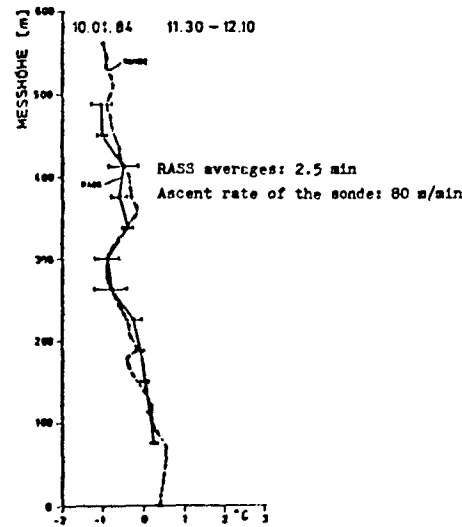


Fig. 10 a: Comparison of a RASS temperature profile and a Radio-sonde profile (s. Peters et al., 1983).

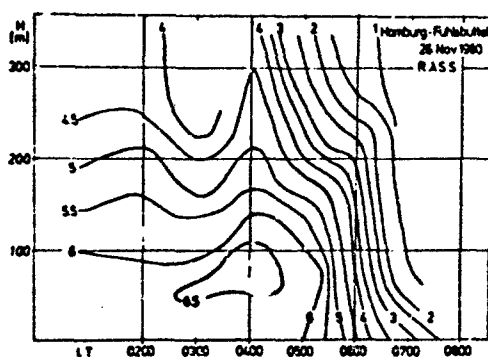


Fig. 11: Contour plot (height/time) of isotherms in 0.5 K intervals (90 s averages) measured by RASS during a cold front passage (Peters et al., 1983).

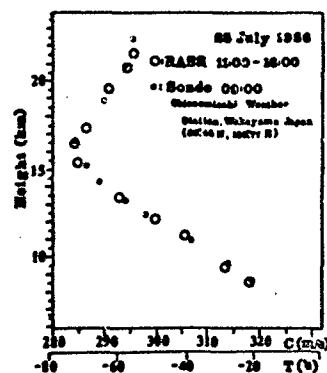


Fig. 12: Comparison between a RASS temperature profile and a Radio-sonde profile (Masuda, 1988).

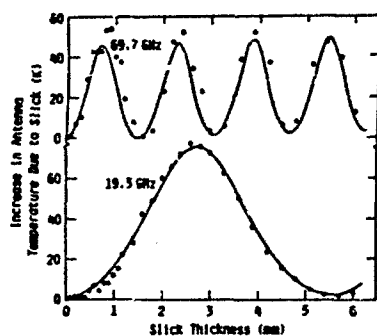


Fig. 13: Increase in antenna temperature due to fuel oil spread over a smooth water surface in a test tank as function of film thickness (measurements and calculations) (Hollinger, 1974).

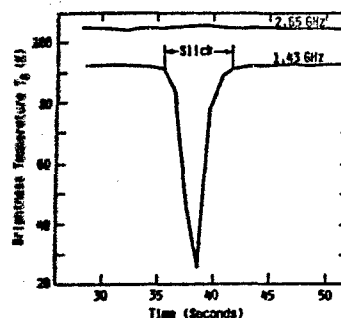


Fig. 14: Brightness temperature at 1.43 GHz and 2.65 GHz as measured by airborne radiometer systems during a pass over a spreading monomolecular oil film (Alpers et al., 1982).

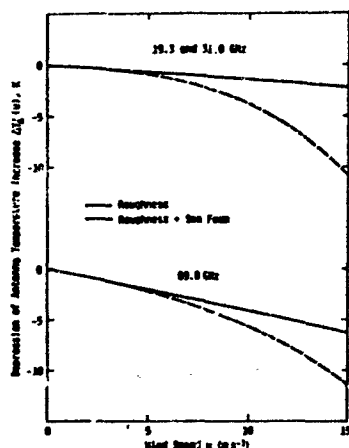


Fig. 15: Depression (of antenna temperature increase) due to the presence of oil on the water surface as function of wind speed. The increase (compared with a smooth and clean surface) is caused by oil, roughness, and foam (Hollinger, 1974).

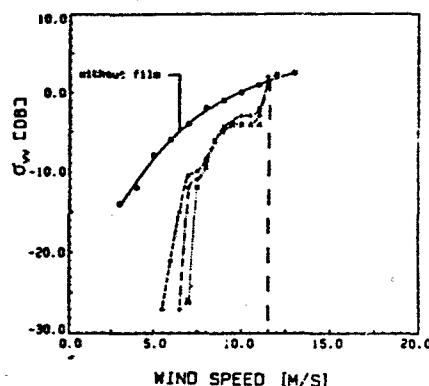


Fig. 16: Wind wave tank measurements of radar cross section of a clean water surface (upper curve) and of water surfaces covered with hexadecanol (triangles), oleyl alcohol (pluses), and CEX3AB (crosses) as function of wind speed; incidence angle 54°, VV polarization (Feindt, 1985).

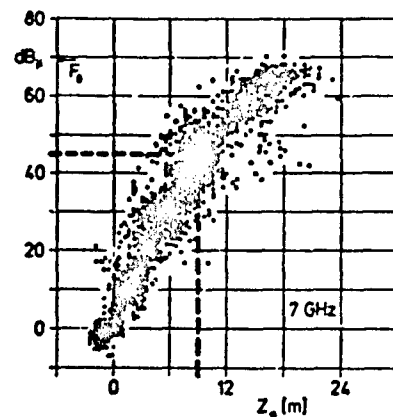


Fig. 17: Correlation diagram of field strength (7 GHz over-the-horizon path) and evaporation duct thickness; July 1965 and Febr. 1 to 10, 1967 (hourly averages,  $F_0 = 1 \text{ dB } \mu$ , free-space level  $F_0 = 69.2 \text{ dB } \mu$ ) (Jes. 3, 1971).

#### DISCUSSION

A. FRASER-SMITH, US

Most fog and rain in the world today is polluted to some extent by pollutants such as  $\text{SO}_2$ , which make the water acidic. Does this alter the microwave absorption characteristics of fog and rain (aerosols are also important). If so, can microwave techniques be used to measure the acidity of fog, rain, & aerosols?

AUTHOR'S REPLY

There will be an effect via the changed dielectric constant of the polluted drops, but water is the determining material, and the effect will be of second order. Applicable microwave techniques via propagation effects are not known, perhaps one idea is the determination of droplet characteristics by polarization vectors.

J. H. RICHTER, US

RASS cannot separate vertical wind fluctuations from temperature changes. Were the vertical wind fluctuations considered in the example presented?

AUTHOR'S REPLY

The data presented were averaged over many minutes and, unless there is a constant bias, fluctuations due to wind should not be important. In addition, the measurements shown were supported by independent measurements of the vertical wind component.

E. SCHWEICHER, BE

How do you define the visibility distance you used on your plot of the rain attenuation as a function of the frequency? Is it the distance at which you perceive a unitary contrast for pattern with a contrast of 21?

AUTHOR'S REPLY

Yes, this is the normal meteorological process to estimate the visibility.

# Ionospheric Modification and Imaginable System Applications

by

H. J. Albrecht

FGAN - Neuenahrstr. 20 - D-5307 Nachtberg-Werthhoven  
Germany

## Summary

This paper attempts to review the nowadays predominant areas of imaginable system applications of anthropogenic modifications applied to the ionosphere. Relevant conditions are indicated, such as the natural systems environment, areas of possible modifications, and aspects of compatibility and interference. This discussion then leads to resultant criteria of applications to systems and required support measures.

## 1. Introduction

Ever since the effect of wave-interaction or ionospheric cross-modulation between two radio transmissions, or the so-called "Luxembourg-Effect", was first verified in the early 1930s and published in 1933 (1.1), there has been no doubt that the entire field of changing the ionosphere by artificial means represents a fascinating area of research. The use of this region of the Earth's atmosphere - and thus a classical propagation medium - as a huge laboratory has certainly yielded a considerable amount of insight into physical processes in the ionosphere, and promises to be of such service in the future.

Further development up to the early 1970s and the establishment of ground-based high-power facilities to "heat" ionospheric regions led to a wide spectrum of results which also indicated some preliminary concepts with regard to a system-oriented evaluation (1.2 - 1.5).

Within the activities of the AGARD Panel on Electromagnetic Wave Propagation, a number of scientific meetings contained, in their proceedings, contributions on the subject, as, for example, those held in 1973 (1.6), 1976 (1.7), 1977 (1.8), 1979 (1.9), 1980 (1.10, 1.11), 1982 (1.12), 1983 (1.13), 1988 (1.14), and 1988 (1.15). Of these, the one in 1976 (1.7) actually concentrated on the topic of artificial modification of propagation media.

Cooperated with the early investigations, continuing research and more advanced technology have augmented the data reservoir in the field of ionospheric modification. Ionospheric heating at various power levels and chemical releases in the ionospheric region have been documented in a large number of review papers (e.g. 1.16 - 1.25). Reference is also made to relevant chapters in recent editions of the Reviews of Radio Science which are issued at triennial intervals by the International Union of Radio Science (U.R.S.I.) (1.26 - 1.31). In an appropriate section of this paper, more details are to be summarized with respect to system-related aspects.

Apart from modification experiments for pure research, the importance of system applications increases, also in proportion to costs of investigations. At the same time, the chances of seriously considering actual engineering applications improve with the progress made in a detailed knowledge of physical processes initiated by modification experiments, and thus with their reproducibility. The still rather dynamical development and the continuous augmentation of results suggest that anticipated system implementations are served best by identifying general boundary conditions connected to such applications; it will be attempted to meet such an objective as well as possible.

A summary of the natural propagation conditions encountered by systems is followed by sections on areas of possible modification, and on compatibility and interference; then criteria of system applications and required support measures are addressed. In addition to publications in the open literature, the material used for and the contents of this paper consist of unclassified and generally available information kindly supplied for this purpose by the USAF Geophysics Laboratory and the Allied Radio Frequency Agency (ARFA) as well as documentation of the Comité Consultatif International de Radiodiffusion (CCIR) of the International Telecommunication Union (ITU).

## 2. Natural Propagation Environment of Systems

### 2.1 General Propagation Conditions

To consider the effects of any modification it is undoubtedly essential to look at the appropriate conditions prevailing in the absence of or prior to such manipulation. In discussing the system applications of ionospheric modifications, the natural propagation environment encountered by typical system categories shall thus be used as a guideline.

The overall frequency spectrum of interest extends up to about 1000 THz; table 1 shows the nomenclature generally considered valid, as well as typical system features. As a summary of propagation effects on all paths other than those depending on ground characteristics, fig. 1 illustrates the atmospheric propagation environment and its effects within the spectrum 10 kHz to 100 GHz (2.1). For the troposphere, a distinction has been made for typical altitude ranges of clouds in lower, medium and upper heights. Ionospheric layers are also indicated, as well as orbital altitudes of geo-stationary satellites and the acon.

Effects resembling reflections in the ionosphere are the governing factor up to frequencies of about 30 MHz, with some partial transparency in the lower frequency range. The range of ionospheric scatter propagation and meteor backscatter may extend up to 100 MHz; a higher limit would be valid for artificially produced scattering.

The preferred spectral range for communication via and remote sensing from satellites and other spacecraft commences at about 100 MHz; above about 10 GHz, high signal attenuation may be experienced due to precipitation and to absorption by tropospheric gases, e.g. by oxygen around 60 GHz. Of far more importance for this review are ionospheric scintillations which may severely affect space-Earth propagation paths in the lower part of this spectral range.

### 2.2 Typical System Areas

Basically, application areas of electromagnetic wave propagation may be subdivided into communication, remote sensing, and navigation. Typical propagation paths may be identified for any one of these categories, yet that of communications includes all possible kinds and thus allows to discuss the largest possible variety. Fig. 2 depicts paths in terms of frequency ranges and special features, such as distances, bandwidths, and predominant medium parameters or corresponding limiting characteristics in very general terms. This brief review concentrates on system areas susceptible to ionospheric modification.

The left-hand column, referring to line-of-sight (L-O-S) and groundwave paths, is included for completeness' sake. Applications addressed hereby are certainly essential to cover relatively short ranges, up to the order of 100 km, and refer to a majority of systems; on the other hand, the chances of influencing them by artificial modifications in the ionosphere are rather minute.

The second column in fig. 2 deals with classical propagation paths using effects resembling reflections in the ionosphere. Worldwide distances may be covered at relatively narrow bandwidths. Depending on a number of factors, such as diurnal ionization changes and effects of solar activity, the propagation conditions are rather variable and influence the reliability of systems unless deviations from normal conditions can be predicted and allowed for in an adequate and timely manner. Performance conditions have been known for decades (e.g. 2.2 - 2.4); artificial means of improving circuit reliability would certainly be welcome.

Using long-distance paths in the HF-range as an example and imagining, ideally, a concentric structure of a constant-altitude ionosphere, such large distances would be covered by several hops with intermediate ground reflections, each hop being geometrically limited to about 4000 km. However, a more realistic concept is that of an ionospheric layer structure with inclinations with respect to the Earth's surface and/or horizontal ionization gradients. This is one basis for chordal-hop paths which do not touch the Earth's surface and show better system performance with less path loss; they were investigated and verified in the 1950s on long-distance paths from Australia (2.5, 2.6); reference is also made to more recent reviews of such chordal-hop propagation (2.7 - 2.9).

Features of another typical application area, the use of scattering, are illustrated in the third column of fig. 2. In this case, the so-called scatter volume in the atmosphere is illuminated by a high-power transmitter, and the energy scattered towards the receiving terminal is used for communication links. Whereas tropospheric scatter propagation is employed rather widely, the here more relevant ionospheric scatter has not led to as many applications. In this case, irregularities or variations of electron density in about the height region of the D-layer are one basis of a scattering volume, providing channels of moderate bandwidth over maximum distances of the order of 1000 km (2.10).

In addition, and roughly within the last-mentioned category, the passage of meteors through the atmosphere causes a short-lived existence of ionized trails which lead to intermittent reflections, useful for burst communications. Modern methods of signal processing have increased the possible usefulness of such applications. Furthermore, diffuse reflections may be due to the sporadic E-layer, or due to irregularities in the upper F2-layer (2.11, 2.12).

The right-hand column of fig. 2 illustrates the features of paths between the Earth's surface and terminals in space. In principle, they resemble line-of-sight paths on frequencies in the range of atmospheric transparency up to optical wavelengths. Nowadays, a majority of worldwide system applications uses Earth/space paths.

Severe limitations may be present with various applications in this category; they depend upon space orbit, frequency, and geographical location of surface terminals. Of particular importance are constant and/or variable attenuation (fading) and also time-delay errors encountered in the atmosphere. Limitations are due to irregularities of various nature, electron-density fluctuations, turbulence, and clouds for higher frequencies. Within the scope of this review paper, the effects of scintillations due to atmospheric irregularities are of special interest (2.13 - 2.16).

### 2.3 Prediction and Adaptive Operation

Above-mentioned typical propagation characteristics indicate that, in practically all cases, limitations are experienced with regard to the desired operational reliability of systems. On the basis of decades of research and engineering experience, numerous mathematical models and operational simulation methods are now available - and the optimization process continues. These approaches allow the prediction of average behaviour of the relevant propagation environment. Timely predictions of - and thus the appropriate response to - short-term variations of propagation conditions are still difficult (2.17 - 2.22).

Modern technological development promises to permit significant progress in operational management of systems. The implementation of real-time channel analysis and automatic selection of optimum operating conditions will result in a favourable influence on performance and adaptivity of systems (2.23 - 2.25).

There is certainly room for further improvements with predictions as with adaptive operation which seems to represent an additional chance for artificial modification of propagation media. A system-oriented approach in the engineering development of appropriate methods appears to be a promising remedy for at least some of the problems encountered with present systems.

## 3. Areas of Possible Modification

### 3.1 Predominant Activities

Although a kind of artificial modification is also possible in the tropospheric region of the atmosphere, the emphasis is in this paper directed at experiments in the ionosphere, and, in particular, at the employment of their results to improve the usability and reliability of operational systems.

As has already been mentioned in the Introduction, the historical basis for modification studies had been the identification of cross-modulation effects about 60 years ago. Work in this field has continued and yielded a large quantity of results (3.1).

Further development of high-power transmitters, and thus the possibility of actually "heating" ionospheric regions from sources located at the Earth's surface, as well as progress with chemical releases, have led to the present state of the art. So far, research interests have largely predominated; activities will probably - and hopefully - continue for the benefit of widening our knowledge on possibilities but also on limitations of approaches employed (1.1 - 1.3, 1.14 - 1.25, 3.2).

A number of reviews and contributed papers have referred to recent investigations and can be considered to provide full documentation on the state of research achievements up to this juncture. Activities proceed in several geographical regions; as an example, fig. 3 shows approximate locations of some high-power sources especially established for ionospheric modification experiments.



Considering the ultimate objective, even the following brief identification of modification areas has to take into account some criteria for system applications which seem to be fundamental and are to be addressed later:-

- controllability
- compatibility
- and - cost-effectiveness

In view of the large amount of material published on ionospheric modifications, and regrettably, the references cited in the following summaries can only represent examples indicating a relevancy to system aspects or providing appropriate cross-references, without any claim of chronological completeness.

### 3.2 Summary of Results and Trends of High-Power Sources

Results and trends in the field of ionospheric modification (IONMOD) by high-power sources may be presented in various ways. Suitable guidelines for the intended system-oriented summary may be altitude or frequency ranges. However, the versatility of possible effects does not facilitate a categorization a systematic as would perhaps be desired.

Fig. 4 represents an attempt of such a display. Effects may be found in various atmospheric altitude regions and are not necessarily restricted to the heights shown; some of the approaches may develop the required system feasibility in the future. Physical processes are only indicated to identify the methods (see references for details); key-words refer to the following modifications:-

\* Absorption may be produced and may affect passing signals (3.3,3.4) (see also section 3.5 below);

\* Radio waves may be generated at very low frequencies, using various processes, such as the modulation of passing ionospheric currents, polar or equatorial electrojet, and non-linear wave interaction. Effective ELF/VLF power radiated is considered low (3.5 - 3.8);

\* The apparently largest effects of rather versatile influence upon all sorts of systems are those producing HF/VHF/UHF-scattering; geographical conditions have to be taken into account:-

- In general, the production of a scattering volume may have the facilitating or positive effect of allowing the establishment of an HF/VHF/UHF scattering link or at least the improvement of an existing one;

- A related modification may be considered on HF if scattering regions can be placed at suitable distances from the end-points of a long-distance path, such that a more persistent chordal hop propagation path may be initiated and maintained; its advantages have already been mentioned in section 2.2. Experimental data of such modification experiments have been reported (3.9);

- On the other hand, scattering within a region affecting Earth/space paths is an example of a disturbing or negative action, or even a shielding one on VHF, UHF, and higher frequencies, as has also been indicated in section 2.2. Again, results of relevant experiments have been reported (3.10 - 3.12);

\* Other propagation characteristics of ionosphere and magnetosphere may be changed. Effects in higher altitude regions, instabilities in the magnetosphere have been addressed in the literature (3.13 - 3.15).

For completeness' sake, the concept of an artificial ionospheric mirror ("AIM") should also be listed. High-power heating is to be used to create patches of ionization at about D-layer altitudes. These may lead to an effective reflector for signals (3.16,3.17). Appropriate future research work should clarify aspects of feasibility; successful results would indicate that direct control of the propagation medium may thus be achieved.

The capability of producing artificial optical emissions had already been summarized many years ago (3.18); further progress might lead to masking effects by emissions in optical and infrared ranges (3.16).

Literature also contains first references to the interpretation of results in view of possible engineering applications (e.g. 3.18,3.2,3.15). To confirm system feasibility, more studies are essential in all relevant areas.

Apart from intensity and duration of effects, the basic criteria mentioned earlier (see section 3.1) are important for a consideration with respect to system-oriented parameters. Of these, the controllability would, for example, be a particularly critical feature if the initiation of perturbations of some persistence, such as magnetic storms, would be possible and would even be planned. - On the other hand, the artificial production of irregularities seems to be most advanced at this juncture; it may thus represent a promising area of actual system applications.

### 3.3 Summary of Results and Trends for Chemical Releases

Another important category of ionospheric modification employs chemical releases. The production of depletions of ionization in the F-region and other effects by rocket launches have led to appropriate analytical studies (3.19 - 3.22). Such ionospheric "holes" may also extend to larger areas. In addition, travelling ionospheric disturbances have been found in the F-region as a rocket-induced perturbation.

For research purposes, injections of substances have been made for the last three decades; they have contributed significantly to the knowledge on physical processes in the atmosphere (3.22 - 3.25).

Again, the question of duration of effects is important. In this regard, results seem to indicate that the persistence of disturbances does not extend largely beyond the period of the actual occurrence; in other words, effects may be somewhat controllable. As in the case of high-power sources, the results of further studies should allow more definite conclusions regarding system applications.

### 3.4 Aspects of Availability and Overall Effectiveness

Questions of overall effectiveness and availability arise with particular regard to a system-oriented use of ionospheric modification. For example, the geographical availability seems to remain a serious problem. Data bases seem to grow on relevant requirements of power and duration of the modifying action.

Basically, sufficiently mobile modification equipment or a proven effectiveness of remote modification by "heating" at oblique incidence would be needed. Experiments have been mentioned in the literature (3.16, 3.26, 3.27). It is not known if results may be satisfactory for the purposes here addressed.

The geographical availability may also be assisted by an in-situ modification from spacecraft within the ionosphere, by energetic charged particle or photon beams, or by the release of neutral gas (3.28, 3.29).

A possibility of increasing the overall effectiveness is the combination of modifications by high-power radio waves and chemical releases. Relevant concepts have recently been addressed (3.16, 3.30).

### 3.5 Inadvertent Modification in the Ionosphere

Any unintended influence of systems upon natural ionospheric conditions may be recognized as a kind of system application of artificial modifications. Any such anthropogenic and electromagnetic "pollution" of our planet's atmosphere undoubtedly requires appropriate monitoring and even the termination of transmissions, if necessary. In addition, proper recognition and analysis of effects and their results yield additional data on modification effectiveness.

Chemical releases as a consequence of rocket launches lead to modifications already mentioned in section 3.3. Effects seem to follow a regular and largely predictable pattern, and may thus be considered reasonably controllable and localized (3.19 - 3.22).

An example of inadvertent modification by high-power sources would have been represented by the energy-production using solar power satellites. During this concept's popularity peak in the late 1970s and early 1980s, several studies addressed possible effects. These may comprise a modification of the ionospheric plasma through ohmic heating by the passage of a high-power microwave beam with the possible consequence of increased absorption for passing radio waves and also the formation of irregularities with results already discussed in previous sections. An additional effect could have been acting upon the propagation path of the microwave power beam itself. However, all these effects in the ionosphere should be of a localized nature (3.31 - 3.33).

Wide-band absorption produced by radio waves has already been mentioned (see section 3.2). There is the possibility that such absorption may also be caused unintentionally. Data of studies may allow an estimate regarding the severity of effects (3.3, 3.4, 3.34, 3.35).

Another possible case of inadvertent modification refers to the transmission of high-power HF-broadcasting stations (3.36 - 3.39). With the apparent popularity of increasing power levels for such applications, the subject may deserve even more attention in the future (3.40). An attempt has been made to indicate the geographical distribution of power levels in fig. 5 which displays a world-map showing cumulative HF-BC-power per Mersden square, as estimated from an appropriate list (3.41). With unknown periods, directions, angles, etc. of transmissions, it is obvious that this information has to be taken cum grano salis, and that no definite conclusions can be drawn from such a map; yet, it may represent some food for thought to authorities responsible for spectrum management. In addition, MF and LF broadcast transmission have been reported to cause an ELF/VLF generation (3.42,3.43).

#### 4. Aspects of Compatibility and Interference

##### 4.1 Coordination and Frequency Management

Whenever new services emitting electromagnetic waves or new system applications of this kind are intended, appropriate frequencies have to be provided within the spectral range desired. In other words, proper assignments have to be made to fit the desired transmissions into the large number of existing allocations. Studies on the probability of co-channel interference and thus on the compatibility are required.

The above conditions apply to any use of frequencies, and ionospheric modification is no exception. To assist with and to contribute to its implementation, attention is here drawn to the need of such prerequisite studies and the probable objectives. It is assumed that these would have to address two major criteria:-

- extent and effect of modification of the propagation medium on all services using this medium, the ones to be improved as well as others;
- extent of the probable, perhaps rather localized, interference caused by the source equipment.

As an example, attention may be drawn to modification processes which require frequencies belonging to the HF portion of the spectrum. This range displays a considerable amount of congestion (4.1,4.2). The situation may also be illustrated on the basis of documentation of the International Frequency Registration Board (IFRB). With the exception of broadcast and amateur bands, figs. 6a and 6b display the number of assignments per frequency in the range between 3 and 15 MHz, while the total bandwidths (in kHz) per frequency are shown in figs. 7a and 7b (4.3). The requirement of optimum compatibility is an obvious consequence.

##### 4.2 Methods of Mitigating Coordination Problems

As has already been emphasized on several occasions in this paper, the controllability of modification effects may be considered of paramount importance. It requires adequate knowledge on the actual physical processes causing and accompanying the modification.

Connected to the controllability are, as other desirable assets, information on and the use of the minimum power required to guarantee the intended modification effect.

Attention to both examples of remedies should permit the preparation of the modifying action as an adaptive system component which would enable a flexible ad hoc adjustment to the actual need of modification; this requirement may also vary in accordance with changes of the natural propagation conditions.

#### 5. Criteria of System Applications and Required Support Measures

##### 5.1 System-Oriented Features of Ionospheric Modification

Relevant facilitating as well as disrupting, or positive and negative, effects of ionospheric modification have already been addressed. An attempt has been made to summarize the essential and system-relevant items in fig. 8 which is based on fig. 2. It should again be emphasized that the indications given depend on the information available so far.

As has been mentioned before, no modification effects are anticipated in the left-hand column which refers to line-of-sight paths. In the other columns, a "+"-sign indicates a facilitating action for systems, and a "-"-sign a disturbing effect.

The chart does not specifically mention the use of artificially generated ELF-VLF waves or modifications affecting propagation in these frequency ranges. Present VLF systems, for example navigational nets, are fully operational and profit from the relative stability of natural propagation conditions but improvements may still be possible. - Future ELF-generation studies may demonstrate relevant system maturity and thus provide a useful asset to systems in this frequency range.

For ionospheric long distance paths, the establishment of chordal-hop paths (see sections 2.2 and 3.2) is considered a possibility, while the ionospheric layer may also be transformed to effective shields or, at least, to absorbers for such propagation paths.

Scatter paths may actually be made possible by modification effects or they may, at least, be assisted in their operational performance (availability, reliability, bandwidth). A destructive action is again that of disturbing or even shielding scatter.

In the case of Earth/space paths, negative consequences seem to be likely with irregularities causing scintillations, attenuation or even shielding, as with the other system areas.

One of the critical questions still to be solved is the availability of modification facilities whenever and wherever they are needed to support systems. From the standpoint of systems, they are in fact tools which are to be adapted to system requirements. In the interest of future applications, there is optimism that the continuing research work will improve the possibilities of equipment mobility and remote modification by oblique heating.

The above considerations should be considered preliminary in view of the presently still rather developmental stage of ionospheric modifications; as yet, it appears to be difficult to reach a kind of system maturity. In addition, the necessary adherence to operational criteria might furthermore be disadvantageous for the present possibilities of implementing artificial ionospheric modification.

## 5.2 Operational Criteria

There can be no doubt that any application of ionospheric modification to systems should aim at their improvement. At the same time, coordination and compatibility are essential with respect to the system to be improved as well as to others using the same propagation environment. Aspects addressed in previous sections thus lead to a kind of recommended menu for operational planning:-

- (a) Analyze existing propagation assets and identify relevant problem areas
- (b) Identify ionospheric modification methods to mitigate conditions found in (a)
- (c) Analyze methods selected under (b) and assess their
  - CONTROLLABILITY
  - COMPATIBILITY w.r.t. to other services
  - and - COST-EFFECTIVENESS
- (d) Adapt ionospheric modification to actual needs (a) to comply with results of (c)
- (e) Monitor operation to maintain full compatibility
- (f) Terminate operation when natural propagation conditions are adequate with respect to (a)

With exception of the rather self-explanatory requirement of cost-effectiveness, the above items are in fact a summary of the views expressed in the previous sections of this paper. The list represents an attempted compromise of the undoubtedly controversial requirements of, for example, the use of high-power sources to increase effects and compatibility with other services.

### 5.3 Required Support Measures

To optimize results of implementations, particular attention should be directed at good engineering planning. Certain support measures are considered to belong to the absolute necessities.

An obvious requirement is the capability of predicting and monitoring the natural propagation conditions for the system path envisaged, for long-term average as well as for short-term changes, including the channel performance with respect to the system needs. Facilities should exist to adjust the prediction on a quasi real-time basis.

As an equally important condition, the effects of the modification should be predicted and monitored continuously; diagnostic methods and equipment presently employed should be a good basis for such operational use.

Another example is the need for a permanent and reliable communication facility to the institution responsible for spectrum management; this would enable the operating agency to adjust the modifying operation as required by an integrated and responsive structure of frequency management. In view of the complexity of the situation, and the need for rapid decision making, the results of analytical assessments might need to be incorporated into some form of expert system.

### 6. Concluding Remarks

An attempt has been made to review the predominant areas of imaginable system applications of ionospheric modification methods as they have become known up to this juncture. Admittedly, the results had to be expressed in general terms; this is due to the present state of the art and the still rather dynamical development of this highly interesting field of ionospheric research.

The research results presently available are impressive with respect to the versatility of possibilities and also with regard to the amount of data collected so far. It is hoped that the degree of further analysis of physical processes and thus the controllability of modifying effects will continue to improve. It may be anticipated that future work will add to the progress made so far and will allow criteria to be satisfied adequately.

### Acknowledgements.

The author is much obliged to Dr. P.A. Kossey and Dr. J.E. Rasmussen for a large amount of material; the compilation of this paper would not have been possible without it. In addition, he wishes to express his particular thanks to Dr. T.K. FitzSimons for information on IFRB documentation and other data regarding spectrum management, and to Dr. Th. Damboldt and Dr. K.J. Hortenbach for recent CCIR documentation.

Table 1: Frequency Ranges

FREQUENCY WAVELENGTH		BAND	SYSTEM FEATURES (Typical Applications, Bandwidth)
0.03 - 3 kHz	Extremely Low	E L F	R & D, very narrow bandwidth
10 - 0.1 cm			
3 - 30 kHz	Very Low	V L F	Navigation, 50 Hz
100 - 10 Hz			
30 - 300 kHz	Low	L F	Navigation, Broadcasting, 1 kHz
10 - 1 Hz			
0.3 - 3 MHz	Medium	M F	Broadcasting, Navigation, 5 kHz
1 - 0.1 cm			
3 - 30 MHz	High	H F	Communication, Radar, 10 kHz
100 - 10 m			
30 - 300 MHz	Very High	V H F	Communication, Radar, 10 kHz, 5 MHz
10 - 1 m			
0.3 - 3 GHz	Ultra High	U H F	Communication, Radar, 10 kHz, 10-50 MHz
100 - 10 cm			
3 - 30 GHz	Super High	S H F	Communication, Radar, 50 MHz
10 - 1 cm			
30 - 300 GHz	Extremely High	E H F	R & D
10 - 1 mm			
1 - 400 THz	Infrared	I R	R & D
300 - 0.75 micron			
400 - 800 THz	Optical		R & D
0.75 - 0.375 micron			

## References

- <1.1> Tellegen, B.D.H., Interaction between radio-waves, *Nature*, 131, p.840, 1933
- <1.2> Utlaut, W.F., An ionospheric modification experiment using very high power, high frequency transmission, *J. Geophys. Res.*, vol. 75, pp. 6402-6405, 1970
- <1.3> Gordon, W.E., Carlson, H.C., Snowden, R.L., Ionospheric heating at Arecibo: first tests, *J. Geophys. Res.*, vol. 76, pp. 7808-7813, 1971
- <1.4> Utlaut, W.F., Violette, E.J., Further ionospheric modification by a high-powered HF transmitter, *J. Geophys. Res.*, vol. 77, pp. 6804-6818, 1970
- <1.5> Thorne, B.D., Blood, D.W., First observations of RF backscatter from field-aligned irregularities produced by ionospheric heating, *Radio Sc.*, vol. 9, pp. 917-921, 1974
- <1.6> Fejer, J.A. (ed.), Non-linear effects in electromagnetic wave propagation, AGARD-EPP Nov. 1973, Conf. Proc. CP 133, Techn. Edit. & Reprod. Ltd., London May 1974
- <1.7> Albrecht, H.J. (ed.), Artificial modification of propagation media, AGARD-EPP April 1976, Conf. Proc. CP 192, Techn. Edit. & Reprod. Ltd., London Jan. 1977
- <1.8> Ince, A.N. (ed.), Aspects of electromagnetic wave scattering in radio communications, AGARD-EPP Oct. 1977, Conf. Proc. CP 244, Techn. Edit. & Reprod. Ltd., London Sept. 1978
- <1.9> Coyne, V.J. (ed.), Special topics in HF propagation, AGARD-EPP May/June 1979, Conf. Proc. CP 263, Techn. Edit. & Reprod. Ltd., London Nov. 1979
- <1.10> Albrecht, H.J. (ed.), Propagation effects in space/Earth paths, AGARD-EPP May 1980, Conf. Proc. CP 284, Techn. Edit. & Reprod. Ltd., London Aug. 1980
- <1.11> Schaeferling, E. (ed.), The physical basis of the ionosphere in the solar-terrestrial system, AGARD-EPP Oct. 1980, Conf. Proc. CP 293, Techn. Edit. & Reprod. Ltd., London Febr. 1981
- <1.12> Soicher, M. (ed.), Propagation aspects of frequency sharing, interference, and system diversity, AGARD-EPP Oct. 1982, Conf. Proc. CP 332, Techn. Edit. & Reprod. Ltd., London March 1983
- <1.13> Soicher, M. (ed.), Propagation effects on military systems in the high-latitude region, AGARD-EPP June 1985, Conf. Proc. CP 382, Techn. Edit. & Reprod. Ltd., London Nov. 1985
- <1.14> Bossy, L., Schunk, R.W. (eds.), Ionospheric structure and variability on a global scale and interactions with atmosphere and magnetosphere, AGARD-EPP May 1988, Conf. Proc. CP 441, Techn. Edit. & Reprod. Ltd., London April 1989
- <1.15> Belrose, J., Boutelard, C. (eds.), Propagation effects and circuit performance of military radio systems with particular emphasis on those employing bandspreading, AGARD-EPP Oct. 1988, Conf. Proc. CP 442, Techn. Edit. & Reprod. Ltd., London Dec. 1989
- <1.16> Utlaut, W.F., A survey of ionospheric modification effects produced by high-power HF radio waves, paper no. 3 in <1.6>, 1974
- <1.17> Gordon, W.E., Carlson, H.C., Parametric instabilities in the ionosphere excited by powerful radio waves observed over Arecibo, paper no. 4 in <1.6>, 1974
- <1.18> Utlaut, W.F., Ionospheric modification induced by high-power HF transmitters - potential for communication and plasma physics research, paper no. 6 in <1.7>, 1977
- <1.19> Gordon, W.E., Carlson, H.C., The heating experiment at Arecibo, paper no. 7 in <1.7>, 1977
- <1.20> Minkoff, J., Meissner, I., A review of VHF/UHF scattering from a heated ionospheric volume, paper no. 8 in <1.7>, 1977
- <1.21> Haerendel, G., Modification of ionized media by chemical substances - a review of physical processes, paper no. 13 in <1.7>, 1977
- <1.22> Bernhardt, P.A., da Rosa, A.V., Park, C.S., Chemical depletion of the ionosphere, paper no. 15 in <1.7>, 1977
- <1.23> Barrett, T.J., Augmentation of HF propagation, paper no. 8 in <1.9>, 1979

- (1.24) Jones, T.D., Robinson, T., Stubbs, P., Kopke, H., Anomalous absorption effects produced by high power radio waves in the high latitude ionosphere, paper no. 5 in (1.12), 1983
- (1.25) Fejer, J.A., Ionospheric irregularities due to powerful HF radio transmissions, paper no. 30 in (1.14), 1989
- (1.26) Bowhill, S.A. (ed.), Review of Radio Science 1972-1974, URSI, Brussels, 1975
- (1.27) Bowhill, S.A. (ed.), Review of Radio Science 1975-1977, URSI, Brussels, 1978
- (1.28) Bowhill, S.A. (ed.), Review of Radio Science 1978-1980, URSI, Brussels, 1981
- (1.29) Bowhill, S.A. (ed.), Review of Radio Science 1981-1983, URSI, Brussels, 1984
- (1.30) Hyde, G. (ed.), Review of Radio Science 1984-1986, URSI, Brussels, 1987
- (1.31) Hyde, G. (ed.), Review of Radio Science 1987-1989, URSI, Brussels, in print
- 
- (2.1) Albrecht, H.J., Electromagnetic wave propagation in aerospace research and development, AGARD Highlights 78/2, pp. 7-15, 1978
- (2.2) Davies, K., Ionospheric radio propagation, U.S. Dept. Commerce NBS, Monograph 80, 1965
- (2.3) Manning, L.A., Bibliography of the ionosphere, Stanford University Press, Stanford, 1962
- (2.4) C.C.I.R. Report 725-1, Ionospheric properties
- (2.5) Albrecht, H.J., Investigations on great-circle propagation between Eastern Australia and Western Europe, Geof. pura e appl., vol. 38, pp. 169-189, 1957
- (2.6) Albrecht, H.J., Further studies on the chordal-hop theory of ionospheric long-range propagation, Archiv. Met. Geoph. Biokl. Ser. A, vol. 11, pp. 84-92, 1959
- (2.7) C.C.I.R.-Report 250-5, Long-distance ionospheric propagation without intermediate ground reflection
- (2.8) Toman, K., High-frequency ionospheric ducting - a review, Radio Sc., vol. 14, pp. 447-453, 1979
- (2.9) Nortonbach, K.J., Rogler, F., On the propagation of short waves over very long distances: predictions and observations, ITU Telecommunication J., vol. 44, pp. 320-327, 1979
- (2.10) C.C.I.R.-Report 260-3, Ionospheric scatter propagation
- (2.11) C.C.I.R.-Report 251-4, Communications by meteor-burst communications
- (2.12) Haldoupis, C., A review of radio studies of auroral E-region ionospheric irregularities, paper no. 31 in (1.14), 1989
- (2.13) Aaron, J., Global morphology of ionospheric scintillations, Proc. IEEE, vol. 70, pp. 360-378, 1982
- (2.14) C.C.I.R.-Report 263-6, Ionospheric effects upon Earth/space propagation
- (2.15) Goodman, J.M., Environmental constraints in Earth-space propagation - a review paper, paper no. 33 in (1.10), 1980
- (2.16) Yeh, K.C., Ionospheric irregularities and their effects on electromagnetic waves propagating through them, paper no. 32 in (1.14), 1989
- (2.17) C.C.I.R.-Report 886-1, Short-term forecasting of critical frequencies, operational maximum usable frequencies and total electron content
- (2.18) C.C.I.R.-Report 255-6, Long-term ionospheric propagation predictions
- (2.19) C.C.I.R.-Report 894-1, Simple HF propagation prediction method for MUF and field strength
- (2.20) Goodman, J.M., The development of an ionospheric model thesaurus and user's guide, paper no. 13 in (1.12), 1983
- (2.21) Rush, C.M., Ionospheric radio propagation models and predictions - a mini-review, IEEE-Trans. Ant. & Prop., vol. AP-34, pp. 1163-1170, 1986

- <2.22> Szuaszewicz, E.P., Wolf, R.A., Fejer, B.G., Schunk, R.W., Rosloff, E., Coordinated multi-parameter measurements and predictions of the global-scale ionosphere, paper no. 38 in <1.14>, 1989
  - <2.23> Darnell, H., Adaptive signal selection for dispersive channels and its practical implications in communications system design, paper no. 23 in Blackband, M.T. (ed.), Radio systems and the ionosphere, AGARD-EPP Conf. Proc. CP 173, Techn. Edit. & Reprod. Ltd., London Jan. 1976
  - <2.24> Aaron, J., Grossi, M.D., HF propagation factors affecting the design and operation of real time, channel evaluation, adaptive systems, paper no. 8 in Albrecht, M.J. (ed.), Propagation effects of ECR resistant systems in communication and navigation, AGARD-EPP Conf. Proc. CP 331, Techn. Edit. & Reprod. Ltd., London Aug. 1982
  - <2.25> C.C.I.R.-Report 889-1, Real-time channel evaluation of ionospheric radio circuits
- 
- <3.1> C.C.I.R.-Report 574-2, Ionospheric cross-modulation
  - <3.2> C.C.I.R.-Report 728-2, Ionospheric modification by ground-based high-power radio transmissions
  - <3.3> Toeko, A.A., Ferraro, A.J., Lee, H.S., D-region absorption effects during high-power radio wave heating, Radio Sc., vol. 15, pp. 673-681, 1980
  - <3.4> Utlaut, W.F., Violante, E.J., A summary of vertical incidence radio observations of ionospheric modifications, Radio Sc., vol. 9, pp. 895-903, 1974
  - <3.5> Stubbe, P., Kopka, H., Modulation of the polar electrojet by powerful HF waves, J. Geophys. Res., vol. 82, pp. 2319-2323, 1977
  - <3.6> Ganguly, S., Gordon, W.E., Papadopoulos, K., Active non-linear ultra-low frequency generation in the ionosphere, Phys. Rev. Lett., vol. 57, pp. 641-644, 1986
  - <3.7> Barr, R., Rietveld, M.T., Stubbe, P., Kopka, H., Ionospheric heater beam scanning: a realistic model of this mobile source of ELF/VLF radiation, Radio Sc., vol. 23, pp. 379-388, 1988
  - <3.8> Noble, S.T., Gordon, W.E., Duncan, L.N., McCoy, J.E., HF sideband generation in the ionosphere, Radio Sc., vol. 24, pp. 265-269, 1989
  - <3.9> Elkins, T.J., Toman, K., Sales, G.S., Theoretical and experimental studies of HF ducted propagation, Report K-DC-TR-87-360, December 1980
  - <3.10> Bowhill, S.A., Satellite transmission studies of spread-F produced by artificial heating of the ionosphere, Radio Sc., vol. 9, p. 975, 1974
  - <3.11> Basu, S., Basu, S., Johnson, A.L., Klobuchar, J.A., Rush, C.M., Preliminary results of scintillation measurements associated with ionosphere heating and possible implications for the solar power satellite, Geophys. Res. Lett., vol. 7, p. 609, 1980
  - <3.12> Pope, J.H., Fritz, R.B., Observations of artificially produced scintillation using satellite transmissions, J. Geophys. Res., vol. 79, p. 1074, 1974
  - <3.13> Helliwell, R.A., Katsufakis, J.P., Bernhardt, P.A., Modification of the propagation characteristics of the ionosphere (and the magnetosphere) by injection into the magnetosphere of whistler-mode waves, paper no. 11 in <1.7>, 1977
  - <3.14> Helliwell, R.A., VLF wave injection from the ground, Proc. Int. Symp. on active experiments in space, Alpbach, Austria, 1983
  - <3.15> Ganguly, S., Effects of ionospheric modification on system performance, paper no. 28 in <1.15>, 1989
  - <3.16> Kossey, P.A., AFBL, private communication, 1989
  - <3.17> Burevich, A.V., Nonlinear phenomena in the ionosphere, Springer-Verlag, Berlin - New York, 1978

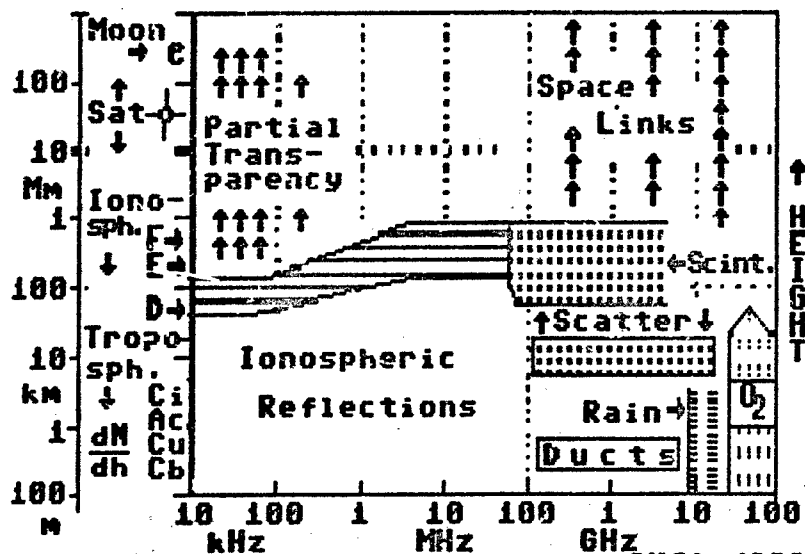


- (3.18) Utlaut, W.F., Cohen, R., Modifying the ionosphere with intense radio waves, Science, vol. 174, pp. 245-254, 1971
- (3.19) Mendillo, M., Hawkins, G.B., Klobuchar, J.A., A sudden vanishing of the ionospheric F-region due to the launch of Skylab, J. Geophys. Res., vol. 80, pp. 2217-2228, 1975
- (3.20) Mendillo, M., Forbes, J., Spatial-temporal development of molecular release capable of creating large-scale F-region holes, paper no. 14 in (1.7), 1977
- (3.21) Mendillo, M., Forbes, J., A summary of F-region ionospheric perturbations, paper no. 17 in (1.11), 1981
- (3.22) C.C.I.R.-Report 1011, Artificial Modification of the ionosphere by chemical injections
- (3.23) Bernhardt, P.A., Park, C.G., Banks, P.M., Depletion of the F2-region ionosphere and protonosphere by the release of molecular hydrogen, Geophys. Res. Lett., vol. 2, pp. 341-344, 1975
- (3.24) Bernhardt, P.A., A critical comparison of ionospheric depletion chemicals, J. Geophys. Res., vol. 92(A5), pp. 4617-4628, 1987
- (3.25) Klobuchar, J.A., Aodu, M.A., Equatorial ionospheric irregularities produced by the Brazilian ionospheric modification experiment (BIME), J. Geophys. Res., vol. 94(A3), pp. 2721-2726, 1989
- (3.26) Bochkarev, G.S., Kiz, V.Y., Lobachevsky, L.A., Lyannoi, B.E., Migulin, V.V., Sergeenko, D.S., Cherkashin, Y.N., Interaction of decametre radio waves at frequencies close to the F2 MUF in oblique propagation, Geosagn. Aeron., vol. 19, pp. 830-833, 1979
- (3.27) Bochkarev, G.S., Erewhko, V.A., Lobachevsky, L.A., Lyannoi, B.E., Migulin, V.V., Cherkashin, Y.N., Non-linear interaction of decametre radio waves at close frequencies in oblique propagation, J. Atm. Terr. Phys., vol. 44, pp. 1137-1141, 1982
- (3.28) Banks, P.M., Gilchrist, B.E., Artificial plasma density structures produced by energetic electron beams from rockets and spacecraft, Geophys. Res. Lett., vol. 12, pp. 175-178, 1985
- (3.29) Banks, P.M., Fraser-Smith, A.C., Gilchrist, B.E., Harker, K.J., Storey, L.R.G., Williamson, P.R., New concepts in ionospheric modification, Report AFBL-TR-88-0133, 1987
- (3.30) Bernhardt, P.A., Duncan, L.M., The theory of ionospheric focused heating, J. Atm. Terr. Phys., vol. 49, pp. 1107-1117, 1987
- (3.31) C.C.I.R.-Report 893-1, Solar power satellites and the ionosphere
- (3.32) Hughes, K.A., The interactions of a solar power satellite transmission with the ionosphere and troposphere, paper no. 38 in (1.10), 1980
- (3.33) Grant, W., Rush, C.M., Morrison, E.L., Potential impact of the satellite power system on communication and electronic systems and the ionosphere, paper no. 41 in (1.10), 1980
- (3.34) Graham, K.N., Fejer, J.A., Anomalous radio wave absorption due to ionospheric heating effects, Radio Sc., vol. 11, pp. 1057-1063, 1976
- (3.35) Kopka, H., Stubbs, P., Jones, T.B., Robinson, T., Non-linear reflectivity of high-power radio waves in the ionosphere, Nature, vol. 195, no. 5851, p. 680, 1982
- (3.36) Utlaut, W.F., Violette, E.J., Melanson, L.L., Radar cross section measurements and vertical incidence effects observed with Plateville at reduced power, Radio Sc., vol. 9, pp. 1033-1040, 1974
- (3.37) Utlaut, W.F. comment in discussion RTD II-5, in (1.7), 1977
- (3.38) Saksena, R.C., Sahu, A.K., Ionospheric modification by high power HF band broadcast transmitters, paper no. 13, Session G3, URSI, 22nd General Assembly, Washington 1981
- (3.39) Saksena, R.C., Propagation of anomalous long-distance TV signals and artificial modification of ionosphere, Indian J. Radio & Space Phys., vol. 17, pp. 172-178, 1989
- (3.40) C.C.I.R.-Recommendation 532, Ionospheric modification by high power transmissions

- (3.41) Both, C.J., The world's radio broadcasting stations & European FM/TV, De Mulderkring BV, Netherlands, 1989
- (3.42) Cannon, P.S., Ionospheric ELF radio signal generation due to LF and/or MF radio transmissions - I. Experimental results, J. Atm. Terr. Phys., vol. 44, pp. 819-829, 1982
- (3.43) Cannon, P.S., Turunen, T., Rycroft, M.J., Ionospheric ELF radio signal generation due to LF and/or MF radio transmissions - II. Interpretation, J. Atm. Terr. Phys., vol. 44, pp. 831-841, 1982

- (4.1) Gott, B.F., Dutta, S., Mong, M.F., Occupancy measurements across the entire HF spectrum, paper no. 32 in (1.12), 1983
- (4.2) Mong, M.F., Gott, B.F., Barclay, L.W., HF spectral occupancy and frequency planning, Proc. IEE, vol. 132, Pt. F, pp. 548-557, 1985
- (4.3) FitzSimons, T.K., ARFA/ENC, private communication, 1990

## EM WAVE PROPAGATION ENVIRONMENT



## NATURAL PROPAGATION PATHS





P A T H S	L-G-S & GROUND- WAVE	IONO- PATHS	SCATTER	SAT
				
FREQ	ALL	<30 MHz	>30 MHz	>100 MHz
DIST	<100 km	WORLDWIDE	<1500 km	WORLDWIDE
B-WTH	WIDE	NARROW	MODERATE	WIDE
EFFECTS of MEDIUM	MULTIPATH TROPOSPH. CONDITIONS	VARIABLE IONOSPHERIC CONDITIONS SUNSPOT CYCLE	VARIABLE SCATTER CONDITION	ATMOSPHERIC SCINTILLATION & ABSORPTION GEOGRAPHIC LIMITATION

Fig. 2

[KJA '81]

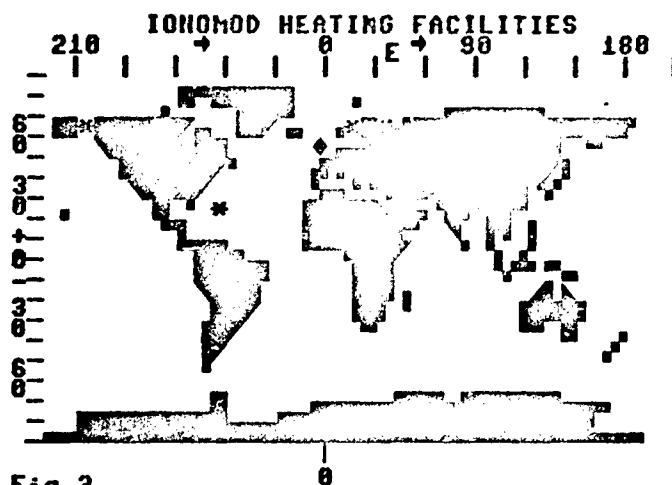


Fig. 3  
Locations of some High-Power Sources

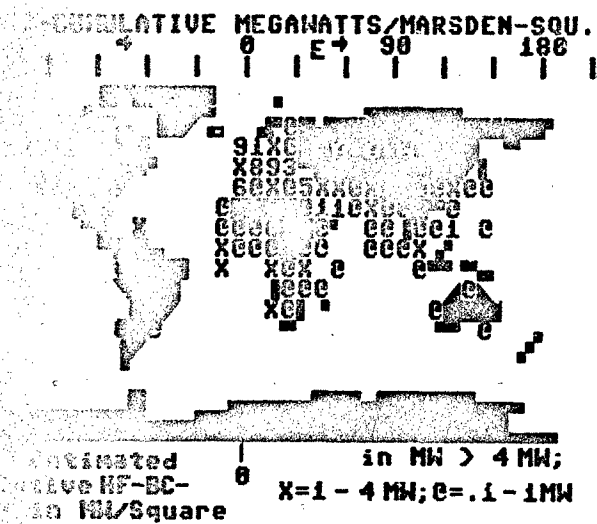
# IONOSPHERIC EFFECTS on SYSTEMS (EXAMPLES)

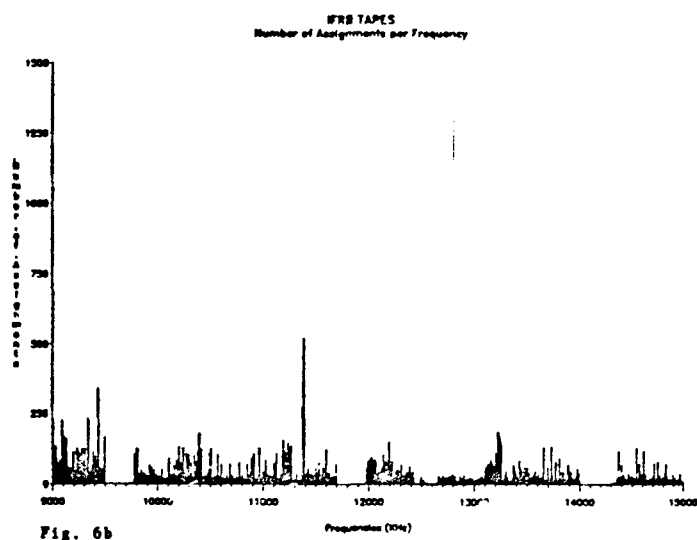
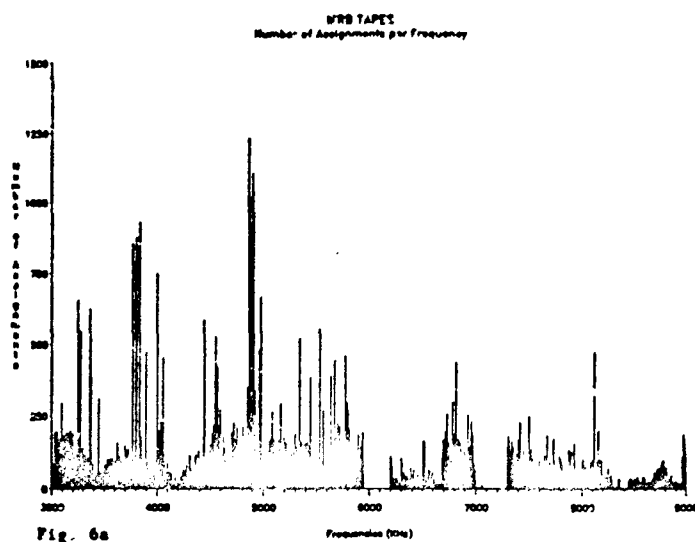
- \* INSTABILITIES  
in MAGNETOSPHERE
- \* SCATTERING on  
HF/VHF/UHF
- due to:-
  - PLASMA INSTABILITY
  - IRREGULARITIES
  - TURBULENCE

ULF-GENERATION

RECEPTION

Fig.4 Examples of  
Modification Effects





# PROPAGATION PATHS with IONOMOD

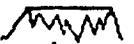

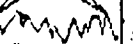

PATHS	L-O-S GROUND-WAVE	IONO- PATHS	SCATTER	SAT
				
FREQ	ALL	<30 MHz	>30 MHz	>100 MHz
DIST	<100 km	WORLDWIDE	<1500 km	WORLDWIDE
B-WTH	WIDE	NARROW	MODERATE	WIDE
EFFECTS of IONOMOD	NONE	[+]: CHORDAL PATHS	[+]: SCATTER PATHS	[-]: SCINTIL. SHIELDS
		[-]: SHIELDS ABSORBER	[-]: SHIELDS	

Fig. 8

[HJA '89]

## DISCUSSION

A. FRASER-SMITH, US

Dr. Albrecht, I would like to add to your fine review by 1) pointing out the ionospheric modification capability of the power transmission systems in use all around the world. They radiate, in total, a very large amount of energy at 50 and 60 Hz, and at their harmonics. This radiation penetrates up through the ionosphere and interacts with the energetic charged particles in the radiation belts, causing them to precipitate out into the ionosphere, which is modified. Next, 2) I would like to stress the importance of the polar region and the need to separate it out from the rest of the world as a region for modification. The reason for this is the occurrence of major natural modifications such as those that accompany large magnetic storms and solar proton effects. Any man-made modifications will have to compete with these natural modifications.

### AUTHOR'S REPLY

Thank you very much for this comment. It will certainly be increasingly important to analyze the effects of man-made modifications.

W. GORDON, US

Ionospheric modification has been part of basic studies of the upper atmosphere. Military support of basic studies has led to communication systems of value to military with important spin-offs to commercial communications.

### AUTHOR'S REPLY

I certainly agree that the use of the atmosphere as a "laboratory-without-walls" has contributed significantly to our present knowledge on the propagation medium and has thus assisted greatly in the improvements of systems.

### Artificial Ionospheric Mirrors for Radar Applications

Robert D. Short, Tom Wallace,  
Clayton V. Stewart, Pierre Lallement, and Peter Koert  
ARCO Power Technologies, Inc.  
1250 24th Street, NW  
Washington, D.C. 20037 (USA)

#### Abstract

Recognition of performance limitations associated with traditional skywave over-the-horizon (OTH) high frequency (HF) radars has led a number of investigators to propose the creation of an Artificial Ionospheric Mirror (AIM) in the upper atmosphere, in order to reflect ground-based radar signals for OTH surveillance. The AIM is produced by beaming sufficient electromagnetic power to the lower ionosphere (around 70 km) to enhance the in situ ionization level to  $10^7 - 10^8$  electrons/cm<sup>3</sup>, thereby providing an ionized layer capable of reflecting radar frequencies of 5 - 90 MHz. This paper presents a baseline AIM system concept and an associated performance evaluation, based upon the relevant ionization and propagation physics and in the context of air surveillance for the cruise missile threat. Results of the subject study indicate that a system using this concept would both complement and enhance the performance of the existing skywave OTH radars.

#### 1.0 AIM System Concept

Strategic air defense depends upon detecting and tracking potential threats approaching at long ranges, allowing adequate time for assessment and reaction. The threats of particular current interest are penetrators with small radar cross sections, including air launched and submarine launched cruise missiles (ALCM and SLCM). These threats will become more important in theater warfare as well over the next few decades. The ability to supplement current wide area surveillance with reliable, all weather, continuous detection and tracking of low flying, low observable targets is essential to the successful implementation of both strategic and tactical air defense.

Recognition of the performance limitations associated with using the natural ionosphere as a radar reflector motivated a number of investigators to propose the creation of an Artificial Ionospheric Mirror (AIM) in the upper atmosphere, in order to reflect ground-based radar signals for OTH surveillance [1,2]. The Air Force Geophysics Laboratory (AFGL) has sponsored a comprehensive study of the ionization and propagation physics associated with AIM. An important element of this work has been the development and evaluation of a system concept to provide reliable detection and tracking of low RCS targets. The AIM is produced by beaming sufficient electromagnetic power to the lower ionosphere to enhance the in situ ionization level to  $10^7 - 10^8$  electrons/cm<sup>3</sup>, thereby providing an ionized layer capable of reflecting radar frequencies of 5-90 MHz. This paper presents an AIM system concept and a performance evaluation, based upon the relevant ionization and propagation physics, in the context of air surveillance. Results of the subject study indicate that a system using this concept would both complement and enhance the performance of existing skywave OTH radars, as illustrated in Figure 1.

The performance characteristics of a stand-alone AIM system are highlighted by

- 200-1200 km detection/tracking ranges (depending on target altitude),
- azimuth coverage over 360°, or any fractional sector,
- beam grazing angles of less than 10 degrees (for 65-80 km high AIM),
- good horizontal polarization control,
- operation at RF's in the HF to low VHF (to about 90 MHz), and
- 90% detection probability of a -25 dBsm target at 1,000 km range, providing 30 dB of margin for typical low observable (LO) threat projections at VHF.

The performance of a normal skywave OTH system can be enhanced by providing an additional AIM sector (Figure 2), which has sustained operation in the VHF band independent of time of day, latitude and ionospheric state. An AIM adjunct to a conventional HF skywave radar can offer substantially improved performance with regard to:

- filling in the range hole that exists out to about 1000 km due to the minimum HF hop distance,
- mitigation of auroral effects in polar directed surveillance sectors,
- sustained operation through periods of ionospheric disturbance,
- availability of the upper end of the HF spectrum during the diurnal ionospheric cycle, and
- improved detection of LO targets through frequency selection and positive polarization control.

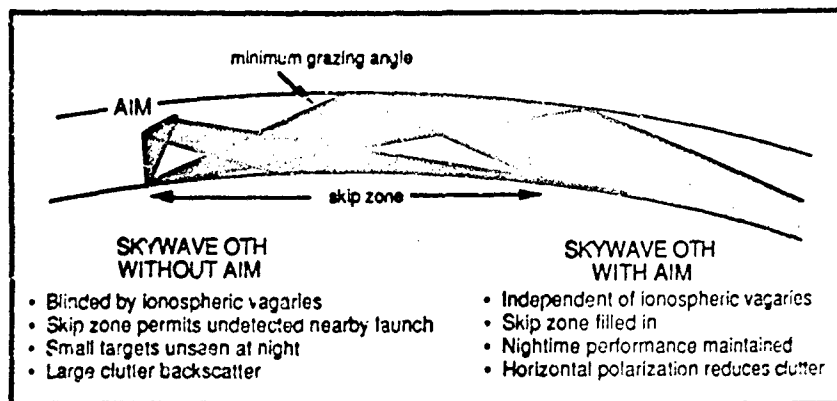


Figure 1. An AIM-Based Radar as a Complement to a Skywave OTH Radar

In addition, an AIM based system is not restricted to the HF band, but can operate in the lower VHF band, which has several advantages over HF:

- less crowded band permits broader bandwidths, better resolution and increased sensitivity.
- lower noise temperature allows higher signal-to-noise ratios.
- operation near resonant frequencies for cruise missile type targets, allowing long range detection of otherwise very difficult to detect threats, as illustrated in Figure 2.

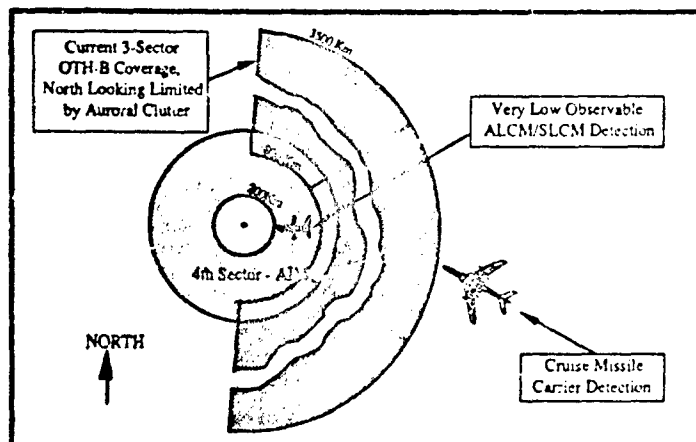


Figure 2. AIM Provides an Additional High Resolution, Highly Available Surveillance Sector

Specific issues influencing an AIM system design fall into one of three primary categories:

- heater design issues, which determine how well one can control the production of an AIM layer,
- RF propagation effects, which allow one to assess the quality of the reflected radar wave (eg. absorption, wavefront distortions, doppler spreading, and Faraday rotation), and
- Environmental and operational requirements, which determine the threat and mission context in which the AIM system must perform.

Here we present results concerning each of these issues, examining those most critical in determining the radar system performance.



## 2.0 AIM Formation and Control

### 2.1 Background

Results from theoretical analysis and numerical modelling indicate that a useful AIM consists of an ionized layer, with an electron density gradient increasing with altitude from the ambient state to a density with plasma frequency corresponding to the radar frequency. The AIM layer is oriented with an inclination ( $\sim 40^\circ$ - $45^\circ$ ) and has a slight curvature to allow the radar wave to refract over a  $15^\circ$  elevation beamwidth, providing range coverage from 200 to 1,200 km. In addition, the AIM azimuth orientation is incrementally stepped over the desired range of surveillance.

Figure 3 illustrates the system timing dependence between the AIM heater operation and the surveillance sequence of the radar. The size and orientation of the AIM relative to the spot size of the focussed RF heater beam ( $\sim 36$  m diameter) requires that the AIM creation be performed with a scanning procedure. As Figure 3 indicates, a complete AIM is formed by moving the heater focus along a stepped sequence of horizontal sweeps. The altitude at which ionization occurs is where the power density exceeds the breakdown threshold. Positive control of this altitude is achieved by using a large, partially filled, array and focussing the beam so that the AIM is formed on the front side of the focus. The focal position is controlled to follow a surface contour having the desired azimuth and elevation orientation and a slight curvature to allow for radar beam divergence over the range required for surveillance. This procedure is referred to as "painting" and is notionally illustrated in Figure 4. Based on current understanding of ionization physics and technology, a typical AIM will require on the order of a 10 to 50 ms to paint.

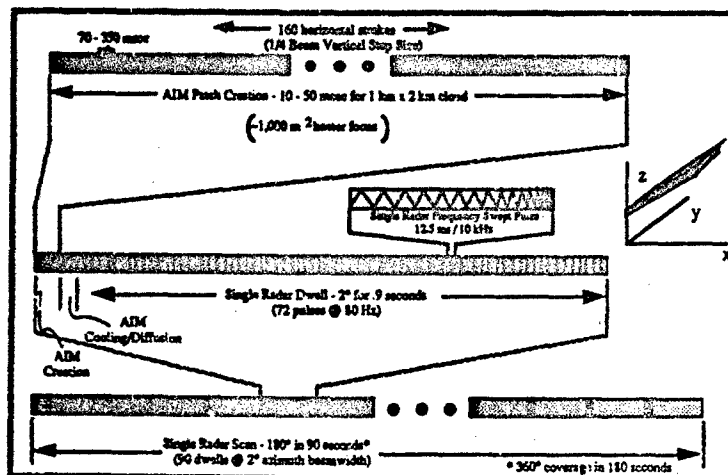


Figure 3. AIM System Timing Diagram

A central issue concerned with evaluating the feasibility of the AIM concept is how reliably the AIM can be created within tolerances necessary for useful reflection of the radar signal. Issues that directly impact usefulness include: size, shape, orientation, uniformity, smoothness, peak electron density, steepness of the density gradient, and density lifetime. In order to adequately address these issues, a comprehensive understanding of the phenomenology (validated experimentally) and a careful analysis of the heater system design parameters as they impact plasma formation control are needed.

Results of investigations to date indicate that the AIM can be created using current technology, with the necessary radar reflective characteristics to provide wide area surveillance and early detection and tracking of the ALCM/SLCM threat of the future. Specific results of the system trade-off studies are presented in the following discussions.

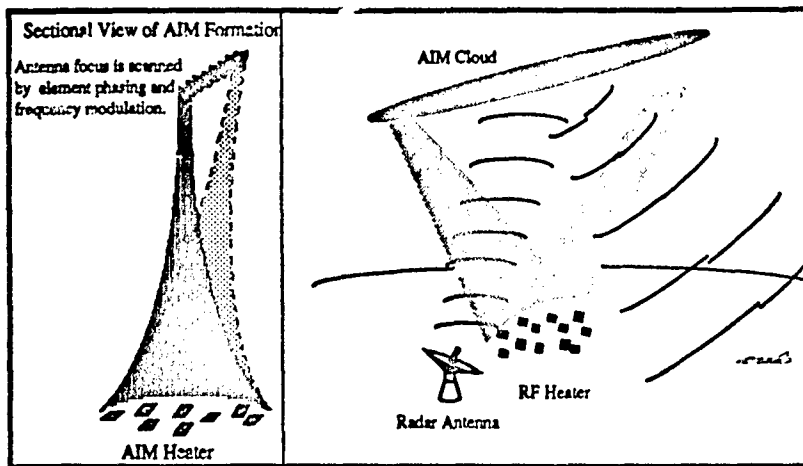


Figure 4. The Large, Sparse Heater Can Paint a Smooth, Homogeneous AIM Patch

## 2.2 Vertical Electron Density Profile Control

As indicated above, altitude control of the AIM formation is achieved by utilizing a large focussed heater array, so that ionization begins on the front edge of the focus (power density is increasing with altitude). Breakdown initiates where the power density reaches a threshold level ( $\sim 30 \text{ kW/m}^2$  @ 70 km altitude and heater frequency,  $f_h = 425 \text{ MHz}$ ), and rapidly increases in ionization rate above this level. As the number of electrons increase, absorption of the heater wave reduces the power reaching altitudes above the critical altitude until it drops below the threshold. This "self-absorption" mechanism limits plasma frequencies to well below the heater frequency. Figure 5 illustrates a time evolution of the ionization process as a function of altitude. This figure clearly shows the limiting of the peak density and the steepening of the electron density profile over time.

This steepening is due to the fact that self-absorption causes the ionization to stop at the higher altitudes first and then to walk down toward the critical altitude.

While many factors impact the resulting electron density profile, the major ones within control of the system designer are the heater RF, dwell time, and the power density gradient. Increasing the heater RF reduces the absorption rate, allowing higher peak plasma densities. Longer dwell time allows the the profile to walk further back toward the critical altitude, hence increasing the final density gradient. The third factor, power density gradient, determines how rapidly the power density is increasing beyond the threshold density and consequently how much absorption is required to reduce the field strength down to the critical level. While higher power density gradients produce higher peak plasma frequencies, increased gradients are obtained at the expense of smaller beam widths and thus smaller ionization areas.

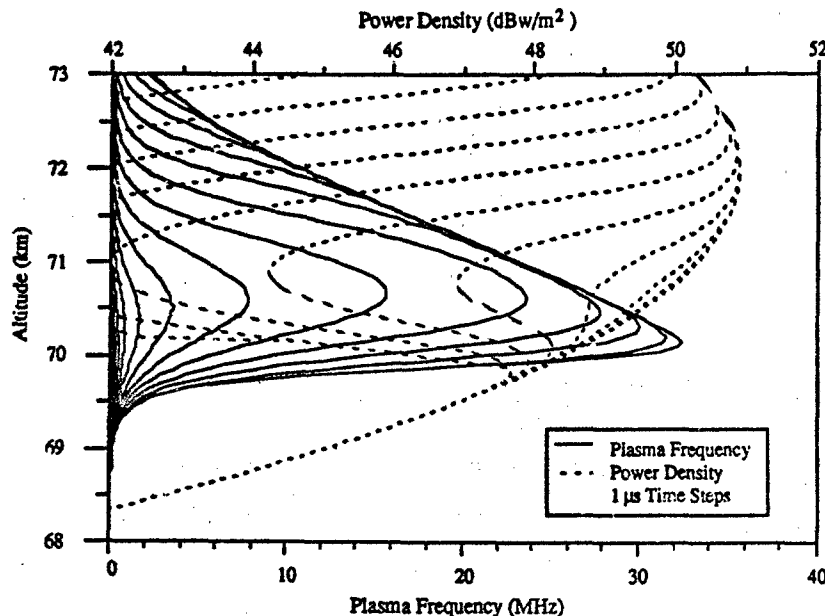


Figure 5. Growth Through Time of AIM Cloud with  $f_h = 425$  MHz,  $t = 12 \mu s$  ( $1 \mu s$  step size)

### 2.3 Heater Control Errors

Since neutral and electron density spatial variations are less than .05% over AIM scale lengths [3], the primary source of plasma irregularities are due to heater scanning and control. Here we present some rough measures of sensitivity between the uncertainties in generating the individual heater element waveforms, the resulting perturbations in AIM breakdown location, and the impact on radar system performance. Deviations in waveform generation at the element level result in corresponding deviations in the desired power density profile in the breakdown region. Three specific potential sources of error are considered:

- simple additive noise,
- amplitude distortions, and
- phase distortions.

Potential causes of these errors include quantization errors in the digital circuitry, digital-to-analog conversion errors, power amplifier gain deviations and distortions, and timing errors in the waveform control circuitry. Each of these factors is considered relative to what is readily achievable with current technology and how these performance limitations impact the patch integrity.

Results of this analysis indicate that although the power density/breakdown dependencies require relatively accurate control of the power density profile (e.g. to within .003 dB, which corresponds to a SNR at the focal point of 68 dB), the large number of independent heater elements results in significant integration gains (e.g. a configuration of 40,000 elements reduces the 68 dB requirement at the focal point by 46 dB to only 22 dB at the element level). For a surveillance radar operating at 50 MHz, the patch irregularities indicated by the cumulative error are on the order of .06 wavelengths. As indicated by Greene's analysis [4], an aperture with rms phase errors of this order will experience minimal performance degradation (< .3 dB reduction in gain, < .2% increase in beamwidth, rms beam canting < 10% of the beamwidth). Furthermore, when path averaging of the radar wave within the plasma is taken into account, the results indicate that the net effect on radar performance is negligible (~.02 dB).

In the following section, we examine the relationship between element waveform errors and errors in plasma breakdown location. Each potential error source is related to an equivalent element waveform error. These two relationships are then combined to determine the sensitivity of the AIM breakdown location to each factor.

#### 2.4 AIM Variations Due to Finite Step Heater Scanning

In the following discussion, we address the issue of AIM irregularities due to the heater's finite step beam motion in the direction of the AIM inclination. Figure 6 illustrates the step scanning of the heater beam along a short segment of the AIM contour. In this figure, the heater dwells for a given time,  $t$  seconds, and then steps the focal point a third of a beamwidth in the cross beam direction and a corresponding distance in the bore-sight direction. This dwell and step process is repeated for the extent of the AIM. As Figure 6 shows, while the desired constant electron density contour is a line inclined at  $45^\circ$ , the actual contour due to the quantization of the beam step has a ripple that oscillates about the desired contour. This irregularity in the AIM will produce a corresponding ripple in the phase front of the refracted radar wave. The extent of wavefront ripple will depend both upon the magnitude of the contour ripple, as well as the depth of the plasma density. A deeper plasma provides more refraction and correspondingly more smoothing of the AIM irregularity, thus less phase front distortion as discussed in earlier sections.

The objective of this section is to quantify the magnitude of these contour fluctuations and determine what beam step sizes are required for acceptable radar performance. These irregularities are studied both from a theoretical perspective, as well as from a straight-forward numerical simulation of the heater step scanning and consequent ionization along the desired constant electron density contour. Quantitative results are provided for the analytic derivations and compared to electron density irregularities produced by the numerical simulation. These results indicate that, within the nominal parameter regime for the current AIM conceptual design.

- 1) the magnitude of electron density irregularities falls off rapidly for paint step sizes less than  $1/2$  beam width and
- 2) a  $1/4$  beam step size produces a density fluctuation with magnitude less than .1% of the average and a corresponding location fluctuation less than .1 m.

Figure 7 shows the quantitative tradeoff between the heater's scanning step size and the resulting electron density fluctuation and corresponding altitude fluctuation for the heater parameters given above. As this plot indicates, the density fluctuation drops dramatically as the scan step size decreases below the half beamwidth size. For a  $1/4$  beam increment, density fluctuations are less than .1%, with corresponding location errors less than .1 meter.

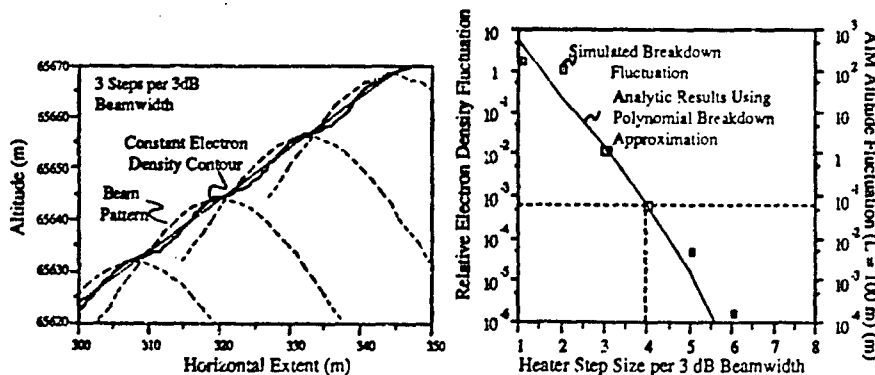


Figure 6. Illustration of Heater Step Scanning

Figure 7. Electron Density Fluctuations Versus Heater Step Size

### 3.0 AIM Propagation Effects

#### 3.1 Background

We begin our discussion of the radar system performance with a brief derivation of a radar range equation appropriate for AIM detection analysis. The AIM geometry differs from that of a traditional radar by the introduction of the reflecting layer in the propagation path. This layer intercepts the radar beam and refracts the intercepted wave toward the direction of the target. Accounting for the reflecting area, losses during the reflection process, and the two phases of spreading loss (pre- & post-reflection) makes up the major difference between an AIM range equation and a line-of-sight, monostatic radar.

The relevant radar system parameters are defined below:

$P_t$ = average transmitted power	$h$ = AIM altitude
$P_r$ = average received power	$R$ = range from the AIM to target
$G_t$ = transmit antenna gain	$\theta$ = incidence angle at the AIM
$f$ = RF frequency ( $\lambda$ = wavelength)	$D_a$ = azimuthal dispersion off the AIM
$A_r$ = receive aperture	$D_e$ = elevation dispersion off the AIM
$\Phi_s$ = angle of surveillance coverage	$w$ = AIM width
$T_s$ = scan time	$l$ = AIM length
$T_d$ = dwell time	$L_p$ = AIM one-way absorption
$L_s$ = radar system losses	$\gamma_p$ = one-way Faraday rotation $P_{hv}/P_{hh}$
$\sigma_t$ = target cross section	$\psi$ = grazing angle at surface
$\Delta_a$ = azimuthal beamwidth	$T$ = total effective noise temperature (including atmospheric noise)

The appropriate expression for received power can be best understood by considering four segments of the radar wave's propagation to and back scatter from the target. These four segments are transmitter-to-patch, patch-to-target, target-to-patch, and patch-to-receiver. The power density at the end of each segment is summarized by

$$P_r = \left[ \frac{P_t G_t}{4\pi h^2} \right] \cdot \left[ \frac{A_p G_p}{4\pi R^2} \right] \cdot \left[ \frac{\sigma_t}{4\pi R^2} \right] \cdot \left[ \frac{A_r G_r}{4\pi h^2} \right] \cdot A_r L_s \quad (1)$$

In (1) the effective AIM reflecting aperture and gain,  $A_p$  and  $G_p$  respectively, are given by

$$A_p = L_p w l \cos(\theta) \quad (2)$$

and

$$G_p = \frac{4\pi}{\Delta_a \Delta_e} \quad (3)$$

For a coherent dwell, the signal-to-noise ratio at the radar is

$$SNR = \frac{P_r T_d}{k T} \quad (4)$$

Substituting equation (1) into (4) and combining terms gives

$$SNR = \left[ \frac{P_t G_t A_p^2 G_r^2 \sigma_t A_r L_s T_d}{(4\pi)^4 h^4 R^4 k T} \right] \quad (5)$$

Equation (1) assumes that any losses due to Faraday rotation during the wave's transit is negligible (i.e.  $\gamma_p \ll 1$ ). However, in the case of clutter backscatter (particularly sea clutter), even small amounts of rotation can result in significant increases in clutter returns. This is due to the large differences between horizontal and vertical clutter cross sections ( $\sigma_{hh}$  and  $\sigma_{vv}$ ). Typical ratios are on the order of 20 dB or more. Taking these cross sections into account, the signal-to-clutter ratio (prior to clutter cancellation) for a horizontal transmit and horizontal receive configuration in sea clutter is given by

$$SCR = \frac{\cos(\psi)}{(\sigma_{hh} + \sigma_{vv} \gamma_p^2) \frac{L_s}{2B} \Delta_a R} \quad (6)$$

where  $B$  is the radar waveform bandwidth, and  $c$  is the speed of light. As will be discussed below, the small, predictable amount of polarization rotation imposed by the plasma layer allows an AIM system to exploit the large difference between horizontal and vertical backscatter.

### 3.2 Absorption and Dispersion Losses

Figure 8 illustrates the loss trade-off between absorption and beam dispersion as a function of patch depth. In this figure the electron density profile is assumed to be linear with altitude and the patch depth is measured as the distance from the ambient density to the plasma density corresponding to the critical density (ie.  $\omega_p = \omega$ ).

### 3.3 Faraday Rotation

Depending on the geographical location and orientation of the patch, the geomagnetic field will cause some amount of Faraday rotation of the polarization of the reflected radar signal. In some cases, such as a system viewing targets over land, this may be of little importance. As discussed in Section 3.1 scattering characteristics of sea clutter are strongly polarization dependent. Figure 9 shows the HF vertical and horizontal co-polarization cross sections for a moderate level sea state, based upon a widely accepted model for backscatter from the sea [5]. These curves show  $\sigma_{HH}$  to be on the order of 20 dB down from  $\sigma_{VV}$ . Therefore, the preferred polarization for reducing sea clutter returns is a linear horizontal electric field. From Equation (6) we see that as long as the Faraday rotation can be kept to less than 10% (ie.  $\gamma_p < .1$ ) the horizontal backscatter will be the dominant clutter return. This assessment assumes that the polarization separation is limited by the rotation in the AIM, rather than at the transmit and receive channels.

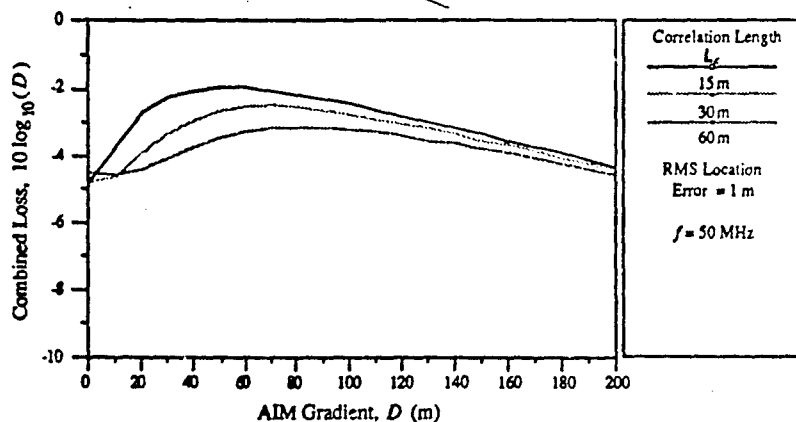


Figure 8. Typical Trade-off For AIM Losses vs Depth of AIM Cloud

Computations using typical profiles produced by simulations of the plasma formation process show rotations of as much as 2-3 radians for the worst-case location and patch orientation. In these cases, it may be necessary to precompensate for Faraday rotation by adjusting the polarization of the transmitted signal. Because the amount of rotation depends only on the depth, location, and orientation of the patch, the amount of compensation required can be computed or determined by experiment and applied each time a patch is created. It is important to note that any AIM radar system which scans in azimuth, and which uses polarization control to take advantage of the difference in sea reflectivity, must already have the ability to transmit varying polarizations; so using this capability to compensate for Faraday rotation does not add additional complexity to the system.

#### 4.0 Projected Threat and AIM System Performance

##### 4.1 The Cruise Missile Threat

In order to quantify the potential performance of an AIM based system, a specific surveillance mission and associated threat was selected. Because of the potential use of this type of system as an adjunct to a traditional skywave OTH radar and the importance of the mission, we have selected the continental United States strategic defense as the candidate mission, and the corresponding threat is a low-flying air or sub launched cruise missile. Selection of this mission and threat presents a number of challenging problems.

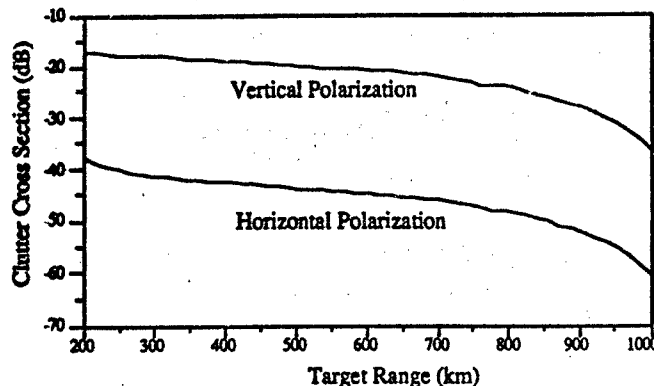


Figure 9. Sea Clutter Cross Sections for a Moderate Sea State

First, the surveillance environment consists primarily of long-range (beyond-the-horizon) air space over the sea. In order to provide OTH coverage, the AIM will be created at approximately 70 km altitude, giving a down looking beam. The corresponding grazing angle will vary from 0° at the AIM horizon (~ 1100 km) to 15° at 200 km. Therefore, as Figure 9 illustrates sea clutter backscatter will become a limiting factor as the target closes in range. In order to help reduce the sea clutter, a horizontal polarization is preferred.

The second issue to be considered is the relative geometry of a low-flying target over a conducting surface, such as the sea. As is well known, this geometry can give rise to severe multipath nulls. An effective approach to dealing with multipath is the use of frequency diversity. As the transmit frequency is changed, the multipath nulls move in range (with the exception of the first null at the AIM horizon). This effect is illustrated in Figure 10, where a single frequency multipath response is compared to the average response due to a transmit frequency that is hopped between three frequencies: 43 MHz, 49 MHz, and 54 MHz. As these curves illustrate, the use of frequency diversity all but eliminates the multipath nulls.

Finally, the radar cross section characteristics of a cruise missile play an important role in how well the radar will be able to detect and maintain a track on the target. Figure 11 shows a numerically calculated radar cross section of a cruise missile like target at grazing incidence. The target consists of a metallic cigar-shaped cylinder with metal fins. The dimensions of the target approximate those of a typical cruise missile. While the resulting cross section calculations do not exactly match those of a real cruise missile, they do give a good indication of the relative dependence upon frequency and polarization. As the curves in Figure 11 indicate, resonance occurs in the 50 - 100 MHz range, with a consequent fall off as  $f^4$  below this region (corresponding to Rayleigh scattering). Additionally, for low grazing angle, closing geometries there is a strong dependence on polarization, with horizontal polarization providing from 10 to 20 dB advantage. Therefore, the positive frequency and polarization control offered by AIM can be used to simultaneously exploit the cross section characteristics of both the target and the sea clutter.

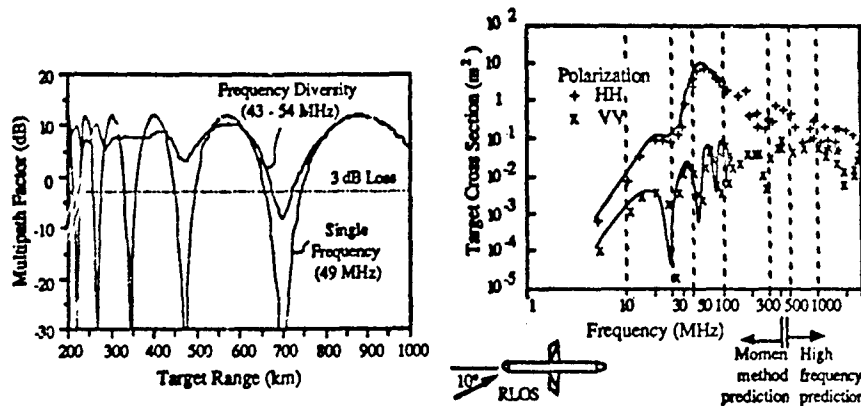


Figure 10. Impact of Multipath Can be Limited by Using Frequency Diversity (50 m Target) Figure 11. Numerical Model for a Cruise Missile Like Target [6]

#### 4.2 A Baseline System and Its Predicted Performance

##### Baseline Heater:

This section describes the current baseline heater system and describes trade studies that have been performed to arrive at this baseline. There are two rather distinctive approaches for simultaneously obtaining the high ERP, achieving the positive field gradient needed for controlled breakdown, and controlling the plasma cloud with sufficient precision that it may be used for the radar application:

- 1) a large, solid-state phased array, or
- 2) high-power tubes (klystrons, likely) feeding several dishes.

Our current understanding of the phenomenology and the available technology leads us to favor the solid-state approach for the Full Scale Engineering Development system because of its greater controllability, likely lower life cycle costs, and greater reliability. The tube approach is currently favored for an atmospheric proof of principle demonstration because of its lower development cost.

Based on our study of the plasma creation process and associated control requirements, formation of an AIM that will efficiently reflect HF/VHF radar waves requires a heater with baseline design characteristics as follows:

- Heater frequency in the UHF band,
- Moderate (about 10%) frequency agility,
- Effective radiated power of 156 dBW,
- Duty cycle of 0.1-5 %,
- Average power of 1 - 5 MW, and
- Flexible and accurate control of the E field focus.

The current baseline concept for the heater antenna consists of a large, phased array (about  $4 \text{ km}^2$ ) with solid state transmit elements, each radiating at a nominal frequency of 425 MHz. While the number and placement of the antenna elements is still subject to a detailed design, the general trade-off is one of increasing the number of elements (ie. radiating aperture) in order to reduce the required heater energy per AIM cloud. As the array area is filled, it becomes more efficient in terms of placing radiated power at the heater focus, consequently requiring less total radiated power.



### Baseline Radar:

The baseline AIM radar consists of a phased array aperture operating in the 30 - 60 MHz range, with an ERP of 98 to 104 dBW. The radar will operate with a frequency-swept FM pulsed waveform, where the pulse width is chosen to match the 540 km two-way propagation time, from the radar to the initial range of surveillance. This will provide maximum average power, compressed range resolution, and co-location of the transmit and receive aperture. Table 1 summarizes the pertinent radar/patch parameters for 25 MHz and 50 MHz baseline designs.

System Parameters	HF AIM	VHF AIM
Average Power	1.2 MW	1.2 MW
Antenna Aperture (Gain)	250 x 250 m (37 dB)	250 x 250 m (43 dB)
Frequency	25 MHz	50 MHz
Bandwidth	10 kHz	100 kHz
Effective Noise Temperature	13,000° K	7,000° K
System Losses	10 dB	10 dB
Patch Parameters		
Size	1.3 x 3.0 km	1.4 x 2.0 km
Altitude	70 km	70 km
Inclination	40° to 45°	40° to 45°
Propagation Loss	4 dB (one-way)	5.5 dB (one-way)
Relative Polarization (VV/HH)	-24 dB	-28 dB
Beam Dispersion	1.5° az, 15° el	1.5° az, 15° el

Table 1. Two Baseline Radar Configurations

### Baseline Performance:

Figure 12 indicates the expected performance of the two baseline radars shown in Table 5 using AIM against targets at 200 - 1,000 km ranges. These curves illustrate the sensitivity of the radar detection performance in a moderate level sea clutter and in noise. All AIM and system related losses have been included in the analysis. The minimum detectable target is defined as the minimum radar cross section required for a probability of detection exceeding 90% with a false alarm rate of  $10^{-3}$  (~ 100 pre-tracking false alarms per scan). As can be seen, the VHF radar has over 30 dB margin against the target illustrated in Figure 10.

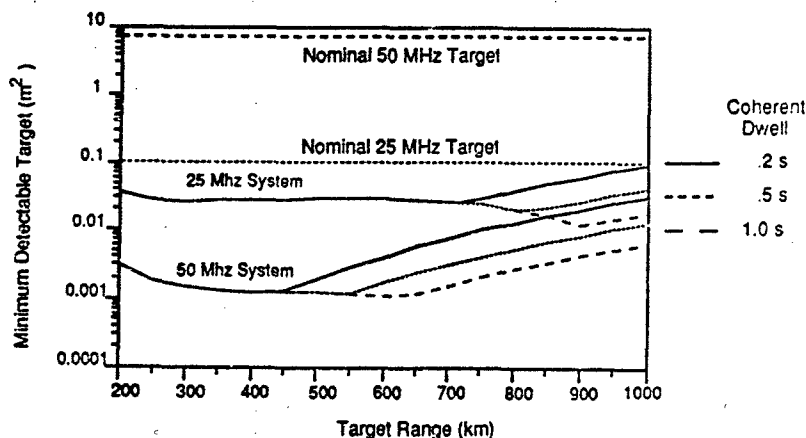


Figure 12. AIM Detection Performance Provides 30 dB Margin at VHF.

### 5.0 Summary

As the results in this paper have indicated, the operational geometry and radar characteristics of an AIM based surveillance radar can provide system performance that is well suited to the long-range detection and tracking of small, low-flying targets, as exemplified by the ALCM and SLCM threats. The basic questions concerning the feasibility of the AIM concept all relate to how reliably one can create the AIM within tolerances necessary for useful reflection of the radar signal. Issues that directly impact AIM utility (size, shape, orientation, uniformity, smoothness, peak electron density, steepness of the density gradient, and density lifetime) have been addressed above. While some uncertainties still remain, efforts to-date have reduced these uncertainties to the extent that there appears to be no phenomenological issue preventing realization of the AIM concept. This is based upon extensive physics studies and system trade-off considerations. Results of these investigations indicate that the AIM can be created using current technology, with the necessary radar reflective characteristics to provide wide area surveillance and early detection and tracking of the ALCM/SLCM threat of the future. Based on these results, the next phase of effort should include the careful design and planning of an atmospheric demonstration of the AIM concept.

### 6.0 Bibliography

1. J.M. Headrick and M.I. Skolnik, "Over-the-Horizon Radar in the HF Band", *Proceedings of the IEEE*, Vol. 62, No. 6, June 1974.
2. A. Drobot, K. Papadopoulos, and R. Hirsch, "Artificial Ionospheric Ionization for Radar Applications", Presentation to Project Forecast II, U. S. Air Force, February 1987.
3. S. P. Blood, et al., "Studies of High Latitude Mesospheric Turbulence by Radar and Rocket 2: Measurements of Small Scale Turbulence", *Journal of Atmospheric and Terrestrial Physics*, Vol. 50, No. 10/11, 1988.
4. C. A. Greene and R. T. Moller, "The Effect of Normally Distributed Random Phase Errors on Synthetic Array Gain Patterns", *IRE Transactions on Military Electronics*, Vol. MIL-6, No. 2, April 1962, pp 130-139.
5. D. Barrick, "First Order Theory and Analysis of MF/HF/VHF Scatter from the Sea", *IEEE Transactions on Antennas and Propagation*, vol. AP-20, no. 1, January 1972.
6. C. C. Cha, "An RCS Analysis of Generic Airborne Vehicles Dependence on Frequency and Bistatic Angle", *Proceedings of IEEE National Radar Conference*, Ann Arbor, Michigan, April 1988.

### DISCUSSION

R. L. SHOWN, US

In addition to a sharp profile onset to reduce absorption, there are other features of the AIM patches which will be relevant to its use in a radar. For example, have you considered patch turbulence or the noise temperature of the patch? Also, what sub-clutter-visibility (SCV) do you envision for your 25 or 50 MHz radar? Over the horizon (OTH) radars at HF would require about 80 dB.

AUTHOR'S REPLY

Yes, we have looked at quite a number of other effects: turbulence in the patch and the effect of wind shears on the position of the patch are important questions for which there is not a lot of experimental data to provide answers. We have no reason to expect turbulence at 70 km sufficient to cause us problems in our Doppler processing, but there is not a lot of available data to show definitively that these problems do not exist. The SCV that we need is going to be somewhat less than for OTH because we have polarization control and OTH is forced to operate with essentially random polarization. This is a key feature of this system in that it gives polarization control and the ability to operate against a 20 dB lower clutter cross-section. Typically we would like to operate at 50-60 dB SCV, although there is no fundamental reason why we couldn't achieve a SCV similar to that of OTH, the only limit would be the coherent integration time limiting our frequency resolution.

W. ARMSTRONG, US

Collateral effects can sometimes be viewed as damaging or as applications, and there can be a long list which many in this audience haven't heard of before, but such lists would take too long and I will try to restrict my questions to the application here of radar, but a longer list should be discussed later. The intermediate radar range discussed here is also covered by airborne radar systems. Coverage of an airborne system is < 4% of an AIM system but is mobile. Please comment further on comparison of AIM and airborne radar systems.

AUTHOR'S REPLY

Airborne radar systems suffer from two major limitations when compared with AIM-based radars. First, current airborne radar systems are incapable of detecting small RCS targets, which an AIM radar would be capable of detecting. Second, although an airborne system could, in principle, be built with performance similar to an AIM-based radar, it would still suffer from the cost and logistics burden imposed by the need to keep many aircraft aloft constantly to cover the same area.

## Electrojet Modulation ELF Communications

K. Papadopoulos<sup>1</sup>, R.A. Shanny, L. Susman, M. Machina, P. Stamboulis

ARCO Power Technologies Inc., 1250 Twenty-fourth St. NW, Washington, DC 20037

**Abstract.** The causes for the inefficient conversion of HF to ELF waves by ionospheric heating observed in recent experiments are examined. It is found that for the low frequency HF range 2.5–4 MHz used in the present experiments the modified conductance saturates during a fraction of the HF irradiation cycle. As a result most of the HF energy is transferred to processes that do not affect the conductance significantly. This was experimentally confirmed using the HIPAS facility. Techniques relying on fast HF antenna sweeping by which the efficiency can increase by more than two orders of magnitude are presented.

## 1 Introduction

The potential for using the ionosphere as an active medium to transform ground based HF power to ELF power and its significance to submarine communications was first noted in an internal report at the Naval Research Laboratory (Papadopoulos, 1973). The original premise was that when the ionosphere is irradiated with an electromagnetic (em) signal that contains two carrier frequencies  $\omega_1$  and  $\omega_2$ , the ionospheric plasma acts as an active, nonlinear medium producing signals at the frequency difference  $\omega \approx \omega_1 - \omega_2$  (Fig. 1). The effect was experimentally confirmed for the first time in Gorky USSR (Germantsev et al., 1974). In the course of subsequent experimental and theoretical studies (Kotik et al., 1975) it was found that for the HF powers used the effect was strongest in the presence of ambient ionospheric currents, in which case the frequency conversion could be accomplished by either the two frequency technique or by simple amplitude modulation of the HF carrier at the desirable low frequency. The experimental and theoretical work in the seventies was conducted predominantly in the USSR (see Belyaev et al., 1987 for a comprehensive review). Following the success of the USSR experiments Stubbe and Kopka (1977) suggested that the high latitude ionosphere could be a much more efficient frequency converter due to the presence of strong electrojet currents. A powerful HF facility built by the Max-Planck Institut für Aeronomie in Tromsø Norway was the dominant site of experimentation in the 80's (Stubbe et al., 1981, 1982; Barr and Stubbe, 1984a,b; Barr et al., 1985). These experiments were extremely successful in producing large ELF/VLF signals on the ground by amplitude modulation of the HF power incident in the ionosphere. The Tromsø HF transmitter operated in the frequency range of 2.5–5 MHz with an effective radiated power (ERP) of 100–300 MW. However, in the context of ELF submarine communications, the results were rather disappointing since the overall HF to ELF power conversion efficiency was found to be of the order of  $10^{-8}$  while the conventional ground based ELF facility in operation at Wisconsin (WTF) has a conversion efficiency of  $10^{-6}$ . The purpose of this paper is to examine the reasons for the low conversion efficiency and suggest techniques under which HF facilities similar to the Tromsø facility can improve their conversion efficiency by two to three orders of magnitude. In addition to the theoretical results we present below preliminary experimental investigations using the HIPAS facility in Fairbanks, Alaska, which confirm the theoretical premise for the inefficiency of downconversion and the suggested improvements. This paper concentrates on frequency conversion in the low D-region of the ionosphere ( $< 80$  km) where the HF power, for the low frequency ( $f < 5$  MHz) and low power density ( $< 1 - 2 \frac{\text{mW}}{\text{m}^2}$ ) range is absorbed. Even larger efficiency gains can be achieved by using higher frequency ( $f > 5$  MHz) higher power densities ( $> 5 - 10 \frac{\text{mW}}{\text{m}^2}$ ) transmitters, in which case the HF power is absorbed in the lower E region (85–95 km). This topic forms the subject of a separate paper (Papadopoulos et al., 1990a).

## 2 Baseline ELF Generation and Scaling

The process by which the HF power is converted to ELF in the lower D-region where the ambient electron neutral collision frequency for momentum transfer  $\nu_0$  is smaller than the electron cyclotron frequency  $\Omega$  is the following (Chang et al., 1961). At high latitudes the solar wind interaction with earth's magnetosphere results in the creation of an electromotive force (emf). Since at high altitude the magnetic field lines are equipotential lines, the high altitude electric field  $E_0 = E_0 \hat{e}_x$  maps in the lower ionosphere where collisional processes allow for the generation of cross field currents. Two types of currents flow across the magnetic field  $B = B_0 \hat{e}_z$ .

<sup>1</sup>Permanent address: Department of Physics and Astronomy, University of Maryland, College Park, MD 20742

The Pedersen current

$$j_p = \sigma_p E_{\phi z} \quad (2.1)$$

in the direction of the electric field  $E_{\phi}$ , and the Hall current

$$j_H = \sigma_H E_{\phi y} \quad (2.2)$$

perpendicular to  $E_{\phi}$  and  $B_0$ . In eqs. (2.1) and (2.2)  $\sigma_p$  and  $\sigma_H$  are the Pedersen and Hall conductivities defined as

$$\sigma_p = \frac{ne^2}{m\Omega^2} \left( \frac{\nu_o}{1 + \nu_o^2/\Omega^2} \right) \quad (2.3a)$$

$$\sigma_H = \frac{ne^2}{m\Omega^2} \left( \frac{\Omega}{1 + \nu_o^2/\Omega^2} \right) \quad (2.3b)$$

where  $n$  is the ambient electron density. It is clear that

$$\frac{j_p}{j_H} = \frac{\nu_o}{\Omega}$$

Charge neutrality requires that the ambient ionospheric currents be divergent free, i.e.

$$\nabla \cdot j = 0 \quad (2.4)$$

Periodic electron heating at the HF modulation frequency  $\omega$ , leads to a periodic conductivity modulation in the heated volume if  $\omega\tau_e \lesssim 1$  where  $\tau_e$  is the electron cooling time. In order to maintain the divergence free condition imposed by the quasineutrality requirement, a polarization electric field  $E_1$  builds in the modified region to maintain the divergence free condition, i.e.

$$\nabla \cdot [\underline{\sigma} \cdot (\underline{E}_0 + \underline{E}_1)] = 0 \quad (2.5)$$

Introducing the height integrated conductivity  $\Sigma$ , eq. (2.5) with  $\underline{E}_1 = -\nabla\phi$  becomes (Chang et al., 1981)

$$\begin{aligned} \frac{\partial}{\partial x} \left( \Sigma_p \frac{\partial \phi}{\partial x} \right) + \frac{\partial}{\partial y} \left( \Sigma_p \frac{\partial \phi}{\partial y} \right) + \frac{\partial \Sigma_H}{\partial x} \frac{\partial \phi}{\partial y} - \frac{\partial \Sigma_H}{\partial y} \frac{\partial \phi}{\partial x} \\ = \left( \frac{\partial \Sigma_p}{\partial x} - \frac{\partial \Sigma_H}{\partial y} \right) E_o \end{aligned} \quad (2.6)$$

Figure 2 shows the difference in the height integrated current  $j_1$  and the electric field  $E_1$  before and after the modification for a Gaussian modified region with radius  $R$ ;  $j_1$  and  $E_1$  are the sources of radiation at the low frequency  $\omega$ . From eqs. (2.3) and  $\nu \gg \Omega$  we see that the fractional change in Hall conductivity is larger than the fractional change of the Pedersen conductivity. We, thus, examine the modification of the height integrated Hall current only. If the HF absorption occurs over a region  $\Delta z \approx a$ , to zero order the radiating current will be

$$j_{1H} \approx (E_o a) \frac{ne^2}{m\nu_o \nu_o} \left( 1 - \frac{\nu_o^2}{\nu_F^2} \right) \quad (2.7)$$

where  $\nu_F$  is the modified collision frequency. Taking as  $L^2$  the horizontal area of the heated region we find that the radiating source at ELF is an horizontal electric dipole with moment  $M$

$$M \approx (E_o a) L^2 \frac{ne^2}{m\nu_o \nu_o} \left( 1 - \frac{\nu_o^2}{\nu_F^2} \right) \quad (2.8)$$

The reason for the inefficiency of HF to ELF conversion can be identified by rewriting (2.8) as

$$M = (E_o a) L^2 \Delta \sigma_H \quad (2.9)$$

$$\Delta \sigma_H = \frac{ne^2}{m\nu_o \nu_o} \left( 1 - \frac{\nu_o^2}{\nu_F^2} \right) \quad (2.10)$$

Notice that  $\nu \sim T_e$ , where  $T_e$  is the electron temperature, which in its turn is proportional to HF power density

$$S = \frac{P_o G}{4\pi z_o^2} \quad (2.11)$$

where  $z_o$  is the absorption height,  $P_o$  the ground HF power and  $G$  the antenna gain.

Figure 3 shows the saturated value of  $\Delta\sigma_H$  computed using a kinetic code as a function of the power density  $S$  for a HF frequency of 2.8 MHz (Papadopoulos et al., 1990). It is clear that  $\Delta\sigma_H$  after an initial linear increase with  $S$  saturates. Further increase of  $S$  or equivalently of the ERP does not produce additional modification. For the Tromso heater  $S \approx 2 \text{ mW/m}^2$  is above the optimum value resulting in waste of the HF power. The behavior seen in Fig. 3 can be understood on the basis of eq. (2.10). For low values of  $S$ , we can write

$$\nu_F \approx \nu_o + \Delta\nu$$

with  $\Delta\nu/\nu_o \ll 1$ . As a result

$$\Delta\sigma_H \approx 2 \frac{ne^2}{m\nu_o\nu_o} \frac{\Omega \Delta\nu}{\nu_o} \sim S \quad (2.12)$$

For higher values of  $S$ , and  $\Delta\sigma_H$  saturates at the value

$$\Delta\sigma_H \approx \frac{ne^2}{m\nu_o\nu_o} \Omega \quad (2.13)$$

For the low power density regime from eqs. (2.9) and (2.12) we find

$$\begin{aligned} M &\sim (E_o a) L^2 S \\ &\sim (E_o a) \frac{1}{G} P_o G \sim (E_o a) P_o \end{aligned} \quad (2.14)$$

where we used  $L^2 \sim \frac{1}{G}$ . Namely the ELF power scales as  $P_o^2$ . However, for the high power regime

$$M \sim (E_o a) \frac{1}{G} \frac{ne^2}{m\nu_o} \sim (E_o a) \frac{1}{G} \quad (2.15)$$

Namely for values of  $S$  larger than saturation, efficient ELF production requires smaller values of  $G$ , which of course result in larger radiating moments. This effect was first noted in Chang et al. (1981). Returning to Fig. 3, we note that  $\Delta\sigma_H$  deviates from linearity at  $S_o \approx 5 \times 10^{-4} \text{ W/m}^2$ . For the Tromso facility  $P_o \approx 1 \text{ MW}$ ,  $P_o G \approx 150 \text{ MW}$  and  $S \approx 2 \text{ mW/m}^2$ . It is obvious that an HF to ELF efficiency will increase by a factor of 16 (i.e.  $\frac{1}{4}$ ) if we decrease the gain of the antenna by a factor of 4 so that  $S = S_o \approx .5 \text{ mW/m}^2$  at 70 km.

The final factor that could affect the conversion efficiency is the scaling of the absorption height  $a$  with power density. To examine its effect we rewrite  $M$  from eq. (2.9) as

$$M \approx E_o L^2 \Delta\Sigma_H \quad (2.16)$$

$$\Delta\Sigma_H = a(\Delta\sigma_H) \quad (2.17)$$

For constant gain  $L^2 \approx \text{const.}$  and

$$M \sim \Delta\Sigma_H \quad (2.18)$$

Figure 4 shows the scaling of  $\Delta\Sigma_H$  as a function of PG from a numerical computation at 2.8 MHz. It is clear that the scaling of the ELF to the HF power is weaker than linear.

### 3 Efficiency Increase by Antenna Scanning

Further efficiency increase can be achieved by relying on the following basic non-linearities of the electron heating in the ionosphere.

- (i) The value of  $\nu \sim T_e$  resulting in fast (exponential) electron heating.
- (ii) The cooling rate decreases as a function of  $T_e$  for  $T_e$  in the range of 600°K and 2000°K (Fig. 5).
- (iii) For  $S_o > .5 \frac{\text{mW}}{\text{m}^2}$  the heating is of the runaway type for  $T_e < 2000^\circ\text{K}$  and thus very little energy is wasted in excitation of rotational levels.

This technique again relies on the fact that  $M \sim L^2$  and major efficiency increase can be accomplished by increasing the modified area  $L^2$  by electronically scanning the HF transmitter. The underlying physics of the efficiency increase can be understood by referring to Fig. 6a,b (Papadopoulos et al., 1989). Figure 6a shows the temperature variation for the case where a single spot in the ionosphere was continuously irradiated by the HF over a time  $\frac{1}{2}\tau_{ELF}$  where  $\tau_{ELF} = \frac{2L^2}{c}$ . The periodic modulation in the temperature results in modulating the conductivity and the ionospheric current, which is the basis of the ionospheric ELF antenna. Figure 6b shows the temperature variation if we send short pulses of duration  $1.2 \times 10^{-3} \tau_{ELF}$  with a repetition rate of  $5 \times 10^{-2} \tau_{ELF}$  over the half period instead of irradiating it continuously. The resultant temperature was only  $\frac{2}{3}$  of the one for the standard case, resulting in a lower conductivity variation by a factor of 2. However, the HF energy expenditure over the  $\tau_{ELF}$  time is 40 times lower, resulting in extreme increase in the efficiency of HF to ELF conversion.

The validity of this concept was demonstrated experimentally using the HIPAS facility last summer (Papadopoulos, 1990b). Figure 7 shows the relative field amplitude measured on the ground for pulses equal with  $\tau_p = 5 \tau_{ELF}$ . For technical reasons only nonrepetitive single pulse irradiation could be performed at  $f = \frac{1}{\tau_{ELF}} = 833 \text{ Hz}$ . For the cases where  $\tau_p > .25 \tau_{ELF}$  the value of B measured on the ground was independent of the HF energy per  $\tau_{ELF}$ , indicative of efficiency improvements. The technique by which this concept can lead to much higher ELF powers without increasing the ground HF power or the antenna gain was discussed in detail in Papadopoulos et al. (1989). The scheme shown in Fig. 8 relies on scanning of the HF antenna very fast so that it can irradiate other spots during its off time  $\tau_{off}$  increasing the effective ELF antenna area. The estimated increase in efficiency was of the order of 400.

#### 4 Summary and Conclusions

In this paper we identified the causes for the low efficiency of HF to ELF conversion observed in the recent ionospheric experiments. It was shown theoretically and experimentally that for low altitude heating the conductivity modification saturates at insident power densities of the order  $5 - 1 \frac{\text{mW}}{\text{m}^2}$ . Increase of the power density past the  $5 \frac{\text{mW}}{\text{m}^2}$  results in excitation of molecular lines or electron heating but weak increase in the conductance. A technique was suggested by which the conversion efficiency can increase by more than two orders of magnitude.

#### Acknowledgement

Work supported in part by DARPA and ONR (K.P.) and in part by APTI internal funds.

#### References

- Barr, R. and P. Stubbe, *J. Atmos. Terr. Phys.*, 46, 315, 1984a.
- Barr, R. and P. Stubbe, *Radio Sci.*, 19, 1111, 1984.
- Barr, R., M.T. Rietveld, P. Stubbe, and H. Kopka, *J. Geophys. Res.*, 90, 2861, 1985.
- Belyaev, P.P., D.S. Kotik, S.N. Mityakov, S.V. Polyzkov, V.O. Rapoport and V. Yu. Trakhtengerts, *Radiophysics* 30, 248, 1987.
- Chang, C.L., V. Tripathi, K. Papadopoulos, J. Fedder, P.J. Palmadesso, and S.L. Ossakow, Effect of the Ionosphere on Radiowave Systems, edited by J.M. Goodman, p. 91, U.S. Government Printing Office, Washington, D.C., 1981.
- Germantsev, G.G., N.A. Zulkov, D.S. Kotik, L.F. Mironenko, N.A. Mityakov, V.O. Rapoport, Yu. A. Sazonov, V. Yu. Trakhtengerts, and V. Ya. Eidman, *JETP Lett.*, 20, 229, 1974.
- Gurevich, A.V., *Nonlinear Phenomena in the Ionosphere*, Springer-Verlag, 1978.
- Kotik, D.S. and V. Yu. Trakhtengerts, *JETP Lett.*, 21, 51-52, 1975.
- Papadopoulos, K. 1973, Naval Res. Lab., Plasma Physics Division (internal report).
- Papadopoulos, K., K. Ko, A. Reiman and V. Tripathi, *ESA SP-195*, pp. 11-28, 1983.
- Papadopoulos, K., A.S. Sharma and C.L. Chang, *Comments Plasma Phys. Controlled Fusion*, 13(1), 1-17, 1989.
- Papadopoulos, K., C.L. Chang, P. Vitello and A. Drobot, (in press), 1990a.
- Papadopoulos, K., Final report submitted to ONR, 1990b.
- Stubbe, P. and H. Kopka, *J. Geophys. Res.*, 82, 2315-2325, 1977.
- Stubbe, P., H. Kopka and R.L. Dowden, *J. Geophys. Res.*, 86, 9073, 1981.
- Stubbe, P., H. Kopka, M.T. Rietveld and R.L. Dowden, *J. Atmos. Terr. Phys.*, 44, 1123, 1982.

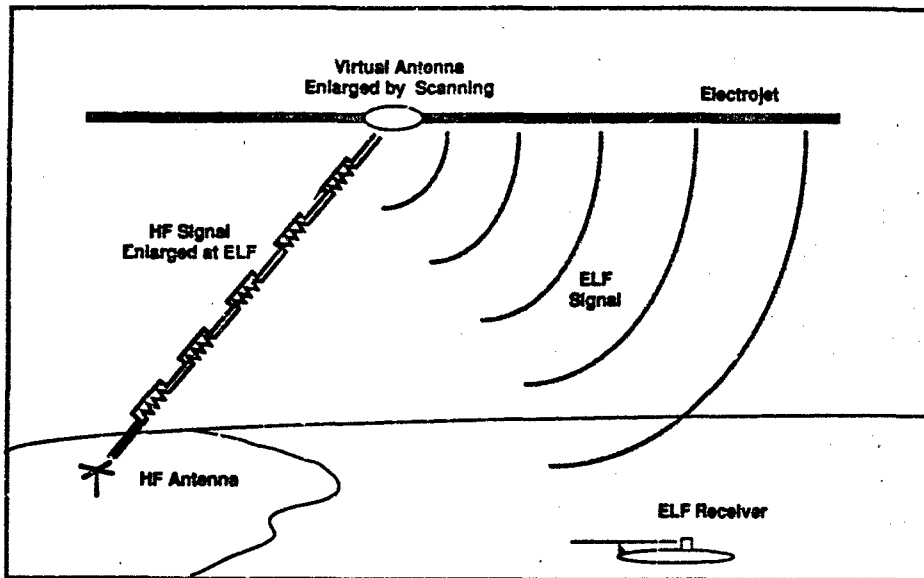


Figure 1. HF to ELF Conversion Process

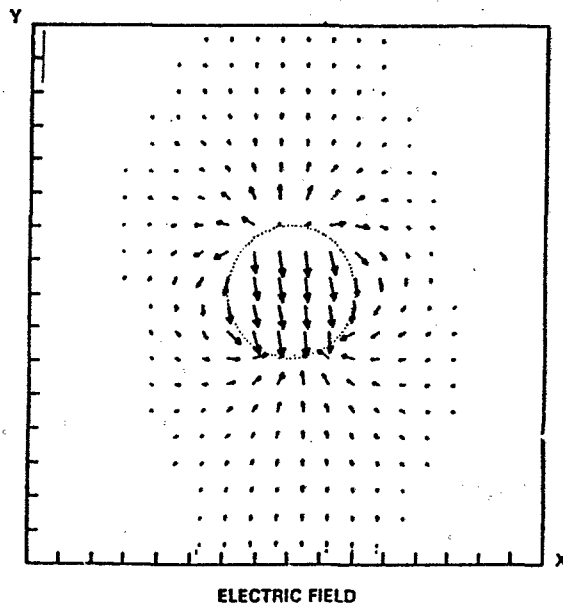


Figure 2 (a). Electric Field Established by Heating Modification

37A-6

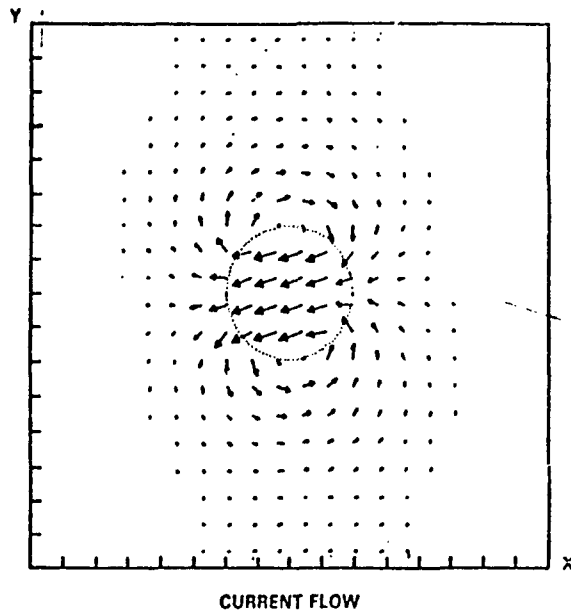


Figure 2 (b). Current Produced by Heating Modification

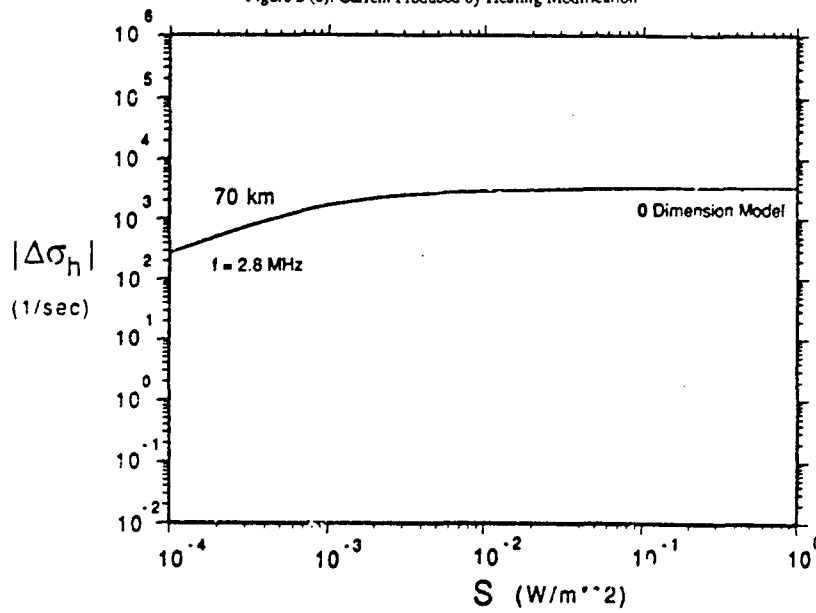


Figure 3. Modification of Hall Conductivity vs. Power Density



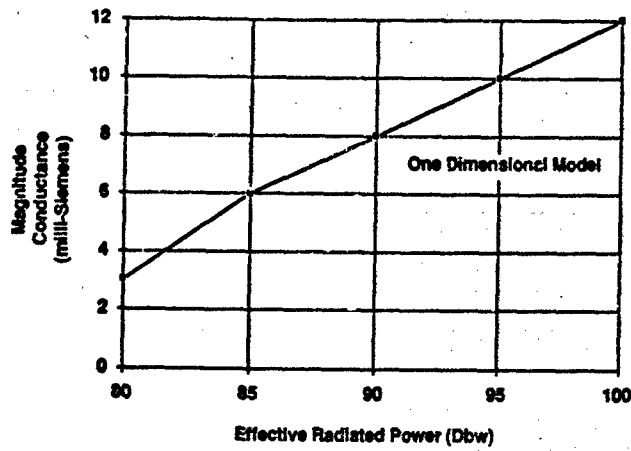


Figure 4. Modification of Hall Conductance at 2.8 MHz

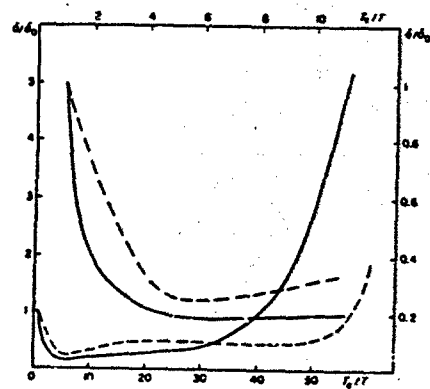


Figure 5. Electron Cooling Rate vs. Temperature

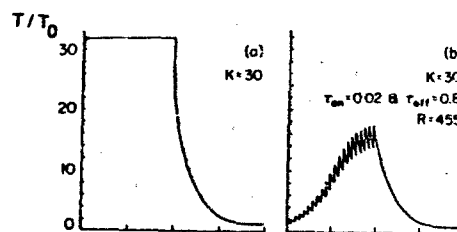


Figure 6. Ionospheric Electron Temperature

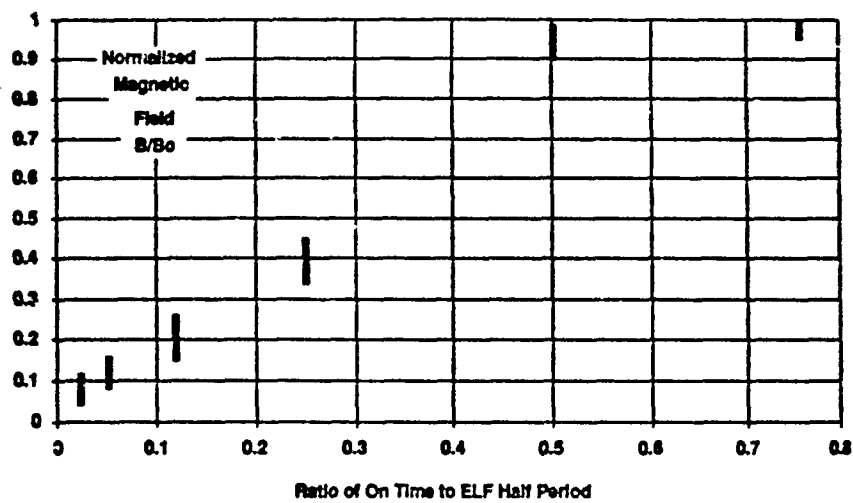


Figure 7. HIPAS Experimental Results

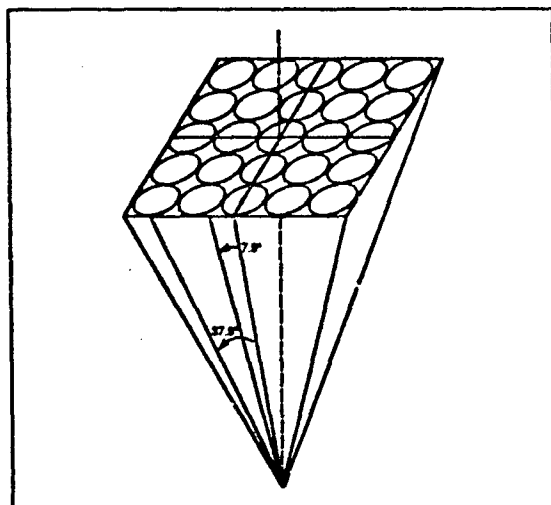


Figure 8. ELF Power Enhanced by Factor of 400

PAPER NO. 37A

## DISCUSSION

U. S. IMAN, US

I would like to point out that I showed in my talk (yesterday) that substantial wave energy can be deposited at ~ 95 km altitude with 60 dBW at VLF frequencies and resulting in conductivity changes of factors of 3-5. I think this represents an alternative scheme for generating ULF/ELF in the ionosphere via heating by modulated VLF waves.

## AUTHOR'S REPLY

If it is possible to heat the electrojet region at 90-95 km preferentially with VLF waves, it will be clearly a technique competitive to HF and a proper trade-off study should be conducted.

INVESTIGATION OF THE POLAR ELECTROJET CURRENT SYSTEM  
USING RADIO WAVE HEATING FROM A GROUND-BASED FACILITY

by

D. H. Werner, A. J. Ferraro  
Communications and Space Sciences Laboratory  
The Pennsylvania State University  
University Park, PA, USA 16802

R. G. Brandt  
Physics Division  
Office of Naval Research  
Arlington, VA, USA 22217-5000

The High Power Auroral Stimulation (HIPAS) heating facility has been used to modulate D region ionospheric currents at high latitudes, producing very low frequency (VLF) radio wave emissions. The behavior of these ionospheric currents can be deduced from a comprehensive study of the VLF signals received at a local field site. This paper examines the relationship between the VLF magnetic field strength measured on the ground and the intensity of an overhead electrojet current for the purpose of enhancing communications. The mapping of the polar electrojet current from the E region down through the D region, where it can then be modulated by the heater beam, is investigated. A finite difference solution to the electrojet mapping problem is presented in which arbitrary conductivity profiles can be specified. Results have been obtained using a simple Cowling model of the electrojet. These results indicate that for electrojets flowing between 100 and 110 km with scale sizes in excess of 100 km, the mapping of the horizontal current density can be completely characterized in terms of the Pedersen and Hall conductivities. This indicates that the mapping becomes independent of scale sizes which exceed 100 km. A promising new diagnostic technique, for studying ionospheric D region currents, has been implemented using the HIPAS facility. This technique involves high frequency (HF) beam steering for localized VLF generation in the mapped region below electrojets. Beam steering has been used to estimate the strength and current distribution of the polar electrojet, and for charting the movements of overhead currents.

## I. Introduction

The generation of ELF/VLF signals by modulation of the dynamo current system using the HF heating facility located near Arecibo, Puerto Rico, has been reported by Ferraro et al. [1] and Ferraro et al. [2]. Radiation from a heated and modulated equatorial electrojet current system was detected by Lunnan et al. [3]. Ionospherically produced signals resulting from periodic plasma heating of the polar electrojet current system have been studied by Stubbe et al. [4], Rietveld et al. [5], Rietveld et al. [6], and more recently by Ferraro et al. [7].

A series of ionospheric heating experiments have been conducted at the HIPAS facility near Fairbanks, Alaska, over a period of two years from June 1987 to August 1989. The transmitting system consists of eight individual HF heating transmitters which feed the eight antennas that comprise the HIPAS heating array. The HIPAS array has a total of eight crossed-dipoles, seven of which are equally spaced around the circumference of a 340 foot radius circle, with an eighth one situated at the center. Ionospheric heating is achieved by modulating the HF continuous wave output of the transmitter.

A reconfigurable ELF/VLF receiver was positioned 47 km west of HIPAS at a University of Alaska Geophysical Institute field site [8]. A polarimeter was set up at the receiving site in order to monitor the polarization characteristics of the incoming ELF/VLF signals at the ground. This polarimeter consisted of two orthogonal loop antennas, one with its plane oriented in the magnetic north-south direction and the other with its plane in the east-west direction. The components of the ELF/VLF signals which were intercepted by each of the tuned loops would undergo preamplification and filtering. Lock-in analyzers then extracted the in-phase (I) and quadrature (Q) components of the signals using narrowband coherent detection. The outputs of the lock-in analyzers were digitized by a data acquisition system for analysis, display, and storage via a microcomputer. Highly stable crystal frequency standards were used at both the transmitter and receiver locations to insure precise frequency coherence and sampling accuracy.

Experiments were carried out in which the HIPAS heater beam was conically scanned at an angle of 30° with respect to the vertical. The total time to complete one of these scans was two minutes. Some conical scanning VLF data is presented and interpreted in this paper.

## II. The Downward Mapping of the Polar Electrojet Current

A simple Cowling model was used by Werner and Ferraro [9] to represent the polar electrojet current. The potential associated with an electrojet current was found to be

$$\Phi(x,y,z) = -\Phi_0 \sin(\beta_1 x + \beta_2 y) Z(z) \quad (1)$$

where

$$\beta_1 = \frac{2\pi}{\lambda_1} \quad (2)$$

$$\beta_2 = \frac{2\pi}{\lambda_2} \quad (3)$$

The parameters  $\lambda_1$  and  $\lambda_2$  are the spatial wavelengths in the geomagnetic east-west and north-south directions, respectively, of an electrojet flowing at an altitude of  $s_1$ . The spatial wavelengths determine scale size of an electrojet and are related by

$$\lambda_1 \sigma_1(z) = \lambda_2 \sigma_2(z) \quad (4)$$

The function  $Z(z)$  appearing in Eq. (1) is the solution of a boundary value problem characterized by

$$\frac{d}{dz} \left( \sigma_3 \frac{dZ}{dz} \right) - \beta_0^2 \sigma_3 Z = 0 \quad (5)$$

$$Z(0) = 0 \quad (6)$$

$$Z(z) = 1 \quad (7)$$

where

$$\beta_0 = \frac{2\pi}{\lambda_0} = \sqrt{\beta_1^2 + \beta_2^2} \quad (8)$$

is the effective wave number of the electrojet. The generalized form of Ohm's law for a plasma in a magnetic field is used to relate the current density to the potential function given in Eq. (1),

$$\mathbf{J} = -\sigma \nabla \Phi \quad (9)$$

where

$$\sigma = \begin{bmatrix} \sigma_1 & \sigma_2 & 0 \\ -\sigma_2 & \sigma_1 & 0 \\ 0 & 0 & \sigma_3 \end{bmatrix} \quad (10)$$

is the ionospheric conductivity tensor. The term  $\sigma_3$  is known as the direct conductivity,  $\sigma_1$  the Petersen conductivity, and  $\sigma_2$  the Hall conductivity. An expression for the normalized magnitude of the horizontal current density is given by

$$\frac{|\mathbf{J}_h(z)|}{J_0} = Z(z) \sqrt{\frac{\sigma_1^2(z) + \sigma_2^2(z)}{\sigma_1^2(z) + \sigma_3^2(z)}} \quad (11)$$

where

$$J_0 = \beta_1 \sigma_1(z) \Phi_0 \quad (12)$$

and

$$\sigma_3 = \frac{(\sigma_1^2 + \sigma_2^2)}{\sigma_1} \quad (13)$$

is the Cowling conductivity. The corresponding angle of the horizontal current density, measured in degrees south of west, is then

$$\phi_h(z) = \tan^{-1} \left[ \frac{\sigma_p(z)\sigma_1(z) - \sigma_e(z)\sigma_2(z)}{\sigma_1(z)\sigma_1(z) + \sigma_p(z)\sigma_2(z)} \right] \quad (14)$$

The boundary value problem described by Eq. (5), Eq. (6), and Eq. (7) must be solved numerically, with the exception of a few special cases of the conductivities [9]. A finite difference scheme was used by Werner [10] to obtain a numerical solution to this boundary value problem. The ability to specify arbitrary conductivity profiles has been incorporated into the numerical mapping model. The differential equation Eq. (5) can be approximated at  $z=z_i$  by the difference equation

$$\frac{Z_{i+1} - 2Z_i + Z_{i-1}}{h^2} - p(z_i) \frac{Z_{i+1} - Z_{i-1}}{2h} - r(z_i)Z_i = 0 \quad 2 \leq i \leq N \quad (15)$$

with the boundary conditions

$$Z_1 = 0 \quad (16)$$

$$Z_{N+1} = 1 \quad (17)$$

where

$$p(z_i) = \frac{\ln \sigma_p(z_{i-1}) - \ln \sigma_p(z_{i+1})}{2h} \quad (18)$$

$$r(z_i) = \frac{\sigma_p^2(z_i)}{\sigma_1^2(z_i)} \quad (19)$$

$$z_i = (i-1)h \quad \text{for } i=1, 2, \dots, N+1 \quad (20)$$

$$h = \frac{z_2}{N} \quad (21)$$

Figure 1 shows some normalized horizontal current density profiles for the altitude range between 100 km and 60 km. Profiles for several different effective wavelengths are included (dashed curves), while the solid curve represents the profile to which the horizontal current density converges with  $\lambda_e > 100$  km. This curve is characterized by

$$\frac{J_h(z)}{J_s} \sim \sqrt{\frac{\sigma_p^2(z) + \sigma_1^2(z)}{\sigma_1^2(z) + \sigma_p^2(z)}} \quad \text{for } \lambda_e > 100 \text{ km} \quad (22)$$

which only depends on the Hall and Petersen conductivities. The current density profiles of Figure 1 were obtained assuming the presence of an intense magnetic storm during sunspot maximum daytime conditions. An electrojet source height of 100 km was assumed in accordance with the results of Kamide and Brekke [11]. The ionospheric conductivity model corresponding to sunspot maximum daytime conditions was adopted from Hughes and Scuthwood [12].

### III. The Ambient and Modulated D Region Current Densities

The VLF ionospheric source can be treated as an incremental volume element  $\Delta x \Delta y \Delta z$  with a modulated horizontal current density of  $[\Delta J_h]$  centered at the altitude of maximum heating. For typical experimental conditions, the extent of the effective radiating layer  $\Delta z$  is approximately 1 km and the layer is assumed to be centered at 70 km. The current density of the modulated ionosphere  $\Delta J$  can be related to the current density of the ambient ionosphere  $J_s$  by

$$\Delta J = [\sigma(T) \sigma(T)^{-1} - I] J_0 \quad (23)$$

where

$$\Delta J = \Delta \sigma(T) E_0 \quad (24)$$

and

$$\Delta \sigma(T) = \sigma(T_0) - \sigma(T_0) \quad (25)$$

For a vertical geomagnetic field, the ambient (unprimed) and the heated (primed) conductivity tensors are given by

$$\sigma(T_0) = \sigma = \begin{bmatrix} \sigma_1 & \sigma_2 & 0 \\ -\sigma_2 & \sigma_1 & 0 \\ 0 & 0 & \sigma_0 \end{bmatrix} \quad (26)$$

and

$$\sigma(T_0) = \sigma' = \begin{bmatrix} \sigma'_1 & \sigma'_2 & 0 \\ -\sigma'_2 & \sigma'_1 & 0 \\ 0 & 0 & \sigma'_0 \end{bmatrix} \quad (27)$$

It follows from Eq. (23), Eq. (26), and Eq. (27) that

$$\sigma \sigma^{-1} - I = \begin{bmatrix} \left( \frac{\sigma_1 \sigma'_1 + \sigma_2 \sigma'_2}{\sigma_1^2 + \sigma_2^2} \right) - 1 & \left( \frac{\sigma_1 \sigma'_2 - \sigma_2 \sigma'_1}{\sigma_1^2 + \sigma_2^2} \right) & 0 \\ - \left( \frac{\sigma_1 \sigma'_2 - \sigma_2 \sigma'_1}{\sigma_1^2 + \sigma_2^2} \right) & \left( \frac{\sigma_1 \sigma'_1 + \sigma_2 \sigma'_2}{\sigma_1^2 + \sigma_2^2} \right) - 1 & 0 \\ 0 & 0 & \frac{\sigma'_0}{\sigma_0} - 1 \end{bmatrix} \quad (28)$$

If we let

$$a_{11} = \left( \frac{\sigma_1 \sigma'_1 + \sigma_2 \sigma'_2}{\sigma_1^2 + \sigma_2^2} \right) - 1 \quad (29)$$

and

$$a_{12} = \left( \frac{\sigma_1 \sigma'_2 - \sigma_2 \sigma'_1}{\sigma_1^2 + \sigma_2^2} \right) \quad (30)$$

then the modulated horizontal current densities can be expressed in terms of the ambient horizontal current densities in the following way

$$\begin{bmatrix} \Delta J_x \\ \Delta J_y \end{bmatrix} = \begin{bmatrix} a_{11} & a_{12} \\ -a_{12} & a_{11} \end{bmatrix} \begin{bmatrix} J_x \\ J_y \end{bmatrix} \quad (31)$$

Using Eq. (31), it can be shown that the magnitude of the total horizontal ambient current density and the total horizontal modulated current density are related by

$$\mu_J = \frac{|\Delta J|}{\sqrt{a_{11}^2 + a_{12}^2}} \quad (32)$$

The horizontal modulated current density may be estimated from the intensity of the VLF magnetic field measured on the ground. The values of  $\Delta_0$  are determined using ionospheric heating theory [13], [14]. The ambient horizontal current density can then be calculated from Eq. (32). Finally, the strength of the electrojet current  $J_e$  can be found using the results of mapping theory Eq. (22). Figure 2 shows a block-diagram of the model developed to study the relationship between the VLF magnetic field intensity measured on the ground and the strength of the polar electrojet.

#### IV. Estimation of Electrojet Current Density

The Alaska meridian chain of magnetometers was used to confirm the presence of an electrojet over the HIPAS facility when heating experiments were in progress. The Alaska meridian chain consists of several flux-gate magnetometers located, approximately, along a line of constant geomagnetic longitude. Each magnetometer measures three components of the earth's vector magnetic field in a coordinate system in which the M-component represents magnetic north, the D-component represents magnetic east, and the Z-component points down towards the ground. In general, currents flow in the east-west direction in the high-latitude ionosphere.

Figures 3, 4, and 5 show the M-, D-, and Z-traces, respectively, for July 22, 1988 [15]. The magnetometer stations of greatest interest are Talkeetna (TLK) which is south of Fairbanks, and Fort Yukon (FYU) which is north of Fairbanks. At 0335 local time (1135 UT) on July 22, the HIPAS HF heater beam was being modulated at a 5 kHz rate in the vertical position. The corresponding B-field intensity measured on the ground was 0.68 pT. The magnetograms for this period indicated that there was a negative perturbation in the M-component measured at the FYU and TLK stations. There was no perturbation in the D-component measured at FYU and TLK. The Z-component was positive to the north (FYU) and negative to the south (TLK) of Fairbanks. These measurements indicate that there was a westward traveling electrojet present over Fairbanks during this time.

A VLF B-field of 0.68 pT corresponds to a horizontal modulated current density of  $1.72 \times 10^3$  A/km, assuming that the altitude of maximum heating is 75 km. Papadopoulos et al. [14], evaluate the level of conductivity modulation at various ionospheric heights as a function of incident HF power density. The value of  $\Delta_0$ , and  $\Delta_0$ , and hence  $a_{||}$  and  $a_{\perp}$ , can be found from these curves assuming an altitude of 75 km and an HF power density at this height of 1 mW/m<sup>2</sup>. The corresponding values of  $a_{||}$  and  $a_{\perp}$  are 0.6255 and 0.3526, respectively. These modulated conductivity values used in conjunction with Eq. (32) imply that the horizontal ambient current density  $J_H$  at a 75 km altitude was  $2.4 \times 10^3$  A/km. If it is assumed that the electrojet was flowing at an altitude of 100 km and had an effective wavelength which exceeded 100 km, then Figure 1 suggests that the strength of the electrojet  $J_e$  must have been 4.8 A/km. This electrojet current density is within the range of values reported by Kamide and Brekke [11].

#### V. The Conical Scanning Experiment

A promising new diagnostic technique, for studying ionospheric D region currents, has recently been implemented at the HIPAS facility [16]. This technique permits a localized cross section of the ionosphere to be probed by steering the HF heater beam. The VLF signals resulting from this beam steering are monitored and recorded at a field site on the ground via a coherent detection scheme. This beam steering diagnostic technique was successfully demonstrated during a HIPAS ionospheric heating campaign which took place in July of 1988.

Scanning of the HIPAS heater beam in a conical fashion was investigated during the July 1988 campaign. The conical scan was primarily used for diagnostics of the ionospheric current system in the vicinity of the HIPAS facility. Under ideal conditions of a uniform overhead current, the signature of the VLF received on the ground resulting from a conical scan should exhibit a certain characteristic shape. Any deviation from this shape may indicate the movement of a current into the path of the conically scanning heater beam. Since the position of the heater beam is known, it is possible to use the conical scanning technique to pinpoint the geographic (or geomagnetic) location of the influx current.

The geometry illustrating the conical scanning mode of operation is shown in Figure 6. The location of the receiver site is 47 km due west of the HIPAS facility, i.e.  $d=47$  km and  $\phi'=270^\circ$ . The coelevation  $\theta$  of the HIPAS heater beam is fixed at  $30^\circ$  while the azimuth  $\phi$  of the beam is incremented  $18^\circ$  every 6 seconds with geographic east ( $\phi=90^\circ$ ) as the starting point. This produces a conical scanning of the heater beam which traces out a circle in the ionosphere above HIPAS once every two minutes.

An incremental volume of current radiating in free space was adopted to model the VLF ionospheric source. The incremental current volume was chosen because it can be used as a basic unit to construct more complex radiating structures. The VLF source model relates the magnetic field strength measured on the ground to the strength of the modulated horizontal current density at the altitude of maximum heating. This elementary source model was used in the analysis of conical scan data.

Typical VLF magnitude and phase data obtained from a conical scan is shown in Figures 7 and 8, respectively. These measurements were made from 0558-0600 local time (1358-1400 UT) just prior to an electrojet event on July 21, 1988. The transition of the heater beam from a vertical position to the scanning mode is visible during the first few seconds of the conical scan data and should be disregarded. The frequency of VLF signals generated during the conical scanning experiment was 5 kHz.

The dashed curve appearing in Figure 7 represents the normalized field strength



that would result from a uniform ionospheric current flowing at an altitude of 70 km. The magnitude data is not exactly symmetrical indicating that heating by sidelobe may produce VLF radiation which interferes with the radiation generated by heating from the main beam. Figure 9 is a current map showing the relative intensity of the ionospheric currents associated with the E-W conical scan magnitude data of Figure 7. The length of each line segment in the current map is proportional to the ratio of the measured conical scan data to the theoretical values for a uniform current. If the length of the line segment is less than one unit, then the ionospheric current is weaker than that predicted by the uniform current model. And if the length of the line segment is greater than one unit, then the ionospheric current is stronger than that predicted by the uniform current model. The coordinates used for the current map are geomagnetic.

The results presented above suggest that conical scanning could be used for communications purposes as well as diagnostics. The heater beam could be adaptively steered to the region of the ionosphere where the strongest current was detected by a conical scan. This procedure could be repeated periodically to account for any changes in the location of the most intense current brought about by the dynamic polar ionosphere.

Figures 10 and 11 show the VLF magnitude and phase data resulting from a conical scan made during 0434-0436 local time (1234-1236 UT) on July 21, 1988. The magnitude data for this conical scan reveals that the strongest current was located to the geographic north-west of HIPAS. If this were an adaptive conical scan the heater beam would subsequently be parked at a coelevation of  $30^\circ$  and an azimuth of  $324^\circ$ . The current map corresponding to the E-W magnitude of this conical scan is shown in Figure 12.

## VI. Conclusion

The relationship between the VLF magnetic field strength measured on the ground and the intensity of an overhead electrojet current has been treated in this paper. The currents that are being modulated in the D region map down from the E region where the electrojet source current flows. A finite difference scheme was implemented to find a numerical solution to the electrojet mapping boundary value problem. This numerical mapping model accommodates arbitrary conductivity profiles.

The VLF source was modeled as an incremental volume of current radiating in free space. This source model relates the magnetic field strength measured by a ground-based receiver to the strength of the modulated horizontal current density at the altitude of maximum heating. The associated ambient (DC) current was then determined. Finally, using this information, the strength of the polar electrojet could be estimated. The results of this analysis agreed favorably with values of electrojet current densities reported elsewhere in the literature.

The use of the HF beam steering VLF generation technique as a diagnostic tool was introduced. Results were presented from beam steering experiments performed during an electrojet event which occurred on July 21, 1988. Conical scanning data was used to infer ionospheric D region currents.

## References

1. Ferraro, A. J., H. S. Lee, R. Allshouse, K. Carroll, A. A. Tzako, F. J. Kelly, and R. C. Joiner, VLF/ELF radiation from the ionospheric dynamo current system modulated by powerful HF signals, *J. Atmos. Terr. Phys.*, 44, 12, 1982, 1113-1122.
2. Ferraro, A. J., H. S. Lee, R. Allshouse, K. Carroll, and R. Lunnen, Characteristics of ionospheric ELF radiation generated by HF heating, *J. Atmos. Terr. Phys.*, 46, 10, 1984, 855-865.
3. Lunnen, R. J., H. S. Lee, A. J. Ferraro, R. F. Woodman, and T. Collins, Detection of radiation from a heated and modulated equatorial electrojet current system, *Nature*, 311, 5982, 1984, 134-135.
4. Stubbe, P., H. Kopka, H. Lauche, M. T. Rietveld, A. Brekke, O. Holt, T. B. Jones, T. Robinson, A. Hedberg, B. Thide, M. Crochet, and M. T. Lotz, Ionospheric modification experiments in Northern Scandinavia, *J. Atmos. Terr. Phys.*, 44, 12, 1982, 1025-1041.
5. Rietveld, M. T., H. Kopka, and P. Stubbe, D-region characteristics deduced from pulsed ionospheric heating under auroral electrojet conditions, *J. Atmos. Terr. Phys.*, 48, 4, 1986, 311-326.
6. Rietveld, M. T., H. P. Mauelshagen, P. Stubbe, H. Kopka, and E. Nielsen, The characteristics of ionospheric heating-produced ELF/VLF waves over 32 hours, *J. Geophys. Res.*, 92, A8, 1987, 8707-8722.
7. Ferraro, A. J., H. S. Lee, T. W. Collins, M. Baker, D. Werner, J. M. Zain, and P. J. Li, Measurements of extremely low frequency signals from modulation of the polar electrojet above Fairbanks, Alaska, *IEEE Trans. Antennas Propagat.*, AP36, 6, 1988, 802-805.
8. Baker, M. R., Development of a diagnostic system for ionospheric modification studies at high latitudes, M. S. Thesis. The Pennsylvania State University.

University Park, PA, 1988.

9. Werner, D. E., and A. J. Ferraro, Mapping of the polar electrojet current down to ionospheric D-region altitudes, Accepted for publication in a Special Issue of Radio Science on Ionospheric Modification in the Polar Region, 1990.
10. Werner, D.H., An investigation of the polar electrojet current system using radio wave heating of the lower ionosphere, Ph.D. Thesis, The Pennsylvania State University, University Park, PA, 1989.
11. Kamide, Y. R., and A. Brekke, Altitude of the eastward and westward auroral electrojets, J. Geophys. Res., 82, 19, 1977, 2851-2853.
12. Hughes, W. J., and D. J. Southwood, The screening of micropulsation signals by the atmosphere and ionosphere, J. Geophys. Res., 81, 19, 1976, 3234-3240.
13. Tonko, A. A., Nonlinear phenomena arising from radio wave heating of the lower ionosphere, Rep. PSU-IRL-SCI-470, Communications and Space Sciences Lab, The Pennsylvania State University, University Park, PA, 1981.
14. Papadopoulos, K., C. L. Chang, P. Vitello, and A. Drobot, On the efficiency of ionospheric ELF generation, Submitted for publication in a Special Issue of Radio Science on Ionospheric Modification in the Polar Region, 1990.
15. Olson, J. V., The University of Alaska at Fairbanks Geophysical Institute, Private Communication, 1988.
16. Wong, A. Y., and M. McCarrick, The University of California at Los Angeles Plasma Physics Laboratory, Private Communication, 1988.

#### DISCUSSION

L. DUNCAN, US

I think this is a very interesting concept for application both to study of the electrojet itself and to improvement of the ELF generation technique. I was a little confused about the approach's ability to detect and locate spatial variations in the electrojet when in the introduction you assumed essentially no spatial variation ( $\lambda > 100$  km).

AUTHOR'S REPLY

It's a different use of the term. By spatial variations I meant movement of spatial location, so if the electrojet had no spatial structure, i.e., was spatially homogeneous, but moved in location overhead you could track that spatially homogeneous electrojet. If in fact one had a very fine beam then one could also look at discerning spatial structure in the electrojet, which would be a finer resolution kind of measurement.

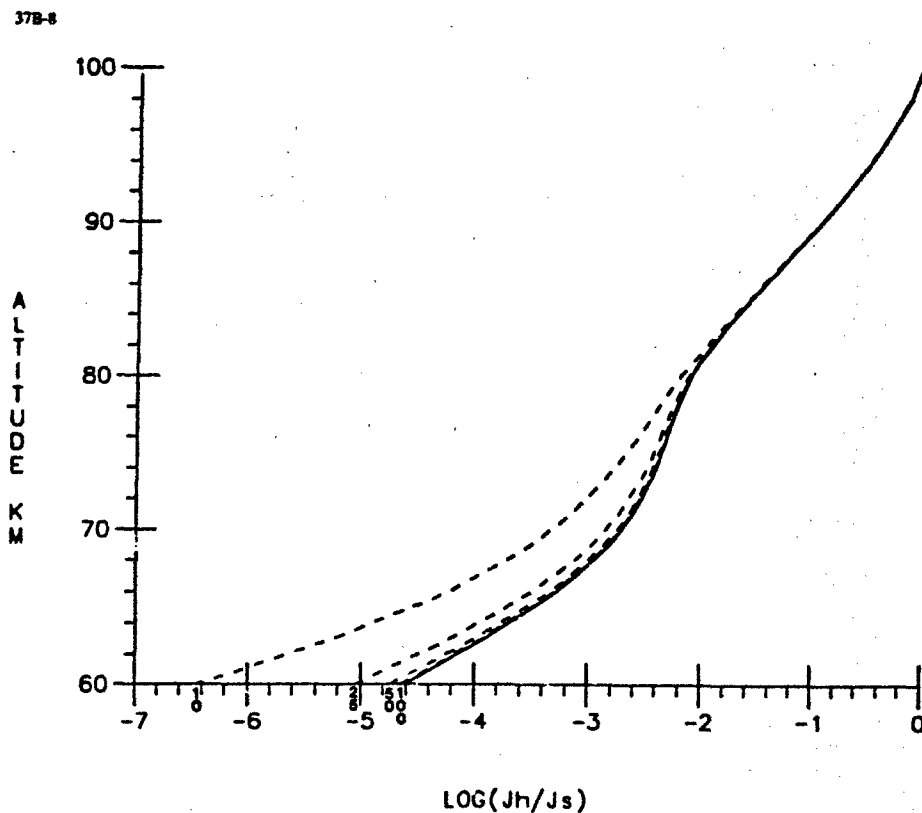


Figure 1. Normalized horizontal current density profiles for the altitude range between 100 km and 60 km.

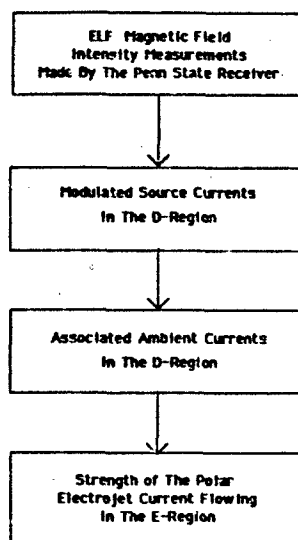


Figure 2. Block-diagram of the model.

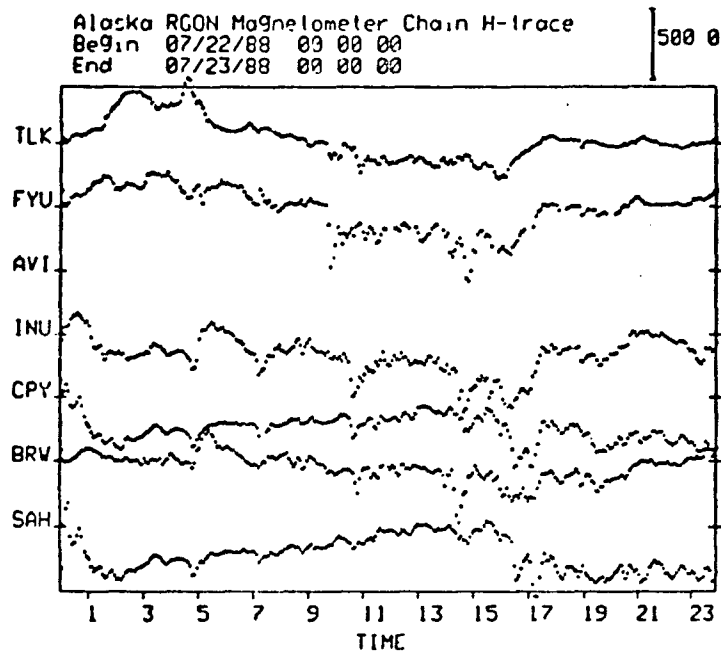


Figure 3. Magnetometer records for July 22, 1988. Alaska RCON magnetometer chain H-traces.

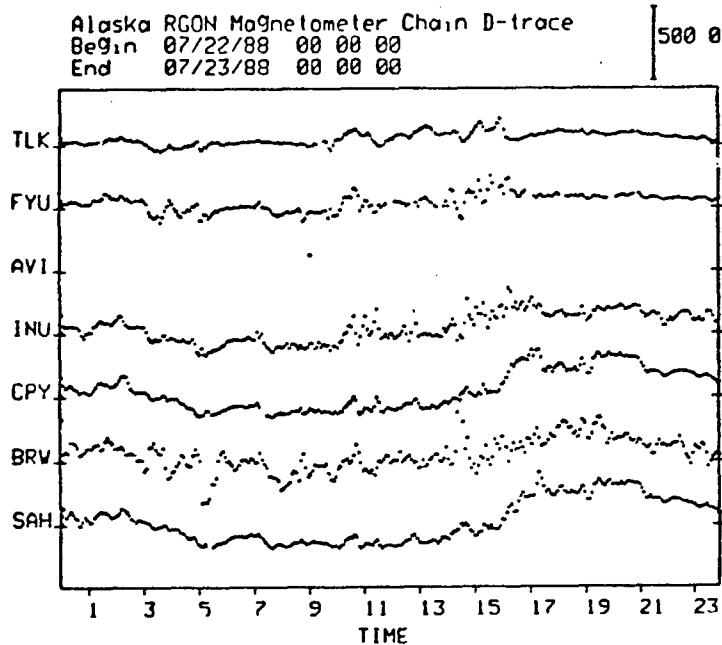
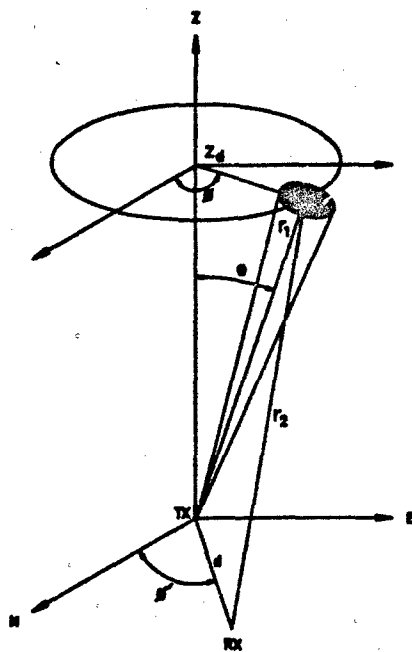
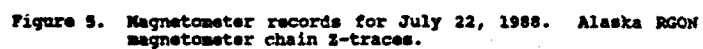


Figure 4. Magnetometer records for July 22, 1988. Alaska RCON magnetometer chain D-traces.



**Figure 6. Geometry for the conical scanning experiment.**

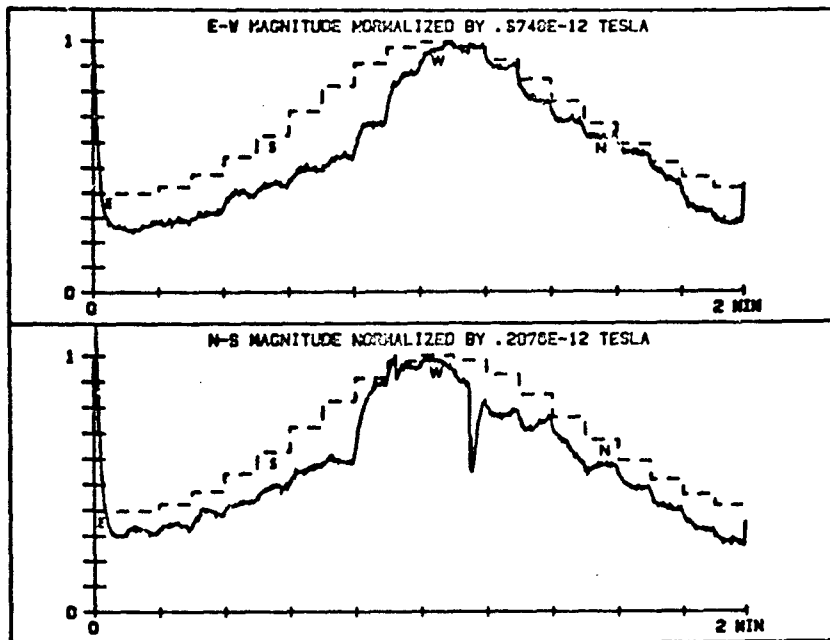


Figure 7. Conical scan VLF magnitude data for the period 1358-1400 UT on July 21, 1988.

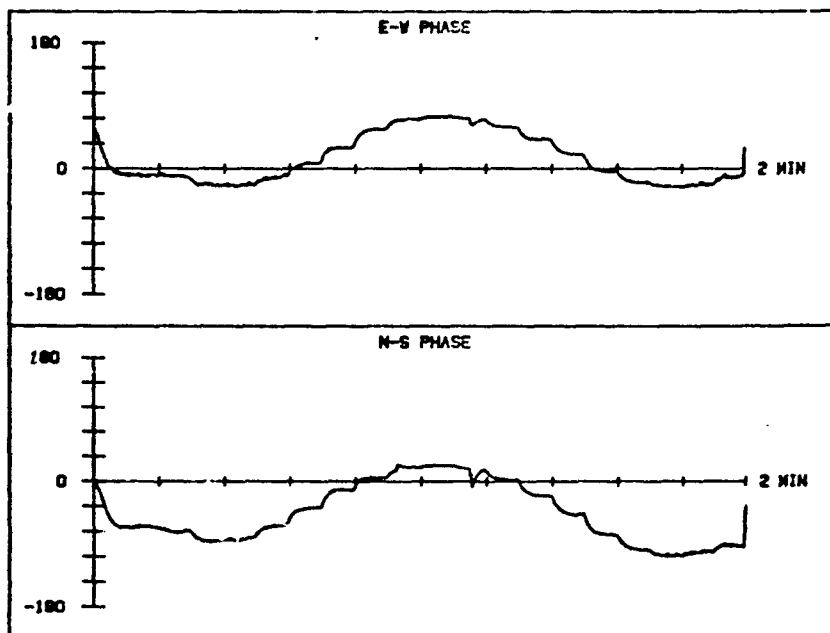


Figure 8. Conical scan VLF phase data for the period 1358-1400 UT July 21, 1988.

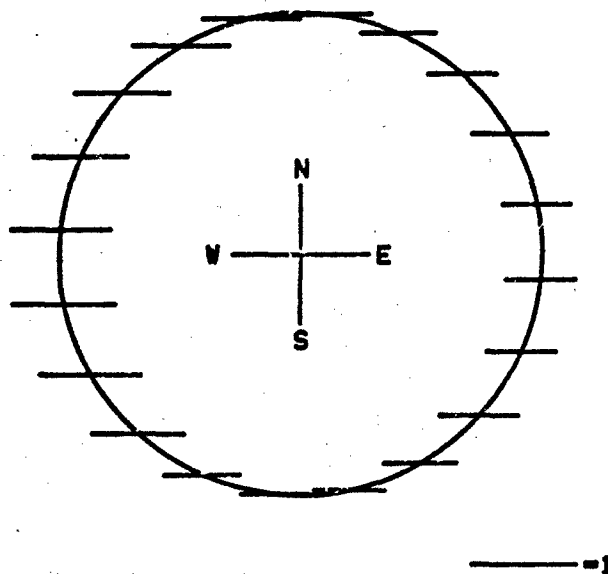


Figure 9. The relative intensity of the E-W component of the D region ionospheric currents associated with the E-W VLF magnitude data of Figure 7.

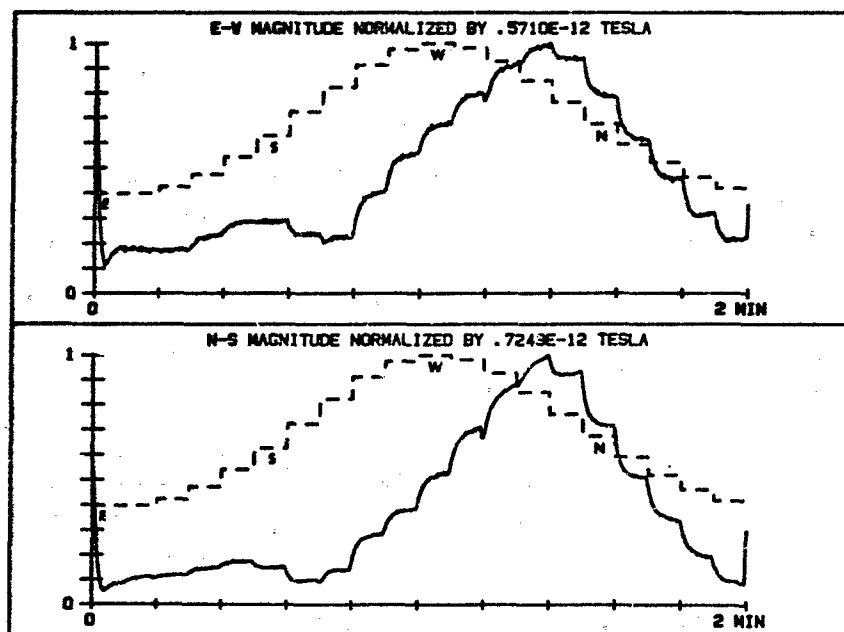


Figure 10. Conical scan VLF magnitude data for the period 1234-1236 UT on July 21, 1988.

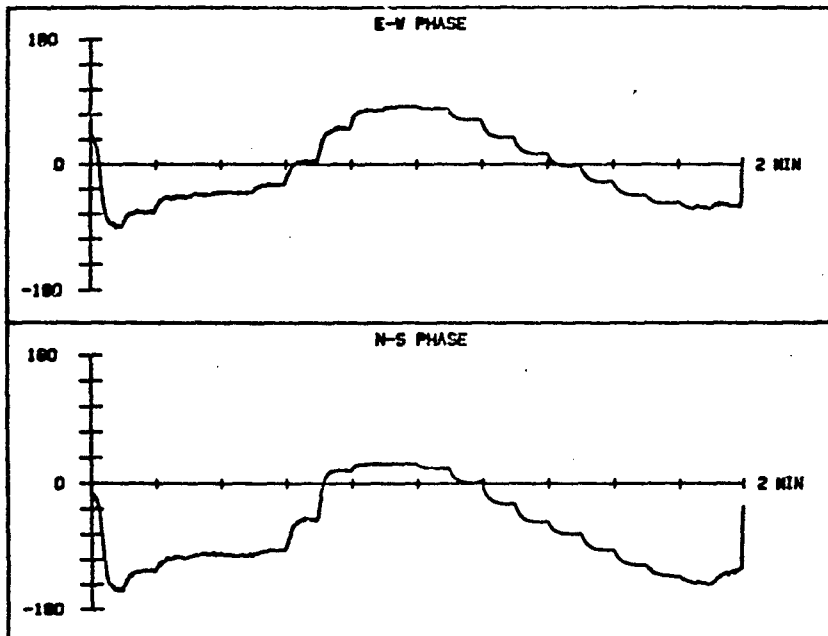


Figure 11. Conical scan VLF phase data for the period 1234-1236 UT on July 21, 1988.

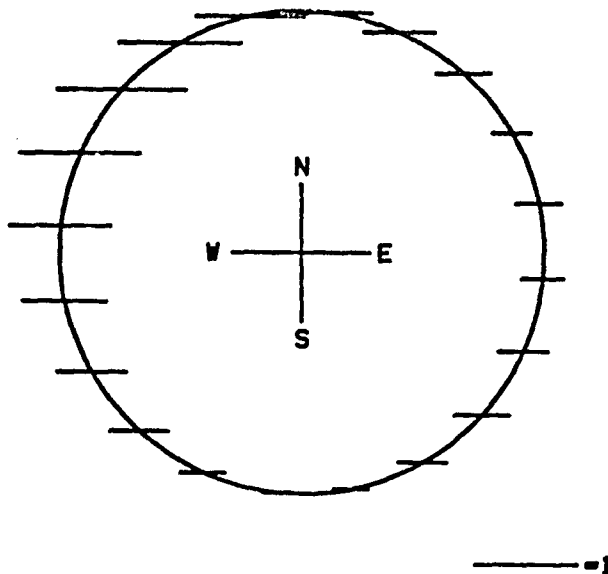


Figure 12. The relative intensity of the E-W component of the D region ionospheric currents associated with the E-W VLF magnitude data of Figure 10.



## THE GENERATION OF ULF WAVES IN THE IONOSPHERE

by

S. T. Noble and W. E. Gordon  
Department of Space Physics and Astronomy  
Rice University  
P. O. Box 1892  
Houston, TX, USA 77251

### SUMMARY

One explanation for the generation of HF sidebands during two-frequency heating experiments is based on the interaction between the beat frequency wave and the HF waves. To test this, simultaneous HF sideband and ULF measurements have been made using the facilities at the National Astronomy and Ionosphere Center at Arecibo, Puerto Rico. The ULF measurement techniques and recent findings are discussed. At the core of the ULF receiving system are three mutually perpendicular magnetometer sensors. For most studies, only the band 0.5-20 Hz is utilized. Although based upon a limited data set, underdense heating has yielded no signs of ULF production in the ionosphere. This is not surprising, since the achievable field strengths during underdense heating are well below the predicted threshold required for beat frequency wave production. Proposed improvements to the Arecibo HF facility, if undertaken, and the resulting increases in effective radiated power could greatly improve the chances of exciting this mode. Although HF swelling near the reflection height can amplify the fields significantly during overdense heating, no signs of ULF have been observed at these times either. This is possibly a result of geometrical limitations imposed by this type of ionospheric heating.

### BACKGROUND

For the past half decade two-frequency heating experiments have been conducted at the Arecibo Observatory, Puerto Rico, using the high-power high-frequency facility at Isotot. Most of the observations have centered on the generation of HF sidebands<sup>1</sup>. Shortly after they were first observed, two processes which could account for their production gained attention. One of these is the phase modulation theory<sup>2</sup> and the other is based on the mixing of the beat frequency wave<sup>3,4,5</sup> with the HF signals. It is the second process, that involving ULF wave generation in the ionosphere and the measurement of the ULF signal during recent HF sideband experiments, which is discussed here. Attention is focused on the design of the receiver system and its capabilities. Recent data are discussed along with future plans.

### SYSTEM DESIGN AND CALIBRATION

In the first experiment<sup>6</sup> designed solely to measure the ULF wave, strong ULF signals were observed at the beat frequency and attributed to ionospheric mixing of the two HF signals. A few years lapsed before this initial experiment was repeated in 1983 in conjunction with the HF sideband studies. Since 1988, experimental campaigns have been conducted annually and consist of approximately 15-30 hours of heater time each year. All of the HF sideband experiments to date which have included ULF measurements have used a transportable ULF receiving station situated on Mona Island. As shown in Figure 1, this station is located about 140 km southwest of Arecibo and is accessible by boat or small aircraft. Since only generator power is used on the island and there are no major artificial sources of electrical noise, this site is nearly ideal for measurements in this lower band of the frequency spectrum.

The receiver system is diagramed in Figure 2. At the core of the receiving system are three Electromagnetic Instruments Model BF-4 magnetic field sensors arranged along three mutually perpendicular axes and buried to minimize mechanically introduced interference. The sensors are designed to cover the frequency band from 0.1 to 1000 Hz. The sensors contain a preamplifier which is powered by a remotely located DC power supply. For ULF studies in the band between 0.5 and 20 Hz the signals from the sensors are passband filtered to eliminate components related to our AC power system. Once filtered, the signals are amplified and recorded on magnetic tape. Although HF sideband measurements are attempted at difference frequencies (i.e.,  $f_{HF1} - f_{HF2}$ ) up to ~2 kHz, simultaneous ULF studies at frequencies above 20 Hz are not typically done. In the rare instances when such studies are attempted the signals are preamplified as before, but no further signal conditioning is performed. At these higher frequencies analog recordings on tape are not made. For all studies, real-time signal processing is accomplished using an Hewlett-Packard Model 3561 Signal Analyzer with 80 dB dynamic range.

In the past we have experienced problems with the linearity of the sensors when subjected to multifrequency HF fields. To shield the sensors from these fields, they are wrapped in a brass wire cloth and then insulated from the ground, and any ground currents, by being placed in PVC tubes. The sensors and the electronics associated with the sensors are electrically isolated from the remainder of the receiving system by optical isolators. To ensure that the system behaves appropriately, two portable low-power HF transmitters are used to calibrate the ULF receiver prior to each experiment. These transmitters are capable of simulating the HF field strengths found on Mona Island from waves launched at Isotot and reflected by the ionosphere. Furthermore, an HF receiver is operated during the experiment and the level of the heater wave on Mona recorded. Since these procedures were not followed prior to 1989 and the system has been shown to respond nonlinearly to multifrequency HF fields when not configured as described, albeit only when the HF field strengths are near the high end of those expected on Mona Island during overdense heating, all prior results based on pre 1989 data should be viewed with caution.

## RECENT FINDINGS

The safeguards implemented to minimize HF effects on the ULF receiver system are recent. HF receivers were first used in 1989 and the local HF sources in 1990. The findings from these and other data are given next and are not encouraging. Data accumulated from 1988-90 during periods of underdense heating have shown no signs of ULF wave generation. These data were taken in the morning and evening around the time of sunrise and sunset and comprise only about 4 hours of time during which the HF system operated at full capacity, i.e., four transmitters at 100 kW each. The fact that ULF was not detected at these times is perhaps not surprising as typical field strengths in the ionosphere without invoking focusing instabilities is  $<0.5$  V/m. The theoretical field strength required for beat wave excitation in the F region is estimated at  $\sim 5$  V/m, or roughly an order of magnitude greater than the field strength achievable with the Arecibo system in an underdense ionosphere free from focusing instabilities. Perhaps on rare occasions when field amplification occurs due to wave focusing and the proper geometrical conditions are satisfied would the Arecibo system under its current configuration yield an ionospherically produced ULF wave in an underdense ionosphere. In this regard, proposed improvements at the Arecibo HF facility, if implemented, and the associated increase in effective radiated power will be beneficial to this and similar programs designed to determine threshold and saturation characteristics of HF induced phenomena. To substantially increase the probability of exciting the beat frequency wave mode, such improvements to the heating facility should include a minimum 6-10 dB increase in the effective radiated power.

The situation is slightly better in an overdense ionosphere near the reflection level where swelling of the HF wave causes significant increases in the field strength (1-3 V/m). If the geometry is also satisfactory, which may not be the case for a vertically incident wave, then beat frequency effects in the form of ULF wave production could potentially occur during times when field strengths increase beyond those normally encountered. About 24 hours of data has been collected during overdense periods. The heating was conducted at night and at frequencies of 3 and 5 MHz with difference frequencies between 0.1 and 37 Hz. The outcome of this study is the same as for the underdense case, that is, no ULF was observed. Geometrical limitations may be in part responsible for this.

## REFERENCES

- <sup>1</sup>Ganguly, S., and W. E. Gordon, Nonlinear mixing in the ionosphere, *Geophys. Res. Lett.*, **13**, 1986.
- <sup>2</sup>Huang, Z. H., and J. A. Fejer, Nonlinear sidebands of two powerful waves at closely spaced frequencies in the ionosphere, *Radio Sci.*, **22**, 4, 1987, 663-670.
- <sup>3</sup>Sturmer, J. A., K. Papadopoulos, R. N. Sudan, S. O. Dean, and E. A. McLean, Spontaneous Magnetic Fields in laser-produced plasmas, *Phys. Rev. Lett.*, **26**, 17, 1971, 1012-1015.
- <sup>4</sup>Papadopoulos, K., K. Ko, and V. Tripathi, Efficient parametric decay in dissipative media, *Phys. Rev. Lett.*, **51**, 6, 1983, 463-466.
- <sup>5</sup>Papadopoulos, K., and C. L. Chang, Generation of ELF/ULF waves in the ionosphere by dynamo processes, *Geophys. Res. Lett.*, **12**, 5, 1985, 279-282.
- <sup>6</sup>Ganguly, S., W. E. Gordon, and K. Papadopoulos, Active nonlinear ultralow-frequency generation in the ionosphere, *Phys. Rev. Lett.*, **57**, 5, 1986, 641-644.
- <sup>7</sup>Ko, K., C. R. Menyuk, A. Reiman, V. Tripathi, P. Palmadesso, and K. Papadopoulos, ELF generation in the lower ionosphere via collisional parametric decay, *J. Geophys. Res.*, **91**, A9, 1986, 10097-10107.

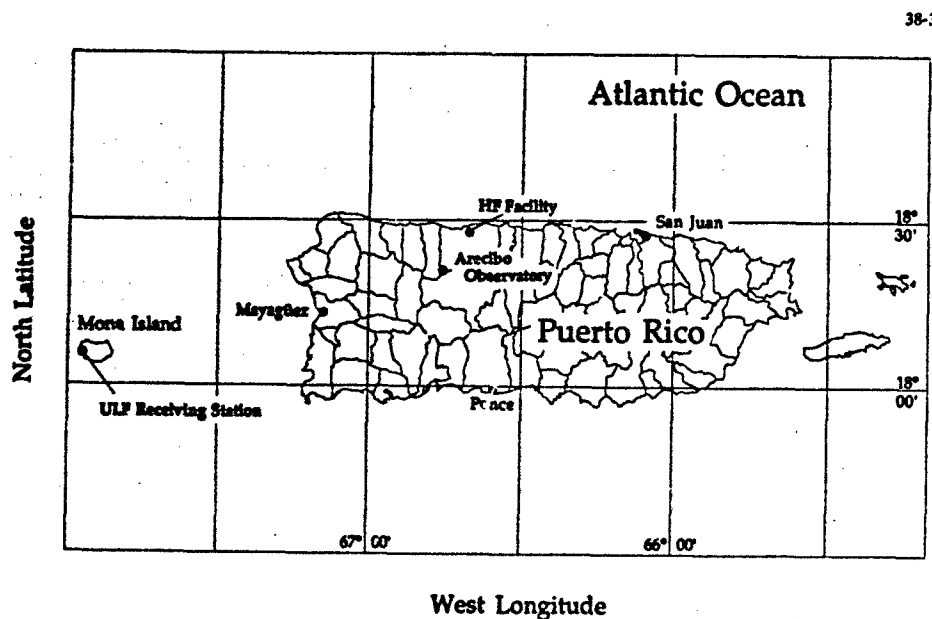


Figure 1. Location of the facilities used during two-frequency heating experiments.

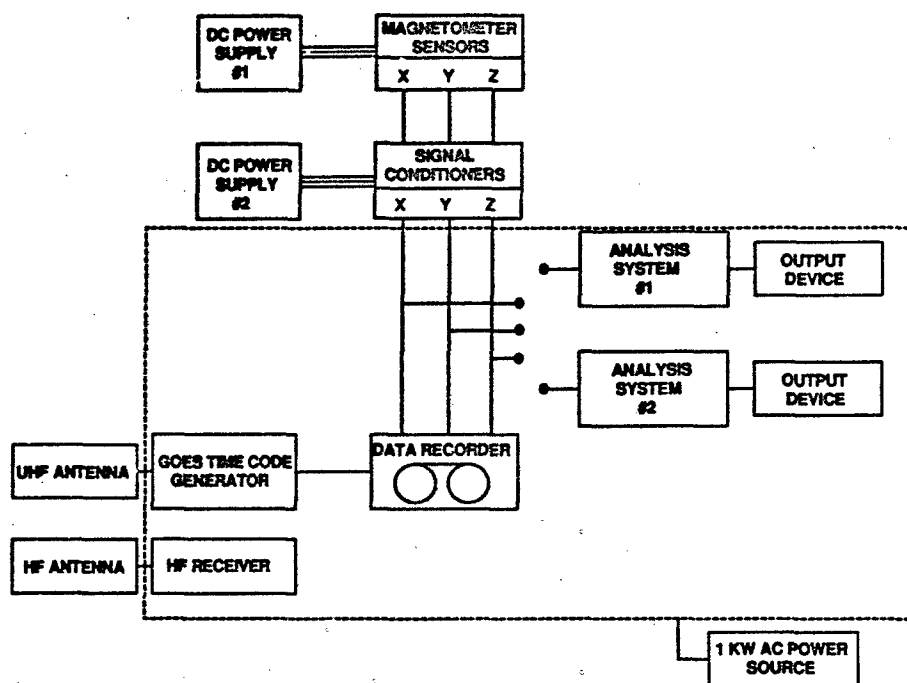


Figure 2. Schematic of the Mona Island ULF receiving system.

## DISCUSSION

## A. FRASER-SMITH, US

You say that no ULF signals were observed over the past two experiment periods. However, it is possible that ULF signals were generated and that they were just too weak to be detected by your instrumentation. Was your measurement system calibrated? Can you say what the noise amplitudes were in your band of operation when you were unable to detect ULF signals? In other words, how small must the ULF signals have been for you not to be able to detect them?

## AUTHOR'S REPLY

The measurement system is calibrated prior to each experimental campaign (under the assumption that the sensors are up to specifications, since they are not calibrated with the rest of the system). Concerning the second question, we have all the information required to determine the noise amplitude. However, I cannot provide the value at this time, since it has not as of yet been determined. One additional point: the receiving system does not provide the limiting noise; therefore, if the excited ULF modes are at a strength greater than ambient, we would detect them.

# HF PROPAGATION THROUGH ACTIVELY MODIFIED IONOSPHERES - MODELLING AND EXPERIMENTAL RESULTS

Paul E. Argo, T. Joseph Fitzgerald,  
John M. Wolcott, and David J. Simons  
Los Alamos National Laboratory  
Atmospheric Sciences  
Los Alamos, New Mexico 87545

## SUMMARY

We have developed a computer modelling capability for predicting the effects of localized electron density perturbations created by ionospheric chemical releases upon oblique, one-hop HF propagation paths. We have included a 3-D deterministic description of the depleted or enhanced ionization, including formation, evolution, and drift. The code uses a homing ray trace technique to calculate the energy propagation paths through the modified ionosphere and hence can predict multipath effects. We participated in the NASA Nickel Carbonyl Release Experiment (NICARE) ionospheric chemical depletion campaign in October of 1989 to validate this code. We will present preliminary results of this experiment here.

## RAYTRACING PROGRAM

Our TRACKER computer program "tracks" the three-dimensional paths of radio waves through model ionospheres by numerically integrating Hamilton's equations. The Hamiltonian method, by using continuous models, avoids false caustics and discontinuous raypath properties often encountered in conventional raytracing methods. In addition to computing the ray path, TRACKER also calculates group path, phase path, geometrical path, and Doppler shift (if the time variation of the ionosphere is explicitly included). This program is an extension of the three-dimensional Hamiltonian integration code developed in the late 1960s by R. Michael Jones and J.M. Stevenson, commonly referred to as the Jones code. We have substituted a modern linear differential equation solving routine (Hindmarsh, 1980) for the Runge-Kutta solver in the Jones code. TRACKER calculates gradients in the index of refraction explicitly, thus allowing for non-analytic ionospheric forms and perturbations.

Raytracing codes cannot in general compute the raypath that connects a specified source and receiver. 'Homing' is usually achieved by launching a fan of rays at small azimuth and elevation increments, and linearly interpolating to find a ray that reaches the receiver location. Since we need to find raypaths that arrive at the receiver within a fraction of a wavelength, TRACKER includes a formalism to treat this homing problem as a differential equation. In this case the one dimensional zero crossings of the rayfans are calculated (azimuth and elevation are treated independently). These are solved sequentially and iterated until a homed ray of the required accuracy is found.

The outputs of the TRACKER raytracing program are tailored to the study of propagation through ionospheric perturbations. Figure 1 shows three rays, directed into a pair of chemical releases, with the ionospheric plasma density contours shown. The depletions are evident, as are the effects on propagation. These effects can in general be described as those of a focusing lens. Figure 2 shows the multiplicity of paths that can be formed by a pair of chemical releases. Two of the five paths are disturbed low and high rays, and the other three are new modes generated by the focusing effects of the depletions. The time delays and signal strengths from each mode can be added to provide an estimate of multipath fading.

## NICARE EXPERIMENT AND PRELIMINARY RESULTS

To validate our model, we participated in the NASA NICARE campaign. This campaign consisted of two 300 km altitude chemical releases from a single rocket launched at Wallops Island, Virginia on the night of October 21, 1989. The chemicals were nickel carbonyl ( $\text{Ni(CO)}_4$ ) and trifluoromethyl bromide ( $\text{CF}_3\text{Br}$ ). Both chemicals reduce electron density by dissociative attachment (Bernhardt, 1988).

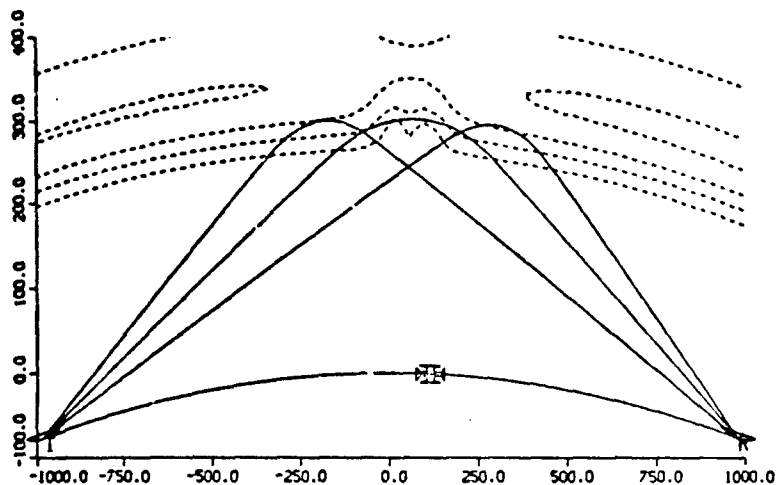
Our experimental sites consisted of HF transmitters in Florida and Bermuda and HF receivers in Ohio and Nova Scotia (Figure 3). These locations were selected to place the mid point of the HF propagation path near the ionospheric depletions. The receiving stations were instrumented to measure changes in the propagation channel as the ionospheric depletions developed. The transmitters and receivers were locked to Rubidium clocks to give very high frequency stability. Each transmitter site broadcast four cw frequencies simultaneously, with frequency separations ranging from 10 to 70 kHz. The receiver sites consisted of spaced arrays with antenna separations ranging from 50 to 750 m. The received signals were reduced to a beat frequency of 10 Hz, and digitized at a rate of 100 Hz for later analysis.

In addition to the HF bistatic links, we had supporting diagnostics, including optical sites at Duck, North Carolina, and Wallops Island, Virginia, a digital ionosonde at Wallops Island, and the Millstone Hill incoherent scatter radar. There were also *in situ* plasma diagnostics on the daughter payload that passed through the releases a few seconds (and kilometers) behind the release payload.

40-2

Time = 500.00

Ray30 of 3/25/86



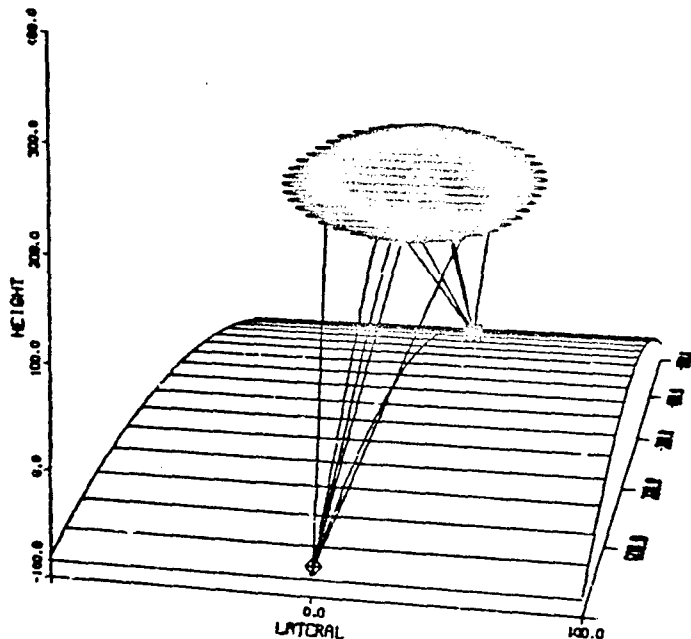
MACDATA  
INCLCC  
freq: 7.00  
RAY: ORD  
dip: 60.32  
fgy: 1.47  
APPLETON  
SS: 50.

shots:  
el az

	Lat	Long	Mhe
Pole	78: 0' 0"	-73: 0' 0"	
Transmitter	32: 0' 0"	-64: 0' 0"	BER
Disturbance	37:3028'	-74: 0' 0"	
Receiver	41: 8' 0"	-82:58' 0"	TOL
I-O-R-I	993.830	0.000	1968.220

FRAME  
09:57:14  
24-JUN-8

Figure 1. Rayfan through a pair of chemical releases seen in the plasma density contours.



81888 882885

Figure 2. Chemical depletion showing the formation of new propagation paths.

## NICARE

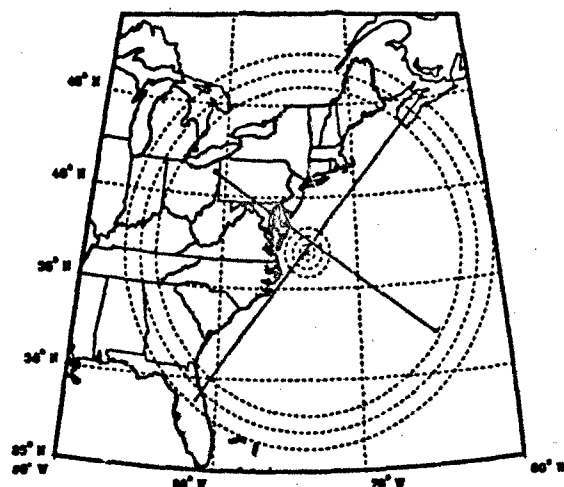


Figure 3. Map showing the two Hf transmission paths. The circle indicates the location and expansion of the second chemical release.

The first (nickel carbonyl) canister released its contents slowly, instead of in a burst as intended, so it did not produce the planned depletion. *In situ* measurements showed strong local depletion effects from both releases, and the Wallops Island ionosonde showed a new reflection following the  $\text{CF}_3\text{Br}$  release from the second canister, indicating that major ionospheric changes had occurred. Data from many of the diagnostics are still being analyzed.

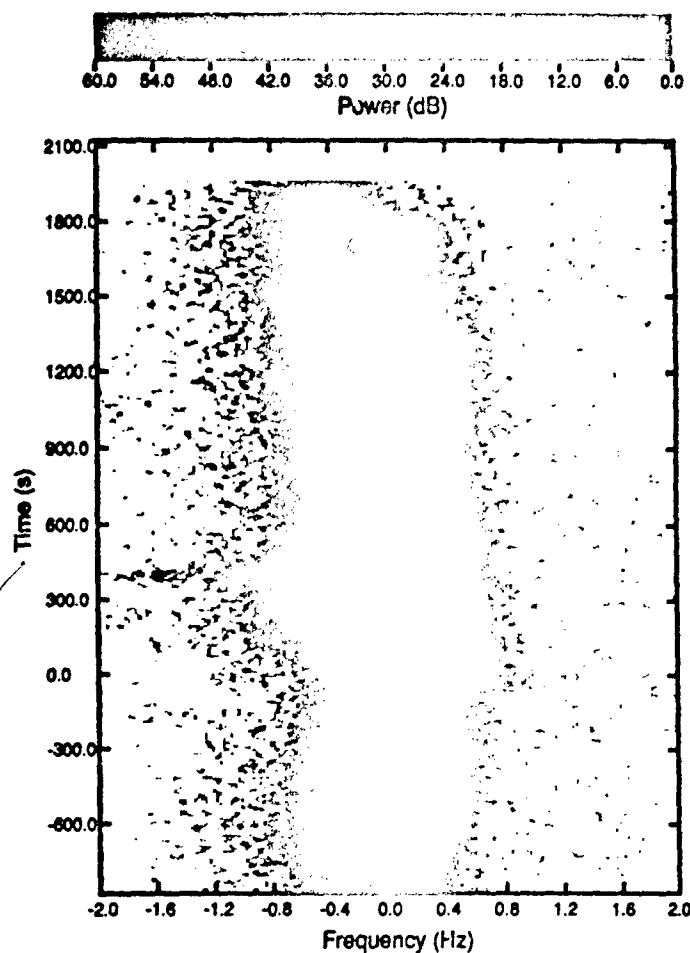
Treating our HF receiver arrays as radio telescopes and using Doppler filtering, we have been able to construct a fairly complete picture of the  $\text{CF}_3\text{Br}$  created depletion. In general, the release behaved as expected in that it appeared as a large focussing lens to our probe radio waves. As the depletion grew and filled in, it created new propagation modes on the Florida to Nova Scotia path, which interfered with signals following the original path and generated strong fadings. By using the spaced antennas at the receiver site we have been able to specify the arrival direction of the new signals, and in all cases they closely matched the model predictions.

#### DOPPLER SPECTRA ON FLORIDA-NOVA SCOTIA PATH

We analyze our cw signals by examining the time behavior of the Doppler power spectra. Time variations in the ionosphere result in small Doppler shifts of cw transmissions that depend on the exact ray path. Negative Doppler shifts correspond to increasing phase path. Multipath often appears as multiple peaks in the power spectra with different Doppler shifts for each component. The time variation of the centroid of the peak reveals the temporal evolution of the ionosphere along that particular ray. Moreover, weak modes may become apparent because they are Doppler shifted away from the more dominant modes. Our method of calculating the evolution of the Doppler power spectra is based on the short-term Fourier transform. We divide the total time series into sub-intervals (10-40 s) over which the spectra appear stable, and calculate the spectrum during that sub-interval. The length of the sub-interval is adjusted to give adequate frequency resolution without smearing produced by changes during the sub-interval. The sub-window is then advanced some fraction of its length and a new power spectrum calculated. The results may be visualized as a three dimensional grey scale plot which displays power as a function of frequency and time.

In this paper, we will only examine the data set for the Florida to Nova Scotia path beginning at 1:43:02 UT and extended to 2:32 UT. The second release occurred at 2:04:13, giving us approximately 26 minutes of data following release #2. A disturbance corresponding to a weak mode with a relative high chirped negative Doppler was observed almost immediately after the second release. This is illustrated in Figure 4, which displays the Doppler spectrum versus time after the rocket launch (1:58:00 UT). We used a 40 s sub-interval to calculate the spectrum every 6 s. The first mode associated with release #2 decreases in Doppler with time and it appears to cross the Doppler track of the preexisting modes at about 600 s, finally stabilizing at a Doppler of about 0.1 Hz. The spectral peak for this mode is broad, indicating that it is made up of at least two paths with slightly differing Doppler shifts.

The behavior of the spectra in Figure 4 indicates that release #2 produced new and relatively stable ray paths for at least 20 minutes. We note that there is a significant increase in signal strength after 600 s on the mode at about -0.2 Hz Doppler. A more detailed picture of the spectra



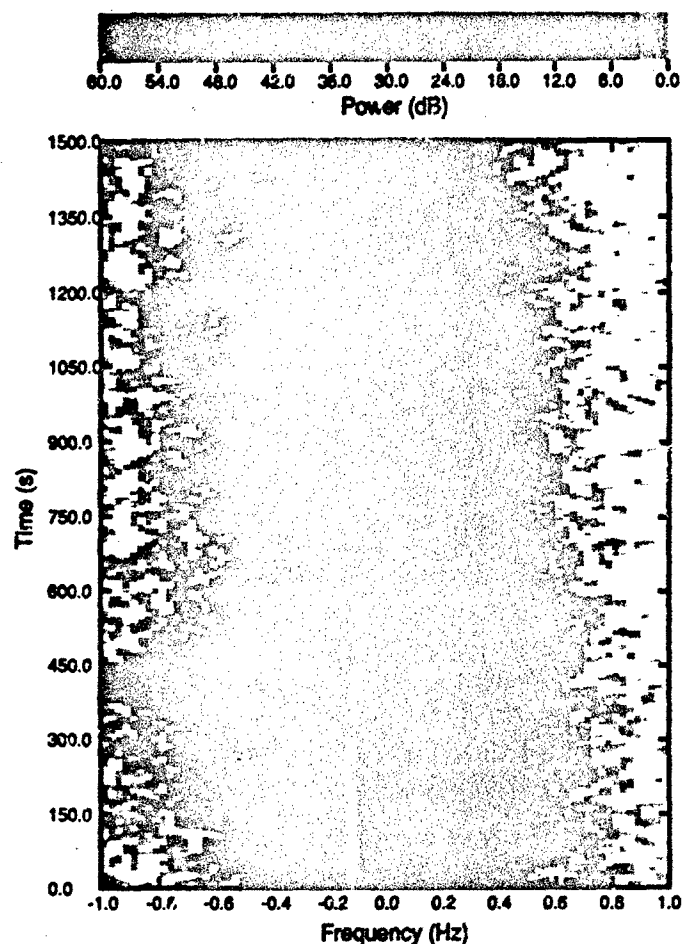
STANLEY/1:43 13.60MHZ CH0\$

Figure 4. Gray scale plot of the Florida to Nova Scotia data plotted as Doppler shift as a function of time, with 0 time being the time of rocket launch. The 60 db gray scale is shown at the top. The negative Doppler excursions at about 400 s result from the second release.

between 0 and 1500 s after launch is shown in Figure 5, where the spectra were calculated every 3 s using a 40 s window. There is a clear transition in the width of the spectra before and after the release; the width before the release is approximately 0.1 Hz while afterwards it is 0.3 Hz. We would expect to observe this effect as an increase in the fading rate after the release.

During the period before the launch, two peaks in the Doppler spectra with a separation of about 0.1 Hz indicate the presence of two modes, which we ascribe to low and high rays. We note that the transmission frequency was too high to support two-hop propagation, and it is also unlikely that two-hop sporadic E propagation would have been possible. No sporadic E was observed at this time period on the ionograms recorded at Wallops Island. The broad noise in the spectra at the 10 to 20 dB level surrounding the peaks is highly correlated between receivers and is likely to be produced by phase jitter on the Rubidium frequency standards [Jacobson, 1990].





STANLEY/1:43 13.60MHZ CH05

Figure 5. Same data as Figure 4 with slightly different processing, and expanded Doppler and time scales.

#### ANGLE OF ARRIVAL ON FLORIDA-NOVA SCOTIA PATH

The elements at each receiver station which shared a common frequency were phase coherent and therefore could be used as a synthesized radio telescope to determine angle of arrival. The Nova Scotia array (Figure 6) consisted of six elements with a maximum aperture of 764 m in the transverse direction and 365 m in the longitudinal direction. Since the nominal elevation angle for the Stanley receiver was about  $9^\circ$ , the effective meridional aperture was approximately 60 m. Because there was only one element off the transverse axis, the angle of arrival estimates are subject to aliasing (different elevation angles giving same phase).

Angle of arrival measurements obtained from the receiver array in Nova Scotia clearly indicate the production of azimuthal multipath following the second release. The signals from the various receivers have unknown phase shifts due to circuit and cable length differences; we therefore cannot determine absolute direction of arrival. However, when phase shifts are constant for the duration of a data set, we can determine relative angle of arrival. We select a time period during which the spectra are quiet and assume that the elevation angle is that given by ray tracing through a model ionosphere corrected using the Wallops Island ionograms. From the measured phase differences during this time period, we can find the relative phase changes needed to align the brightness to the nominal direction of arrival. We then correct the whole data set using these phase corrections, and our calculated directions of arrival will then be relative to this nominal ray.

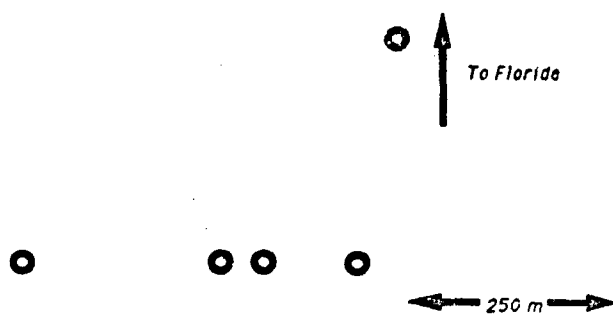


Figure 6. Schematic layout of the Stanley, Nova Scotia spaced receiver array.

For the Florida-Nova Scotia path we assume that the elevation angle of the nominal ray is  $9^\circ$ . Ray tracing indicates that the nominal ray would arrive from slightly west of the great circle path due to ionospheric tilts. We selected a time period from 100 to 200 s after launch, when the spectra showed only one major peak, to determine the phase correction. The brightness during that time period is shown in Figure 7; the peak in the lower center, just above the horizon, represents the ray; the duplicate peak at  $\sin(\eta) = 0.925$  is a grating pattern (usually called aliasing in time series data) caused by under sampling in the longitudinal direction. This could have presented an identification problem since this phantom peak cannot be distinguished from the real peak, but it is unlikely that rays would arrive with such a high elevation angle for the conditions during this experiment.

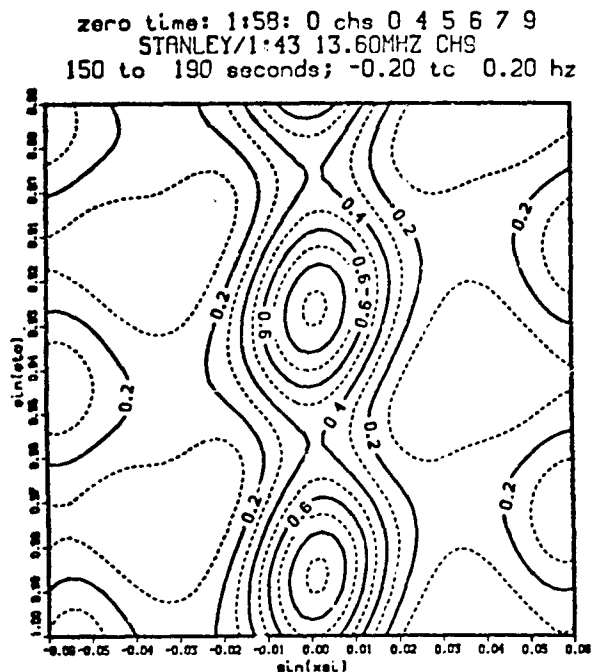


Figure 7. Brightness plot of the Stanley array data.  $\xi$  is the azimuth angle, with  $0^\circ$  directed toward the transmitter in Florida, and  $\eta$  is the zenith angle. The brightness peak in the lower center is the undisturbed ray, and the peak above it is a result of aliasing due to insufficient antenna coverage in the elevation axis.

We cannot obtain an accurate direction of arrival for the weak disturbance occurring immediately after the second release. However, once the power in the negative Doppler peak increases we can identify a direction distinctly to the east of the nominal path and at about the same elevation angle (Figure 8). This direction was obtained between 390 and 420 s after launch at Doppler shifts between -0.8 and -0.6 Hz. The peak near 0 Hz showed no significant change during that time. The direction of arrival of the new mode remained displaced to the east and at somewhat lower elevation angle compared to the nominal direction for several minutes. Thus the second release immediately formed a weak, rapidly varying path, with the negative Doppler shift indicating that the phase path was increasing. This new mode gradually decreased in Doppler shift while increasing in strength to form a relatively stable path arriving from the east of the nominal path. During approximately the first 175 s following the release the nominal path remained undisturbed, indicating that the release was in between the two ray paths and had a diameter of less than 40 km up to at least 175 s after release.

zero time: 1:58: 0 chs 0 4 5 6 7 9  
STANLEY/1:43 13.60MHZ CH9  
390 to 420 seconds; -0.80 to -0.60 hz

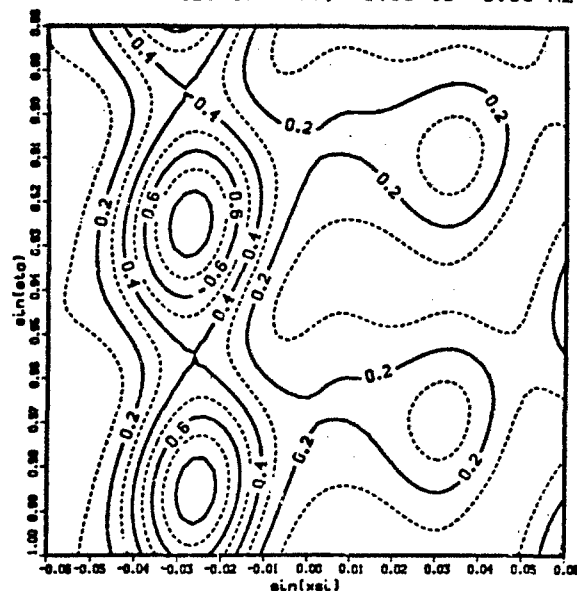


Figure 8. Negative Doppler peak with direction of arrival to the east of the nominal path and at about the same elevation angle. This direction was obtained between 390 and 420 s after launch at Doppler shifts between -0.8 and -0.6 Hz.

During the period from 550 to 650 s, the Doppler shifts of the two modes overlap so that filtering is impossible. The most likely interpretation of Figure 5 is that the modes cross during this time period, and this interpretation is consistent with the direction of arrival of the mode near 0 Hz Doppler between 750 and 800 s, which is displaced towards the east (Figure 9). The mode at about -0.1 Hz Doppler is displaced to the west (Figure 10) during that time period; 100 s earlier the same mode was displaced a somewhat lesser amount to the west (Figure 11). Apparently, by 750 s the new mode had stabilized in phase path so that the Doppler had decreased to almost 0 Hz, but the direction of arrival remained displaced to the east. Sometime after 550 s the original mode started being displaced to the west; the negative Doppler indicates a growing phase path consistent with such a displacement. Indeed, at 750 s there is a third mode displaced towards the east with a somewhat higher elevation angle than the other (Figure 12).

Between 750 and 1500 s the spectra are highly structured but consistently show modes displaced to the east as well as a mode that moves increasingly to the west with time. Apparently the eastward side of the depletion remained relatively stable while the westward side, after reaching the nominal path at about 550 s, continued to expand to the west for the duration of the data set. During the period from 1000 to 1500 s, the increasing displacement moved to the west with the speed of approximately 40 m/s transverse to the path. The directions of arrival of the most positive Doppler mode during the same period remained displaced to the east with a relatively low elevation angle.

zero time: 1:58: 0 chs 0 4 5 6 7 9  
 STANLEY/1:43 13.60MHZ CH9  
 750 to 800 seconds; -0.05 to 0.05 hz

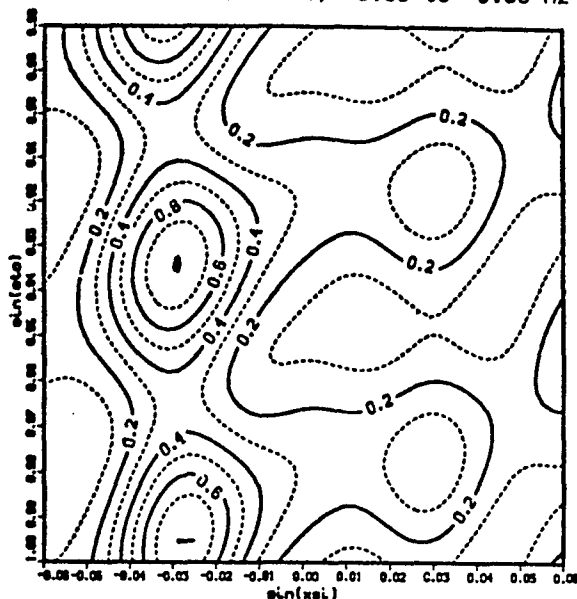


Figure 9. Direction of arrival of the mode near 0 Hz Doppler between 750 and 800 s, indicating displacement towards the east.

zero time: 1:58: 0 chs 0 4 5 6 7 9  
 STANLEY/1:43 13.60MHZ CH9  
 750 to 800 seconds; -0.20 to -0.10 hz

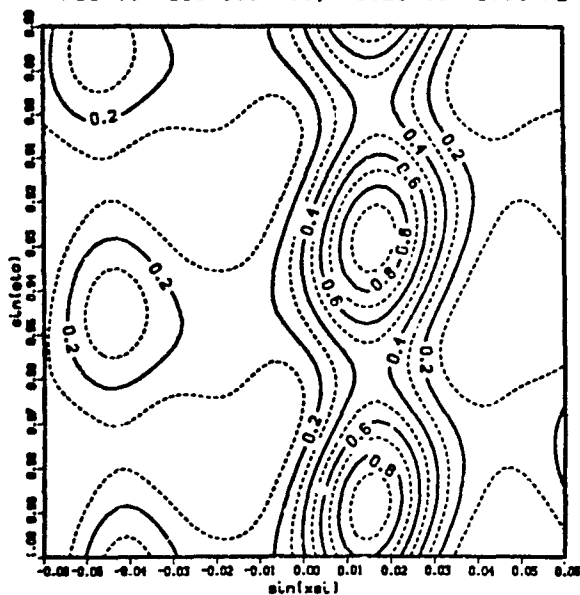


Figure 10. The mode at about -0.1 Hz Doppler showing displacement to the west during the 750 to 800 s time period.

zero time: 1:58: 0 chs 0 4 5 6 7 9  
 STANLEY/1:43 13.60MHZ CH9  
 650 to 700 seconds; -0.14 to -0.06 hz

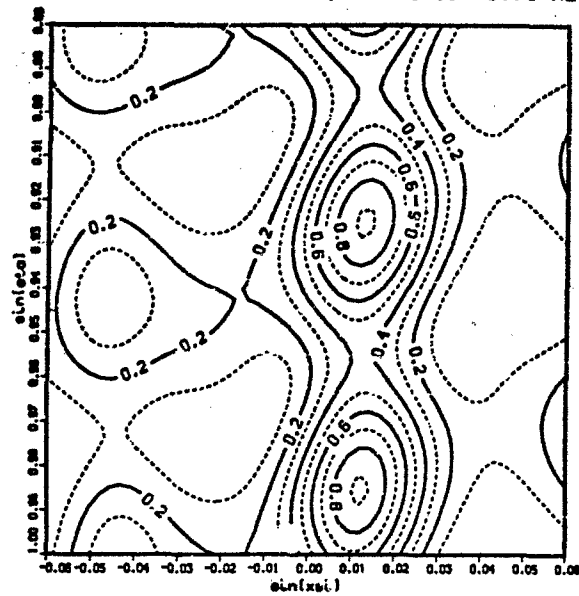


Figure 11. 100 s earlier the same mode was displaced a somewhat lesser amount to the west.

zero time: 1:58: 0 chs 0 4 5 6 7 9  
 STANLEY/1:43 13.60MHZ CH9  
 750 to 800 seconds; 0.05 to 0.15 hz

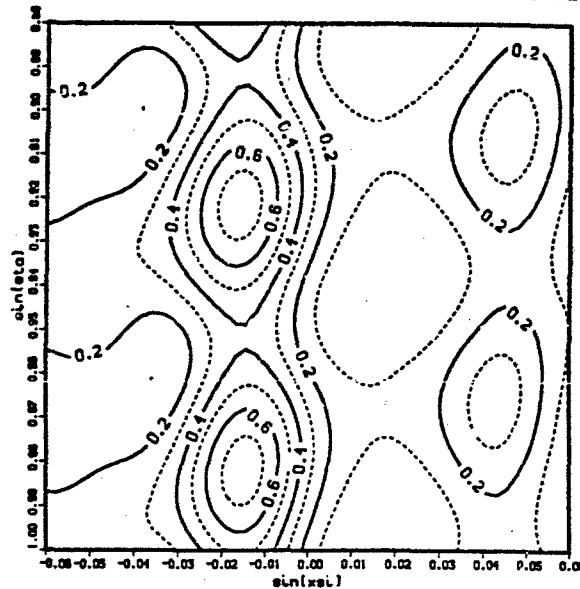


Figure 12. Indeed, at 750 s there is a third mode at 0.1 Hz displaced towards the east with a somewhat higher elevation angle than the other modes.

## DISCUSSION AND CONCLUSIONS

The first MICARE chemical release did not produce a wide spread ionospheric depletion due to failure of the canister release mechanism. The second release produced a significant ionospheric modification that lasted for at least 1200 s, and was seen by our HF diagnostic paths as well as the Wallops Island ionosonde. We have been able to construct a fairly complete picture of this depletion. In general, the release behaved as expected, in that it appeared as a large focussing lens to our probe radio waves. This lens created at least one additional HF path that passed around the east side of the depletion while the original path remained on the west side but was deflected by the expanding depletion. This experiment also demonstrated that our TRACKER code can successfully model ionospheric chemical depletions, as well as HF propagation through them.

## REFERENCES

- Bernhardt, P. A., Cross-S Convection of Artificially Created, Negative-Ion Clouds and Plasma Depletions: Low-Speed Flow, *Journal of Geophysical Research*, Vol. 93, No. A8, pp. 8696-8704.
- Hindmarsh, A. C., LSODE and LSODEI, two new initial value ordinary differential equation solvers, *ACM-SIGNUM Newsletter*, Vol. 15, No. 4, 1980, pp. 10-11.
- Jacobson, A. R., Los Alamos National Laboratory, Private communication, 1990.

## ACKNOWLEDGMENTS

This work was performed under the auspices of the U.S. Department of Energy.

## DISCUSSION

G. TACCONT, IT

Generally speaking, the artificial ionization (deterministic) you introduce in the natural medium (stochastic), should intentionally produce an improvement in the performances of a relevant transmission channel.

AUTHOR'S REPLY

Only under very special conditions would a chemical depletion guarantee an improvement in a transmission channel. In general, the multiple modes excited will create fading and decrease the performance of the channel.

ARMSTRONG, US

The modeling of ray paths suggests dominant rays from the edge of the depletion. Can this result be used to infer the ray path convergence in other locations and hence, the "lensing" efficiency of the depletion?

AUTHOR'S REPLY

The ray paths are selected by the model, and hence are very model dependent. The rays will meet very stringent conditions, including background modeled ionosphere, magnetic field, and modeled disturbance. This leads to the finite number of rays, whereas in the real case many more rays will find the right conditions. The model could be set to run a simple geometry to confirm "lensing". Our data, however, shows only a few rays that are Doppler separated.

## 46TH EPP SYMPOSIUM, BERGEN, NORWAY, 28 - 31 MAY, 1990

Bergen High Technology Center

LIST OF PARTICIPANTS

AFONSO, Capt. Antonio Jorge AFONSO, Direccao de Electrotecnica, CLAPA, Base de Alfragide, 2700 Amadora, PO

ALBRECHT, Dr. H.J. ALBRECHT, FGAN, Meuenahrer Strasse 23, D-5307 Vachtberg-Werthhoven, GE

ALVAREZ, Ing. Antonio SEGURA ALVAREZ, INTA, Departamento P. Especiales, Carretera de Ajalvir 8/N, Torrejon de Ardoz, Madrid, SP

ARMSTRONG, Dr. W.T. ARMSTRONG, SST-7, MS D466, Los Alamos National Laboratory, Los Alamos, NM 87545, US

BANKS, Prof. Peter M. BANKS, STAR Laboratory/Durand 202, Stanford University, Stanford, CA 94305-4055, US

BARR, Dr. R. BARR, Max-Planck Institut für Aeronomie, Postfach 20, D-3411 Katlenburg-Lindau 3, GE

BELROSE, Dr. John S. BELROSE, Director, Radio Prop. Laboratory, Communications Research Center, PO Box 11490, Station N, Ottawa, K2N 8S2, CA

BERSON, Dr. Robert F. BERSON, Code 692, Goddard Space Flight Center, Greenbelt, MD 20771, US

BENZINGER, Mr. J. BENZINGER, W.T.O 81, D-223, D-8547 Greding, GE

BERNHARDT, Dr. Paul A. BERNHARDT, Code 4780, Naval Research Laboratory, Washington, DC 20375-5000, US

BLANC, Dr. Elisabeth BLANC, Commissariat à l'Energie Atomique, Laboratoire de Détection et de Géophysique, BP 12, 91680 Bruyères-le-Châtel, FR

BRANDT, Dr. Richard G. BRANDT, Office of Naval Research, Code 1112, 800 N. Quincy Street, Arlington, VA 22217, US

BREKKE, Prof. Asgeir BREKKE, INR, University of Tromsø, N-9000 Tromsø, NO

BRUNELLI, Lt. Col. P.A. BRUNELLI, AGARD, EPP Executive, 7, rue Ancelle, 92200 Neuilly sur Seine, FR

BURKE, Dr. William J. BURKE, Geophysics Laboratory/Space Physics, Laboratory, Hanscom AFB, MA 01731, US

CANNON, Dr. Paul S. CANNON, Applied Ionospheric Physics Lab., Flight Management Department, Royal Aerospace Establishment, Farnborough, Hampshire, GU14 6TD, UK

CARATORI, Dr. Julien CARATORI, L.E.T.T.I., S.P. 16, 94230 Cachan, FR

CARLSON, Dr. Herbert CARLSON, Geophysics Laboratory / LI, Hanscom Air Force Base, Hanscom AFB, MA 01731, US

CASSARA, Lt. Col. A. CASSARA, Aeronautica Militare DASE/RASA, 00040 Pratica di Mare, IT

CHESTERFIELD, Mr. S.R. CHESTERFIELD, FPC 117, British Aerospace (Dynamics) Ltd, PO Box 5, Filton, Bristol, BS12 7QW, UK

CHRISTOPHE, Mr. P. CHRISTOPHE, Dept. Micro-Ondes, ONERA-CERT, BP 4025, 31055 Toulouse Cedex, FR

CRESCIMBENI, CDR Fernando CRESCIMBENI, Mariteleradar, Viale Italia 72, 57100 Livorno, IT

CROSIGNANI, Prof. B. CROSIGNANI, Università di Roma, Dipartimento di Fisica, Piazzale A. Moro, 2, 00185 Roma, IT

DARNELL, Prof. M. DARNELL, Dept. of Electronic Engineering, University of Hull, Hull, HU6 7RX, UK

DUNCAN, Dr. Lewis M. DUNCAN, Assoc. Dean College of Sciences, Clemson University, Clemson, SC 29634-1901, US

FIELD, Dr. Edward C. FIELD, Jr., Pacific-Sierra Research Corporation, 12340 Santa Monica Boulevard, Los Angeles, CA 90025, US

FLOOD, Dr. Valter A. FLOOD, Director, Geosciences Div., US Army Research Office, PO Box 12211, Research Triangle Park, NC 27709, US

FRASER-SMITH, Dr. Anthony C. FRASER-SMITH, STAR Laboratory Durand 202, Stanford University, Stanford, CA 94305-4055, US

GRICOPoulos, Dr. B. GRICOPoulos, Hellenic Air Force, Research Technology Center -  
 KETA, Post Office Terpsithea, 16501 GlyfaDa, Athens, GR  
 GONCALVES, Mr. Carlos A. GONCALVES, Instituto Nacional Meteorologica e Geofisica,  
 Rua C de Aeroporto, 1700 Lisboa, PO  
 GORDON, Dr. W.E. GORDON, Rice University, PO Box 1892, Houston, TX 77251, US  
 GRIFFITHS, Mr. W.Y.G. GRIFFITHS, C/o Dr. P.B. Cannon, Flight Management Dept., Royal  
 Aerospace Establishment, Farnborough P 161 Bldg, Farnborough GU14 6TD, UK  
 HANSEN, Mr. Alfred HANSEN, The Auroral Observatory, University of Tromsø, PO Box  
 953, N-9001 Tromsø, NO  
 BECKESCHER, Mr. J.L. BECKESCHER, Geophysics Laboratory / LID, Hanscom Air Force Base,  
 Hanscom AFB, MA 01731-5000, US  
 HØEG, Dr. P. HØEG, Danish Meteorological Institute, Svanemøllens Kaserne, Bygn-1,  
 DK-2100 Copenhagen, DE  
 HÖHN, Dr. D.H. HÖHN, Director, Forschungsinstitut für Optik, FOM, Schloss  
 Krossbach, D-7400 Tübingen, SE  
 HORTENBACH, Dr. E.J. HORTENBACH, Deutsche Welle, PO Box 100 444, D-5000 Köln 1, GE  
 INAN, Dr. Umut S. INAN, STAR Laboratory Durand 321, Stanford University, Stanford,  
 CA 94305-4055, US  
 JESKE, Prof. Dr. H. JESKE, University of Hamburg, Meteorologisches Institut,  
 Bundesstr. 55, D-2000 Hamburg 13, GE  
 JODALEN, Ms. Vivianne JODALEN, N.D.R.E., PO Box 25, N-2007 Kjeller, NO  
 JONES, Prof. T.B. JONES, Physics Department, University of Leicester, University  
 Road, Leicester, LE1 7RH, UK  
 KESKINEN, Dr. M.J. KESKINEN, Code 4781, Naval Research Laboratory, Washington, DC  
 20375-5000, US  
 KOSSEY, Dr. Paul A. KOSSEY, Geophysics Laboratory/LID, Hanscom AFB, MA 01731-5000,  
 US  
 KUO, Prof. S.P. KUO, Weber Research Institute, Polytechnic University, Route 110,  
 Farmingdale, NY 11735, US  
 LAI, Dr. S.T. LAI, Geophysics Laboratory, PHK, Hanscom AFB, MA 01731-5000, US  
 LEE, Dr. M.C. LEE, Plasma Fusion Center (NV 1-234), Massachusetts Institute, of  
 Technology, Cambridge, MA 02139, US  
 LEFEUVRE, Dr. F. LEFEUVRE, C.N.R.S., Laboratoire de Physique et Chimie, de  
 l'Environnement, 3A, Av. de la Recherche Scientifique, 45071 Orléans Cedex, FR  
 NAERLUM, Dr. B.H. NAERLUM, Norwegian Defence Research Est., PO Box 25, 2007 Kjeller,  
 NO  
 NJØLHUS, Dr. E. NJØLHUS, I.M.R., University of Tromsø, 9000 Tromsø, NO  
 NOURENAS, Dr. D. NOURENAS, C.N.R.S., Laboratoire de Physique et Chimie, de  
 l'Environnement, 3A, Av. de la Recherche Scientifique, 45071 Orléans Cedex, FR  
 NULDREW, Mr. D.B. NULDREW, Communications Research Center, Dept. of Communications,  
 PO Box 11490, Station 'N', Ottawa, Ontario K2H 8S2, CA  
 NOBLE, Dr. S. T. NOBLE, SPC, NASA Road 1, Suite 100, Houston, TX 77058, US  
 ØYTA, Mr. ØYTA AYUNU, Statens Telfervaltning, PO Box 2592 Solli, 0203 Oslo 2, NO  
 OSSAKOV, Dr. Sidney L. OSSAKOV, Superintendent, Plasma Physics Div., Naval Research  
 Laboratory, Code 4700, Washington, DC 20375-5000, US  
 PAPADOPOULOS, Dr. K. PAPADOPOULOS, University of Maryland, 3705 Raymond Street,  
 Chevy Chase, MD 20815, US  
 PATRICIO, Ing. J.F. PATRICIO, Rua Alferes, Barrilero Ruas No 1, 8 Dt, 1800 Lisboa,  
 PO  
 PATTANAYAK, Dr. Deva N. PATTANAYAK, GE Corporate Research & Development, KVC 604, PO  
 Box 8, Schenectady, NY 12301, US  
 PAUL, Dr. Adolf K. PAUL, Code 542, Naval Ocean Systems Center, San Diego, CA  
 92152-5000, US  
 PROCHASKA, Mr. R.D. PROCHASKA, FTD / VE, Wright-Patterson AFB, OH 45433-6508, US



RASMUSSEN, Mr. John E. RASMUSSEN, Geophysics Laboratory / LIR, Hanscom Air Force Base, Hanscom AFB, MA 01731, US  
 RICHTER, Dr. Juergen M. Richter, Head, Ocean and Atmospheric Sciences Division, Code 54, Naval Ocean Systems Center, San Diego, CA 92152-5000, US  
 RIETVELD, Dr. Michael T. RIETVELD, EISCAT, N-9027 Ramfjordbotn, NO

RIPIN, Dr. Barrett M. RIPIN, Naval Research Laboratory, Space Plasma Branch, Code 4780, Washington, DC 20375-5000, US  
 ROGGE, Mr. J. ROGGE, Royal Military Academy, PO Box 90154, 4800 RG Breda, NE

RYCROFT, Dr. M.J. RYCROFT, British Antarctic Survey, Madingley Road, Cambridge CB3 0ET, UK

SALES, Dr. Garry S. SALES, University of Lowell, Center for Atmospheric Research, Lowell, MA 01854, US

SCHWEICHER, Prof. Dr. E. SCHWEICHER, ERN, Chaire OM, 30, Avenue de la Renaissance, B-1040 Bruxelles, BE

SHANNY, Dr. Romy A. SHANNY, President, ARCO Power Technologies, Inc. Suite 850, 1250 24th Street N.W., Washington, DC 20037, US

SHOUCRI, Dr. M. SHOUCRI, TRW-R1/2120, One Space park, Redondo Beach, CA 90278, US

SHOWEN, Dr. R.L. SHOWEN, SRI International 30160, 333 Ravenswood, Menlo Park, CA 94025, US

SKAUG, Mr. B. SKAUG, Norwegian Defence Research Establishment, Division for Electronics, PO Box 25, N-2007 Kjeller, NO

STOCKER, Mr. A.J. STOCKER, Physics Department, University of Leicester, University Road, Leicester, LE1 7RH, UK

STORKE, Mr. Knut M. STORKE, S.T.F., PU Box 2592, Seili, 0203 Oslo 2, NO

STROENSES, Mr. Odbjorn STROENSES, Navy Material Command, N-5078 Naakonsvern, NO

TAAHNOLT, Mr. J. TAAHNOLT, Danish Polar Center, Haeusergade 3, DK-128 Copenhagen K, DE

TACCONI, Prof. G. TACCONI, Universita' di Genova, Dip. Ingegneria Biofisica, Via all'Opera Pia 11/A, 16145 Genova, IT

TOKER, Prof. Dr. C. TOKER, Dept. of Electrical Engineering, Elektrik Muh. Bolumu, ODTU Ankara, TU

TORUN, Capt. E. TORUN, Ministry of Defence - NSB, Research and Development Dept., ARGE, 06650 Ankara, TU

VISSINGA, Ir. B. VISSINGA, van Kempenstraat 30, 2252 VM Voorsooten, NE

VLAHAKIS, Capt. Georgios VLAHAKIS, Hellenic Air Force - KETA, Post Office Thessalonika, 16501 Glyfada, Athens, GR

WOLCOTT, Dr. John H. WOLCOTT, SST-7, MSD466, Los Alamos National Laboratory, Los Alamos, NM 87545, US

WALLACE, Mr. T.M. WALLACE, 1250 24th St., NW STE 850, Washington, DC 20037, US

YAVUZ, Dr. D. YAVUZ, SHAPE Technical Center, COM/R, PO Box 174, 2501 CD Den Haag, NE

YEN, Prof. K.C. YEN, Everitt Laboratory, University of Illinois, 1406 W. Green Street, Urbana, IL 61801-2991, US

YUKON, Dr. Stanford P. YUKON, RADC / EECF, Hanscom AFB, MA 01731-5000, US

## ROUND TABLE DISCUSSION

L. DOWMAN (US): Radio science and ionospheric effects have traditionally been affiliated with military applications for many, many years, including telecommunications, radars, and other forms of remote sensing, although those applications have not always been anticipated. In the spirit of the comments which Prof. Gordon gave in the opening session, it behooves us to recognize that we live in a world where political changes and associated changes in military posture and missions are evolving much faster than anyone could have anticipated even just a few years ago, and that it's inevitable that those changes will have some influence on military applications for RF and other forms of ionospheric modification. We should begin to think about how those changes might affect what we're doing. With respect to ionospheric physics changes (our future that we can look forward to) and new opportunities that are coming up in the next few years that we're aware of, I think we should recognize that this meeting is in some sense a transition, from ionospheric modification being a multidisciplinary science to one which is becoming more interdisciplinary. Although that sounds like semantics, we have had in this room all week presentations, not only from the "heaters", (the RF ionospheric modification people), but also from the chemical release community, the wave injection (particularly VLF) community, and even the beam injection people represented primarily in the talk of Dr. Banks. So we're seeing that the community in a sense is coming together a little, including both the physics and chemistry of RF heating, other RF heating, the microwave work of artificial ionization, beams, chemicals, and wave injections.

All of this is at a time when there are new facilities becoming available within the next decade. In the HF world, we're seeing possible upgrades to Arecibo, definite upgrades to be completed very soon at EISCAT, and a transition of the EISCAT heating facility into the more general EISCAT community; the opportunity that was never there before to make use of facilities in the Soviet Union to extend both the power and the frequency range in which some of those experiments can be conducted; new facilities being talked about in Alaska in the next few years; use of nondedicated facilities like the Voice of America transmitting site; and even further down the road, perhaps the possibility of microwave breakdown experiments using Arecibo or a more dedicated facility.

In the chemical release world, there are many new opportunities coming. One that has been mentioned several times during this symposium are the CRES releases which will be both from sounding rockets and satellites this coming summer. Others include a new rocket range being built in Puerto Rico in conjunction with the Arecibo observatory, and the opportunity for satellite experiments, not only for chemical releases, but using space platforms for beam injections and wave injections. I hope members of those communities will present their future plans in more detail than this quick summary has.

In nonlinear physics, speaking mainly to the high power RF community, one of the very hot topics in the coming years will be to address the issues associated in the debate of what's really happening. Is it weak turbulence, or are most of the phenomena we are seeing a result of strong laminar turbulence? Tremendous theoretical gains over the last several years have now challenged the experimentalists to go out and prove what's actually happening. I look for rapid advances in that area, and full well believe that once the dust has settled, we'll find that there are no winners or losers, but that weak and strong laminar turbulence are contributing in different regimes to the variety of phenomena we see. Similarly, nonlinear plasma physics questions are going to need to be addressed in experiments like AIM. This artificial ionization cloud, were we ever to produce it in the atmosphere, clearly could have a number of instabilities that we haven't anticipated.

And finally, it was a pleasure to hear us discuss at this meeting some of the environmental questions which are coming up, questions that we haven't asked ourselves very often in the past. We're becoming more aware of putting significant amounts of power up into the atmosphere, that we have in the past waved our hands and said that if everything seems to recover within some often undefined time scale after we turn it off, it must be okay. But we are beginning to get to critical regimes, both in terms of ionospheric modification by high power radio waves and the ability to deposit large amounts of chemicals. If P. Bernhardt were here, he would tell you, so in his absence I will, that he has gone through an extraordinary list of exotic chemicals that might be deposited, and environmental concerns are important there. Again, I would like to hear from the beam and wave injection communities -- their thoughts on the matter. But it's a pleasure to hear that we're beginning to ask the right questions about the environmental consequences, both EM and true atmospheric environmental effects, of our experiments. And so with those opening remarks I would like to open the floor to comments from the audience as to where they think the physics of ionospheric modification is going in the coming years.

R. BENSON (US): I would like to respond and make a few comments pertaining to wave injection from space vehicles. As was mentioned after P. Banks' talk, there are still plans to do a WISP (Waves In Space Plasmas) experiment. The portion that is being planned is the high frequency portion. This is really designed as an experiment to study certain plasma physics and geophysics problems in space on a short time scale where we are looking for specific solutions to specific questions. What really seems to be needed in addition to this, in the long range, is something that's in a monitoring nature. Dr. Albrecht, toward the end of his talk, made several points: the number one requirement is to monitor the state of the ionosphere, to know what it's like, what conditions can we expect for propagation, and if modification is necessary, we usually have to start from that point, and can know how to modify it. Now this problem of monitoring often comes up in meetings I attend. In fact I think it was the AGARD meeting in Munich where the topic of geophysical monitoring

and the need for such monitoring to know the state of affairs was discussed. It's always hard, at least from my experience through the NASA end, to try to get any program approved that has anything to do with monitoring, because usually things are geared toward specific physics -- you have to go out and solve a specific problem. I think that there is a need for something like the topside sounder program that we had in the Alouette/ISIS days, to monitor the ionosphere on a global nature. Ironically, the great success of the Alouette/ISIS program -- I think there are over 50 satellite-years of sounder data available -- has almost been a kiss of death for trying to get something like that approved in the future. When one talks about any program in the future to do more ionospheric modeling, the question is, "Well you know you have so many millions and billions of ionograms, why do you need any more?" The other point is something D. Muldrew reminded me of earlier, that the amount of power from a topside sounder at a distance of about 1 km is equivalent to the radiated power deposited in the F-region from a ground-based heater. Many of the plasma phenomena excited by the ISIS satellites occur well within that 1 km region, so there is a lot of interesting plasma physics that can be studied in regions where the field strengths are much stronger than those from ground-based heaters. If there is some way we can sell this to get missions of that type going, it would be good for global morphology and also for ionospheric physics related to specific ionospheric modification problems. The problem is, to try to get any sounder on a satellite with passive instruments is almost impossible, because the passive people do not like an active instrument on board. What's really needed is a dedicated system where the primary thing is the sounder. And I think maybe we should think in the future of somehow trying to get back to those days again when we can have a state-of-the-art sounder designed with present day equipment.

L. DUNCAN (US): Bob, let me respond to something that you reminded me of. The challenge, maybe even greater than the one you described, is on the chemical release side, at least in the US. The latest announcement of opportunity that came out of NASA specifically excluded chemical releases which were to be used for basic plasma physics studies in which the upper atmosphere was a plasma lab. So the basic physics side of active experiments often falls through the cracks somewhere between applications and those who identify their mission as studying the atmosphere as it exists and not as a laboratory. Both in terms of topside sounders and some other active experiments, it's very hard to sell to some of the funding agencies.

D. PAPADOPOULOS (US): Listening to you and to Bob, one thing that comes to mind in terms of wave plasma interactions and issues of strong and weak turbulence, is the commonality of this subject in terms of electron beam injection, in terms of ionospheric modifications, and in terms of wave injection in space. Now we went through a long period in the '70s in which we debated whether weak or strong turbulence was the relevant issue in beam plasma interactions. Finally it turned out that strong turbulence dominated in almost every case that we could measure the data. Weak turbulence was almost a set of measure zero. Even in Type III radio bursts with  $10^{-5}$   $n_{beam}/n_{plasma}$  density ratio, strong turbulence dominated. There is a lot of understanding that can be directly transferred because in the beam plasma interaction you have a very long wave which is electrostatic, but long waves, electrostatic or electromagnetic, behave similarly; that's the dipole approximation. The thing we didn't have there is the density gradient. In the experiments that can be done with the means that Bob is suggesting, you have the injection of a high frequency wave without the gradient, and you can study both decay instabilities and strong turbulence in a homogeneous medium. And then the strong/weak turbulence issues come along. And then finally, in the experiments in Arecibo and the other HF facilities, the strong turbulence is induced mainly because of the large fields created at the reflection point. The Scandinavian experiments should provide us also with the opportunity of studying that in an underdense fashion in terms of the  $2\omega_u$  underdense Raman scattering. So all I wanted to point out was the commonality that runs through all these subjects.

L. DUNCAN (US): I might point out I was pleased to see a talk at this meeting that was a unified theory of turbulence by Dr. Mjølhus who talked about how weak and strong Langmuir turbulence might actually be described in a common framework which I think is a promising step forward.

M. KESKINEN (US): I have three comments on what I have heard this week, particularly in the HF area. One is that I think the theory of HF interactions in the ionosphere is not well developed and is way behind the laboratory plasma physics community. There is some crossover that Dennis [Papadopoulos] has talked about, that we might take from the small scale laboratory plasmas and transfer to the space plasmas, but there is very little nonlinear work that has been done for the large scale plasmas, particularly in the thermal self-focusing instabilities, etc. It is very crucial to make some more gains in this area. A second comment is that when you have small scales you have very short time scale phenomena, and when you have large scales you can have very long time scale phenomena. The connection between the two, how they interact and how you bring a unified picture into the program is going to be very important in the next few years. The third point is we really have to know what the natural ionosphere is doing before we turn the heater on, especially at high latitudes, and how one might affect the naturally occurring irregularities with the heater and vice versa, and try to come up with some kind of a self-consistent analysis of the problem. Those three areas I think are going to be very important in the next few years and we at NRL are looking in all these areas. In terms of theoretical advances, that is where they are going to be made.

L. DUNCAN (US): I would like to second your last comment, which was that high latitudes are going to be tough. We could fill volumes with irreproducible results obtained at Arecibo where the ionosphere is relatively calm, so at high latitudes where the environment is a lot more variable it's going to be really tough to decipher what's happening.

**T. JONES (UK):** I really must take exception with those last comments. I think one of the things that has not come across in this meeting, and I'm very disappointed that it hasn't, is the tremendous amount of work that has been done at Tromsø. We've been heating the ionosphere at Tromsø for almost eight years now. We are well aware of the things that you have just mentioned. We are well aware that the preconditioning of the ionosphere is important. I would take objection with you that the theory of HF interaction is not well understood; I think it is well understood. I think it is a great shame that the German group has not shown up here. I think if P. Stubbe, and Kopka, and the people from Lindau were here, you would have heard a lot more about that kind of work. So I really do see a danger here of the work that has been done at Tromsø being ignored and the whole "wheel" being rediscovered in Alaska, and I think that is a very dangerous situation to get in. I think the papers that have been published, particularly in JAGP, are not well known on the other side of the Atlantic, and I think the people involved in the planning really ought to look very hard at what has been published, all in the open literature I might say, using the highlighted heater. It's a great shame that the Germans aren't here.

**L. DUNCAN (US):** I think, Tudor, that Mike's [Kasinen] comments were primarily directed toward the theoretical side of what's been done, basically that there hasn't been the parallel computer simulations, numerical simulations, that have gone on in beam plasma work.

**T. ARMSTRONG (US):** With regards to some of the new facilities that are being talked about, in the context of what you were saying, Levin, about a changing political and therefore defense related environment, what character would the new facilities take? One thing I'm hearing that distracts me a little is that they're focused for a particular application and not necessarily for versatility. I would suggest two areas that haven't been mentioned here that would be new horizons and that would require some versatility in the new facilities. An AIM facility has been discussed primarily in the context of a reflecting layer, while a new HF heating facility would be primarily an ELF generation instrument. Both of these facilities, if they were to be built with their higher power capabilities, have the potential first of doing beat wave heating at plasma resonances on the topside of the ionosphere, which I find an especially intriguing possibility, with different density gradients and different conditions than have been previously accessible. Second, if the HF facility is high enough in frequency, and if the AIM facility (if it were UHF) had good phase coherence, both could be considered as potential radars for accessing much higher altitudes, up into the magnetosphere. Both these possibilities I think are extremely intriguing, are within the realm of operation of these new facilities, and should be considered. (Ref: Thidé, HISCAT Proposal, Swedish Institute of Space Physics).

**M. SHOUCRI (US):** I'll make two comments along the lines similar to both M. Kasinen and T. Jones. Experimentalists for the past few years have refined techniques that were developed over the last 10-15 years, so what people do for plasma line measurements in 1990 is completely different than what used to be done in 1974. There has been great experimental development done both in Tromsø, and in Arecibo and other places. However, I think we've hit a limit from the experimental point of view by the fact that we're limited to the ground and more specifically to the backscatter condition, where we sit down there and look at what's going on at a finite frequency at a finite wavelength, looking at 35 km structures, and ignoring completely what may in reality be happening in the ionosphere. I'll just take two examples to make my point. There is need for more comprehensive types of experiments, where simultaneous measurements are done, backscattered yes, but also bistatically and specifically from space. There's a great need for some kind of ionospheric type of satellite, or a shuttle type of flight, that can do simultaneous measurements of what's happening in the ionosphere while the radar is measuring backscatter on the ground. That kind of three dimensional information, that can measure spatial and temporal evolution, can then go and lead the theoretician as to whether indeed thermal self-focusing is due to micro effects or macro effects; this is one example as far as ionospheric modification. A second example would be ELF generation, where for years now we've been sticking up loops anywhere from 10 to 500 km from where the modification region is. For ELF purposes, this is near field. If we indeed would like to know if we do generate ELF, one would think of what happened for instance with, I think it was, the ISIS or the GEOS satellite where Gordon James captured the ducted waves on the satellite. You would then go to global measurements, go to the conjugate point, go under the transmitter, go to all such places and make simultaneous measurements to really validate a system of that type. So here are two examples that tell you we've reached a limit if we keep doing the same type of experiments that we've been doing so far. Incidentally in ionospheric modification, again to the credit of the Europeans, the HERO experiments generated an incredible wealth of information from in-situ measurements, and we should head in that direction as a suggestion for the future.

**T. JONES (UK):** Could I just comment on that? I don't want to be blowing trumpets about Tromsø and the facility there, but the HERO experiment is a good one. There are two rocket ranges there. There is Andoya and Esrange. The instrumented rockets have been flown through the heater, a volume to measure electric fields and some particle precipitation and energies and so on. We have EISCAT which is the only tristatic incoherence scatter radar in operation at the present time which gives you good handles on electric fields which you can't measure elsewhere. We have the STARE system, and SABRE can look into that area, and also we have all the usual ground-based instrumentation. So I don't think you can say that that system is under-instrumented. Maybe we're not doing the right experiments, but certainly the facilities are there.

**L. DUNCAN (US):** A comment I would like to add in addition to Merit's [Shoucri], and that is next summer, summer of 1991, when the rocket range is installed in Arecibo, there will be a series of eight or nine rockets flown during the campaign. Six or seven will be CRRES, and another two rockets are non-CRRES. Four of the CRRES chemical releases and one instrumented rocket which is not officially part of the CRRES campaign will all fly through

RTD-4

the heater volume, and are in fact HF experiments. There is one rocket inappropriately named the SOLITON rocket that Mike Kelley and I are on and Los Alamos is on as well. It's intended to take very rapid measurements as you fly through the heater volume. One of the problems with measurements of HF effects from space, at least from a satellite, is that you go through the heater volume very quickly and so it's important that allowance is made for very fast data rates. One of the limitations of the past was, some of the interesting physics is on very small scales that were not previously resolved.

**W. IKAN (US):** I think what I want to say is relevant to what Lewis [Duncan] talked about: wave injection. Dr. Armstrong talked about versatility of the systems that you put together and opportunities for international collaboration that are now facilitated in the present climate, and I would like to announce to the community an initiative that Stanford is in the process of putting together, and has been for the last year and a half, which involves an international ELF/VLF wave injection facility in Antarctica. This is a really major undertaking for us. We're in the process of putting together a proposal, and have already demonstrations of significant support from our Soviet colleagues and colleagues also from Japan and the UK. We had a workshop at Stanford last year, and we put together a report which is available which describes the detailed scientific opportunities in the area of wave-particle interactions, heating of the lower ionosphere, heating of the upper ionosphere at altitudes of 1000 km or so which leads to production of ion conics which is a subject that wasn't discussed here of course but is very interesting in terms of the coupling between the ionosphere and magnetosphere. Basically, the facility involves antennas strung out on the Antarctic ice (about 3000 m thick) and the antennas are 200 km long. There are five of them separated by 20 km which operate at frequencies as low as 500 Hz; it's resonant at 500 Hz. And I think it is an alternative scheme for generating ELF -- not too low in the ELF range, but at 500 Hz and above. By varying the antenna length, it can be made to operate at higher frequencies all the way up to 500 kHz. So I think the ability to inject rays over a wide spectrum into the ionosphere and look at their effects will be there, and I would like very much for members of this community to participate in this. We are in the process of putting together proposals; we're envisioning a facility like EISCAT that will be usable by members of the community; and we hope that we will get funding support for this from the Division of Polar Programs. I hope also that nations that are participating are going to get their own funding. So if you have any questions, please let me know.

**J. BELROSE (CA):** Stanford University has been carrying out experiments like that for the past decade. What new do you expect to learn?

**W. IKAN (US):** That's a very good question. The past experiment was basically a demonstration of capability of doing this conjugate experiment at 5 kHz to basically 2.5 MHz and at very minimal radiated power, in the range of 1 to 3 kW. What we are now aiming at is a very substantial increase in that radiated power, by factors of ten or more, so we are talking about 40 kW at 5 kHz. Predictions are that precipitation of particles from the radiation belts at L-shells of four to five will become feasible very easily within the parameter ranges that we have, so we can produce artificial aurora and investigate the response of the ionosphere to the artificial aurora. We can study the generation of lower hybrid rays at altitudes of 1000 km and look at ion conics. We can look at possible triggering of AKR for example. There is a wide range of scientific issues that were not addressed by the previous facility, and I would like to talk to you more about those and send you the report.

**D. YAVUZ (ME):** I'm not an expert in this area. I'm on the periphery of the physics communication engineer, but I would like to pose the following question to those of you who are involved with the modeling of the nonlinear aspects. All the effects that we are talking about in this symposium are highly nonlinear effects, and as you probably know, in the last 5-6 years there's been a revolution in the analysis of nonlinear dynamical systems. It goes sort of under the name of "chaos" but it's actually far more revolutionary and fundamental than that; that nonlinear coupled equations have a behavior in which the phase space produces fractal trajectories, which then indicates that some of these nonlinear phenomena which we thought were predictable in the short term, like weather patterns, like precipitation initiation in the meteorological sense, are now known to be physically impossible from that analysis, from a theoretical viewpoint. This also implies that unless you are able to define the initial conditions almost to an infinite resolution, you cannot predict the performance or the evolution of that particular nonlinear phenomena. These are just beginning to be emerging from the work of people like Leon Choi at Berkeley and some of the other people working in nonlinear dynamics. I would like to know your comments on whether you feel that perhaps somebody should look, or perhaps somebody is looking at this effect, and that these highly nonlinear effects have some chaotic trajectories in phase space that perhaps indicate some of the work is being done unnecessarily or without understanding the chaotic nature of the coupling effects.

**M. KESKINEN (US):** Some of the parametric instabilities that have been invoked in ionospheric heating have also been studied in laboratory plasmas, in particular laser fusion plasmas; these have been looked at initially in terms of nonlinear dynamics and chaotic behavior. Particularly at the University of Maryland several people have looked at it there, and some other places also. I don't think it's been applied to the ionospheric case, but it can very easily be.

**D. PAPAIOPOULOS (US):** We do have an active program of chaotic studies of ionospheric responses, and today actually, I was supposed to be giving an invited talk at the AGU on exactly that subject with respect to the AE index and the KP index; one of my colleagues is giving it because I am here. There are a lot of things that are very, very important and it's not so much the unpredictability. By looking up [certain factors] of the AE index, for example, we can find out the length of predictability. We can find out the substorm

time scales. These methods right now are being used very, very effectively in understanding the coupling of the solar wind to the magnetosphere and to the ionosphere. That's one part. On the micro physics we have looked that the collapse essentially is a chaotic phenomenon, namely when the wave turbulence  $W/n_p$ , where  $n_p$  is the plasma density, exceeds one-ninth, then what you end up with is a very chaotic behavior, and a very broadband signal comes out of that due to exactly chaos, so it is not neglected. I think we have about five people working right now at the University of Maryland on that area.

L. DUNCAN (US): Very good, that was a nice question as well. Now perhaps we can move on toward the more applied side of all of this.

J. BELROSE (CA): I'll start with a few remarks. My remarks will be slanted to my own personal feelings and from a Canadian point of view. Canada is a high latitude nation. In fact we own a significant part of the disturbed ionosphere. The dip pole and the L-shell or corrected geomagnetic pole both lie in Canada. Ionospheric modification is not my field of expertise, except I know quite a lot about the basic physics of the phenomena because the subject and I have been around for quite a long time. But this doesn't stop me from making a few remarks. I guess I can't lose too much. If I say something foolish, this perhaps will stimulate some discussion. If I should manage to make it say something provocative, this will also stimulate perhaps even more interesting discussion. I intend to address not the physics of the phenomena, but mainly the application of it, and from a Canadian high latitude point of view.

We at the Communications Research Center in Ottawa, have tried very hard to get in to this subject field for a number of years. When I say "tried very hard," I mean from a ground-based experimental point of view. Gordon James together with Don Muldrew have looked at interactions of waves in space from the ISIS and Alouette satellites, and Don Muldrew has participated in analysis of Arecibo data. We intended to do the Fejer type of experiment, to measure electron densities in the D-region. But in 1961 when we turned on our relatively low power then, 100 kW transmitter, feeding a 4-dipole antenna array, the first day we turned it on, lo and behold there was no ionospheric echo. In fact there was only one echo from 45 km. We were right in the middle of a major solar proton event which had extended as far south as Ottawa. I can assure Dr. Papadopoulos there are going to be many occasions in sunspot maximum years when his superb method of painting ELF antennae in the sky just won't work because his paintbrush won't get there. In the final development of the 2.66 MHz system which I just referred to a moment ago, we had a 40-dipole antenna array and powers up to 1 MW and durations up to 10 ms. Ten millisecon was the largest capacity that our power supply could handle. We had an estimated radiated power of 80 dBW. We had other operating frequencies: 4.6 and 6.2 MHz. The latter employed a 100 kW transmitter and 128-dipole array. At Ft. Churchill we had at this frequency a 100 kW transmitter and 128-dipole array. We could measure electron density profiles and winds in the mesosphere. We never observed wave interaction effects, although we did try. We looked at pulse distortion (We thought perhaps there might be something interesting in this). For the 2.66 MHz transmitter, we didn't need to use a receiver, and the transmitter was a perfectly trapezoidal pulse so we could connect an oscilloscope to the antenna, and at full power, the E-region echo was running around a third to half a volt across the input terminals of the oscilloscope, so there was no distortion in the receiver from the pulse. We increased the powers up from the 100 kW to 1000 kW of transmitter power, and while the edges of the pulse did round a little bit, there was nothing exciting in that. We looked for the third harmonic which might be generated in the ionosphere, but there was no detectable third harmonic. We sat at the foot of the field line that passed through the heated region and looked with our maximum transmitter pulse duration, 10 ms, and full transmitter power. We used a 440 MHz transmitter: 1 kW feeding 32, and in the ultimate end, 64 ten-element Yagis. Jules Fejer had speculated that sitting at the foot of the field line we might see these plasma resonance lines many dB stronger. Well we saw no discernable signal. So much for our attempts; it was a bit disappointing.

Bragg scatter has been mentioned in this meeting a number of times; it's very aspect sensitive, and if we produce field-aligned irregularities in Canada which one can Bragg scatter VHF/UHF signals from, field lines in Canada are almost vertical, and there's nowhere in Canada where we could in fact set a transmitter and receiver and see reflections from these field-aligned irregularities. If we did have a powerful heating source in Canada, we would produce reflectors for our neighbors to the south, the US, who might find something interesting in this. All this leads me to the general remark: wave interaction is a very interesting subject. A great deal has been learned about it, and we've heard some of it at this meeting, particularly about the plasma, using it as a tool to measure the plasma, and about energetic particle precipitation. But from a communications point of view, I wonder if there's anything practically applicable.

My particular interests, I guess, are sort of in the possibility of ELF generation. Getting the signals to the places where they need to be at the electrojet is going to be impossible under a number of occasions on sunspot maximum years because of polar cap absorption events, and in other years due to high energetic electron precipitation, relativistic electron events, which produce ionization so low down that any transmitter power which we've used in Canada (and I've mentioned some of them) have not produced reflections from the ionosphere on many occasions. The possibility of using VLF transmitters we heard from the Maryland group, wasn't a very good method of producing ELF because the signals wouldn't get to the height where they needed to get to, to use the electrojet as an antenna. But I wonder how thoroughly founded that kind of an observation is, and have we really looked at the ideal experimental situation where you have a VLF transmitter running a megawatt of power at the highest latitude at which VLF transmitters exist at the present time, and you are transmitting on a pair of frequencies whose separation might be something of the order

RTD-6

of 100 Hz. I guess to be useful we have to know, "Is it detectable?" Well certainly it is, or certainly it would be, but is the amplitude useful, and would it be there for a significant amount of time? From a point of view of a researcher in the high latitude region, it doesn't look to me like there is a great future for ionospheric modification being useful for a communication means.

D. PAPADOPOULOS (US): The point I want to make is with respect to wanting to put the energy where we have to. There is no reason to put the energy at 90 km if I have a lot of electrons at 50 km. The beauty of the ELF generation is that if I have a lot of electrons at 50 km, even if it won't go to 90 km, it will be absorbed at 50 km; it will modulate, and it will give me as much power as I would have gotten at 90 km. All I need is an electric field -- an electric field of the order of a few millivolts per meter which is very, very low and has very high probability of occurring. Actually under nuclear conditions, I will have the best ELF generation system ever because I will have a lot of electrons low down, so I do not believe that this is a restriction. With respect to really getting the whistler range, the low frequency range up, I believe that it's a very good idea to be looked at, and especially with respect to the bit excitation, because the Manley-Rowe relations are very, very good for that possibility. We have not looked into that point in detail.

T. JONES (UK): I would like to take up something that J. Belrose mentioned in his presentation. I think it has been somewhat of a disappointment to me, personally, in this meeting that we have spent most of our time, as far as systems are concerned, talking about OTH systems and introducing the artificial mirrors, and we've talked a lot about ULF generation. We have not talked very much about anything else at all, and I think there are many more things you can do with ionospheric modification than just those two possible applications. For example, we did hear a little bit about lenses; I know L. Duncan, for example, has done much work on lenses and introducing HF signals into ionospheric ducts, the generation of new ducts, and the long distance, low attenuation propagation of HF waves in ducts, and the uses that one can put these kinds of propagation to. I just wondered if there were people in the audience who felt, like I do, that perhaps we should have opened this up to a much more wide ranging discussion as far as the applications are concerned than we have done.

G. TACCONI (IT): About the communication aspect in application, we can consider for instance a medium, or the space like a medium, as a part of a communication channel. The modification with a deterministic procedure of this development of the medium can probably produce certain efficient effects in the improvement of the final transmission channel. So I wonder whether some artificial modification could be introduced into the, generally speaking, "transmission channel" in order to improve the communication properties of the channel.

R. SPANNEY (US): I think Dr. Jones brought out very well that Tromso has done a large number of experiments which are extremely well funded compared to US efforts. In order to get funding in the US at this time, I believe that one has to come up with applications. Like Dr. Jones said, we have to come up with things which are specific. The Defense Department is not willing to pay a lot of money to enhance most communication system capabilities, and most ionospheric work does demand quite a bit of money. ELF and OTH radars are two areas where more monies could be spent. The ionospheric community has not come up with enough applications through the years, and that's the only way that there will be support for it. Otherwise it will just be research for semi-random individual physics issues, without the methodical approach behind it, and we are not going to get anywhere. Hopefully the Europeans will keep getting funded and we can moderate our own sponsors in the States to maybe come up to speed.

W. GORDON (US): I would like to make two points. First, responding to the last comment about the applications that come out of the work that the community does. I thought we had agreed that the basic studies that have gone on over the years have produced military systems, communication systems, that have been remarkably useful in Canada, in high latitudes, across Europe and many other places, that are still in use in some cases and have had spin-offs into the commercial world that matter. The other point I would like to make has to do with the spin-offs. One of the most important communication applications may, in fact, be satellite communication and the TV news that's carried by satellite communication worldwide where you can see the events taking place in Tienanmen Square, in Dresden, in Romania, wherever. That I think is the most powerful force for peacekeeping that there is. And it may be a twist of the military purpose, but if the military has a function to defend us and to defend a peaceful world, it seems to me that this is an important contribution that they have made through years of contributing to what amounts to basic science.

T. JONES (UK): Yes, can I just add one comment, not to what W. Gordon has just said, but just going back one step. One of the interesting things that people who work in satellite-to-ground systems are concerned with is scintillation, both in amplitude and in phase, and one of the techniques that they have recently been very concerned with is what is known as ionospheric tomography. This is essentially the transfer of medical imaging techniques to the ionosphere. It is similar to brain scanning, and with the placement of a number of sensors you can do the same thing with the ionosphere: you put a number of receivers on the ground, you have a satellite as your source, and then you measure the image on the ground of the scintillators. Now why hasn't anybody done this for the heated volume? I mean this seems such an obvious thing to do that I would have thought somebody, especially the satellite people amongst us, would have come up with ideas of imaging both the RF heating and perhaps the chemical releases. The application of tomography techniques, I would have

thought, would have been a good thing to do both from a scientific point of view and an applications point of view.

**P. ROSEY (US):** With regard to a subject that Tudor Jones briefly mentioned earlier, there are plans in the US to use a heater to generate field-aligned irregularities in the ionosphere for the purpose of scattering HF signals from ground-based transmitters into and out of elevated ionospheric ducts. The ducts are located around 250 km altitude in the ionosphere, and are not usually accessible to ground-based HF signals, because of their normal propagation angles. The use of the heater-generated irregularities will provide a controlled mechanism for accessing the ducts. Observations of the signals will be made on a satellite that will be launched sometime in the next year or so. Such issues as the efficiency of coupling HF energy into and out of ducts and the propagation characteristics of HF waves in elevated ducts, including such things as attenuation rates and HF bandwidths that can be sustained, will be investigated. The temporal and spatial characteristics of the ducts will also be studied. Such data will be useful in assessing the potential for exploiting ducted HF modes for long range communication and surveillance applications. The program is being conducted by the US Air Force's Rome Air Development Center.

**ARMSTRONG (US):** With regards to tomography, just a month ago at the Ionospheric Effects Symposium in D. C., there were several papers given about the theoretical modeling of that and description of a system. There is no hardware in place for it yet, but certainly there is thought going on in that area, and is prime and ready to go.

**A. FRASER-SMITH (US):** I just want to make a sort of general comment based on Tudor's (Jones) observation that we may not have had as many people here as we could have talking ionospheric modification. In fact I've been very impressed with the big community of people here talking ionospheric modification. In fact I have been following ionospheric modification for many years since I worked on the Platteville heater array in Colorado. But one thing I have noticed over the many years since I did become involved is that although there is a big community of interest, there is no formal manner in which in which this can express itself; we all act as individuals doing our various bits and pieces. Now, it so happens that I am Associate Editor of the journal Radio Science, and one thing I think would be interesting would be a special issue in which there might be some overview papers dealing with the progress of ionospheric modification over the years, with some other smaller papers pointing out the future of various activities in this area, so that there will be in one location, something dealing generally with ionospheric modification. Now I am not trying to compete with the AGARD Proceedings, which I think would be very valuable, but this would be more of a series of overview type things for people interested in radio science generally. I'm just talking about this -- it would have to be taken up by the editor, Allen Waterman -- but if there is interest, I'm sure he would consider taking some action on that.

**T. JONES (UK):** Let's say something to that. Most of you are aware of the Suzdal meetings that are held every two years, one year in the Soviet Union and one year in Western Europe, organized by the Soviets and by our German colleagues at the Max Planck Institute, Lindau who actually built and operated the Tromsø heater. So I think there is this very important meeting every two years on ionospheric modification and I think the proceedings of that meeting are available. There have now been two or three of these meetings and I think they have been very successful meetings, although I've never been to them.

**L. DUNCAN (US):** Maybe I could clarify that, because the proceedings are not published from that, but the papers are available. This is the year for that meeting, but it will not be held because of the General Assembly. It has been delayed a year, and so the Suzdal meeting, which normally would have fallen on this year, will be held next year, and plans are well under way; Prof. Gordon is also one of the organizers of that symposium. It's a special forum primarily for heating, RF ionospheric modification, although we were just discussing today that it may well be appropriate to broaden the scope. The next meeting outside of the Soviet Union may well be held at Arecibo or someplace. It is not strictly Western Europe although the last meeting was held in Tromsø.

**J. BELROSE (CA):** I would like to return, before we close this afternoon, to my comment about generating ELF using a VLF transmitter. It suddenly occurred to me, after I stopped speaking, that the station, Cutler, in Maine, in fact has two antennas. I believe that the transmission system is in fact duplicated. I believe there are two 500 kW transmitters which can be operated in parallel into both antennas. Presumably they could operate, if we could persuade the US Navy to do so, a 500 kW transmitter into each antenna system, in other words, transmit on a pair of frequencies separated by an ELF frequency. Also, I would like to make one comment about the paper by Dr. Noble and Gordon. The one thing that was particularly noticeable in the slides that we saw was the insignificant small size of the coils which were used in that receiver. I know a little bit about receiving ULF and ELF signals because we've looked at it. In fact we've built equipment in Canada to do that kind of thing. Some people use a device called a SQUID magnetometer which uses cryogenically cooled coils so as to get enormous sensitivity. We've always been of the opinion that you didn't need to go to that extent, but on the other hand, we have used in receiving systems that we've built, antennas which are significantly large compared to what we saw in the photograph, as used at Arecibo. If I can recall the numbers correctly, maybe not exactly, we use one meter loops; we had crossed loops (in general we use crossed loops so we can measure in the two planes). They were aircore loops, and they had something like 640 turns of copper wire on them. You could hardly lift one of the loops. You had to be awfully careful with them so that there would be no wind-induced noise whatsoever. They sort of had to be on sandy soil and not shake too much. The house about them mustn't touch them so that they had to have no wind-induced noise whatsoever. In other words, one does need



RID-8

to take a great deal of care, and I think Dr. Noble had suggested that, in fact, they were going to look at the sensitivity of their system. My feeling is, without looking at the numbers, just at the pictures, is that the sensitivity was perhaps not quite adequate, although he did say that they could see human resonances and things like that. Anyway, I would urge perhaps if there is any interest in the US -- NRL people or whoever -- to maybe at least think of the possibility of the Cutler, Maine station transmitting on a pair of frequencies during certain intervals of time.

S. Noble (US): These sensors actually were compared with the SQUIDS and in this band they are every bit as sensitive.

W. KRAM (US): I'm quite interested in your comment, Jack [Belrose], because we have already talked to Gracen Joiner to use the Cutler, Maine transmitter to generate both ELF and ULF. We can go, I think, with the present modulations available on it, as far as 30 Hz, but this idea of using two generators to drive them separately with maybe 100 Hz or so separation is also a good one. I don't know that Gracen will be able to do this for us, but I have already written to him and discussed in detail the use of NAA. We have used it in the past, so I don't see a problem with it, but that's the appropriate transmitter to use indeed.

P. ROBERT (US): I don't want to speak for the Navy, but in the 1970s I believe that they tried such an experiment, using the NAA transmitter in Cutler, Maine. I'm not sure of the overall results, but I believe they have been reported in open reports out of the Naval Research Laboratory.

L. DUNCAN (US): Unless there is anyone with a burning issue, we'll close the panel discussion and move on to the closing ceremonies.

REPORT DOCUMENTATION PAGE			
1. Recipient's Reference	2. Originator's Reference	3. Further Reference	4. Security Classification of Document
	AGARD-CP-485	ISBN 92-835-0590-5	UNCLASSIFIED
5. Originator	Advisory Group for Aerospace Research and Development North Atlantic Treaty Organization 7 rue Ancelle, 92200 Neuilly sur Seine, France		
6. Title	IONOSPHERIC MODIFICATION AND ITS POTENTIAL TO ENHANCE OR DEGRADE THE PERFORMANCE OF MILITARY SYSTEMS		
7. Presented at	the Electromagnetic Wave Propagation Panel Symposium held in Bergen, Norway, 28th—31st May 1990.		
8. Author(s)/Editor(s)	Various		9. Date October 1990
10. Author's/Editor's Address	Various		11. Pages 490
12. Distribution Statement	This document is distributed in accordance with AGARD policies and regulations, which are outlined on the Outside Back Covers of all AGARD publications.		
13. Keywords/Descriptors	<div style="display: flex; justify-content: space-between;"> <div> Ionospheric modifications Heating processes Artificial mirrors </div> <div> ULF-ELF-VLF OTH communications </div> </div>		
14. Abstract	<p>The propagation medium is, in effect, an integral part of many military systems. For the most part, interest in the propagation medium has been focussed on identifying and quantifying the limitations it imposes on systems, rather than on ways it might be altered, or controlled. The results of on-going theoretical and experimental research show potential for modifying selected regions of the ionosphere in order to affect radio wave propagation. A variety of modification techniques are being investigated, both ground- and space-based, to increase or decrease existing ionization or to create independent artificial plasmas. These techniques include high power radio waves, lasers, particle beams, and chemical releases. In addition, recent developments in high power RF sources raise concerns over system limitations due to self induced anomalous absorption, ray path deviation and clutter. These proceedings present the current state of ionospheric modification technology, with emphasis on potential applications for enhancing or degrading the performance of military communications, surveillance and navigation systems.</p>		

<p>AGARD Conference Proceedings No.485 Advisory Group for Aerospace Research and Development, NATO IONOSPHERIC MODIFICATION AND ITS POTENTIAL TO ENHANCE OR DEGRADE THE PERFORMANCE OF MILITARY SYSTEMS Published October 1990 490 pages</p> <p>The propagation medium is, in effect, an integral part of many military systems. For the most part, interest in the propagation medium has been focused on identifying and quantifying the limitations it imposes on systems, rather than on ways it might be altered, or controlled. The results of on-going theoretical and experimental research show potential for modifying selected regions of the ionosphere</p> <p>P.T.O.</p>	<p>AGARD-CP-485</p> <p>Ionospheric modifications Heating processes Artificial mirrors ULF-ELF-VLF OTH communications</p>	<p>AGARD Conference Proceedings No.485 Advisory Group for Aerospace Research and Development, NATO IONOSPHERIC MODIFICATION AND ITS POTENTIAL TO ENHANCE OR DEGRADE THE PERFORMANCE OF MILITARY SYSTEMS Published October 1990 490 pages</p> <p>The propagation medium is, in effect, an integral part of many military systems. For the most part, interest in the propagation medium has been focused on identifying and quantifying the limitations it imposes on systems, rather than on ways it might be altered, or controlled. The results of on-going theoretical and experimental research show potential for modifying selected regions of the ionosphere</p> <p>P.T.O.</p>	<p>AGARD-CP-485</p> <p>Ionospheric modifications Heating processes Artificial mirrors ULF-ELF-VLF OTH communications</p>
<p>AGARD Conference Proceedings No.485 Advisory Group for Aerospace Research and Development, NATO IONOSPHERIC MODIFICATION AND ITS POTENTIAL TO ENHANCE OR DEGRADE THE PERFORMANCE OF MILITARY SYSTEMS Published October 1990 490 pages</p> <p>The propagation medium is, in effect, an integral part of many military systems. For the most part, interest in the propagation medium has been focused on identifying and quantifying the limitations it imposes on systems, rather than on ways it might be altered, or controlled. The results of on-going theoretical and experimental research show potential for modifying selected regions of the ionosphere</p> <p>P.T.O.</p>	<p>AGARD-CP-485</p> <p>Ionospheric modifications Heating processes Artificial mirrors ULF-ELF-VLF OTH communications</p>	<p>AGARD Conference Proceedings No.485 Advisory Group for Aerospace Research and Development, NATO IONOSPHERIC MODIFICATION AND ITS POTENTIAL TO ENHANCE OR DEGRADE THE PERFORMANCE OF MILITARY SYSTEMS Published October 1990 490 pages</p> <p>The propagation medium is, in effect, an integral part of many military systems. For the most part, interest in the propagation medium has been focused on identifying and quantifying the limitations it imposes on systems, rather than on ways it might be altered, or controlled. The results of on-going theoretical and experimental research show potential for modifying selected regions of the ionosphere</p> <p>P.T.O.</p>	<p>AGARD-CP-485</p> <p>Ionospheric modifications Heating processes Artificial mirrors ULF-ELF-VLF OTH communications</p>

<p>in order to affect radio wave propagation. A variety of modification techniques are being investigated, both ground- and space-based, to increase or decrease existing ionization or to create independent artificial plasmas. These techniques include high power radio waves, lasers, particle beams, and chemical releases. In addition, recent developments in high power RF sources raise concerns over system limitations due to self induced anomalous absorption, ray path deviation and clutter. These proceedings present the current state of ionospheric modification technology, with emphasis on potential applications for enhancing or degrading the performance of military communications, surveillance and navigation systems.</p> <p>Papers presented at the Electromagnetic Wave Propagation Panel Symposium held in Bergen, Norway, 28th—31st 1990.</p> <p>ISBN 92-835-0590-5</p>	<p>in order to affect radio wave propagation. A variety of modification techniques are being investigated, both ground- and space-based, to increase or decrease existing ionization or to create independent artificial plasmas. These techniques include high power radio waves, lasers, particle beams, and chemical releases. In addition, recent developments in high power RF sources raise concerns over system limitations due to self induced anomalous absorption, ray path deviation and clutter. These proceedings present the current state of ionospheric modification technology, with emphasis on potential applications for enhancing or degrading the performance of military communications, surveillance and navigation systems.</p> <p>Papers presented at the Electromagnetic Wave Propagation Panel Symposium held in Bergen, Norway, 28th—31st 1990.</p> <p>ISBN 92-835-0590-5</p>
<p>in order to affect radio wave propagation. A variety of modification techniques are being investigated, both ground- and space-based, to increase or decrease existing ionization or to create independent artificial plasmas. These techniques include high power radio waves, lasers, particle beams, and chemical releases. In addition, recent developments in high power RF sources raise concerns over system limitations due to self induced anomalous absorption, ray path deviation and clutter. These proceedings present the current state of ionospheric modification technology, with emphasis on potential applications for enhancing or degrading the performance of military communications, surveillance and navigation systems.</p> <p>Papers presented at the Electromagnetic Wave Propagation Panel Symposium held in Bergen, Norway, 28th—31st 1990.</p> <p>ISBN 92-835-0590-5</p>	<p>in order to affect radio wave propagation. A variety of modification techniques are being investigated, both ground- and space-based, to increase or decrease existing ionization or to create independent artificial plasmas. These techniques include high power radio waves, lasers, particle beams, and chemical releases. In addition, recent developments in high power RF sources raise concerns over system limitations due to self induced anomalous absorption, ray path deviation and clutter. These proceedings present the current state of ionospheric modification technology, with emphasis on potential applications for enhancing or degrading the performance of military communications, surveillance and navigation systems.</p> <p>Papers presented at the Electromagnetic Wave Propagation Panel Symposium held in Bergen, Norway, 28th—31st 1990.</p> <p>ISBN 92-835-0590-5</p>

**AGARD**

NATO  OTAN

7 RUE ANCELLE - 92200 NEUILLY-SUR-SEINE

FRANCE

Téléphone (1)47.38.57.00 - Telex 610 176

**DIFFUSION DES PUBLICATIONS**

**AGARD NON CLASSIFIEES**

L'AGARD ne détiens pas de stocks de ses publications, dans un but de distribution générale à l'adresse ci-dessus. La diffusion initiale des publications de l'AGARD est effectuée auprès des pays membres de cette organisation par l'intermédiaire des Centres Nationaux de Distribution suivants. Ces Centres disposent parfois d'exemplaires additionnels; dans les cas contraire, on peut se procurer ces exemplaires sous forme de microfiches ou de microcopies auprès des Agences de Vente dont la liste suit.

**CENTRES DE DIFFUSION NATIONAUX**

**ALLEMAGNE**

Fachinformationszentrum,  
Karlsruhe  
D-7514 Eggenstein-Leopoldshafen 2

**BELGIQUE**

Coordonnateur AGARD-VSL  
Etat-Major de la Force Aérienne  
Quartier Reine Elisabeth  
Rue d'Evere, 1140 Bruxelles

**CANADA**

Directeur du Service des Renseignements Scientifiques  
Ministère de la Défense Nationale  
Ottawa, Ontario K1A 0K2

**DANEMARK**

Danish Defence Research Board  
Ved Idrættsparken 4  
2100 Copenhagen Ø

**ESPAGNE**

INTA (AGARD Publications)  
Pinar Rosales 34  
28008 Madrid

**ETATS-UNIS**

National Aeronautics and Space Administration  
Langley Research Center  
M/S 180  
Hampton, Virginia 23665

**FRANCE**

G.N.E.R.A. (Direction)  
29, Avenue de la Division Leclerc  
92320, Châtillon sous Bagneux

**GRECE**

Hellenic Air Force  
Air War College  
Scientific and Technical Library  
Dekelia Air Force Base  
Dekelia, Athens TGA 1010

**ISLANDE**

Director of Aviation  
c/o Flugrad  
Reykjavik

**ITALIE**

Aeronautica Militare  
Ufficio del Delegato Nazionale all'AGARD  
3 Piazzale Adenauer  
00144 Roma EUR

**LUXEMBOURG**

Voir Belgique

**NORVEGE**

Norwegian Defence Research Establishment  
Attn: Biblioteket  
P.O. Box 25  
N-2007 Kjeller

**PAYS-BAS**

Netherlands Delegation to AGARD  
National Aerospace Laboratory NLR  
Kluuyverweg 1  
2629 HS Delft

**PORTUGAL**

Portuguese National Coordinator to AGARD  
Gabinete de Estudos e Programas  
CLAFIA  
Base de Alfragide  
Alfragide  
2700 Amadora

**ROYAUME UNI**

Defence Research Information Centre  
Kentigern House  
65 Brown Street  
Glasgow G2 8EX

**TURQUIE**

Milli Savunma Bakanligi (MSB)  
ARGE Daire Bakanligi (ARGE)  
Ankara

LE CENTRE NATIONAL DE DISTRIBUTION DES ETATS-UNIS (NASA) NE DETIENT PAS DE STOCKS  
DES PUBLICATIONS AGARD ET LES DEMANDES D'EXEMPLAIRES DOIVENT ETRE ADRESSEES DIRECTEMENT  
AU SERVICE NATIONAL TECHNIQUE DE L'INFORMATION (NTIS) DONT L'ADRESSE SUIT.

**AGENCES DE VENTE**

National Technical Information Service  
(NTIS)  
5285 Port Royal Road  
Springfield, Virginia 22161  
Etats-Unis

ESA/Information Retrieval Service  
European Space Agency  
10, rue Mario Nikis  
75015 Paris  
France

The British Library  
Document Supply Division  
Boston Spa, Wetherby  
West Yorkshire LS23 7BQ  
Royaume Uni

Les demandes de microfiches ou de photocopies de documents AGARD doivent comporter le numéro de série AGARD, le titre, le nom de l'auteur ou du rédacteur-coordonnateur et la date de publication. Les demandes adressées au NTIS doivent comporter le numéro matricule NASA du rapport. Des références bibliographiques complètes ainsi que des résumés des publications AGARD figurent dans les journaux suivants:

Scientific and Technical Aerospace Reports (STAR)  
publié par la NASA Scientific and Technical  
Information Branch  
NASA Headquarters (NTI-40)  
Washington D.C. 20546  
Etats-Unis

Government Reports Announcements (GRA)  
publié par National Technical Information Services.  
Springfield  
Virginia 22161  
Etats-Unis



Imprimé par Specialized Printing Services Limited  
40 Chigwell Lane, Loughton, Essex IG10 3TZ

**AGARD**

NATO  OTAN

7 rue Ancelle • 92200 NEUILLY-SUR-SEINE  
FRANCE

Telephone (1)47.38.57.00 • Telex 610 178

**DISTRIBUTION OF UNCLASSIFIED  
AGARD PUBLICATIONS**

AGARD does NOT hold stocks of AGARD publications at the above address for general distribution. Initial distribution of AGARD publications is made to AGARD Member Nations through the following National Distribution Centres. Further copies are sometimes available from these Centres, but if not may be purchased in Microfiche or Photocopy form from the Sales Agencies listed below.

**NATIONAL DISTRIBUTION CENTRES**

**BELGIUM**

Coordonnateur AGARD - VSL  
Etat-Major de la Force Aérienne  
Quartier Reine Elisabeth  
Rue d'Evere, 1140 Bruxelles

**LUXEMBOURG**

See Belgium

**NETHERLANDS**

Netherlands Delegation to AGARD  
National Aerospace Laboratory, NLR

**CANADA**

Director Sci  
Dept of Natl  
Ottawa, Ont



National Aeronautics and  
Space Administration

Postage on Post Paid  
National Aeronautics and  
Space Administration  
NASA-61

Official Business  
Penalty for Private Use \$300



**DENMARK**

Danish Def  
Ved Idraets  
2100 Copenhagen

Washington, D.C.  
20548

**SPECIAL FORTH COMING MAIL  
BOOK**

**FRANCE**

O.N.E.R.A.  
29 Avenue  
92320 Chât

L4 001 AGARDCP485910116S002672D  
DEPT OF DEFENSE  
DEFENSE TECHNICAL INFORMATION CENTER  
DTIC-FDAC  
CAHERON STATION BLDG 5  
ALEXANDRIA VA 223046145

**GREECE**

Hellenic A  
Air War C  
Scientific A  
Dekelia Air Force Base  
Dekelia, Athens TGA 1010

**ICELAND**

Director of Aviation  
c/o Flugrad  
Reykjavik

**ITALY**

Aeronautica Militare  
Ufficio del Delegato Nazionale all'AGARD  
3 Piazzale Adenauer  
00144 Roma/EUR

**UNITED KINGDOM**

Defence Research Information Centre  
Kentigern House  
65 Brown Street  
Glasgow G2 8EX

**UNITED STATES**

National Aeronautics and Space Administration (NASA)  
Langley Research Center  
M/S 180  
Hampton, Virginia 23665

THE UNITED STATES NATIONAL DISTRIBUTION CENTRE (NASA) DOES NOT HOLD STOCKS OF AGARD PUBLICATIONS. AND APPLICATIONS FOR COPIES SHOULD BE MADE DIRECT TO THE NATIONAL TECHNICAL INFORMATION SERVICE (NTIS) AT THE ADDRESS BELOW.

**SALES AGENCIES**

National Technical  
Information Service (NTIS)  
5285 Port Royal Road  
Springfield, Virginia 22161  
United States

ESA/Information Retrieval Service  
European Space Agency  
10, rue Mario Nikis  
75015 Paris  
France

The British Library  
Document Supply Centre  
Boston Spa, Wetherby  
West Yorkshire LS23 7BQ  
United Kingdom

Requests for microfiche or photocopies of AGARD documents should include the AGARD serial number, title, author or editor, and publication date. Requests to NTIS should include the NASA accession report number. Full bibliographical references and abstracts of AGARD publications are given in the following journals:

Scientific and Technical Aerospace Reports (STAR)  
published by NASA Scientific and Technical  
Information Branch  
NASA Headquarters (NTI-40)  
Washington D.C. 20546  
United States

Government Reports Announcements (GRA)  
published by the National Technical  
Information Services, Springfield  
Virginia 22161  
United States



Printed by Specialised Printing Services Limited  
40 Chigwell Lane, Loughton, Essex IG10 3TZ

- ISBN 92-835-0590-5 -